frontiers | Research Topics

Rising stars in precision medicine imprecise medicine is unethical in the big data era 2021

Edited by
David S. Liebeskind and Fu Wang

Published in
Frontiers in Medicine
Frontiers in Oncology

ISSN 1664-8714
ISBN 978-2-8325-2321-6
DOI 10.3389/978-2-8325-2321-6

About Frontiers

Frontiers is more than just an open access publisher of scholarly articles: it is a pioneering approach to the world of academia, radically improving the way scholarly research is managed. The grand vision of Frontiers is a world where all people have an equal opportunity to seek, share and generate knowledge. Frontiers provides immediate and permanent online open access to all its publications, but this alone is not enough to realize our grand goals.

Frontiers journal series

The Frontiers journal series is a multi-tier and interdisciplinary set of open-access, online journals, promising a paradigm shift from the current review, selection and dissemination processes in academic publishing. All Frontiers journals are driven by researchers for researchers; therefore, they constitute a service to the scholarly community. At the same time, the *Frontiers journal series* operates on a revolutionary invention, the tiered publishing system, initially addressing specific communities of scholars, and gradually climbing up to broader public understanding, thus serving the interests of the lay society, too.

Dedication to quality

Each Frontiers article is a landmark of the highest quality, thanks to genuinely collaborative interactions between authors and review editors, who include some of the world's best academicians. Research must be certified by peers before entering a stream of knowledge that may eventually reach the public - and shape society; therefore, Frontiers only applies the most rigorous and unbiased reviews. Frontiers revolutionizes research publishing by freely delivering the most outstanding research, evaluated with no bias from both the academic and social point of view. By applying the most advanced information technologies, Frontiers is catapulting scholarly publishing into a new generation.

What are Frontiers Research Topics?

Frontiers Research Topics are very popular trademarks of the *Frontiers journals series*: they are collections of at least ten articles, all centered on a particular subject. With their unique mix of varied contributions from Original Research to Review Articles, Frontiers Research Topics unify the most influential researchers, the latest key findings and historical advances in a hot research area.

Find out more on how to host your own Frontiers Research Topic or contribute to one as an author by contacting the Frontiers editorial office: frontiersin.org/about/contact

Rising stars in precision medicine 2021: Imprecise medicine is unethical in the big data era

Topic editors

David S. Liebeskind — University of California, Los Angeles, United States
Fu Wang — Xi'an Jiaotong University, China

Citation

Liebeskind, D. S., Wang, F., eds. (2023). *Rising stars in precision medicine 2021: Imprecise medicine is unethical in the big data era*. Lausanne: Frontiers Media SA. doi: 10.3389/978-2-8325-2321-6

Table of contents

05 Editorial: Rising stars in precision medicine 2021: imprecise medicine is unethical in the big data era
David S. Liebeskind

07 Oridonin Alleviates LPS-Induced Depression by Inhibiting NLRP3 Inflammasome *via* Activation of Autophagy
Chunyan Li, Yuehua Zhu, Yuanyuan Wu, Meiyuan Fu, Yiling Wu, Yuehong Wu, Yinger Qiu, Hui Zhang and Mingxing Ding

23 Molecular Characterization and Clinical Relevance of ALDH2 in Human Cancers
Bo Ma, Zaoqu Liu, Hui Xu, Long Liu, Tao Huang, Lingfang Meng, Libo Wang, Yuyuan Zhang, Lifeng Li and Xinwei Han

33 Investigation on the Pathological Mechanism of Frequent Exacerbators With Chronic Obstructive Pulmonary Disease Based on the Characteristics of Respiratory Flora
Li Ke, Luo Chen, Yuan Yaling, Gao Can, Lin Jun and Zhang Chuan

45 The Potential Bioactive Components of Nine TCM Prescriptions Against COVID-19 in Lung Cancer Were Explored Based on Network Pharmacology and Molecular Docking
Lin Du, Yajie Xiao, Yijun Xu, Feng Chen, Xianghui Chu, Yuqi Cao and Xun Zhang

57 Over-Expression and Prognostic Significance of FN1, Correlating With Immune Infiltrates in Thyroid Cancer
Qi-Shun Geng, Tao Huang, Li-Feng Li, Zhi-Bo Shen, Wen-Hua Xue and Jie Zhao

71 Depiction of Aging-Based Molecular Phenotypes With Diverse Clinical Prognosis and Immunological Features in Gastric Cancer
Fang He, Huan Ding, Yang Zhou, Yuanzhen Wang, Juan Xie, Shaoqi Yang and Yongzhao Zhu

87 Study of Allosteric Transitions of Human P-Glycoprotein by Using the Two-State Anisotropic Network Model
Hongwu Li and Weikang Gong

99 Complementing Tissue Testing With Plasma Mutation Profiling Improves Therapeutic Decision-Making for Patients With Lung Cancer
Yukti Choudhury, Min-Han Tan, Jun Li Shi, Augustine Tee, Kao Chin Ngeow, Jonathan Poh, Ruth Rosalyn Goh and Jamie Mong

110 Roles of Pyroptosis-Related Gene Signature in Prediction of Endometrial Cancer Outcomes
Yili Chen, Yuandong Liao, Qiqiao Du, Chunliang Shang, Shuhang Qin, Kaping Lee, Qiaojian Zou, Junxiu Liu and Shuzhong Yao

123 Factors Influencing Total Delay of Breast Cancer in Northeast of China
Sihang Ren, Yuting Zhang, Pan Qin and Jia Wang

129 The Efficacy and Safety of Transurethral 2 μm Laser Bladder Lesion Mucosal En Bloc Resection in the Treatment of Cystitis Glandularis
Changyuan Zhao, Kexin Wang, Chao Men, Yue Xin and Haibo Xia

136 Identification of an Immune Classification and Prognostic Genes for Lung Adenocarcinoma Based on Immune Cell Signatures
Lili Deng, Fei Long, Ting Wang, Ling Dai, Huajian Chen, Yujun Yang and Guoming Xie

151 Effect of Hydrogen Inhalation Therapy on Hearing Loss of Patients With Nasopharyngeal Carcinoma After Radiotherapy
Xiaofeng Kong, Tianyu Lu, You-Yong Lu, Zhinan Yin and Kecheng Xu

162 Nonoxid-HMGB1 Attenuates Cognitive Impairment After Traumatic Brain Injury in Rats
Jun-Quan Chen, Shuang-Qi Gao, Lun Luo, Zong-Yuan Jiang, Chao-Feng Liang, Hai-Yong He and Ying Guo

174 A Network Pharmacology Study: Reveal the Mechanisms of Palovarotene Against Heterotopic Ossification
Junchao Huang, Dachuan Liu, Jingwei Zhang and Haijun Xiao

188 Deep Sequencing of Serum Exosomal microRNA Level in Psoriasis Vulgaris Patients
Xiu-Min Chen, Dan-Ni Yao, Mao-Jie Wang, Xiao-Dong Wu, Jing-Wen Deng, Hao Deng, Run-Yue Huang and Chuan-Jian Lu

200 Construction and Analysis of a Joint Diagnosis Model of Random Forest and Artificial Neural Network for Obesity
Jian Yu, Xiaoyan Xie, Yun Zhang, Feng Jiang and Chuyan Wu

211 Identification of Epigenetic-Dysregulated lncRNAs Signature in Osteosarcoma by Multi-Omics Data Analysis
Junchao Huang, Jingwei Zhang and Haijun Xiao

frontiers | Frontiers in Medicine

TYPE Editorial
PUBLISHED 18 April 2023
DOI 10.3389/fmed.2023.1181788

EDITED AND REVIEWED BY
Alice Chen,
Consultant, Potomac, MD, United States

*CORRESPONDENCE
David S. Liebeskind
✉ davidliebeskind@yahoo.com

RECEIVED 07 March 2023
ACCEPTED 03 April 2023
PUBLISHED 18 April 2023

CITATION
Liebeskind DS (2023) Editorial: Rising stars in precision medicine 2021: imprecise medicine is unethical in the big data era.
Front. Med. 10:1181788.
doi: 10.3389/fmed.2023.1181788

Editorial: Rising stars in precision medicine 2021: imprecise medicine is unethical in the big data era

David S. Liebeskind[1,2]*

[1]Neurovascular Imaging Research Core, University of California, Los Angeles, Los Angeles, CA, United States, [2]Comprehensive Stroke Center and Department of Neurology, Geffen School of Medicine at the University of California, Los Angeles, Los Angeles, CA, United States

KEYWORDS

precision medicine, data science, innovation, imaging, biomarkers, clinical trials

Editorial on the Research Topic
Rising stars in precision medicine 2021: imprecise medicine is unethical in the big data era

The publication of this open-access Research Topic on innovative approaches to and aspects of precision medicine across a diverse set of clinical conditions underscores the recent evolution and ethical considerations of translational research in medicine. The Research Topic includes 17 distinct articles on data science methods across a diverse range of conditions to discern the impact of baseline patient characteristics, medical decision-making and specific therapeutic interventions on outcomes (Chen J-Q. et al.; Chen X-M. et al.; Chen Y. et al.; Choudhury et al.; Deng et al.; Du et al.; Geng et al.; He et al.; Huang, Liu et al.; Huang, Zhang et al.; Ke et al.; Kong et al.; Li et al.; Li and Gong; Ma et al.; Yu et al.; Zhao et al.). A variety of biomarkers are used, including standard diagnostic tests, imaging, proteomics and genomics to classify and study subsets of disease with novel methodologies. The clinical topics vary from oncology to pulmonary disease, dermatology, and traumatic brain injury. A variety of patient-specific biomarkers are highlighted, including genetic profiles, RNA signatures and routine serum assays that may be used to more precisely classify individual patients and predict their long term outcomes or therapeutic response. The broad range of highly specialized conditions covered on this topic is expansive yet demonstrates the critical roles of open access publication in data sharing, translation of data science methods across disciplines, and real-world data to drive future improvements in patient outcomes.

Precision medicine is not new. Although references to precision medicine have proliferated since the Human Genome Project, focusing extensively on individual-specific genetic characteristics, the conceptual basis has been implemented in medical practice for centuries. Since ancient times, it has been understood that individual patients respond differently to the same treatments due to underlying biological diversity in the pathophysiology or patient-specific features. Genomics, however, did provide a great example of how biomarkers may be employed in translational research. Although monogenic disorders may occur, most disease states likely involve complex and potentially, subtle, genome-wide associations, and interactions with environmental factors during life. The genomics, proteomics and other biomarkers are likely informative of potential therapeutic response to specific interventions at different disease stages or timing.

The imprecise medicine of many traditional clinical research paradigms has skewed the development of novel therapeutics and has often failed to address the overwhelming disparities manifest in patient presentations around the world, as only select patient populations and standard analytic approaches have been applied. Paradoxically, clinical research methodologies have been ensconced in concerns regarding ethical principles, benevolence and doing what is right for each individual patient, yet perpetuating imprecise medicine is inherently, unethical. Informed consent of patients and institutional review of research protocols enhance ethics of specific studies or clinical trials, yet biases regarding healthcare disparities, access to care and access to research remain tremendous challenges. Numerous clinical and translational research vehicles exist, such as phased clinical trials with the ultimate randomized, controlled trial (RCT) as the pinnacle, yet multiple alternative pathways exist; however, they are less valued. RCTs are overly obsessed with data collection, with paradoxical paucity of details on data quality or validity, such as independent adjudication of imaging measures by a core lab or related methodology. Post-marketing surveillance of most therapeutic drugs or devices is largely non-existent in most geographies around the world, including the United States. Registries and vehicles to evaluate quality of healthcare delivery are largely unfunded, unregulated, and devoid of validated data checks or measures to assess generalizability in routine clinical practice across most geographical regions.

Perhaps such gaps in translational research could be excused in prior years, yet the abundance of patient-specific information in the current big data era should prompt a reconsideration of traditional research paradigms. The big data era has not only sparked interest in large, diverse datasets, as it has also heralded the emergence of big data analytics, including artificial intelligence methods that can be readily deployed with current clinical data. In the United States, The Health Insurance Portability and Accountability Act of 1996 (HIPAA) was intended to promote data sharing and interoperability of clinical data systems, rather than to solely ensure individual patient privacy. Unfortunately, HIPAA has been cited to restrict data sharing rather than the original purpose of portability and dissemination of data and related findings. Data sharing at the National Institutes of Health and other platforms is a now a top priority. In routine care, the electronic health record systems, individual hospitals, institutions, provider groups, and academicians limit data sharing due to competition with others and the relative strength in controlling or restricting such data access. The marked expansion of knowledge with artificial intelligence is almost unbelievable with recent advances such as ChatGPT and likely future development of related medical applications, yet access to data is a starting point. Medical or clinical data has already been simplified and codified by common data elements or variables that exist in most medical specialties, laboratory assays and medical imaging modalities. Simultaneously, data scientists know of such potential yet lack the clinical expertise to apply such analytical techniques to specialized clinical topics. Unsupervised machine learning or artificial intelligence will likely always depend on periodic retraining by expert annotations or clinical guidance, yet patterns may rapidly emerge from machine learning that human efforts would take generations to realize. Unlike recent concerns over false ground truths inadvertently used to train machine learning, most medical data relate to timed, quantitative measures of biological significance such as physiological measures (e.g., vital signs), laboratory values, imaging, and increasing use of functional outcome measures that are widely available.

These changes sparked by the big data era and continued practice of imprecise medicine pose an ethical conundrum regarding current clinical research methodology and the responsibility of various parties. Academicians often initiate, design and perpetuate clinical research constructs such as trial design, the nature of clinical trials, statistical measures employed, and many entrenched traditional approaches, yet there is no concrete imperative to innovate such methodology. Industry partners are often seen as biased in trying to accelerate innovation of products, yet they need clinical research data not just leading up to RCTs, but afterwards in routine clinical practice. Regulatory bodies revert to predicate methods without clear imperative to facilitate advances, with a much larger concern for patent safety, far before efficacy. Yet once approved, most therapies go largely unmonitored in the general population. Fortunately, regulatory bodies are now implementing diversity requirements in prospective clinical trials. Routine healthcare providers remain relatively passive, as they can only use established methods or approved products. The most responsible and ethical approach for all would start with dissemination of data to collaboratively mine and discern potentially subtle yet pivotal insights on how precision medicine of individual patient response to a specific therapy is practiced on a daily basis around the world.

Open access publications, as in this Research Topic, and collaborative data sharing are critical in the big data era and further advances in precision medicine. This selective example of research articles provides an example to demonstrate such progress toward a broader swath of specific medical disciplines or specialties to be covered in future years. There is undoubtedly an indirect yield or benefit of disruptive innovation that may emerge from applying such novel methodologies or even medical therapies such as drugs or devices to other medical conditions. Open access is a critical barrier to overcome disparities in low income countries, to encourage collaboration and to promote data sharing as the initial steps in our transformation from imprecise medicine to precision medicine of the 21st century.

Author contributions

DL conceived the design and content of this editorial manuscript, drafted, revised, and approved the submitted version.

Conflict of interest

The author declares that the research was conducted in the absence of any commercial or financial relationships that could be construed as a potential conflict of interest.

Publisher's note

frontiers in Medicine

ORIGINAL RESEARCH
published: 12 January 2022
doi: 10.3389/fmed.2021.813047

Oridonin Alleviates LPS-Induced Depression by Inhibiting NLRP3 Inflammasome *via* Activation of Autophagy

Chunyan Li[1], Yuehua Zhu[2], Yuanyuan Wu[1], Meiyuan Fu[3], Yiling Wu[3], Yuehong Wu[4], Yinger Qiu[5], Hui Zhang[5] and Mingxing Ding[3]*

[1] Nursing Faculty, School of Medicine, Jinhua Polytechnic, Jinhua, China, [2] Department of Psychiatry, Affiliated Jinhua Hospital, Zhejiang University School of Medicine, Jinhua, China, [3] Medical Molecular Biology Laboratory, School of Medicine, Jinhua Polytechnic, Jinhua, China, [4] Department of Psychiatry, The Second Hospital of Jinhua, Jinhua, China, [5] Jinhua Center of Laboratory Animals, Jinhua Municipal Food and Drug Inspection Institute, Jinhua, China

Objective: Oridonin (Ori) is a diterpene compound that has multiple biological properties. Here, our study was conducted to observe the therapeutic effect of Ori on depression as well as to uncover the mechanism.

Methods: Lipopolysaccharide (LPS)-induced depression models were established both in C57BL/6 mice and primary astrocytes, which were treated with Ori, autophagy agonist Rapamycin (Rap) and autophagy inhibitor 3-Methyladenine (3-MA). The depressive-like behaviors were assessed with behavioral tests. Autophagy was evaluated in the hippocampus and astrocytes by investigating autophagosomes under transmission electron microscope (TEM) and detecting LC3II/I, Beclin1 and P62 through western blotting. Astrocyte marker glial fibrillary acidic protein (GFAP) was investigated by immunofluorescence. NLRP3 inflammasome activation was evaluated by detecting IL-1β, NLRP3, ASC and Caspase-1 expression and reactive oxygen species (ROS) accumulation was quantified *via* DCFH-DA probe. Autolysosomes, autophagosomes and mitophagy were separately observed through mTag-Wasabi-LC3 plasmid, MitoTracker Deep Red staining, and TEM.

Results: Our results showed that Ori administration alleviated LPS-induced depressive-like behaviors and increased GFAP expression in the hippocampus. Furthermore, Ori treatment promoted autophagy activation and cell viability as well as weakened NLRP3 inflammasome activation and ROS accumulation both in LPS-induced mice and astrocytes. Ori promoted the autophagic flux unblocked through enhancing fusion of autophagosomes with lysosomes as well as enhanced mitophagy in LPS-treated astrocytes. The therapeutic effect of Ori was enhanced by Rap and weakened by 3-MA.

Conclusion: Collectively, our findings provided a promising antidepressant drug and uncovered that Ori alleviated LPS-induced depression by inhibiting NLRP3 inflammasome through activation of autophagy.

Keywords: Oridonin, depression, autophagy, NLRP3 inflammasome, LPS

OPEN ACCESS

Edited by:
Fu Wang,
Xi'an Jiaotong University, China

Reviewed by:
Lijie Chen,
Sheng Jing Hospital of China Medical University, China
Tahir Ali,
Peking University, China

****Correspondence:***
Mingxing Ding
mtd5tc@163.com

Specialty section:
This article was submitted to Precision Medicine, a section of the journal Frontiers in Medicine

Received: *11 November 2021*
Accepted: *14 December 2021*
Published: *12 January 2022*

Citation:
Li C, Zhu Y, Wu Y, Fu M, Wu Y, Wu Y, Qiu Y, Zhang H and Ding M (2022) Oridonin Alleviates LPS-Induced Depression by Inhibiting NLRP3 Inflammasome via Activation of Autophagy. Front. Med. 8:813047. doi: 10.3389/fmed.2021.813047

INTRODUCTION

Depression represents a severe psychiatric disease, with a cluster of symptoms such as anhedonia, depressed mood, pessimism, and cognitive impairment (1). More than 350 million people suffer from depression worldwide (2). Depression, as one of the main mental diseases that cause mental and behavioral disorders, is an important factor leading to the global burden of disease (3). It is expected that depression will rise to the top factor resulting in the global burden of diseases by 2030 (4). Although the research on antidepressants, psychotherapy for depression and physical and mental treatment has made significant progress in recent years, there is still no completely satisfactory treatment strategy against depression (5).

It has been found that inflammatory response is implicated in the pathophysiology of depression (1). Increasing evidence suggests that various inflammatory factors are involved in the pathogenesis of depression (6). Among them, interleukin-1β (IL-1β) is closely related to abnormal mood and behaviors caused by stress (7). The cleavage and maturation of IL-1β precursor requires IL-1β converting enzyme, and IL-1β converting enzyme is an important component of the inflammasome (8). The inflammasome mainly modulates the function of the innate immune system as well as the mechanism of a series of inflammatory diseases (9). NLRP3 inflammasome is composed of NOD-like receptors, adaptor protein ASC and effector protein Caspase-1 (i.e., IL-1β converting enzyme), which can promote IL-1β, IL-18 and IL-33 shearing and maturation (10). NLRP3 inflammasome can be activated by a variety of exogenous or endogenous stress factors such as infection, reactive oxygen species (ROS), injury, and metabolites (11). NLRP3 inflammasome mediates the pathogenesis of depression *via* neuroinflammation (12), but it is not clear whether and how NLRP3 inflammasome is involved in the molecular mechanism of depression. Autophagy is an evolutionary conserved intracellular pathway, ensuring energy, organelle, and protein homeostasis by lysosomal degradation of damaged macromolecules or organelles (13). Emerging evidence suggests that autophagy is closely linked to stress-related diseases including depression (14). Studies have found that autophagy negatively modulates inflammasome activation; the occurrence of autophagy depends on specific inflammasome recognizers; inflammasomes are degraded through selective autophagy receptors; autophagy plays an important role in the secretion of the pro-inflammatory factor IL-1β (15–17). The basal level of autophagy regulates the activation of inflammasomes (18). If autophagy is inhibited, it leads to the accumulation of depolarized mitochondria, and then the leaked substances become endogenous inflammasome activators, such as mitochondrial DNA and ROS (19). Therefore, enhancing the level of autophagy can weaken inflammasome activation in depression.

Oridonin (Ori) is the main active ingredient of Rabdosia rubescens, which is widely used in Chinese medicine (20, 21). Ori has obvious anti-cancer activities such as inducing cell cycle arrest and apoptosis, inhibiting angiogenesis, etc. (22–24). But due to its relatively mild and imprecise mechanism of action, it greatly hinders the clinical application of Ori in cancer treatment. Ori can inhibit the activation of immune-related pathways, and inhibit the release of pro-inflammatory cytokines such as TNF-α and IL-6, which exhibits anti-inflammatory and protective effects in colitis, sepsis and neuroinflammation, etc. (25–27). Recent research has reported that Ori has the effect of suppressing depressive behaviors (28), but the detailed mechanisms are still unclear. Herein, we hypothesized that Ori may inhibit NLRP3 inflammasome activation by promoting autophagy, thereby having the function of alleviating depression.

MATERIALS AND METHODS

Animals and Drug Administration

Healthy 8-week-old C57BL/6 mice with 18–22 g were provided from the Jinhua Center of Laboratory Animals (Zhejiang, China). All mice were raised at 18–22°C with 12 h light/12 h dark cycle, with free access to diet and water. All the experimental procedures were performed in line with the protocols approved by the Institutional Animal Care and Use Committee of School of Medicine, Jinhua Polytechnic (2019019). After 1 week of adaptive feeding, all mice were randomly separated into five groups ($n = 6$ each group): control group; lipopolysaccharide (LPS) group; LPS + Ori group; LPS + Ori + autophagy agonist Rapamycin (Rap) group; LPS + Ori + autophagy inhibitor 3-Methyladenine (3-MA) group. Ori (Sigma, USA) was dissolved in dimethyl sulfoxide (DMSO) and then diluted in 0.9% saline to a final concentration of 0.1% DMSO. Mice were given 20 mg/kg Ori by gavage (29) or were injected intraperitoneally by 3 mg/kg Rap or 10 mg/kg 3-MA daily for 7 consecutive days (30). Thirty min after the drug administration on the 7th day, mice were injected intraperitoneally with 1.2 mg/kg/day LPS or an equal amount of normal saline (31, 32). After 24 h of the LPS administration, all mice were subjected to behavioral tests before being perfused with glutaraldehyde and PFA, and were anesthetized by inhaling 4% halothane and subsequently sacrificed by cervical dislocation until the heartbeat and breathing stopped completely and the reflex disappeared. At last, brain tissues were collected and were stored at −80°C until before use.

Sucrose Preference Test

As previously described (33), after 12 h of water deprivation, the mice were given pre-quantified 1% sucrose water and tap water at the same time. The position of the two tubes was changed after 6 h to prevent mice from having a position preference. After the mice drank freely for 12 h, the sucrose water pipe and the tap water pipe were collected and weighed. The sucrose preference rate (%) was determined according to the formula: sucrose preference rate (%) = sucrose water drinking amount (g)/(sucrose water drinking amount (g) + tap water drinking amount (g)) × 100%.

Abbreviations: IL-1β, interleukin-1β; ROS, reactive oxygen species; Ori, Oridonin; LPS, lipopolysaccharide; Rap, Rapamycin; 3-MA, 3-Methyladenine; FST, forced swimming test; TST, tail suspension test; TEM, transmission electron microscope; IF, immunofluorescence; GFAP, glial fibrillary acidic protein; RT-qPCR, real-time quantitative polymerase-chain reaction; IHC, immunohistochemistry; CCK-8, Counting kit-8.

Forced Swimming Test (FST)

As previously described (34), the mice were placed in glass beakers (height 24 cm, and diameter 13 cm) with a water depth of 14 cm and the water temperature was 22 ± 1°C. A video camera was used to record the behavior of the mice within 6 min. ForcedSwimScan^{TM} software (Clever Sys Inc., VA, USA) was used for analysis, and the immobility time of mice in the last 4 min was counted.

Tail Suspension Test (TST)

As previously described (35), medical tape was utilized to fix the tail of mice on the top of the experiment box. A video camera was used to record the behavior of mice within 6 min. Tail Suspension Scan^{TM} software (Clever Sys Inc., VA, USA) was used for analysis. The time that mice's limbs and trunk were completely immobile in the last 4 min was counted.

Transmission Electron Microscope (TEM)

After anesthesia with intravenous injection of pentobarbital sodium (5 mg/ 100 g), the mice were perfused by 2.5% glutaraldehyde as well as fixed *via* 4% paraformaldehyde. Then, secondary euthanasia was performed by cervical dislocation. Primary astrocytes were precipitated and fixed in 1% glutaraldehyde. About 1 mm^3 hippocampus tissues or primary astrocytes were sectioned and incubated for 2 h at 4°C. After being postfixed by 1% osmium tetroxide, sections were treated with aqueous uranyl acetate. Afterwards, sections were dehydrated, embedded in epoxy resin as well as treated with lead citrate. Images were observed under a TEM (HT7700; Hitachi, Japan).

Western Blotting

Brain tissues and primary astrocytes were lysed *via* RIPA on the ice lasting 30 min. The specimens were centrifuged at 12,000 g lasting 10 min at 4°C. The supernatant was gathered as well as protein concentrations were quantified utilizing BCA protein assay kits (P0009; Beyotime, Shanghai, China). Protein was separated *via* 12% SDS-PAGE, followed by being transferred onto a PVDF membrane. The membrane was sealed through 5% milk/TBST at room temperature for 1 h as well as incubated by primary antibody at 4°C overnight. Afterwards, the membrane was incubated by HRP-labeled goat anti-rabbit secondary antibodies (1/5000; SA00001-2; Proteintech, Wuhan, China) or HRP-labeled goat anti-mouse secondary antibodies (1/5000; SA00001-1; Proteintech, Wuhan, China) at room temperature lasting 1 h, and developed through ChemiDoc MP imaging system (Bio-Rad, USA). Primary antibodies included LC3 (1/2000; 14600-1-AP; Proteintech, Wuhan, China), Beclin1 (1/1000; 11306-1-AP; Proteintech, Wuhan, China), p62 (1/2000; 18420-1-AP; Proteintech, Wuhan, China), IL-1β (1/1000; 16806-1-AP; Proteintech, Wuhan, China), NLRP3 (1/1000; DF7438; Affinity, USA), ASC (1/2000; 10500-1-AP; Proteintech, Wuhan, China), Caspase-1 (1/1000; 22915-1-AP; Proteintech, Wuhan, China) and GAPDH (1/5000; ATPA00013Rb; AtaGenix, Wuhan, China). The results were quantified with ImageJ software (version 1.48; National Institutes of Health).

Immunofluorescence (IF)

Hippocampus sections were permeated by 0.5%Triton X-100 at room temperature for 20 min and blocked by normal goat serum (C0265; Beyotime, Shanghai, China) at room temperature for 30 min. The sections were incubated by glial fibrillary acidic protein (GFAP) antibody (1/100; 16825-1-AP; Proteintech, Wuhan, China) at 4°C overnight and incubated by Alexa Fluor 488-conjugated AffiniPure Goat Anti-Rabbit IgG (H + L) (srbAF488-1; Proteintech, Wuhan, China) for 1 h. Images were captured under a BX53 fluorescence microscope (Olympus, Japan). The results were quantified with ImageJ software (version 1.48; National Institutes of Health).

Real-Time Quantitative Polymerase-Chain Reaction (RT-qPCR)

RNA was extracted from brain tissues or primary astrocytes *via* Trizol (10606ES60; YEASEN, Shanghai, China) and reverse transcribed to cDNA in line with the following procedures: at 25°C lasting 5 min; at 42°C lasting 30 min and at 85°C lasting 5 min. Primer sequences included: GAPDH: 5′-TGTTT CCTCGTCCCGTAGA-3′ (forward) and 5′-GATGGCAACA ATCTCCACTTTG-3′ (reverse), 116 bp; IL-1β: 5′-GTTCC CATTAGACAACTGC-3′ (forward) and 5′-GATTCTTTCC TTTGAGGC-3′ (reverse), 199 bp; NLRP3: 5′-CTCGCATTGG TTCTGAGCTC-3′ (forward) and 5′-AGTAAGGCCGGAATT CACCA-3′ (reverse), 153 bp; ASC: 5′-CAATGACTGTGCTTA GAGACATG-3′ (forward) and 5′-ACTTCTGTGACCCTG GCAATG-3′ (reverse), 175 bp; Caspase-1: 5′-CTGACTGGGA CCCTCAAGTT-3′ (forward) and 5′-TCAACTTGAGCTCCA ACCCT-3′ (reverse), 170 bp. RT-qPCR was presented through ABI 12K RT-qPCR instrument (ABI QuantStudio^{TM} 12K Flex; ABI, USA). Relative mRNA expression was determined with $2^{-\Delta\Delta Ct}$ method.

Immunohistochemistry (IHC)

Brain tissue specimen was fixed *via* 4% paraformaldehyde and embedded in paraffin. The section was cut into 4 µm. After xylene deparaffinization, hydration and antigen retrieval, the section was sealed through normal goat serum (C0265; Beyotime, Shanghai, China) lasting 20 min at room temperature. Then, the section was treated by primary antibodies against NLRP3 (1/100; NBP2-12446; Novus, USA) and IL-1β (1/50; Abs126104; absin, Beijing, China) at 37°C for 90 min and incubated by secondary antibody (1/100; SA00001-2/SA00001-1; Proteintech, Wuhan, China) lasting 30 min at room temperature. The color developing was presented *via* DAB reagent for 5 min. The nucleus was counterstained through hematoxylin (B600020; Proteintech, Wuhan, China) lasting 3 min as well as the section was washed by running water. After dehydration, the section was transparent and sealed with neutral gum. Images were acquired through an IX71 microscope (Olympus, Japan). The results were quantified with ImageJ software (version 1.48; National Institutes of Health).

Primary Cell Culture and Treatment

Primary astrocytes were purchased from Procell company (CP-M157; Wuhan, China; https://www.procell.com.cn/), which were maintained in DMEM (SH30243.01B; Hyclone, USA) containing 10% fetal bovine serum (SH30084.03; Hyclone, USA), 100 U/mL penicillin, and 100 U/mL streptomycin in an environment of 37°C and 5% CO_2. Astrocytes were treated with 0.1, 1.0 and 10 μM Ori. Astrocytes were induced by 2 μg/ml LPS to construct a depression *in vitro* model. Autophagy was activated by 25 ng/mL Rap and inhibited by 5 mM 3-MA.

Cell Viability Assay

Counting kit-8 (CCK-8) detection kit (CK04; Dojindo, Shanghai, China) was utilized for detecting the cell viability. Primary astrocytes were seeded onto a 96-well plate (10^4 cells/well). Each group was set to three repetitions. After incubation overnight, 20 μl of CCK-8 was added to each well and cells were incubated lasting 4 h. The absorbance values at 450 nm were examined with a microplate reader.

Detection of ROS

ROS detection kit (CA1410; Solarbio, Beijing, China) was employed for examining ROS in primary astrocytes. DCFH-DA was diluted with serum-free culture medium according to 1:1000 to make the final concentration 10 μmol/L. After 48 h of drug treatment, astrocytes were incubated with 300 μl DCFH-DA at 37°C for 30 min. Then, astrocytes were washed with PBS to eliminate DCFH-DA which did not enter the astrocytes. In the culture plate, the slides with the climbed cells were immersed in PBS. Primary astrocytes were permeabilized through 0.5% Triton X-100 (T8787; Sigma, USA) at room temperature lasting 20 min as well as the slides were immersed in PBS. After absorbing the PBS with absorbent paper, normal goat serum (C0265; Beyotime, Shanghai, China) was added dropwise on the glass slide, and blocked for 30 min at room temperature. DAPI was added dropwise and incubated for 5 min in the dark to stain the nucleus, and the excess DAPI (D9542; Sigma, USA) was washed away with PBST. Following absorbing the liquid on the slide, the slides were mounted with a mounting solution containing anti-fluorescence quencher, and then observed and collected the images under a BX53 fluorescence microscope (Olympus, Japan).

Transfection

Primary astrocytes were inoculated on the glass coverslip in a 24-well plate (1×10^6 cells / well). 0.5 μg mTag-Wasabi-LC3 plasmids (800 ng/well) were transfected into astrocytes *via* Lipofectamine 2000 (Invitrogen, USA). The mTag-Wasabi-LC3 plasmid contained a red fluorescent protein mTagRFP, a green fluorescent protein mWasabi and an amino terminal of autophagy-labeled protein LC3 that was used for monitoring autophagic flux. In green/red merged images, yellow puncta indicated autophagosomes, and red puncta indicated autolysosomes. Following transfection for 6 h, LC3 fluorescent spot was acquired under a BX53 fluorescence microscope (Olympus, Japan). The vesicle of autolysosome was counted through Image-Pro Plus 6.0 software [National Institutes of Health (NIH)]. In total, 30 fields were randomly chosen for each sample.

Measurement of Mitochondrial Activity

Primary astrocytes were seeded to poly-l-lysine-handled glass coverslips, followed by GFP-LC3 transfection. Mitochondria of astrocytes was stained by 100 nM MitoTracker Deep Red staining solution in the dark for 15 min. Images were captured by a BX53 fluorescence microscope (Olympus, Japan). Mitochondrial fluorescence intensity was quantified by ImageJ software (version 1.48; National Institutes of Health).

Statistical Analysis

Statistical analysis was implemented with GraphPad Prism software (version 8.0.1). Each experiment was independently repeated three times. Data are displayed as mean ± standard deviation. Comparisons between two groups were analyzed with unpaired student's t test. Meanwhile comparisons between three or more groups were performed using one-way analysis of variance (ANOVA) followed by Turkey's *post-hoc* test. $P < 0.05$ indicated statistical significance.

RESULTS

Ori Alleviates LPS-Induced Depressive-Like Behaviors

To determine whether Ori may prevent the development of LPS-induced depressive-like behaviors, this study preliminarily administrated mice with 20 mg/kg/day Ori and on the 7th day, 30 min after administration, the mice were injected intraperitoneally by 1.2 mg/kg LPS. Following 24 h of LPS injection, we evaluated depressive-like behaviors. The results showed that LPS significantly decreased sucrose preference (**Figure 1A**) as well as increased FST immobility (**Figure 1B**) and TST immobility (**Figure 1C**). On the contrary, Ori administration markedly elevated sucrose preference (**Figure 1A**) as well as reduced FST immobility (**Figure 1B**) and TST immobility (**Figure 1C**), indicative of the anti-depression roles of Ori. Under co-administration by autophagy inhibitor 3-MA, the therapeutic effects of Ori on sucrose preference and FST immobility were significantly weakened in LPS-induced mice. However, autophagy agonist Rap did not affect the roles of Ori on anti-depression.

Ori Administration Enhances Autophagy Activation in the Hippocampus of LPS-Induced Depression Mouse Models

Autophagosomes with a vacuum-like bilayer structure enveloping the cell contents were investigated with TEM, which were pointed out by red arrows, as shown in **Figure 1D**. Compared with controls, the size and number of autophagosomes was increased in the hippocampus of LPS-induced depression mice. Both Ori and autophagy agonist Rap significantly enhanced the formation of autophagosomes and the converse results were found when treated by autophagy inhibitor 3-MA. Autophagy primarily involves three processes: formation of autophagosomes, transportation to the lysosomes as well as lysosomal degradation (36). We observed that LC3II/I and Beclin1 expression was significantly increased and P62

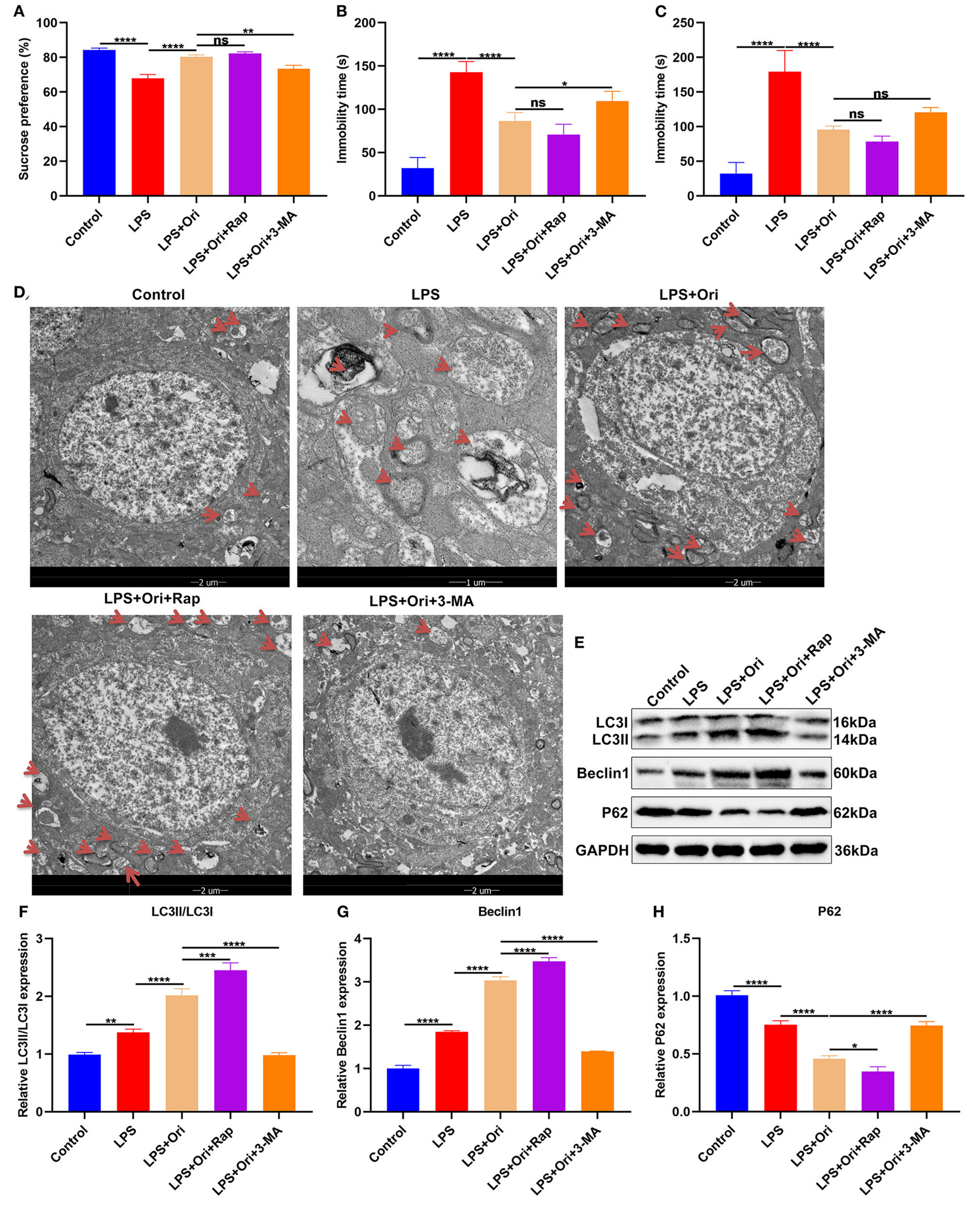

FIGURE 1 | Effects of Ori, autophagy agonist Rap and inhibitor 3-MA on depressive-like behaviors in LPS-induced depression mouse models. **(A–C)** Sucrose preference, immobility time of FST and TST in each group. **(D)** TEM showing the size and number of autophagosomes in the hippocampus in each group. Red arrows, autophagosomes. Magnification, 5000× (1 μm) and 1700× (2 μm). **(E–H)** Western blotting for detecting LC3II/I, Beclin1 as well as P62 levels in the hippocampus of each group. $N = 6$ each group. P values were calculated with ANOVA with Turkey's *post-hoc* test. Ns, not significant; $^{*}p < 0.05$; $^{**}p < 0.01$; $^{***}p < 0.001$; $^{****}p < 0.0001$.

expression was markedly reduced in the hippocampus of LPS-induced depression mice (**Figures 1E–H**). Evidence suggests that enhancing the level of autophagy can treat LPS-induced depression (19). Herein, both Ori and autophagy agonist Rap distinctly enhanced LC3II/I and Beclin1 expression as well as significantly attenuated P62 expression, on the contrary when treated with autophagy inhibitor 3-MA. These data indicated that Ori administration enhanced autophagy activation in the hippocampus of LPS-induced depression mice.

Ori Administration Protects Against LPS-Induced Astrocyte Damage *via* Autophagy Activation

To detect the involvement of astrocytes in LPS-mediated neuroinflammation, the expression of astrocyte activation marker GFAP was evaluated by IF staining. We observed that GFAP expression in the hippocampus was markedly reduced by LPS treatment, indicating that astrocytes were damaged (**Figures 2A,B**). Intriguingly, Ori administration prominently reduced the inhibitory effects of LPS on astrocytes. Hence, above findings supported that Ori administration protected against LPS-induced astrocyte damage. Furthermore, autophagy agonist Rap enhanced the protective effects of Ori on astrocytes and opposite results were observed when co-treatment with autophagy inhibitor 3-MA. This indicated that autophagy activation could be an indispensable factor for Ori-mediated astrocyte protection.

Ori Administration Reduces NLRP3 Inflammasome Activation *via* Autophagy Activation in LPS-Induced Depression Mouse Models

We observed that the expression of NLRP3 inflammasome members IL-1β, NLRP3, ASC and Caspase-1 mRNAs was significantly up-regulated in the hippocampus of LPS-induced mice, indicative of the activation of NLRP3 inflammasome (**Figures 3A–D**). But Ori administration prominently reduced their mRNA expression in LPS-induced mice. Either autophagy agonist Rap or autophagy inhibitor 3-MA did not affect the inhibitory effects of Ori on the mRNA expression of IL-1β, NLRP3 and Caspase-1. Nevertheless, autophagy activation significantly enhanced the inhibitory effects of Ori on ASC expression and opposite results were investigated when autophagy was inhibited. As depicted in western blotting results, LPS treatment prominently induced the increase in IL-1β, NLRP3, ASC, pro-Caspase-1 and cleaved-Caspase-1 expression in the hippocampus (**Figures 3E–J**). Nevertheless, Ori administration markedly attenuated LPS-induced increase in IL-1β, NLRP3, ASC, pro-Caspase-1 and cleaved-Caspase-1 expression. Autophagy agonist Rap significantly strengthened the inhibitory effects of Ori administration on IL-1β, NLRP3, ASC and cleaved-Caspase-1 expression but did not affect pro-Caspase-1 expression in LPS-induced mice. Meanwhile, autophagy inhibitor 3-MA markedly attenuated the inhibitory effects of Ori on IL-1β, NLRP3, ASC, pro-Caspase-1 and cleaved-Caspase-1 expression. IHC staining was also presented for examining IL-1β and NLRP3 expression in the hippocampus. The results showed that LPS treatment markedly elevated IL-1β and NLRP3 expression in the hippocampus, which was prominently weakened by Ori administration (**Figures 3K–M**). The inhibitory effects of Ori on IL-1β and NLRP3 proteins were enhanced by autophagy agonist Rap, whereas were attenuated by autophagy inhibitor 3-MA. Hence, Ori administration significantly decreased NLRP3 inflammasome activation *via* autophagy activation in the hippocampus of LPS-induced depression mouse models.

Ori Treatment Promotes Autophagy Activation of Astrocytes

The effects of Ori treatment on autophagy were observed in primary astrocytes. Astrocytes were treated with 0, 0.1, 1 and 10 μM of Ori for 2, 6, 12 and 24 h. After treatment for 2 h, 0.1 μM Ori not 1 and 10 μM Ori significantly reduced the expression of LC3II/I in astrocytes, while 1 and 10 μM Ori not 0.1 μM Ori significantly decreased P62 expression (**Figures 4A–C**). Following treatment for 6 h, as the concentration of Ori increased, LC3II/I levels were gradually elevated and P62 levels were markedly reduced in astrocytes (**Figures 4D–F**). At 12 h of treatment, we found that LC3II/I expression exhibited significant increase gradually with an increase in concentration of Ori (**Figures 4G,H**). Meanwhile, Ori treatment significantly weakened the expression of P62, while P62 expression displayed the lowest expression under treatment with 1 μM Ori (**Figures 4G,I**). After treatment for 24 h, we observed that LC3II/I expression was gradually elevated with an increase in concentration of Ori (**Figures 4J,K**). Meanwhile, 1 and 10 μM Ori not 0.1 μM Ori markedly reduced P62 expression (**Figures 4J,L**). Taken together, our findings supported the stimulating effects of Ori treatment on autophagy activation in astrocytes. One μM Ori was selected as the optimal concentration and 6 h of treatment was selected as the optimal time.

Ori Treatment Inhibits NLRP3 Inflammasome Activation and ROS Accumulation in Astrocytes

For confirming the protective roles of Ori on astrocytes, this study assessed cell viability through CCK-8 assay. We observed that 1 μM Ori distinctly promoted the viability of astrocytes (**Figure 5A**), indicative of the protective roles of Ori on astrocytes. The effects of Ori treatment on NLRP3 inflammasome activation were then investigated. The RT-qPCR results showed that 1 μM Ori markedly reduced the mRNA expression of IL-1β, NLRP3, ASC as well as Caspase-1 in astrocytes (**Figures 5B–E**). Meanwhile, we also investigated the decrease in IL-1β, NLRP3, ASC, pro-Caspase-1 as well as cleaved-Caspase-1 expression after treatment with 1 μM Ori (**Figures 5F–K**). These data were indicative of the inhibitory effects of 1 μM Ori on NLRP3 inflammasome activation in astrocytes. ROS may trigger NLRP3 inflammasome activation. Hence, we detected ROS accumulation by H2DCF-DA fluorescent probe in astrocytes. As expected, ROS expression was markedly weakened by 1 μM Ori treatment, suggesting that Ori could prevent ROS accumulation in astrocytes (**Figures 5L,M**).

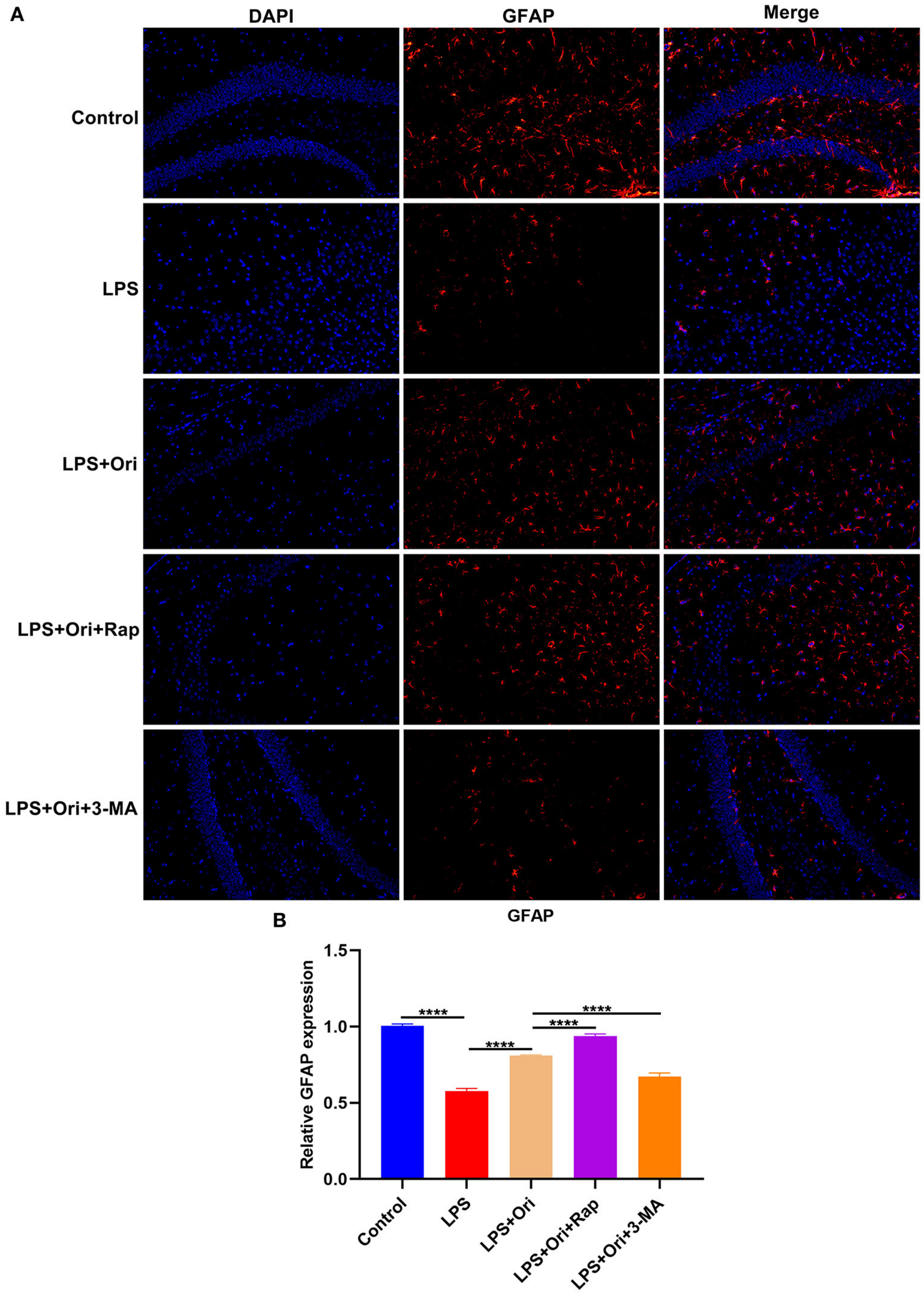

FIGURE 2 | Effects of Ori, autophagy agonist Rap and inhibitor 3-MA on astrocyte activation in the hippocampus of LPS-induced depression mouse models. **(A)** Representative IF staining of GFAP in the hippocampus in each group. Magnification, 200× (50 μm). **(B)** Quantification of GFAP expression according to the IF staining results. $N = 6$ each group. P values were calculated with ANOVA followed by Turkey's *post-hoc* test. $^{****}P < 0.0001$.

Ori Treatment Promotes Autophagy Activation in Astrocytes

Here, mTag-Wasabi-LC3 dual fluorescence staining was utilized for detection of the autolysosome and autophagosome accumulation. This study determined the effects of 1 μM Ori on autolysosomes and autophagosomes in astrocytes. In green/red merged images, yellow puncta indicated autophagosomes, while red puncta indicated autolysosomes. We found that 1 μM Ori

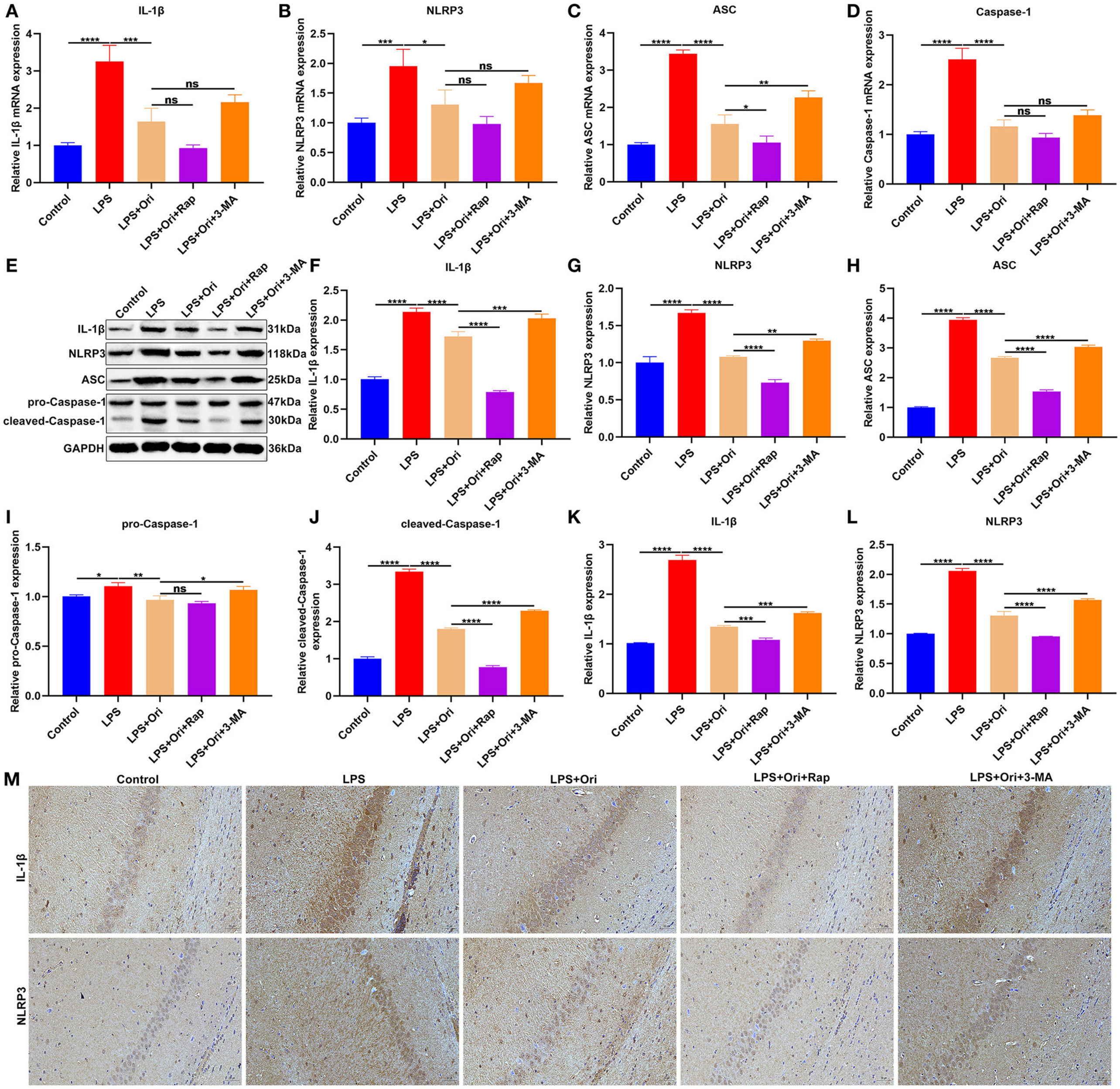

FIGURE 3 | Effects of Ori, autophagy agonist Rap and autophagy inhibitor 3-MA on NLRP3 inflammasome in LPS-induced depression mouse models. **(A–D)** RT-qPCR for examining the relative mRNA levels of IL-1β, NLRP3, ASC as well as Caspase-1 in the hippocampus in each group. **(E)** Representative blots showing IL-1β, NLRP3, ASC, pro-Caspase-1, and cleaved-Caspase-1 in the hippocampus. **(F–J)** Quantitative analysis of IL-1β, NLRP3, ASC, pro-Caspase-1, and cleaved-Caspase-1 expression according to the western blotting results. **(K–M)** IHC showing the expression IL-1β and NLRP3 in the hippocampus. Magnification, 200× (50 μm). *N* = 6 each group. *P* values were calculated with ANOVA followed by Turkey's *post-hoc* test. Ns, not significant; **p* < 0.05; ***p* < 0.01; ****p* < 0.001; *****p* < 0.0001.

distinctly induced autolysosome and autophagosome formation in astrocytes (**Figures 6A,B**). This showed that the acid-labile protein GFP-LC3 expressed by the fluorescent plasmid was degraded in the acidic environment inside the lysosome, indicating that the binding of autophagosomes and lysosomes was not hindered, and the autophagy flux remained unblocked after Ori was given. The effects of Ori on mitophagy were further observed. GFP-LC3 plasmid was transfected into astrocytes and MitoTracker Deep Red dye was used to label the mitochondria after 1 μM Ori treatment for 24 h. Each green fluorescent spot represented an autophagosome, and the red spot represented mitochondria in the cytoplasm. After 1 μM Ori treatment,

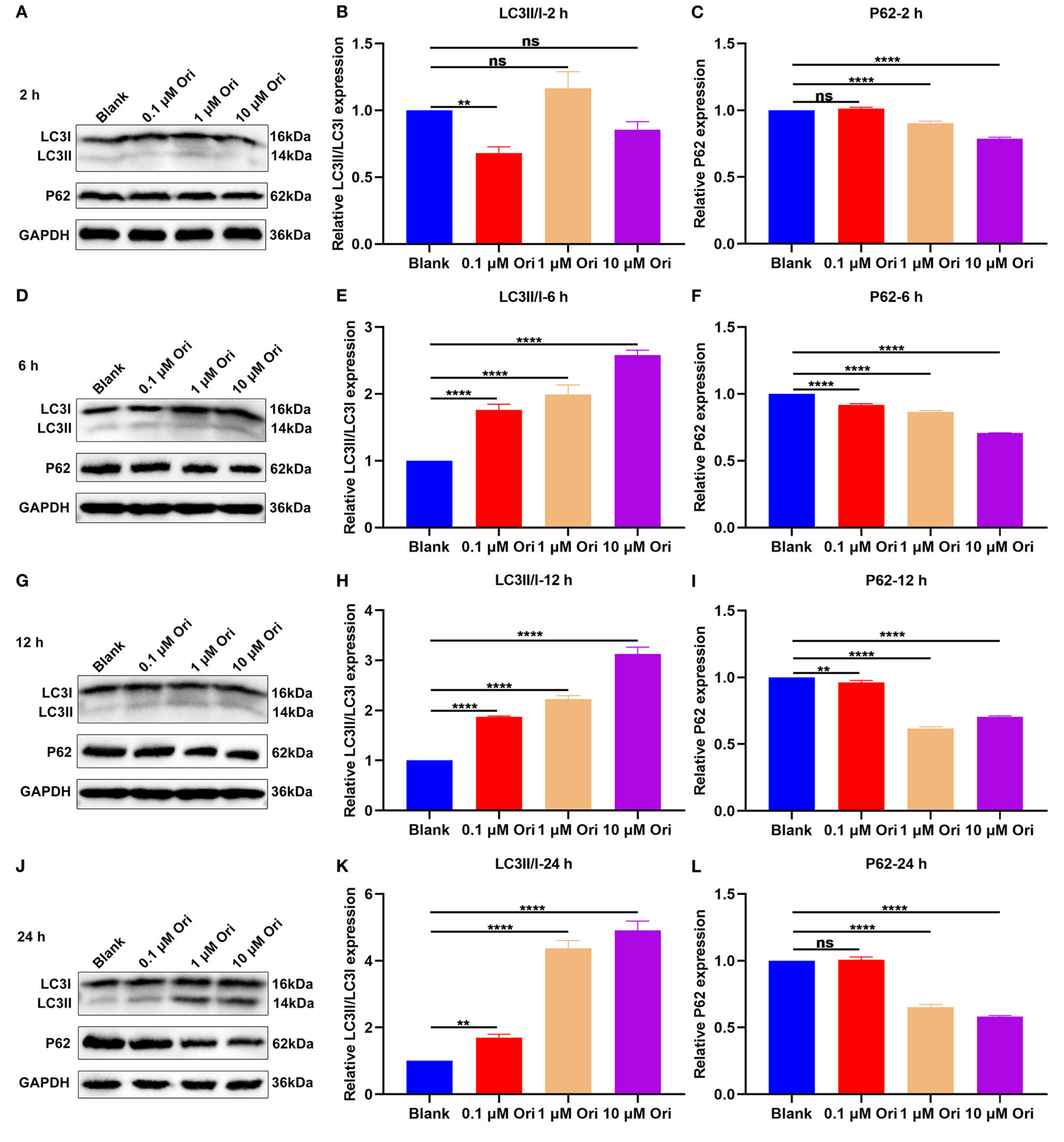

FIGURE 4 | Effect of Ori treatment on autophagy activation in astrocytes. **(A–C)** Western blotting showing the expression of LC3II/I and P62 in astrocytes treated with 0, 0.1, 1 and 10 μM of Ori for 2 h. **(D–F)** Western blotting detecting the expression of LC3II/I and P62 in astrocytes treated with 0, 0.1, 1 and 10 μM of Ori for 6 h. **(G–I)** Western blotting quantifying the expression of LC3II/I and P62 in astrocytes treated with 0, 0.1, 1 and 10 μM of Ori for 12 h. **(J–L)** Western blotting quantifying the expression of LC3II/I and P62 in astrocytes treated with 0, 0.1, 1 and 10 μM of Ori for 24 h. *N* = 3 each group. *P* values were calculated with ANOVA followed by Turkey's *post-hoc* test. Ns: not significant; $^{**}p < 0.01$; $^{****}p < 0.0001$.

we observed a significant increase in autophagosomes and its co-localization with mitochondria (**Figures 6C,D**), suggesting that Ori significantly promoted mitophagy in astrocytes. Autophagosomes were also monitored by TEM analysis. Our results showed that 1 μM Ori distinctly increased the number of autophagosomes in astrocytes (**Figure 6E**).

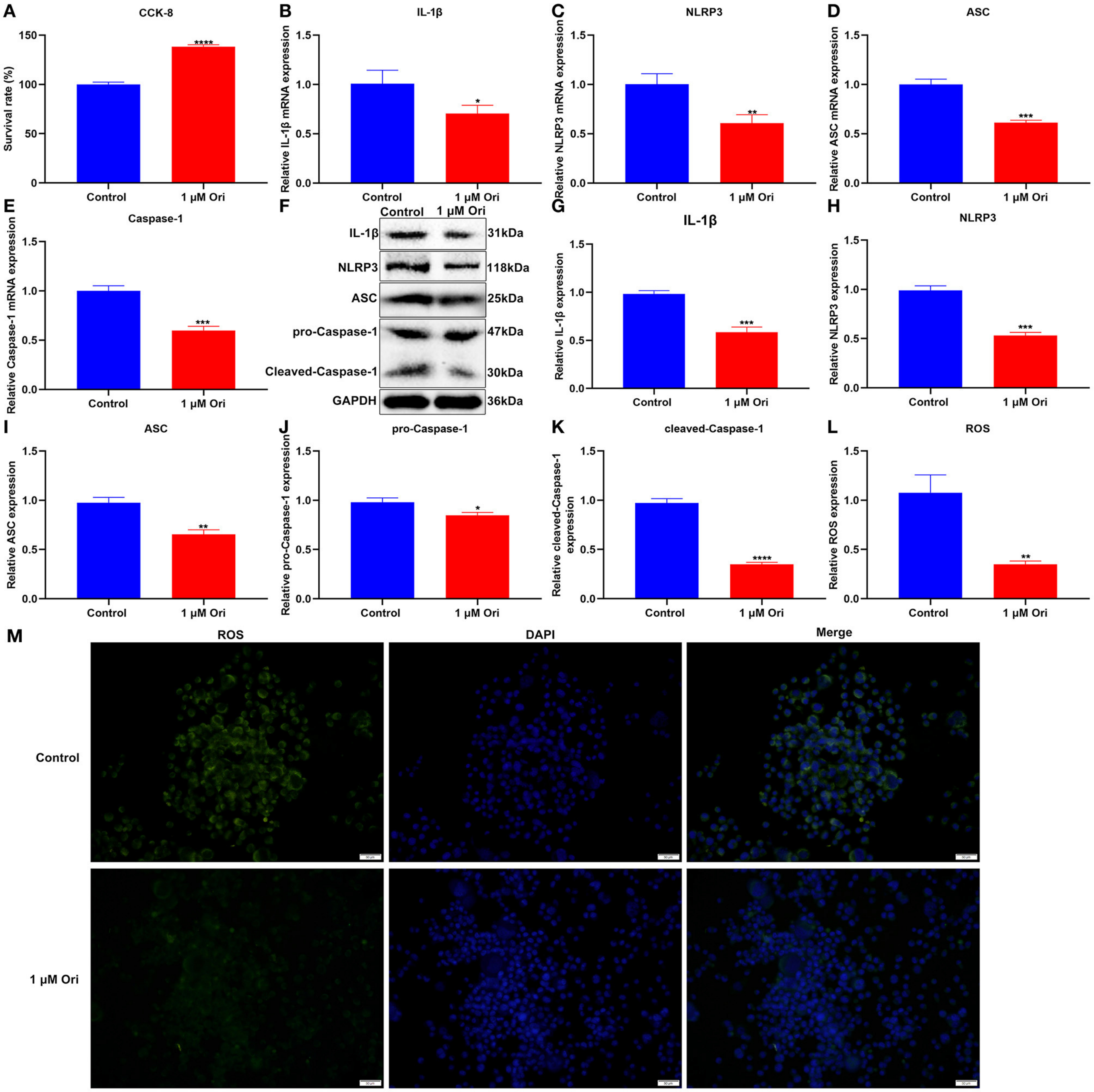

FIGURE 5 | Effect of 1 μM Ori on NLRP3 inflammasome activation and ROS accumulation in astrocytes. **(A)** The cell viability of astrocytes treated with 1 μM Ori according to CCK-8 assay. **(B–E)** RT-qPCR of the relative mRNA expression of IL-1β, NLRP3, ASC and Caspase-1 in astrocytes treated with 1 μM Ori. **(F)** Representative blots showing IL-1β, NLRP3, ASC, pro-Caspase-1, and cleaved-Caspase-1 in astrocytes treated with 1 μM Ori. **(G–K)** Quantitative analysis of the expression of IL-1β, NLRP3, ASC, pro-Caspase-1, and cleaved-Caspase-1 according to the western blotting results. **(L)** Representative H2DCF-DA fluorescence staining of ROS in astrocytes treated with 1 μM Ori. **(M)** Quantitative analysis of the expression of ROS based on the H2DCF-DA fluorescence staining results. Magnification, 200× (50 μm). $N = 3$ each group. P values were calculated with student's t test. $^{*}p < 0.05$; $^{**}p < 0.01$; $^{***}p < 0.001$; $^{****}p < 0.0001$.

Ori Treatment Protects Against NLRP3 Inflammasome Activation and ROS Accumulation *via* Autophagy Activation in LPS-Treated Astrocytes

Primary astrocytes were induced by LPS to construct depression *in vitro* models. Cell viability of primary astrocytes was markedly reduced by LPS treatment (**Figure 7A**). Compared with primary astrocytes, cell viability was significantly enhanced by autophagy agonist Rap and the opposite results were observed when treated with autophagy inhibitor 3-MA, indicating that autophagy activation may protect astrocytes against damage. One μM Ori and Rap co-treatment significantly ameliorated LPS-induced cell damage while 1 μM Ori administration markedly

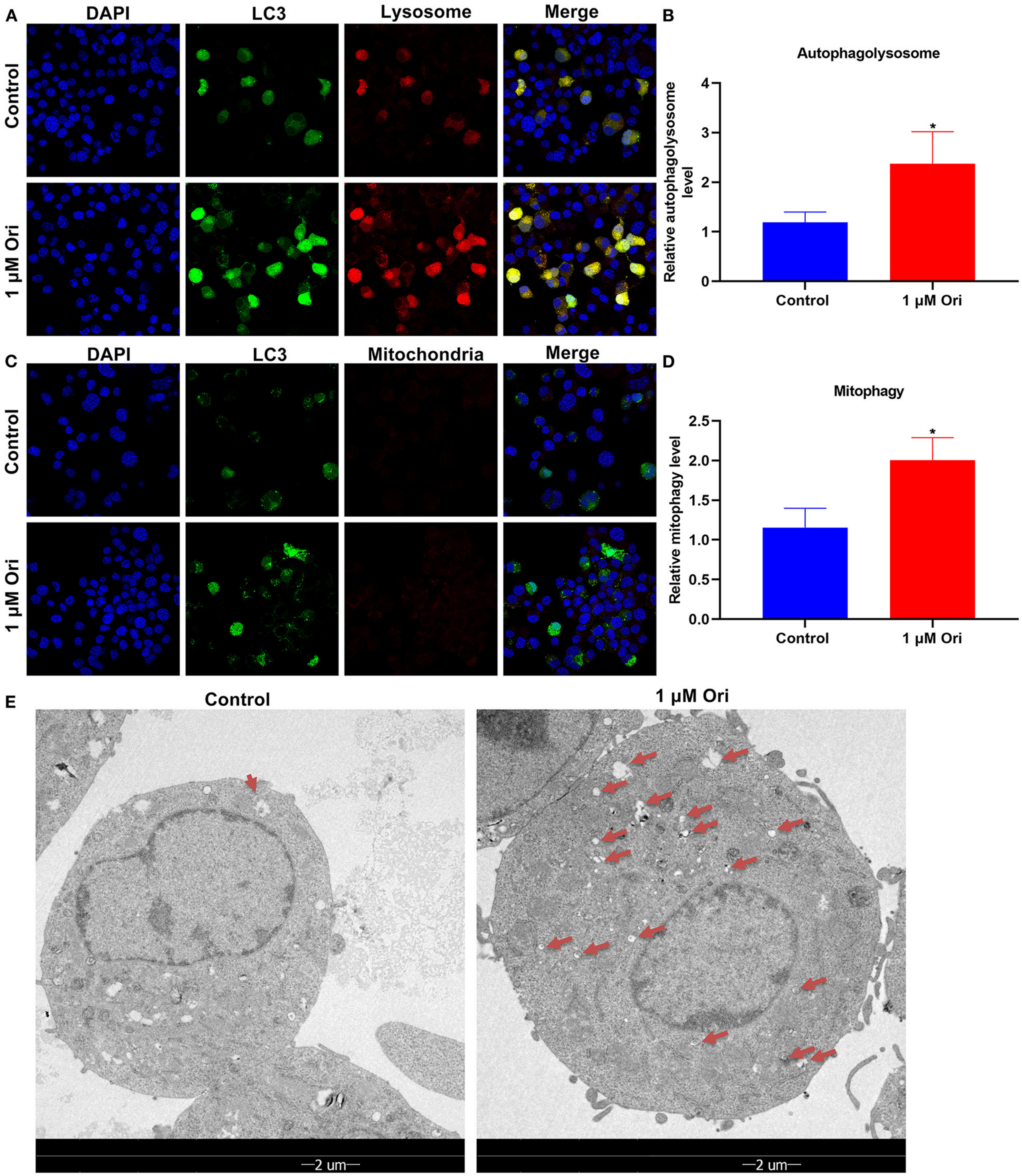

FIGURE 6 | Effect of 1 μM Ori on autophagy activation in astrocytes. **(A)** IF staining for astrocytes transfected by mTag-Wasabi-LC3 plasmids. Magnification, 200× (50 μm). **(B)** Autolysosomes were counted in astrocytes treated with 1 μM Ori. **(C)** Astrocytes administrated by 1 μM Ori of which mitochondria were marked through MitoTracker Deep Red. Magnification, 200× (50 μm). **(D)** Mitophagy was quantified in astrocytes treated with 1 μM Ori. **(E)** TEM showing the morphology and number of autophagosomes in astrocytes treated with 1 μM Ori. Red arrows, autophagosomes. Magnification, 1700× (2 μm). $N = 3$ each group. *P* values were calculated with student's *t* test. $^*P < 0.05$.

alleviated LPS-induced cell damage despite the existence of 3-MA. Thus, 1 μM Ori may protect against LPS-induced astrocyte damage *via* activating autophagy. Autophagy level was assessed through detecting the expression of LC3II/I, Beclin1 and P62. We observed that 1 μM Ori treatment markedly enhanced LC3II/I and Beclin1 expression and decreased P62 expression in LPS-treated astrocytes (**Figures 7B–E**). Meanwhile, 1 μM Ori treatment significantly ameliorated the inhibitory effects of 3-MA on autophagy in LPS-treated astrocytes. NLRP3 inflammasome activation was examined by detection of IL-1β, NLRP3, ASC, pro-Caspase-1 and cleaved-Caspase-1 in astrocytes (**Figures 7F–J**). Their expression was markedly increased by LPS and autophagy inhibitor 3-MA. Also, we observed that autophagy agonist Rap treatment significantly reduced IL-1β and cleaved-Caspase-1 levels in astrocytes. One μM Ori prominently reduced IL-1β, NLRP3, ASC, pro-Caspase-1 as well as cleaved-Caspase-1 expression in LPS-treated astrocytes under the existence of Rap or 3-MA. Above data suggested that 1 μM Ori weakened NLRP3 inflammasome activation through activating autophagy in LPS-treated astrocytes. ROS levels were increased in LPS-treated astrocytes, which was alleviated by 1 μM Ori treatment despite the existence of Rap or 3-MA (**Figures 7K,L**).

Ori Treatment Enhances Autophagy in LPS-Treated Astrocytes

Through mTag-Wasabi-LC3 dual fluorescence staining, the autolysosome and autophagosome accumulation was detected in astrocytes. We observed that 1 μM Ori combined with Rap distinctly promoted autolysosome and autophagosome formation in LPS-treated astrocytes (**Figures 8A,B**). Furthermore, 1 μM Ori treatment combined with Rap significantly increased autophagosome formation and its co-localization with mitochondria (**Figures 8C,D**), suggesting that Ori significantly promoted mitophagy in LPS-treated astrocytes. However, 3-MA significantly weakened the stimulating effect of Ori on autophagy in LPS-treated astrocytes.

DISCUSSION

The cytokine theory, also known as the inflammatory response theory, has attracted more and more attention from researchers in the mechanisms of depression (37). The cytokine theory is based on the immunological changes in patients with depression. This theory believes that the inflammatory cytokines produced by the over-activated immune system play an important role in the pathogenesis of depression (38). At present, the cytokine theory has been confirmed by the research results of a series of clinical trials and animal experiments, so anti-inflammation therapy has increasingly become an emerging research direction in the prevention and treatment of depression (39). Here, we observed the therapeutic effects of Ori on depression by inhibiting NLRP3 inflammasome *via* activation of autophagy both in LPS-induced depression mice and LPS-treated astrocytes.

Our results showed that Ori treatment alleviated LPS-induced depressive-like behaviors in mice according to sucrose preference, FST and TST assays that have been widely applied as animal models for screening potential antidepressants. As previous evidence, autophagy inhibition induces depressive-like behaviors (40). Autophagy inhibitor 3-MA weakened the therapeutic effects of Ori on depressive-like behaviors. Furthermore, Ori treatment enhanced autophagy activation in the hippocampus of the LPS-induced depression model and LPS-treated astrocytes, indicating that Ori improved depressive-like behaviors through enhancing autophagy. Astrocytes are the richest glial cells in the mammalian brain, which act as a key regulator of cerebral development as well as survival and growth of normal neurons, formation of synapses, and action potential propagation (41). Astrocytes have special glial fibrils, which are composed of GFAP (42). Thus, GFAP can be used as a marker of astrocytes. Due to different dose, and different time line of administration of drugs compared with previous research (3), our results showed that GFAP expression was decreased in the hippocampus of mice after 1.2 mg/kg LPS administration, indicating that a single dose of LPS can damage astrocytes. We found that Ori improved the reduction of GFAP expression in the hippocampus of the LPS-induced depression model. Meanwhile, autophagy agonist Rap enhanced the promotion of Ori on GFAP expression, while autophagy inhibitor 3-MA abolished the protective role of Ori on astrocytes in the depression models, indicating that Ori can protect astrocytes by enhancing autophagy.

The inflammasome, a cytosolic multi-protein complex, includes NLRs, adaptor protein ASC and Caspase-1 (11). The NLRP3 inflammasome acts as a major pathway, which induces Caspase-1 activation as well as subsequent maturation of IL-1β (11). Our results for the first time showed that Ori treatment reduced the expression of NLRP3 inflammasome components including IL-1β, NLRP3, ASC and Caspase-1 both in the hippocampus of the LPS-induced depression models and LPS-treated astrocytes, which was enhanced by autophagy agonist Rap and weakened by autophagy inhibitor 3-MA. Previous evidence has shown that autophagy may suppress the NLRP3 inflammasome (16). ROS accumulation stimulates tissue inflammatory response and induces NLRP3 inflammasome activation (18). Our results demonstrated that Ori treatment weakened the production of ROS in LPS-treated astrocytes. Hence, Ori treatment could reduce LPS-induced NLRP3 inflammasome *via* enhancing autophagy. Under the TEM, we observed that Ori treatment significantly increased the formation of autophagosomes both in the hippocampus of the LPS-induced depression mice and LPS-treated astrocytes. To clarify what kind of autophagosome increased phenomenon belonged to, we used mTag-Wasabi-LC3 plasmid to transfect primary astrocytes. Our results showed that autophagosomes and autophagolysosomes were significantly increased in LPS-treated astrocytes after Ori treatment, indicating that autophagosome maturation was inhibited, that was, autophagosomes could not be combined with lysosomes made autophagosomes unable to degrade and accumulate. Mitophagy is a process of selectively removing damaged mitochondria through autophagy (43). Generally, the energy production of astrocytes is mainly based on mitochondrial oxidative metabolism in response to neuronal activity. Therefore,

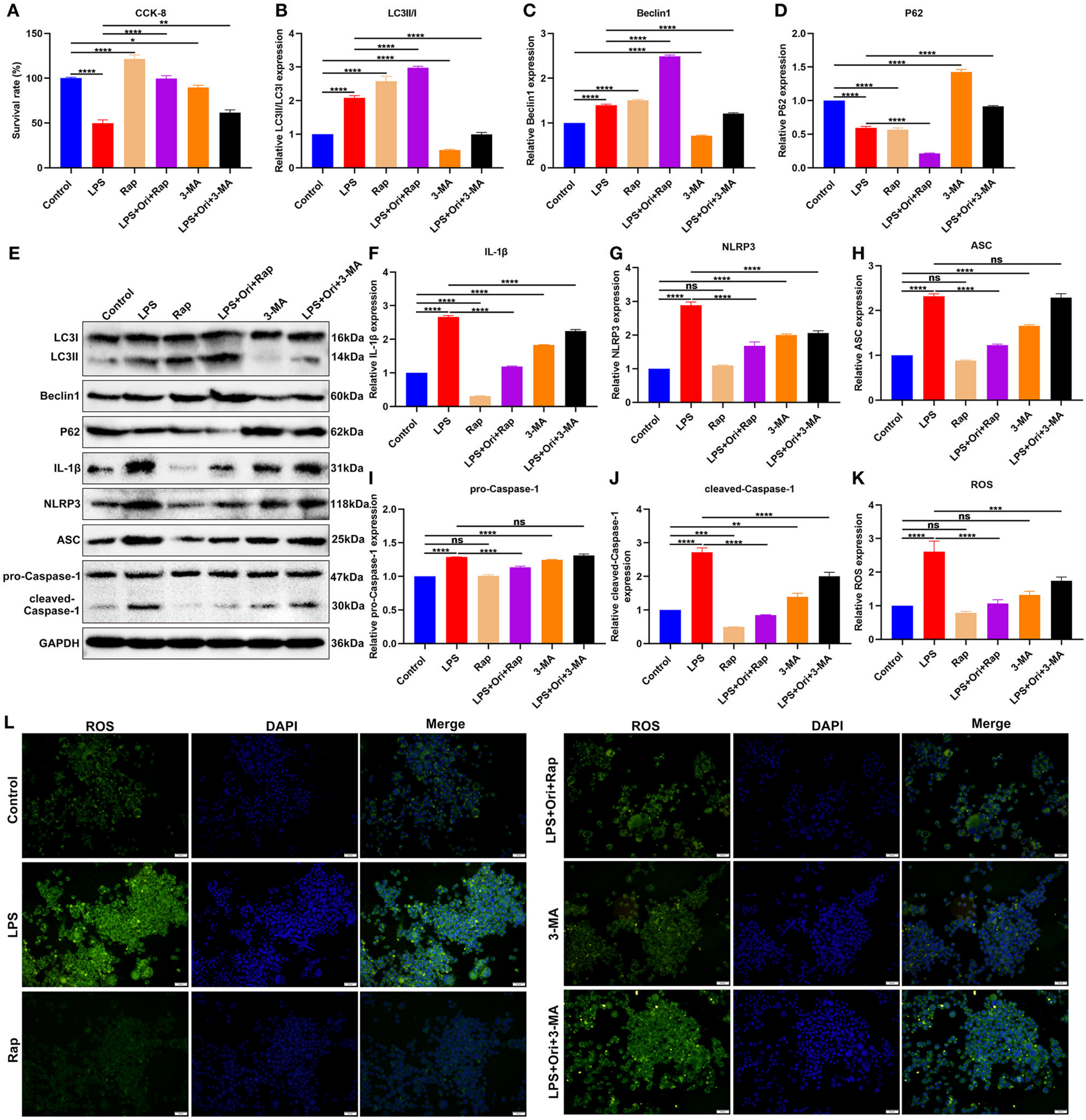

FIGURE 7 | Effects of Ori, autophagy agonist Rap, and autophagy inhibitor 3-MA on NLRP3 inflammasome activation and ROS accumulation in LPS-treated astrocytes. **(A)** CCK-8 detecting the viability of astrocytes in each group. **(B–E)** Western blotting examining the expression autophagy markers LC3II/I, Beclin1 and P62 in astrocytes. **(F–J)** Western blotting testing the levels of NLRP3 inflammasome proteins IL-1β, NLRP3, ASC, pro-Caspase-1 as well as cleaved-Caspase-1 in astrocytes. **(K)** Quantitative analysis of the expression of ROS based on the H2DCF-DA fluorescence staining results. **(L)** Representative H2DCF-DA fluorescence staining of ROS in astrocytes. Magnification, 200× (50 μm). $N = 3$ each group. P values were calculated with ANOVA followed by Turkey's *post-hoc* test. Ns, not significant; $^{*}p < 0.05$; $^{**}p < 0.01$; $^{***}p < 0.001$; $^{****}p < 0.0001$.

mitophagy as a selective autophagy plays a key role in determining the fate of astrocytes in depression. In this study, we found that Ori enhanced LPS-induced mitophagy in astrocytes, indicating that Ori promoted astrocyte autophagy flux and increased the clearance rate of damaged mitochondria in LPS-induced astrocytes. Damaged or non-functional mitochondria may release excessive ROS and cause cell damage (44). Our results showed that Ori treatment reduced the accumulation

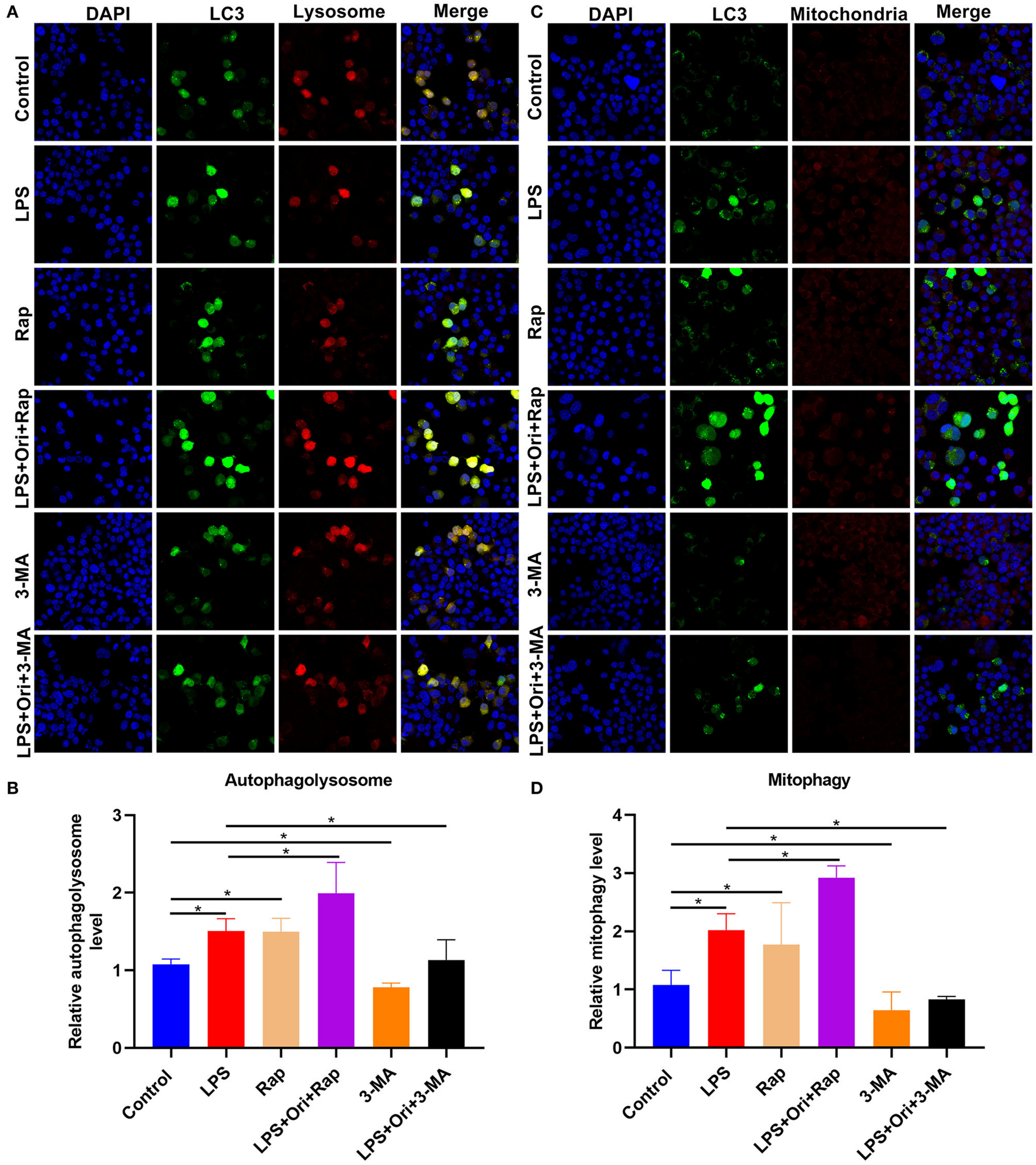

FIGURE 8 | Effects of Ori, autophagy agonist Rap, and autophagy inhibitor 3-MA on autophagy activation in astrocytes. **(A)** IF staining showing astrocytes transfected by mTag-Wasabi-LC3 plasmids. Magnification, 200× (50 μm). **(B)** Quantification of autolysosomes in astrocytes. **(C)** Labeling mitochondria of astrocytes through MitoTracker Deep Red. Magnification, 200× (50 μm). **(D)** Quantification of mitophagy in astrocytes. $N = 3$ each group. P values were calculated with ANOVA followed by Turkey's *post-hoc* test. $^*p < 0.05$.

of ROS induced by LPS, indicating that Ori could eliminate excessive mitochondrial ROS accumulation, thereby reducing cell death caused by mitochondrial damage. Therefore, Ori promoted autophagy to eliminate damaged mitochondria and reduce cell death, ultimately improving the pathological changes of hippocampal astrocytes in depression.

Herein, LPS exposure was used to induce neuroinflammation and depressive-like behaviors both in mice and astrocytes. Previous research has showed that Ori can significantly ameliorate depressive-like behaviors of mice partly through regulating PPAR-γ/AMPA receptor signaling in the prefrontal cortex (28). Moreover, Ori ameliorates depressive-like behaviors *via* suppressing neuroinflammation and autophagy impairment in rat models with chronic unpredictable mild stress. However, the specific molecular mechanisms are lack of more experimental evidences. Herein, our study for the first time demonstrated that Ori treatment could reduce LPS-induced NLRP3 inflammasome *via* enhancing autophagy of astrocytes. However, there are a few limitations in our study. Firstly, we did not use a reference drug (antidepressant) like fluoxetine, though Ori possessed a remarkable anti-depressant property. Secondly, more experiments will be carried out for revealing the molecular mechanisms of Ori in treatment of depression. Thirdly, the therapeutic effect of Ori on depressive behaviors will be investigated in more studies.

CONCLUSION

Taken together, our findings demonstrated that Ori could become a promising antidepressant drug. Ori may alleviate LPS-induced depression by inhibiting NLRP3 inflammasome through activation of autophagy both in the hippocampus of the LPS-induced depression model mice and LPS-treated astrocytes, which unveiled the new protective mechanism of Ori treatment in depression.

DATA AVAILABILITY STATEMENT

The original contributions presented in the study are included in the article/supplementary material, further inquiries can be directed to the corresponding author.

ETHICS STATEMENT

The study was approved by the Ethics Committee of School of Medicine, Jinhua Polytechnic (2019019).

AUTHOR CONTRIBUTIONS

MD conceived and designed the study. CL, YZ, YuaW, and MF conducted most of the experiments and data analysis, and wrote the manuscript. YiW, YueW, YQ, and HZ conducted a small number of experiments and data analysis, and contributed to the writing of the manuscript. MD and CL confirm the authenticity of all the raw data. All authors reviewed and approved the manuscript.

FUNDING

This work was funded by the Basic Public Welfare Research Program of Zhejiang Province (LGD20H090002) and the Science and Technology Project of Jinhua City in China (2019-4-070).

REFERENCES

1. Beurel E, Toups M, Nemeroff CB. The bidirectional relationship of depression and inflammation: double trouble. *Neuron.* (2020) 107:234–56. doi: 10.1016/j.neuron.2020.06.002
2. Malhi GS, Mann JJ. Depression. *Lancet.* (2018) 392:2299–312. doi: 10.1016/S0140-6736(18)31948-2
3. Li W, Ali T, He K, Liu Z, Shah FA, Ren Q, et al. Ibrutinib alleviates LPS-induced neuroinflammation and synaptic defects in a mouse model of depression. *Brain Behav Immun.* (2021) 92:10–24. doi: 10.1016/j.bbi.2020.11.008
4. Dwyer JB, Aftab A, Radhakrishnan R, Widge A, Rodriguez CI, Carpenter LL, et al. Hormonal treatments for major depressive disorder: state of the art. *Am J Psychiatry.* (2020) 177:686–705. doi: 10.1176/appi.ajp.2020.19080848
5. Rein T. Is autophagy involved in the diverse effects of antidepressants? *Cells.* (2019) 8:44. doi: 10.3390/cells8010044
6. Troubat R, Barone P, Leman S, Desmidt T, Cressant A, Atanasova B, et al. Neuroinflammation and depression: a review. *Eur J Neurosci.* (2021) 53:151–71. doi: 10.1111/ejn.14720
7. Das R, Emon MPZ, Shahriar M, Nahar Z, Islam SMA, Bhuiyan MA, et al. Higher levels of serum IL-1β and TNF-α are associated with an increased probability of major depressive disorder. *Psychiatry Res.* (2021) 295:113568. doi: 10.1016/j.psychres.2020.113568
8. Moretti J, Blander JM. Increasing complexity of NLRP3 inflammasome regulation. *J Leukoc Biol.* (2021) 109:561–71. doi: 10.1002/JLB.3MR0520-104RR
9. Lahooti B, Chhibber T, Bagchi S, Varahachalam SP, Jayant RD. Therapeutic role of inflammasome inhibitors in neurodegenerative disorders. *Brain Behav Immun.* (2021) 91:771–83. doi: 10.1016/j.bbi.2020.11.004
10. Kinra M, Joseph A, Nampoothiri M, Arora D, Mudgal J. Inhibition of NLRP3-inflammasome mediated IL-1β release by phenylpropanoic acid derivatives: in-silico and in-vitro approach. *Eur J Pharm Sci.* (2021) 157:105637. doi: 10.1016/j.ejps.2020.105637
11. Kelley N, Jeltema D, Duan Y, He Y. The NLRP3 inflammasome: an overview of mechanisms of activation and regulation. *Int J Mol Sci.* (2019) 20:3328. doi: 10.3390/ijms20133328
12. Wang D, Wang H, Gao H, Zhang H, Zhang H, Wang Q, et al. P2X7 receptor mediates NLRP3 inflammasome activation in depression and diabetes. *Cell Biosci.* (2020) 10:28. doi: 10.1186/s13578-020-00388-1
13. Mizushima N, Levine B. Autophagy in human diseases. *N Engl J Med.* (2020) 383:1564–76. doi: 10.1056/NEJMra2022774
14. Gassen NC, Rein T. Is there a role of autophagy in depression and antidepressant action? *Front Psychiatry.* (2019) 10:337. doi: 10.3389/fpsyt.2019.00337
15. Biasizzo M, Kopitar-Jerala N. Interplay between NLRP3 inflammasome and autophagy. *Front Immunol.* (2020) 11:591803. doi: 10.3389/fimmu.2020.591803
16. Cao Z, Wang Y, Long Z, He G. Interaction between autophagy and the NLRP3 inflammasome. *Acta Biochim Biophys Sin (Shanghai).* (2019) 51:1087–95. doi: 10.1093/abbs/gmz098
17. Chung C, Seo W, Silwal P, Jo EK. Crosstalks between inflammasome and autophagy in cancer. *J Hematol Oncol.* (2020) 13:100. doi: 10.1186/s13045-020-00936-9

18. Zhou R, Yazdi AS, Menu P, Tschopp J. A role for mitochondria in NLRP3 inflammasome activation. *Nature.* (2011) 469:221–5. doi: 10.1038/nature09663
19. Deretic V, Levine B. Autophagy balances inflammation in innate immunity. *Autophagy.* (2018) 14:243–51. doi: 10.1080/15548627.2017.1402992
20. Zhang Y, Wang S, Dai M, Nai J, Zhu L, Sheng H. Solubility and bioavailability enhancement of oridonin: a review. *Molecules.* (2020) 25:332. doi: 10.3390/molecules25020332
21. Cheng W, Huang C, Ma W, Tian X, Zhang X. Recent development of oridonin derivatives with diverse pharmacological activities. *Mini Rev Med Chem.* (2019) 19:114–24. doi: 10.2174/1389557517666170417170609
22. Guo J, Chen T, Ma Z, Qiao C, Yuan F, Guo X, et al. Oridonin inhibits 4T1 tumor growth by suppressing Treg differentiation *via* TGF-β receptor. *Int Immunopharmacol.* (2020) 88:106831. doi: 10.1016/j.intimp.2020.106831
23. Yang H, Gao Y, Fan X, Liu X, Peng L, Ci X. oridonin sensitizes cisplatin-induced apoptosis *via* AMPK/Akt/mTOR-dependent autophagosome accumulation in A549 cells. *Front Oncol.* (2019) 9:769. doi: 10.3389/fonc.2019.00769
24. Kou B, Yang Y, Bai YE, Shi YH, Gao RX, Yang FL, et al. Oridonin induces apoptosis of laryngeal carcinoma *via* endoplasmic reticulum stress. *Cancer Manag Res.* (2020) 12:8387–96. doi: 10.2147/CMAR.S271759
25. Zhao YJ, Lv H, Xu PB, Zhu MM, Liu Y, Miao CH, et al. Protective effects of oridonin on the sepsis in mice. *Kaohsiung J Med Sci.* (2016) 32:452–7. doi: 10.1016/j.kjms.2016.07.013
26. Wang S, Zhang Y, Saas P, Wang H, Xu Y, Chen K, et al. Oridonin's therapeutic effect: suppressing Th1/Th17 simultaneously in a mouse model of Crohn's disease. *J Gastroenterol Hepatol.* (2015) 30:504–12. doi: 10.1111/jgh.12710
27. He H, Jiang H, Chen Y, Ye J, Wang A, Wang C, et al. Oridonin is a covalent NLRP3 inhibitor with strong anti-inflammasome activity. *Nat Commun.* (2018) 9:2550. doi: 10.1038/s41467-018-04947-6
28. Liu P, Du J. Oridonin is an antidepressant molecule working through the PPAR-γ/AMPA receptor signaling pathway. *Biochem Pharmacol.* (2020) 180:114136. doi: 10.1016/j.bcp.2020.114136
29. Xu M, Wan CX, Huang SH, Wang HB, Fan D, Wu HM, et al. Oridonin protects against cardiac hypertrophy by promoting P21-related autophagy. *Cell Death Dis.* (2019) 10:403. doi: 10.1038/s41419-019-1617-y
30. Salazar G, Cullen A, Huang J, Zhao Y, Serino A, Hilenski L, et al. SQSTM1/p62 and PPARGC1A/PGC-1alpha at the interface of autophagy and vascular senescence. *Autophagy.* (2020) 16:1092–110. doi: 10.1080/15548627.2019.1659612
31. Yu H, Zou Z, Zhang X, Peng W, Chen C, Ye Y, et al. Inhibition of phosphodiesterase 4 by FCPR03 alleviates lipopolysaccharide-induced depressive-like behaviors in mice: involvement of p38 and JNK signaling pathways. *Int J Mol Sci.* (2018) 19:513. doi: 10.3390/ijms19020513
32. Zou ZQ, Chen JJ, Feng HF, Cheng YF, Wang HT, Zhou ZZ, et al. Novel phosphodiesterase 4 inhibitor FCPR03 alleviates lipopolysaccharide-induced neuroinflammation by regulation of the cAMP/PKA/CREB signaling pathway and NF-κB inhibition. *J Pharmacol Exp Ther.* (2017) 362:67–77. doi: 10.1124/jpet.116.239608
33. Liu MY, Yin CY, Zhu LJ, Zhu XH, Xu C, Luo CX, et al. Sucrose preference test for measurement of stress-induced anhedonia in mice. *Nat Protoc.* (2018) 13:1686–98. doi: 10.1038/s41596-018-0011-z
34. Petit-Demouliere B, Chenu F, Bourin M. Forced swimming test in mice: a review of antidepressant activity. *Psychopharmacology (Berl).* (2005) 177:245–55. doi: 10.1007/s00213-004-2048-7
35. Cryan JF, Mombereau C, Vassout A. The tail suspension test as a model for assessing antidepressant activity: review of pharmacological and genetic studies in mice. *Neurosci Biobehav Rev.* (2005) 29:571–625. doi: 10.1016/j.neubiorev.2005.03.009
36. Yu L, Chen Y, Tooze SA. Autophagy pathway: cellular and molecular mechanisms. *Autophagy.* (2018) 14:207–15. doi: 10.1080/15548627.2017.1378838
37. Koo J, Marangell LB, Nakamura M, Armstrong A, Jeon C, Bhutani T, et al. Depression and suicidality in psoriasis: review of the literature including the cytokine theory of depression. *J Eur Acad Dermatol Venereol.* (2017) 31:1999–2009. doi: 10.1111/jdv.14460
38. Köhler O, Benros ME, Nordentoft M, Farkouh ME, Iyengar RL, Mors O, et al. Effect of anti-inflammatory treatment on depression, depressive symptoms, and adverse effects: a systematic review and meta-analysis of randomized clinical trials. *JAMA Psychiatry.* (2014) 71:1381–91. doi: 10.1001/jamapsychiatry.2014.1611
39. Kohler O, Krogh J, Mors O, Benros ME. Inflammation in depression and the potential for anti-inflammatory treatment. *Curr Neuropharmacol.* (2016) 14:732–42. doi: 10.2174/1570159X14666151208113700
40. Ali T, Rahman SU, Hao Q, Li W, Liu Z, Ali Shah F, et al. Melatonin prevents neuroinflammation and relieves depression by attenuating autophagy impairment through FOXO3a regulation. *J Pineal Res.* (2020) 69:e12667. doi: 10.1111/jpi.12667
41. Zhang HY, Wang Y, He Y, Wang T, Huang XH, Zhao CM, et al. A1 astrocytes contribute to murine depression-like behavior and cognitive dysfunction, which can be alleviated by IL-10 or fluorocitrate treatment. *J Neuroinflammation.* (2020) 17:200. doi: 10.1186/s12974-020-01871-9
42. Li Y, Li L, Wu J, Zhu Z, Feng X, Qin L, et al. Activation of astrocytes in hippocampus decreases fear memory through adenosine A(1) receptors. *Elife.* (2020) 9:e57155. doi: 10.7554/eLife.57155
43. Liu J, Liu L, Han YS Yi J, Guo C, Zhao HQ, et al. The molecular mechanism underlying mitophagy-mediated hippocampal neuron apoptosis in diabetes-related depression. *J Cell Mol Med.* (2021) 25:7342–53. doi: 10.1111/jcmm.16763
44. Lin Q, Li S, Jiang N, Shao X, Zhang M, Jin H, et al. PINK1-parkin pathway of mitophagy protects against contrast-induced acute kidney injury *via* decreasing mitochondrial ROS and NLRP3 inflammasome activation. *Redox Biol.* (2019) 26:101254. doi: 10.1016/j.redox.2019.101254

Conflict of Interest: The authors declare that the research was conducted in the absence of any commercial or financial relationships that could be construed as a potential conflict of interest.

ORIGINAL RESEARCH
published: 13 January 2022
doi: 10.3389/fmed.2021.832605

Molecular Characterization and Clinical Relevance of ALDH2 in Human Cancers

Bo Ma[1†], Zaoqu Liu[1,2,3†], Hui Xu[1,2,3†], Long Liu[4], Tao Huang[5], Lingfang Meng[6], Libo Wang[4], Yuyuan Zhang[1], Lifeng Li[7*] and Xinwei Han[1,2,3*]

[1] *Department of Interventional Radiology, The First Affiliated Hospital of Zhengzhou University, Zhengzhou, China,* [2] *Interventional Institute of Zhengzhou University, Zhengzhou, China,* [3] *Interventional Treatment and Clinical Research Center of Henan Provice, Zhengzhou, China,* [4] *Department of Hepatobiliary and Pancreatic Surgery, The First Affiliated Hospital of Zhengzhou University, Zhengzhou, China,* [5] *Medical School, Huanghe Science and Technology University, Zhengzhou, China,* [6] *Department of Infection Management, The Second Affiliated Hospital of Zhengzhou University, Zhengzhou, China,* [7] *Internet Medical and System Applications of National Engineering Laboratory, Zhengzhou, China*

Background: Aldehyde dehydrogenase 2 (ALDH2) is well-known to be a key enzyme in alcohol metabolism. However, a comprehensive understanding of ALDH2 across human cancers is lacking.

Methods: A systematic and comprehensive analysis of the molecular alterations and clinical relevance for ALDH2 in more than 10,000 samples from 33 cancer types was performed. qRT-PCR was performed on 60 cancer and 60 paired nontumor tissues.

Results: It was observed that ALDH2 was generally downregulated in most cancers, which was mainly driven by DNA hypermethylation rather than mutations or copy number variations. Besides, ALDH2 was closely related to the inhibition and activation of tumor pathways and a variety of potential targeted agents had been discovered in our research. Last but not least, ALDH2 had the best prediction efficacy in assessing immunotherapeutic response compared with PD-L1, PD-1, CTLA4, CD8, and tumor mutation burden (TMB) in cutaneous melanoma. According to the analysis of large-scale public data and 60 pairs of clinical cancer samples, we found the downregulation of ALDH2 expression tends to suggest the malignant phenotypes and adverse prognosis, which might enhance the precise diagnosis and timely intervention of cancer patients.

Conclusion: This study advanced the understanding of ALDH2 across cancers, and provided important insight into chemotherapy, immunotherapy and prognosis of patients with cancer.

Keywords: ALDH2, pan-cancer, genetic alterations, drug sensitivity, immunotherapy, survival

Edited by:
Fu Wang,
Xi'an Jiaotong University, China

Reviewed by:
Zhang Yizhe,
Shanghai Jiaotong University School of Medicine, China
Nan Li,
Ludwig Maximilian University of Munich, Germany
Enoch Xu,
Lanzhou University Second Hospital, China

***Correspondence:**
Xinwei Han
fcchanxw@zzu.edu.cn
Lifeng Li
lilifeng0317@163.com

[†] *These authors have contributed equally to this work*

Specialty section:
This article was submitted to Precision Medicine, a section of the journal Frontiers in Medicine

Received: 10 December 2021
Accepted: 23 December 2021
Published: 13 January 2022

Citation:
Ma B, Liu Z, Xu H, Liu L, Huang T, Meng L, Wang L, Zhang Y, Li L and Han X (2022) Molecular Characterization and Clinical Relevance of ALDH2 in Human Cancers. Front. Med. 8:832605. doi: 10.3389/fmed.2021.832605

INTRODUCTION

Aldehyde dehydrogenase 2 (ALDH2) is one of the aldehyde dehydrogenase family of enzymes. As another member of the aldehyde dehydrogenase family, ALDH1 is widely known for its key role in carcinogenesis and cancer treatment (1). Nonetheless, ALDH2 is well-known to be a key enzyme in alcohol metabolism and has a major contribution in oxidizing endogenous aldehydic products arising from lipid peroxidation such as 4-hydroxy-2-nonenal (4-HNE) and malondialdehyde under oxidative stress (2). The dysfunction of ALDH2 has a tight correlation with multiple diseases such as diabetes, cardiovascular disease, osteoporosis, and cancers (3). As the rate-limiting enzyme of alcohol metabolism, ALDH2 has a profound impact on the clearance process of toxic acetaldehyde. Low expression or genetic polymorphism of ALDH2 dramatically reduce its enzyme activity, and the accumulation of acetaldehyde can further damage normal cells and lead to cancers (4).

Previous studies have shown that ALDH2 has profound impacts on the prognosis and treatment of tumors. For example, prognostic analysis revealed the low expression of ALDH2 indicated adverse overall survival (OS) in patients with lung, liver, or bladder cancer (5, 6). Hou et al. have demonstrated that ALDH2 modulates the adenosine 5 ’-monophosphate (AMP) -activated protein kinase pathway in mice, which in turn inhibits the progression of hepatocellular carcinoma (7). ALDH2 has also been reported to regulate tumor proliferation by catabolizing some endogenous substrates derived from normal cell metabolism (e.g., 4-HNE) (8). In addition, ALDH2 has been demonstrated to be tightly associated with the sensitivity and resistance of multiple targeted drugs including 4-Hydroxycyclophosphamide, Doxorubicin, Cisplatin, Vincristine, and Disulfiram (9–12). Therefore, a comprehensive understanding of ALDH2 on the molecular characterization and clinical relevance across human cancers is necessary. Understanding the abnormal expression and genomic alterations of ALDH2 may help elucidate its role in cancer prognosis and therapy.

In this study, we are committed to systematically and comprehensively exploring the molecular alterations, prognosis, and therapeutic value of ALDH2 in 33 cancer types. It was proven that aberrant expression and genetic alterations of ALDH2 are widespread in different types of cancer. By assessing the correlation between ALDH2 and cancer pathway activity as well as its clinical value, ALDH2 was found to be a potential biomarker for immunotherapeutic evaluation and prognostic stratification. In a word, our study demonstrates the important value of ALDH2 in cancer and lays the foundation for translational medicine development of ALDH2.

MATERIALS AND METHODS

Multi-Omics Data of 33 Cancer Types in TCGA

33 different cancer cohorts were collected from The Cancer Genome Atlas Research Network (TCGA, https://portal.gdc.cancer.gov/). The RNA-seq, copy number variation (CNV), and survival information were downloaded from UCSC Xena website (https://xenabrowser.net/datapages/). The somatic mutation (VarScan2 variant aggregation and masking) and HumanMethylation450 array were derived from TCGA GDC portal. Tumor mutation burden (TMB) was defined as the total number of non-silent somatic mutations in each sample (13). The correlation between methylation sites and ALDH2 expression was evaluated by Pearson Correlation Coefficient and the methylation site with $r < -0.3$ and false discovery rate (FDR) <0.05 was considered as hypermethylation. The proteomics data were retrieved from the Clinical Proteomic Tumor Analysis Consortium (CPTAC, https://proteomics.cancer.gov/programs/cptac), and the protein expression levels of ALDH2 in human tumors and normal tissues were determined by Human Protein Atlas (HPA, https://www.proteinatlas.org/). See **Supplementary Material** for the detailed description.

Immunotherapeutic Cohorts

Three independent cohorts containing immunotherapy information and expression data were retrieved from Gene Expression Omnibus (GEO, https://www.ncbi.nlm.nih.gov/geo/). (1) GSE100797: melanoma patients treated with adoptive T cell therapy (ACT) (14); (2) GSE78220: melanoma patients treated with anti-PD-1 (15); (3) GSE91061: melanoma patients treated with anti-PD-1 (16). Based on the RECIST v1.1 criterion, 21 patients in GSE100797, 28 patients in GSE78220, as well as 49 patients in GSE91061 were finally determined. A detailed description is provided in the **Supplementary Material**.

Estimation of Drug Response

Predicted responses of cancer patients to 138 anticancer drugs were collected from existing studies to evaluate drug response for TCGA samples (17). Half maximum inhibitory concentration (IC50) was used to assess drug sensitivity. Besides, the correlation between imputed drug response and ALDH2 mRNA expression was calculated by Pearson correlation and drugs with top 10 $|r|$ and FDR <0.05 were considered to be the latent targets for ALDH2.

Oncogenic Pathway Activity and Immune Infiltration Assessment

The FPKM normalized gene expression of TCGA database was performed to Gene Set Variation Analysis (GSVA), which is a non-parametric, unsupervised method for estimating variation of gene set enrichment through the samples of an expression data set. The correlation between ALDH2 and oncogenic pathways was verified by Gene set enrichment analysis (GSEA). 50 gene sets were enrolled from Molecular Signatures Database (MSigDB, https://www.gsea-msigdb.org/gsea/msigdb/) v7.2 Hallmark database and FDR <0.05 was considered statistically significant. Single sample gene set enrichment analysis (ssGSEA) algorithm implemented in GSVA package was applied to estimate the relative infiltration abundance of tumor microenvironment (TME) cells. The gene sets for marking 28 immune cell types were collected from Charoentong et al. (18). Furthermore, we evaluated the correlation between

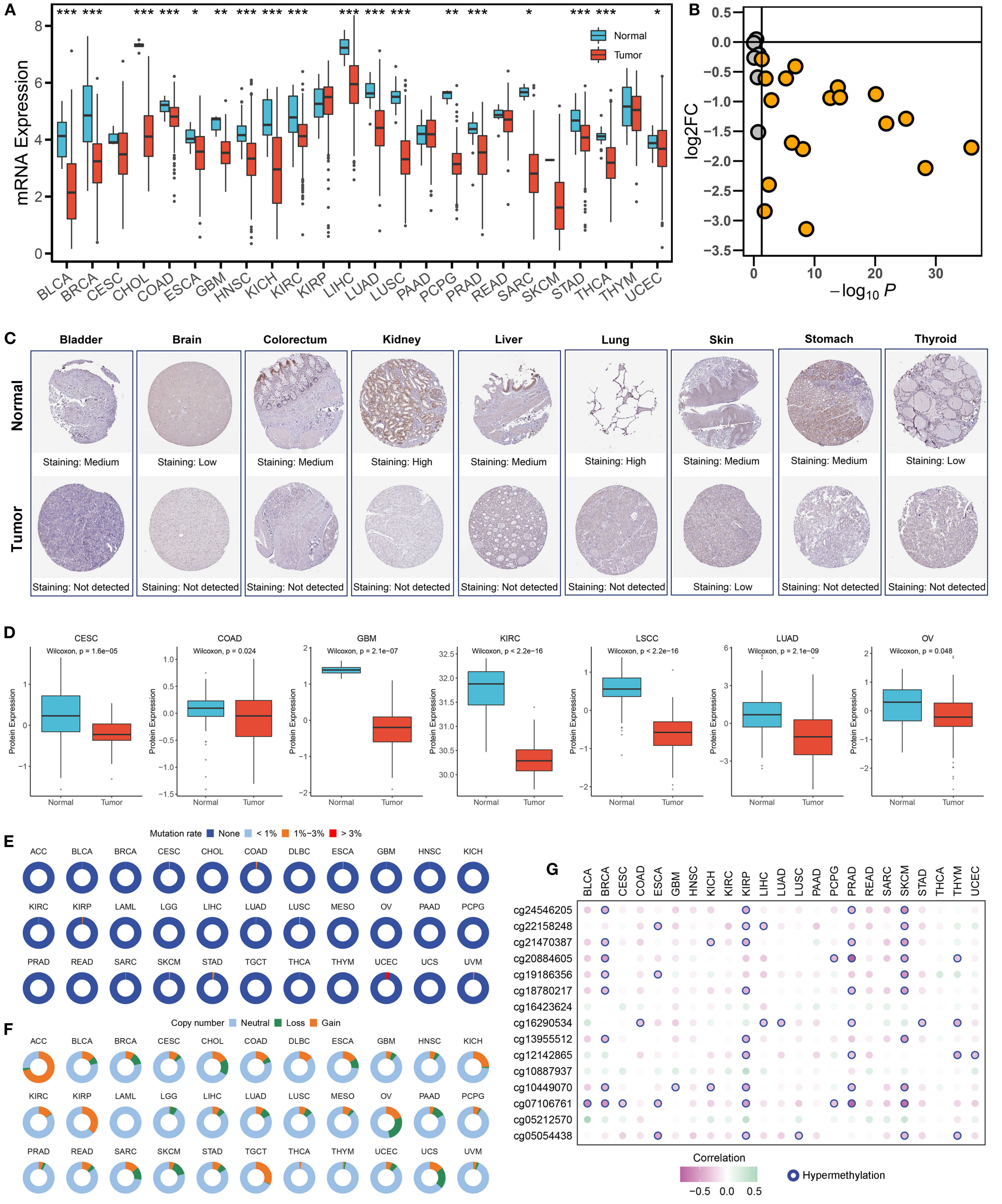

FIGURE 1 | Multi-omics landscape of ALDH2 in cancers. **(A)** The expression of ALDH2 between normal and tumor tissue across human cancers. Wilcoxon rank-sum test: $^{*}P < 0.05$; $^{**}P < 0.01$; $^{***}P < 0.001$. **(B)** The log2 fold change (FC) and *P*-value distribution of ALDH2 between normal and tumor across human cancers. **(C)** The immunohistochemical results displayed that lighter protein staining in tumor relative to normal tissue. **(D)** The protein level of ALDH2 between normal and tumor across human cancers. **(E)** The mutation frequency of ALDH2 across 33 cancer types. **(F)** The copy number variation frequency of ALDH2 across 33 cancer types. **(G)** Pearson correlation between the expression of ALDH2 and the methylation beta value of 15 corresponding CpG site. Hypermethylation represents the methylation site with $r < -0.3$ and FDR <0.05.

ALDH2 expression and pathway or cell activity using Pearson correlation coefficient.

Human Cancer Specimens and Clinical Information

A total of 60 cancer tissues and matched adjacent nontumor tissues were enrolled from The First Affiliated Hospital of Zhengzhou University, including 5 pairs of pancreatic cancers, 10 pairs of paired liver cancers, 5 pairs of bile duct cancers, and 40 pairs of colorectal cancers. All patients signed written informed consent. See **Supplementary Material** for the inclusion criteria of patients. The clinical characteristics of patients included gender, clinical stage, distant metastasis status, lymph metastasis status, vessel invasion status, nerve invasion status, disease-free survival (DFS), and OS. Refer to **Supplementary Table S1** for details of the baseline information.

RNA Preparation and Quantitative Real-Time PCR

Total RNA was isolated from cancer tissues and paired adjacent nontumor tissues with RNAiso Plus reagent (Takara, Dalian, China) according to the manufacturer's instructions. RNA quality was evaluated using a NanoDrop One C (Waltham, MA, USA), and RNA integrity was assessed using agarose gel electrophoresis. An aliquot of 1 μg of total RNA was reverse-transcribed into complementary DNA (cDNA) according to the manufacturer's protocol using a High-capacity cDNA Reverse Transcription kit (TaKaRa BIO, Japan). Quantitative real-time PCR (qRT-PCR) was performed using SYBR Assay I Low ROX (Eurogentec, USA) and SYBR® Green PCR Master Mix (Yeason, Shanghai, China) to detect the expression. The data were normalized to the expression of GAPDH. The sequences of the primers were as follows:

GAPDH forward (5'- to 3'-): GGAGCGAGATCCCTCCAAAAT

GAPDH reverse (5'- to 3'-): GGCTGTTGTCATACTTCTCATGG

ALDH2 forward (5'- to 3'-): GTTTGGAGCCCAGTAACCCTT

ALDH2 reverse (5'- to 3'-): CCCACACTCACAGTTTTGAATT.

Statistical Analysis

The correlation between two variables was assessed using Pearson correlation. Correlations with $|r| > 0.3$ and FDR < 0.05 were significant and labeled as "SigCor" in the genomic analysis. The *survminer* package was utilized to determine the optimal cut-off value of ALDH2 expression based on survival information. The *survival* package was employed for Kaplan-Meier survival analysis and the different significance was defined by the log-rank test. The *pROC* package was utilized to plot the receiver operating characteristic (ROC) curves. The area under ROC curve (AUC) was used to compare the accuracy of predicting immunotherapeutic response of ALDH2, CD8, CTLA-4, PD-1, PD-L1, and TMB. Differences in ALDH2 expression between the two groups were compared by Wilcoxon rank sum test or independent samples *T*-test. Multiple comparisons were performed using ANOVA or Kruskal-Wallis tests. Paired *T*-test was used to analyze ALDH2 expression differences between paired tumor samples and matched adjacent nontumor samples. All statistical *P* values were two-sided, and $P < 0.05$ was defined as statistically significant. Adjust *P* value was performed using Benjamini-Hochberg (BH) multiple test correction. All plotting and data processing were completed in R 4.0.2 software.

RESULTS

Multi-Omics Landscape of ALDH2 in Cancers

As illustrated in **Figures 1A,B**, ALDH2 presented universally lower mRNA expression in almost all tumors. Immunohistochemical results also displayed that lighter protein staining in tumors relative to normal tissue (**Figure 1C**). The proteomics data of multiple cancers further validated these results in protein level (**Figure 1D**). The above suggested ALDH2 was significantly downregulated in human cancers. In order to clarify the factors affecting ALDH2 expression, we further investigated the genomic variation of ALDH2 across tumors. Interestingly, despite ALDH2 polymorphism being closely related to many diseases such as cardiovascular and digestive diseases, the mutational events were extremely rare in cancers, and the mutation rate of most cancers were <1% (**Figure 1E**). Therefore, the mutation is not the major driver for the downregulation of ALDH2. Conversely, ALDH2 presented extensive copy number variation (CNV) in cancers (**Figure 1F**). To assess the impact of CNV on ALDH2 expression, we further investigated the correlation between CNV and expression of ALDH2. Notably, CNV had little impact on ALDH2 expression in most cancers, which also indicated CNV was not an important factor downregulating ALDH2 expression (**Supplementary Figure S1**). DNA hypermethylation is another essential factor that regulates gene expression, which is also a ubiquitous feature of carcinogenesis. ALDH2 has 15 methylation sites in HumanMethylation450 array. Our results indicate that the expression of ALDH2 in most tumors was negatively correlated with DNA methylation. The multiple cancers displayed plenty of hypermethylation sites, particularly KIRP and SKCM (**Figure 1G**). Overall, the downregulation of ALDH2 was driven by DNA hypermethylation rather than mutation or CNV.

Functional Analysis of ALDH2

The correlation between ALDH2 expression and the activity of pathways involved in 50 cancer hallmarks was explored to further understand the molecular mechanism of ALDH2 involvement in cancer. The results indicate that ALDH2 expression was closely correlated with inhibition or activation of multiple oncogenic pathways (**Figure 2A**). For instance, the expression of ALDH2 was predominantly positive related to immune related pathways such as interferon and complement response in TGCT, DLBC, and SKCM, metastasis-related pathways such as epithelial mesenchymal transition and angiogenesis in THYM, and lipid metabolism-related pathways such as adipogenesis and fatty acid metabolism in COAD,

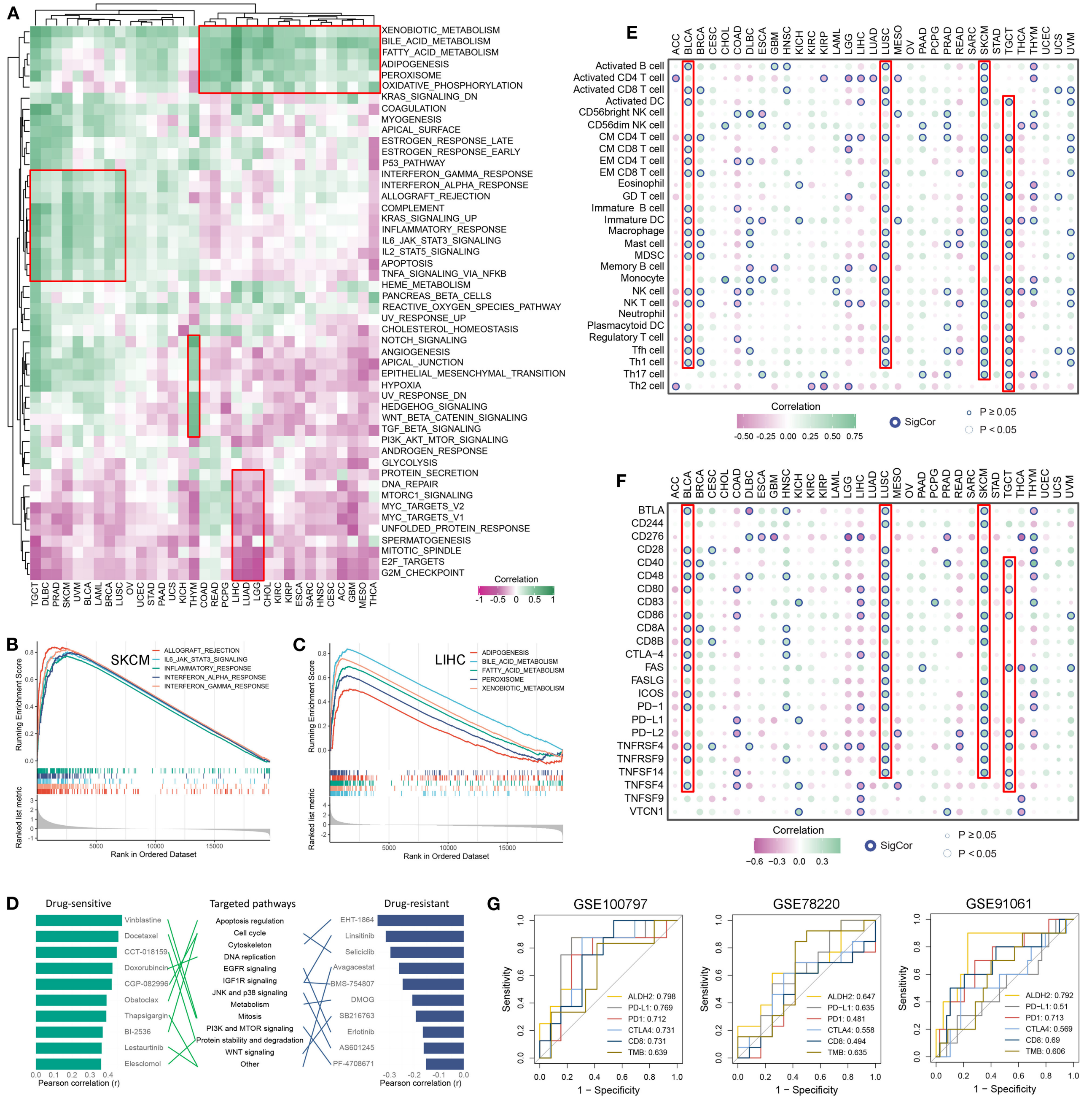

FIGURE 2 | Functional analysis and cancer therapy implication of ALDH2. **(A)** Correlation between ALDH2 expression and 50 oncogenic pathways activity across 33 cancer types. **(B,C)** The top 5 pathways with FDR <0.05 and NES >0 was retrieved form GSEA results of SKCM **(B)** and LIHC **(C)**. **(D)** The potential roles of ALDH2 in cancer drug therapy. **(E,F)** Correlation between ALDH2 expression and 28 immune cells infiltration **(E)** and 24 immune checkpoints expression **(F)** across 33 cancer types. **(G)** Comparison of the predictive accuracy of ALDH2, PD-L1, PD-1, CTLA4, CD8, and TMB for immunotherapy in GSE100797, GSE78220, and GE91061.

READ, and LIHC, etc. Moreover, ALDH2 expression also had a significantly negative correlation with proliferation-related pathways such as DNA repair, MYC and E2F targets, and G2M checkpoint in LIHC, LUAD, and LGG, etc. Based on the ALDH2 expression group, GSEA analysis verified the above results. SKCM presented intense immune-related pathways (**Figure 2B**); LIHC significantly enriched in lipid metabolism-related pathways (**Figure 2C**); THYM displayed canonical metastasis-related pathways (**Supplementary Figure S2A**); and LUAD was negatively related to proliferation-related pathways (**Supplementary Figure S2B**). Collectively, ALDH2 might play multiple functional roles in distinct cancers.

Implications of ALDH2 for Cancer Chemotherapy and Immunotherapy

Furthermore, based on the relationship between ALDH2 expression and impute drug response of each patient, we identified the potential roles of ALDH2 in cancer drug therapy (**Figure 2D**). Obviously, we found ALDH2 might enhance the drug sensitivity of Vinblastine, Docetaxel, CCT-018159, Doxorubicin, CGP-082996, Obatoclax, Thapsigargin, BI-2536, Lestaurtinib, and Elesclomol; elevate the drug resistant of EHT-1864, Linsitinib, Selicicib, Avagacestat, BMS-754807, DMOG, SB216763, Erlotinib, AS601245, and PF-4708671. Some of our results are consistent with previous studies (6–8). Of note, ALDH2 may have different drug responses to the same targeted pathway. For example, the targeted pathway of Obatoclax, BI-2536, and Selicicib is cell cycle, but ALDH2 enhances drug sensitivity of Obatoclax and BI-2536, and decreases the drug sensitivity of Selicicib. These results might advance clinical drug selection and facilitate precision therapy in human cancers.

Due to the enriched immune-related pathway across cancers (**Figures 2A,B**), we further assessed the correlation between ALDH2 expression and 24 immune checkpoints expression and 28 immune cells infiltration (**Figures 2E,F**). It was observed that predominantly correlation in multiple cancers, particularly in those with well immunotherapeutic efficacy, such as BLCA, LUSC, SKCM, and TGCT. Thus, we hypothesized ALDH2 might be a latent biomarker for predicting immunotherapeutic response. Three independent SKCM cohorts containing expression data and immunotherapeutic information were enrolled. We compared the accuracy of ALDH2 in predicting immunotherapeutic response with that of existing biomarkers such as CD8, CTLA4, PD-1, PD-L1, and TMB. The results demonstrated that ALDH2 had the highest accuracy in predicting the effect of immunotherapy compared with other biomarkers (**Figure 2G**). These findings suggested ALDH2 was a promising biomarker for assessing immunotherapeutic efficacy in SKCM.

Clinical Relevance of ALDH2 Across Cancers

We further revealed the clinical value of ALDH2 in cancers subsequently. As shown in our results, there was no correlation between ALDH2 expression and age (**Figure 3A**). Male patients had predominant higher ALDH2 expression relative to female patients (**Figure 3B**). In addition, downregulation of ALDH2 was associated with malignant phenotypes of cancers (**Figures 3C,D**). Notably, metastasis tumors had the lowest ALDH2 expression compared with primary and recurrent tumors, and there was no significant difference between recurrent and primary tumors (**Figure 3E**). Furthermore, univariate Cox regression revealed ALDH2 was a protective factor of survival (disease-specific survival, overall survival, progression-free interval, and disease-free interval) in most cancers (**Figure 3F**). The Kaplan-Meier survival analysis also demonstrated the same results in human cancers (**Figure 3G**). The significant clinical relevance of ALDH2 may provide important insight into translational medicine developments.

Validating the Role of ALDH2 Across Tumors in Our Cohort

A total of 60 cancer tissues and matched adjacent nontumor tissues were enrolled from The First Affiliated Hospital of Zhengzhou University, including 5 pairs of pancreatic cancers, 10 pairs of paired liver cancers, 5 pairs of bile duct cancers, and 40 pairs of colorectal cancers. As illustrated in **Figure 4A**, the expression of ALDH2 was significantly downregulated across all cancers relative to their corresponding adjacent nontumor tissues (T-test: all $P < 0.05$). Patients with high ALDH2 expression possessed better OS and DFS compared to patients with low ALDH2 expression (Log-rank test: both $P < 0.05$; **Figure 4B**). Moreover, highly expressed ALDH2 was more likely to appear in male tumor patients (T-test: $P < 0.05$; **Figure 4C**). Consistent with the above results, the low expression of ALDH2 tended to indicate a malignant clinical outcome. For example, patients with malignant phenotypes such as advanced AJCC stage, distant metastasis, and vessel invasion had the inferior ALDH2 expression (All $P < 0.05$; **Figures 4D–F**). Of note, when lymph metastasis or nerve invasion events occurred, patients had predominantly downregulated ALDH2 expression although there were no statistically significant (**Figures 4G,H**). Overall, the downregulation of ALDH2 expression tends to suggest malignant phenotypes, which might enhance the precise diagnosis and timely intervention of cancer patients.

DISCUSSION

In our study, we systematically and comprehensively explored the molecular alterations, prognosis, and therapeutic value of ALDH2 in 33 cancer types. It was found that ALDH2 was downregulated in most cancer, which was mainly driven by DNA hypermethylation rather than mutation or CNV. The aberrant expression of ALDH2 is dramatically correlated with the activity of cancer pathways. Moreover, ALDH2 was proved to be a potentially useful biomarker for immunotherapy assessment and prognostic stratification.

ALDH2 is a mitochondrial enzyme that is closely associated with the degradation of acetaldehyde. Acetaldehyde is a toxic substance, and its accumulation in cells causes acetaldehyde-induced DNA interstrand crosslinks (AA-ICLs), which further induces the initiation and progression of many tumors such as liver cancer, colorectal cancer, gastric cancer, esophageal cancer, and lung cancer (4, 19). In this study, we demonstrated that ALDH2 is defective in most tumors relative to normal tissues on both mRNA and protein expression levels, which was further validated by *in vitro* experiments. In order to find out the potential reasons leading to the downregulation of A LDH2 expression. We analyzed somatic mutations, CNV, and DNA methylation of ALDH2 across 33 cancer types. We observed that ALDH2 displayed low mutations. Previous researches demonstrated ALDH2 polymorphism was common in the Asian population (4, 19). As far as we know, the population of TCGA was mainly from the United States. Thus, the aberrant expression of ALDH2 was not driven by mutation in the United States. Notably, ALDH2 displayed broad CNV alterations, while there

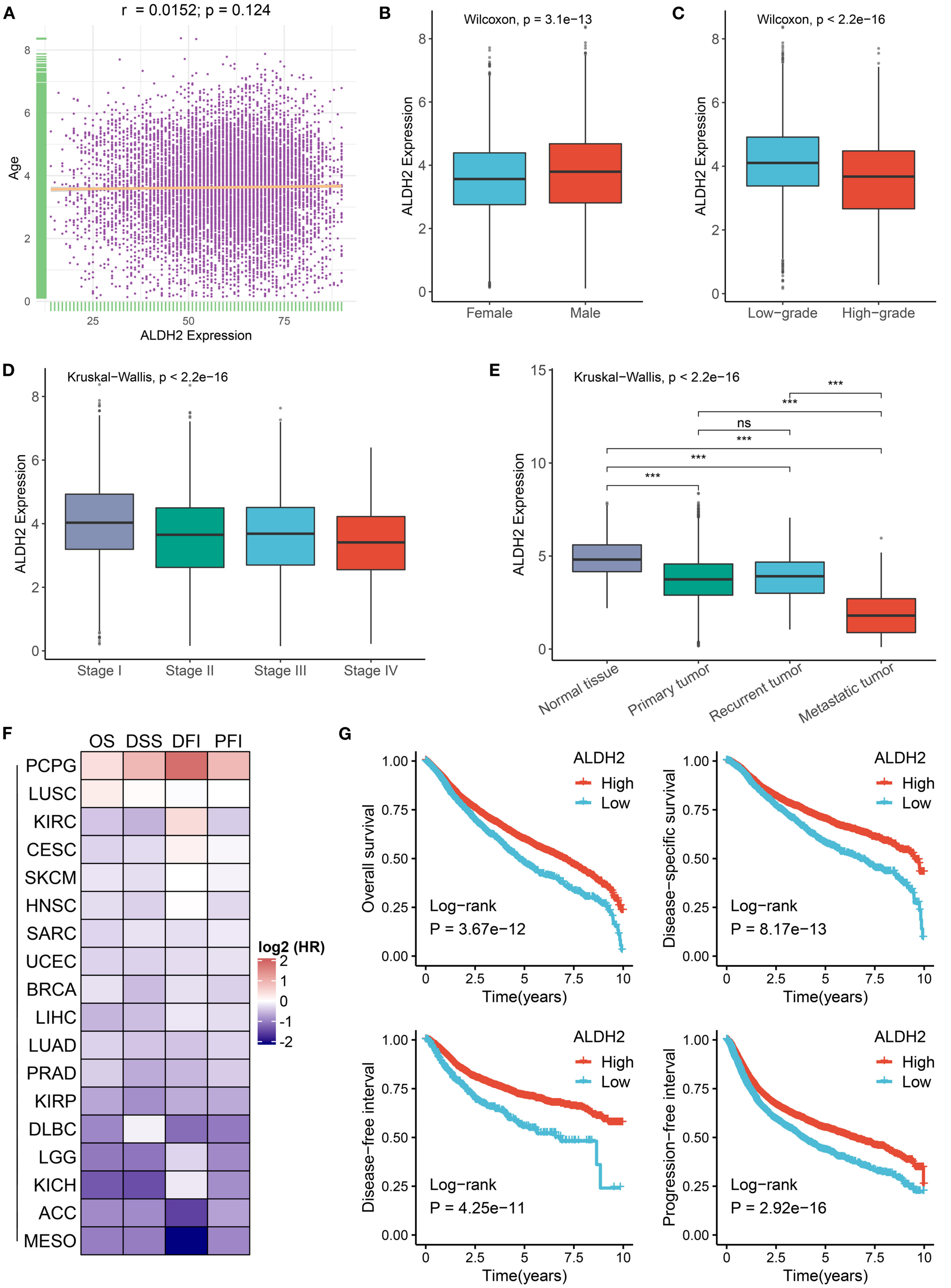

FIGURE 3 | Clinical relevance of ALDH2 across cancers. **(A)** Correlation between ALDH2 expression and age in cancers. **(B)** The difference of ALDH2 expression between female and male groups. **(C)** The difference of ALDH2 expression between low grade (G1, G2 or low grade in cancers) and high grade (G3, G4 or high grade in cancers). **(D)** The distribution of ALDH2 expression among distinct AJCC stages. **(E)** The distribution of ALDH2 expression among different categories tissues

(Continued)

FIGURE 3 | including solid normal tissue, primary tumor, recurrent tumor, and metastatic tumor. ns, $P > 0.05$; ***$P < 0.001$. **(F)** Heatmap showing the hazard ratio (HR) of overall survival, disease specific survival, disease free interval, and progression free interval for ALDH2 in human cancers. The cell value represents log2 (HR). **(G)** Kaplan-Meier survival curve of ALDH2 for overall survival, disease specific survival, disease free interval, and progression free interval.

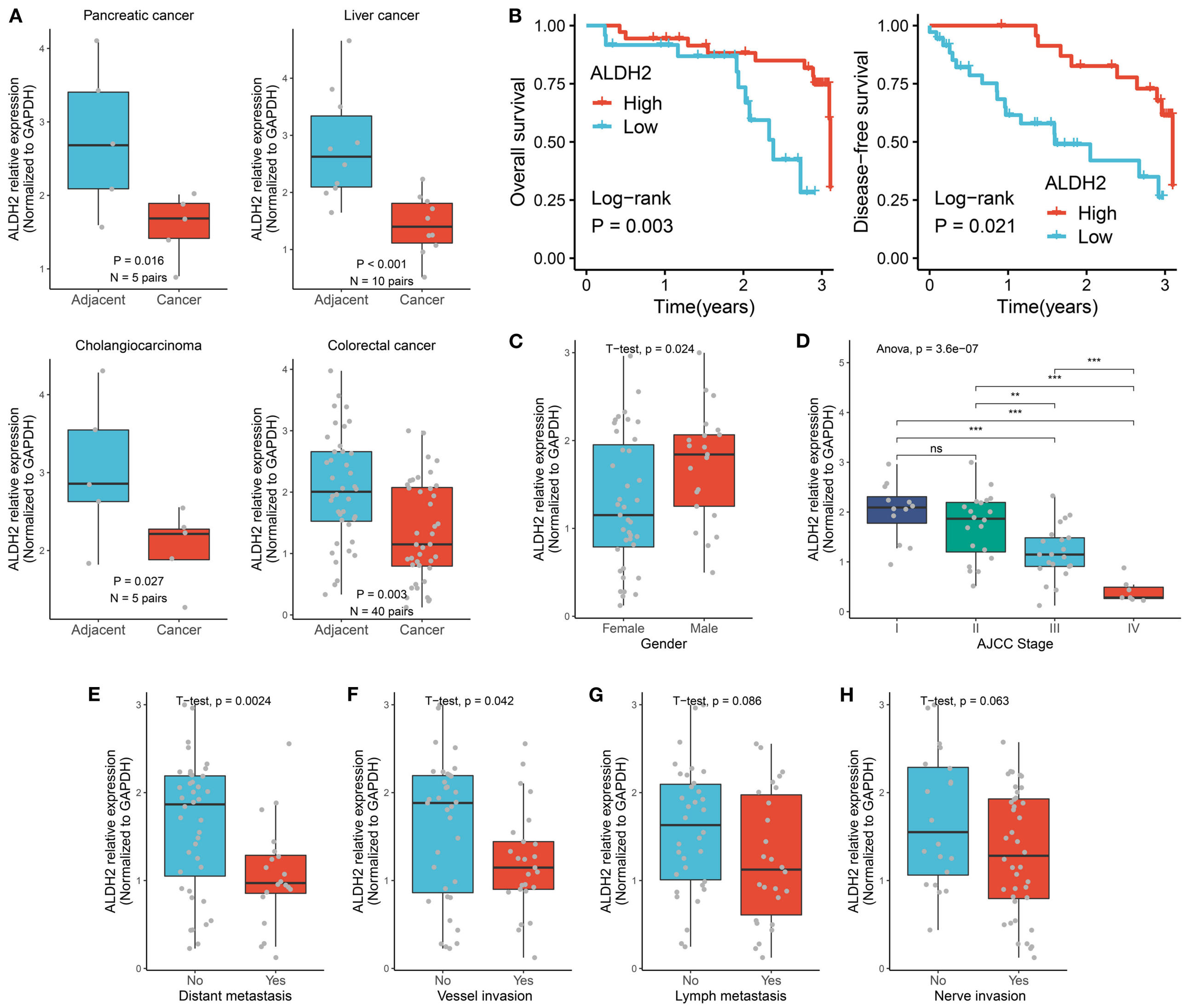

FIGURE 4 | Validating the role of ALDH2 across tumors in our cohort. **(A)** qRT-PCR displayed the mRNA expression level of ALDH2 between cancer tissues and their corresponding adjacent nontumor tissues. **(B)** Kaplan-Meier survival curve of ALDH2 for overall survival, disease-free survival. **(C)** The difference of ALDH2 expression between female and male groups. **(D)** The distribution of ALDH2 expression among distinct AJCC stages. *T*-test: ns, $P > 0.05$; **$P < 0.01$; ***$P < 0.001$. **(E)** The difference of ALDH2 expression in the groups with or without distant metastasis. **(F)** The difference of ALDH2 expression in the groups with or without vessel invasion. **(G)** The difference of ALDH2 expression in the groups with or without lymph metastasis. **(H)** The difference of ALDH2 expression in the groups with or without nerve invasion.

was no significant correlation between the expression and CNV. Finally, we found that ALDH2 hypermethylation was an essential mechanism in the downregulation of ALDH2 in human cancers.

Our research demonstrated the close correlation between the aberrant expression of ALDH2 and the activity of cancer pathways. Of note, ALDH2 might be involved in the different processes of initiation and progression in different tumors. For instance, ALDH2 is mainly associated with metabolic pathways in respiratory and digestive system tumors, metastasis-related pathways in THYM, and immune-related pathways in SKCM. The multiple roles of ALDH2 in cancers might give rise to diverse reflections on cancer treatments. Previous studies have proved that ALDH2 is closely correlated with the sensitivity and resistance of multiple targeted drugs such as 4-Hydroxycyclophosphamide, Doxorubicin, Cisplatin, Vincristine, and Disulfiram (9–12). In this study, based on the imputed tumor response of 138 anticancer-drugs from a large cohort, we provided potential sensitive or resistant drug resources for ALDH2-deficient tumors. Moreover, due to the enriched immune-related pathway and immune infiltration in SKCM, we further assessed the accuracy of ALDH2 in predicting immunotherapy response of three SKCM cohorts, and found the predictive performance of ALDH2 was better than popular indicators such as CD8, CTLA4, PD-1, PD-L1, and TMB. This interesting finding suggested that ALDH2 might be a reliable and promising biomarker for evaluating immunotherapy response in SKCM.

In addition, we have proven ALDH2 has significant clinical value in both large-scale public datasets and 60 pairs of clinical cancer samples. We found that male patients have a superior expression of ALDH2 compared with female patients. Patients with low ALDH2 expression possessed an adverse prognosis. The low expression of ALDH2 tended to indicate malignant phenotypes such as advance stage, high metastasis tendency, and vessel invasion. These results indicated ALDH2 deficiency is a good indicator for assessing the clinical outcome of patients with cancer.

Collectively, we have demonstrated ALDH2 is prevalent downregulation in most cancers, which is mainly driven by DNA hypermethylation rather than mutation or CNV. ALDH2 is not only tightly associated with the activation and inhibition of cancer pathways, but also displays a predominant correlation with the sensitivity and resistance of multiple drugs, and has the best prediction efficacy in assessing immunotherapeutic response compared with CD8, CTLA4, PD-1, PD-L1, and TMB in SCKM. In addition, the deficiency of ALDH2 tends to suggest malignant phenotypes and adverse prognosis, which might enhance the precise diagnosis and timely intervention of cancer patients. This study advanced the understanding of ALDH2 across cancers, and laid a foundation for the translational medicine developments of ALDH2.

DATA AVAILABILITY STATEMENT

The datasets presented in this study can be found in online repositories. The names of the repository/repositories and accession number(s) can be found in the article/**Supplementary Material**.

ETHICS STATEMENT

The studies involving human participants were reviewed and approved by Ethics Committee of the First Affiliated Hospital of Zhengzhou University. The patients/participants provided their written informed consent to participate in this study.

AUTHOR CONTRIBUTIONS

ZL made the conceptualization, data curation, formal analysis, investigation, methodology, resources, software, validation, visualization, and writing. BM supported the funds and reviewed the manuscript. HX, LoL, TH, LM, LW, YZ, LiL, and XH reviewed and edited the manuscript. All authors agree to publish this manuscript.

FUNDING

This study was supported by Key Research Projects of Henan Higher Education (No.16A320053) and Youth Innovation Fund of the First Affiliated Hospital of Zhengzhou University to BM.

SUPPLEMENTARY MATERIAL

The Supplementary Material for this article can be found online at: https://www.frontiersin.org/articles/10.3389/fmed.2021.832605/full#supplementary-material

REFERENCES

1. Shao C, Sullivan JP, Girard L, Augustyn A, Yenerall P, Rodriguez-Canales J, et al. Essential role of aldehyde dehydrogenase 1A3 for the maintenance of non-small cell lung cancer stem cells is associated with the STAT3 pathway. *Clin Cancer Res.* (2014) 20:4154–66. doi: 10.1158/1078-0432.CCR-13-3292
2. Chen CH, Ferreira JC, Gross ER, Mochly-Rosen D. Targeting aldehyde dehydrogenase 2: new therapeutic opportunities. *Physiol Rev.* (2014) 94:1–34. doi: 10.1152/physrev.00017.2013
3. Wang LS, Wu ZX. ALDH2 and cancer therapy. *Adv Exp Med Biol.* (2019) 1193:221–28. doi: 10.1007/978-981-13-6260-6_13
4. Chang JS, Hsiao JR, Chen CH. ALDH2 polymorphism and alcohol-related cancers in Asians: a public health perspective. *J Biomed Sci.* (2017) 24:19. doi: 10.1186/s12929-017-0327-y
5. Chen X, Legrand AJ, Cunniffe S, Hume S, Poletto M, Vaz B, et al. Interplay between base excision repair protein XRCC1 and ALDH2 predicts overall survival in lung and liver cancer patients. *Cell Oncol (Dordr).* (2018) 41:527–39. doi: 10.1007/s13402-018-0390-8
6. Andrew AS, Gui J, Hu T, Wyszynski A, Marsit CJ, Kelsey KT, et al. Genetic polymorphisms modify bladder cancer recurrence and survival in a USA population-based prognostic study. *BJU Int.* (2015) 115:238–47. doi: 10.1111/bju.12641
7. Hou G, Chen L, Liu G, Li L, Yang Y, Yan HX, et al. Aldehyde dehydrogenase-2 (ALDH2) opposes hepatocellular carcinoma progression by regulating AMP-activated protein kinase signaling in mice. *Hepatology.* (2017) 65:1628–44. doi: 10.1002/hep.29006
8. Muzio G, Maggiora M, Paiuzzi E, Oraldi M, Canuto RA. Aldehyde dehydrogenases and cell proliferation. *Free Radic Biol Med.* (2012) 52:735–46. doi: 10.1016/j.freeradbiomed.2011.11.033
9. Moreb JS, Ucar D, Han S, Amory JK, Goldstein AS, Ostmark B, et al. The enzymatic activity of human aldehyde dehydrogenases 1A2 and 2 (ALDH1A2 and ALDH2) is detected by Aldefluor, inhibited by diethylaminobenzaldehyde and has significant effects on cell proliferation and drug resistance. *Chem Biol Interact.* (2012) 195:52–60. doi: 10.1016/j.cbi.2011.10.007
10. Kim J, Chen CH, Yang J, Mochly-Rosen D. Aldehyde dehydrogenase 2*2 knock-in mice show increased reactive oxygen species production in response to cisplatin treatment. *J Biomed Sci.* (2017) 24:33. doi: 10.1186/s12929-017-0338-8
11. Wang NN, Wang LH, Li Y, Fu SY, Xue X, Jia LN, et al. Targeting ALDH2 with disulfiram/copper reverses the resistance of cancer cells to microtubule

inhibitors. *Exp Cell Res.* (2018) 362:72–82. doi: 10.1016/j.yexcr.2017.11.004

12. Liu P, Brown S, Goktug T, Channathodiyil P, Kannappan V, Hugnot JP, et al. Cytotoxic effect of disulfiram/copper on human glioblastoma cell lines and ALDH-positive cancer-stem-like cells. *Br J Cancer.* (2012) 107:1488–97. doi: 10.1038/bjc.2012.442
13. Hellmann MD, Callahan MK, Awad MM, Calvo E, Ascierto PA, Atmaca A, et al. Tumor mutational burden and efficacy of nivolumab monotherapy and in combination with ipilimumab in small-cell lung cancer. *Cancer Cell.* (2019) 35:329. doi: 10.1016/j.ccell.2019.01.011
14. Lauss M, Donia M, Harbst K, Andersen R, Mitra S, Rosengren F, et al. Mutational and putative neoantigen load predict clinical benefit of adoptive T cell therapy in melanoma. *Nat Commun.* (2017) 8:1738. doi: 10.1038/s41467-017-01460-0
15. Hugo W, Zaretsky JM, Sun L, Song C, Moreno BH, Hu-Lieskovan S, et al. Genomic and transcriptomic features of response to Anti-PD-1 therapy in metastatic melanoma. *Cell.* (2016) 165:35–44. doi: 10.1016/j.cell.2016.02.065
16. Riaz N, Havel JJ, Makarov V, Desrichard A, Urba WJ, Sims JS, et al. Tumor and microenvironment evolution during immunotherapy with nivolumab. *Cell.* (2017) 171:934–49 e16. doi: 10.1016/j.cell.2017.09.028
17. Geeleher P, Zhang Z, Wang F, Gruener RF, Nath A, Morrison G, et al. Discovering novel pharmacogenomic biomarkers by imputing drug response in cancer patients from large genomics studies. *Genome Res.* (2017) 27:1743–51. doi: 10.1101/gr.221077.117
18. Charoentong P, Finotello F, Angelova M, Mayer C, Efremova M, Rieder D, et al. Pan-cancer immunogenomic analyses reveal genotype-immunophenotype relationships and predictors of response to checkpoint blockade. *Cell Rep.* (2017) 18:248–62. doi: 10.1016/j.celrep.2016.12.019
19. Hodskinson MR, Bolner A, Sato K, Kamimae-Lanning AN, Rooijers K, Witte M, et al. Alcohol-derived DNA crosslinks are repaired by two distinct mechanisms. *Nature.* (2020) 579:603–08. doi: 10.1038/s41586-020-2059-5

Conflict of Interest: The authors declare that the research was conducted in the absence of any commercial or financial relationships that could be construed as a potential conflict of interest.

frontiers in Medicine

ORIGINAL RESEARCH
published: 20 January 2022
doi: 10.3389/fmed.2021.816802

Investigation on the Pathological Mechanism of Frequent Exacerbators With Chronic Obstructive Pulmonary Disease Based on the Characteristics of Respiratory Flora

Li Ke[1]*, Luo Chen[2], Yuan Yaling[1], Gao Can[1], Lin Jun[1] and Zhang Chuan[1]

[1] Department of Laboratory Medicine, Chongqing the Seventh People's Hospital, Chongqing, China, [2] Department of Respiratory and Critical Care, Chongqing the Seventh People's Hospital, Chongqing, China

Chronic obstructive pulmonary disease (COPD) is a common obstructive respiratory disease characterized by persistent respiratory symptoms and limited airflow due to airway obstruction. The present study investigates the distribution characteristics of respiratory tract flora in both frequent and infrequent exacerbators of COPD. The 16S sequencing technique was adopted to differentiate the inherent differences of respiratory tract flora between frequent exacerbators and infrequent exacerbators. Additionally, cell counting kit 8 (CCK8), lactate dehydrogenase (LDH) test, flow cytometry, enzyme-linked immunosorbent assay (ELISA), and western blot were carried out in human bronchial epithelial cells cultured *in vitro* and the regulatory effects of differential flora were verified. The results revealed that the observed species index, Chao1 index, and the ACE estimator of COPD frequent exacerbators were markedly higher than those of COPD infrequent exacerbators. The top five strains of COPD frequent exacerbators included g_Streptococcus (15.565%), g_Prevotella (10.683%), g_Veillonella (6.980%), g_Haemophilus (5.601%), and g_Neisseria (4.631%). Veillonella parvula generated obvious cytotoxicity and substantially reduced the activity of human bronchial epithelial cells ($p < 0.01$). Furthermore, the results of flow cytometry indicated that the proportion of human bronchial epithelial cells in both the S phase and G2 phase decreased following Veillonella parvula treatment indicated that Veillonella parvula inhibited cell proliferation. Meanwhile, being treated using Veillonella parvula, the expressions of interleukin-1 (IL-1), IL-6, Tumor Necrosis Factor α (TNF-α), and p-nuclear factor kappa B (NF-κB) of the cells were increased markedly ($p < 0.01$). Taken together, the current research demonstrated that the relative abundance of Veillonella in COPD frequent exacerbators was higher than that of infrequent exacerbators. Veillonella parvula activated the inflammatory pathway, ultimately destroyed the cell viability, and greatly impaired the activity of human bronchial epithelial cells, thereby inhibiting cell proliferation.

Keywords: COPD frequent exacerbators, COPD infrequent exacerbators, bacterial flora analysis, Veillonella parvula, COPD

Edited by:
Fu Wang,
Xi'an Jiaotong University, China

Reviewed by:
Jian Xu,
Chongqing Medical University, China
Yuanxue Yi,
Army Medical University, China
Deyu Zuo,
Chongqing Hospital of Traditional Chinese Medicine, China

***Correspondence:**
Li Ke
Like1234511@outlook.com

Specialty section:
This article was submitted to Precision Medicine, a section of the journal Frontiers in Medicine

Received: *17 November 2021*
Accepted: *15 December 2021*
Published: *20 January 2022*

Citation:
Ke L, Chen L, Yaling Y, Can G, Jun L and Chuan Z (2022) Investigation on the Pathological Mechanism of Frequent Exacerbators With Chronic Obstructive Pulmonary Disease Based on the Characteristics of Respiratory Flora. Front. Med. 8:816802. doi: 10.3389/fmed.2021.816802

INTRODUCTION

Chronic obstructive pulmonary disease (COPD) has emerged as the third most common cause of death globally, and it is estimated to become the fifth financially burdened disease (1, 2). The acute exacerbation of COPD is mainly responsible for this burden. Clinically, patients with COPD are divided into frequent exacerbators and infrequent exacerbators. The former is defined as those who suffer from twice of exacerbated episodes within 12 months, and the morbidity and mortality are higher than infrequent exacerbators (3, 4). Increasing evidence has indicated that COPD frequent exacerbation is intimately associated with the unbalanced normal bacterial flora colonization in the respiratory tract, but there are obvious regional differences in the distribution characteristics of the bacterial flora, and the relationship between the airway flora and the phenotype of exacerbation is unclear (5–7).

The next-generation sequencing technique is available for simultaneous sample detection of thousands of bacteria covered in the database (5–7). The 16S sequencing refers to selecting one or several variant regions of 16S rDNA, selecting universal primers for PCR amplification of environmental sample microorganisms, then performing high-throughput sequencing on the PCR products, and comparing the obtained sequencing data with the existing 16S rDNA database. The core is species analysis, such as the types of microorganisms, the relative abundance of different species, the species differences between different groups, and system evolution. Researchers have introduced this approach to detect respiratory disease specimens obtained from the respiratory tract, hoping to discover the correlation between the distribution of bacterial flora and the occurrence and development of diseases (8, 9). These studies have covered disorders of bronchial asthma, cystic fibrosis, and COPD, which contributes a lot in broadening our recognition and understanding of respiratory etiology. Results of bacterial flora analysis have revealed that Streptococcus, Prevotella, and Haemophilus influenzae are common bacteria in the respiratory tract (10). Fusobacterium and Pseudomonas are also colonized in the lower respiratory tract (11, 12). Based on existing studies, during the period of COPD exacerbation, the α-diversity of the flora decreases compared with the stable period, and the ratio of Proteobacteria/Firmicutes increases. Moreover, during the period of acute exacerbation, the relative abundance of Moraxella is significantly increased, whereas Haemophilus presents no significant increase compared with the stable period (13–15). Investigation on respiratory microbiome began in 2010 and remains in an early stage. Moreover, related data are insufficient globally, most research has limited samples, and the research conducted in China is even rarer. Therefore, many biomarkers are still under the stage of identification and more further cohort data from different regions are to be validated (16).

This project explores the distribution characteristics of the respiratory tract flora in both COPD frequent exacerbators and infrequent exacerbators in the local region and to identify the inherent differences in the respiratory flora between COPD frequent exacerbators and infrequent exacerbators. We attempted to determine the risk-related target flora with COPD frequent exacerbators and verified in human bronchial epithelial cells cultured *in vitro*. The present project was expected to open up a novel approach for the prevention and treatment of COPD frequent exacerbators.

MATERIALS AND METHODS

Clinical Data

This research was a prospective and observational study, which was approved and documented by the Medical Ethics Committee of Chongqing the Seventh People's Hospital (approval number: 202019). COPD frequent exacerbators (48 cases) and COPD infrequent exacerbators (32 cases) were recruited from Chongqing Seventh People's Hospital, and sputum samples were collected.

Collection of Sputum Specimens

The collection procedures were strictly performed following the aseptic operation requirements. The surface of fresh sputum was removed using a sterile cotton swab to avoid being mixed with other sundries. The inner layer of the sputum sample was obtained and transferred into a sterile cryotube using a new cotton swab. Immediately after sample collection, the specimens were stored in a refrigerator at −20°C, transferred to the laboratory within 24 h, and kept in a refrigerator at −80°C for later use.

DNA Extraction and Purification of Bacterial Flora in Sputum Samples

A QlAamp DNA Stool Mini Kit (Qiagen Company, Germany) was employed to extract DNA, and a Qubit Fluorometer Kit (Life Technologies, Carlsbad, CA, USA) was adopted to detect DNA concentration, and 1% agarose gel electrophoresis was performed to detect sample integrity. Taq enzyme (Sangon Biotech, Shanghai, China) was used to amplify selected regions (V3–V4 regions), PCR primers were 338F (5'-ACTCCTACGGGAGGCAGCA-3') and 806B (5'-GGACTACHVGGGTWTCTAAT-3'). After passing the 1% agarose gel electrophoresis test, the samples were delivered for high-throughput sequencing of 16S analysis of bacteria in the laboratory.

High-Throughput Sequencing of 16S Analysis of Bacteria

Illumina Hiseq 2500 (Illumina, San Diego, CA, USA) sequencing platform was employed for PE250 library construction and sequencing, using pair-end sequencing (Pair-end) method, each sequence generates 250 reads from the 5′ and 3′ end. The raw data obtained for sequencing were trimmed and filtered before being applied for analysis, and the low-quality reads were filtered out and only valid data were retained. The reads were spliced into Tags using overlapped valid data, and the target fragments were obtained by further filtering. Using 97% similarity, the Tags were clustered into operational taxa (OTU) and compared with the 16S database of known species for OTU species annotation, and the community composition of each sample was subsequently obtained.

Bacterial Flora Analysis Method

QIIME2 software (Version 2.0.2, https://qiime2.org/) was used to analyze the microbiome sequence data. The 16S rRNA representative sequence was constructed using the silva-138-99 (QIIME 2 2020.8 Species Annotation Database) provided by SILVA (https://www.arb-silva.de/) amplicon database with a similarity threshold of 97%. To remove the potential signals in the contaminants, we removed the analytical taxa with a relative abundance of 10% in the sample and the OTUs with a total abundance of 1 in the sample from the analytical taxa. The remaining reads were aggregated into 3,942 OTUs.

Alpha diversity used Observed species index (the actual number of OTUs observed), Chao1 index (estimated total number of OTUs contained in the sample), ACE index (estimated total number of OTUs contained in the sample), Shannon index (estimated microbial community diversity), and The Simpson index (estimated microbial community diversity) to compare the Alpha-diversity of the microbial community in the HIV group and the Norma group. Pie charts and histograms were used to show the proportion of genus-level microorganisms in the sample, that is, the relative abundance of microorganisms. Linear discriminant analysis effect size (LEfSe) was a method of discovering biomarkers to determine the best characteristic genus for each study group. The LEfSe score measures and analyzes the consistency of the relative abundance differences of taxa in each group. The higher the score, the higher the consistency. We considered that the groups with Linear Discriminant Analysis (LDA) score >4 and $p < 0.05$ were significant. The different species at the genus level and the provided physiochemical factors were applied to calculate the Spearman correlation between the species and the physiochemical factors. R software (4.1.0, https://www.r-project.org/) psych package/The reshape2 package/ggplot2 package was used to plot heat maps to reveal the essential connection between both aspects.

Culture of Human Bronchial Epithelial Cells

Human bronchial epithelial cells were purchased from American Type Culture Collection and cultured in a complete medium containing 10% fetal bovine serum (FBS) and 1% penicillin-streptomycin. The cells were categorized into a control group and a model group. Following 24 h of inoculation, the cells in the model group were added 50 μl of active Veillonella parvula (ATCC #10790) and 50 μl of bacteria through high-temperature sterilization to the control group. After 24 h, the effect of Veillonella parvula on human bronchial epithelial cells was determined.

Cell Counting Kit (CCK8) Assay

The cells were placed in a 96-well plate with 100 μl per well, and there were three multiple wells in each group. Cell modeling and grouping were subsequently managed as per the abovementioned conditions, and the cells were placed in a carbon dioxide incubator. After 24 h of incubation, the 96-well plate was taken out and 10 μl of CCK8 solution (AC11L054, Life-iLab, China) was supplemented to each well. The culture plate was kept in the incubator for 4 h and then terminate the culture. The absorbance of each well was determined at 450 nm using an enzyme-linked immunometric meter.

Lactate Dehydrogenase (LDH Detection)

After the stimulation, the cell culture plate was centrifuged at 400 g for 5 min in a multi-well plate centrifuge. The supernatant was aspirated as much as possible. Subsequently, 150 μl of the LDH release reagent was added, which was supplied with a 10-fold PBS diluted kit, mixed well by moderately vibrating the culture plate, and then continued to incubate in the cell culture incubator for 1 h. Subsequently, the cell culture plate was centrifuged at 400 g for 5 min using the multi-well plate centrifuge. In total, 120 μl of the supernatant was obtained from each well, added to the corresponding well of a new 96-well plate, and proceeded to sample determination instantly. Of 60 μl LDH detection working solution (C0016, Beyotime, China) was supplied to each well, mixed evenly, incubated at 25°C in the dark for 30 min, and measured the absorbance at 490 nm. Cytotoxicity or mortality (%) = (absorbance of treated samples – absorbance of samples in control hole)/(absorbance of cells with maximum enzyme activity – absorbance of samples in control hole) × 100.

Detection of Cell Cycles by Flow Cytometry

The cells were cultured in a 6-well plate. When the cell growth was reached 60–70%, they were aspirated into a 1.5 ml centrifuge tube after cell treatment and centrifuged at 2,000 rpm for 5 min. The cells were rinsed twice with PBS and centrifuged at 2,000 rpm for 5 min. Then, the cells were added in 1 ml of pre-cooled 70% ethanol in an ice bath, blown gently to mix well, and fixed at 4°C for 2 h. The cells were precipitated after centrifugation at about 1,000 rpm for 5 min, added about 1 ml of ice-cooled PBS for cell resuspension, centrifuged again, and carefully aspirated the supernatant. Of 0.5 ml propidium iodide staining solution was added to each tube with sample cells. Cell precipitation was suspended slowly and fully, warm bathed at 37°C for 30 min, and kept away from light. After that, the cells were stored either at 4°C or kept in an ice bath away from light. It is advisable to perform flow cytometry within 24 h after staining. Red fluorescence and light scattering were subjected to flow cytometry at an excitation wavelength of 488 nm.

Enzyme-Linked Immunosorbent Assay (ELISA)

The interleukin-1 (IL-1β), IL-6, and Tumor Necrosis Factor α (TNF-α) ELISA kits (RX106152H, RX106126H, RX104793H, Ruixin BIO, China) were purchased from Ruixin Biotech, and the tests were carried out as per product instructions of use. The required plates were prepared firstly, marked standard wells and sample wells, added 50 μl of standard products of different concentrations to each standard wells and 50 μl of the sample to be tested to the sample wells. Detection antibody labeled by horseradish catalase 100 μl was supplemented to each standard solution well and sample well, respectively. Following the plate was blocked with sealing membrane, it was incubated at 37°C for 60 min. After the incubation was completed, discarded the liquid of the wells, dried it on a piece of absorbent paper, filled each well with washing solution, let stand for 1 min, discarded the washing solution, dried it again on a piece of absorbent paper, and repeated five times. Following the addition of substrates A and B 50 µl, respectively, to each well, incubation was performed at 37°C for 15 min in dark. When the incubation was completed, a termination solution at a quantity of 50 µl was added to each well. optical density (OD) value of each well was measured at 450 nm wavelength within 15 min.

Western Blot (WB) Detects the Expressions of p-Nuclear Factor Kappa B (NF-κB) and NF-κB

Prepared gel was taken out from a refrigerator at 4°C and placed in an electrophoresis tank. Of 500 µg, total proteins were taken from each sample and mixed with 5 × Sodium dodecyl sulfate (SDS) loading sample buffer at a ratio of 4:1. The concentration of protein in the mixture was about 3.3 µg/µl, and the proteins were denatured by metal bath heating at 100°C for 6 min. The denatured total proteins of 60 g were selected for sample loading. After running at 80 V using spacer gel, the voltage was switched to 120 V and waited until the bromophenol orchid just covered the bottom of the gel plate without spilling out. The clip was loosed to level at the black side horizontally and placed sponge pad, filtering paper, gel, polyvinylidene fluoride (PVDF) membrane, filtering paper, and sponge pad in turn. The current was set at a constant 250 mA for 30 min. The membrane was taken out, marked well on both sides, washed in tris buffered saline with tween (TBST) for 1 min, and sealed with 5% skimmed milk blocking buffer at room temperature for 1 h. After sealing, the membrane was washed with TBST three times, 5 min each time. Primary antibody was diluted with primary antibody diluent at 1:1,000, incubated overnight at 4°C, and rinsed with TBST for three times, 10 min each. Secondary antibody was diluted using the blocking buffer, incubated for 1.0 h at room temperature, and rinsed with TBST for three times, 10 min each time. The ECL exposure solution was mixed with liquid A and B at a 1:1 rate and then evenly covered on the entire membrane. After reaction for 1 min, it was loaded in the exposure meter for detection. Antibodies used were as follows: p-NF-κB (3033T, CST, Danvers, MA, USA); NF-κB (10745-1-AP, Proteintech, Rosemont, IL, USA); GAPDH (A19056, Abclonal, China); HRP-Goat-anti-Rabbit (AS014, Abclonal, China).

Statistical Analysis

SPSS 22.0 statistical analysis software was employed for data analysis, and the measurement index was expressed as mean ± SEM. A *t*-test was adopted for the data in conformity to normal distribution. The comparison of categorical count indexes was tested by the χ^2 tests or Fisher's exact probability method. The hypothesis testing used two-sided testing to obtain test statistics and their corresponding *p* values, and $p < 0.05$ was considered as the standard of significant difference.

RESULTS

Analysis of Microbial Diversity in Sputum Samples of COPD Frequent Exacerbators and Infrequent Exacerbators

This study analyzed the sputum samples obtained from 48 COPD frequent exacerbators and 32 cases of infrequent exacerbators using the 16S sequencing technique. A total of 8,741,237 reads were collected from all samples, and 4,440 OTUs were obtained by clustering. Based on the dilution curve, the curve line had a tendency of going stable and the quantity of sequencing data was sufficient. It was therefore that the sequencing results of this project could reflect most of the microbial diversity information in the samples (**Figure 1A**). QIIME software was applied to calculate the index values of Alpha diversity in both groups of samples, and it was found that the Observed species index, Chao1 index, and ACE index of COPD frequent exacerbators were markedly higher than COPD infrequent exacerbators ($p < 0.05$; **Figure 1B**).

Beta Analysis of Microbial Diversity in Samples

Subsequently, a Beta analysis of microbial diversity was performed. The results revealed that there were significant differences in the variety and quantity of microorganisms between COPD frequent and infrequent exacerbators ($p < 0.05$; **Figure 2**).

Clustering of Bacterial Species

Community compositions of both sample groups were analyzed, and there were 30 primary bacterial species identified in the samples of the two groups (**Figure 3A**). Comparison of relative abundance of intestinal dominant flora and species clustering between the two groups at the genus level, it was found that the top five strains of COPD frequent exacerbators were g_Streptococcus (15.565%), g_Prevotella (10.683%), g_Veillonella (6.980%), g_Haemophilus (5.601%), and g_Neisseria (4.631%; **Figure 3B**). The first five strains of COPD infrequent exacerbators included g_Streptococcus (17.509%), g_Prevotella (10.6593%), g_Neisseria (5.925%), g_Pseudomonas (4.63%), and g_Haemophilus (4.382%; **Figure 3C**).

Next, LDA Effect Size (LEfSe analysis) was performed to estimate the abundance influence of each strain on the effect of difference and to identify which colonies had a significant difference in sample classification. **Figure 4A** presents a clustering tree. Red represents the group of COPD frequent exacerbators, green represents the group of COPD infrequent exacerbators, and nodes of different colors represent the importance of the microbiome in the represented group. The yellow nodes indicate that the microbiota did not play an important role in both groups. Similarly, the relative abundance of Veillonella in COPD frequent exacerbators was higher than that of COPD infrequent exacerbators (**Figure 4B**).

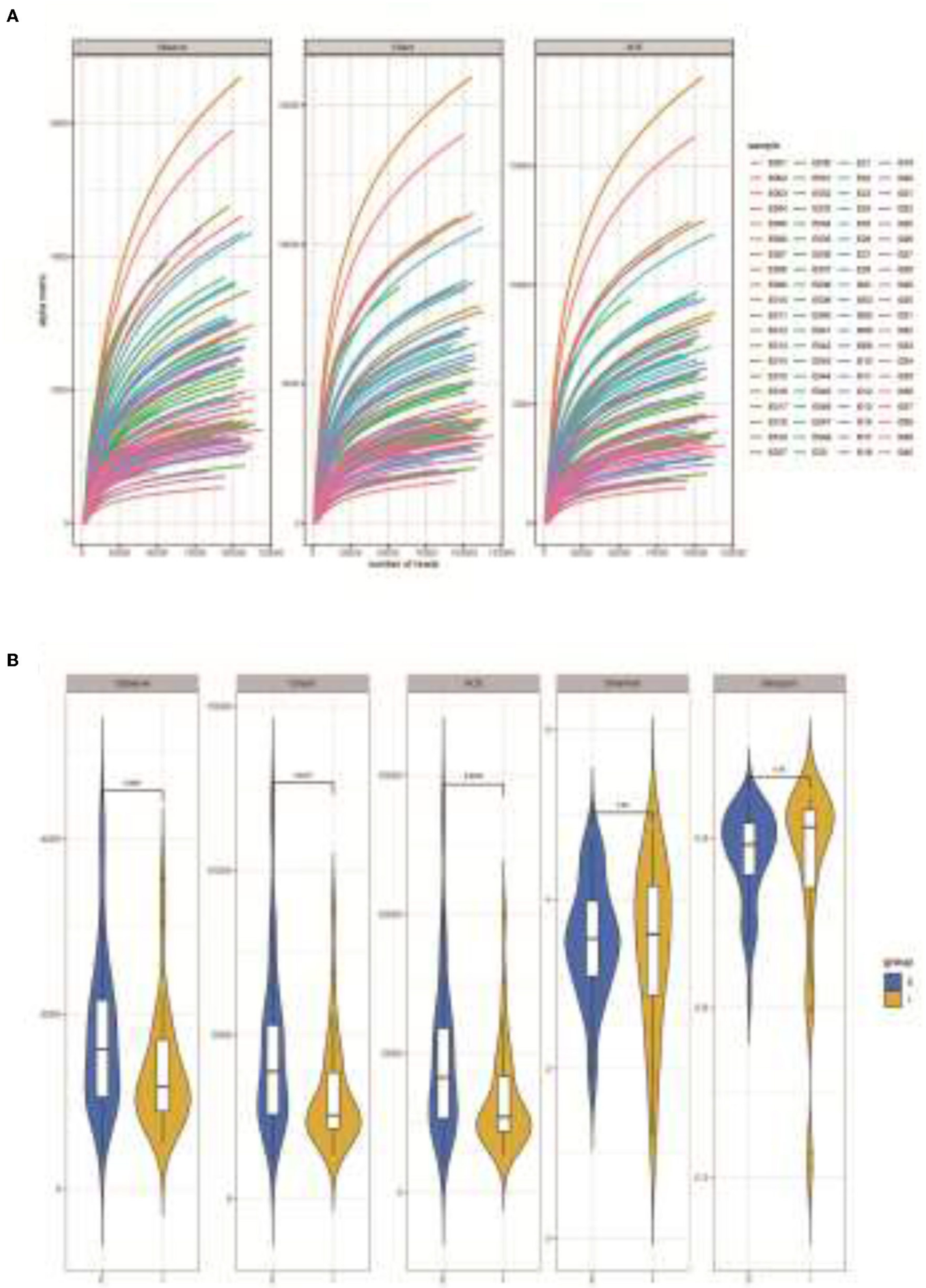

FIGURE 1 | Analysis of microbial diversity in sputum samples of COPD frequent exacerbators and infrequent exacerbators. **(A)**, 16S sequencing dilution curve results. **(B)**, QIIME software was used to calculate the Alpha diversity index of both sample groups. E represented COPD frequent exacerbators; I represented COPD infrequent exacerbators. COPD, chronic obstructive pulmonary disease.

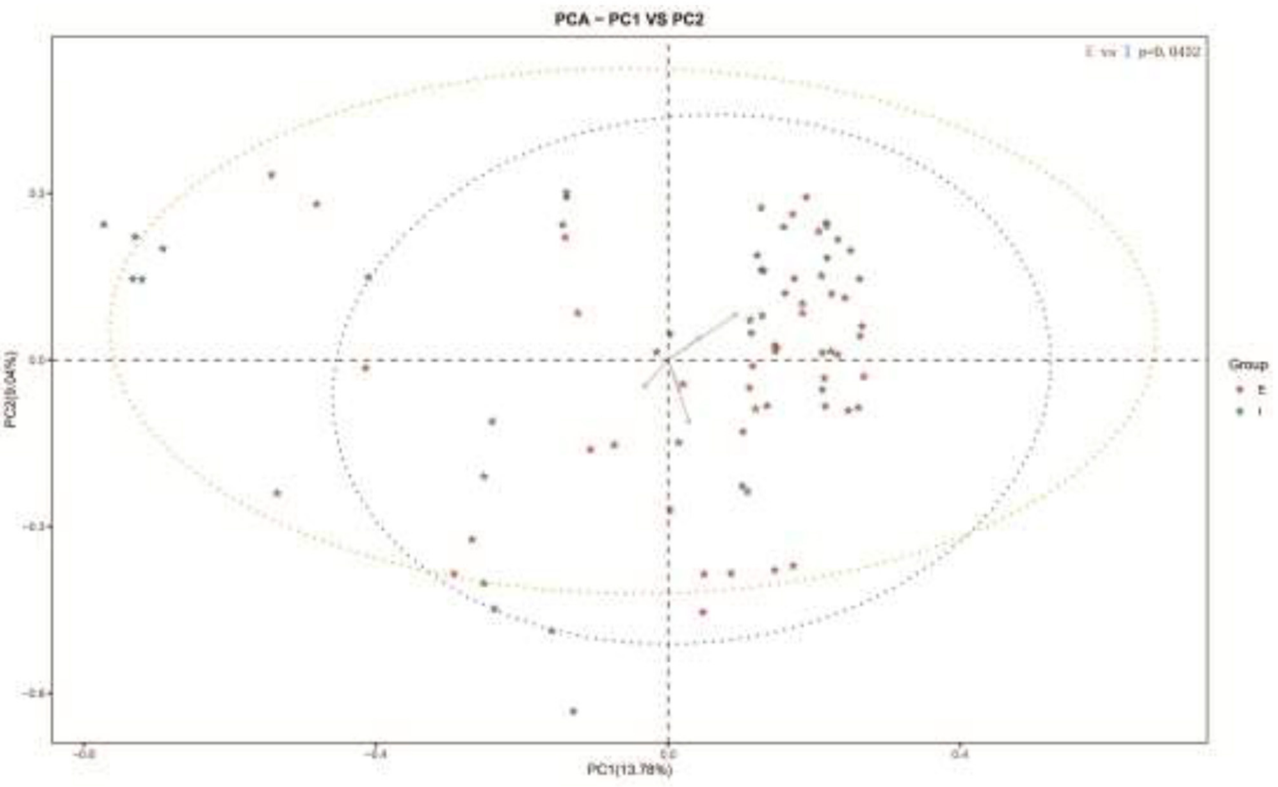

FIGURE 2 | Beta analysis of microbial diversity in sputum samples of COPD frequent exacerbators and COPD infrequent exacerbators. E represented COPD frequent exacerbators; I represented COPD infrequent exacerbators. COPD, chronic obstructive pulmonary disease.

The Regulatory Effect of Veillonella on the Activity of Human Bronchial Epithelial Cells

Subsequently, we added Veillonella parvula to human bronchial epithelial cells cultured *in vitro* (**Figure 5A**) and determined the regulatory effect of Veillonella parvula on human bronchial epithelial cells. The results indicated that Veillonella parvula markedly reduced the activity of human bronchial epithelial cells ($p < 0.01$; **Figure 5B**). The LDH content was increased substantially, indicating that Veillonella parvula produced apparent cytotoxicity (**Figure 5C**), causing cell membrane rupture and cell death. Furthermore, the results of flow cytometry indicated that the proportion of human bronchial epithelial cells in both the S phase and G2 phase decreased following Veillonella parvula treatment, indicating that Veillonella parvula inhibited cell proliferation (**Figure 5D**).

Veillonella Parvula Regulates the Expressions of Inflammatory Factors

To clarify the effect of Veillonella parvula on the expressions of cell inflammatory factors, ELISA and western blot assays were performed to detect the expressions of inflammatory factors. After Veillonella parvula treatment, the expressions of IL-1, IL-6, and TNF-α in cells were increased greatly ($p < 0.01$; **Figures 6A–C**), and the expression of p-NF-κB was increased significantly (**Figures 6D–F**), indicating that Veillonella parvula activated the inflammatory pathway and ultimately destroyed cell viability.

DISCUSSION

The mucosal epithelium of the respiratory tract is the first natural barrier of the body and the external environment, which is the first natural barrier against microbial infections. COPD is a frequent obstructive respiratory disease characterized by persistent respiratory symptoms and limited airflow due to airway obstruction (17, 18). As COPD has been reported as the third leading cause of death worldwide since 2020, the treatment of COPD acute exacerbators is of vital importance to the standardized management, prevention, and control of COPD (19). Bacterial or viral respiratory infections are the principal factor leading to acute exacerbation of COPD victims. This project aimed to study the distribution characteristics of flora in the respiratory tract among frequent and infrequent exacerbators in this region and to distinguish the inherent differences of flora in the respiratory tract between frequent and infrequent exacerbators. This study revealed that the Observed species index, Chao1 index, and ACE index of COPD frequent exacerbators were markedly higher than those of COPD infrequent exacerbators. The top five strains of COPD frequent exacerbators included g_Streptococcus (15.565%), g_Prevotella

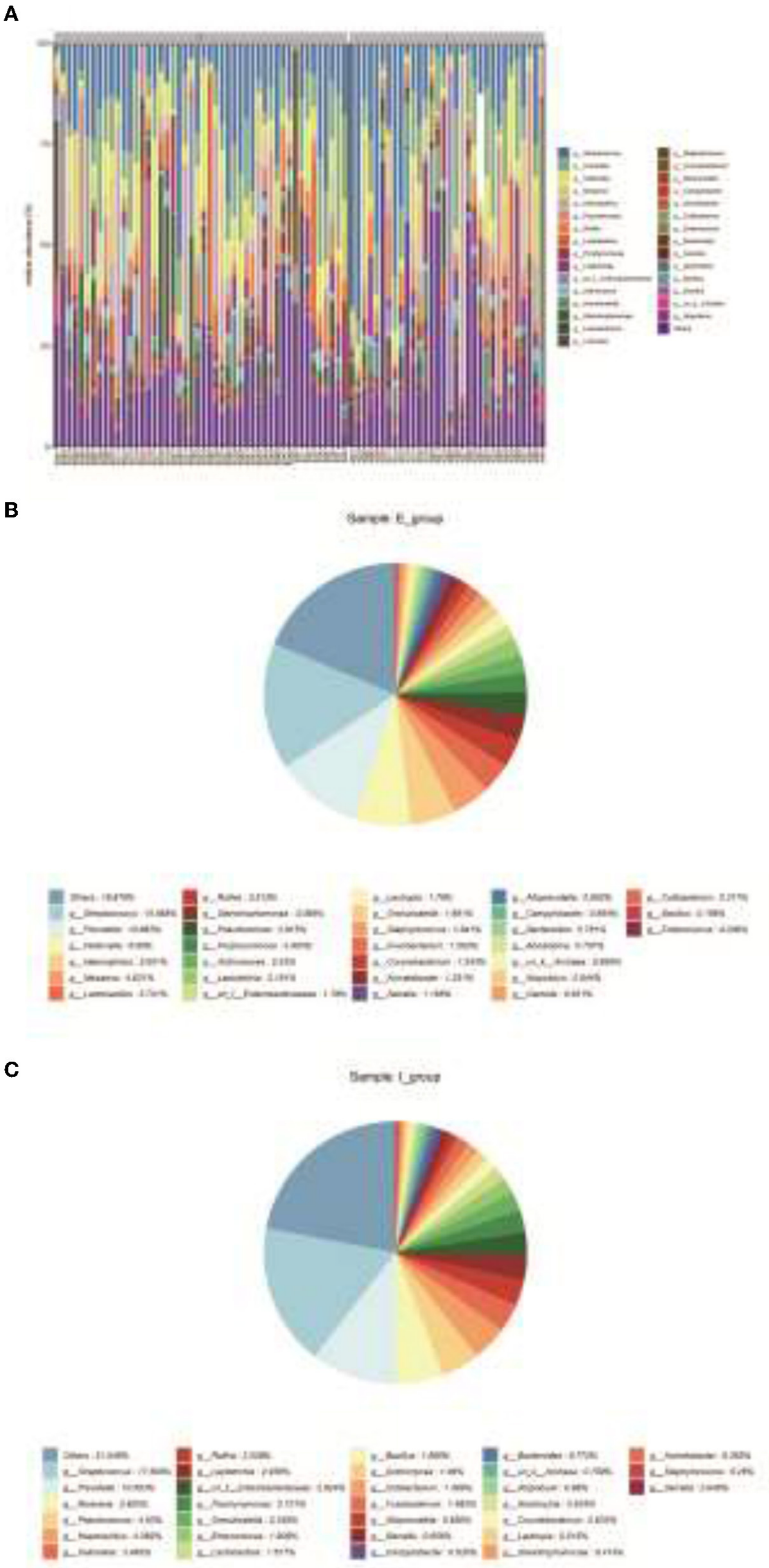

FIGURE 3 | Clustering of bacterial species. **(A)**, Community compositions of both sample groups were analyzed and there were 30 primary bacterial species identified in the samples of the two groups. **(B)**, Relative abundance of intestinal dominant flora and cluster analysis of species in COPD frequent exacerbators at the genus level. **(C)**, Relative abundance of intestinal dominant flora and cluster analysis of species in COPD infrequent exacerbators at the genus level. E represented COPD frequent exacerbators; I represented COPD infrequent exacerbators. COPD, chronic obstructive pulmonary disease.

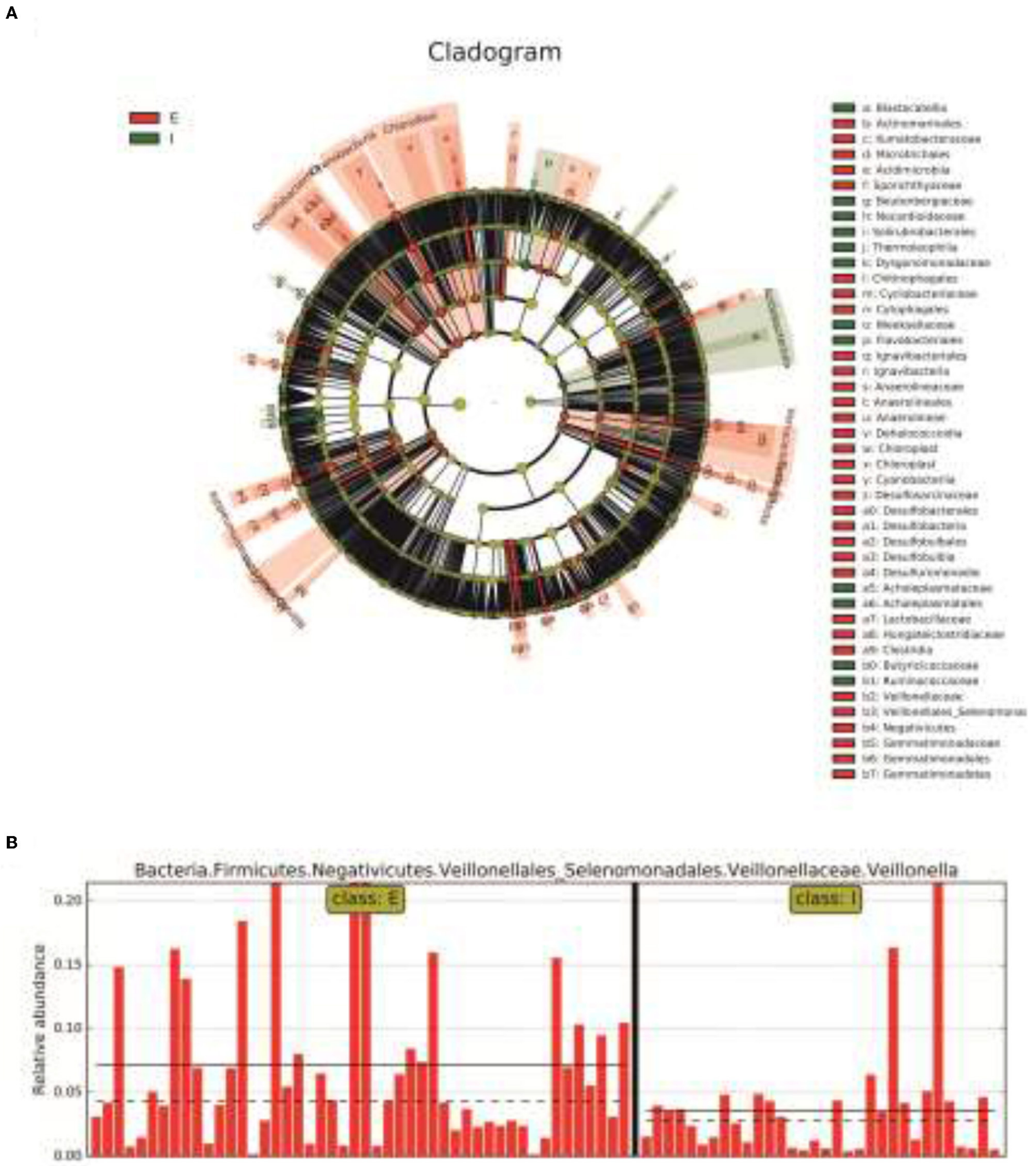

FIGURE 4 | The LEfSe analysis was used to estimate the abundance influence of each strain on the difference. **(A)**, Cluster tree analysis. Red represents the group of COPD frequent exacerbators, green represents the group of COPD infrequent exacerbators, and nodes of different colors represent the importance of the microbiome in the representated group. The yellow nodes indicate the microbiota that did not play an important role in both groups. **(B)**, The abundance analysis of Veillonella in COPD frequent exacerbators and COPD infrequent exacerbators. E represented COPD frequent exacerbators; I represented COPD infrequent exacerbators. LEfSe, linear discriminant analysis effect size; COPD, chronic obstructive pulmonary disease.

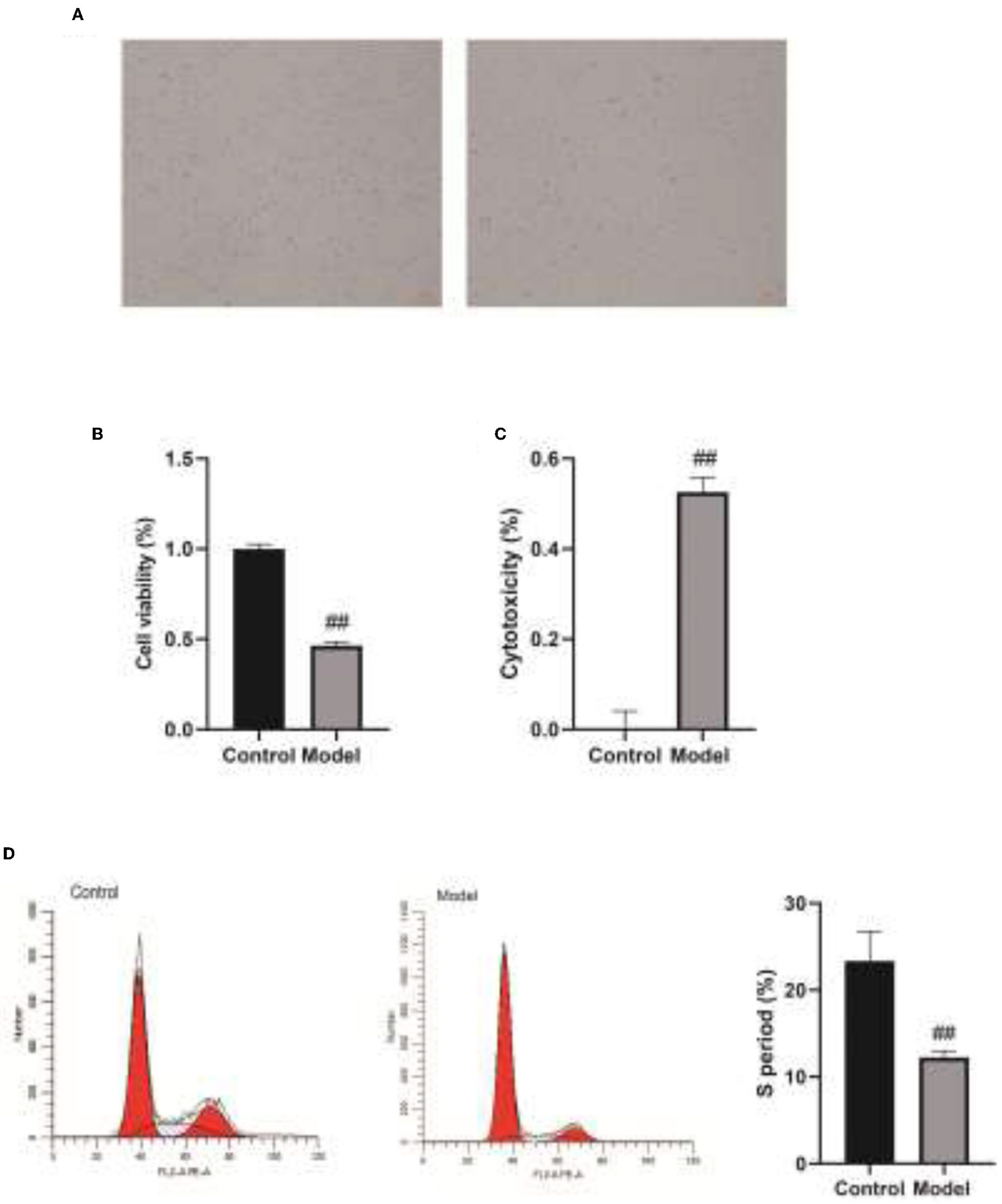

FIGURE 5 | The regulatory effect of Veillonella on the activity of human bronchial epithelial cells. **(A)**, Human bronchial epithelial cells cultured *in vitro*. **(B)**, Cell viability detected by CCK8. **(C)**, LDH content determination. **(D)**, Cell cycles detection by flow cytometry. ##, $p < 0.01$. LDH, lactate dehydrogenase; CCK8, cell counting kit 8.

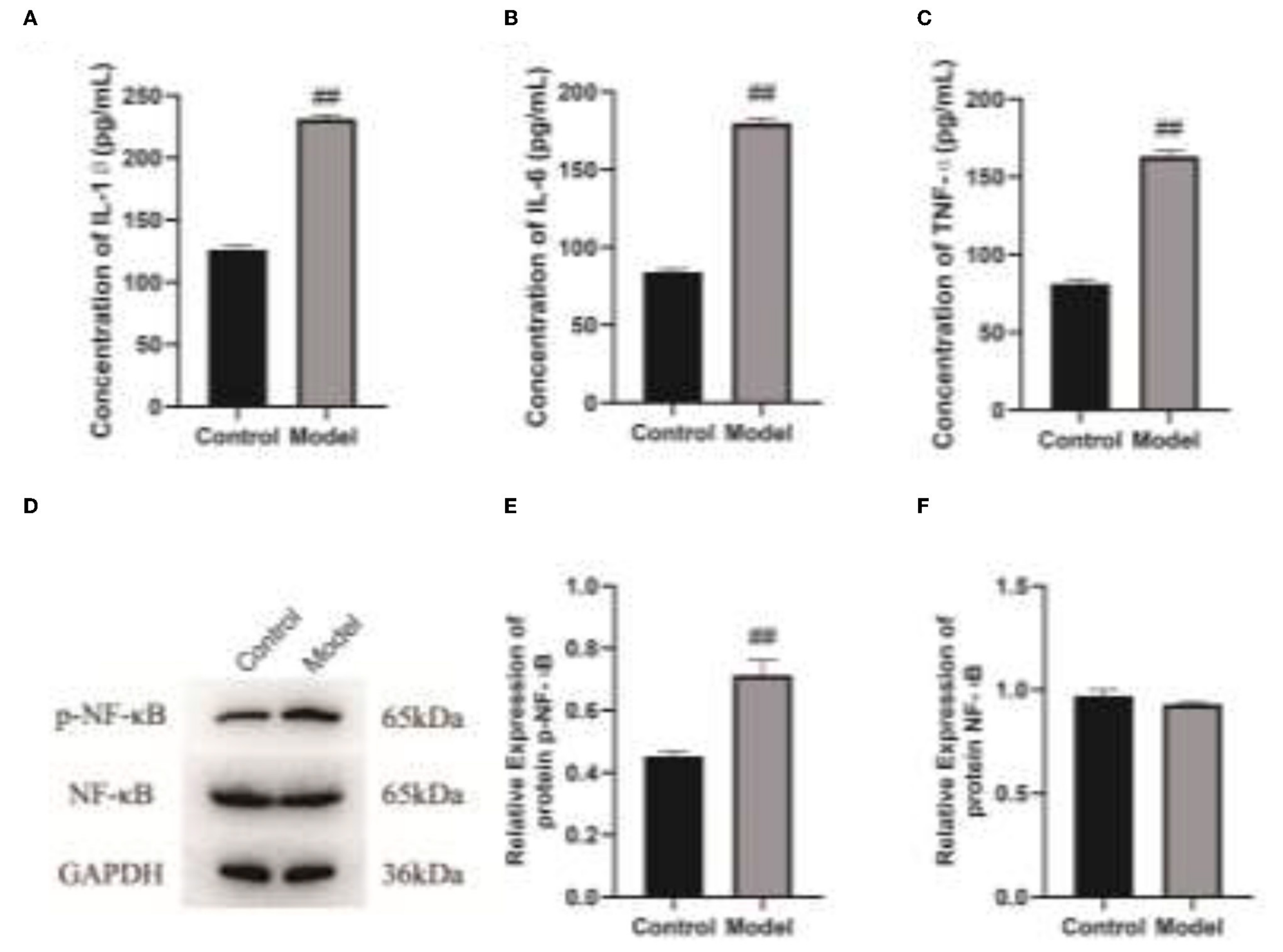

FIGURE 6 | Veillonella parvula regulates the expressions of inflammatory factors. **(A–C)**, Expressions of IL-1, IL-6, and TNF-α detected by ELISA. **(D)**, The expressions of NF-κB and p-NF-κB detected by Western blot. **(E,F)**, Gray value analysis of NF-κB and p-NF-κB proteins. ## $p < 0.01$. IL-6, interleukin-L; TNF-α, Tumor Necrosis Factor α; ELISA, enzyme-linked immunosorbent assay.

(10.683%), g_Veillonella (6.980%), g_Haemophilus (5.601%), and g_Neisseria (4.631%). We found that the relative abundance of Veillonella in COPD frequent exacerbators was higher than that of COPD infrequent exacerbators.

After the balance of the flora is broken, it will lead to changes in the local environment of the tissue. In addition, the increase or decrease of some flora can cause host infection and some other diseases. After the bacteria invaded tissue cells, they could replicate and survive in the cells. Meanwhile, some bacteria activated the cellular anti-apoptotic pathway, thereby evading immunity elimination of the host, which could directly induce the death of host cells and aggravate the damage of tissue cells. Veillonella represents an anaerobic gram-negative coccus, which can parasitize in the oral cavity, gastrointestinal tract, and female reproductive tract (20). Thirteen species of this genus have been identified, of which six species have been isolated from the human oral cavity. It has been reported that Veillonella is a copolymer with streptococcus (21). It was previously considered non-pathogenic and rarely caused serious infections. However, in recent years, there have been increasing reports of human infections in immunocompromised individuals. Statistics of the literature from 1976 to October 2015 have reported 31 cases of human infection with Veillonella. Of these cases, five cases were musculoskeletal infections caused by Veillonella parvula, such as four spinal infections. Additional reports also revealed cases of extramembranous abscess in patients with sclerocarcinoma affected by Veillonella parvula (22, 23). Veillonella parvula seems to be an opportunistic pathogen that affects immunocompromised patients. The present study indicated that the addition of Veillonella parvula to human bronchial epithelial cells cultured *in vitro* markedly reduced the viability of human bronchial epithelial cells. The LDH content in the cells was increased significantly, indicating that Veillonella parvula generated obvious cytotoxicity, which caused cell membrane rupture and cell death.

In addition, some studies have confirmed that COPD acute exacerbators are greatly affected by the persistent inflammation in the airway induced by bacterial infection (24, 25). Statistics results have indicated that the expression of IL-1β in COPD patients is increased, and the expression level of IL-1β is positively correlated with the increase of airway neutrophils and the decline of lung function index. The level of IL-1β in the airway (sputum) is recognized as a bacteria-associated biomarker of COPD acute exacerbators (26). Proteomic analysis of the sputum samples obtained from patients with COPD revealed that the proteomics characteristics of IL-1β-related sputum samples were identified. It also confirmed that the expressions of TNF-α and IL-6 were elevated and regulated by the IL-1β pathway. Elevated IL-1β and serum IL-6 expression levels in patients with COPD can activate the IL-1β-system inflammatory axis pathway and pose an increased risk for COPD frequent exacerbators (27, 28). The results of this study indicated that after Veillonella parvula treatment, the expressions of IL-1, IL-6, and TNF-α in the cells were elevated markedly, and the expression of p-NF-κB was increased substantially, indicating that Veillonella parvula activated the inflammatory pathway and ultimately destroyed cell viability. The findings also implied that Veillonella parvula could aggravate the response of airway inflammation, thereby promoting the susceptibility to COPD acute exacerbation.

Currently, the high-throughput sequencing of 16S amplicon is mainly introduced for the research on respiratory flora with a large sample size (29–31). This technique is only available for accurately identifying all bacterial components to the genus level. Luckily, the approach of metagenomic analysis can accurately determine the components of the microbial population, identify the functional areas of microorganisms combined with the macro transcriptome approach, and explore whether the entire microbial community can affect the metabolism of other microorganisms and/or hosts by generating signal molecules through the expression of specific genes, thereby further recognition of the signal transmission on the promotion of COPD occurrence and development. In the study of the microbiome, the concept of the brain-gut axis has been recognized by the public. COPD represents a systemic inflammatory disease of the lung affected by inflammation. The permeability of both the respiratory tract and intestinal mucosa may increase, which also provides the possibility for the migration or circulation of lung and intestinal flora. The previously described concerns will be potential research trends of respiratory flora in the future. This study has only verified the regulatory function of Veillonella parvula in cultured cells *in vitro* and has not been able to verify the function of more strains, nor has it been further verified in model animals. We know that the regulatory role of intestinal flora should be extensive, and only by understanding the regulatory network can we further formulate clinical medication and treatment plans. In future research, we will further verify the function of differentially expressed flora at the animal level and explore the possibility of improving the efficacy of clinically commonly used drugs or new drugs on COPD.

CONCLUSION

The present study revealed that the relative abundance of Veillonella in COPD frequent exacerbators was higher than that of COPD infrequent exacerbators. Veillonella parvula activated the inflammatory pathway, ultimately destroyed the cell viability, and greatly impaired the activity of human bronchial epithelial cells, thereby inhibiting cell proliferation.

DATA AVAILABILITY STATEMENT

The data are deposited in https://submit.ncbi.nlm.nih.gov/subs/sra/, accession number SUB10905251.

ETHICS STATEMENT

This research was a prospective and observational study, which was approved and documented by the Medical Ethics Committee of Chongqing the Seventh People's Hospital. The patients/participants provided their written informed consent to participate in this study.

AUTHOR CONTRIBUTIONS

LK, LC, and YY performed the experiment and collected the data. GC and LJ analyzed and interpreted the data. LK and ZC participated in writing this manuscript. All authors conceived and designed the study and approved this final manuscript.

FUNDING

This work was funded by Chongqing Science and Technology Bureau of Banan District (No. 2020SHSY08).

SUPPLEMENTARY MATERIAL

The Supplementary Material for this article can be found online at: https://www.frontiersin.org/articles/10.3389/fmed.2021.816802/full#supplementary-material

REFERENCES

1. Tiew PY, Jaggi TK, Chan L, Chotirmall SH. The airway microbiome in COPD, bronchiectasis and bronchiectasis-COPD overlap. *Clin Respir J.* (2021) 15:123–33. doi: 10.1111/crj.13294
2. Agusti A, Vogelmeier C, Faner R. COPD 2020: changes and challenges. *Am J Physiol Lung Cell Mol Physiol.* (2020) 319:L879–83. doi: 10.1152/ajplung.00429.2020
3. Matera MG, Cazzola M, Page C. Prospects for COPD treatment. *Curr Opin Pharmacol.* (2021) 56:74–84. doi: 10.1016/j.coph.2020.11.003

4. Gordon A, Young M, Bihler E, Cheema T. COPD maintenance pharmacotherapy. *Crit Care Nurs Q.* (2021) 44:19–25. doi: 10.1097/CNQ.0000000000000336
5. Nowinski A, Korzybski D, Bednarek M, Goljan-Geremek A, Puscinska E, Sliwinski P. Does bronchiectasis affect COPD comorbidities? *Adv Respir Med.* (2019) 87:214–20. doi: 10.5603/ARM.2019.0059
6. Labaki WW, Han MK. Antibiotics for COPD exacerbations. *Lancet Respir Med.* (2017) 5:461–2. doi: 10.1016/S2213-2600(17)30166-2
7. Ghosh A, Boucher RC, Tarran R. Airway hydration and COPD. *Cell Mol Life Sci.* (2015) 72:3637–52. doi: 10.1007/s00018-015-1946-7
8. Chang WA, Tsai MJ, Jian SF, Sheu CC, Kuo PL. Systematic analysis of transcriptomic profiles of COPD airway epithelium using next-generation sequencing and bioinformatics. *Int J Chron Obstruct Pulmon Dis.* (2018) 13:2387–98. doi: 10.2147/COPD.S173206
9. Yeo J, Morales DA, Chen T, Crawford EL, Zhang X, Blomquist TM, et al. RNAseq analysis of bronchial epithelial cells to identify COPD-associated genes and SNPs. *Bmc Pulm Med.* (2018) 18:42. doi: 10.1186/s12890-018-0603-y
10. Connolly E, Hussell T. The impact of type 1 interferons on alveolar macrophage tolerance and implications for host susceptibility to secondary bacterial pneumonia. *Front Immunol.* (2020) 11:495. doi: 10.3389/fimmu.2020.00495
11. Rubbert-Roth A, Aletaha D, Devenport J, Sidiropoulos PN, Luder Y, Edwardes MD, et al. Effect of disease duration and other characteristics on efficacy outcomes in clinical trials of tocilizumab for rheumatoid arthritis. *Rheumatology.* (2021) 60:682–91. doi: 10.1093/rheumatology/keaa259
12. Garg N, Luzzatto-Knaan T, Melnik AV, Caraballo-Rodriguez AM, Floros DJ, Petras D, et al. Natural products as mediators of disease. *Nat Prod Rep.* (2017) 34:194–219. doi: 10.1039/C6NP00063K
13. Leitao FF, Takiguchi H, Akata K, Ra SW, Moon JY, Kim HK, et al. Effects of Inhaled Corticosteroid/long-acting beta-2 agonist combination on the airway microbiome of patients with COPD: a randomized controlled trial (DISARM). *Am J Respir Crit Care Med.* (2021) 204:1143–52. doi: 10.1164/rccm.202102-0289OC
14. Tiew PY, Dicker AJ, Keir HR, Poh ME, Pang SL, Mac AM, et al. A high-risk airway mycobiome is associated with frequent exacerbation and mortality in COPD. *Eur Respir J.* (2021) 57:2002050. doi: 10.1183/13993003.02050-2020
15. Liu H, Zheng D, Lin Y, Liu Z, Liang Z, Su J, et al. Association of sputum microbiome with clinical outcome of initial antibiotic treatment in hospitalized patients with acute exacerbations of COPD. *Pharmacol Res.* (2020) 160:105095. doi: 10.1016/j.phrs.2020.105095
16. Xia C, Rook M, Pelgrim GJ, Sidorenkov G, Wisselink HJ, van Bolhuis JN, et al. Early imaging biomarkers of lung cancer, COPD and coronary artery disease in the general population: rationale and design of the ImaLife (Imaging in Lifelines) study. *Eur J Epidemiol.* (2020) 35:75–86. doi: 10.1007/s10654-019-00519-0
17. Li S, Ma H, Gan L, Ma X, Wu S, Li M, et al. Cancer antigen-125 levels correlate with pleural effusions and COPD-related complications in people living at high altitude. *Medicine.* (2018) 97:e12993. doi: 10.1097/MD.0000000000012993
18. Kharbanda S, Anand R. Health-related quality of life in patients with chronic obstructive pulmonary disease: a hospital-based study. *Indian J Med Res.* (2021) 153:459–64. doi: 10.4103/ijmr.IJMR_1812_18
19. Barker RE, Brighton LJ, Maddocks M, Nolan CM, Patel S, Walsh JA, et al. Integrating home-based exercise training with a hospital at home service for patients hospitalised with acute exacerbations of COPD: developing the model using accelerated experience-based co-design. *Int J Chron Obstruct Pulmon Dis.* (2021) 16:1035–49. doi: 10.2147/COPD.S293048
20. Bathini A, Maxwell CR, Hedayat H, Barrett J, Hakma Z. Case report: vertebral osteomyelitis secondary to a dental abscess. *Bmc Infect Dis.* (2020) 20:133. doi: 10.1186/s12879-020-4857-7
21. Edlund A, Garg N, Mohimani H, Gurevich A, He X, Shi W, et al. Metabolic fingerprints from the human oral microbiome reveal a vast knowledge gap of secreted small peptidic molecules. *Msystems.* (2017) 2(2017) 2:e00058–17. doi: 10.1128/mSystems.00058-17
22. Chen YC, Ko PH, Yang CJ, Chen YC, Lay CJ, Tsai CC, et al. Epidural abscess caused by veillonella parvula: case report and review of the literature. *J Microbiol Immunol Infect.* (2016) 49:804–8. doi: 10.1016/j.jmii.2014.05.002
23. Prod'Homme M, Pfander G, Pavese P, Cech A, Abouelnaga I, Helfer L. Acromioclavicular septic arthritis caused by veillonella parvula. *Case Rep Orthop.* (2019) 2019:7106252. doi: 10.1155/2019/7106252
24. Knobloch J, Feldmann M, Wahl C, Jungck D, Behr J, Stoelben E, et al. Endothelin receptor antagonists attenuate the inflammatory response of human pulmonary vascular smooth muscle cells to bacterial endotoxin. *J Pharmacol Exp Ther.* (2013) 346:290–9. doi: 10.1124/jpet.112.202358
25. Chan S, Selemidis S, Bozinovski S, Vlahos R. Pathobiological mechanisms underlying metabolic syndrome (MetS) in chronic obstructive pulmonary disease (COPD): clinical significance and therapeutic strategies. *Pharmacol Ther.* (2019) 198:160–88. doi: 10.1016/j.pharmthera.2019.02.013
26. Paplinska-Goryca M, Misiukiewicz-Stepien P, Proboszcz M, Nejman-Gryz P, Gorska K, Krenke R. The expressions of TSLP, IL-33, and IL-17A in monocyte derived dendritic cells from asthma and COPD patients are related to epithelial-macrophage interactions. *Cells Basel.* (2020) 9:1944. doi: 10.3390/cells9091944
27. Che L, Yu C, Chen G, Lin J, Xie Z, Xia T, et al. The inflammatory response induced by RELMbeta upregulates IL-8 and IL-1beta expression in bronchial epithelial cells in COPD. *Int J Chron Obstruct Pulmon Dis.* (2021) 16:2503–13. doi: 10.2147/COPD.S321877
28. Osei ET, Brandsma CA, Timens W, Heijink IH, Hackett TL. Current perspectives on the role of interleukin-1 signalling in the pathogenesis of asthma and COPD. *Eur Respir J.* (2020) 55:1900563. doi: 10.1183/13993003.00563-2019
29. Bouquet J, Tabor DE, Silver JS, Nair V, Tovchigrechko A, Griffin MP, et al. Microbial burden and viral exacerbations in a longitudinal multicenter COPD cohort. *Respir Res.* (2020) 21:77. doi: 10.1186/s12931-020-01340-0
30. Beech AS, Lea S, Kolsum U, Wang Z, Miller BE, Donaldson GC, et al. Bacteria and sputum inflammatory cell counts; a COPD cohort analysis. *Respir Res.* (2020) 21:289. doi: 10.1186/s12931-020-01552-4
31. Keir HR, Contoli M, Chalmers JD. Inhaled corticosteroids and the lung microbiome in COPD. *Biomedicines.* (2021) 9:1312. doi: 10.3390/biomedicines9101312

Conflict of Interest: The authors declare that the research was conducted in the absence of any commercial or financial relationships that could be construed as a potential conflict of interest.

frontiers in Medicine

ORIGINAL RESEARCH
published: 20 January 2022
doi: 10.3389/fmed.2021.813119

The Potential Bioactive Components of Nine TCM Prescriptions Against COVID-19 in Lung Cancer Were Explored Based on Network Pharmacology and Molecular Docking

Lin Du[1], Yajie Xiao[2], Yijun Xu[1], Feng Chen[1], Xianghui Chu[1], Yuqi Cao[1] and Xun Zhang[1]*

[1] Department of Thoracic Surgery, Tianjin Chest Hospital, Tianjin, China, [2] Department of Clinical Translational Medicine, YuceBio Technology Co., Ltd., Shenzhen, China

Objective: The purpose of this study was to screen active components and molecular targets of nine prescriptions recommended by the National Health Commission (NHC) of China by network pharmacology, and to explore the potential mechanism of the core active components against COVID-19 with molecular docking.

Methods: Differentially expressed genes of lung adenocarcinoma (LUAD) screened by edgeR analysis were overlapped with immune-related genes in MMPORT and COVID-19-related genes in GeneCards. The overlapped genes were also COVID-19 immune-related genes in LUAD. TCMSP platform was used to identify active ingredients of the prescription, potential targets were identified by the UniProt database, and the cross genes with COVID-19 immune-related genes in LUAD were used to construct a Chinese Medicine-Logy-immune target network. Gene Ontology (GO) and Kyoto Encyclopedia of Genes and Genomes (KEGG) enrichment analyses were performed on the target genes of each prescription. Finally, the key active components were selected for molecular docking simulation with ACE2.

Results: We obtained 15 overlapping immunization target genes from FPQXZ, HSYFZ, HSZFZ, and QFPDT, 16 overlapping immunization target genes from QYLFZ, SDYFZ, SRYFZ, and YDBFZ, and 17 overlapping immunization target genes from QYLXZ. ADRB2, FOS, HMOX1, ICAM1, IL6, JUN, NFKBIA, and STAT1 also had the highest-ranked therapeutic targets for 9 prescriptions, and their expressions were positively correlated with TME-related stromal score, immune score, and ESTIMATE score. Among 9 compounds with the highest frequency of occurrence in the 9 prescriptions, baicalein had the highest ACE2 binding affinity and can be well-combined into the active pocket of ACE2 It is stabilized by forming hydrogen bonds with ASN290 and ILE291 in ACE2 and hydrophobic interaction with PHE438, ILE291, and PRO415.

Conclusion: The nine Chinese medicine prescriptions may play an anti-SARS-CoV-2 role *via* regulating viral transcription and immune function through multi-component, multi-target, and multi-pathway.

Keywords: COVID-19, Chinese medicine, network pharmacology, baicalein, molecular docking

OPEN ACCESS

Edited by:
Fu Wang,
Xi'an Jiaotong University, China

Reviewed by:
Fengsen Li,
The Traditional Chinese Medicine Hospital Affiliated to Xinjiang Medical University, China
Mingfen Li,
First Affiliated Hospital of Guangxi University of Chinese Medicine, China
Min Wei,
Shanghai Jiao Tong University, China

****Correspondence:***
Xun Zhang
zhangxun69@163.com

Specialty section:
This article was submitted to Precision Medicine, a section of the journal Frontiers in Medicine

Received: *11 November 2021*
Accepted: *13 December 2021*
Published: *20 January 2022*

Citation:
Du L, Xiao Y, Xu Y, Chen F, Chu X, Cao Y and Zhang X (2022) The Potential Bioactive Components of Nine TCM Prescriptions Against COVID-19 in Lung Cancer Were Explored Based on Network Pharmacology and Molecular Docking. Front. Med. 8:813119. doi: 10.3389/fmed.2021.813119

INTRODUCTION

Coronavirus disease 2019 is a viral infection triggered by severe acute respiratory syndrome coronavirus 2 (SARS-CoV-2) (1). COVID-19 has spread rapidly, posing a serious threat to human health all over the world. Until August 11, 2021, there were nearly 205 million confirmed COVID-19 cases worldwide, resulting in more than 4.32 million deaths (https://www.worldometers.info/coronavirus/). It has been reported that patients with lung cancer are more likely to be infected with SARS-COV-2 and have a higher risk of death than normal ones due to impaired basic lung function and immunosuppression (2). The current challenge in treating patients with lung cancer is the balance between the risk of a potentially life-threatening infection with COVID-19 and the consequences of delayed treatment or non-treatment of lung cancer (3). Food and Drug Administration has approved antivirals, immune-modulators, nucleotide analogs, and convalescent plasma therapy for emergency treatment of COVID-19 (4). Many clinical studies have shown that the effectiveness of Chinese medicine interventional therapy for COVID-19 can reach higher than 90% (5). Recent clinical studies have combined both Chinese and Western medicine to treat COVID-19 with great success (6). The results of a meta-analysis demonstrated that integrated Traditional Chinese and Western medicine treatment for COVID-19 was more effective than applying conventional Western medicine treatment, with a better improvement of patients' clinical symptoms, chest CT and infection indicators (7). To date, there are more than 133 ongoing registered clinical studies of Chinese medicine/integrated Chinese and Western medicine (8). Although Chinese medicine has significant advantages in the treatment of COVID-19 and has strong clinical support, it is still considered as an alternative or complementary medicine mainly due to unspecific biochemical active ingredients of its prescriptions and unclear mechanism of action (9). Therefore, the problem that active ingredients and their mechanism of action should be explored.

The emergence of network pharmacology has provided great convenience for the study of pharmacological action and mechanisms of Chinese medicine. With network pharmacology, researchers can mine drug and disease targets from vast amounts of data to understand the mechanisms of action and regulatory pathways (10). In this study, we used online pharmacology to screen active ingredients and potential targets of nine prescriptions recommended by the National Health Commission (NHC) of China. Moreover, the potential mechanism of the anti-COVID-19 action of the core active ingredient through the molecular docking method was investigated. The current findings provide a reference for clinical treatment and mechanism study of Chinese medicine.

MATERIALS AND METHODS

Data Gathering and Processing

The IMMPORT (Division of Systems Medicine, Department of Pediatrics, Stanford University School of Medicine)

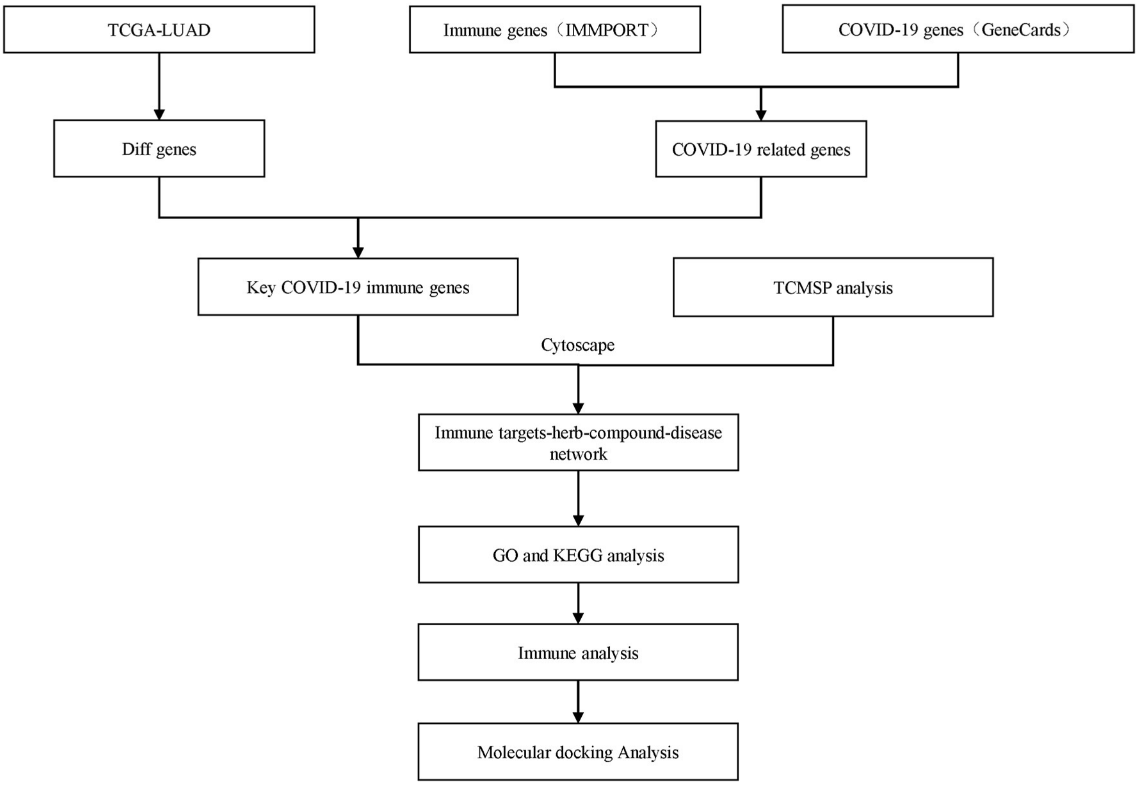

FIGURE 1 | Workflow chart.

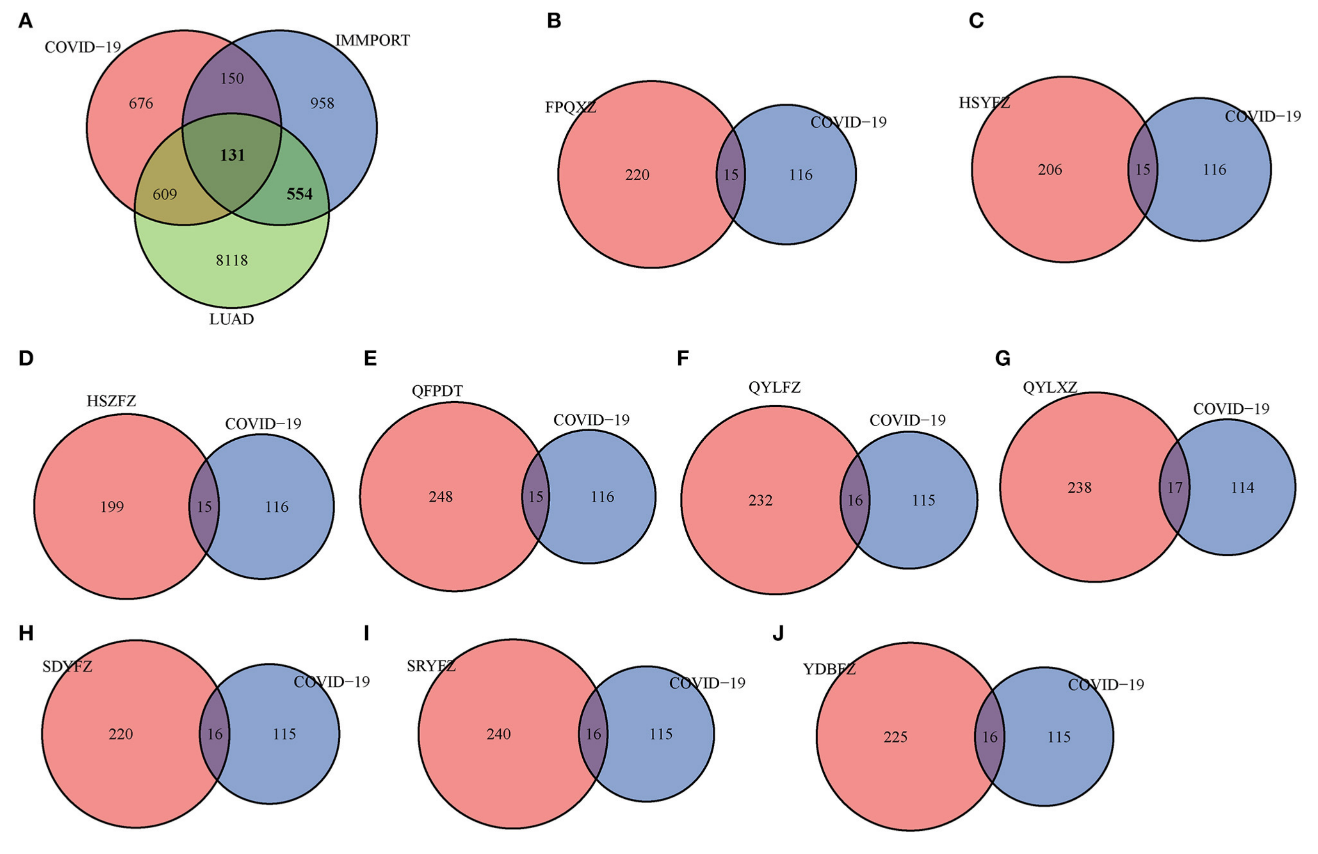

FIGURE 2 | Active ingredients and targets prescribed for COVID-19 treatment. **(A)** Intersection analysis of differentially expressed genes, immune-related genes, and COVID-19 related genes in CLUAD. The Venn diagram of FPQXZ **(B)**, HSYFZ **(C)**, HSZFZ **(D)**, QFPDT **(E)**, QYLFZ **(F)**, QYLXZ **(G)**, SDYFZ **(H)**, SRYFZ **(I)**, and YDBFZ **(J)** with COVID-19 immune-related genes in LUAD.

(https://www.immport.org) database (11) was used to retrieve and collate 1,793 immune-related genes. A total of 1,566 COVID-19 related genes were acquired from Genecards (Department of Molecular Genetics, Weizmann Institute of Science) (https://www.genecards.org/) (12). The RNA sequencing data of TCGA-LUAD patients was obtained from the TCGA data portal (https://tcga-data.nci.nih.gov/tcga/). We downloaded the RNA-seq FPKM data set and further transformed the expression profile into transcripts per kilobase million (TPM). Differential expression of coding genes between tumor tissue and normal tissue was analyzed using edgeR (Institute of Molecular Life Sciences, University of Zurich) (13) (V3.26.8) to take the intersection of immune-related genes in MMPORT and COVID-19 related genes in GeneCards. The results of overlapping genes were shown by Venn Diagram (Informatics and Biocomputing Platform, Ontario Institute for Cancer Research) (14). The workflow chart is shown in **Figure 1**.

Screening of Active Ingredients for COVID-19 Treatment and Prediction of Corresponding Targets

A total of 9 prescriptions of Chinese medicine were selected from "Novel Coronavirus Pneumonia Diagnosis and Treatment Scheme (Trial Edition 8)" issued by the National Health Commission of China, including Qing-Fei-Pai-Du-Tang (QFPDT), Shi-Re-Yun -Fei-Zheng (SDYFZ), Shi-Du-Yu-Fei-Zheng (SDYFZ), Han-Shi-Yu-Fei-Zheng (HSYFZ), Yi-Du-Bi-Fei-Zheng (YDBFZ), Han-Shi-Zu-Fei-Zheng (HSZFZ), Fei-Pi-Qi-Xu-Zheng (FPQXZ), Qi-Ying-Liang-Fan-Zheng (QYLFZ), and Qi-Yin-Liang-Xu-Zheng (QYLXZ). Bioactive ingredients of each prescription were searched through the Chinese Medicine Database and Analysis Platform (Center for Bioinformatics, College of Life Science, Northwest A&F University) (15) (TCMSP, https://tcmsp-e.com/). The most commonly used screening parameter for web-based pharmacological analysis was oral bioavailability (OB) (16), drug-likeness (DL) (17), and intestinal epithelial permeability (Caco-2) (18). In this method, the criteria of OB $\geq$ 30% and drug-likeness $\geq$ 0.18 were applied to screen bioactive components and their potential targets, and the target was annotated in UniProt (European Molecular Biology Laboratory, European Bioinformatics Institute (EMBL-EBI), Wellcome Trust Genome Campus) (https://www.uniprot.org/). The intersected genes of COVID-19 target genes and prescription target gene sets using The Venn Diagram package in the R software.

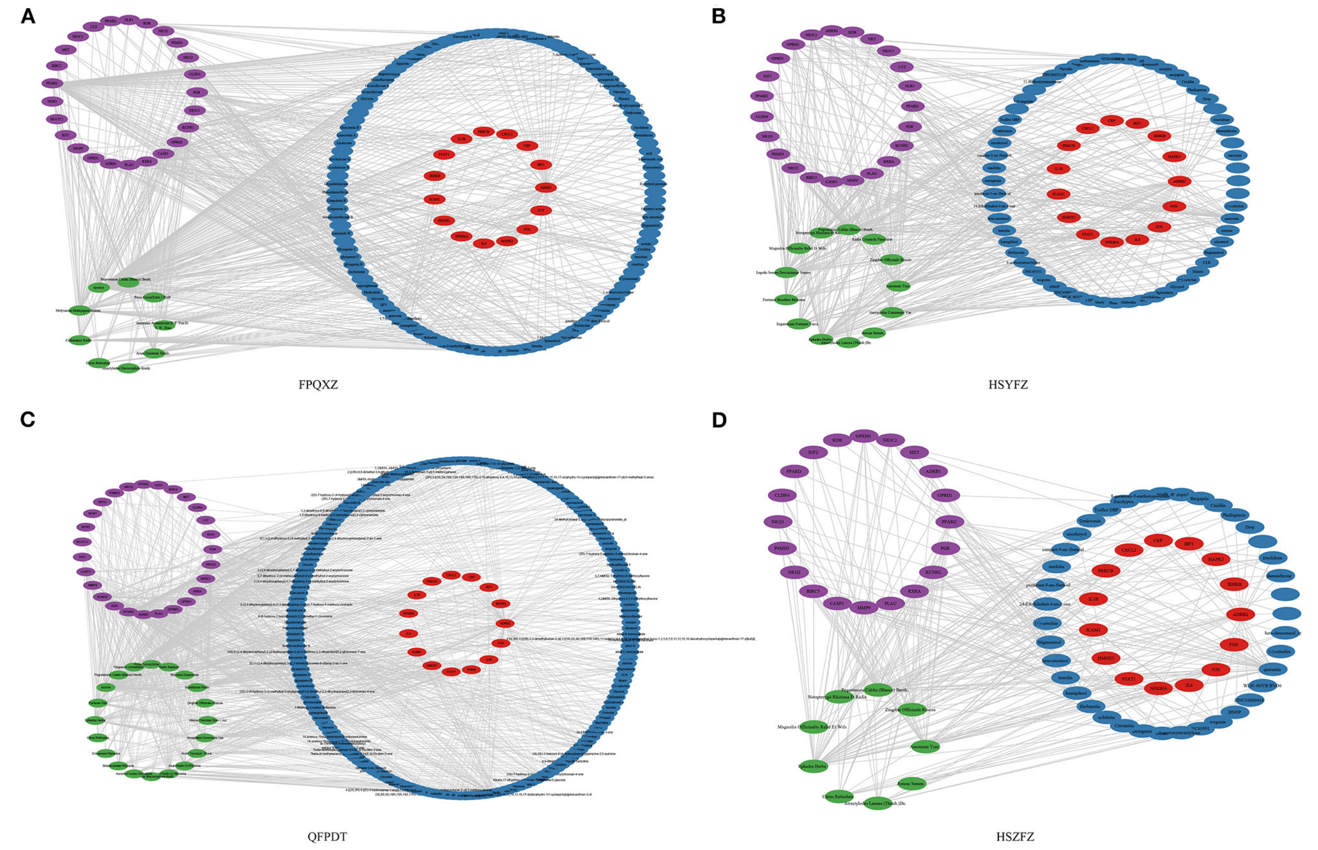

FIGURE 3 | The Chinese medicine herb- constituent -immune target network. **(A)** FPQXZ's Chinese medicine herb—constituent -immune target regulatory network. **(B)** HSYFZ's Chinese medicine herb—constituent -immune target network. **(C)** QFPDT's Chinese medicine herb—constituent -immune target network. **(D)** Chinese medicine herb—constituent -immune target interaction network of HSZFZ.

TABLE 1 | The top 10 key compounds in FPQXZ.

Compound	Degree	Betweenness centrality
Quercetin	29	0.01015208
Kaempferol	13	0.00336682
Luteolin	11	0.00193848
Stigmasterol	9	0.0006946
Beta-sitosterol	8	0.00041647
Baicalein	7	0.0016664
Irisolidone	7	0.00038325
Cavidine	7	0.00034745
7-O-methylisomucronulatol	7	0.00034529
Shinpterocarpin	7	0.00030962

TABLE 2 | The top 10 core targets in FPQXZ.

Gene	Degree	Betweenness centrality
ADRB2	50	0.07531967
JUN	14	0.00682336
ICAM1	7	0.00088071
HMOX1	7	0.00088071
FOS	6	0.00214445
NFKBIA	6	0.00073893
IL6	6	0.00073893
IL1B	5	0.0002301
STAT1	5	8.54E-05
IRF1	4	4.83E-05

Construction of Chinese Medicine-Constituent-Immune Target

To construct the Chinese medicine herb-constituent-immune target network, CytoScape (Institute for Systems Biology) (V3.7.2) (19) was used in order to reflect the complex relationship among active Chinese medicine, compounds, and filtrated targets. Topology analysis of networks was carried out according to the values of degree centrality, betweenness centrality, and closeness centrality. The protein-protein interaction data set comes from the stringdb database (https://cn.string-db.org/) (Department of Molecular Life Sciences and Swiss Institute of Bioinformatics, University of Zurich) (20).

Gene Ontology (GO) and KEGG Pathway Enrichment Analysis

To conduct GO and KEGG enrichment analyses, the ClusterProfiler (Institute of Life and Health Engineering, Key Laboratory of Functional Protein Research of Guangdong Higher Education Institutes, Jinan University) database was used by importing the list of intersection target gene names and setting the species as "hsa" for customized analysis with a filter P-value of < 0.05.

Simulated Molecular Docking

The active ingredient with the highest content in nine kinds of Chinese medicine was selected, and the chemical structure of the active ingredient and ACE2 was downloaded from PubChem (National Center for Biotechnology Information, National Library of Medicine, National Institutes of Health, Department of Health and Human Services). AutoDock Vina software (Department of Molecular Biology, The Scripps Research Institute) (21) was used to simulate molecular docking. AutoDockTools processed the ACE2 protein, added polar hydrogen, calculated the Gasteiger charge, and set all ligand rotatable bonds. The targets and drugs were prepared and molecular docking performed inside a grid box (40 Å × 40 Å × 40 Å). A lamarckian genetic algorithm was applied to calculate protein docking with the ligand. All docking was run with default settings. The exhaustiveness level was set to 8 and the output maximum was set to 10.

RESULTS

Collection of Active Ingredients and Target Gene Screening for Prescribing Treatments for COVID-19

A total of 9,412 differentially expressed genes were screened from TCGA-LUAD by performing differential analysis. One hundred and thirty-one genes were determined as COVID-19 immune-related and LUAD-related (**Figure 2A**). According to OB value and DL index, the active ingredients of nine prescriptions were obtained from TCMSP. Then the target genes of each prescription were predicted to take the intersection with COVID-19 immune-related genes in LUAD. In this study, 15 immune target genes were obtained from FPQXZ, HSYFZ, HSZFZ, and QFPDT, 16 immune target genes were obtained from QYLFZ, SDYFZ, SRYFZ, and YDBFZ, and 17 were obtained from QYLXZ (**Figures 2B–J**). We used WebGestaltR to analyze the function of these gene immune target genes. We can observe that they are mainly related to cytokine receptor interaction, JAK-STAT signaling pathway, and MAPK signaling pathway, such as **Supplementary Figure 1A**. In addition, they are also related to blood vessel morphogenesis, positive regulation of MAPK cascade Regulation of signaling receiver activity is related to biological processes (**Supplementary Figure 1B**). Cell composition analysis shows that these genes are mainly enriched in the side of the membrane, receiver complex, external side of the plasma membrane, and other components (**Supplementary Figure 1C**). They are also enriched in receiver regulator activity, receiver live activity Cytokine receptor binding, and other molecular functions (**Supplementary Figure 1D**). These results prove the relationship between these genes and the immune process.

TABLE 4 | The common immune target genes of each prescription were counted.

Gene	Freq
ADRB2	9
FOS	9
HMOX1	9
ICAM1	9
IL6	9
JUN	9
NFKBIA	9
STAT1	9
IL1B	7
PRKCB	7
IKBKB	3
IRF1	1

Construction of Chinese Medicine-Constituent-Immune Target Network

The interaction network of the Chinese medicine-constituent-immune target network was constructed by introducing each Chinese medicine prescription, its active ingredient, and predicted target into Cytoscape. As shown in **Figure 3** and **Supplementary Figure 2**, the nodes of the Chinese medicine—constituent -immune target network of each prescription could be observed. Among them, green, blue, red, and purple circles represented Chinese medicine prescription, compounds, immune target genes, and non-immune target genes of the prescription, respectively. We also analyzed the degree distribution and eigenvector centrality of each network. It can be observed that the moderate distribution of these networks presents a dark rate form, which is consistent with the characteristics of biological networks. The eigenvector centrality shows a similar situation, as shown in **Supplementary Figure 3**, In In each Chinese medicine prescription network, one compound acted on a multitarget, and different compounds could also simultaneously interact with an immune target. Moreover, the top 10 key compounds of the top 10 core targets in FPQXZ were identified according to the degree value as shown in **Tables 1**, **2**. **Table 3** showed predicted targets of the top 10 active ingredients, with their corresponding genes in FPQXZ.

Analysis of GO Function and KEGG Enrichment of Related Targets

Gene ontology (GO) and KEGG analyses were performed on the targets of each prescription to obtain enriched ontology clusters. A total of 309 GO terms including 284 biological processes (BPs), eight cellular components (CCs), and 17 molecular functions (MFs) were found in the GO functional annotation of FPQXZ target genes (**Figure 4A**). For BPs, the targets were mainly involved in transcriptional regulation, response to hormones, and harmful factors. CCs terms demonstrated that the targets

TABLE 3 | Predicted targets of the top 10 active ingredients, with their corresponding genes in FPQXZ.

MolId	Mol name	Target	Symbol	Herb
MOL000098	Quercetin	Beta-2 adrenergic receptor	ADRB2	Hedysarum Multijugum Maxim.
MOL000098	Quercetin	Beta-2 adrenergic receptor	ADRB2	Licorice
MOL000098	Quercetin	Beta-2 adrenergic receptor	ADRB2	Pogostemon Cablin (Blanco) Benth.
MOL000449	Stigmasterol	Beta-2 adrenergic receptor	ADRB2	Amomum Aurantiacum H. T. Tsai Et S. W. Zhao
MOL000449	Stigmasterol	Beta-2 adrenergic receptor	ADRB2	Arum Ternatum Thunb.
MOL000449	Stigmasterol	Beta-2 adrenergic receptor	ADRB2	Codonopsis Radix
MOL000358	Beta-sitosterol	Beta-2 adrenergic receptor	ADRB2	Amomum Aurantiacum H. T. Tsai Et S. W. Zhao
MOL000358	Beta-sitosterol	Beta-2 adrenergic receptor	ADRB2	Arum Ternatum Thunb.
MOL005916	Irisolidone	Beta-2 adrenergic receptor	ADRB2	Pogostemon Cablin (Blanco) Benth.
MOL002670	Cavidine	Beta-2 adrenergic receptor	ADRB2	Arum Ternatum Thunb.
MOL000378	7-O-methylisomucronulatol	Beta-2 adrenergic receptor	ADRB2	Hedysarum Multijugum Maxim.
MOL004891	Shinpterocarpin	Beta-2 adrenergic receptor	ADRB2	Licorice
MOL000098	Quercetin	Transcription factor AP-1	JUN	Hedysarum Multijugum Maxim.
MOL000098	Quercetin	Transcription factor AP-1	JUN	Licorice
MOL000098	Quercetin	Transcription factor AP-1	JUN	Pogostemon Cablin (Blanco) Benth.
MOL000422	Kaempferol	Transcription factor AP-1	JUN	Hedysarum Multijugum Maxim.
MOL000422	Kaempferol	Transcription factor AP-1	JUN	Licorice
MOL000006	Luteolin	Transcription factor AP-1	JUN	Codonopsis Radix
MOL000358	Beta-sitosterol	Transcription factor AP-1	JUN	Amomum Aurantiacum H. T. Tsai Et S. W. Zhao
MOL000358	Beta-sitosterol	Transcription factor AP-1	JUN	Arum Ternatum Thunb.
MOL005916	Irisolidone	Transcription factor AP-1	JUN	Pogostemon Cablin (Blanco) Benth.
MOL000098	Quercetin	Intercellular adhesion molecule 1	ICAM1	Hedysarum Multijugum Maxim.
MOL000098	Quercetin	Intercellular adhesion molecule 1	ICAM1	Licorice
MOL000098	Quercetin	Intercellular adhesion molecule 1	ICAM1	Pogostemon Cablin (Blanco) Benth.
MOL000422	Kaempferol	Intercellular adhesion molecule 1	ICAM1	Hedysarum Multijugum Maxim.
MOL000422	Kaempferol	Intercellular adhesion molecule 1	ICAM1	Licorice
MOL000006	Luteolin	Intercellular adhesion molecule 1	ICAM1	Codonopsis Radix
MOL000098	Quercetin	Heme oxygenase 1	HMOX1	Hedysarum Multijugum Maxim.
MOL000098	Quercetin	Heme oxygenase 1	HMOX1	Licorice
MOL000098	Quercetin	Heme oxygenase 1	HMOX1	Pogostemon Cablin (Blanco) Benth.
MOL000422	Kaempferol	Heme oxygenase 1	HMOX1	Hedysarum Multijugum Maxim.
MOL000422	Kaempferol	Heme oxygenase 1	HMOX1	Licorice
MOL000006	Luteolin	Heme oxygenase 1	HMOX1	Codonopsis Radix
MOL000098	Quercetin	Proto-oncogene c-Fos	FOS	Hedysarum Multijugum Maxim.
MOL000098	Quercetin	Proto-oncogene c-Fos	FOS	Licorice
MOL000098	Quercetin	Proto-oncogene c-Fos	FOS	Pogostemon Cablin (Blanco) Benth.
MOL002714	Baicalein	Proto-oncogene c-Fos	FOS	Arum Ternatum Thunb.
MOL000098	Quercetin	NF-kappa-B inhibitor alpha	NFKBIA	Hedysarum Multijugum Maxim.
MOL000098	Quercetin	NF-kappa-B inhibitor alpha	NFKBIA	Licorice
MOL000098	Quercetin	NF-kappa-B inhibitor alpha	NFKBIA	Pogostemon Cablin (Blanco) Benth.
MOL000006	Luteolin	NF-kappa-B inhibitor alpha	NFKBIA	Codonopsis Radix
MOL000098	Quercetin	Interleukin-6	IL6	Hedysarum Multijugum Maxim.
MOL000098	Quercetin	Interleukin-6	IL6	Licorice
MOL000098	Quercetin	Interleukin-6	IL6	Pogostemon Cablin (Blanco) Benth.
MOL000006	Luteolin	Interleukin-6	IL6	Codonopsis Radix
MOL000098	Quercetin	Interleukin-1 beta	IL1B	Hedysarum Multijugum Maxim.
MOL000098	Quercetin	Interleukin-1 beta	IL1B	Licorice
MOL000098	Quercetin	Interleukin-1 beta	IL1B	Pogostemon Cablin (Blanco) Benth.
MOL005916	Irisolidone	Interleukin-1 beta	IL1B	Pogostemon Cablin (Blanco) Benth.

(Continued)

TABLE 3 | Continued

MolId	Mol name	Target	Symbol	Herb
MOL000098	Quercetin	Signal transducer and activator of transcription 1-alpha/beta	STAT1	Hedysarum Multijugum Maxim.
MOL000098	Quercetin	Signal transducer and activator of transcription 1-alpha/beta	STAT1	Licorice
MOL000098	Quercetin	Signal transducer and activator of transcription 1-alpha/beta	STAT1	Pogostemon Cablin (Blanco) Benth.
MOL000422	Kaempferol	Signal transducer and activator of transcription 1-alpha/beta	STAT1	Hedysarum Multijugum Maxim.
MOL000422	Kaempferol	Signal transducer and activator of transcription 1-alpha/beta	STAT1	Licorice
MOL000098	Quercetin	Interferon regulatory factor 1	IRF1	Hedysarum Multijugum Maxim.
MOL000098	Quercetin	Interferon regulatory factor 1	IRF1	Licorice
MOL000098	Quercetin	Interferon regulatory factor 1	IRF1	Pogostemon Cablin (Blanco) Benth.

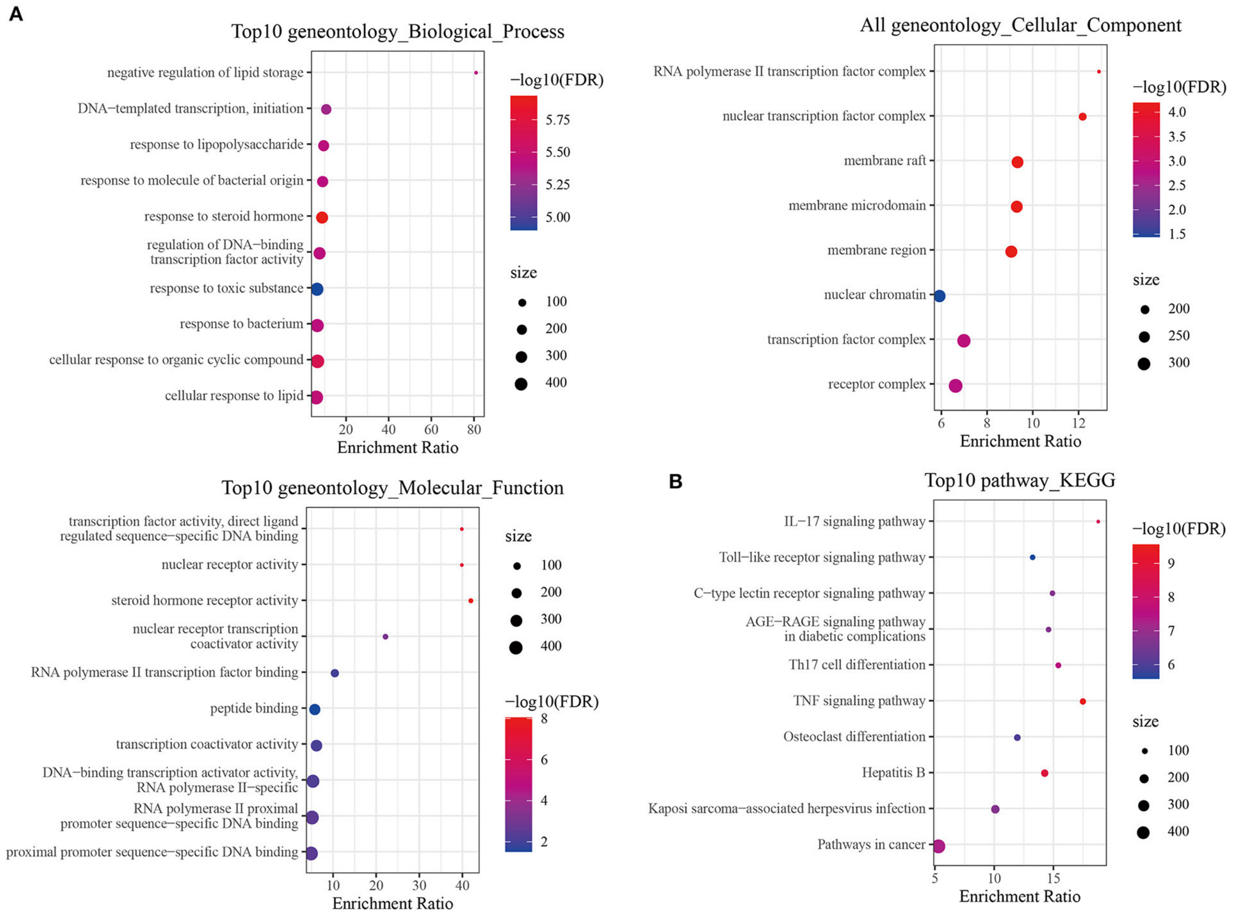

FIGURE 4 | GO and KEGG analysis of FPQXZ target genes. **(A)** GO terms of FPQXZ target genes. The top 10 GO functional categories were selected. **(B)** KEGG bubble diagram showed the top 10 pathways of FPQXZ target genes.

were associated with transcription factor complex and membrane raft. From MFs analysis, it could be found that the targets were mainly associated with nuclear receptor activity, steroid hormone receptor activity, peptide binding, etc. The enrichment analysis of KEGG signal pathways included 87 pathways. From the visual results of the first 10 pathways, the target gene of the main signaling pathways of prescription was concentrated in pathways in the IL−17 signaling pathway, Th17 cell differentiation, TNF signaling pathway, Hepatitis B, etc. (**Figure 4B**). The GO function and KEGG enrichment results of the target genes of the other eight Chinese medicine prescriptions were displayed in **Supplementary Figure 4**.

Correlation Between Tumor Environment (TME) and Immune Target Gene of Chinese Medicine Prescription

Comparison analysis showed that eight (ADRB2, FOS, HMOX1, ICAM1, IL6, JUN, NFKBIA, and STAT1) out of the top 10 immune target genes of each prescription were therapeutic

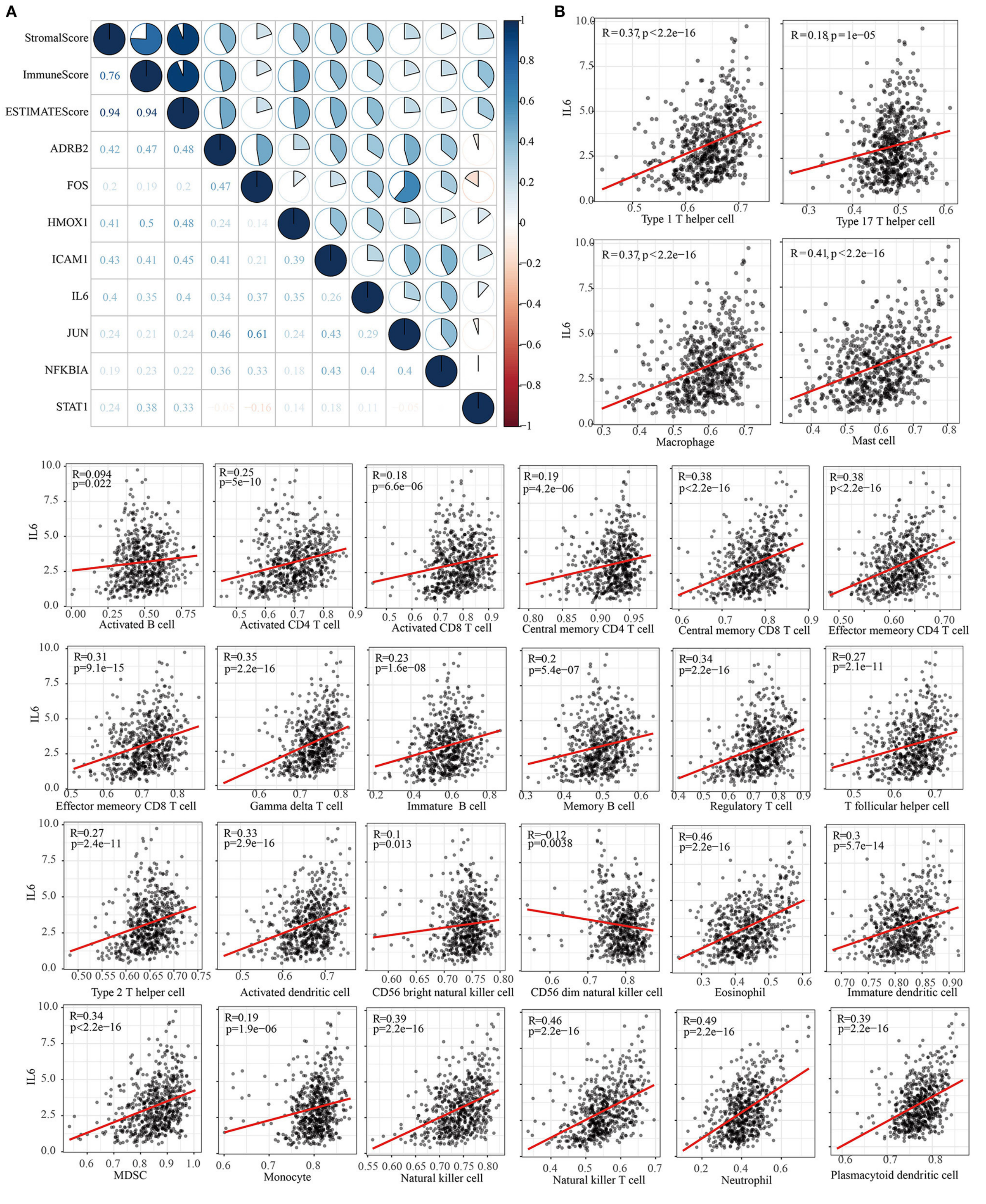

FIGURE 5 | Correlation analysis between immune target genes and TME in Chinese medicine prescription. **(A)** Correlation between immune target genes and stromal score, immune score, and ESTIMATE score in Chinese medicine prescription. **(B)** Pearson correlation analysis between IL6 expression level and ssGSEA score of 28 immune cells.

targets of 9 kinds of prescription (**Table 4**). Eight immune target genes were significantly differentially expressed in cancer and adjacent tumors. Except for STAT1, the other seven genes were low expressed in tumor samples (**Supplementary Figure 5A**). Stromal score, immune score, and ESTIMATE score of LUAD in TCGA were obtained through ESTIMATE, and correlation analysis was conducted between these TME-related scores and 8 immune target genes. Three TME-related scores were found to be positively correlated with 8 immune target genes (**Figure 5A**). According to single-gene GSEA (ssGSEA), the infiltration score of 28 types of immune cells was assessed, including activated B cell, activated CD4 T cell, activated CD8 T cell, central memory CD4 T cell, central memory CD8 T cell, effector memory CD4 T cell, effector memory CD8 T cell, gamma delta T cell, immature B cell, memory B cell, regulatory T cell, follicular helper T cell, type 1 T helper cell, type 17 T helper cell, type 2 T helper cell, activated dendritic cell, CD56 bright natural killer cell, CD56 dim natural killer cell, eosinophil, immature dendritic cell, macrophage, mast cell, MDSC, monocyte, natural killer cell, natural killer T cell, neutrophil, plasmacytoid dendritic cell. The Pearson correlation analysis between IL6 and 28 kinds of immune cells showed that the expression of IL6 was negatively correlated with the scores of CD56 dim natural killer cell, and positively correlated with the scores of the other 27 kinds of cells (**Figure 5B**).

Molecular Docking

Among the top 10 compounds in each prescription, we selected the compounds that occur more than or equal to five times in nine prescriptions, and these included beta-sitosterol, kaempferol, luteolin, quercetin, stigmasterol, shinpterocarpin, wogonin, baicalein, and irisolidone (**Table 5**). The docking results of the nine compounds with ACE2 were shown in **Table 6**. The binding free energy of each compound to ACE2 was lower than 0, indicating that all the nine compounds could well-bind to ACE2, and baicalein had the highest binding affinity to ACE2 among all the nine compounds. So the molecular docking pattern between baicalein and ACE2 was simulated here. It was found that baicalein could well-bind to the active pockets of ACE2, and was stabilized through forming hydrogen bonds with ASN290 and ILE291 in ACE2 and hydrophobic interactions with PHE438, ILE291, and PRO415 (**Figures 6A,B**). The 100 ns simulation of baicalein combined with ACE2 showed the conformational change of baicalein in the binding pocket of ACE2, and that the root mean square deviation (RMSD) of each moment was almost the same (**Figure 6C**). These findings indicated that baicalein may bind to ACE2, thereby inhibiting the host-virus protein interactions in which they were involved.

TABLE 5 | The frequency of occurrence of different compounds in nine prescriptions.

Compound	Freq
Beta-sitosterol	9
Kaempferol	9
Luteolin	9
Quercetin	9
Stigmasterol	9
Shinpterocarpin	6
Wogonin	6
Baicalein	5
Irisolidone	5
Sitosterol	4
Cavidine	3
7-Methoxy-2-methyl isoflavone	2
7-O-methylisomucronulatol	2
Estrone	2
l-SPD	2
Naringenin	2
1-Methoxyphaseollidin	1
Arachidonic acid	1
Cryptotanshinone	1
Eucalyptol	1
Nobiletin	1
Tanshinone iia	1

TABLE 6 | Binding free energy of nine compounds to ACE2.

Compounds	Score (kcal/mol)	Hydrogen-bond	Hydrophobic-bond
Baicalein	−9.6	ASN290, ILE291	PHE438, ILE291, PRO415
Stigmasterol	−9.3	GLU406	PHE438, LEU370, ALA413, ILE291, LYS441
Beta-sitosterol	−9.3	GLU406	LEU370, MET366, ALA413, PRO415, ILE291, PHE438, LYS441
Luteolin	−9.1	ILE291	PHE438, ILE291, THR434, PRO415
Kaempferol	−8.8	ASN290, ILE291, HIS540	PHE438, ALA413, THR434, PRO415
Wogonin	−8.5	ASP431, THR434	PHE438, PRO415, ILE291
Irisolidone	−8.3	LYS423	PHE420, PRO397, ILE273, MET348
Shinpterocarpin	−8.2	SER44, ALA348	ASP350, PHE40
Quercetin	−7.7	ALA413, ASP367, THR434	PHE438, MET366

DISCUSSION

The interaction of COVID-19 virus spike protein with host angiotensin-converting enzyme 2 (ACE2) receptor is the primary mechanism for SARS-CoV-2 entry into host cells (22). Therefore, a strategy that interferes with such an interaction may be an effective strategy for treating SARS-CoV-2. There is already a wealth of research data and findings in this area. Suresh Gangadevi et al. (23) showed that blocking the interaction between ACE2 receptor and S1-RBD *in vitro* could serve as a lead compound against COVID-19. Withanone in *Withania Somnifera* effectively inhibited the interaction between SARS-CoV-2 RBD and host ACE2 in a dose-dependent manner, and this can be used as a potential antiviral drug (24). A recent study applied multidisciplinary approaches to show that 12 ACE2

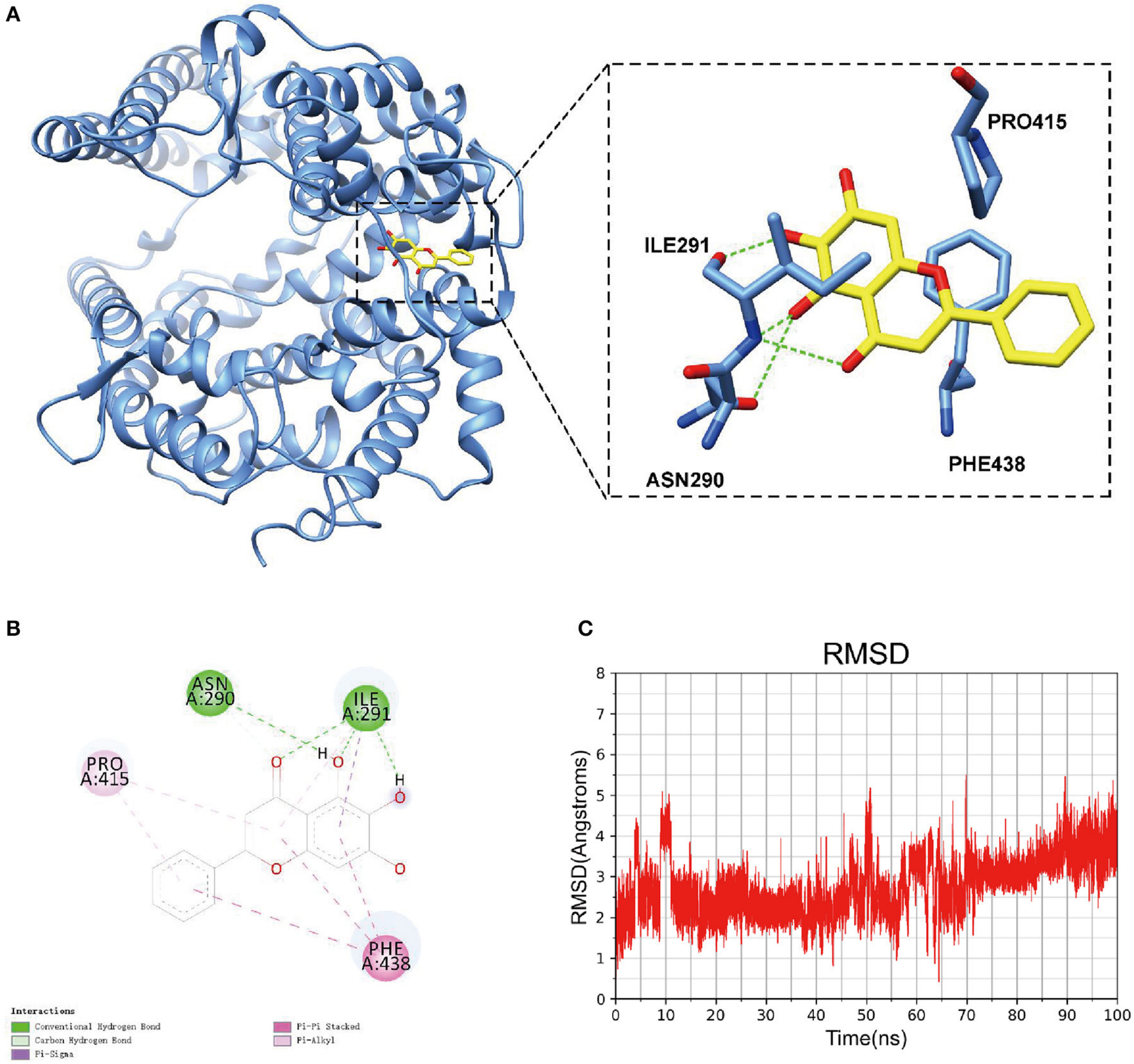

FIGURE 6 | Molecular docking patterns of baicalein and ACE2. **(A)** The pose of baicalein within the binding site of ACE2. The yellow confirmation was the baicalein, and the green dotted line was the hydrogen bond. **(B)** 2D-interaction diagram of ACE2 -baicalein interaction. **(C)** RMSD of baicalein combined with ACE2 for 100 ns.

binders and 6 of the RBD binders competed with the RBD-ACE2 interaction, which may be explored as inhibitors to SARS-COV-2 (25). Some Chinese medicine prescriptions have also been clinically proven to be effective in treating COVID-19, however, due to their multi-component and multi-target characteristics, the active ingredients and mechanisms remain unknown.

This study applied network pharmacology to explore the active ingredients and therapeutic targets of nine approved Chinese medicine prescriptions, and combined with simulated molecular docking to analyze the important components with a high binding ability to COVID-19 targets. We screened eight common immune target genes from nine Chinese medicine prescriptions. JUN, NFKBIA, and ICAM1 have been reported as key genes related to COVID-19 (26). ADRB2, FOS, and IL-6 were found to be associated with COVID-19 inflammation (27–29). Dysregulation of HMOX1 was relevant to ARS-CoV-2 and cancer (30). A study of Toshifumi Matsuyama indicated that enhanced STAT1 activity could be used in the treatment of COVID-19 (31). In addition, we also found that ADRB2 and STAT1 were significantly correlated with the prognosis of patients with lung cancer (**Supplementary Figure 5B**). ADRB2 was a protective factor, while STAT1 was a risk factor. ADRB2 was closely related to a variety of diseases, such as ADRB2 signaling by inhibiting HIF1 α Autophagy degradation to promote HCC progression and sorafenib resistance (32). ADRB2 hypermethylation induced β 2AR down regulation inhibits PI3K / Akt, resulting in cardiac dysfunction (33). STAT1 involves M1 macrophage polarization, which may affect osteolysis and bone remodeling of extrapulmonary tuberculosis (34). STAT1 activation induces PRMT1 expression and regulates the remodeling of primary human lung fibroblasts (35). In addition, we also analyzed the expression relationship between these eight genes and ACE2.

Generally speaking, the correlation between these genes and ACE2 is weak, suggesting that these eight genes may not directly co-express with ACE2 and participate in the immune pathway (**Supplementary Figure 5C**). Here, we found that they were positively correlated with TME, and the inhibition of the nine Chinese medicine prescriptions on COVID-19 may be partially achieved *via* acting on these targets.

We also listed the top 10 compounds in each prescription and identified at least nine compounds with high content in the five prescriptions. Through literature review, we learned that hydrogen bonding, hydrophobic, and van der Waals force interactions between Beta-Sitosterol and ACE2 (36). Kaempferol only formed a single hydrogen bond with ACE2 with low affinity but showed a high affinity with Akt1 (37, 38). Luteolin, quercetin can form strong hydrogen bonds with polar amino acid residues R273, D269, and N149 in ACE2 pocket, and weak hydrogen bonds with hydroxyl groups of Y127. At the same time, the top dihydroxyl group can form a double hydrogen bond with the -Co group on the N149 skeleton, with a free energy of binding of −7.92 kcal/mol (37), which was close to our estimated binding free energy of −7.7 kcal/mol. In addition, a study has calculated that the free energy of the combination of stigmasterol and ACE2 was −8.3 kcal/mol (39), and this was also consistent with our calculation. Tao et al. (40) reported that baicalein regulated multiple signaling pathways through ACE2. However, the conformation and stability of the two combinations are still unclear. Here, our results indicated that baicalein was an active component with the highest free binding energy to ACE2 among the nine compounds, and can be embedded in the active pocket of ACE2 to form a stable conformation through the formation of hydrogen bonds and hydrophobic interactions.

Our results suggested that baicalein may be the core ingredient in several Chinese medicine prescriptions for the effective treatment of COVID-19. This study may provide a theoretical basis for the development of anti-COVID-19 drugs. Even so, network pharmacology only analyzed the main active components and targets of drugs, its predicted targets and specific regulatory mechanisms need further experimental verification and exploration.

DATA AVAILABILITY STATEMENT

Publicly available datasets were analyzed in this study. This data can be found at: the IMMPORT (https://www.immport.org) database was used to retrieve and collate 1,793 immune-related genes. A total of 1,566 COVID-19 related genes were acquired from Genecards (https://www.genecards.org/). The RNA sequencing data of TCGA-LUAD patients was obtained from the TCGA data portal (https://tcga-data.nci.nih.gov/tcga/).

AUTHOR CONTRIBUTIONS

LD, YXi, and YXu: statistical analysis. XC, YC, and XZ: acquisition of data. FC: obtaining funding. All authors contributed to the article and approved the submitted version.

SUPPLEMENTARY MATERIAL

The Supplementary Material for this article can be found online at: https://www.frontiersin.org/articles/10.3389/fmed.2021.813119/full#supplementary-material

REFERENCES

1. Guan WJ, Ni ZY, Hu Y, Liang WH, Ou CQ, He JX, et al. Clinical characteristics of coronavirus disease 2019 in China. *N Engl J Med.* (2020) 382:1708–20. doi: 10.1056/NEJMoa2002032
2. Mehta V, Goel S, Kabarriti R, Cole D, Goldfinger M, Acuna-Villaorduna A, et al. Case fatality rate of cancer patients with COVID-19 in a New York Hospital System. *Cancer Discov.* (2020) 10:935–41. doi: 10.1158/2159-8290.CD-20-0516
3. Singh AP, Berman AT, Marmarelis ME, Haas AR, Feigenberg SJ, Braun J, et al. Management of lung cancer during the COVID-19 pandemic. *JCO Oncol Pract.* (2020) 16:579–86. doi: 10.1200/OP.20.00286
4. Saleem A, Akhtar MF, Haris M, Abdel-Daim MM. Recent updates on immunological, pharmacological, and alternative approaches to combat COVID-19. *Inflammopharmacology.* (2021) 29:1331–46. doi: 10.1007/s10787-021-00850-7
5. Huang YF, Bai C, He F, Xie Y, Zhou H. Review on the potential action mechanisms of Chinese medicines in treating Coronavirus Disease 2019 (COVID-19). *Pharmacol Res.* (2020) 158:104939. doi: 10.1016/j.phrs.2020.104939
6. Wang SX, Wang Y, Lu YB, Li JY, Song YJ, Nyamgerelt M, et al. Diagnosis and treatment of novel coronavirus pneumonia based on the theory of traditional Chinese medicine. *J Integr Med.* (2020) 18:275–83. doi: 10.1016/j.joim.2020.04.001
7. Yin B, Bi YM, Sun L, Huang JZ, Zhao J, Yao J, et al. Efficacy of integrated traditional Chinese and Western medicine for treating COVID-19: a systematic review and meta-analysis of RCTs. *Front Public Health.* (2021) 9:622707. doi: 10.3389/fpubh.2021.622707
8. Ni L, Chen L, Huang X, Han C, Xu J, Zhang H, et al. Combating COVID-19 with integrated traditional Chinese and Western medicine in China. *Acta Pharm Sin B.* (2020) 10:1149–62. doi: 10.1016/j.apsb.2020.06.009
9. Zhang ZJ, Wu WY, Hou JJ, Zhang LL, Li FF, Gao L, et al. Active constituents and mechanisms of Respiratory Detox Shot, a traditional Chinese medicine prescription, for COVID-19 control and prevention: network-molecular docking-LC-MS(E) analysis. *J Integr Med.* (2020) 18:229–41. doi: 10.1016/j.joim.2020.03.004
10. Hao da C, Xiao PG. Network pharmacology: a Rosetta Stone for traditional Chinese medicine. *Drug Dev Res.* (2014) 75:299–312. doi: 10.1002/ddr.21214
11. Bhattacharya S, Andorf S, Gomes L, Dunn P, Schaefer H, Pontius J, et al. ImmPort: disseminating data to the public for the future of immunology. *Immunol Res.* (2014) 58:234–9. doi: 10.1007/s12026-014-8516-1
12. Barshir R, Fishilevich S, Iny-Stein T, Zelig O, Mazor Y, Guan-Golan Y, et al. GeneCaRNA: a comprehensive gene-centric database of human non-coding RNAs in the genecards suite. *J Mol Biol.* (2021) 433:166913. doi: 10.1016/j.jmb.2021.166913
13. Nikolayeva O, Robinson MD. edgeR for differential RNA-seq and ChIP-seq analysis: an application to stem cell biology. *Methods Mol Biol.* (2014) 1150:45–79. doi: 10.1007/978-1-4939-0512-6_3
14. Chen H, Boutros PC. VennDiagram: a package for the generation of highly-customizable Venn and Euler diagrams in R. *BMC Bioinformatics.* (2011) 12:35. doi: 10.1186/1471-2105-12-35

15. Ru J, Li P, Wang J, Zhou W, Li B, Huang C, et al. TCMSP: a database of systems pharmacology for drug discovery from herbal medicines. *J Cheminform.* (2014) 6:13. doi: 10.1186/1758-2946-6-13
16. Sietsema WK. The absolute oral bioavailability of selected drugs. *Int J Clin Pharmacol Ther Toxicol.* (1989) 27:179–211.
17. Proudfoot JR. Drugs, leads, and drug-likeness: an analysis of some recently launched drugs. *Bioorg Med Chem Lett.* (2002) 12:1647–50. doi: 10.1016/S0960-894X(02)00244-5
18. Li Y, Chu F, Li P, Johnson N, Li T, Wang Y, et al. Potential effect of Maxing Shigan decoction against coronavirus disease 2019 (COVID-19) revealed by network pharmacology and experimental verification. *J Ethnopharmacol.* (2021) 271:113854. doi: 10.1016/j.jep.2021.113854
19. Shannon P, Markiel A, Ozier O, Baliga NS, Wang JT, Ramage D, et al. Cytoscape: a software environment for integrated models of biomolecular interaction networks. *Genome Res.* (2003) 13:2498–504. doi: 10.1101/gr.1239303
20. Szklarczyk D, Gable AL, Nastou KC, Lyon D, Kirsch R, Pyysalo S, et al. Correction to 'The STRING database in 2021: customizable protein-protein networks, and functional characterization of user-uploaded gene/measurement sets'. *Nucleic Acids Res.* (2021) 49:10800. doi: 10.1093/nar/gkab835
21. Trott O, Olson AJ. AutoDock Vina: improving the speed and accuracy of docking with a new scoring function, efficient optimization, and multithreading. *J Comput Chem.* (2010) 31:455–61. doi: 10.1002/jcc.21334
22. Shang J, Ye G, Shi K, Wan Y, Luo C, Aihara H, et al. Structural basis of receptor recognition by SARS-CoV-2. *Nature.* (2020) 581:221–4. doi: 10.1038/s41586-020-2179-y
23. Gangadevi S, Badavath VN, Thakur A, Yin N, De Jonghe S, Acevedo O, et al. Kobophenol A inhibits binding of host ACE2 receptor with spike RBD domain of SARS-CoV-2, a lead compound for blocking COVID-19. *J Phys Chem Lett.* (2021) 12:1793–802. doi: 10.1021/acs.jpclett.0c03119
24. Balkrishna A, Pokhrel S, Singh H, Joshi M, Mulay VP, Haldar S, et al. Withanone from *Withania somnifera* attenuates SARS-CoV-2 RBD and host ACE2 interactions to rescue spike protein induced pathologies in humanized Zebrafish model. *Drug Des Devel Ther.* (2021) 15:1111–33. doi: 10.2147/DDDT.S292805
25. Day CJ, Bailly B, Guillon P, Dirr L, Jen FE, Spillings BL, et al. Multidisciplinary approaches identify compounds that bind to human ACE2 or SARS-CoV-2 spike protein as candidates to block SARS-CoV-2-ACE2 receptor interactions. *mBio.* (2021) 12:20. doi: 10.1128/mBio.03681-20
26. Sharma P, Pandey AK, Bhattacharyya DK. Determining crucial genes associated with COVID-19 based on COPD findings (sextile,sextilesextile). *Comput Biol Med.* (2021) 128:104126. doi: 10.1016/j.compbiomed.2020.104126
27. Barbieri A, Robinson N, Palma G, Maurea N, Desiderio V, Botti G. Can Beta-2-adrenergic pathway be a new target to combat SARS-CoV-2 hyperinflammatory syndrome?-lessons learned from cancer. *Front Immunol.* (2020) 11:588724. doi: 10.3389/fimmu.2020.588724
28. Zhu QC, Li S, Yuan LX, Chen RA, Liu DX, Fung TS. Induction of the proinflammatory chemokine interleukin-8 is regulated by integrated stress response and AP-1 family proteins activated during coronavirus infection. *Int J Mol Sci.* (2021) 22:115646. doi: 10.3390/ijms22115646
29. Erdogan M, Kaya Kalem A, Ozturk S, Erdol MA, Kayaaslan B, Ozbebek YE, et al. Interleukin-6 level is an independent predictor of right ventricular systolic dysfunction in patients hospitalized with COVID-19. *Anatol J Cardiol.* (2021) 25:555–64. doi: 10.5152/AnatolJCardiol.2021.24946
30. Satu MS, Khan MI, Rahman MR, Howlader KC, Roy S, Roy SS, et al. Diseasome and comorbidities complexities of SARS-CoV-2 infection with common malignant diseases. *Brief Bioinform.* (2021) 22:1415–29. doi: 10.1093/bib/bbab003
31. Matsuyama T, Kubli SP, Yoshinaga SK, Pfeffer K, Mak TW. An aberrant STAT pathway is central to COVID-19. *Cell Death Differ.* (2020) 27:3209–25. doi: 10.1038/s41418-020-00633-7
32. Wu FQ, Fang T, Yu LX, Lv GS, Lv HW, Liang D, et al. ADRB2 signaling promotes HCC progression and sorafenib resistance by inhibiting autophagic degradation of HIF1alpha. *J Hepatol.* (2016) 65:314–24. doi: 10.1016/j.jhep.2016.04.019
33. Yang X, Zhao T, Feng L, Shi Y, Jiang J, Liang S, et al. PM25-induced ADRB2 hypermethylation contributed to cardiac dysfunction through cardiomyocytes apoptosis *via* PI3K/Akt pathway. *Environ Int.* (2019) 127:601–14. doi: 10.1016/j.envint.2019.03.057
34. Liang T, Chen J, Xu G, Zhang Z, Xue J, Zeng H, et al. STAT1 and CXCL10 involve in M1 macrophage polarization that may affect osteolysis and bone remodeling in extrapulmonary tuberculosis. *Gene.* (2022) 809:146040. doi: 10.1016/j.gene.2021.146040
35. Sun Q, Liu L, Mandal J, Molino A, Stolz D, Tamm M, et al. induces PRMT1 expression through ERK1/2 dependent STAT1 activation and regulates remodeling in primary human lung fibroblasts. *Cell Signal.* (2022) 89:110114. doi: 10.1016/j.cellsig.2021.110114
36. Sankar M, Ramachandran B, Pandi B, Mutharasappan N, Ramasamy V, Prabu PG, et al. *In silico* screening of natural phytocompounds towards identification of potential lead compounds to treat COVID-19. *Front Mol Biosci.* (2021) 8:637122. doi: 10.3389/fmolb.2021.637122
37. Pan B, Fang S, Zhang J, Pan Y, Liu H, Wang Y, et al. Chinese herbal compounds against SARS-CoV-2: puerarin and quercetin impair the binding of viral S-protein to ACE2 receptor. *Comput Struct Biotechnol J.* (2020) 18:3518–27. doi: 10.1016/j.csbj.2020.11.010
38. Xia QD, Xun Y, Lu JL, Lu YC, Yang YY, Zhou P, et al. Network pharmacology and molecular docking analyses on Lianhua Qingwen capsule indicate Akt1 is a potential target to treat and prevent COVID-19. *Cell Prolif.* (2020) 53:e12949. doi: 10.1111/cpr.12949
39. Gao K, Song YP, Song A. Exploring active ingredients and function mechanisms of Ephedra-bitter almond for prevention and treatment of Corona virus disease 2019 (COVID-19) based on network pharmacology. *BioData Min.* (2020) 13:19. doi: 10.1186/s13040-020-00229-4
40. Tao Q, Du J, Li X, Zeng J, Tan B, Xu J, et al. Network pharmacology and molecular docking analysis on molecular targets and mechanisms of Huashi Baidu formula in the treatment of COVID-19. *Drug Dev Ind Pharm.* (2020) 46:1345–53. doi: 10.1080/03639045.2020.1788070

Conflict of Interest: Author YX was employed by YuceBio Technology Co., Ltd.

The remaining authors declare that the research was conducted in the absence of any commercial or financial relationships that could be construed as a potential conflict of interest.

frontiers in Medicine

ORIGINAL RESEARCH
published: 24 January 2022
doi: 10.3389/fmed.2021.812278

Over-Expression and Prognostic Significance of FN1, Correlating With Immune Infiltrates in Thyroid Cancer

Qi-Shun Geng [1], Tao Huang [2], Li-Feng Li [3], Zhi-Bo Shen [3], Wen-Hua Xue [1] and Jie Zhao [1,3]*

[1] Department of Pharmacy, The First Affiliated Hospital of Zhengzhou University, Zhengzhou, China, [2] Huanghe Science and Technology University, Zhengzhou, China, [3] Internet Medical and System Applications of National Engineering Laboratory, The First Affiliated Hospital of Zhengzhou University, Zhengzhou, China

Background: Thyroid cancer (THCA) is a malignancy affecting the endocrine system, which currently has no effective treatment due to a limited number of suitable drugs and prognostic markers.

Methods: Three Gene Expression Omnibus (GEO) datasets were selected to identify differentially expressed genes (DEGs) between THCA and normal thyroid samples using GEO2R tools of National Center for Biotechnology Information. We identified hub gene *FN1* using functional enrichment and protein-protein interaction network analyses. Subsequently, we evaluated the importance of gene expression on clinical prognosis using The Cancer Genome Atlas (TCGA) database and GEO datasets. MEXPRESS was used to investigate the correlation between gene expression and DNA methylation; the correlations between *FN1* and cancer immune infiltrates were investigated using CIBERSORT. In addition, we assessed the effect of silencing *FN1* expression, using an *in vitro* cellular model of THCA. Immunohistochemical(IHC) was used to elevate the correlation between *CD276* and *FN1*.

Results: *FN1* expression was highly correlated with progression-free survival and moderately to strongly correlated with the infiltration levels of M2 macrophages and resting memory CD4+ T cells, as well as with *CD276* expression. We suggest promoter hypermethylation as the mechanism underlying the observed changes in *FN1* expression, as 20 CpG sites in 507 THCA cases in TCGA database showed a negative correlation with *FN1* expression. In addition, silencing *FN1* expression suppressed clonogenicity, motility, invasiveness, and the expression of CD276 *in vitro*. The correlation between FN1 and CD276 was further confirmed by immunohistochemical.

Conclusion: Our findings show that *FN1* expression levels correlate with prognosis and immune infiltration levels in THCA, suggesting that *FN1* expression be used as an immunity-related biomarker and therapeutic target in THCA.

Keywords: thyroid cancer, biomarker, FN1, immunity, survival

OPEN ACCESS

Edited by:
Fu Wang,
Xi'an Jiaotong University, China

Reviewed by:
Zhuo Li,
Sun Yat-sen Memorial Hospital, China
Mengyan Li,
Sun Yat-sen University Cancer Center (SYSUCC), China

***Correspondence:**
Jie Zhao
zhaojie@zzu.edu.cn

Specialty section:
This article was submitted to Precision Medicine, a section of the journal Frontiers in Medicine

Received: 10 November 2021
Accepted: 15 December 2021
Published: 24 January 2022

Citation:
Geng Q-S, Huang T, Li L-F, Shen Z-B, Xue W-H and Zhao J (2022) Over-Expression and Prognostic Significance of FN1, Correlating With Immune Infiltrates in Thyroid Cancer. Front. Med. 8:812278. doi: 10.3389/fmed.2021.812278

INTRODUCTION

Thyroid carcinoma (THCA) is the most common type of endocrine cancer (1). Its prevalence has sharply increased in recent decades. In the US, the annual incidence of thyroid cancer increased from 4.9/100,000 in 1975 to 14.3/100,000 in 2009 (2). The observed increase in the incidence is partly due to the increased detection rate. In Beijing, China, the detection rate significantly increased from 16.8% in 1994 to 69.8% in 2015 ($P < 0.01$) (3). THCA can be subclassified into several histological subtypes, which include papillary thyroid carcinoma (PTC), follicular thyroid carcinoma (FTC), undifferentiated or anaplastic thyroid carcinoma (ATC), and medullary thyroid carcinoma (MTC). THCA occurs mostly in young adults (the average age of diagnosis is 40 years), and more frequently in females (4). The most common treatment of thyroid cancer consists of surgical resection combined with radiotherapy or chemotherapy. However, for PTC, ATC, and MTC, a satisfactory resection is not always feasible, and even after radiotherapy, the risk of cancer recurrence is still high (5, 6). In addition, recently personalized therapy approaches directed against specific targets have become available, only a few suitable targets have been identified thus far. Although the survival rate of patients with thyroid cancer is very high, with the rapid increase in THCA incidence, this disease poses a serious threat to human health (7).

Immune-related processes play an important role in the development of thyroid cancer, and hence, immunotherapy strategies are considered the most promising candidates for the treatment of thyroid cancer in the future (8). Many studies have shown that tumor-infiltrating lymphocytes, such as tumor-associated macrophages, tumor-associated dendritic cells, and tumor-infiltrating neutrophils, affect the prognosis of THCA patients and the efficacy of chemotherapy and immunotherapy (9). Therefore, there is an urgent need to understand which immune cells play a role in the development of THCA, as well as to explore novel immune-related biomarkers that could aid in the diagnosis and prognosis of this disease.

Fibronectin 1 (*FN1*) encodes a glycoprotein present in a soluble dimeric form in the plasma and a dimeric or multimeric form at the cell surface and in the extracellular matrix. FN1 is involved in cell adhesion and migration processes during embryogenesis, wound healing, blood coagulation, host defense, and metastasis, as well as in cell proliferation (10). Multiple studies have established its involvement in the development of cancer, including oral squamous cell carcinoma (11), renal cancer (12), and thyroid cancer (13). Previous studies have indicated that FN1 is involved in NKp46 receptor-mediated interferon-γ (IFN-γ) production by natural killer cells, with respect to the control of tumor architecture and metastasis (14). BAG5 also promotes invasion of papillary thyroid cancer cells *via* upregulation of FN1 at the translational level (15). In addition, FN1 plays an important role in glioblastomagrowth and invasion, and is correlated with the low elasticity of thyroid nodules and Malignancy of THCA (16, 17). These findings suggest that FN1 has multifaceted functional roles in tumor progression.

In this study, we comprehensively analyzed the correlation between *FN1* expression with the prognosis of patients with THCA, as well as with the presence of tumor-infiltrating immune cells. Our findings highlight the important role of *FN1* expression in THCA, and suggest a potential correlation between *FN1* expression and tumor-immune interactions. Furthermore, the results were validated by immunohistochemistry and cell biology experiments, which indicate that *FN1* is a potential prognostic and immunity-related biomarker in THCA and could potentially be used as a drug target in THCA therapy.

MATERIALS AND METHODS

Cell Lines and Reagents

The cell lines B-CPAP and KTC-1, belonging to the thyroid cancer cell lines, were obtained from the Institute of Biochemistry and Cell Biology of the Chinese Academy of Sciences, Shanghai, China. All cells were cultured in Roswell Park Memorial Institute (RPMI) 1640 medium (Gibco, Grand Island, NY, USA) supplemented with 10% fetal bovine serum (10%FBS), 100 U/mL penicillin, and 100 mg/mL streptomycin (Invitrogen, Carlsbad, CA, USA). Cells were incubated in a 5% CO_2/95% O_2 in a humidified atmosphere at 37°C.

Data Sources and Identification of Differentially Expressed Genes (DEGs)

TCGA is a landmark cancer genomics program that characterized over 20,000 primary cancer samples, spanning 33 cancer types and matched to the respective normal samples. Samples are molecularly characterized, and multi-omics data are provided, including gene transcripts, miRNA expression data, and DNA methylation state data. Additionally, it contains abundant and standardized clinical data. All datasets used were downloaded from the Cancer Genomics Browser website of the University of California, Santa Cruz (18). The GEO database (http://www.ncbi.nlm.nih.gov/geo/) stores original submitter-supplied records (series, samples, and platforms), as well as the curated datasets. Using the selection criteria of a number of samples >20 and <1,000, we selected three gene expression profiles [GSE33630 (19), GSE58545 (20), and GSE60542 (21)]. Among them, GSE33630 (105 samples) and GSE60542 (45 samples) are based on the GPL570 platform, and GSE58545 (92 samples) was obtained with the GPL96 platform. According to the commonly used threshold parameters (adjusted $P < 0.05$, $|\log_2 \text{FoldChange}| \geq 2.0$) (22), we determined the DEGs between THCA and normal thyroid samples using the GEO2R online analysis tool, accessible *via* the National Center for Biotechnology Information website. Then, the interactive tool Venny2.1.0 (23) was used to create a Venn diagram of the DEGs

---

Abbreviations: THCA, Thyroid cancer; GEO, the Gene Expression Omnibus database; DEGs, the differentially expressed genes; DAVID, the Database for Annotation, Visualization, and Integrated Discovery; STRING, the Retrieval of Interacting Genes; PPI, the protein–protein interaction; GEPIA, Gene expression profiling and interactive analyses; PTC, papillary thyroid carcinoma; FTC, follicular thyroid carcinoma; ATC, undifferentiated thyroid carcinoma; MTC, medullary thyroid carcinoma; IHC, Immunohistochemistry.

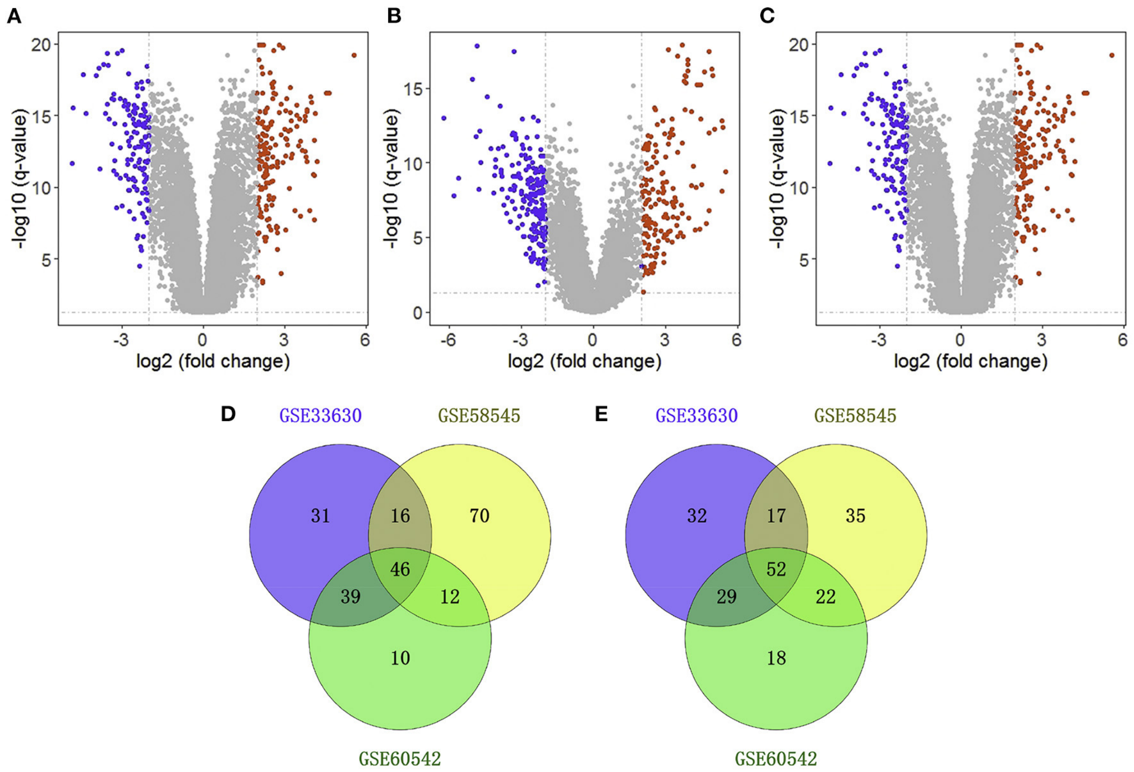

FIGURE 1 | Identification of differentially expressed genes (DEGs). Volcano plot showing the differentially expressed genes of GSE33630 **(A)**, GSE58545 **(B)**, and GSE60542 **(C)**. Veen diagram of downregulated **(D)** and upregulated **(E)** common DEGs to three gene expression profiles.

to determine the common DEGs between the three analyzed gene expression profiles.

Functional Enrichment Analysis and Identification of Hub Genes

Gene Ontology (GO) is an initiative that provides a standardized classification of genes by accounting for their functions, biological pathways they participate in, and the cell localization of the corresponding proteins. Genes are categorized into three domains: biological process (BP), molecular function (MF), and cellular component (CC) (24). We annotated the identified DEGs according to the GO classification system using the Database for Annotation, Visualization, and Integrated Discovery (DAVID) tool (https://david.ncifcrf.gov/) (25). The threshold criteria to determine the significantly enriched GO terms were $P < 0.05$ and gene counts ≥ 5. To identify the hub genes, a protein-protein interaction (PPI) network was constructed for the DEGs that had been annotated in the category BP ($P < 0.05$) using Search Tool for the Retrieval of Interacting Genes (STRING) (http://string-db.org/) (26). PPI pairs with a combined confidence score ≥ 0.4, were visualized using Cytoscape (version 3.7.2) (27). The Cytoscape plugin Molecular Complex Detection (MCODE) (version 1.4.2), an app to cluster any given network, was used to identify the most important module in the PPI network, and the plugin CytoHubba was used to identify the hub genes in the PPI networks by calculating the degree of connectivity between DEGs. The selection criteria were as follows: MCODE score > 5 points, degree cut-off $= 2$, node score cut-off $= 0.2$, maximum depth $= 100$, and k-score $= 2$.

Correlation Between Gene Expression and Survival

ONCOMINE is an online cancer microarray database (www.oncomine.org) (28). Gene expression profiles from the website were used to analyze the transcription levels of *FN1* in THCA. Furthermore, the correlation between *FN1* expression and progression-free survival (PFS) and clinical parameters was analyzed using the TCGA database. In addition, the UALCAN (29), a web resource to analyze cancer OMICS data, was used to investigate the correlation between *FN1* expression and cancer stage, and between *FN1* expression and promoter methylation level.

Methylation and Immunity Correlation Analysis

MEXPRESS (https://mexpress.be/) is a data visualization tool designed for easy visualization of TCGA expression, DNA methylation, and clinical data, as well as the correlations between them (30, 31). We used this tool to investigate the correlation between hub gene expression and the degree of methylation of the gene promoters. CIBERSORT is an analytical tool used to estimate the abundance of cell types

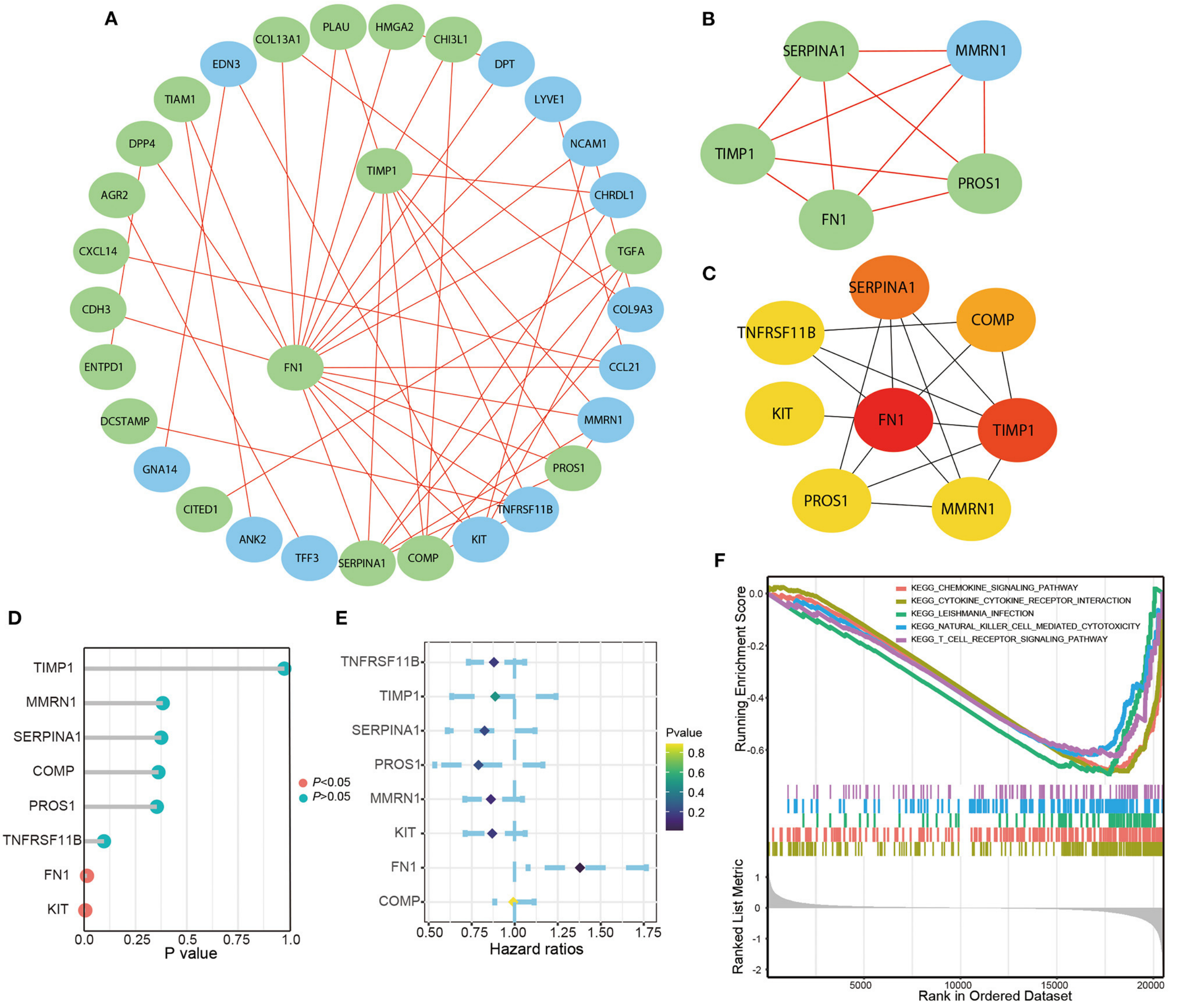

FIGURE 2 | The Screening and identification of key genes. **(A)** PPI network constructed with the DEGs in biological progress. **(B)** The most significant module obtained from PPI network. **(C)** The top eight hub genes. The logrank analysis of hub genes **(D)** and the multivariate cox logistic regression analysis **(E)** of hub genes based on the TCGA database. **(F)** The significant kegg pathways of FN1 in THCA obtained by GSEA.

in a mixed cell population using gene expression data (32). We used this tool to assess the degree of immune infiltration. The co-expression analysis of *FN1* and B7 family members (including *CD274, CD80, CD86, CD276, CD273, CD275, B7-H4, B7-H5, CD28, B7-H7, CD152, CD279, CD278, TLT-2*, and *NKp30*) was assessed in the normal thyroid samples and in the THCA samples from TCGA database. The correlation between *FN1, CD273, CD274, CD275, B7-H4*, and *CD276* was further analyzed in the THCA cohort. GEPIA (http://gepia.cancer-pku.cn/detail.php) (33) and TIMER (39) were used to plot the expression scatterplots between any pair of genes in a given cancer type, while including the Spearman correlation and the statistical significance.

Silencing of FN1 by Small Interfering RNA (siRNA)

The siRNA targeting human *FN1* (siFN1) and a non-specific scrambled siRNA sequence (siNC) were purchased from Shanghai Gene Pharma and transiently transfected into B-CPAP and KTC-1 cells using Lipofectamine 3000 (Invitrogen, Carlsbad, CA, USA) according to the manufacturer's instructions. The target sequence in *FN1* was: 5′-CAGUCAAAGCAAGCCCGGUUGUUAU-3′. Subsequently, assays were performed 48 h after the transfection. Cell viability was assessed 24, 48, or 72 h after transfection using the commercial kit Cell Counting Kit-8 (CCK-8, Beyotime Biotechnology, China) according to manufacturer's instructions.

TABLE 1 | The information related to biological processes of statistical significance.

Term	Describe	*P*-value	Gene	Count
GO:0007155	Cell adhesion	1.61E-06	PLXNC1, CYP1B1, CLDN10, MMRN1, CDH3, NCAM1, LAMB3, LYVE1, CDH16, SORBS2, COMP, ENTPD1, DPT, FN1	14
GO:0007165	Signal transduction	0.012464	GNA14, EDN3, CRABP1, RAP1GAP, KIT, HMGA2, LYVE1, TNFRSF11B, CXCL14, ANK2, TENM1, IGSF1, GDF15, PLAU	14
GO:0030198	Extracellular matrix organization	0.000814	CSGALNACT1, TNFRSF11B, LAMB3, COL9A3, COL13A1, COMP, FN1	7
GO:0010628	Positive regulation of gene expression	0.00353	ANK2, KIT, HMGA2, CDH3, AGR2, CITED1, FN1	7
GO:0008284	Positive regulation of cell proliferation	0.046698	EDN3, TIAM1, TGFA, KIT, DPP4, FN1, TIMP1	7
GO:0007596	Blood coagulation	0.046698	SERPINA1, MMRN1, ENTPD1, PROS1, PAPSS2, PLAU	6
GO:0042060	Wound healing	0.046698	TGFA, TFF3, CDH3, FN1, TIMP1	5
GO:0002576	Platelet degranulation	0.046698	SERPINA1, MMRN1, PROS1, FN1, TIMP1	5
GO:0007399	Nervous system development	0.046698	CSGALNACT1, CHRDL1, TENM1, BEX1, MPPED2	5

Quantitative Reverse Transcription-Polymerase Chain Reaction (RT-qPCR)

RNA was isolated using TRIzol reagent (Invitrogen, Carlsbad, CA, USA), followed by transfer into RNA-free EP tubes and storage at −80°C. Complementary DNA (cDNA) was synthesized from total RNA using the PrimeScript RT reagent Kit (Takara, Dalian, China), and PCR was performed using the SYBR Green RT-PCR Kit (AG11701, Accurate Biotechnology, Hunan, Co., Ltd). PCR was performed on the StepOne Plus Real-Time PCR System (Applied Biosystems, Foster City, CA, USA). Data were analyzed using the $2^{-\Delta\Delta CT}$ method. The primer sequences used in the experiment are as follows: FN1, 5′-CGGTGGCTGTCAGTCAAAG-3′ (forward), 5′-AAACCTCGGCTTCCTCCATAA-3′ (reverse); CD276, 5′-CTCCCTACAGCTCCTACCCTC-3′ (forward), 5′-TGGTCTGTGTATCGCATCCTT-3′ (reverse).

TABLE 2 | Hub genes with higher degree of connectivity.

Gene symbol	Gene title	Degree	Gene nature
FN1	Fibronectin 1	17	UP
TIMP1	TIMP metallopeptidase inhibitor 1	9	UP
SERPINA1	Serpin family A member 1	6	UP
COMP	Cartilage oligomeric matrix protein	5	UP
PROS1	Protein S (alpha)	4	UP
MMRN1	Multimerin 1	4	DOWN
KIT	KIT proto-oncogene receptor tyrosine kinase	4	DOWN
TNFRSF11B	TNF receptor superfamily member 11b	4	DOWN

Immunohistochemistry (IHC) Staining

Samples from cancer patients were obtained from thyroid cancer arrays (DC-Thy11004 Avira Biotechnology Co., Ltd., China), which included 24 cases of thyroid cancer and corresponding paracancerous tissues. Tumor tissues chip were deparaffinized and rehydrated, followed by antigen retrieval. The sections were then blocked with 5% BSA in PBS and incubated with FN1 antibody (1 mg/mL, 1:200; Affinity) and CD276 antibody (1 mg/mL, 1:200; Affinity) at 4°C overnight. After three times washing, tissue sections were incubated with the secondary antibody conjugated with streptavidin–horseradish peroxidases for 1 h at room temperature. The slides were stained with 3, 3-diaminobenzidine tetrahydrochloride (DAB), and the nuclei were counterstained with hematoxylin. Marker density was scored independently by two investigators as follows: 0, negative; 1, weak; 2, moderate; or 3, strong.

Statistical Analyses

All statistical analyses were performed using GraphPad Prism 5.0 (San Diego, CA, USA) and R version 3.6.1. Data from independent experiments performed in triplicate are presented as mean ± standard deviation (SD). Multivariate survival analysis was carried out for all parameters that were significant in the univariate analysis using the Cox regression model. To analyze the significance of differences between groups, unpaired two-tailed Student's *t*-test and

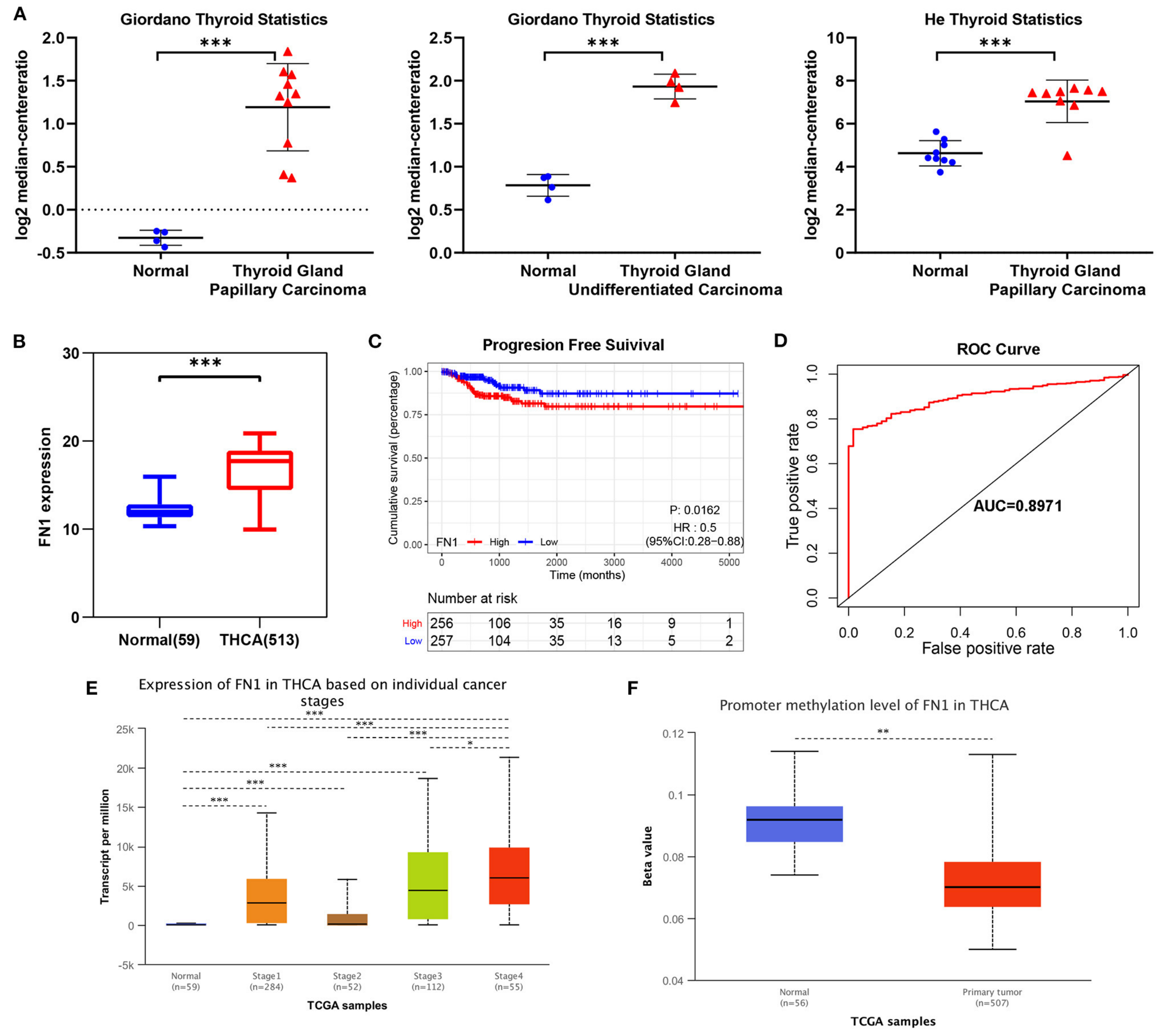

FIGURE 3 | Transcriptional expressions of FN1 significantly correlated with poor survival outcomes in THCA patients from TCGA cohort. **(A)** The expression of FN1 in different subtypes of THCA. **(B)** The expressions of FN1 in THCA patients from TCGA-THCA cohort, **(C)** The correlation between the expression of FN1 and PFS, **(D)** ROC curve with an AUC of 0.8971. Transcriptional expression of FN1 was significantly correlated with individual cancer stages **(E)** and promoter methylation **(F)**. $^*p < 0.05$, $^{**}p < 0.01$, $^{***}p < 0.001$.

one-way analysis of variance (ANOVA) were performed, and multiple comparisons were accounted for using Bonferroni's correction. Differences were considered significant at $P < 0.05$.

RESULTS

Identification of the Common DEGs Between the Datasets Used

We obtained three gene expression profiles (GSE33630, GSE58545, and GSE60542) from the GEO database. GSE33630 includes 45 normal thyroid samples and 60 THCA samples; GSE58545 includes 18 normal thyroid samples and 27 THCA samples; GSE60542 includes 30 normal thyroid samples and 33 THCA samples. According to the conventional criteria (adjusted $P < 0.05$ and $|\log_2 \text{FoldChange}| \geq 2.0$), 263 genes were identified as DEGs in GSE33630, of which 133 were downregulated and 130 were upregulated; moreover, GSE58545 included 270 DEGs, including 144 downregulated genes and 126 upregulated genes, and GSE60542 contained 228 DEGs, including 107 downregulated genes and 121 upregulated genes (**Figures 1A–C**). A Venn diagram showed that 98 genes were differentially expressed in the three datasets, of which 46 were downregulated, and 52 were upregulated (**Figures 1D,E**).

Functional Enrichment Analysis of the Common DEGs

In this study, we performed GO functional analysis of the common DEGs using the tool DAVID. Then, we filtered the results to improve the confidence according to the standard criteria ($P < 0.05$ and gene counts $\geq$ 5) (**Supplementary Table 1**). GO analysis showed that the common DEGs were mainly enriched in the CC category, including the plasma membrane, extracellular exosome, extracellular region, and extracellular space. DEGs annotated as BP were enriched in cell adhesion, signal transduction, extracellular matrix organization, positive regulation of gene expression, positive regulation of cell proliferation, blood coagulation, wound healing, platelet degranulation, and nervous system development, all of which are processes associated with the occurrence and development of tumors.

Identification and Analysis of the Hub Genes

We selected 46 DEGs involved in specific BP ($P < 0.05$) to build the PPI network (**Figure 2A**; **Table 1**). The most important module was obtained using the plugin MCODE in Cytoscape (**Figure 2B**). The top eight genes, including *FN1, TIMP1, SERPINA1, COMP, PROS1, MMRN1, KIT,* and *TNFRSF11B*, were identified as potential hub genes according to the degree score generated by the plugin CytoHubba (**Figure 2C**; **Table 2**). This was consistent with their enrichment in the top module determined using MCODE. Among them, *FN1* had the highest degree of connectivity in the PPI network. Furthermore, logrank regression and multivariate Cox regression analysis were used to calculate the correlation between gene expression and PFS (**Figures 2D,E**), indicating *FN1* appeared to be the most attractive drug target and prognostic marker. GSEA was used to perform kegg analysis for FN1. The results suggested that most of the involved significant pathways including chemokine signaling pathway, cytokine receptor interaction, Leishmania infection, natural killer cell-mediated cytotoxicity, and T cell receptor signaling pathway, as it has been established that FN1 plays a crucial role in tumor architecture and controls metastasis (**Figure 2F**) (13).

Expression Levels of *FN1* in THCA and Evaluation of Its Value as a Prognostic Marker

We analyzed the expression levels of *FN1* in THCA using the Oncomine database. We found that *FN1* expression was upregulated in almost all different subtypes of THCA, including PTC and ATC (**Figure 3A**). We validated these results using the TCGA database, in which *FN1* was also significantly high expressed in THCA samples than in normal thyroid samples ($P < 0.05$) (**Figure 3B**);. and *FN1* expression level was also correlated with PFS of THCA ($P < 0.05$) (**Figure 3C**). The area under the curve (AUC) of *FN1* from the TCGA dataset was 0.8971 (**Figure 3D**), highlighting the value of *FN1* as a diagnostic marker in THCA. We compared the clinical characteristics (including age, sex, location, clinical stage, progression state, lymph node metastasis, and distant metastasis) between the *FN1*-high expression and *FN1*-low expression groups, and observed statistically significant differences in lymph node metastasis, distant metastasis, and progression state, although no significant differences were identified for other clinical features (**Table 3**). Furthermore, univariate and multivariate Cox regression models revealed that clinical stage and *FN1* expression were independent prognostic factors for PFS in patients with THCA (**Table 4**). In addition, analysis of the UALCAN database showed that *FN1* expression levels were closely correlated to cancer stage (**Figure 3E**) and that the degree of methylation of the *FN1* promoter was lower in THCA than that in normal tissues (**Figure 3F**),

TABLE 3 | Comparison of clinical characteristics between low FN1 group and high FN1 group in THCA cohort.

Variable	Case no. (%)	FN1		*P*
		High	Low	
Sample	505	253	252	
Age (Year)				
≥60	118	62	56	0.544
<60	387	191	196	
Gender				
Female	366	182	184	0.786
Male	139	71	68	
Clinical stage				
I	287	136	151	
II	52	13	39	**<0.001**
III	111	65	46	
IV	55	39	16	
Lymph node metastasis				
Yes	227	84	143	
No	229	152	77	**<0.001**
Unknown	49	17	32	
Distant metastases				
Yes	280	157	123	
No	9	3	6	**0.009**
Unknown	216	93	123	
Location				
Left lobe	176	89	87	
Right lobe	219	105	114	0.348
Bilateral	88	44	44	
Isthmus	22	15	7	
Progression state				
Yes	53	35	18	**0.014**
No	452	218	234	

P-values less than 0.05 are bold.

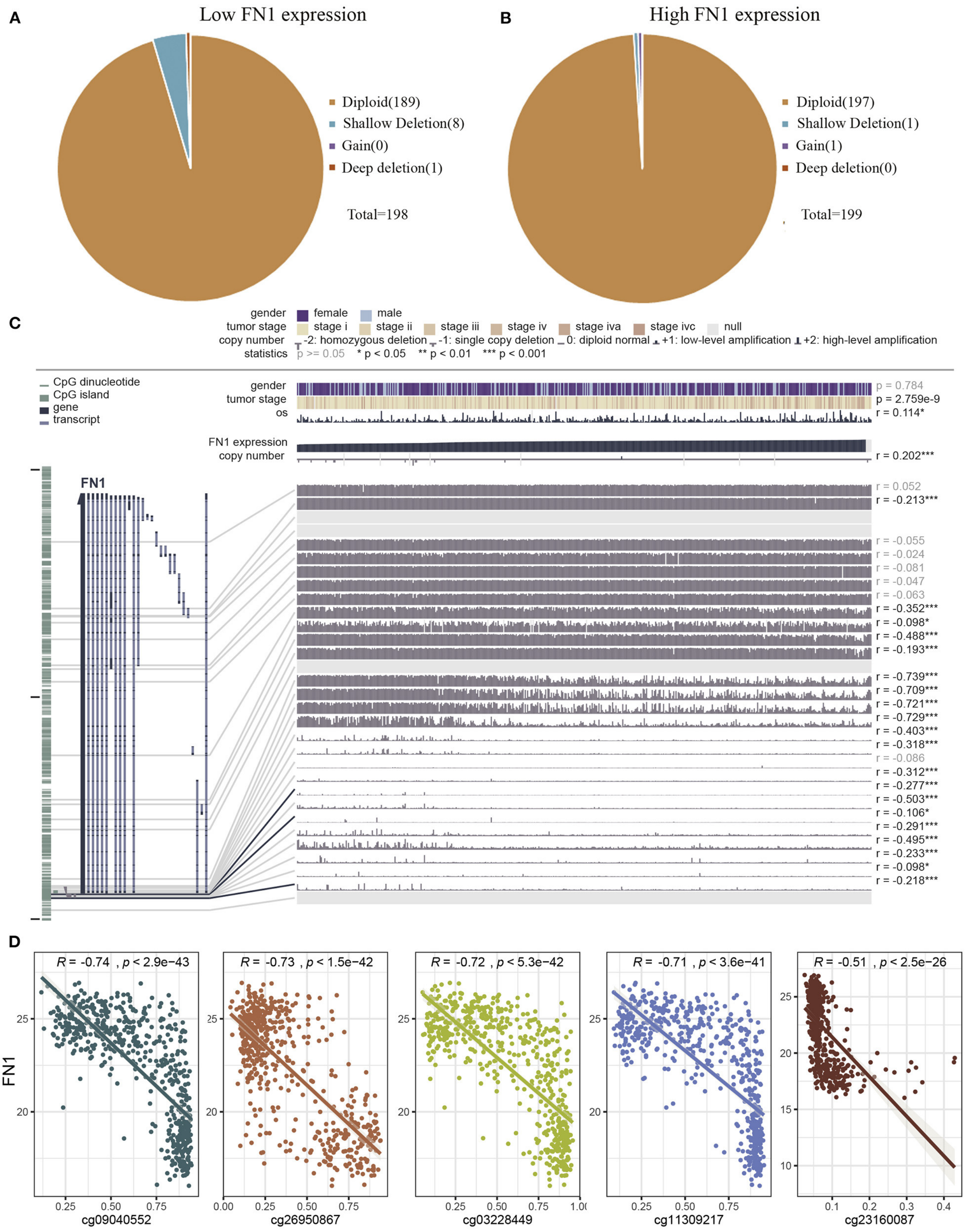

FIGURE 4 | Analysis of the potential genetic and epigenetic alterations associated with FN1 dysregulation. **(A,B)** The CNAs in FN1-high and low expression groups. **(C)** Analysis of CpG island methylation and abnormal FN1 expression using TCGA-THCA dataset. **(D)** Correlation between FN1 expression and CpG island methylation was performed. *$p < 0.05$, **$p < 0.01$, ***$p < 0.001$.

TABLE 4 | Univariate and Multivariate Cox logistic regression analysis of FN1 for predicting PFS in TCGA cohort (PFS, progression free survival; TCGA, The Cancer Genome Atlas).

Variable	**Univariate**			**Multivariate**		
	HR	**(95% CI)**	***P***	**HR**	**(95% CI)**	***P***
Age (ref. <60)	2.10	1.20∼3.70	**0.007**	1.49	0.78∼2.80	0.225
Gender (ref. Male)	0.58	0.33∼1.00	0.055	0.69	0.39∼1.20	0.211
Clinical stage (ref. I–II)	2.60	1.50∼4.40	**<0.001**	1.94	1.03∼3.60	**0.039**
Lymph node metastasis (ref. No)	1.60	0.91∼2.80	0.11	1.13	0.62∼2.10	0.687
Distant metastases (ref. No)	1.50	0.88∼2.60	0.13	1.65	0.95∼2.90	0.076
Location (ref. left and right lode)	0.90	0.45∼1.80	0.77	0.84	0.42∼1.70	0.632
FN1 expression (ref. low)	1.90	1.10∼3.40	**0.022**	1.83	1.01∼3.30	**0.046**

P-values less than 0.05 are bold.

indicating that *FN1* may be involved in the development of THCA.

Analysis of the Potential Genetic and Epigenetic Alterations Underlying *FN1* Dysregulation

Next, we investigated the underlying mechanism of *FN1* dysregulation in THCA. To determine whether copy number alterations (CNAs) are responsible for the abnormal expression of *FN1* in THCA, we analyzed 397 cases from the TCGA database for which CNAs data was available. No differences were observed for CNAs in the FN1-high and FN1-low groups (**Figures 4A,B**). Another mechanism that could underlie the altered *FN1* expression profile observed in THCA samples is promoter hypermethylation, which plays an important role in the occurrence and development of several types of tumors (34, 35). To investigate whether DNA methylation results in FN1 dysfunction, we examined the status of CpG sites in 507 THCA cases from the TCGA database using the tool MEXPRESS. We found that 27 CpG sites had associated data; among which 20 CpG sites showed a negative correlation with *FN1* expression (**Figure 4C**). The Pearson correlation coefficient was calculated for the five CpG sites with the highest correlation coefficient, including cg21494132, cg09040552, cg11309217, cg03228449, and cg03228449 (**Figure 4D**, all $P < 0.05$). Our results demonstrate the correlation between DNA methylation and abnormal expression levels of *FN1* in THCA, highlighting the need for further investigation of the underlying mechanism.

Correlation Between FN1 and Inflammatory Activities

Considering the strong association between *FN1* expression levels and THCA prognosis, we hypothesized that FN1 may be associated with inflammatory responses, leading to enhanced survival rates. To identify the FN1 associated immune signature in THCA, we assessed the degree of immune infiltration with CIBERSORT. *FN1* expression was closely correlated to the degree of M2 macrophages, resting memory CD4$^+$ T cells, follicular helper T cells, and CD8$^+$ T cell infiltration. The increase in *FN1* expression was associated with an increase of the proportion of M2 macrophages and resting memory CD4$^+$ T cells and a decrease of the proportion of follicular helper T cells and CD8$^+$ T cells (**Figure 5A**). To further investigate the correlation between *FN1* and inflammation, we analyzed the co-expression of *FN1* and members of the B7-CD28 ligand-receptor family, including *CD274, CD80, CD86, CD276, CD273, CD275, B7-H4, B7-H5, CD28, B7-H7, CD152, CD279, CD278, TLT-2,* and *NKp30*, which are closely correlated to T cell function. The result demonstrated that FN1 exhibited a significant co-expression trend with CD273, CD274, CD275, CD276 and B7-H4 (**Figure 5B**). Furthermore, we investigated the correlation between *FN1, CD273, CD274, CD275, CD276,* and *B7-H4* expression in the THCA cohort, and found a close positive correlation between *FN1* and *CD276* expression ($R = 0.55$, $P = 0$) (**Figures 5C,D**). This result was validated using TIMER and GEPIA, which provided *R*-values of 0.682 and 0.79, respectively, for the correlation between *FN1* and *CD276* in THCA ($P < 0.001$) (**Figures 5E,F**).

Down-Regulation of *FN1* Inhibited Cell Proliferation and Invasion and Decreased *CD276* Expression Levels in THCA Samples

To explore the biological significance of *FN1* in THCA tumorigenesis, KTC-1 and B-CPAP cells were transfected with siRNA targeting *FN1* (siFN1) or negative control siRNA (siNC). Efficient depletion of *FN1* expression was confirmed *via* RT-qPCR ($P < 0.05$, **Figure 6A**). Moreover, we found that downregulation of *FN1* significantly reduced the expression of *CD276* in KTC-1 and B-CPAP cells compared with siNC transfection (**Figure 6A**), indicating that that the interactions between FN1 and CD276 could be a potential mechanism for the correlation of FN1 expression with immune infiltration and poor prognosis in THCA. Then, we studied the effect of *FN1* on THCA cell proliferation and invasion *in vitro*. The wound-healing assay, cell viability, and cytotoxicity CCK-8 assay, and clone formation assay revealed that downregulation of *FN1* in both cell types significantly inhibited cell proliferation and invasion compared to that in the control cells ($P < 0.05$, **Figures 6B–D**). These results suggest that the downregulation of *FN1* reduces the viability of THCA cell lines.

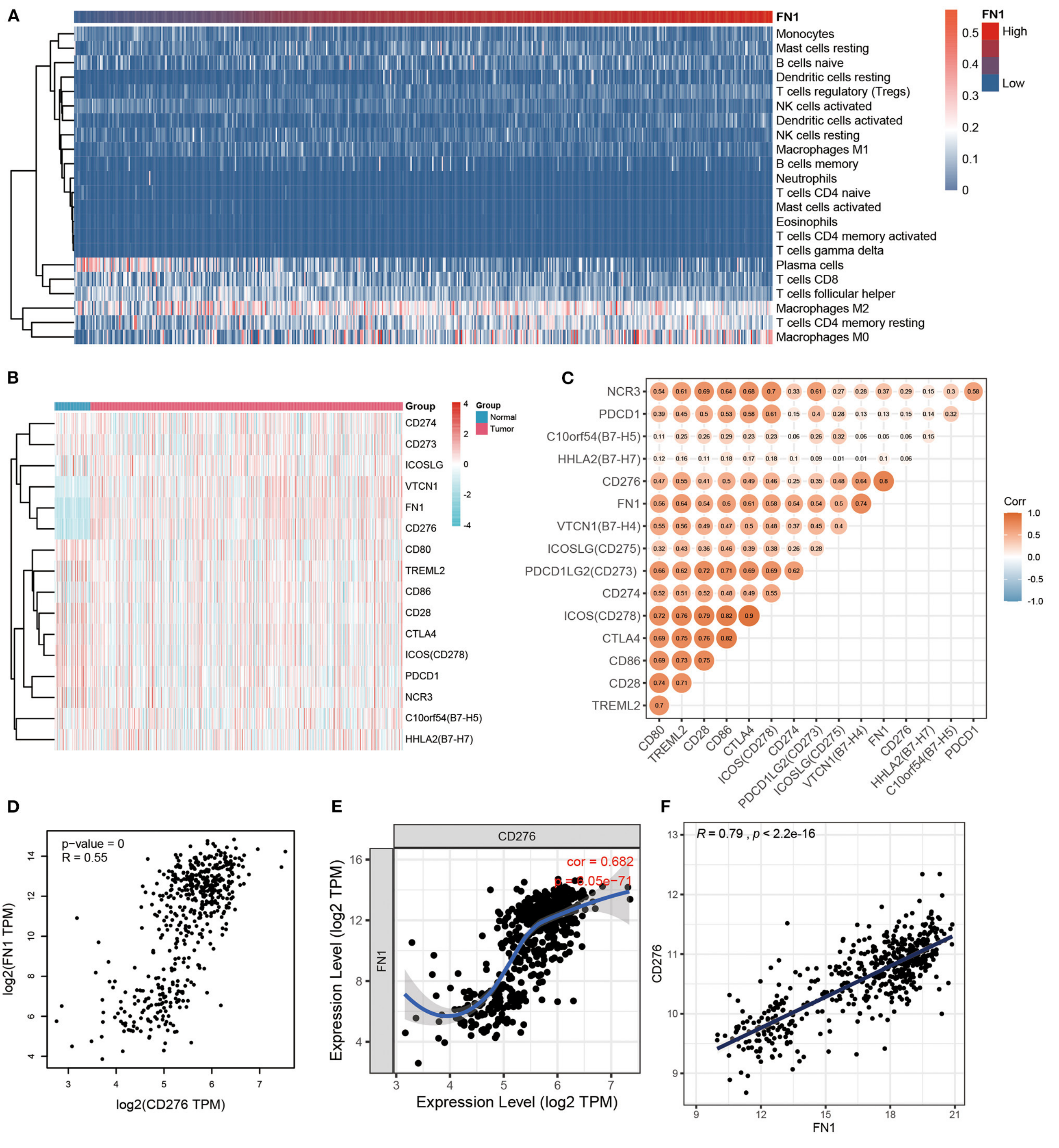

FIGURE 5 | The correlation between FN1 and inflammatory activities. **(A)** The heatmap of immune infiltration analysis. **(B)** The coexpression between FN1 and the B7-CD28 ligand-receptor family. **(C)** The correlation between FN1, CD273, CD274, CD275, CD276, and B7-H4 in THCA cohort. The correlation between FN1 and CD276 analyzed by THCA datasets **(D)**, TIMER **(E),** and GEPIA **(F)**.

FN1 Is Positively Correlated With CD276

In order to assess FN1 correlation with CD276, we analyzed FN1 and CD276 expression in tumor sites and the adjacent no-tumor samples (**Figure 7A**). We found that FN1 and CD276 showed significantly higher expression in tumor sites than in the adjacent no-tumor samples ($P < 0.05$, **Figures 7C,D**). Furthermore, we divided the tumor sites into two groups according to FN1 expression and found that CD276 levels

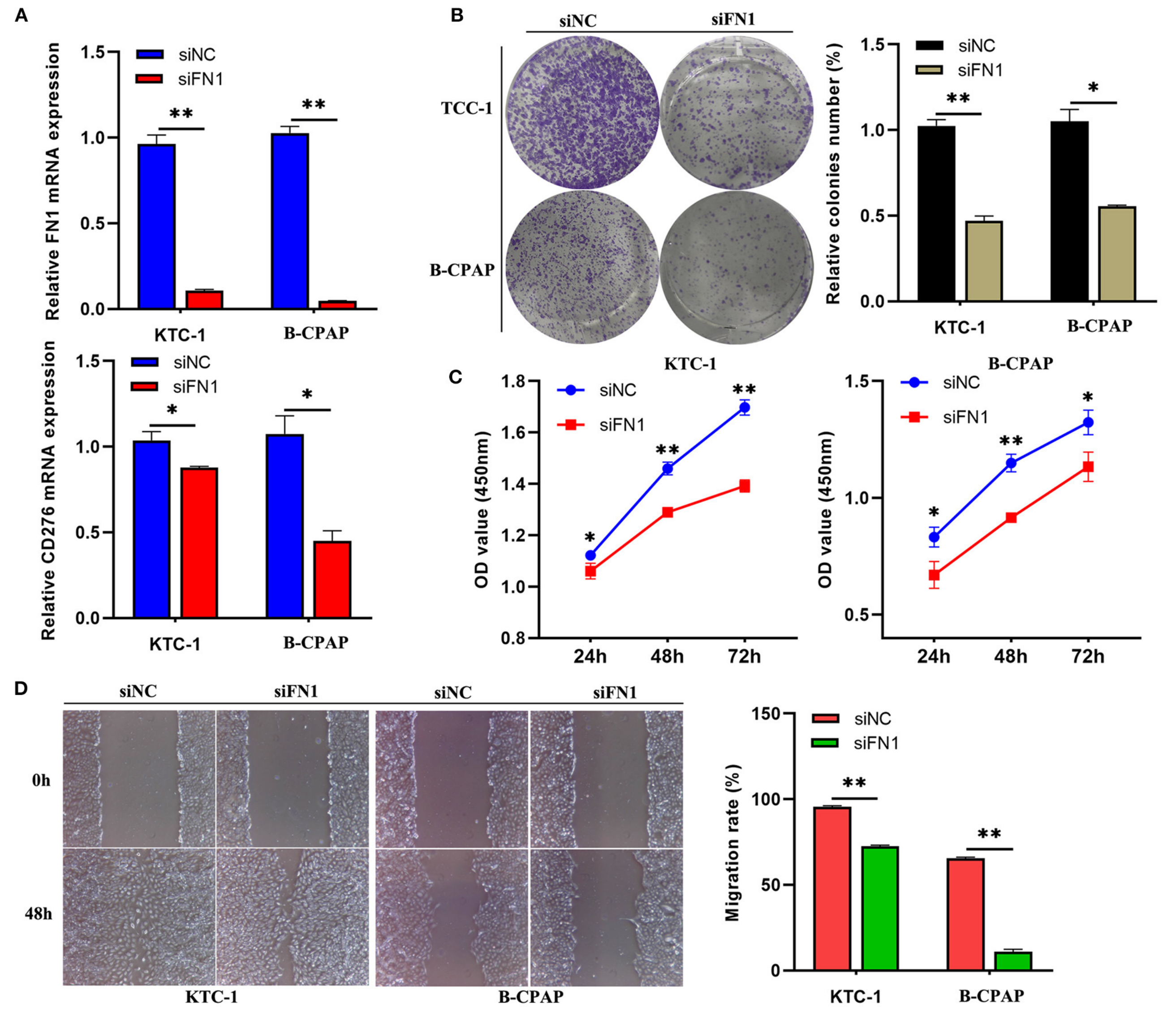

FIGURE 6 | Down-regulation of FN1 suppressed THCA cell migration and invasion *in vitro*. **(A)** qRT-PCR showing the efficient depletion of FN1 expression and the expression of CD276 in B-CPAP and KTC-1 cells compared with siNC transfection. Representative photo-images (left) and histograms (right) of the effect of siFN1 on the clone formation **(B)** and migration **(D)** of B-CPAP and KTC-1 cells. **(C)** The proliferative ability of B-CPAP and KTC-1 cells after transfection was evaluated by CCK-8 assay. $^*p < 0.05$, $^{**}p<0.001$.

were positively correlated with the level of FN1($P < 0.05$, **Figures 7B,E**).

DISCUSSION

FN1 is a member of the FN family widely expressed in multiple cell types and is involved in cellular adhesion and migration processes (36). Here, we report that variations in *FN1* expression levels correlate with prognosis in THCA patients. High expression levels of *FN1* are associated with a poorer prognosis in THCA, indicating that *FN1* expression could be used to predict tumor patient' prognosis. Furthermore, our analysis show that immune infiltration levels and immune markers are correlated with *FN1* expression level in THCA, suggesting a potential role of *FN1* in tumor immunology and its possible used as a cancer biomarker.

In this study, we screened DEGs from three GEO datasets based on functional enrichment analysis and PPI network maps. *FN1*, which is closely correlated to disease-free survival, was identified as a hub gene. In addition, we found that the promoter region of *FN1* had significantly lower methylation levels ($P < 0.05$) in THCA than in normal thyroid tissues. GSEA analysis also showed that *FN1* plays a role in the chemokine signaling pathway, cytokine receptor interaction, natural killer cell-mediated cytotoxicity, and T cell receptor

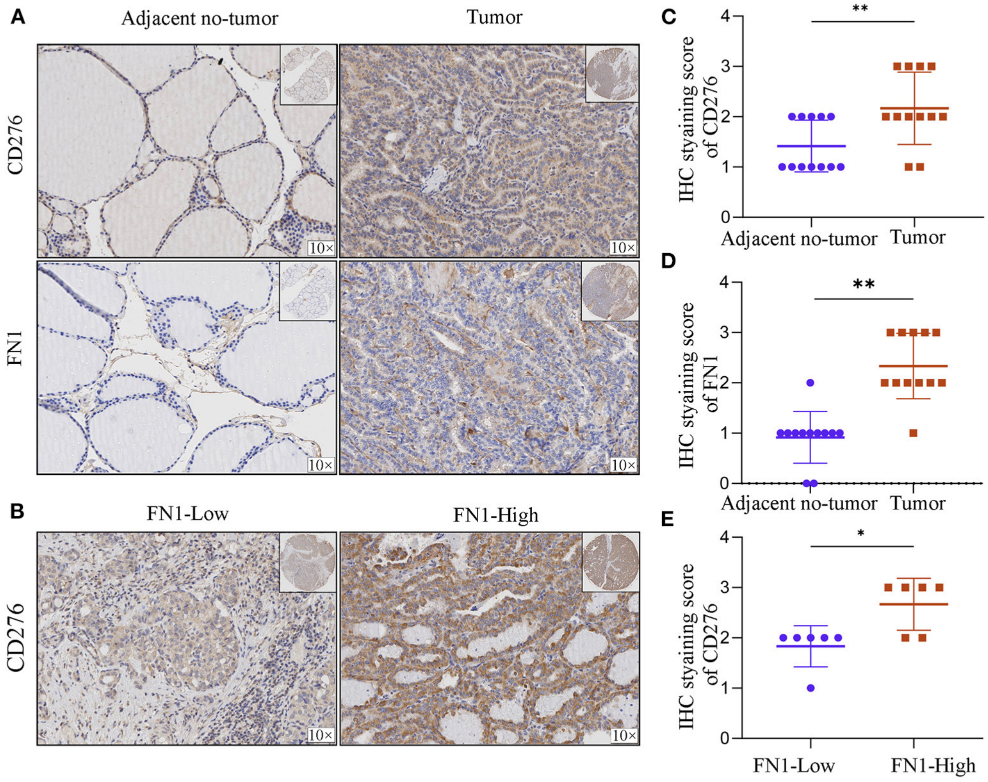

FIGURE 7 | The correlation between FN1 and CD276 in THCA. **(A)** Representative IHC staining of CD276 and FN1 in tumors and adjacent no-tumor tissues from THCA patients. **(B)** Representative IHC staining of CD276 in tumor tissues from FN1-high and low patient groups. IHC score of CD276 **(C)** and FN1 **(D)** in adjacent no-tumor tissues and tumor tissues form patients with THCA. **(E)** IHC score of CD276 in tumor tissues from FN1-high and low patient groups, $^{*}p < 0.05$, $^{**}P < 0.01$.

signaling pathway, which is closely correlated to tumorigenesis. Importantly, immune infiltration analysis showed that immune infiltration level and diverse immune marker sets were correlated with *FN1* expression level. Therefore, *FN1* can be a potential immunity-related biomarker and therapeutic target in THCA. Moreover, using quantitative proteomic approaches, previous studies have proved that *FN1* can be a potential novel candidate prognostic biomarker in THCA (37). However, these studies did not specify the exact range of effects of genes on disease prognosis, lacked certain clinical significance. In this study, three GEO datasets were combined to screen the hub genes, providing results with a high statistical and clinical significance. Our research further demonstrates that *FN1* is a potential prognostic biomarker and therapeutic target in THCA from the perspective of DNA methylation and tumor immunology.

The important aspect of this study is that *FN1* expression is correlated with diverse immune infiltration level in THCA. An increase in *FN1* expression level was positively correlated with the proportion of M2 macrophages and resting memory $CD4^{+}$ T cells but negatively correlated with the proportion of follicular helper T cells and $CD8^{+}$ T cells. To further investigate the correlation between *FN1* and inflammatory activities, the correlation between *FN1* and members of the B7-CD28 ligand-receptor family was analyzed, and a close positive correlation between *FN1* and *CD276* was identified. *CD276*, a member of the B7 superfamily, has been previously identified as a poor prognostic factor. A previous study demonstrated that *CD276*, expressed in multiple tumor lines, tumor-infiltrating dendritic cells, and macrophages, can inhibit T-cell activation and autoimmunity (38). Therefore, the interactions between *FN1* and *CD276* could be a potential mechanism underlying the correlation of *FN1* expression with immune infiltration and poor prognosis in THCA.

In summary, increased *FN1* expression correlated with poor prognosis and altered immune infiltration levels in THCA, indicating that *FN1* is a potential immunity-related biomarker. This study was based on a statistical analysis of bioinformatics methods, and the conclusions obtained were supported by experimental data and multiple databases. Therefore, it is reasonable to believe that FN1 plays an important role in the diagnosis, treatment, and prognosis of THCA.

CONCLUSION

In summary, we performed a comprehensive analysis using the TCGA dataset and multiple online databases and identified *FN1* as a potential immunity-related biomarker and a prognostic marker in THCA. Our results suggest FN1 has a significant part in the diagnosis, treatment, and prognosis of THCA, highlighting the necessity of future clinical research in the topic.

DATA AVAILABILITY STATEMENT

The datasets presented in this study can be found in online repositories. The names of the repository/repositories and accession number(s) can be found in the article/**Supplementary Material**.

ETHICS STATEMENT

All the patients' data involved in this study is open source which is freely available in the public research databases including the Cancer Genome Atlas (TCGA) and Gene Expression Omnibus (GEO). The application of the public data is already properly anonymized and informed consent was also obtained at the time of the original data collection. Samples from cancer patients were obtained from thyroid cancer arrays (DC-Thy11004 Avira Biotechnology Co., Ltd., China). The data is already properly anonymized and informed consent was also obtained at the time of the original data collection.

AUTHOR CONTRIBUTIONS

Q-SG is responsible for the acquisition of the data, analysis and interpretation of the data. TH and L-FL are responsible for the drafting of the manuscript, and statistical analysis. Z-BS, W-HX,and JZ contributed to the critical revision of the manuscript. All authors contributed to the article and approved the submitted version.

FUNDING

This work was supported by the Collaborative Innovation Major Project of Zhengzhou (Grant No. 20XTZX08017), National Natural Science Foundation of China (Grant Nos. 82002433 and 82002998), Science and Technology Project of Henan Provincial Department of Education (Grant Nos. 18A320044 and 21A320036), Henan Province Medical Science and Technology Research Project Joint Construction Project (Grant Nos. LHGJ20190003, LHGJ20190055, and LHGJ20190042), First-class Postdoctoral Research Grant in Henan Province (Grant No. 201901007), and Youth Talent Support Project of Henan Province (Grant No. 2021HYTP045) also support this work.

SUPPLEMENTARY MATERIAL

The Supplementary Material for this article can be found online at: https://www.frontiersin.org/articles/10.3389/fmed.2021.812278/full#supplementary-material

Supplementary Figure 1 | Flow diagram of the study.

Supplementary Table 1 | The significantly enriched GO terms of the common DEGs (BP, biological process; CC, cellular component; DEG, differentially expressed gene; GO, Gene Ontology; MF, molecular function).

REFERENCES

1. Bonhomme B, Godbert Y, Perot G, Al GA, Bardet S, Belleannee G. Molecular pathology of anaplastic thyroid carcinomas: a retrospective study of 144 cases. *Thyroid.* (2017) 27:682–92. doi: 10.1089/thy.2016.0254
2. Davies L, Welch HG. Current thyroid cancer trends in the United States. *JAMA Otolaryngol.* (2014) 140:317–22. doi: 10.1001/jamaoto.2014.1
3. Zhao L, Pang P, Zang L, Luo Y, Wang F, Yang G. Features and trends of thyroid cancer in patients with thyroidectomies in Beijing, China between 1994 and 2015: a retrospective study. *BMJ Open.* (2019) 9:e0233341. doi: 10.1136/bmjopen-2018-023334
4. Aschebrook-Kilfoy B, Ward MH, Sabra MM, Devesa SS. Thyroid cancer incidence patterns in the United States by histologic type, 1992-2006. *Thyroid.* (2011) 21:125–34. doi: 10.1089/thy.2010.0021
5. Chen AY, Bernet VJ, Carty SE, Davies TF, Ganly I, Inabnet WR. American Thyroid Association statement on optimal surgical management of goiter. *Thyroid.* (2014) 24:181–9. doi: 10.1089/thy.2013.0291
6. Wang, C., Sun, P., Yang, L., i,. J., Yang, W., and Feng, J. (2016). Z, et al. Strategies of laparoscopic thyroidectomy for treatment of substernal goiter via areola approach. *Surg Endosc*. 30, 4721–4730. doi: 10.1007/s00464-016-4814-0
7. Sipos JA, Mazzaferri EL. Thyroid cancer epidemiology and prognostic variables. *Clin Oncol.* (2010) 22:395–404. doi: 10.1016/j.clon.2010.05.004
8. Naoum GE, Morkos M, Kim B, Arafat W. Novel targeted therapies and immunotherapy for advanced thyroid cancers. *Mol Cancer.* (2018) 17:51. doi: 10.1186/s12943-018-0786-0
9. Mlecnik B, Van den Eynde M, Bindea G, Church SE, Vasaturo A, Fredriksen T. Comprehensive intrametastatic immune quantification and major impact of immunoscore on survival. *J Natl Cancer Inst*. (2018) 110:djx123. doi: 10.1093/jnci/djx123
10. Pankov R, Yamada KM. Fibronectin at a glance. *J Cell Sci*. (2002) 115(Pt 20):3861–3. doi: 10.1242/jcs.00059
11. Chen Z, Tao Q, Qiao B, Zhang L. Silencing of LINC01116 suppresses the development of oral squamous cell carcinoma by up-regulating microRNA-136 to inhibit FN1. *Cancer Manag Res.* (2019) 11:6043–59. doi: 10.2147/CMAR.S197583
12. Waalkes S, Atschekzei F, Kramer MW, Hennenlotter J, Vetter G, Becker JU. Fibronectin 1 mRNA expression correlates with advanced disease in renal cancer. *BMC Cancer.* (2010) 10:503. doi: 10.1186/1471-2407-10-503
13. Sponziello M, Rosignolo F, Celano M, Maggisano V, Pecce V, Rose D, et al. RF, et al. Fibronectin-1 expression is increased in aggressive thyroid cancer and favors the migration and invasion of cancer cells. *Mol Cell Endocrinol*. (2016) 431:123–32. doi: 10.1016/j.mce.2016.05.007
14. Glasner A, Levi A, Enk J, Isaacson B, Viukov S, Orlanski S. NKp46 receptor-mediated interferon-γ production by natural killer cells increases fibronectin 1 to alter tumor architecture and control metastasis. *Immunity.* (2018) 48:107–19. doi: 10.1016/j.immuni.2017.12.007
15. Zhang DL, Wang JM, Wu T, Du X, Yan J. Du ZX, et al. BAG5 promotes invasion of papillary thyroid cancer cells via upregulation of fibronectin 1 at the translational level. *Biochim Biophys Acta Mol Cell Res.* (2020) 1867:118715. doi: 10.1016/j.bbamcr.2020.118715
16. Yu S, Yu X, Sun L, Zheng Y, Chen L, Xu H, et al. GBP2 enhances glioblastoma invasion through Stat3/fibronectin pathway. *Oncogene*. (2020) 39:5042–55. doi: 10.1038/s41388-020-1348-7
17. Rago T, Scutari M, Loiacono V, Santini F, Tonacchera M, Torregrossa L, et al. Low elasticity of thyroid nodules on ultrasound elastography is correlated with malignancy, degree of fibrosis, and high expression of galectin-3 and fibronectin-1. *Thyroid*. (2017) 27:103–10. doi: 10.1089/thy.2016.0341
18. Goldman MJ, Craft B, Hastie M, Repečka K, McDade F, Kamath A, et al. Visualizing and interpreting cancer genomics data via the Xena platform. *Nat Biotechnol*. (2020) 38:675–8. doi: 10.1038/s41587-020-0546-8
19. Tomas G, Tarabichi M, Gacquer D, Hebrant A, Dom G, Dumont JE. A general method to derive robust organ-specific gene expression-based differentiation

indices: application to thyroid cancer diagnostic. *Oncogene.* (2012) 31:4490–8. doi: 10.1038/onc.2011.626

20. Rusinek D, Swierniak M, Chmielik E, Kowal M, Kowalska M, Cyplinska R. BRAFV600E-associated gene expression profile: early changes in the transcriptome, based on a transgenic mouse model of papillary thyroid carcinoma. *PLoS ONE.* (2015) 10:e143688. doi: 10.1371/journal.pone.0143688
21. Tarabichi M, Saiselet M, Tresallet C, Hoang C, Larsimont D, Andry G. Revisiting the transcriptional analysis of primary tumours and associated nodal metastases with enhanced biological and statistical controls: application to thyroid cancer. *Br J Cancer.* (2015) 112:1665–74. doi: 10.1038/bjc.2014.665
22. Kameshwar AK, Qin W. Metadata analysis of phanerochaete chrysosporium gene expression data identified common CAZymes encoding gene expression profiles involved in cellulose and hemicellulose degradation. *Int J Biol Sci.* (2017) 13:85–99. doi: 10.7150/ijbs.17390
23. Khan A, Mathelier A. Intervene: a tool for intersection and visualization of multiple gene or genomic region sets. *BMC Bioinformatics.* (2017) 18:287. doi: 10.1186/s12859-017-1708-7
24. Chen L, Zhang YH, Lu G, Huang T, Cai YD. Analysis of cancer-related lncRNAs using gene ontology and KEGG pathways. *Artif Intell Med.* (2017) 76:27–36. doi: 10.1016/j.artmed.2017.02.001
25. Zhao Z, Bai J, Wu A, Wang Y, Zhang J, Wang Z. Co-LncRNA: investigating the lncRNA combinatorial effects in GO annotations and KEGG pathways based on human RNA-Seq data. *Database*. (2015) 2015:bav082. doi: 10.1093/database/bav082
26. Cook HV, Doncheva NT, Szklarczyk D, von Mering C, Jensen LJ. Viruses.STRING: a virus-host protein-protein interaction database. *Viruses*. (2018) 10:519. doi: 10.3390/v10100519
27. Doncheva NT, Morris JH, Gorodkin J, Jensen LJ. Cytoscape StringApp: network analysis and visualization of proteomics data. *J Proteome Res.* (2019) 18:623–32. doi: 10.1021/acs.jproteome.8b00702
28. Rhodes DR, Yu J, Shanker K, Deshpande N, Varambally R, Ghosh D, et al. ONCOMINE: a cancer microarray database and integrated data-mining platform. *Neoplasia*. (2004) 6:1–6. doi: 10.1016/S1476-5586(04)80047-2
29. Chandrashekar DS, Bashel B, Balasubramanya S, Creighton CJ, Ponce-Rodriguez I, Chakravarthi B. UALCAN: a portal for facilitating tumor subgroup gene expression and survival analyses. *Neoplasia.* (2017) 19:649–58. doi: 10.1016/j.neo.2017.05.002
30. Koch A, Jeschke J, Van Criekinge W, van Engeland M, and Meyer De T. MEXPRESS update 2019. *Nucleic Acids Res*. (2019) 47:W561–5. doi: 10.1093/nar/gkz445
31. Huang WY, Hsu SD, Huang HY, Sun YM, Chou CH, Weng SL, et al. A database of DNA methylation and gene expression in human cancer. *Nucleic Acids Res*. (2015) 43:D856–61. doi: 10.1093/nar/gku1151
32. Newman AM, Steen CB, Liu CL, Gentles AJ, Chaudhuri AA, Scherer F. Determining cell type abundance and expression from bulk tissues with digital cytometry. *Nat Biotechnol.* (2019) 37:773–82. doi: 10.1038/s41587-019-0114-2
33. Tang Z, Li C, Kang B, Gao G, Li C, Zhang Z. GEPIA: a web server for cancer and normal gene expression profiling and interactive analyses. *Nucleic Acids Res*. (2017) 45:W98–102. doi: 10.1093/nar/gkx247
34. Morgan AE, Davies TJ, Mc AM. The role of DNA methylation in ageing and cancer. *Proc Nutr Soc.* (2018) 77:412–22. doi: 10.1017/S0029665118000150
35. Flanagan JM, Wilson A, Koo C, Masrour N, Gallon J, Loomis E. Platinum-based chemotherapy induces methylation changes in blood DNA associated with overall survival in patients with ovarian cancer. *Clin Cancer Res.* (2017) 23:2213–22. doi: 10.1158/1078-0432.CCR-16-1754
36. Ruoslahti E. Fibronectin in cell adhesion and invasion. *Cancer Metastasis Rev.* (1984) 3:43–51. doi: 10.1007/BF00047692
37. Zhan S, Li J, Wang T, Ge W. Quantitative proteomics analysis of sporadic medullary thyroid cancer reveals FN1 as a potential novel candidate prognostic biomarker. *Oncologist*. (2018) 23:1415–25. doi: 10.1634/theoncologist.2017-0399
38. Lee YH, Martin-Orozco N, Zheng P, Li J, Zhang P, Tan H, et al. Inhibition of the B7-H3 immune checkpoint limits tumor growth by enhancing cytotoxic lymphocyte function. *Cell Res*. (2017) 27:1034–45. doi: 10.1038/cr.2017.90
39. Li T, Fan J, Wang B, Traugh N, Chen Q, Liu JS, et al. TIMER: a web server for comprehensive analysis of tumor-infiltrating immune cells. *Cancer Res*. (2017) 77:e108–10. doi: 10.1158/0008-5472.CAN-17-0307

Conflict of Interest: The authors declare that the research was conducted in the absence of any commercial or financial relationships that could be construed as a potential conflict of interest.

frontiers in Medicine

ORIGINAL RESEARCH
published: 01 February 2022
doi: 10.3389/fmed.2021.792740

Depiction of Aging-Based Molecular Phenotypes With Diverse Clinical Prognosis and Immunological Features in Gastric Cancer

Fang He[1†], Huan Ding[1†], Yang Zhou[2], Yuanzhen Wang[1], Juan Xie[1], Shaoqi Yang[1] and Yongzhao Zhu[1*]*

[1] General Hospital of Ningxia Medical University, Yinchuan, China, [2] Graduate School, Ningxia Medical University, Yinchuan, China

Objective: Aging acts as a dominating risk factor for human cancers. Herein, we systematically dissected the features of transcriptional aging-relevant genes in gastric cancer from multiple perspectives.

Methods: Based on the transcriptome profiling of prognostic aging-relevant genes, patients with gastric cancer in The Cancer Genome Atlas (TCGA) stomach adenocarcinoma (TCGA-STAD) cohort were clustered with a consensus clustering algorithm. Mutational landscape and chemotherapeutic responses were analyzed and immunological features (immunomodulators, immune checkpoint molecules, cancer immunity cycle, and tumor-infiltrating immune cells) were systematically evaluated across gastric cancer. Weighted gene co-expression network (WGCNA) was conducted for screening aging molecular phenotype-relevant genes, and key genes were identified with Molecular Complex Detection (MCODE) analyses. Expressions of key genes were examined in 20 paired tumors and controls with RT-qPCR and Western blotting. Proliferation and apoptosis were investigated in two gastric cancer cells under MYL9 deficiency.

Results: Three aging-based molecular phenotypes (namely, C1, C2, and C3) were conducted in gastric cancer. Phenotype C1 presented the most prominent survival advantage and highest mutational frequencies. Phenotype C2 indicated low responses to sorafenib and gefitinib, while C3 indicated low responses to vinorelbine and gemcitabine. Additionally, phenotype C2 was characterized by enhanced immune and stromal activation and an inflamed tumor microenvironment. Seven aging molecular phenotype-relevant key genes (ACTA2, CALD1, LMOD1, MYH11, MYL9, MYLK, and TAGLN) were identified, which were specifically upregulated in tumors and in relation to dismal prognosis. Among them, MYL9 deficiency reduced proliferation and enhanced apoptosis in gastric cancer cells.

Conclusion: Collectively, aging-based molecular subtypes may offer more individualized therapy recommendations and prognosis assessment for patients in distinct subtypes.

Keywords: gastric cancer, aging-relevant genes, molecular phenotype, prognosis, tumor immune microenvironment, immunogenomic characteristics

Edited by:
Fu Wang,
Xi'an Jiaotong University, China

Reviewed by:
Francesca Reggiani,
Local Health Authority of Reggio Emilia, Italy
Weimin Zhong,
Xiamen Fifth Hospital, China

***Correspondence:**
Yongzhao Zhu
zhuyongzhao2410@nyfy.com.cn
Shaoqi Yang
shaoqiynh@nyfy.com.cn

† These authors have contributed equally to this work

Specialty section:
This article was submitted to Precision Medicine, a section of the journal Frontiers in Medicine

***Received:** 11 October 2021*
***Accepted:** 10 November 2021*
***Published:** 01 February 2022*

Citation:
He F, Ding H, Zhou Y, Wang Y, Xie J, Yang S and Zhu Y (2022) Depiction of Aging-Based Molecular Phenotypes With Diverse Clinical Prognosis and Immunological Features in Gastric Cancer. Front. Med. 8:792740. doi: 10.3389/fmed.2021.792740

INTRODUCTION

Gastric cancer ranks the sixth most frequent malignancy as well as the fifth major cause of cancer death across the globe (1). When diagnosed at an advanced stage, patients' 5-year overall survival rate is merely 5% (1). As a heterogeneous disease, it has the features of diverse histological and molecular subtypes (2). At present, according to the morphology, differentiation, and cohesion of gland cells, gastric cancer is histopathologically classified as intestinal and diffuse (3). Genomic analyses have become the major methodology applied in international efforts for discovering novel biological targets in gastric cancer (4). It is fundamental to unravel the complicated biology underlying gastric cancer etiology and development for overcoming the highly heterogeneous malignancy.

Accumulated pieces of evidence have uncovered the implication of tumor-associated structures and activated signaling pathways both in tumor cells and in the tumor microenvironment (5). Aging is a complicated process primarily categorized by a reduction in tissues, cells, and organ functions as well as an elevated risk of mortality, which acts as a dominant risk factor of diverse fatal malignancies, especially cancers (6). This process presents prominent correlations to telomere attrition, mitochondrial dysfunction, DNA injury, impaired immune system, and the like (7). Nevertheless, the specific mechanisms involved in aging are still indistinct. Transcriptomic studies have identified abundant human aging-relevant genes (8). The human aging genome resource (HAGR) project offers a powerful set of aging-specific network features, which reveals aging-relevant gene signatures as network hubs through comprehensive analyses of biology and genetics of the human aging process (8). Cellular senescence is a permanent state of stagnant replication of proliferating cells as well as a sign of aging (9). Senescent tumor cells triggered by tumorigenesis may lead to cell cycle arrest, as an antitumor mechanism (10). Nevertheless, senescent cells surrounding tumor cells generate opposite results as well as present prominent correlations with senescence-associated secretory phenotype factor secretions (11). Moreover, senescence displays two-tier influences upon cancer immunity (12, 13). Aging-relevant gene signatures exert critical functions in modulating cellular senescence, not only inhibiting tumor progression through modulating senescence of cancer cells but also promoting malignant progression of cancers and dismal clinical outcomes (14). Nevertheless, there is still a lack of systematic analyses of aging-relevant genes during gastric carcinogenesis. Herein, we identified three aging-based molecular phenotypes that offered more individualized therapy options and prognosis prediction for gastric cancer patients.

MATERIALS AND METHODS

Retrieval and Preprocessing of Genome-Relevant Data and Clinical Information

Raw RNA-seq data [Fragments Per Kilobase Million (FPKM) value] and relevant clinicopathological characteristics for The Cancer Genome Atlas (TCGA) stomach adenocarcinoma (TCGA-STAD) cohort containing 443 patients with gastric cancer were curated from Genomic Data Commons (GDC) data portal (https://portal.gdc.cancer.gov) utilizing TCGAbiolinks package (15). Additionally, normalized microarray expression profiling of 433 patients with gastric cancer in the GSE84437 cohort was curated from the Gene Expression Omnibus (GEO) repository (https://www.ncbi.nlm.nih.gov/gds/) (16). The detailed information of patients with gastric cancer in TCGA and GSE84437 cohorts is listed in **Supplementary Table 1**. The expression profiling (FPKM values) of the TCGA-STAD dataset was transformed into transcripts per kilobase million (TPMs). In total, 307 aging-relevant genes (**Supplementary Table 2**) were curated from the HAGR (https://genomics.senescence.info/) (8). Molecular subtypes [genome stable (GS), microsatellite instability (MSI), EBV infection, and chromosomal instability (CIN)] of gastric cancer samples were retrieved from Liu et al. (17). Somatic mutation data [Mutation Annotation Format (MAF) format] of 433 patients with gastric cancer on the basis of the whole-exome sequencing platforms were curated from the TCGA project. Mutational types and frequencies of genes were analyzed as well as visualized utilizing the maftools package (18). Tumor mutation burden (TMB) was defined as the entire number of non-synonymous variations within the coding regions per megabase (19). In addition, copy number alteration (CNA) data were retrieved from GDAC Firehose (https://gdac.broadinstitute.org), and prominent amplification and deletion across the whole genome were identified with GISTIC2.0 (20). Somatic copy-number alterations (SCNAs) and homologous recombination deficiency (HRD) across gastric cancer specimens were also curated from Davoli et al. (21).

Molecular Characterization for Subtypes

Tumors with qualitatively diverse aging-relevant gene expressions were clustered utilizing hierarchical agglomerative clustering on the basis of Euclidean distance as well as Ward's linkage. Unsupervised clustering method (K-means) was utilized for identifying aging-related molecular phenotypes as well as classifying samples for subsequent analyses. Through consensus clustering algorithm, the number of clusters was determined using TCGA-STAD and GSE84437 cohorts for assessing the stability of the identified molecular phenotypes. This procedure was presented through adopting the ConsensuClusterPlus package as well as repeated 50 times for ensuring the accuracy regarding this classification (22).

Abbreviations: FPKM, Fragments Per Kilobase Million; TCGA, The Cancer Genome Atlas; GDC, Genomic Data Commons; GEO, Gene Expression Omnibus; TPMs, transcripts per kilobase million; TMB, Tumor mutation burden; can, copy number alteration; SCNAs, Somatic copy-number alterations; PCA, Principal component analyses; GSVA, gene set variation analysis; MSigDB, Molecular Signatures Database; Pan-F-TBRS, pan-fibroblast TGF-β response signature; EMT, epithelial-mesenchymal transition; ssGSEA, single sample gene set enrichment analysis; GDSC, Genomics of Drug Sensitivity in Cancer; IC50, half-maximal inhibitory concentration; ESTIMATE, Estimation of Stromal and Immune cells in Malignant Tumor tissues using Expression data; WGCNA, Weighted gene co-expression network analysis; STRING, Search Tool for the Retrieval of Interacting Genes/Proteins; PPI, protein-protein interaction; MCODE, Molecular Complex Detection; RT-qPCR, Real-time quantitative reverse transcription PCR.

Gene Set Variation Analysis (GSVA)

Gene set variation analysis, a non-parametric and unsupervised gene set enrichment algorithm, may infer the enrichment scores of specific pathways or signatures on the basis of transcriptomic profiling (23). The 50 hallmarks of gene signatures were collected from the Molecular Signatures Database (MSigDB) project (24). Moreover, the gene sets of other relevant biological processes were curated from Mariathasan et al. containing CD8 T effectors, DNA damage repair, pan-fibroblast TGF-β response signature (Pan-F-TBRS), antigen-processing machinery, immune checkpoint, epithelial-mesenchymal transition (EMT) markers, FGFR3-related genes, angiogenesis, Fanconi anemia, WNT targets, cell cycle regulators, and the like (25). Utilizing single sample gene set enrichment analysis (ssGSEA) from the GSVA package, gene sets of hallmarks and other relevant biological processes were chosen for presenting quantifications of pathway activity.

Estimation of Chemotherapeutic Response

Chemotherapeutic sensitivity in cancer cells, as well as molecular markers of chemotherapeutic response profiles, were curated from the largest publicly available pharmacogenomics project: the Genomics of Drug Sensitivity in Cancer (GDSC; https://www.cancerrxgene.org/) (26). Four commonly applied chemotherapeutic agents, sorafenib, gefitinib, vinorelbine, and gemcitabine, were chosen. The prediction procedure was implemented *via the* pRRophetic package (27). The half-maximal inhibitory concentration (IC50) values were estimated with the ridge regression method, and the prediction accuracy was assessed through 10-fold cross-verification.

Evaluation of Tumor Immune Microenvironment and Immunogenomic Characteristics

Immunological features of the tumor immune microenvironment contained the expression profiles of immunomodulatory factors and immune checkpoint molecules, the activity of the cancer immunity cycle, and infiltrations of immune cells. In total, 122 immunomodulatory factors comprising MHC, receptor, chemokine, and immune stimulator were curated from Sokolov et al. (28). Immune checkpoint molecules with therapeutic potential were collected from Auslander et al. (29). The cancer immunity cycle uncovers antitumor immune response, and the activity of each step determines the fate of tumor cells (30). Here, the activity of each step was quantified with ssGSEA on the basis of the expression profiling of individual specimens. Thereafter, the ssGSEA algorithm was developed for quantifying the abundance of lymphocytes within the tumor immune microenvironment utilizing bulk RNA-seq profiles. Through Estimation of Stromal and Immune cells in Malignant Tumor tissues using Expression data (ESTIMATE), immune and stromal contents (immune and stromal scores and tumor purity) were inferred across gastric cancer specimens (31). Tumor tissues with abundant immune cell infiltration represented an increased immune score and a decreased level of tumor purity.

Quantification of Gene Expression-Based Stemness Index (MRNAsi)

Through the one-class logistic regression (OCLR) method, the stemness index was calculated on the basis of transcriptome profiling of normal PSCs (32). The stemness signatures were generated with the OCLR algorithm (28). Thereafter, this study estimated Spearman's correlation between the weight vector of the stemness signatures and mRNA expression across gastric cancer. Eventually, the stemness index was mapped onto the range of 0 to 1 utilizing a linear conversion, which subtracted the minimum as well as separated through the maximal correlation coefficient. The stemness index produced from transcriptome profiling was defined as mRNAsi.

Weighted Gene Co-expression Network Analysis (WGCNA)

Weighted gene co-expression network analysis was presented for identifying underlying co-expression modules that were prominently correlated with aging-associated molecular phenotypes. The soft-thresholding for the scale-free network was identified. The topological overlap matrix similarity was adopted for the evaluation of the distance between gene pairs. Furthermore, hierarchical clustering analyses with mean and dynamic methods were utilized for building the clustering tree as well as classifying the gene signatures into diverse modules. Following merging the initial modules in line with their similarity, functional modules were eventually conducted. Spearman's correlation coefficient, as well as matched p-value between aging-associated molecular phenotypes and functional modules, was determined through cor function. For each module, gene significance (GS) and module membership (MM) were calculated. Genes with GS > 0.5 and MM > 0.8 were utilized as aging phenotype-relevant genes. Through the Search Tool for the Retrieval of Interacting Genes/Proteins (STRING) tool (33), protein-protein interaction (PPI) analysis of aging phenotype-relevant genes was carried out. Molecular Complex Detection (MCODE) (34), a plugin in Cytoscape software (35), was used for screening the significant modules of the PPI network in line with the filtrating criteria of degree cutoff = 2, node score cutoff = 0.2, k-core = 2, and depth from depth = 100.

Patients and Specimens

In total, 20 patients with gastric cancer were recruited at the General Hospital of Ningxia Medical University. Adjacent gastric tissues (3–6 cm from the tumor). Tumor tissues and adjacent non-cancerous gastric tissues (>5 cm from the edge of tumor tissues) were harvested during surgical resection. The inclusion criteria included: (1) patients pathologically diagnosed with gastric cancer and (2) patients who did not experience radio- and/or adjuvant chemotherapy prior to surgery. The exclusion criteria included: (1) patients previously diagnosed with other malignancies; (2) patients who were previously treated with radio- or adjuvant chemotherapy; and (3) patients who died within 4 weeks of this surgery. All specimens were frozen in liquid nitrogen at once following collection and were stored at −80°C before usage. This study was conducted in accordance with the

TABLE 1 | Primer sequences used for RT-qPCR.

Gene	Sequence (5′-3′)
MYL9	F: TCTTCGCAATGTTTGACCAGT R: GTTGAAAGCCTCCTTAAACTCCT
ACTA2	F: AAAAGACAGCTACGTGGGTGA R: GCCATGTTCTATCGGGTACTTC
TAGLN	F: AGTGCAGTCCAAAATCGAGAAG R: CTTGCTCAGAATCACGCCAT
MYH11	F: CGCCAAGAGACTCGTCTGG R: TCTTTCCCAACCGTGACCTTC
LMOD1	F: GTAAAAGGGGAGCGTAGGAAC R: CTCGGGTGTTTTGGTCTTGCT
CALD1	F: TGGAGGTGAATGCCCAGAAC R: GAAGGCGTTTTTGGCGTCTTT
MYLK	F: CCCGAGGTTGTCTGGTTCAAA R: GCAGGTGTACTTGGCATCGT
GAPDH	F: CTGGGCTACACTGAGCACC R: AAGTGGTCGTTGAGGGCAATG

guidance of the Declaration of Helsinki. The protocol gained the approval of the Institutional Ethical Committee of General Hospital of Ningxia Medical University (Approval No. 2020-031). All participants signed an informed consent form prior to our study.

Real-Time Quantitative Reverse Transcription PCR

Tissues or cells were lysed with RNAiso plus (Takara, Japan). Thereafter, RNA extraction was presented with the phenol-chloroform/isopropanol method. The cDNA was prepared through PrimeScript RT reagent kits as well as a gDNA eraser. About 20 μl qPCR system was prepared, followed by analysis with GoTaq qPCR Master Mix. The relative mRNA expressions were quantified with the $2^{-\Delta\Delta Ct}$ method, with GAPDH as a control. The primer sequences are listed in **Table 1**.

Western Blotting

Tissues or cells were lysed with RIPA buffer plus protease inhibitor cocktail. Following separation *via* electrophoresis in SDS/PAGE gel, the protein was transferred onto PVDF membranes. The membrane was blocked in PBS-T buffer in supplements of 5% milk/BSA lasting 2 h and presented the incubation with primary antibody targeting MYL9 (1:500; 15354-1-AP; Proteintech, China), ACTA2 (1:1000; 23081-1-AP; Proteintech, China), TAGLN (1:300; 15502-1-AP; Proteintech, China), MYH11 (1:1000; 18569-1-AP; Proteintech, China), LMOD1 (1:500; 15117-1-AP; Proteintech, China), CALD1 (1:2000; 20887-1-AP; Proteintech, China), MYLK (1:500; 21642-1-AP; Proteintech, China), and β-actin (1:5000; 20536-1-AP; Proteintech, China) overnight at 4°C. Following incubation by horseradish peroxidase-labeled HRP-coupled secondary antibodies lasting 1 h, the protein band was visualized with an ECL detection reagent.

Cell Culture

Two gastric cancer cell lines (MGC-803 and BGC-823) were acquired from the Cell Bank of the Chinese Academy of Sciences (Shanghai, China). The cells were cultivated in the Dulbecco's modified Eagle's medium (DMEM; Gibco, United States) with supplements of 10% fetal bovine serum (FBS) as well as 1% antibiotics penicillin/streptomycin. Moreover, all cells were fostered in an incubator with 5% CO_2 at 37°C.

Transfection

For generating MYL9-knockdown clones, two short hairpin RNA (shRNA) sequences against MYL9 were synthesized and cloned into pSUPER-retro-puro plasmids. The recombinant plasmids or negative control vector ligated by scrambled-base hairpin oligos were co-transfected with packaging plasmids pIK into 293T cells. Thereafter, the supernatant was harvested, which was utilized for infecting MGC-803 and BGC-823 cells. The above-mentioned cells were plated into 6-well plates. When the confluency reached 50%, transfections were presented with Lipofectamine 2000 (Invitrogen, United States) in accordance with the manufacturer's instructions. Following 48 h, transfection efficiencies were evaluated.

Cell Counting Kit (CCK)-8

For the determination of viable MGC-803 and BGC-823 cells, CCK-8 (Dojindo, Japan) kits were adopted. In brief, cells were administered on a 96-well plate (3×10^3 cells/well). Following cultivation lasting 24 h, 10 μl of CCK-8 reagent was added, followed by incubation at 37°C lasting 1 h. The absorbance values were tested at 450 nm with an ultraviolet spectrophotometer at diverse time points.

Flow Cytometry

MGC-803 and BGC-823 cells were treated with propranolol lasting 24 h. Thereafter, 100 μl cell suspension was incubated with 5 μl fluorescein isothiocyanate (FITC)-Annexin V as well as 2.5 μl propidium iodide (PI) protecting from light in accordance with the manufacturer's instruction. Apoptosis was under evaluation utilizing flow cytometry on BD FACSCanto II (BD, United States). Flow cytometry was analyzed with FlowJo software.

Statistics

All statistical analyses were conducted with R software and GraphPad Prism software. Measurement data were displayed as mean ± SD. If the variables were normally distributed, comparisons of continuous variables between two or more than two subgroups were presented through a parametric test (Student's *t*-test or ANOVA). Otherwise, a non-parametric test (Wilcoxon rank-sum test or Kruskal–Wallis test) was presented. Principal component analyses (PCAs) were used to present the dissimilarity among diverse clusters. Hazard ratio (HR) was determined with a Cox regression model utilizing a survival package. Analyses of overall survival (OS), disease-free survival (DFS), and disease-specific survival (DSS) were conducted with Kaplan–Meier method, and the log-rank test was adopted for determining the statistical difference. Pearson's or Spearman's

TABLE 2 | Prognostic aging-relevant genes in gastric cancer with univariate-cox regression analyses.

Genes	HR	HR 0.95L	HR 0.95H	*P*-value
GHR	1.5437	1.1596	2.0551	0.0029
POU1F1	3.5083	1.2136	10.142	0.0205
GH1	1.9524	1.0594	3.5981	0.0320
NGF	1.7419	1.2548	2.4180	0.0009
EGF	1.5420	1.1022	2.1572	0.0115
PDGFRB	2.2543	1.1351	4.4766	0.0202
PEX5	0.3813	0.1479	0.9831	0.0460
NR3C1	2.0259	1.1514	3.5646	0.0143
TGFB1	3.0279	1.2103	7.5751	0.0179
APOC3	1.2600	1.0596	1.4984	0.0089
AR	1.3530	1.0050	1.8215	0.0463
FEN1	0.4273	0.1849	0.9872	0.0466
A2M	2.4406	1.0382	5.7374	0.0408
SNCG	1.7807	1.2627	2.5113	0.0010
PON1	1.4702	1.0866	1.9893	0.0125
IL6	1.3283	1.0257	1.7201	0.0314
FGFR1	1.5856	1.0199	2.4652	0.0406
PAPPA	1.6353	1.1335	2.3593	0.0085
EFEMP1	1.9565	1.2875	2.9732	0.0017
AGTR1	1.2752	1.0316	1.5763	0.0246
PDGFRA	1.8412	1.1501	2.9478	0.0110

correlation test was used for evaluating the correlation between variables. For all statistical analyses, a two-tailed $P < 0.05$ indicated significance.

RESULTS

Aging-Genomic Profiles Identify Three Diverse Molecular Phenotypes of Gastric Cancer

This study analyzed the expression patterns of aging-relevant genes across gastric cancer specimens in the TCGA cohort. Through univariate-cox regression analyses, abnormal expression of 24 aging-relevant genes was in relation to gastric cancer prognosis (**Table 2**). With the consensus clustering method, patients with gastric cancer were clustered into three aging-relevant molecular phenotypes (C1, 143 samples; C2, 117 samples; C3, 91 samples) in accordance with the transcriptome profiling of prognostic aging-relevant genes (**Figure 1A**). PCA uncovered the dissimilarity between aging-relevant molecular phenotypes (**Figure 1B**). The prominent discrepancy in expressions of prognostic aging-relevant genes was investigated among phenotypes (**Figure 1C**). Survival analyses demonstrated that three aging-relevant molecular phenotypes presented prominent survival outcomes. C1 phenotype possessed more favorable OS (**Figure 1D**), DFS (**Figure 1E**), and DSS (**Figure 1F**) outcomes than C2 and C3 phenotypes. The classification accuracy was confirmed in the GSE84437 cohort (**Supplementary Figures 1A–D**). **Figure 1G** showed the heterogeneity in the distribution of three aging-relevant molecular phenotypes (C1, C2, and C3) among the most known molecular subtypes (CIN, EBV, GS, and MSI). C1 subtype occupied the highest percentage in EBV and MSI, while C2 occupied the highest percentage in GS. Thus, the aging-relevant molecular phenotypes presented remarkable associations with the most known molecular subtypes of gastric cancer.

Aging-Relevant Molecular Phenotypes With Diverse Cancer Mutational Genome

The preclinical studies and clinical trials have uncovered that somatic mutation is linked to therapeutic response, survival outcome, and clinical benefit of patients with gastric cancer (36). Hence, this study evaluated the distributions of somatic mutations across gastric cancer among three aging-related molecular phenotypes. We investigated that molecular phenotype C1 presented higher mutational frequency (132, 30.48%; **Figure 2A**) compared with C2 (84, 19.4%; **Figure 2B**) and C3 (86, 19.86%; **Figure 2C**). The first 20 genes with the highest mutational frequencies were shown in each phenotype. Gistic2.0 identified 54 amplifications in phenotype C1 (**Figure 2D**), 37 amplifications in phenotype C2 (**Figure 2E**), and 58 amplifications in phenotype C3 (**Figure 2F**). Meanwhile, there were 46 deletions in phenotype C1 (**Figure 2G**), 35 deletions in phenotype C2 (**Figure 2H**), and 51 deletions in phenotype C3 (**Figure 2I**). Collectively, aging-relevant molecular phenotypes presented diverse cancer mutational genomes.

Aging-Associated Molecular Phenotypes With Distinct Activations of Functional Pathways and Chemotherapeutic Responses

We further investigated the mechanisms underlying distinct aging-associated molecular phenotypes. In **Figure 3A**, we observed that immune activation pathways (complement, IL2-STAT5 signaling, inflammatory response, IL6-JAK-STAT3 signaling, allograft rejection, and interferon gamma response) and stromal activation pathways (epithelial-mesenchymal transition, angiogenesis, and WNT β-catenin signaling) were prominently upregulated in aging-associated molecular phenotype C2. Several tumorigenic pathways (mTORC1 signaling, MYC targets, DNA repair, E2F targets, and G2M checkpoint) presented a significant activation in molecular phenotypes C1 and C3. Consistently, pan-F-TBRS, immune checkpoint, EMT1-3, angiogenesis, and WNT target were prominently upregulated in molecular phenotype C2 (**Figure 3B**). The above data demonstrated the immune and stromal activation in molecular phenotype C2. The chemotherapeutic responses to sorafenib, gefitinib, vinorelbine, and gemcitabine were compared among three molecular phenotypes. Our results showed that molecular phenotype C2 presented the lowest therapeutic responses to sorafenib and gefitinib (**Figures 3C,D**) while phenotype C3 had the lowest therapeutic responses to vinorelbine and gemcitabine (**Figures 3E,F**).

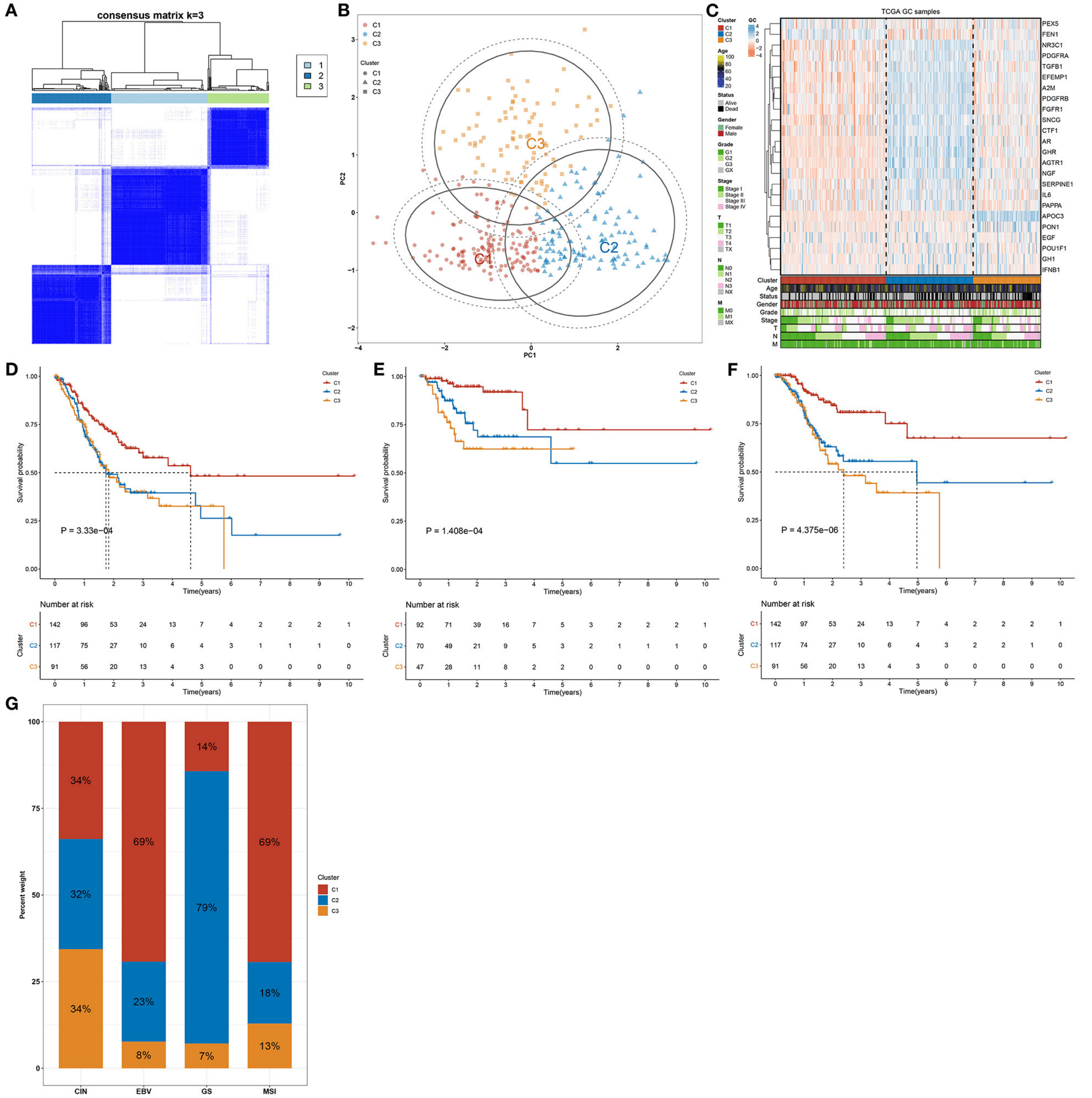

FIGURE 1 | Aging-genomic profiles identify three molecular phenotypes in gastric cancer. **(A)** Heatmap depicted sample clustering at consensus $k = 3$ in accordance with the transcriptome profiling of prognostic aging-relevant genes across gastric cancer samples in the TCGA cohort. **(B)** PCA plots visualized the dissimilarity between aging-relevant molecular phenotypes. **(C)** Heatmap showed the expression patterns of prognostic aging-relevant genes in three aging-relevant molecular phenotypes. **(D–F)** Kaplan–Meier curves of **(D)** OS, **(E)** DFS, and **(F)** DSS were conducted for gastric cancer patients with diverse aging-relevant molecular phenotypes. **(G)** Distribution of aging-related molecular phenotypes C1, C2, and C3 in different molecular subtypes (CIN, EBV, GS, and MSI).

Aging-Associated Molecular Phenotypes Display Diverse Tumor Immune Microenvironment and Immunological Status

In **Figure 4A**, most MHC molecules (HLA-DMB, HLA-DOA, HLA-DOB, HLA-DPA1, HLA-DPB1, HLA-DQA1, HLA-DQB1, HLA-DRA, HLA-DRB1, and HLA-E) presented the highest expressions in aging-associated molecular phenotype C2. This was indicative that the ability of antigen presentation and processing was upregulated in phenotype C2. Additionally, molecular phenotype C2 had the highest expressions of most chemokines (XCL2, CXCL1, CXCL12, CXCL13, CCL11, CCL13, CCL14, CCL16, CCL17, CCL19, CCL2, CCL21, CCL22, CCL23,

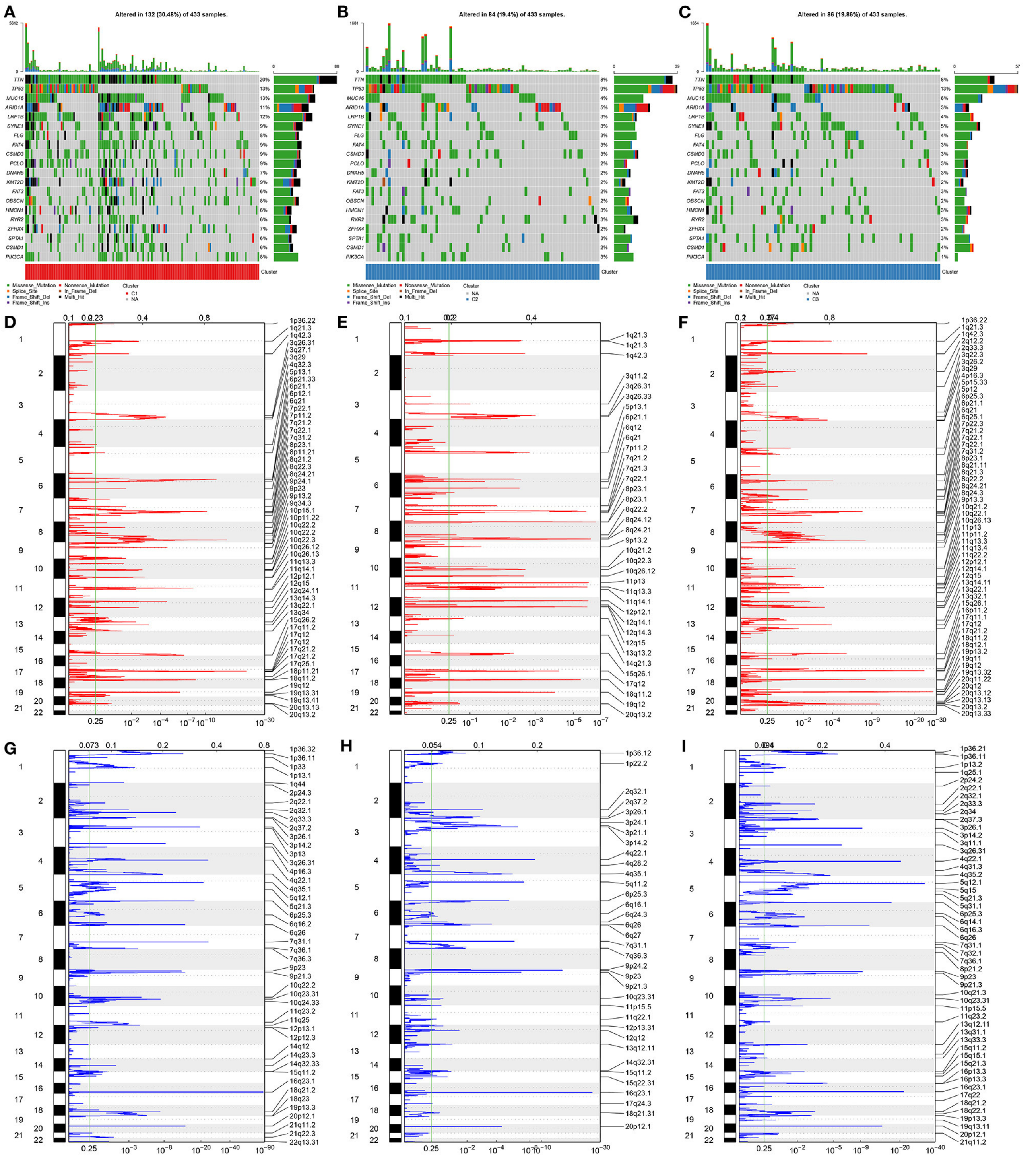

FIGURE 2 | Aging-relevant molecular phenotypes with diverse cancer mutational genomes. **(A–C)** Oncoprint of somatic mutation status across patients with gastric cancer in aging-related molecular phenotypes **(A)** C1, **(B)** C2, and **(C)** C3. Individual patients were represented in each column. The right bar plots showed the mutation frequencies of the first 20 mutated genes in each molecular phenotype. **(D–F)** The amplifications of genes were separately shown in molecular phenotypes **(D)** C1, **(E)** C2, and **(F)** C3. The false-discovery rate (*q* value) and scores for amplifications were plotted against genomic locations. **(G–I)** The deletions of genes were separately shown in molecular phenotypes **(G)** C1, **(H)** C2, and **(I)** C3. The *q*-value and scores for deletions were depicted against genomic locations. Dotted lines indicated the centromeres. The green line represented 0.25 of *q*-value cutoff value that determined significance.

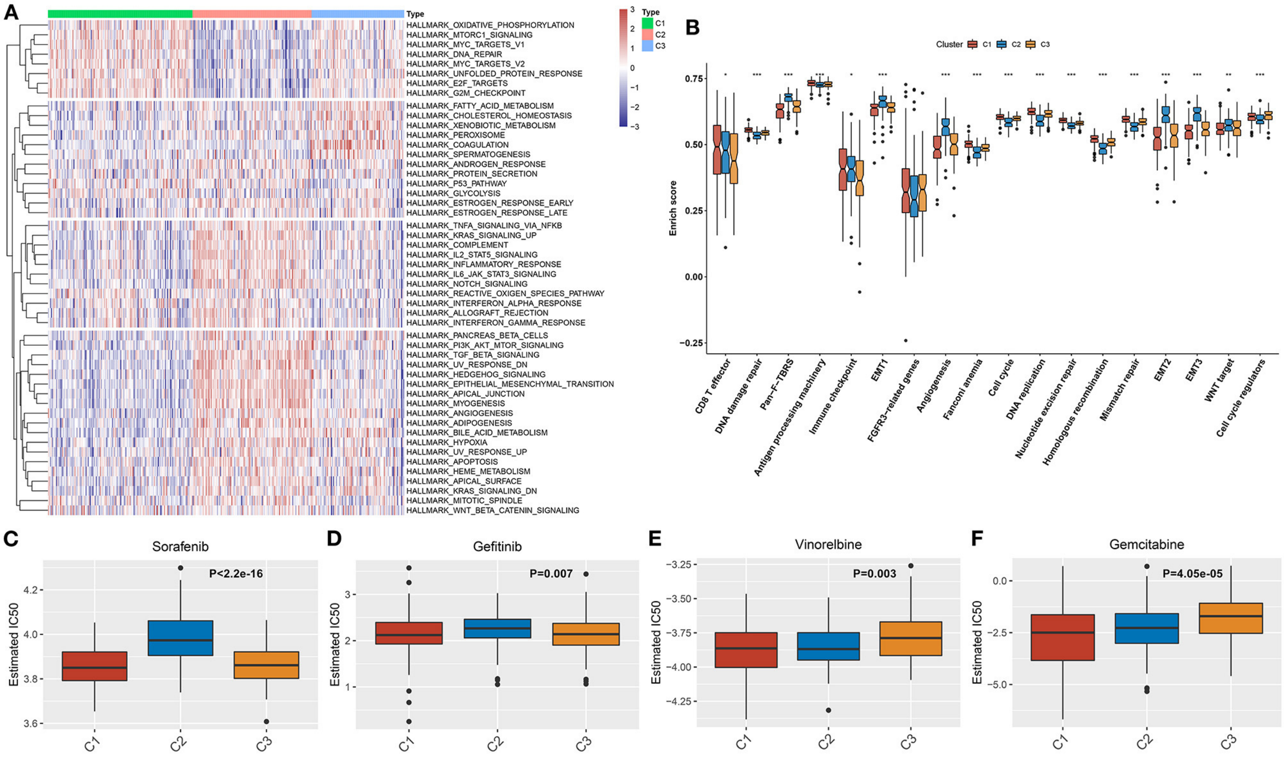

FIGURE 3 | Aging-associated molecular phenotypes with distinct activations of functional pathways and chemotherapeutic responses. **(A)** Heatmap visualized the activities of the 50 hallmark gene sets in three aging-associated molecular phenotypes. **(B)** Comparisons of the activities of common biological processes among distinct molecular phenotypes. **(C–F)** Comparisons of the estimated IC50 values of chemotherapeutic agents, including **(C)** sorafenib, **(D)** gefitinib, **(E)** vinorelbine, and **(F)** gemcitabine. **p* < 0.05; ***p* < 0.01; ****p* < 0.001.

CCL4, and CCL8) and their receptors (XCR1, CCR1, CCR10, CCR2, CCR4, CCR5, CCR6, CCR7, CCR8, CCR9, CXCR1, CXCR3, CXCR4, and CXCR5), and the lowest expression of above molecules was found in molecular phenotype C1 (**Figures 4B,C**). Above chemokines and receptors facilitate the recruitment of effector lymphocytes like CD8+ T cell, TH17 cell, as well as antigen-presenting cells. In **Figure 4D**, molecular phenotype C2 was characterized by the highest expressions of most immune checkpoint molecules (IL2RA, IL6, IL6R, KLRK1, LTA, NT5E, RAET1E, TNFRSF13B, TNFRSF13C, TNFRSF17, TNFRSF4, TNFRSF8, TNFSF13B, TNFSF14, TNFSF18, TNFSF4, ENTPD1, BTNL2, CD27, CD276, CD28, CD40, CD40LG, CD48, and CD86). These data reflected the activated immunological status in molecular phenotype C2. Cancer immunity cycle activity is the overall manifestation of the chemokine system as well as immunomodulatory factors. Most steps in the cancer immunity cycle presented the highest activities in molecular phenotype C2, like cancer cell antigen release and presentation, priming and activation, recruitment of B cell, CD4 T cell, dendritic cell, eosinophil, macrophage, monocyte, T cell, Th17 cell, and Treg (**Figure 4E**). Thereafter, we calculated the infiltration levels of immune cells utilizing the ssGSEA algorithm. The infiltration levels of most immune cells were upregulated in molecular phenotype C2, like activated B cell, activated CD8 T cell, central memory CD4 T cell, central memory CD8 T cell, effector memory CD4 T cell, effector memory CD8 T cell, gamma delta T cell, immature B cell, memory B cell, regulatory T cell, T follicular helper cell, type 1 T helper cell, type 2 T helper cell, activated dendritic cell, eosinophil, immature dendritic cell, macrophage, mast cell, MDSC, natural killer cell, natural killer T cell, and plasmacytoid dendritic cell (**Figure 4F**). Collectively, molecular phenotype C2 had an inflamed tumor microenvironment.

Aging-Associated Molecular Phenotypes Associated With Immunotherapeutic Response Predictors in Gastric Cancer

We investigated the difference in immunotherapeutic responses among three aging-associated molecular phenotypes through comparisons of multiple immunotherapeutic predictors. Aging-associated molecular phenotype C2 presented higher stromal and immune scores as well as reduced tumor purity compared with C1 and C3, indicating that samples in phenotype C2 had increased infiltrations of stromal and immune cells (**Figures 5A–C**). The mRNAsi was quantified for reflecting the levels of cancer stem cells across gastric cancer. There was the lowest mRNAsi in phenotype C2, while the highest mRNAsi in phenotype C1 (**Figure 5D**). Also, we investigated the lowest SCNA in phenotype C2 but the highest SCNA in phenotype

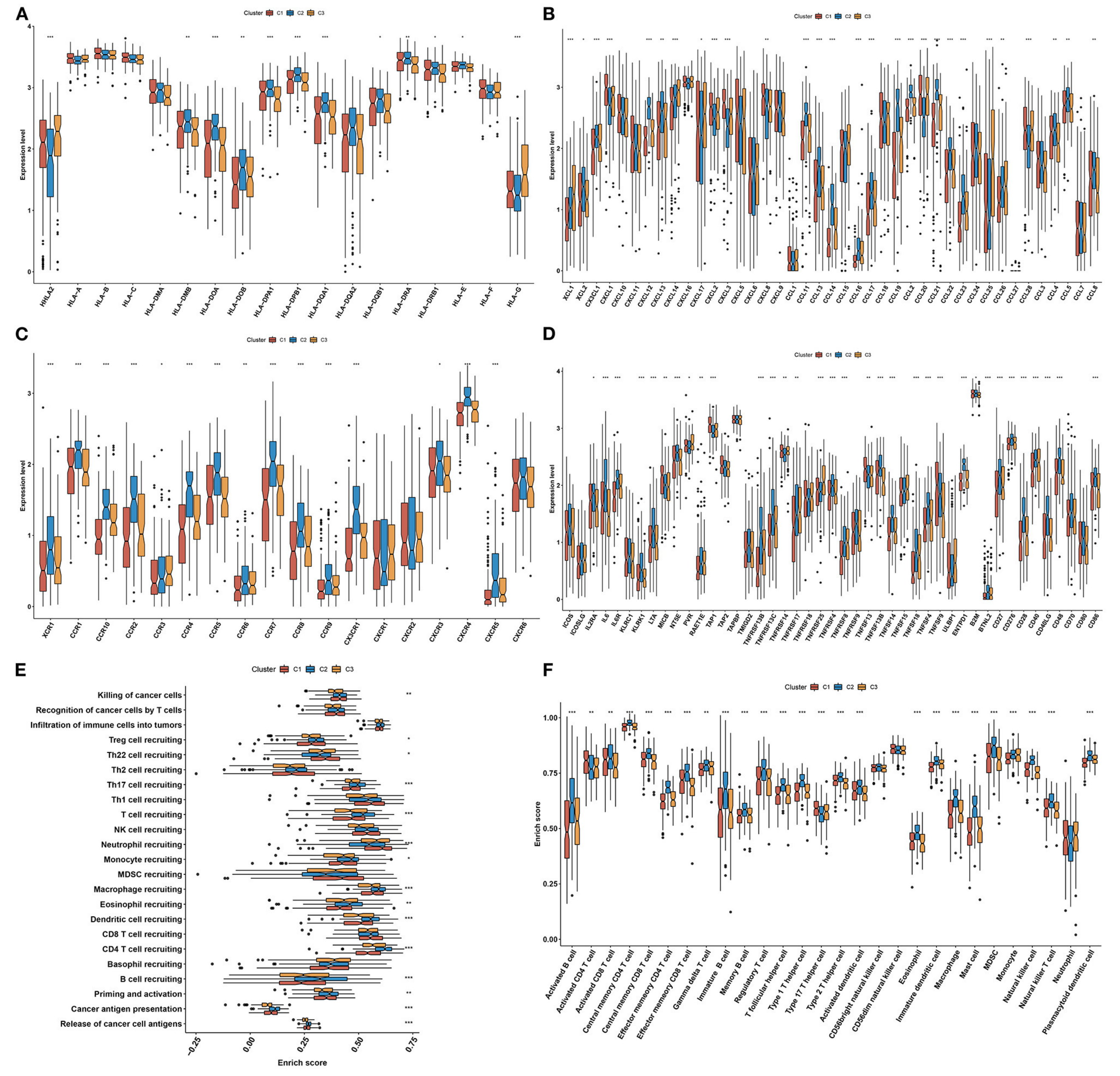

FIGURE 4 | Three aging-associated molecular phenotypes display diverse tumor immune microenvironment and immunogenomic characteristics. **(A–D)** Comparisons of the mRNA expressions of immunomodulators, including **(A)** MHC, **(B)** chemokines, **(C)** receptors, and **(D)** immune checkpoint molecules among three aging-associated molecular phenotypes. **(E)** Comparisons of the activities of all steps in the cancer immunity cycle among three molecular phenotypes. **(F)** Comparisons of the infiltration levels of tumor-infiltrating lymphocytes among three molecular phenotypes. $^*p < 0.05$; $^{**}p < 0.01$; $^{***}p < 0.001$.

C3 (**Figure 5E**). In **Figure 5F**, phenotype C2 displayed the lowest MSI, while phenotype C1 possessed the highest MSI. Phenotype C2 presented the lowest TMB score but C1 had the highest TMB score (**Figure 5G**). We also evaluated the differences in cancer testis antigen (CAT) and HRD score among three aging-associated molecular phenotypes. We investigated that phenotype C3 had the highest CAT score, followed by C2 and C1 (**Figure 5H**). Additionally, the highest HRD score was found in phenotype C3 (**Figure 5I**). The above data suggested that aging-associated molecular phenotypes presented distinct immunotherapeutic responses in gastric cancer.

Identification of Aging Molecular Phenotype-Relevant Key Genes

The WGCNA method was adopted for the construction of a co-expression network as well as finding genes highly

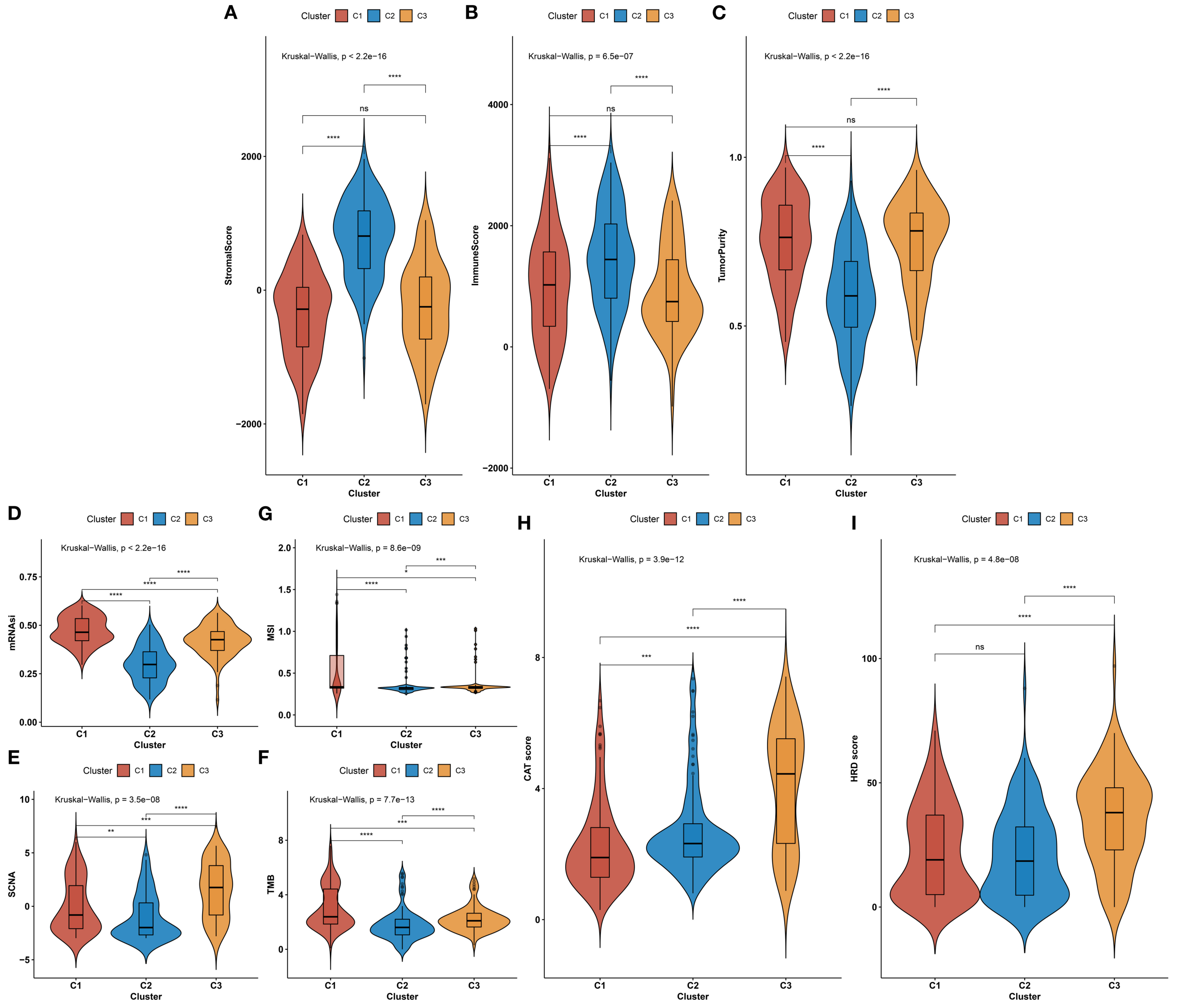

FIGURE 5 | Aging-associated molecular phenotypes associated with immunotherapeutic response predictors in gastric cancer. **(A–C)** Distributions of stromal and immune scores as well as tumor purity among three aging-associated molecular phenotypes. **(D–G)** Comparisons of mRNAsi, SCNA, MSI, and TMB scores among three aging-associated molecular phenotypes. **(H,I)** Comparisons of CAT and HRD scores in diverse aging-associated molecular phenotypes. $^{*}p < 0.05$; $^{**}p < 0.01$; $^{***}p < 0.001$; $^{****}p<0.0001$; ns, not significant.

associated with aging molecular phenotypes. We first detected outliers among gastric cancer specimens on the basis of gene expression profiling. As a result, there was no outlier sample (**Figure 6A**). Thereafter, soft thresholding power β was calculated, and β was set at 5 for ensuring a scale-free network (**Figures 6B,C**). In total, 11 co-expression modules were merged, as depicted in **Figure 6D**. Among them, the brown module presented the strongest association with aging molecular phenotype C2 (**Figure 6E**). Thereafter, we evaluated intramodular analyses of genes in each module. Especially, genes in the brown module had high correlations with aging molecular phenotype C2 (**Figure 6F**). Eventually, 312 genes in this module were selected as aging molecular phenotype-relevant genes in accordance with the criteria of module membership >0.8 and gene significance >0.5 (**Supplementary Table 3**). We further observed the interactions between aging molecular phenotype-relevant genes through the STRING database. With MCODE analyses, seven aging molecular phenotype-relevant hub genes were identified, namely, ACTA2, CALD1, LMOD1, MYH11, MYL9, MYLK, and TAGLN (**Figure 6G**). In **Figure 6H**, we noted that the hub genes displayed remarkable associations with the infiltration levels of immune cells. All of them were negatively correlated to the infiltration levels of activated CD4 T cell, CD56dim natural killer cell, neutrophil, and type 17 T helper cell but were positively associated with the other immune cells.

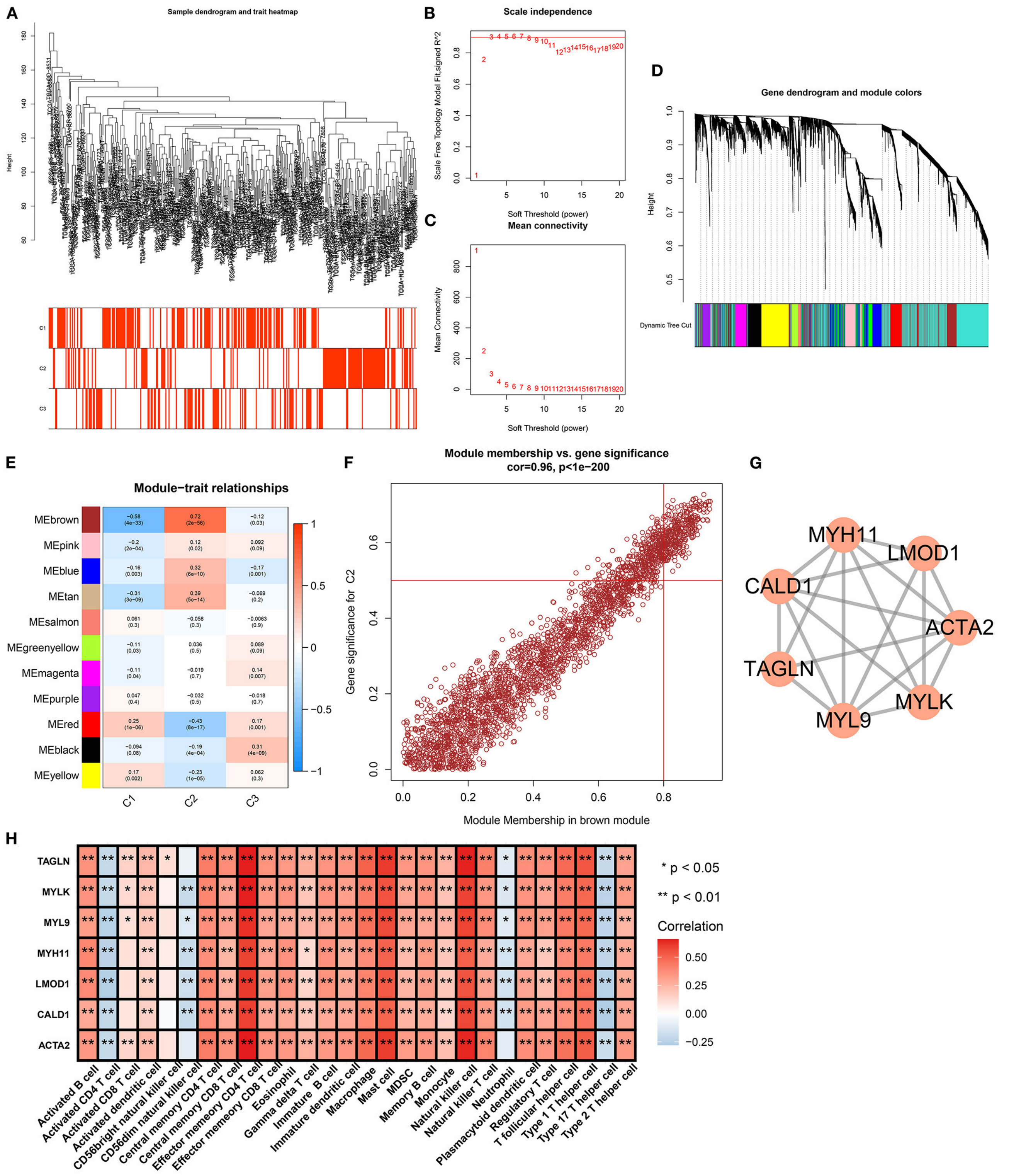

FIGURE 6 | Identification of aging molecular phenotype-relevant key genes. **(A)** Sample dendrogram and heatmap were conducted based on transcriptome data of gastric cancer. The color intensity indicated aging-associated molecular phenotypes (C1, C2, and C3). **(B)** The scale-free fitting index was determined across diverse soft thresholding powers. **(C)** Mean connectivity was analyzed under different soft thresholding powers. **(D)** Clustering dendrogram was conducted on the basis of co-expression network analyses. Totally, 11 co-expression modules were merged as well as uniquely identified by diverse colors. **(E)** Heatmap showed the correlation between co-expression modules and aging-associated molecular phenotypes across gastric cancer. The brown module presented the strongest correlation module with phenotype C2. **(F)** Scatter plots depicted the interactions of module membership in the brown module with gene significance for phenotype C2. **(G)** MCODE analyses identified the most prominent module in the PPI network of genes in the brown module. **(H)** Heatmap visualized the interaction between the hub genes and the infiltration levels of immune cells. *$p < 0.05$; **$p < 0.01$.

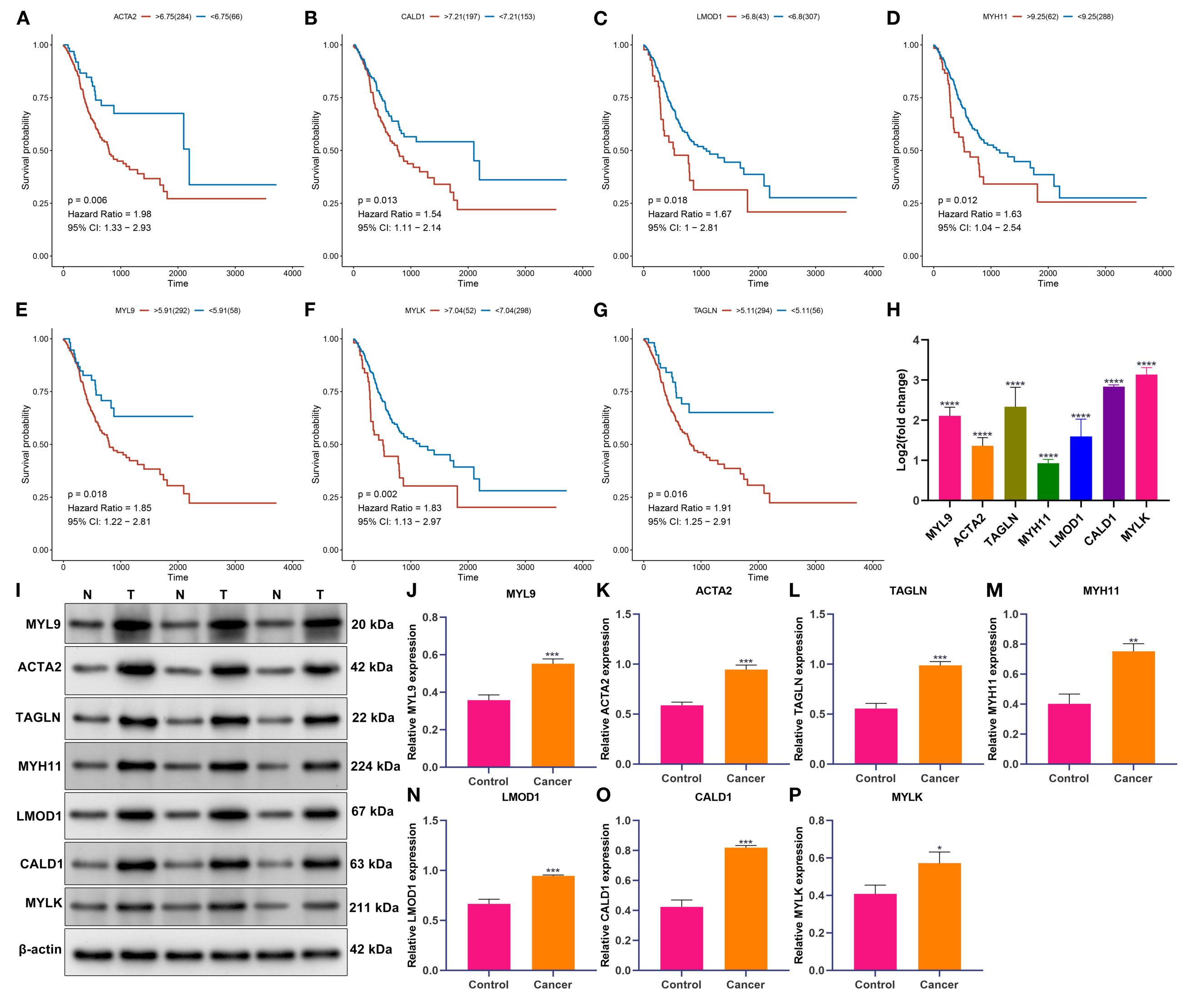

FIGURE 7 | Verification of prognostic implication and deregulated expression of aging molecular phenotype-relevant key genes. **(A–G)** Kaplan–Meier curves were conducted for the investigation of survival significance of MYL9, ACTA2, TAGLN, MYH11, LMOD1, CALD1, and MYLK across patients with gastric cancer patients. **(H)** The mRNA expressions of MYL9, ACTA2, TAGLN, MYH11, LMOD1, CALD1, and MYLK were verified in 20 paired tumors and controls with RT-qPCR. The displayed graph contained normalized data to controls. **(I–P)** Western blotting was conducted for verification of the expressions of MYL9, ACTA2, TAGLN, MYH11, LMOD1, CALD1, and MYLK in tumors and controls. *$p < 0.05$; **$p < 0.01$; ***$p < 0.001$; ****$p < 0.0001$.

Verification of Prognostic Implication and Deregulated Expression of Aging Molecular Phenotype-Relevant Key Genes

Survival analyses were conducted for investigations of the prognostic implications of aging molecular phenotype-relevant key genes across patients with gastric cancer. Our data demonstrated that the upregulations of ACTA2, CALD1, LMOD1, MYH11, MYL9, MYLK, and TAGLN were in relation to more dismal survival outcomes in comparisons with their downregulations (**Figures 7A–G**). We further verified their expressions in 20 paired tumors and controls. In **Figure 7H**, compared with controls, their prominent upregulations were investigated in tumors in line with RT-qPCR. Additionally, Western blotting results confirmed their abnormal expressions of these key genes in gastric cancer (**Figures 7I–P**).

In Gastric Cancer Cells, MYL9 Loss Weakens Proliferation and Triggers Apoptosis

Among aging molecular phenotype-relevant key genes, only the role of MYL9 in gastric cancer remains unknown. Thus, we investigated the function of MYL9 in gastric carcinogenesis. Herein, MYL9 expressions were reduced in

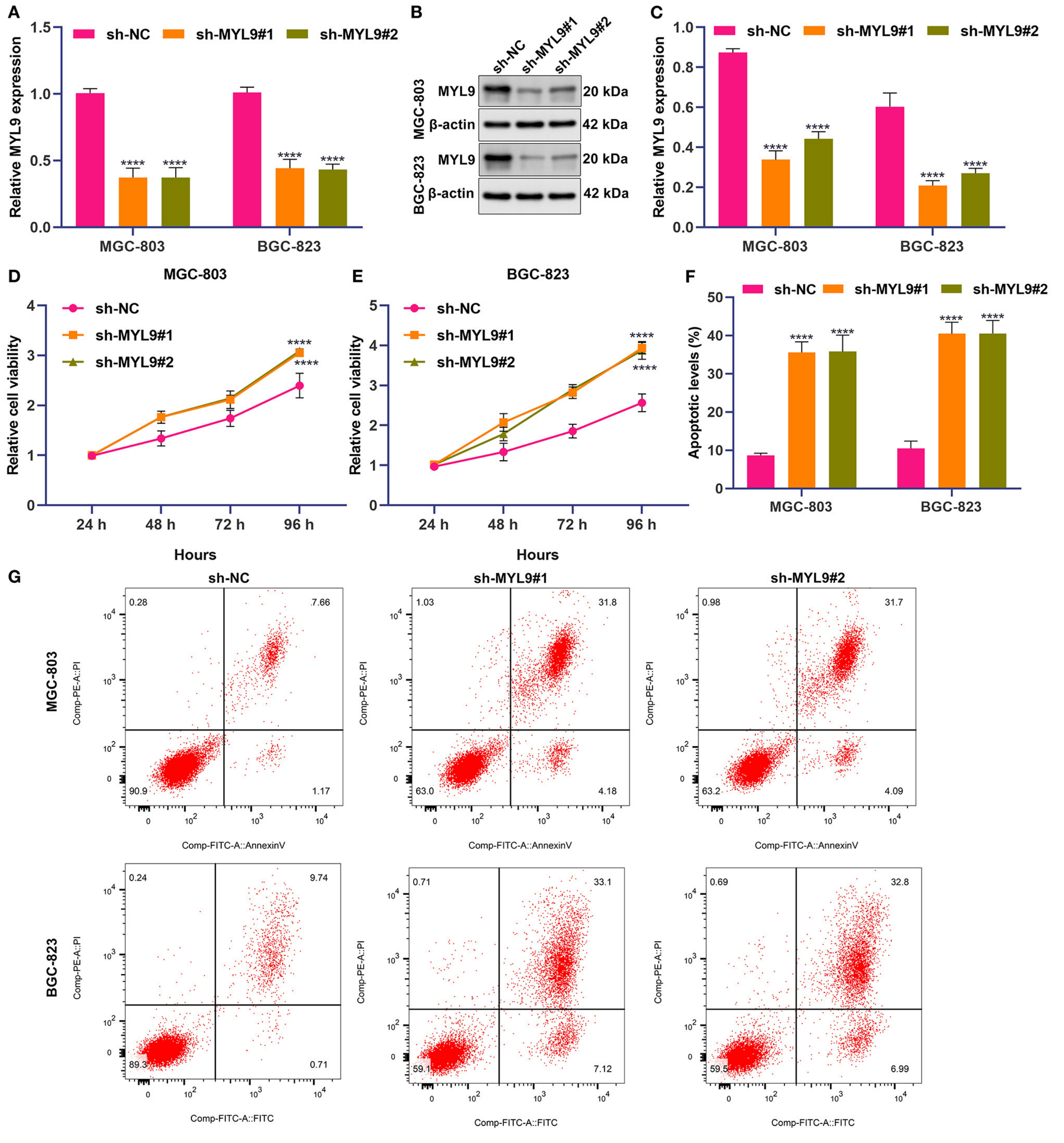

FIGURE 8 | MYL9 loss weakens proliferation and triggers apoptosis in gastric cancer cells. **(A–C)** MYL9 expressions were determined in MGC-803 and BGC-823 cells under shRNAs targeting MYL9 transfections with RT-qPCR and Western blotting. **(D,E)** Viable MGC-803 and BGC-823 cells were evaluated following shRNAs against MYL9 transfections through CCK-8. **(F,G)** Apoptotic MGC-803 and BGC-823 cells were investigated after shRNAs against MYL9 transfections with flow cytometry. ****$p < 0.0001$.

MGC-803 and BGC-823 cells under two shRNAs against MYL9 transfections (**Figures 8A–C**). In accordance with CCK-8 results, MYL9 loss reduced the cell viability of MGC-803 and BGC-823 cells (**Figures 8D,E**). Additionally, apoptosis of MGC-803 and BGC-823 cells was enhanced when MYL9 expressions were defective (**Figures 8F,G**). The above data indicated the gastric tumorigenic roles of MYL9.

DISCUSSION

In our study, we conducted three aging-based molecular phenotypes with a consensus clustering algorithm. Further, aging-based molecular phenotypes were characterized by diverse clinical prognoses, mutational status as well as the immunological status of tumor microenvironment across gastric cancer. In this aspect, our findings offered individualized treatment options and prognosis evaluation for distinct subpopulations based on the aging-related molecular phenotypes.

The tumor microenvironment is comprised of a heterogeneous cellular milieu that influences cancer cell behaviors (3). The feature produces a far-reaching impact on treatment responses like immunotherapy. An inflamed tumor microenvironment combined with preexisting antitumor immunity is necessary for immunotherapy that suppresses tumor growth through tumor-cytotoxic T-cell re-invigoration. In theory, molecules and signals contribute to an inflamed tumor microenvironment that may trigger sensitivity to immunotherapy. Herein, in accordance with immunological features (immunomodulators, immune checkpoint molecules, cancer immunity cycle, and tumor-infiltrating immune cells), aging-based molecular phenotype C2 presented an inflamed tumor microenvironment. This indicated that the subpopulations in this phenotype possessed greater chances of responding to immunotherapy. Cancer stem cells contribute to chemotherapeutic resistance as well as distant metastases due to the self-renewal and tumorigenic capacities (37). Through mRNAsi, we quantified the levels of cancer stem cells across gastric cancer. There was the lowest mRNAsi in phenotype C2, while the highest mRNAsi in phenotype C1. TMB and MSI are capable of predicting the clinical responses to immunotherapy. Nevertheless, the predictors are examined utilizing complex molecular tools that are slow and expensive. Thus, it is an urgent medical requirement for developing faster and economical predictors. Our data indicated that phenotype C2 displayed the lowest MSI and TMB scores, while phenotype C1 possessed the highest MSI and TMB scores. HRD leads to impaired double-strand break repair, which is a common driving factor of carcinogenesis (38). Herein, phenotype C2 presented the features of reduced HRD score, while phenotype C3 was characterized by elevated HRD score.

Through WGCNA combined with MCODE methods, we identified seven aging molecular phenotype-relevant key genes, namely, ACTA2, CALD1, LMOD1, MYH11, MYL9, MYLK, and TAGLN. The above genes displayed the specific upregulations in gastric cancer and contributed to a dismal clinical prognosis. Previously, CALD1 acts as a prognostic indicator and also is in relation to immune infiltrates in gastric carcinoma (39). MYH11 expression is downregulated in gastric carcinoma and is indicative of a dismal clinical prognosis (40). Hypermethylation of MYLK serves as a circulating diagnostic marker of gastric carcinoma (41). Stromal fibroblasts in the microenvironment trigger gastric carcinoma metastases through the upregulation of TAGLN (42). Among them, our experimental pieces of evidence demonstrated that MYL9 deficiency reduced proliferation as well as enhanced apoptosis in gastric carcinoma cells, confirming the tumorigenic function of MYL9. Nevertheless, there were a few limitations in this study. The aging-based molecular phenotypes should be further verified in large patients from multicenter cohorts for identifying the characteristics of clinical prognosis and drug responses. Additionally, we identified aging molecular phenotype-relevant key genes, especially MYL9. Nevertheless, the specific experimental verifications should be designed for the assessment of the biological implications.

CONCLUSION

Herein, our comprehensive assessment of the cellular, molecular, and genetic features correlated with aging-based molecular phenotypes generated novel insights on how gastric tumors responded to immunotherapy and guided the development of more effective combination therapeutic regimens.

DATA AVAILABILITY STATEMENT

The original contributions presented in the study are included in the article/**Supplementary Material**, further inquiries can be directed to the corresponding author/s.

ETHICS STATEMENT

The study was approved by the Ethics Committee of General Hospital of Ningxia Medical University (approval no. 2020-031). The patients/participants provided their written informed consent to participate in this study.

AUTHOR CONTRIBUTIONS

YZhu and SY conceived and designed the study. FH, HD, and YZhou conducted most of the experiments and data analysis and wrote the manuscript. YW and JX participated in collecting data and helped to draft the manuscript. All authors reviewed and approved the manuscript.

FUNDING

This work was funded by the National Key R&D Program of China (MOST-2017YFC0908300) and Ningxia Autonomous Region Key R&D Program Project (2018YBZD0418).

SUPPLEMENTARY MATERIAL

The Supplementary Material for this article can be found online at: https://www.frontiersin.org/articles/10.3389/fmed.2021.792740/full#supplementary-material

Supplementary Figure 1 | Validation of aging-genomic profiles identifies three molecular phenotypes across gastric cancer in the GSE84437 cohort. **(A)** Heatmap depicted sample clustering at consensus $k = 3$ following the transcriptome profiling of prognostic aging-relevant genes. **(B)** PCA plots confirmed the classification accuracy of aging-relevant molecular phenotypes. **(C)** Heatmap showed the expression patterns of prognostic aging-relevant genes in three aging-relevant molecular phenotypes. **(D)** Kaplan–Meier survival curves were conducted for gastric cancer patients with diverse molecular phenotypes.

Supplementary Table 1 | Clinicopathological characteristics of patients with gastric cancer in TCGA and GSE84437 cohorts.

Supplementary Table 2 | The list of aging-relevant genes.

Supplementary Table 3 | The list of 312 genes in the brown module.

REFERENCES

1. Gambardella V, Castillo J, Tarazona N, Gimeno-Valiente F, Martínez-Ciarpaglini C, Cabeza-Segura M, et al. The role of tumor-associated macrophages in gastric cancer development and their potential as a therapeutic target. *Cancer Treat Rev.* (2020) 86:102015. doi: 10.1016/j.ctrv.2020.102015
2. Yan HHN, Siu HC, Law S, Ho SL, Yue SSK, Tsui WY, et al. A Comprehensive human gastric cancer organoid biobank captures tumor subtype heterogeneity and enables therapeutic screening. *Cell Stem Cell.* (2018) 23:882–97.e811. doi: 10.1016/j.stem.2018.09.016
3. Sathe A, Grimes SM, Lau BT, Chen J, Suarez C, Huang RJ, et al. Single-cell genomic characterization reveals the cellular reprogramming of the gastric tumor microenvironment. *Clin Cancer Res.* (2020) 26:2640–53. doi: 10.1158/1078-0432.CCR-19-3231
4. Ho SWT, Tan P. Dissection of gastric cancer heterogeneity for precision oncology. *Cancer Sci.* (2019) 110:3405–14. doi: 10.1111/cas.14191
5. Zeng D, Li M, Zhou R, Zhang J, Sun H, Shi M, et al. Tumor microenvironment characterization in gastric cancer identifies prognostic and immunotherapeutically relevant gene signatures. *Cancer Immunol Res.* (2019) 7:737–50. doi: 10.1158/2326-6066.CIR-18-0436
6. Yang J, Jiang Q, Liu L, Peng H, Wang Y, Li S, et al. Identification of prognostic aging-related genes associated with immunosuppression and inflammation in head and neck squamous cell carcinoma. *Aging (Albany NY).* (2020) 12:25778–804. doi: 10.18632/aging.104199
7. Jia K, Cui C, Gao Y, Zhou Y, Cui Q. An analysis of aging-related genes derived from the Genotype-Tissue Expression project (GTEx). *Cell Death Discov.* (2018) 4:26. doi: 10.1038/s41420-018-0093-y
8. de Magalhães JP, Costa J, Toussaint O. HAGR: the human ageing genomic resources. *Nucleic Acids Res.* (2005) 33:D537–543. doi: 10.1093/nar/gki017
9. Avelar RA, Ortega JG, Tacutu R, Tyler EJ, Bennett D, Binetti P, et al. A multidimensional systems biology analysis of cellular senescence in aging and disease. *Genome Biol.* (2020) 21:91. doi: 10.1186/s13059-020-01990-9
10. Serrano M, Lin AW, McCurrach ME, Beach D, Lowe SW. Oncogenic ras provokes premature cell senescence associated with accumulation of p53 and p16INK4a. *Cell.* (1997) 88:593–602. doi: 10.1016/S0092-8674(00)81902-9
11. Laberge RM, Zhou L, Sarantos MR, Rodier F, Freund A, de Keizer PL, et al. Glucocorticoids suppress selected components of the senescence-associated secretory phenotype. *Aging Cell.* (2012) 11:569–78. doi: 10.1111/j.1474-9726.2012.00818.x
12. Faget DV, Ren Q, Stewart SA. Unmasking senescence: context-dependent effects of SASP in cancer. *Nat Rev Cancer.* (2019) 19:439–53. doi: 10.1038/s41568-019-0156-2
13. Mahmoudi S, Xu L, Brunet A. Turning back time with emerging rejuvenation strategies. *Nat Cell Biol.* (2019) 21:32–43. doi: 10.1038/s41556-018-0206-0
14. Johnson SC, Rabinovitch PS, Kaeberlein M. mTOR is a key modulator of ageing and age-related disease. *Nature.* (2013) 493:338–45. doi: 10.1038/nature11861
15. Colaprico A, Silva TC, Olsen C, Garofano L, Cava C, Garolini D, et al. TCGAbiolinks: an R/Bioconductor package for integrative analysis of TCGA data. *Nucleic Acids Res.* (2016) 44:e71. doi: 10.1093/nar/gkv1507
16. Yoon SJ, Park J, Shin Y, Choi Y, Park SW, Kang SG, et al. Deconvolution of diffuse gastric cancer and the suppression of CD34 on the BALB/c nude mice model. *BMC Cancer.* (2020) 20:314. doi: 10.1186/s12885-020-06814-4
17. Liu Y, Sethi NS, Hinoue T, Schneider BG, Cherniack AD, Sanchez-Vega F, et al. Comparative molecular analysis of gastrointestinal adenocarcinomas. *Cancer Cell.* (2018) 33:721–735.e728. doi: 10.1016/j.ccell.2018.03.010
18. Mayakonda A, Lin DC, Assenov Y, Plass C, Koeffler HP. Maftools: efficient and comprehensive analysis of somatic variants in cancer. *Genome Res.* (2018) 28:1747–56. doi: 10.1101/gr.239244.118
19. Budczies J, Seidel A, Christopoulos P, Endris V, Kloor M, Gyorffy B, et al. Integrated analysis of the immunological and genetic status in and across cancer types: impact of mutational signatures beyond tumor mutational burden. *Oncoimmunology.* (2018) 7:e1526613. doi: 10.1080/2162402X.2018.1526613
20. Mermel CH, Schumacher SE, Hill B, Meyerson ML, Beroukhim R, Getz G. GISTIC2.0 facilitates sensitive and confident localization of the targets of focal somatic copy-number alteration in human cancers. *Genome Biol.* (2011) 12:R41. doi: 10.1186/gb-2011-12-4-r41
21. Davoli T, Uno H, Wooten EC, Elledge SJ. Tumor aneuploidy correlates with markers of immune evasion and with reduced response to immunotherapy. *Science.* (2017) 355:eaaf8399. doi: 10.1126/science.aaf8399
22. Wilkerson MD, Hayes DN. ConsensusClusterPlus: a class discovery tool with confidence assessments and item tracking. *Bioinformatics.* (2010) 26:1572–3. doi: 10.1093/bioinformatics/btq170
23. Hänzelmann S, Castelo R, Guinney J. GSVA: gene set variation analysis for microarray and RNA-seq data. *BMC Bioinformatics.* (2013) 14:7. doi: 10.1186/1471-2105-14-7
24. Liberzon A, Birger C, Thorvaldsdóttir H, Ghandi M, Mesirov JP, Tamayo P. The Molecular Signatures Database (MSigDB) hallmark gene set collection. *Cell Syst.* (2015) 1:417–25. doi: 10.1016/j.cels.2015.12.004
25. Mariathasan S, Turley SJ, Nickles D, Castiglioni A, Yuen K, Wang Y, et al. TGFβ attenuates tumour response to PD-L1 blockade by contributing to exclusion of T cells. *Nature.* (2018) 554:544–8. doi: 10.1038/nature25501
26. Yang W, Soares J, Greninger P, Edelman EJ, Lightfoot H, Forbes S, et al. Genomics of Drug Sensitivity in Cancer (GDSC): a resource for therapeutic biomarker discovery in cancer cells. *Nucleic Acids Res.* (2013) 41:D955–961. doi: 10.1093/nar/gks1111
27. Geeleher P, Cox N, Huang RS. pRRophetic: an R package for prediction of clinical chemotherapeutic response from tumor gene expression levels. *PLoS ONE.* (2014) 9:e107468. doi: 10.1371/journal.pone.0107468
28. Sokolov A, Carlin DE, Paull EO, Baertsch R, Stuart JM. Pathway-based genomics prediction using generalized elastic net. *PLoS Comput Biol.* (2016) 12:e1004790. doi: 10.1371/journal.pcbi.1004790
29. Auslander N, Zhang G, Lee JS, Frederick DT, Miao B, Moll T, et al. Robust prediction of response to immune checkpoint blockade therapy in metastatic melanoma. *Nat Med.* (2018) 24:1545–9. doi: 10.1038/s41591-018-0157-9
30. Chen DS, Mellman I. Oncology meets immunology: the cancer-immunity cycle. *Immunity.* (2013) 39:1–10. doi: 10.1016/j.immuni.2013.07.012
31. Yoshihara K, Shahmoradgoli M, Martínez E, Vegesna R, Kim H, Torres-Garcia W, et al. Inferring tumour purity and stromal and immune cell admixture from expression data. *Nat Commun.* (2013) 4:2612. doi: 10.1038/ncomms3612
32. Malta TM, Sokolov A, Gentles AJ, Burzykowski T, Poisson L, Weinstein JN, et al. Machine learning identifies stemness features associated with oncogenic dedifferentiation. *Cell.* (2018) 173:338–54.e315. doi: 10.1016/j.cell.2018.03.034
33. Szklarczyk D, Gable AL, Nastou KC, Lyon D, Kirsch R, Pyysalo S, et al. The STRING database in 2021: customizable protein-protein networks, and functional characterization of user-uploaded gene/measurement sets. *Nucleic Acids Res.* (2021) 49:D605–12. doi: 10.1093/nar/gkab835
34. Bader GD, Hogue CW. An automated method for finding molecular complexes in large protein interaction networks. *BMC Bioinformatics.* (2003) 4:2. doi: 10.1186/1471-2105-4-2
35. Doncheva NT, Morris JH, Gorodkin J, Jensen LJ. Cytoscape StringApp: network analysis and visualization of proteomics data. *J Proteome Res.* (2019) 18:623–32. doi: 10.1021/acs.jproteome.8b00702
36. Zhang B, Wu Q, Li B, Wang D, Wang L, Zhou YL. m(6)A regulator-mediated methylation modification patterns and tumor microenvironment infiltration characterization in gastric cancer. *Mol Cancer.* (2020) 19:53. doi: 10.1186/s12943-020-01170-0

37. Sun L, Huang C, Zhu M, Guo S, Gao Q, Wang Q, et al. Gastric cancer mesenchymal stem cells regulate PD-L1-CTCF enhancing cancer stem cell-like properties and tumorigenesis. *Theranostics.* (2020) 10:11950–62. doi: 10.7150/thno.49717
38. Nguyen L, Materns, JWM, Van Hoeck A, Cuppen E. Pan-cancer landscape of homologous recombination deficiency. *Nat Commun.* (2020) 11:5584. doi: 10.1038/s41467-020-19406-4
39. Liu Y, Xie S, Zhu K, Guan X, Guo L, Lu R. CALD1 is a prognostic biomarker and correlated with immune infiltrates in gastric cancers. *Heliyon.* (2021) 7:e07257. doi: 10.1016/j.heliyon.2021.e07257
40. Wang J, Xu P, Hao Y, Yu T, Liu L, Song Y, et al. Interaction between DNMT3B and MYH11 via hypermethylation regulates gastric cancer progression. *BMC Cancer.* (2021) 21:914. doi: 10.1186/s12885-021-08653-3
41. Chen L, Su L, Li J, Zheng Y, Yu B, Yu Y, et al. Hypermethylated FAM5C and MYLK in serum as diagnosis and pre-warning markers for gastric cancer. *Dis Markers.* (2012) 32:195–202. doi: 10.1155/2012/473251
42. Yu B, Chen X, Li J, Qu Y, Su L, Peng Y, et al. Stromal fibroblasts in the microenvironment of gastric carcinomas promote tumor metastasis via upregulating TAGLN expression. *BMC Cell Biol.* (2013) 14:17. doi: 10.1186/1471-2121-14-17

Conflict of Interest: The authors declare that the research was conducted in the absence of any commercial or financial relationships that could be construed as a potential conflict of interest.

frontiers in Medicine

ORIGINAL RESEARCH
published: 09 February 2022
doi: 10.3389/fmed.2022.815355

Study of Allosteric Transitions of Human P-Glycoprotein by Using the Two-State Anisotropic Network Model

Hongwu Li [1†] ***and Weikang Gong*** [2*†]

[1] *School of Mathematics and Statistics, Nanyang Normal University, Nanyang, China,* [2] *Faculty of Environmental and Life Sciences, Beijing University of Technology, Beijing, China*

Edited by:
Fu Wang,
Xi'an Jiaotong University, China

Reviewed by:
Suliman Khan,
Second Affiliated Hospital of Zhengzhou University, China
Ghulam Nabi,
Hebei Normal University, China
Min-Chun Wu,
Nanyang Technological University, Singapore

***Correspondence:**
Weikang Gong
N2007046B@e.ntu.edu.sg

† *These authors have contributed equally to this work*

Specialty section:
This article was submitted to Precision Medicine, a section of the journal Frontiers in Medicine

Received: *01 December 2021*
Accepted: *04 January 2022*
Published: *09 February 2022*

Citation:
Li H and Gong W (2022) Study of Allosteric Transitions of Human P-Glycoprotein by Using the Two-State Anisotropic Network Model. Front. Med. 9:815355. doi: 10.3389/fmed.2022.815355

Human P-glycoprotein (P-gp) is a kind of ATP-binding cassette (ABC) transporters. Once human P-gp is overexpressed in tumor cells, which can lead to tumor multidrug resistance (MDR). However, the present experimental methods are difficult to obtain the large-scale conformational transition process of human P-gp. In this work, we explored the allosteric pathway of human P-gp from the inward-facing (IF) to the outward-facing (OF) state in the substrate transport process with the two-state anisotropic network model (tANM). These results suggest that the allosteric transitions proceed in a coupled way. The conformational changes of nucleotide-binding domains (NBDs) finally make the transmembrane domains (TMDs) to the OF state *via* the role of the allosteric propagation of the intracellular helices IH1 and IH2. Additionally, this allosteric pathway is advantageous in energy compared with other methods. This study reveals the conformational transition of P-gp, which contributes to an understanding of the allosteric mechanism of ABC exporters.

Keywords: two-state ANM, P-glycoprotein, allosteric pathway, multidrug resistance, ATP-binding

INTRODUCTION

Long-term contact between cells and drugs can lead to multidrug resistance (MDR). It is also a major obstacle to cancer chemotherapy. MDR is mainly due to the overexpression of antineoplastic drug-efflux transporters (1). Such proteins belong to the ATP-binding cassette (ABC) superfamily and are widely located on the cell membranes. They utilize the energy of ATP hydrolysis to transport substrates across the lipid bilayer, even directly out of cells. The importance of studies on bacteria in elucidating several basic principles pertaining to ABC transporters is emphasized (2, 3). Interindividual differences in drug response are an important cause of treatment failures and adverse drug reactions. Human MDR protein 1, namely P-glycoprotein (P-gp), is an MDR ABC exporter that is widely distributed in the human body, it has a high-level expression generally in the blood–brain barrier and blood testosterone, liver, inner ear, and a variety of stem cells (4). Additionally, it shares a significant sequence identity with protein MsbA from gram-negative bacteria, which has been implicated in MDR. Researchers have found that P-gp has unusually broad polyspecificity, recognizing hundreds of hydrophobic substrates as 330–4,000 Da. It is like a "hydrophobic vacuum cleaner" pulling substrates from the membrane and expelling them to promote MDR. Therefore, it is of great importance to reveal the export process of human P-gp.

P-glycoprotein has been studied as a hotspot for many years because of its clinical relevance. Especially, the structure of mouse P-gp, which has 87% sequence similarity to human P-gp, was obtained by Aller et al. Like mouse P-gp, human P-gp undergoes large-scale conformational changes between inward-facing (IF) and outward-facing (OF) state during a transport event (**Figures 1A,B**). It is a single polypeptide composed of 1,280 residues. It can be arranged as two pseudo homologous halves, named PA and PB (5). Each half (PA/PB) consists of a transmembrane domain (TMD) and a nucleotide-binding domain (NBD). Each TMD of human P-gp contains six helices, as labeled with TM1–TM6 for PA, TM7–12 for PB in **Figure 1**. Extracellular loops EL1, EL2, and EL3 of PA connect TM1–TM2, TM3–TM4, and TM5–TM6 in the periplasmic side, respectively. Intracellular helices IH1 and IH2 of PA connect TM2–TM3 and TM4–TM5 in the cytoplasmic side, respectively. The structure of PB is basically corresponding with PA. The TM helices cross each other to form a cavity in their interfaces. For the IF state, the TM helices are split into two groups forming two branches (TM1–3, 6, 10, 11 and TM4, 5, 7–9, 12) at the cytoplasmic side, resulting in the opening of the putative translocation pore to the cytoplasm (**Figure 1A**). Once the IF state is transferred into the OF state, the packing of TM helices will be rearranged. The helices TM3 and TM6 (TM9 and TM12) are crossed over to associate with the other branch. Thus, for the OF state, two branches are composed of helices TM1–2, 9–12, and TM3–6, 7–8, respectively. The TM1 is elongated to concur with an elongated helix in PA seen in the EM structure. TMDs interact with NBDs through IH1, 2 and IH3, 4. The NBDs of different transporters are highly conserved and responsible for ATP binding and hydrolysis. Each is composed of a RecA-like subdomain and a helical one. The RecA-like subdomain contains one conserved nucleotide-binding site; the helical subdomain includes the ABC family signature motifs. These subdomains constitute a head-to-tail dimer with nucleotide-binding sites at the interface. NBDs utilize the released energy of ATP hydrolysis to transport drug molecules from the inside to the outside of the cellular membrane, and this process accompanies a large-amplitude cooperation motion between the different structural domains of human P-gp.

A simple alternating access model was proposed by Jardetzky (6). In 2004, Higgins and Linton (7) conclusively proposed the ABC transporter conformation transformation model of "ATP-switch" based on a large number of experiments. At present, a lot of experimental information and conformational transformation models about human P-gp have been studied. In 1976, Juliano and Ling (8) first found that P-gp in the Chinese hamster ovary cells was selected for resistance to colchicines. In 1986, Chen et al. (9) discovered human P-gp for the first time. In 2008, Lee et al. (10) manufactured human P-gp of two-dimensional crystals in the phospholipid bilayer, then analyzed by using transmission electron microscopy (TEM) and got a low-resolution (14.6–74.5 Å) three-dimensional structure of human P-gp. Aller et al. (5) resolved three x-ray crystal structures of mouse P-gp with IF conformation in 2009. Later, Paul et al. (11) obtained the higher resolution crystal structures of mouse P-gp. Despite not getting a high-resolution crystal structure of human P-gp, the two have an 87% sequence identity (12). So, the crystal structures of mouse P-gp are chosen as good templates for human P-gp with IF conformation. In 2012, Wise (13) observed the coupled movement between NBDs and TMDs and referred it to the pronounced twisting of NBDs at the same time of closing. Chang et al. (14) explored the atomic detail of the conformational transmission of human P-gp by using targeted molecular dynamics (tMD) simulations and identified six key segments in the allosteric process. Recently, Pan and Aller (15) analyzed the conformational changes of ATP binding using all-atom molecular dynamics (MD) simulations. However, there is very little research on the large conformational transmission and analyses of the energy of human P-gp. Thus, the allosteric transition of human P-gp is still a hot issue.

All-atom MD simulation is an important tool to study protein dynamics and demonstrate their biological function. However, it is difficult to simulate the large-scale functional motion of transmembrane proteins and to obtain the complete information of conformational changes. To solve this problem, researchers put forward the coarse-grained model to steed up simulation with a freezing part of freedom degrees of the system. The Gaussian network model (GNM) (16) and the anisotropic network model (ANM) (17) are relatively simplified models based on the elastic network model (ENM) (18–21). Recently, Pan and Aller (15) analyzed the conformational changes and allosteric regulation of ATP binding by using all-atom MD simulations. Recently, Das et al. proposed a simple and computationally efficient method, the two-state ANM (tANM) (22) to construct a physically reasonable pathway between the two end points. First, a simple ENM representation is adopted for each of the end states, which accounts for the topology of inter-residue contacts in the structure. Second, a very simple two-state potential is constructed by mixing these two ENMs. The potential has a cusp hypersurface where the energies from both the ENMs are identical. Third, a minimum energy structure on the cusp hypersurface is searched and treated as the transition state. Fourth, starting from the transition state, two separate steepest descent minimizations were performed to connect the corresponding end states. Finally, the conformations collected from the two steepest descent paths along with the transition state provide a pathway. The Bahar group tested the Leucine transporter and Glutamate transporter, paving physically significant pathways, and helping generate experimentally testable hypotheses.

In this paper, the allosteric pathway between IF and OF state of human P-gp is explored through the tANM method; a reasonable allosteric pathway is obtained with the optimal energy. This helps to better understand the working mechanism of the human P-gp system.

MATERIALS AND METHODS

Protein System

The x-ray structure of human P-gp in the IF state was modeled by using the Swiss-Model (http://swissmodel.expasy.org/) with a high resolution of mouse P-gp (PDB ID: 4Q9H) with the resolution value of 3.4 Å. The model of an OF conformation was obtained by O'Mara and Tieleman's group (23). The IF state

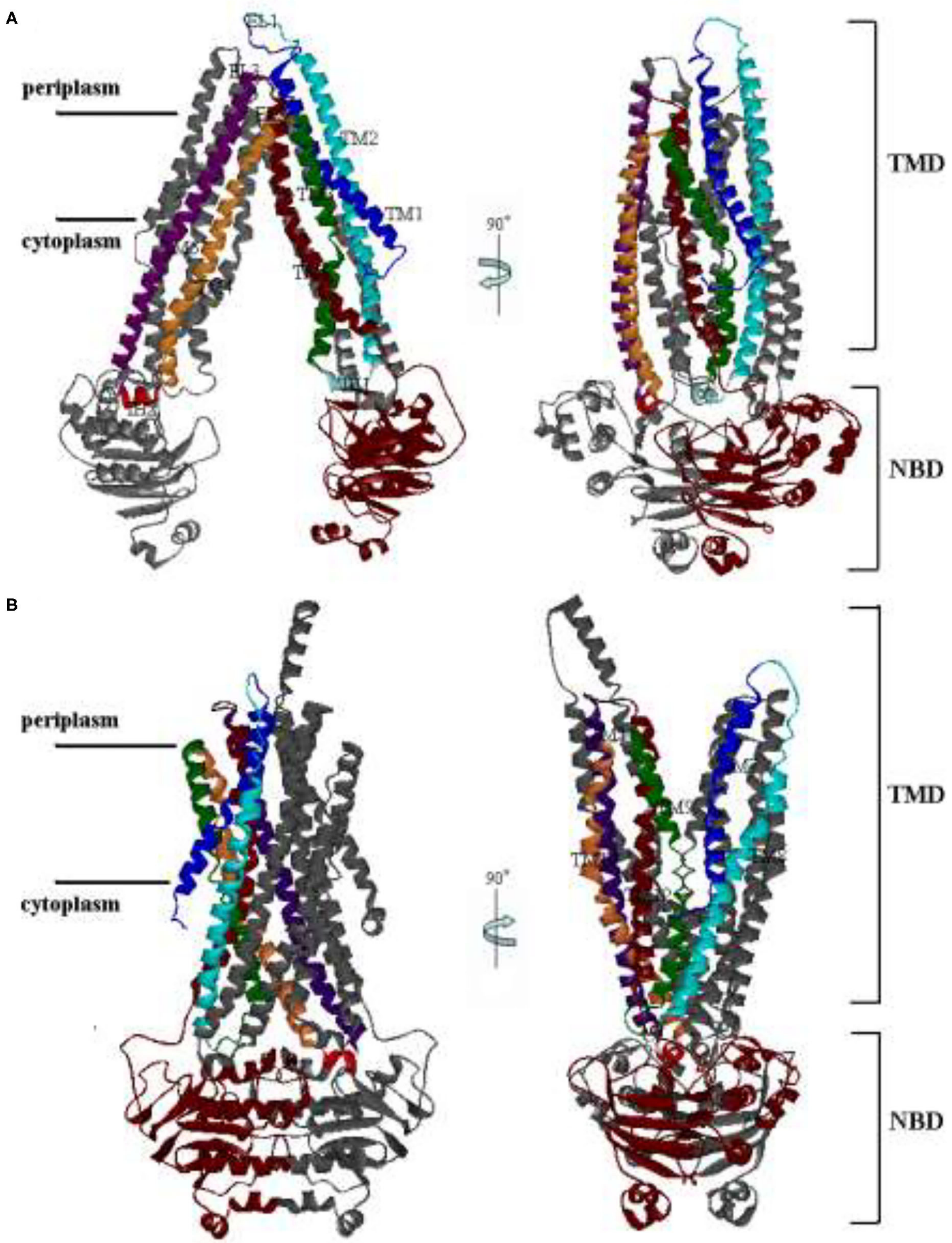

FIGURE 1 | The structures of human P-glycoprotein (P-gp). **(A)** The conformation of the inward-facing (IF) state by the Swiss Model; **(B)** The conformation of the outward-facing (OF) state with O'Mara. The right panel is related to the left one by a 90° rotation around the axis shown.

contains residues from 34–630 and 701–1,275, opposite to 36–631 and 697–1,276 in the OF state, so we work it in mainly 1,170 residues of the two public sections.

Adaptive ANM

For a protein with N residues, the configuration of the system is denoted by an elastic network, a node represents a residue, so ANM is an elastic network model defined around an experimental structure (e.g., x-ray or NMR structure) with the following energy function:

$$U_{ANM}(R) = \frac{\gamma}{2}\sum_{i<j}^{N} C_{ij}(R_{ij}-R_{ij}^{0})^2 = \frac{\gamma}{2}\sum_{i<j}^{N} C_{ij}([(X_i-X_j)^2 + (Y_i-Y_j)^2 + (Z_i-Z_j)^2]^{1/2} - R_{ij}^{0})^2 \tag{1}$$

where γ is the uniform force constant, N is the number of residues, R_{ij} is the distance between the nodes i and j, R_{ij}^{0} is the instantaneous distance between the nodes i and j, $R_i = [X_i, Y_i, Z_i]$ is the coordinate in X, Y, and Z directions of nodes i, C_{ij} is an element of the contact matrix defined by

$$C_{ij} = \begin{cases} 1 \ \ if\ R_{ij} \le r_c \\ 0 \ \ otherwise \end{cases} \tag{2}$$

r_c is the cutoff distance. $U_A(R)$ and $U_B(R)$ are, respectively, the ANM energy function in A and B states. The two-state potential function combines them with the following mixing rule (24):

$$U(R) = \frac{1}{2}\left(U_A(R) + U_B(R) - \sqrt{\left[U_A(R) - U_B(R)\right]^2}\right) \tag{3}$$

tANM Detailed Procedure

1. Two end structures are represented by the positions of their C_α atoms. These structures are aligned, and M-2 new intermediate conformers/images are generated by linearly interpolating between the end structures. The value of M is chosen by the user and is dependent on the value of the tolerance parameter $\varepsilon^{\dagger}$, which is the smallest energy difference between the two conformers that are considered to be different.
2. For each image, the energy is determined to use the two-state potential defined in formula (3). Then, the conformer $R^{\dagger}$ is identified for which energies from both the surfaces [i.e., $U_A(R^{\dagger})$ and $U_B(R^{\dagger})$] are equal within the tolerance parameter $\varepsilon^{\dagger}$.
3. Starting from $R^{\dagger}$, the transition state is searched by the following iterative procedure:
    (a) With appropriate choices of step-sizes s_A and s_B the knowledge of transition state for the present iteration $R^{\dagger}(n)$, one step of the steepest descent minimization is carried out on each surface using the force of the respective surface and two new sets of coordinates $R^A(n+1)$ and $R^B(n+1)$ are generated, where

$$R^A(n+1) = R^{\Psi}(n) + s_A f_A(n) \tag{4}$$

$$R^B(n+1) = R^{\Psi}(n) + s_B f_B(n) \tag{5}$$

and

$$f_A(n) = -\frac{\partial U_A(R)}{\partial R} \quad f_B(n) = -\frac{\partial U_B(R)}{\partial R} \tag{6}$$

    (b) A linear interpolation (LI) is performed between $R^A(n+1)$ and $R^B(n+1)$ to find out the conformer that resides on the cusp hypersurface. This is a new approximation for the transition state, i.e., $R^{\dagger}(n+1)$.
    (c) We iterate steps (3a) and (3b) until the energy difference between the two transition state conformers, obtained in two successive iterations, is less than tolerance ε_{conv}.
4. Two separate steepest descent minimizations are performed, one on each surface, starting from the final transition state conformation $R_f^{\dagger}$ and conformers, and conformers separated by using a user-defined RMSD are collected.
5. The cross-correlation between the displacements of the ith and jth residues at the kth conformer is defined as:

$$C_{A,ij}^{(k)} = \cos(h_{A,i}^{(k)}, h_{A,j}^{(k)}) \tag{7}$$

where $h_{A,i}^{(k)}$ and $h_{A,j}^{(k)}$ are, respectively, the displacements of the ith and jth residues generated from the deformation vector:

$$h_{A,i}^{(k)} = (v_{A,3i-2}^{(k)}, v_{A,3i-1}^{(k)}, v_{A,3i}^{(k)}) \tag{8}$$

$$h_{A,j}^{(k)} = (v_{A,3j-2}^{(k)}, v_{A,3j-1}^{(k)}, v_{A,3j}^{(k)}) \tag{9}$$

The cross-correlation value ranges from −1 to 1. The positive values represent the residues moving in the same direction, and the negative values represent their movement in the opposite direction.

Several parameters listed above need to be specified before performing the calculation. The two-state potential function is characterized by the force constants and cutoff distances of ANMs. The ANM force constant does not affect the qualitative results (or the shape of conformational change driven by the normal modes) but uniformly scales the absolute size of motions. So, the force constants are inconsequential, and the cut-off distance is usually selected in the range of 12–16 Å. The values of $\varepsilon^{\dagger}$ are chosen to be in the range between 10e-4 and 10e-5. The most important parameters for an efficient implementation of the algorithm turned out to be the step sizes involved in the search of the transition state on the cusp hypersurface (and in step 3a). If step-sizes are too large, then the resultant movement of the transition state structure on the cusp hypersurface is large and the minimization algorithm does not work. On the other hand, if the chosen values are too small, then the convergence becomes slow.

In tANM, the cutoff is 13Å with the experimental information, the force constant is 0.1 kcal/(mol·Å^2), the tolerance parameter $\varepsilon^{\dagger}$ is $5{\cdot}10^{-5}$, and ε_{conv} is 10^{-4}. The values of step sizes s_A and s_B are as quickly as possible to find the saddle point on the cusp hypersurface, so they set for 1 first, if the procedure spans the saddle point, turns down the value of step size, then calculates again from the breakpoint, until arriving the tolerance $\varepsilon^{\dagger}$, the RMSD of collecting conformers is 0.1 Å. The tANM has found an energy optimal path from opening to closing in physical.

RESULTS AND DISCUSSION

First, we aligned the two end structures by using VMD: (25), the original RMSD between them is 14.324 Å, and then used tANM to find the allosteric pathway of human P-gp.

Sequence of Transition

After collecting conformers on the cusp hypersurface, we produced 171 intermediate conformers (tr_1-171), of which tr_124 is the conformer of the transition state. Also, we modeled the IF intermediate conformation (IF-II) by using mouse P-gp (PDB ID: 3G5U) with the resolution of 3.8 Å, corresponding to the structure of Wise (13) and Chang's et al. group (14). Further comparison of the conformers of an allosteric pathway with it, the lowest RMSD obtained between IF-II and tr_39 is 4.026 Å (**Figure 2**). To a certain extent, this illustrates the rationality of the pathway we got.

Figure 3 shows five representative snapshots along an allosteric pathway. **Figure 3C** (tr_124) is the transition state, that is to say, its energy is a saddle point on the cusp hypersurface. From **Figures 3A–C** (IF state), it can be seen that NBDs undergo an apparent conformational transition from the open to the nearly closed intermediates, and get affected due to this. The cytoplasmic side of the TMDs also experiences the corresponding changes. While for the periplasmic side, there are hardly evident conformational transitions. These results suggest that the allosteric transitions are more likely to be driven by NBDs, and this point is also hinted at in the following analyses about the changes of distances among some critical residues. Additionally, it is noticed that the relative orientation between the NBDs also changes and has a twisting motion although it is not very evident during this stage. In the transition state (**Figure 3C**), the cytoplasmic side of TMDs gathers into a cluster and NBDs become closed. From **Figures 3C–E** (the OF state), NBDs become completely closed. In addition, the periplasmic side of TMDs opens toward the outside. From **Figure 3** (overall), we can see the whole transport process of human P-gp from IF to OF states. The sequence of transition of human P-gp is similar to exporter MsbA, which is in connection with their similar function and amino acid sequence (26). The sequence consistency of PA, PB part with MA, MB of MsbA are, respectively, 37, 34% by using the BLAST (12).

Analysis of the Energy

We combined different simulation methods to analyze and compare changes in the allosteric energy of human P-gp. LI is a linear fitting with the coordinates of amino acids to get a user-defined number set of conformers between the two states, actually, this is a rigid allosteric process. tMD is based on traditional MD simulation to drive the coordinates of amino acids toward their target coordinates by means of extra potential. All TMD simulations were performed in the isothermal isobaric (substance, pressure and temperature, NPT) ensemble using the NAMD 2.8 software. The temperature was set to 310 K and kept constant during the simulation process using a Langevin thermostat with a damping coefficient of 1.0 ps^{-1}. The two whole systems were first equilibrated for 0.5 ns and then conducted for 1 ns. In **Figure 4**, the reaction coordinate is the projection

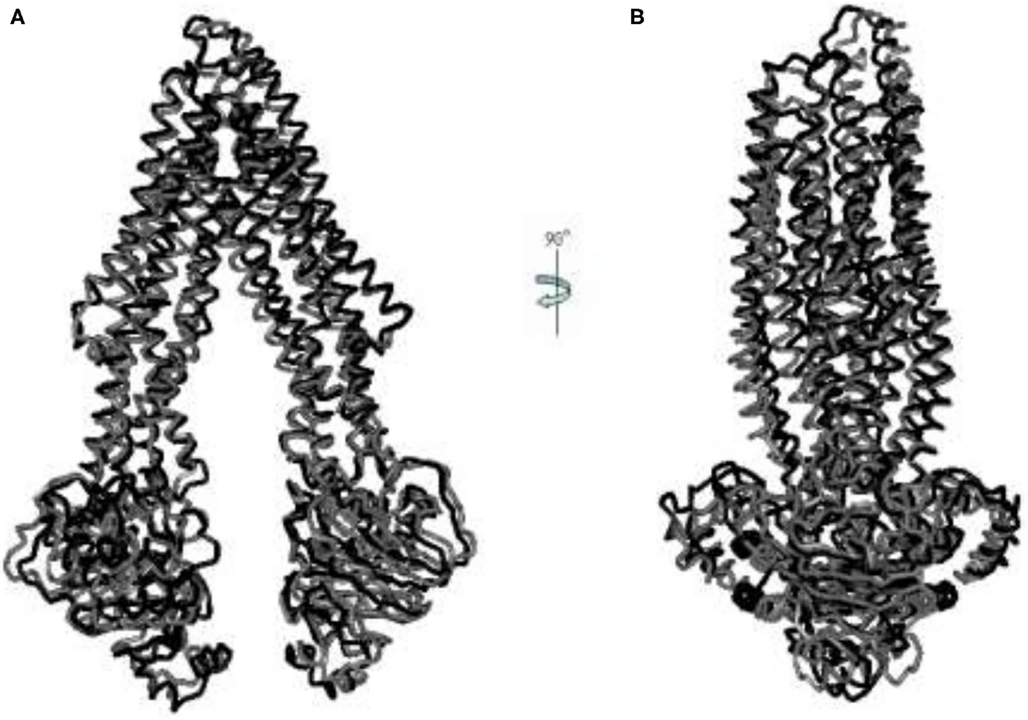

FIGURE 2 | (A,B) The aligned figures of tr_39 and IF_2009. The RMSD of tr_39 (black) and IF_2009 (gray, template: 3G5U, resolution: 3.8 Å) is 4.026 Å.

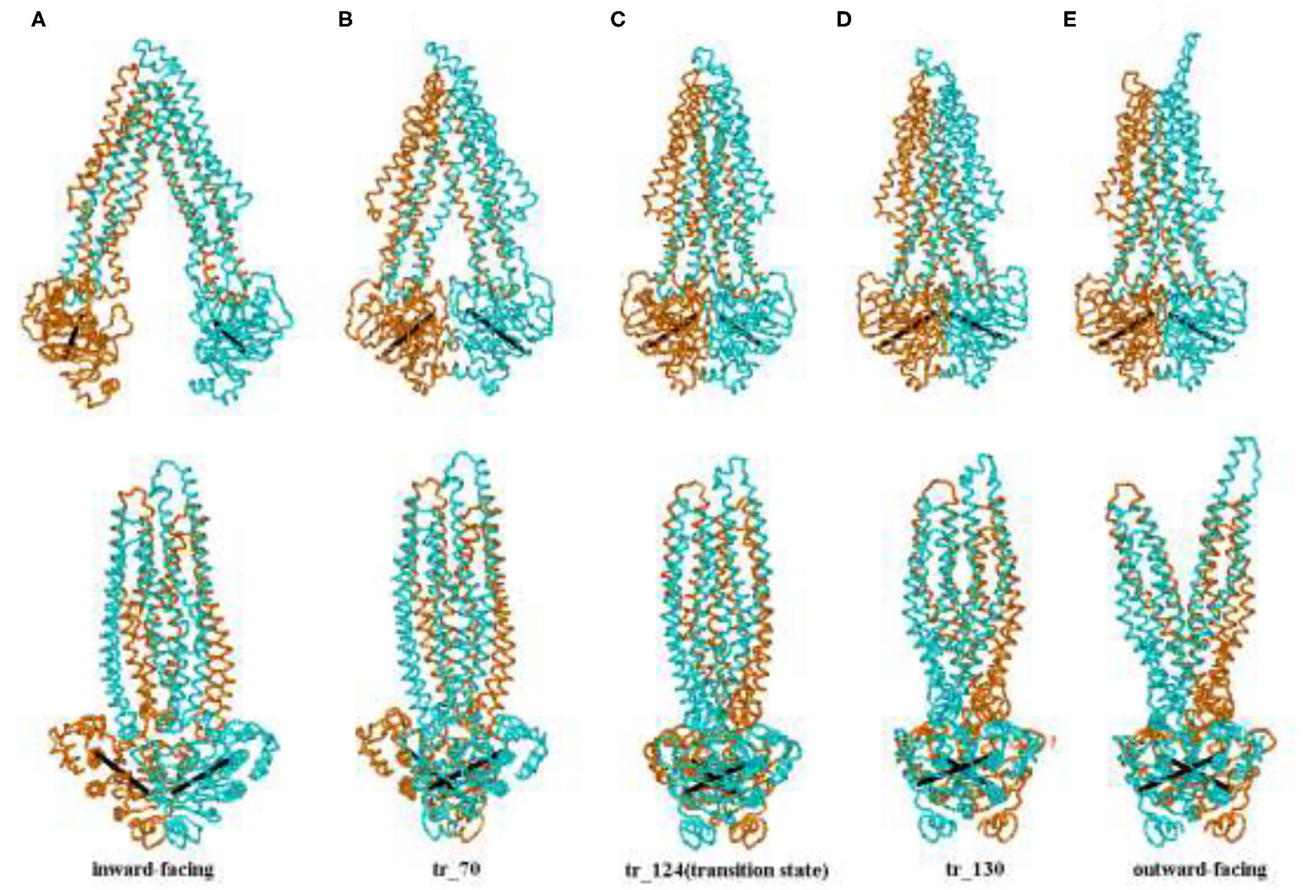

FIGURE 3 | (A–E) Representative conformation sampling along the allosteric pathway. The lower snapshots are obtained by rotating the corresponding upper ones to 90° counterclockwise. The two lines, respectively, connect C_α atoms of the residues L413 and K536, E1059, and K1181 in two-nucleotide binding domain (NBD).

of the cumulative displacement $v^{(n)} = R^{(n)} - R_A^{(n)}$ on the original distance vector $d^{(0)}$, that is, $x(n) = \frac{d^{(0)} \cdot v^{(n)}}{|d^{(0)}|^2}$, with IF and OF states representing the respective limits $x(n) = 0$ and 1. The energy peaks of the three methods are in the middle-late term of allosteric transmission. Compared with tMD and LI, tANM has the lowest energy consumption, the former two simulations are spanned a much taller energy barrier than tANM. To further observe tANM, it is slower in initial or final stages and faster before or after the transition state, which shows that low-frequency slow motions dominated the allosteric process of human P-gp in initial or final stages, then the participation of high-frequency local motions makes it rising rapidly.

Changes of Distances Among Some Critical Residues During Transitions

To study the allosteric details of human P-gp, we analyzed the changes of distances among some critical residues during this transition (**Figure 5**).

For TMDs, the residue pairs PA ASP87-PB ASP743, PA TRP212-PB TRP855, and PA GLY324-PB LEU968 (located in the extracellular loops EL1,4, EL2,5, and EL3,6, respectively), are selected to indicate the movement of the periplasmic side. For the middle part of TMDs, the selected residue pairs are PA MET68-PB PHE728 and PA ASP188-PB SER831 located in the drug-binding sites. The residue pairs PA TRP162-PB TRP803 and PA ILE265-PB VAL908 (respectively, located in the intracellular helix IH1,3 and IH2,4) are used to reflect the changes in the cytoplasmic side (**Figure 5B**). For NBDs, mainly contain a number of critical conserved sequence motifs involved in ATP binding, namely walker A, walker B, and LSGGQ. So, the residue pairs PA GLY430-PB GlY1178, PA GLY533-PB GLY1073, and PA GLU556-PB GLU1201 are, respectively, selected to explain the distance changes of NBDs.

From **Figure 5A**, for the periplasmic side, the distances (PA ASP87-PB ASP743, PA TRP212-PB TRP855, and PA GLY324-PB LEU968) remain nearly invariant at first and gradually increase after the transition state, the periplasmic side is closed before the transition state, it comes to open in the late period of the whole transmission. Due to the elongation of a long helix structure TM1, the distance between the two EL1 leads to the biggest change in the later stage of a process. For the middle part, the residue pair MET68-PHE728 next to the periplasmic side interacts with the drug and the decrease of distance occurs mainly

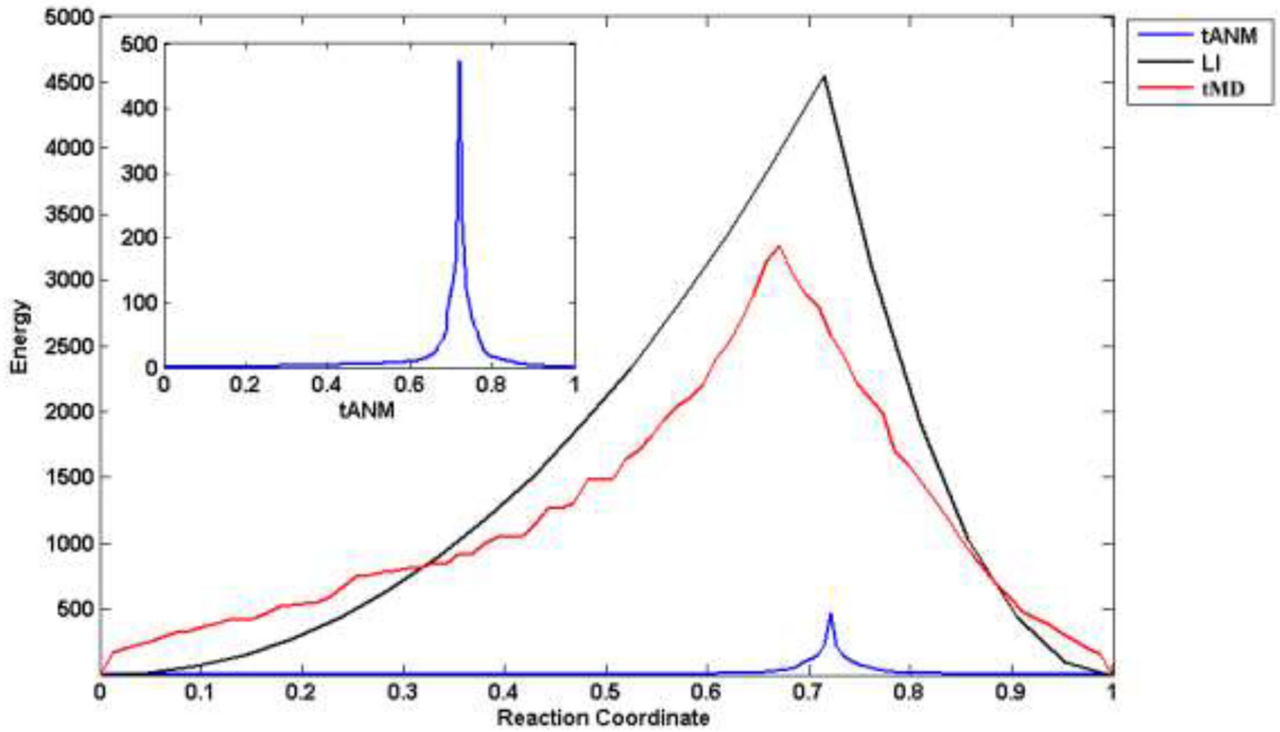

FIGURE 4 | The allosteric energy comparison of different methods. X-axis is the reaction coordinate, that is, the projection of the cumulative displacement on the original distance vector.

near the transition state, and as the TMDs open and drug release in the late process, it slowly increases. The distance of residue pair ASP188-SER831 decreases tardily at the beginning of the allosteric pathway and becomes obvious when the transmission nears the transition state, and because of TMDs open, it increases a little after the transition state and tends to be stable at the end of the pathway. The distances of residue pairs at the cytoplasmic side (PA TRP162-PB TRP803 and PA ILE265-PB VAL908) have an obvious decline trend before the transition state, it corresponds to the closing motion of NBDs and becomes stable in later stages.

Clearly, the closing speed of NBDs is more obvious than that of the TMD cytoplasmic part and much faster than that of the TMD middle part. These results imply that the allosteric transitions may be driven by NBDs. A previous study also indicates that the signals of conformational changes between the two NBDs are transmitted through the NBD–TMD interface to TMDs. When the two NBDs form dimers, an ATP-binding pocket (ABP) is composed of a Walker A and a Walker B with LSGGQ of another NBD. ATP molecules were sandwiched between the two NBDs and formed the “ATP sandwich dimers.” They are known as no. 1 and no. 2 ABP. The residue pairs PA GLY430-PB GlY1178 and PA GLY533-PB GLY1073 (respectively, located at no. 1 and no. 2 ABP) are closer to each other at the beginning of the allostery, and the distance decreases fastly, reaches consistently at the same time in the transition state, and remains stable until the OF state. The change of NBDs mainly occurs before the transition state, and the NBDs of the transition state have been closed, so the distance is basically invariant in the later stage. As to rise slowly of the distance before the transition state, we think it is also related to the twisting motion of NBDs. A specific discussion is given below.

Change of Relative Position Between NBDs

From the abovementioned analysis, in the allosteric process, the NBDs of human P-gp are not only close but also twisted (**Figure 6**). Here, we further analyzed a relative movement between the NBDs.

In the tANM simulation, each α helix and β -fold of NBDs basically remain unchanged, we selected the two lines to connect the residue pairs PA L413-PB K536 and PB E1059-PB K1181 and to illustrate the relative movement between the two NBDs (**Figure 6**). **Figure 7** shows the allosteric degree change of acute angle that is crossed of two lines. We assumed if NBDs only do closing motion, the angle should be determined as invariable. From the IF state to the OF state of human P-gp, the intersection angle is closed to 0° and the two lines remain to be in parallel relationship with each other at the initial of allosteric transitions, due to the movement of NBDs, such as the relative position and angle change, therefore the twisting motions of NBDs have been involved at the initial of allosteric transitions. Then, the lines no longer remain basically parallel, the cross-relationship becomes obvious and the angle is also increasing. After the conformer of the 91st angle increases faster, meanwhile it is the most obvious

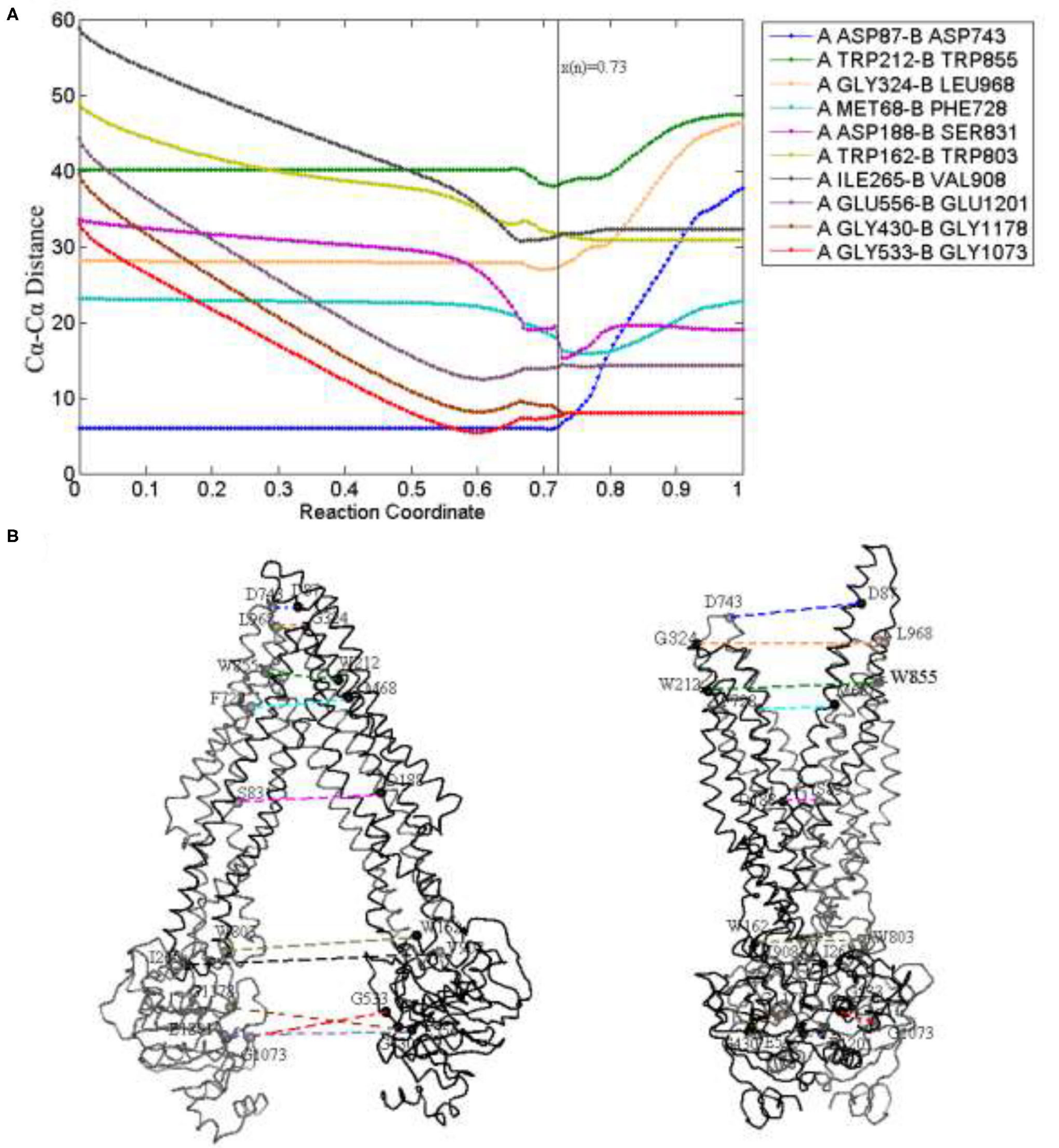

FIGURE 5 | Distance changes **(A)** of some critical residue pairs **(B)** along the reaction coordinate. $x(n) = 0.73$ (black) is the reaction coordinate of the transition state. The color of lines in **(B)** is in correspondence to **(A)**.

moment of the twisting motion of NBDs in the whole allosteric transitions. The angle remains unchanged from the transition state to the OF state. In general, the relative movement between the NBDs results from a closing and twisting motion, and the twisting motion continues in the whole period of closing NBDs. From **Figure 6**, we also see that the relative movement makes

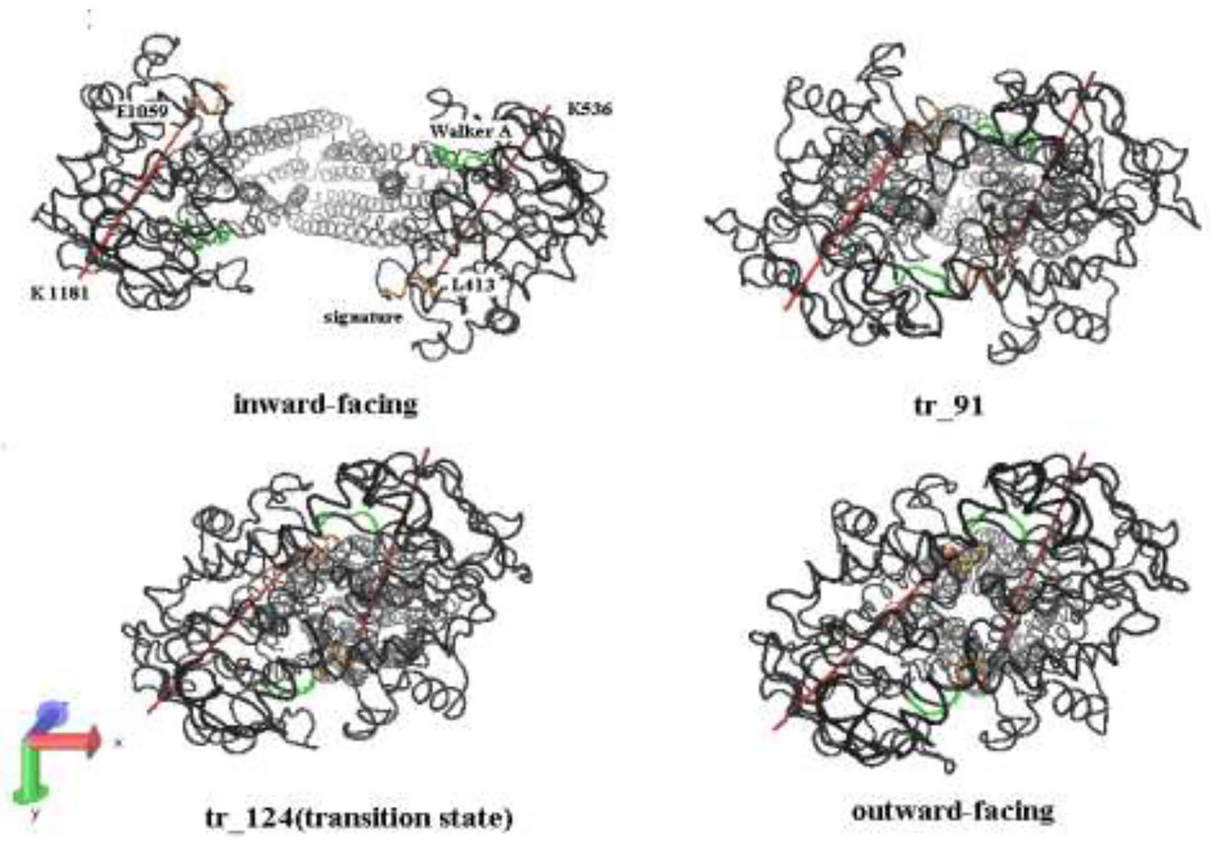

FIGURE 6 | A bottom-up view of human P-gp in different transition intermediates. The red lines represent the distance of residual pairs PA L413-PA K536 and PB E1059-PB K1181 in NBDs. The green and orange, respectively, mark the Walker A and signature motifs in NBDs.

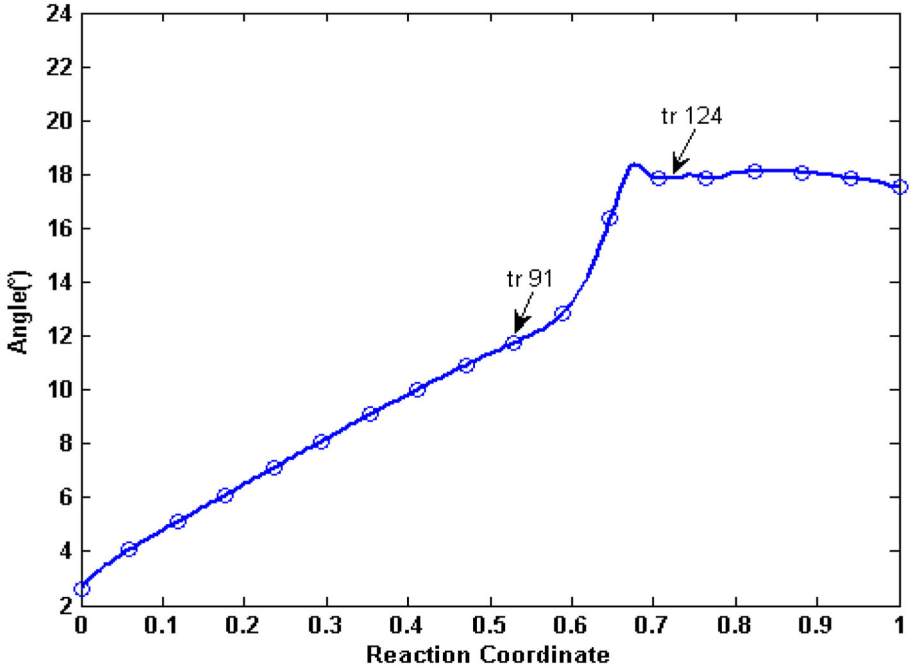

FIGURE 7 | The angle changes of the two lines of PA L413-PA K536 and PB E1059-PB K1181. Arrows represent conformation 91 and conformation 124, respectively.

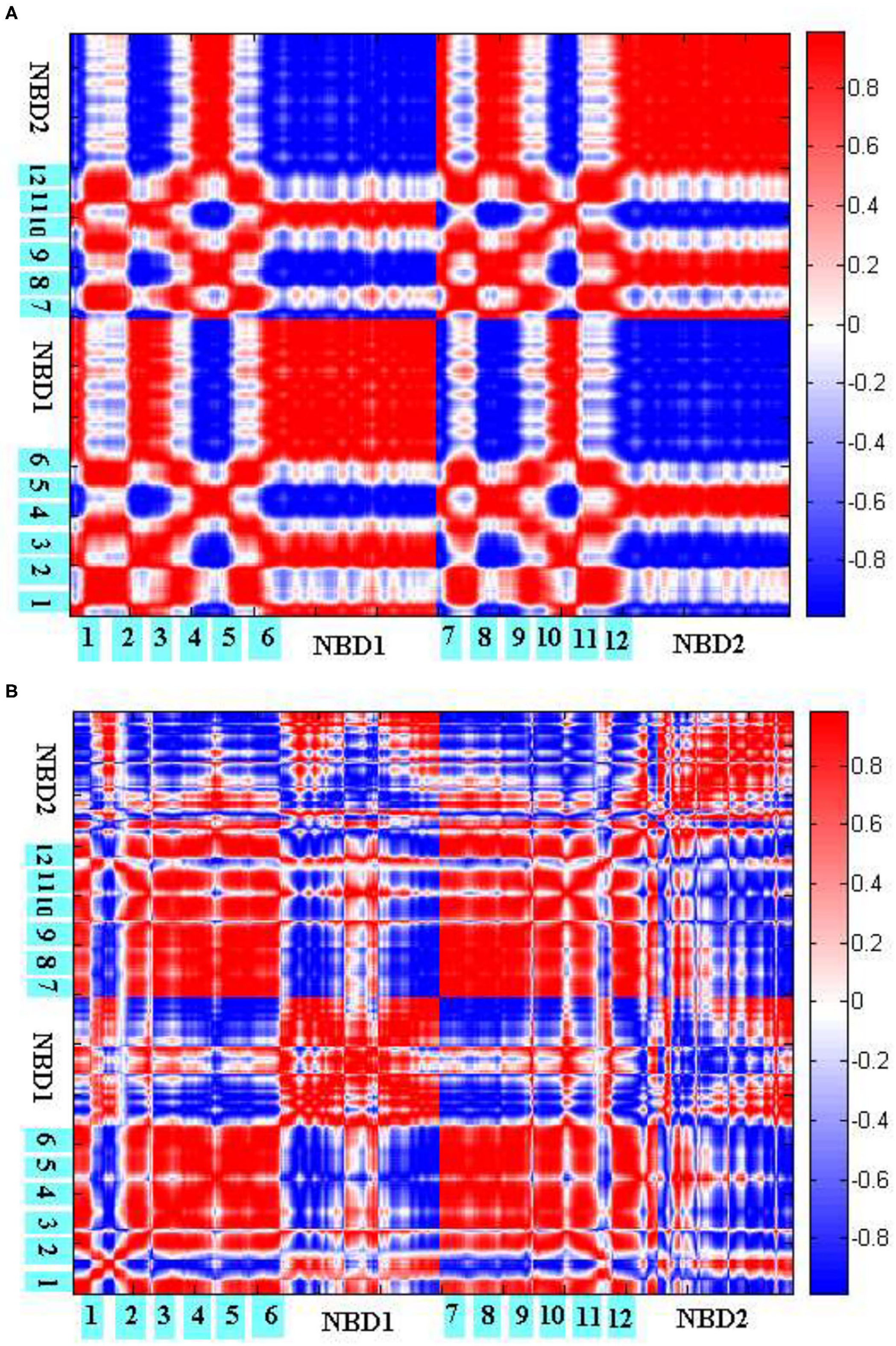

FIGURE 8 | Cross-correlations between the residues of P-gp in the initial **(A)** and final **(B)** stages of allosteric transitions. The TM helices TM1-6 and NBDs are labeled out.

NBDs form a closed dimer and two correct "ABP," so the twisting motion is indispensable in the transformation of human P-gp.

Coupling of the NBDs and TMDs

To explore the coupling mechanism between the different regions of human P-gp, we computed the cross-correlations between the residues of human P-gp according to Equations (7–9), respectively, in the initial (**Figure 8A**) and final (**Figure 8B**) stages of allosteric transitions. From Equations (7–9), the cross-correlations are computed from the recruited low-frequency eigenvectors obtained by ANM for the initial A and final B states. These eigenvectors reflect that the inherent motion modes are determined by the topological structure of the protein. Therefore, the following results of the cross-correlation analyses are closely related to the topological structures of human P-gp in different states.

Figure 8A reflects the coupling inside TMDs, between the NBDs, and between TMDs and NBDs in the initial stage. Overall, PA and PB move in a symmetrical way. For TMDs, they form two branches, with each branch consisting of helices TM1–3, TM6 from one half, and TM4–5 from the other. It is natural that the helices within one branch make strong positive correlations with each other. The correlations are mainly negative between the helices from different branches, which correspond to the closing movements of cytoplasmic and middle parts of TMDs. At the same time, because of the closing movements, both NBDs evidently make strong negative correlations with each other. For the coupling between TMDs and NBDs, it is observed that PA IH1 and IH2 make strong positive correlations with NBDs from PA and PB, respectively, which is consistent with the structural feature that both helices are deeply located into NBDs. In addition, the cytoplasmic parts of PA TM2, TM3 and TM4, TM5 influenced by IH1 and IH2, respectively, form intense positive correlations too with NBDs from PA and PB, respectively. However, their periplasmic parts, far away from IH1 and IH2, exhibit weak correlations with the corresponding NBDs. These results suggest that TMDs and NBDs move in a coupled way, and the helices IH1 and IH2 play an important mediating role. Additionally, TMDs may not move.

Figure 8B reflects the residual coupling of human P-gp in the final stage. Different from the initial stage, TMD helices are rearranged, with TM3 and TM6 splitting away from one branch to another, to adopt the OF conformation. In addition, because of an expanding outward movement, the periplasmic parts of TM1, TM2, and an extracellular loop EL1 make negative correlations with TMDs and positive correlations with NBDs. We could see that in **Figure 8B** TM1–2 makes a positive correlation with TM3–6 because they are consistent with their accumulations of the OF state. But, it is strange that the correlation of intramembrane PA TM3–6 with PB TM3–5 is positive, by comparing the conformers of the P-gp pathway, we can see these residues are connected closely to the intracellular helices IH1 and IH2, which may be related to a coupling effect. Due to the formation of the OF state, the intramembrane PB TM6 makes a negative correlation with another bifurcate half, the periplasmic parts of PB TM6 and NBD from PB exhibit a positive correlation with it. For NBDs, the correlation results show a positive correlation of the part of the RecA-like subdomain from PA with the part of the helical subdomain from PB because the conserved sequence motifs of them form the no. 1 ABP and are twisted together. The residues of no. 2 ABP are the same as those of no. 1. The other parts of NBDs still present a negative correlation, which indicates that the motion of NBDs happens in the whole conformational transition.

CONCLUSIONS

Human P-gp transports intracellular drugs to the outside of cells, and the allosteric mechanism of human P-gp from IF to OF states remains unclear. In this work, the tANM was performed on the exporter human P-gp, we got a transition pathway with the advantage in energy and verified its rationality by using analysis. The results show that the allosteric transitions start from the large-scale closing motion of NBDs that is accompanied by a significant twisting movement between them. The twisting motion becomes more obvious in close to the transition state. The allosteric signal from NBDs is transmitted to TMDs through the intracellular helices IH1 and IH2. The twisting motion between the NBDs plays an important role in the packing rearrangement of TM helices, and the opening of the TMDs to the extracellular side which directly affects whether correctly form ABP. In addition, the movements of TMDs have non-rigid-body properties. This study revealed that the conformation transition of human P-gp could be helpful for human P-gp inhibitors and an understanding of the molecular mechanism of ABC exporters. The conformational rearrangement of human P-gp has been simulated from IF to OF states using targeted MD simulations in the future.

DATA AVAILABILITY STATEMENT

The original contributions presented in the study are included in the article/supplementary material, further inquiries can be directed to the corresponding author/s.

AUTHOR CONTRIBUTIONS

WG and HL designed the research. WG performed data analyses, wrote the manuscript, and developed the program. All authors revised and approved the manuscript.

FUNDING

This work was supported by the Chinese National Science Foundation (31601379).

REFERENCES

1. Goldstein LJ. Clinical reversal of drug resistance. *Curr Prob Cancer.* (1995) 19:65–124. doi: 10.1016/S0147-0272(07)80004-3
2. Higgins CF. ABC transporters-from microorganisms to man. *Ann Rev Cell Biol.* (1992) 8:67–113. doi: 10.1146/annurev.cb.08.110192.000435
3. Higgins CF. ABC transporters: physiology, structure and mechanism-an overview. *Res Microbiol.* (2001) 152:205–10. doi: 10.1016/S0923-2508(01)01193-7
4. Cascorbi I. Role of pharmacogenetics of ATP-binding cassette transporters in the pharmacokinetics of drugs. *Pharmacol Therapeut.* (2006) 112:457–73. doi: 10.1016/j.pharmthera.2006.04.009
5. Aller SG, Yu J, Ward A, Weng Y, Chittaboina S, Zhuo R, et al. Structure of P-glycoprotein reveals a molecular basis for poly-specific drug binding. *Science.* (2009) 323:1718–22. doi: 10.1126/science.1168750
6. Jardetzky O. Simple allosteric model for membrane pumps. *Nature.* (1966) 211:969–70. doi: 10.1038/211969a0
7. Higgins CF, Linton KJ. The ATP switch model for ABC transporters. *Nat Struct Mol Biol.* (2004) 11:918–26. doi: 10.1038/nsmb836
8. Juliano RL, Ling V. Surface glycoprotein modulating drug permeability in chinese-hamster ovary cell mutants. *Biochim Biophys Acta.* (1976) 455:152–62. doi: 10.1016/0005-2736(76)90160-7
9. Chen CJ, Chin JE, Ueda K, Clark DP, Pastan I, Gottesman MM, et al. Internal duplication and homology with bacterial transport proteins in the MDR1 (P-glycoprotein) gene from multidrug-resistant human-cells. *Cell.* (1986) 47:381–9. doi: 10.1016/0092-8674(86)90595-7
10. Lee J, Urbatsch IL, Senior AE, Wilkens S. Nucleotide-induced structural changes in P-glycoprotein observed by electron microscopy. *J Biol Chem.* (2008) 283:5769–79. doi: 10.1074/jbc.M707028200
11. Ward AB, Szewczyk P, Grimard V, Lee C, Martinez L, Doshi R, et al. Structures of P-glycoprotein reveal its conformational flexibility and an epitope on the nucleotide-binding domain. *Proc Natl Acad Sci USA.* (2013) 110:13386–91. doi: 10.1073/pnas.1309275110
12. Altschul SF, Gish W, Miller W, Myers EW, Lipman DJ. Basic local alignment search tool. *J Mol Biol.* (1990) 215:403–10. doi: 10.1016/S0022-2836(05)80360-2
13. Wise JG. Catalytic transitions in the human MDR1 P-glycoprotein drug binding sites. *Biochemistry.* (2012) 51:5125–41. doi: 10.1021/bi300299z
14. Chang S, Liu F, Dong X, Sun Y. Molecular insight into conformational transmission of human P-glycoprotein. *J Chem Phys.* (2013) 139:225102. doi: 10.1063/1.4832740
15. Pan L, Aller SG. Equilibrated atomic models of outward-facing P-glycoprotein and effect of ATP binding on structural dynamics. *Sci Rep.* (2015) 5:7880. doi: 10.1038/srep07880
16. Haliloglu T, Bahar I, Erman B. Gaussian dynamics of folded proteins. *Phys Rev Lett.* (1997) 79:3090–3. doi: 10.1103/PhysRevLett.79.3090
17. Atilgan AR, Durell SR, Jernigan RL, Demirel MC, Keskin O, Bahar I. Anisotropy of fluctuation dynamics of proteins with an elastic network model. *Biophys J.* (2001) 80:505–15. doi: 10.1016/S0006-3495(01)76033-X
18. Zhan M, Li S, Li F. Wavelet transformed Gaussian network model. *J Theor Comput Chem.* (2014) 13:14500539. doi: 10.1142/S0219633614500539
19. Ruvinsky AM, Kirys T, Tuzikov AV, Vakser IA. Structure fluctuations and conformational changes in protein binding. *J Bioinf Comput Biol.* (2012) 10:12410028. doi: 10.1142/S0219720012410028
20. Togashi Y, Flechsig H. Coarse-grained protein dynamics studies using elastic network models. *Int J Mol Sci.* (2018) 19:3899. doi: 10.3390/ijms19123899
21. Anand DV, Meng Z, Xia K. A complex multiscale virtual particle model based elastic network model (CMVP-ENM) for the normal mode analysis of biomolecular complexes. *Phys Chem.* (2019) 21:4359–66. doi: 10.1039/C8CP07442A
22. Das A, Gur M, Cheng MH, Jo S, Bahar I. Exploring the conformational transitions of biomolecular systems using a simple two-state anisotropic network model. *PLoS Comput Biol.* (2014) 10:e1003521. doi: 10.1371/journal.pcbi.1003521
23. O'Mara ML, Tieleman DP. P-glycoprotein models of the apo and ATP-bound states based on homology with Sav1866 and MalK. *FEBS Lett.* (2007) 581:4217–22. doi: 10.1016/j.febslet.2007.07.069
24. Maragakis P, Karplus M. Large amplitude conformational change in proteins explored with a plastic network model: adenylate kinase. *J Mil Biol.* (2005) 352:807–22. doi: 10.1016/j.jmb.2005.07.031
25. Humphrey W, Dalke A, Schulten K. VMD: visual molecular dynamics. *J Mol Graph.* (1996) 14:33–8, 27–8. doi: 10.1016/0263-7855(96)00018-5
26. Seyffer F, Tampe R. ABC transporters in adaptive immunity. *BBA Gen Sub.* (2015) 1850:449–60. doi: 10.1016/j.bbagen.2014.05.022

Conflict of Interest: The authors declare that the research was conducted in the absence of any commercial or financial relationships that could be construed as a potential conflict of interest.

frontiers in Medicine

ORIGINAL RESEARCH
published: 11 February 2022
doi: 10.3389/fmed.2022.758464

Complementing Tissue Testing With Plasma Mutation Profiling Improves Therapeutic Decision-Making for Patients With Lung Cancer

Yukti Choudhury[1], Min-Han Tan[2], Jun Li Shi[3], Augustine Tee[4], Kao Chin Ngeow[1], Jonathan Poh[1], Ruth Rosalyn Goh[1,5] and Jamie Mong[6]*

[1] Lucence Diagnostics Pte. Ltd., Singapore, Singapore, [2] Lucence Health Inc, Palo Alto, CA, United States, [3] Institute of Bioengineering and Nanotechnology, Singapore, Singapore, [4] Department of Respiratory and Critical Care Medicine, Changi General Hospital, Singapore, Singapore, [5] Faculty of Medicine, Imperial College London, London, United Kingdom, [6] Institute of Bioengineering and Bioimaging, Singapore, Singapore

Edited by:
Fu Wang,
Xi'an Jiaotong University, China

Reviewed by:
Caterina De Luca,
University of Naples Federico II, Italy
Wei Wu,
University of California, San Francisco, United States

***Correspondence:**
Jamie Mong
jmong@ibb.a-star.edu.sg

Specialty section:
This article was submitted to Precision Medicine, a section of the journal Frontiers in Medicine

Received: 14 August 2021
Accepted: 04 January 2022
Published: 11 February 2022

Citation:
Choudhury Y, Tan M-H, Shi JL, Tee A, Ngeow KC, Poh J, Goh RR and Mong J (2022) Complementing Tissue Testing With Plasma Mutation Profiling Improves Therapeutic Decision-Making for Patients With Lung Cancer. Front. Med. 9:758464. doi: 10.3389/fmed.2022.758464

Background: Tissue biopsy is an integral part of the diagnostic approach to lung cancer. It is however invasive and limited by heterogeneity. Liquid biopsies may complement tissue testing by providing additional molecular information and may be particularly helpful in patients from whom obtaining sufficient tissue for genomic profiling is challenging.

Methods: Patients with suspected lung cancer ($n = 71$) were prospectively recruited. Blood and diagnostic tissue samples were collected within 48 h of each other. Plasma cell-free DNA (cfDNA) testing was done using an ultrasensitive amplicon-based next-generation sequencing (NGS) panel (plasma NGS testing). For cases diagnosed as non-small cell lung carcinoma (NSCLC) *via* histology or cytology, targeted testing for epidermal growth factor receptor (*EGFR*) mutations was performed using tissue biopsy samples (tissue *EGFR* testing), where available. Concordance of clinically actionable mutations between methods and sample types was assessed.

Results: For confirmed NSCLC cases ($n = 54$), tissue *EGFR* test results were available only for 70.3% (38/54) due to sample inadequacies, compared to blood samples for 98.1% (53/54) cases. Tissue *EGFR* testing identified sensitizing *EGFR* (L858R or exon 19 deletion) mutation in 31.6% (12/38) of cases. Plasma NGS identified clinically actionable mutations in 37.7% (20/53) of cases, including *EGFR* mutations in two cases with no tissue *EGFR* results, and mutations in *KRAS*, *BRAF,* and *MET*. The overall sensitivity of sensitizing *EGFR* mutation detection by plasma NGS was 75% (9/12), and specificity was 100% (25/25) in patients tested in both tissue *EGFR* and plasma NGS ($n = 37$). In this cohort of patients, tissue *EGFR* testing alone informed clinical decisions in 22.2% (12/54) of cases. Adding plasma NGS to tissue *EGFR* testing increased the detection rate of actionable mutations to 42.6% (23/54), representing a 1.9-fold increase in clinically relevant findings. The average turnaround time of plasma NGS was shorter than standard tissue testing (10 vs. 29.9 days, $p < 0.05$).

Conclusions: In the first-line setting, plasma NGS was highly concordant with tissue *EGFR* testing. Plasma NGS increases the detection of actionable findings with a shorter time to results. This study outlines the clinical utility of complementary plasma mutation profiling in the routine management of lung cancer patients.

Keywords: liquid biopsy and circulating tumor DNA, non-small cell lung cancer (NSCLC), plasma-first, next generation sequencing, amplicon-based NGS, tumor heterogeneity, NGS panel testing

INTRODUCTION

Lung cancer is the most common cause of cancer death worldwide and nonsmall cell lung cancer (NSCLC) accounts for 85% of all the lung cancers, making NSCLC a major cause of mortality (1). The 5-year survival rate of lung cancer patients is 18.6% and for late-stage NSCLC the 5-year survival rate stands at 6% (2). The median age of diagnosis of NSCLC is 70 years of age and about 40% of patients are diagnosed with lung cancer at a late stage (2). Given the age profile and time-scarce outlook for the average lung cancer patient, it is important to create diagnostic tools that are fast, sensitive, and accessible by all patients, in particular those of advanced age or cancer stage.

Major progress has been made in the treatment of advanced NSCLC with the identification of specific driver mutations and the development of targeted therapies (3, 4). Although actionable mutations are found in only a subset of patients, progression-free survival was shown to be significantly increased in patients treated with targeted therapy compared to those treated with chemotherapy (5). Molecular diagnostic testing combined with molecular targeted agents directed against driver mutations in *EGFR*, *ALK*, *ROS1*, *BRAF*, *MET, RET*, and most recently *KRAS* has significantly improved the outcomes for patients with advanced disease harboring these alterations (6, 7). The most recent National Comprehensive Cancer Network (NCCN) guideline recommendations (Version 5.2021) for the management of NSCLC now include testing for *EGFR*, *BRAF*, *ALK, ROS1, RET, KRAS, MET* exon 14 skipping, and *NTRK* in nonsquamous lung cancer, as part of broader molecular profiling (8).

Tissue biopsy is the prevailing gold standard for the diagnosis of NSCLC among patients suspected to have lung cancer, and tumor testing is most commonly used for the determination of guideline-recommended biomarkers. In about 15 to 40% of NSCLC cases, comprehensive molecular testing is not feasible due to insufficient tissue samples (9, 10). In the absence of a comprehensive tissue test, a serial testing approach was shown to be successful in only 5% of patients for all the eight guideline-recommended biomarkers (11). Sampling a single lesion may not capture the complete genomic landscape due to molecular heterogeneity of tumors (12). The risk of complications is another concern, rising to 61% with the use of transthoracic needle biopsy, and the incidence of pneumothorax also increases significantly in older patients with obstructive lung disease (13). Another challenge is the time required for guideline-complete tissue testing which can result in a substantial number of patients initiating chemotherapy before diagnostic results become available, with 19% of *EGFR* mutation or ALK rearrangement positive patients initiating first-line chemotherapy while awaiting their biomarker test results (10).

Liquid biopsies present an alternative approach to tissue-based diagnostic testing, with the use of plasma cell-free DNA (cfDNA) as the substrate for molecular profiling. Tumor alterations identified through routine analysis of clinical tissue samples are detected in cfDNA with a sensitivity of ∼80–90% (14). Detection sensitivity is influenced by both anatomical sites of disease and tumor burden which in turn correlates with overall circulating tumor DNA (ctDNA) burden (15–17). A recent study focused on the use of cfDNA for the diagnosis of NSCLC found a pooled sensitivity of 68% *via* a systematic review (18). Currently, the NCCN guidelines only endorse (1) a plasma-first approach for testing for EGFR T790M in patients who have developed resistance to first- or second-generation tyrosine kinase inhibitors (TKIs), with tissue biopsy being recommended in cases where plasma testing is negative (8), and (2) liquid biopsy in specific clinical circumstances where the patient is medically unfit for invasive tissue sampling or when tumor tissue specimen is inadequate or unobtainable, following pathological confirmation of diagnosis, with a follow-up tissue-based analysis in cases where no oncogenic driver is identified in plasma cfDNA (8). This is aligned with the latest recommendations from the International Association for the Study of Lung Cancer (IASLC) for liquid biopsy for NSCLC, where liquid biopsy is recommended for cases where the tissue sample is unavailable ("plasma first" approach), or in cases where tissue biopsy is inadequate for conducting comprehensive tissue genotyping ("complementary" approach) (19). Furthermore, according to the IASLC recommendations, for cases with oncogene-addicted NSCLC progressing after initial targeted therapy, a "plasma first" approach should be considered standard of care (19).

Liquid and tissue biopsies each present their own strengths. In this study, we hypothesize that plasma cfDNA testing using a panel of target genes can complement standard molecular testing using tissue biopsy for NSCLC patients. Here, standard molecular tests encompass single target (e.g., *EGFR*) PCR-based tests, which could require time-consuming serial tissue testing depending on previous findings. For plasma cfDNA testing, next-generation sequencing (NGS)-based approaches, if adequately sensitive and comprehensive, have been shown to identify actionable mutations in plasma cfDNA of advanced NSCLC (20, 21). Therefore, rather than substituting tissue biopsies with liquid biopsies, adding a concurrent plasma NGS test to tissue testing would improve the detection of actionable mutations in patients with NSCLC, improving prognostication in addition to choice and timeliness of treatment initiation. This may translate to a "plasma-first" approach where getting a tissue sample is rendered impractical or extremely difficult (19).

This study focuses on standard tissue testing for mutations in the *EGFR* gene, which is mutated in 40–60% of Asian patients and 10–20% of Caucasian patients with NSCLC (22). Specifically, EGFR L858R and in-frame exon 19 deletions account for 50 and 40% of *EGFR* mutations, respectively, and are sensitizing mutations as tumors harboring these mutations are sensitive to EGFR TKIs (23). Molecular testing for alterations in multiple genes such as *EGFR, ALK, ROS1, RET, BRAF, ERRB2, MET* exon 14, and *NTRK1/2/3* have progressively entered the standard of care over the last 10 years (24). Here, we aim to demonstrate the clinical utility of an ultrasensitive, amplicon-based NGS tool for plasma cfDNA testing alongside standard tissue testing in patients suspected to have lung cancer, to widen the scope of eligibility for treatment and reduce waiting time for molecular test results.

METHODS

Study Design and Patients

Patients with suspected lung cancer ($n = 71$) were prospectively enrolled for this study at the Department of Respiratory Medicine, Changi General Hospital, Singapore between June 2015 and August 2018. Before diagnosis by histology, blood samples for NGS-based plasma genotyping were collected during the patient visit, followed by baseline tissue sampling by bronchoscopy or effusion collection within 48 h. Patients were subsequently diagnosed to have non-small cell lung carcinoma (NSCLC), other cancers, or not cancer based on histology, cytology, or microbiological testing. For NSCLC patients, the standard of care targeted *EGFR* mutation tissue testing was performed on tumor biopsy samples, where available, using the Roche cobas® EGFR Mutation Test or by Sanger sequencing in a College of American Pathologists (CAP)-accredited clinical laboratory, and results were available as clinical reports. For all patients with blood available, targeted NGS plasma testing was performed in a CAP-accredited clinical laboratory, to detect tumor mutations in cfDNA. Similar targeted NGS testing was also performed in matched tissue samples, for cases with additional tissue available. Basic patient characteristics, namely, age, gender, and confirmed histological diagnosis were recorded as part of the study. This study was approved by the institutional review board of Changi General Hospital and is registered under clinical trial number NCT04254497.

Plasma and Tissue NGS Genotyping

Peripheral blood was collected in ethylenediaminetetraacetic acid (EDTA) tubes and blood was processed within 24 h of collection to isolate plasma. Circulating nucleic acid was extracted from plasma samples using the QIAamp Circulating Nucleic Acid Kit (Qiagen) and cfDNA was used to perform an NGS assay (LiquidHALLMARK®) in a CAP-accredited clinical laboratory. LiquidHALLMARK® is a clinically validated, ultrasensitive, and amplicon-based assay for the detection of single nucleotide variants (SNVs), insertion-deletion mutations (indels), and copy number alterations among 49 genes (at the time of this study) (**Supplementary Table 1**) with sensitive detection at variant allele frequencies above 0.1% for SNVs and indels. In this study, clinically actionable mutations were defined as mutations in *EGFR*, *ERBB2*, *BRAF*, *KRAS*, and *MET* (exon 14 skipping and copy number gains) which are therapeutically targetable, guideline-recommended biomarkers or emerging biomarkers for the treatment of metastatic NSCLC (25). Tumor DNA was extracted from remaining available tissue biopsy material using the QIAamp DNA FFPE Tissue Kit (Qiagen) and was also analyzed for panel-wide confirmation and concordance of findings from plasma cfDNA, using the same platform technology as LiquidHALLMARK® (TissueHALLMARK®). The NGS assay did not examine fusions in *ALK*, *RET,* and *ROS1* at the time of this study.

Data Analysis

Concordance analysis between routine molecular tissue testing and plasma samples was focused on the presence of mutations in *EGFR* as this is a routine molecular diagnostic test available for patients with NSCLC, ordered by practicing oncologists. Sensitivity and specificity analyses were performed taking tissue *EGFR* test results as standard. Other actionable mutations (non-*EGFR*) detected in *BRAF*, *KRAS*, *ERBB2,* and *MET* using plasma NGS panel testing were recorded as additional actionable findings, and any other mutations detected among the 49 genes targeted in the NGS assay were recorded as other genomic findings. The overall rate of detection of mutations in plasma cfDNA NGS was analyzed. For panel-wide testing done on matched plasma and tissue samples (where available), positive and negative predictive agreement analysis was performed for all actionable genomic findings. For NGS, variant allele frequencies (VAFs) were analyzed and are defined as the proportions of variant alleles relative to wild-type alleles. For patients with concurrent plasma and tissue NGS tests, correlation analysis of plasma and tissue variant allele frequencies (AFs) was done using Spearman's rank correlation. Fisher's exact test was used to determine associations between detection of actionable mutations and average coverage, and disease stage for NSCLC. All analyses were performed using RStudio V1.2.5033.

Clinical endpoints included test turnaround time (TAT), measured in days from biopsy sampling to reporting of *EGFR* molecular test results, or from blood sampling to reporting of NGS results.

RESULTS

Patient and Sample Characteristics and Test Results Accessibility

A total of 71 patients suspected to have lung cancer, based on their diagnostic scans and symptomatology, were enrolled. Patients were predominantly male (52/71, 73%) and the median age of the patient group was 67 years (range 31–87). Based on histology or cytology specimens, 54 patients (76.1%) were subsequently confirmed to have NSCLC, seven (9.9%) were diagnosed with having other cancers, and the remaining 10 (14.1%) did not have cancer, with diagnosis of tuberculosis,

TABLE 1 | Baseline patient characteristics.

Characteristics	No. (%)
Total	71 (100)
Sex	
Female	19 (27)
Male	52 (73)
Median age, (range), years	67 (31–87)
Diagnosis †	
NSCLC	54 (76)
adenocarcinoma	37 (52)
squamous cell carcinoma	6 (8.5)
large cell carcinoma	1 (1.4)
NOS	6 (8.5)
with neuroendocrine feature	1 (1.4)
lymphoepithelioma-like carcinoma	3 (4.2)
SCLC	4 (5.6)
Hepatocellular carcinoma	1 (1.4)
High-grade undifferentiated sarcoma	1 (1.4)
Ovarian cancer	1 (1.4)
Tuberculosis	3 (4.2)
Pneumonia	2 (2.8)
Inflammation	3 (4.2)
Undetermined, not cancer	2 (2.8)

†Diagnosis was determined by histology or cytology, before any tissue or plasma molecular testing, but after blood collection.

NSCLC, non-small cell lung carcinoma; SCLC, small cell lung carcinoma; NOS, not otherwise specified.

pneumonia or inflammation, or an undetermined noncancer diagnosis (**Table 1**). Blood samples could be obtained for 99% (70/71) patients before diagnostic biopsy sampling. Among NSCLC cases, blood sample was not available for one patient, resulting in an accessibility rate of 98.4% (53/54) for blood samples. Plasma NGS testing was successful for 100% of blood samples collected (70/70), and among 100% of NSCLC patients with blood samples available (53/53). Volume of plasma available ranged from 0.5 to 9 ml (median, 5.5 ml), and yield of cfDNA was in the range of 10–350 ng per ml plasma (median, 19.24 ng per ml plasma) (**Supplementary Figure 1**).

Patients with NSCLC ($n = 54$) were eligible for tissue *EGFR* testing, however, tissue *EGFR* test results were available only for 38 NSCLC patients, resulting in a significantly lower tissue results accessibility rate of 70.4% (38/54), with 29.6% of cases (16/54) having no *EGFR* test results from tissue (**Supplementary Figure 2**). There were two primary reasons for lack of tissue *EGFR* test results for NSCLC patients, namely, failure to obtain adequate biopsy sample due to advanced age of patients or aggressive disease in 37.5% of cases (6/16) and failure to obtain informative *EGFR* test results from collected biopsies for 62.5% of cases (10/16). Patient enrollment, testing workflow and an overview of mutation findings are described in **Figure 1**.

Among NSCLC cases with successful tissue *EGFR* testing using biopsy, an *EGFR* mutation was found in 31.6% of cases (12/38), whereas an *EGFR* sensitizing mutation was found in 20.7% of cases (11/53) that underwent plasma NGS testing. Among NSCLC cases tested by plasma NGS that were negative for *EGFR* sensitizing mutations, additional actionable findings were made in nine of 42 cases (21.4%), and other genomic findings (any other nonactionable mutations from the 49 gene LiquidHALLMARK® panel) were made in 42.8% (18/42) cases. Of the seven cases subsequently diagnosed by histology or cytology to have other non-NSCLC cancers, six cases had $\geq$ 1 mutation identified by plasma NGS testing (**Supplementary Table 2**). In nine of 10 patients with noncancer diagnosis confirmed, no mutations were detected by plasma NGS testing.

Diagnostic Yield From Tissue Biopsy and Plasma

Diagnostic yield was compared for patients with NSCLC where testing was possible with either standard tissue *EGFR* test with concurrent plasma NGS testing, or with plasma NGS only, as dictated by sample availability (**Figure 2A**). Of the NSCLC cases with available tissue *EGFR* test results, 31.6% (12/38) were positive for *EGFR* sensitizing mutations while the remaining 68.4% (26/38) had a negative *EGFR* mutation finding. Of these 38 cases, 37 cases were also tested by plasma NGS (blood was not available for one case) with 24.3% (9/37) having a positive result for *EGFR* sensitizing mutation and the remaining 75.7% (28/37) having a negative *EGFR* mutation result (**Figure 2B**). Specifically, among tissue *EGFR*-negative cases also tested by plasma NGS ($n = 25$), plasma NGS did not identify any further *EGFR* sensitizing mutations (for which FDA-approved therapies are available) but did identify other clinically actionable mutations in six cases, namely, *MET* exon 14 skipping ($n = 1$), *BRAF p*.V600E ($n = 1$), *BRAF p*.K601E ($n = 1$), *KRAS p*,G12D ($n = 2$), and *EGFR* exon 20 insertion ($n = 1$) (**Figure 2B**).

Importantly, where tissue *EGFR* testing results were lacking and only plasma NGS was performed ($n = 16$), clinically actionable mutations were detectable in five cases, namely, sensitizing *EGFR* mutations p.E746_A750del ($n = 1$) and p.L747_P753delinsS ($n = 1$), *BRAF* p.K601E ($n = 1$), *KRAS* p.G12D ($n = 1$), and *MET* exon 14 skipping ($n = 1$) (**Figure 2C**).

The additional diagnostic yield from plasma NGS testing for tissue *EGFR*-negative cases is therefore 24% (6/25), for which other actionable mutations were detected. Among NSCLC samples that totally failed to undergo tissue *EGFR* testing ($n = 16$), plasma NGS provided a diagnostic yield of 31.3% (5/16). The total additional diagnostic yield by plasma NGS is therefore 26.8% (11/41).

In this cohort of 54 patients with NSCLC, irrespective of the availability of tissue *EGFR* testing, a plasma NGS test on its own would have provided clinically actionable mutation information in up to 37% of cases (20/54). In contrast, standard tissue *EGFR* testing (with limitations of tissue sampling and quality and breadth of testing), accurately identified only 22.2% (12/54) of cases with clinical actionability based on *EGFR* sensitizing mutations. Performing both tissue and plasma testing resulted in a diagnostic finding in 42.6% (23/54) of NSCLC cases, considering only tissue *EGFR* test and plasma NGS test not

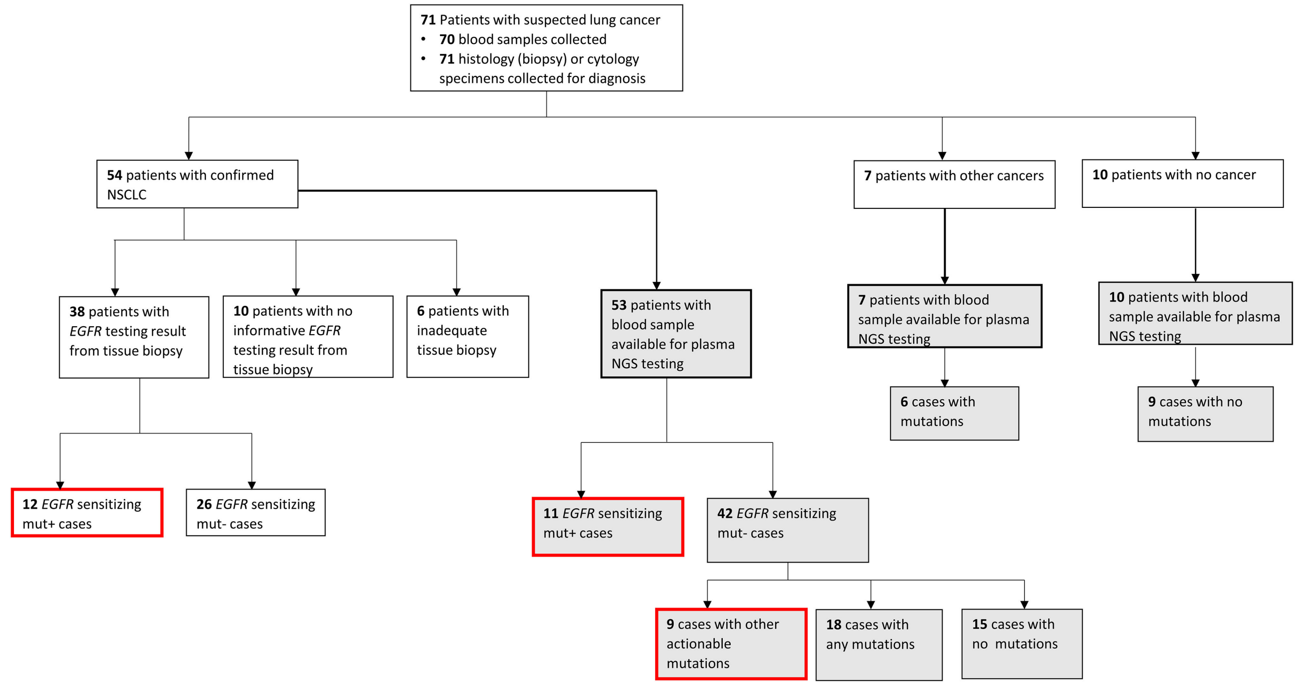

FIGURE 1 | Patient enrollment and testing workflow. Flowchart showing the patient enrolment, diagnosis, sample availability, type of testing conducted, and mutation findings. Gray-filled boxes indicate testing results from plasma next-generation sequencing (NGS) and red-outlined boxes are all clinically actionable findings made in this study for non-small cell lung carcinoma (NSCLC) cases.

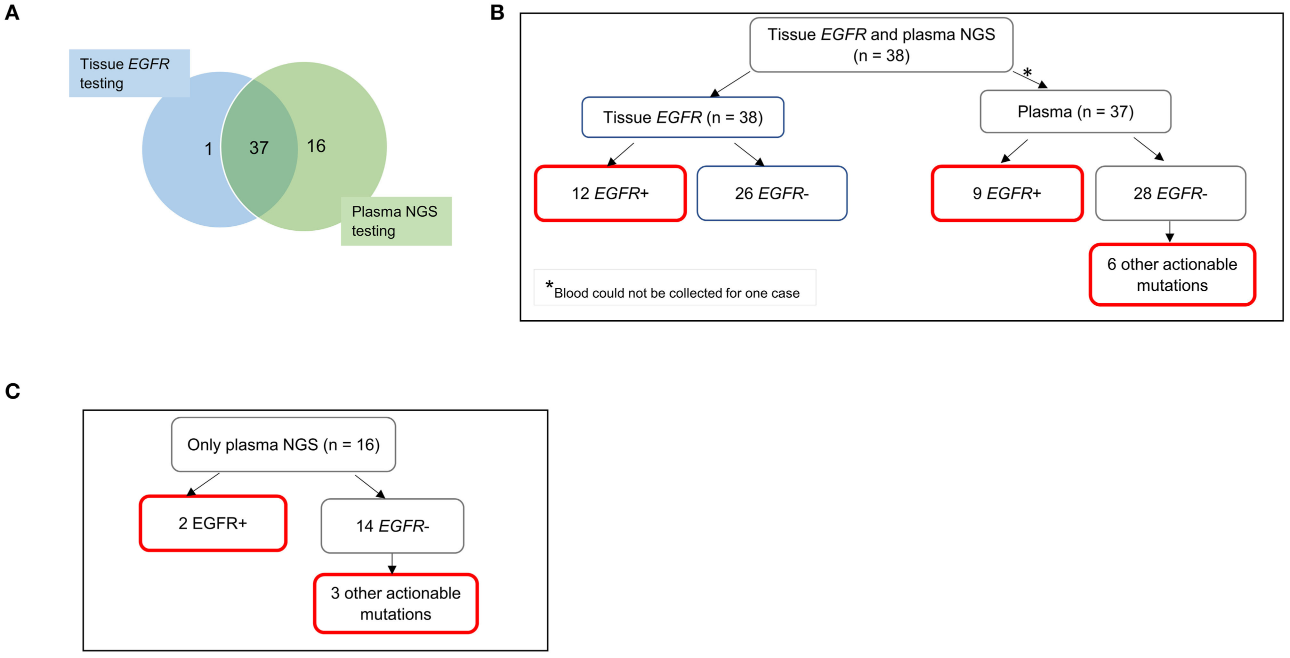

FIGURE 2 | Diagnostic yield from molecular testing of tissue and plasma samples for 54 patients with NSCLC. **(A)** Nearly all 38 patients with informative tissue *EGFR* testing underwent plasma NGS testing (except one). An additional 16 patients had only plasma NGS testing done, due to inadequate tissue biopsy samples for molecular testing or non-informative results from tissue testing. **(B)** Findings of *EGFR* sensitizing mutations and other actionable mutations in cases with both tissue *EGFR* and plasma NGS results. Six other actionable mutations from plasma NGS testing included *MET* exon 14 skipping (n = 1), *BRAF* p.V600E (n = 1), *BRAF* p.K601E (n = 1), *KRAS* p.G12D (n = 2), and *EGFR* exon 20 insertion (n = 1). **(C)** Clinically actionable findings in cases with only plasma NGS testing. Boxes outlined in red indicate clinically actionable diagnostic yield from all testing modalities. EGFR, epidermal growth factor receptor; NGS, next-generation sequencing.

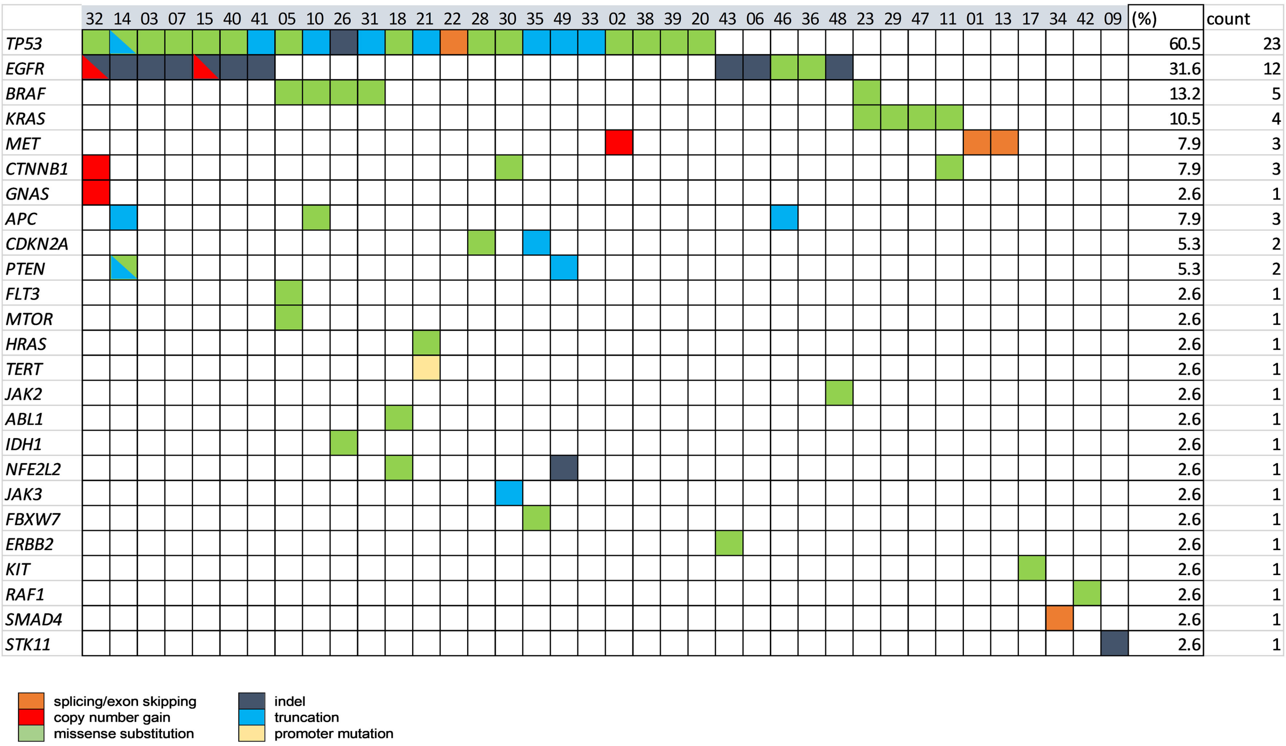

	32	14	03	07	15	40	41	05	10	26	31	18	21	22	28	30	35	49	33	02	38	39	20	43	06	46	36	48	23	29	47	11	01	13	17	34	42	09	(%)	count
TP53	🟩	🟦🟩	🟩	🟩	🟩	🟩	🟦	🟩	🟦	⬛	🟦	🟩	🟦	🟧	🟩	🟩	🟦	🟦	🟦	🟩	🟩	🟩	🟩																60.5	23
EGFR	🟥⬛	⬛	⬛	⬛	🟥⬛	⬛	⬛																	⬛	⬛	🟩	🟩	⬛											31.6	12
BRAF								🟩	🟩	🟩	🟩																		🟩										13.2	5
KRAS																													🟩	🟩	🟩	🟩							10.5	4
MET																				🟥													🟧	🟧					7.9	3
CTNNB1	🟥															🟩																🟩							7.9	3
GNAS	🟥																																						2.6	1
APC		🟦							🟩																	🟦													7.9	3
CDKN2A															🟩		🟦																						5.3	2
PTEN		🟦🟩																🟦																					5.3	2
FLT3								🟩																															2.6	1
MTOR								🟩																															2.6	1
HRAS													🟩																										2.6	1
TERT													🟨																										2.6	1
JAK2																												🟩											2.6	1
ABL1												🟩																											2.6	1
IDH1										🟩																													2.6	1
NFE2L2												🟩						⬛																					2.6	1
JAK3																🟦																							2.6	1
FBXW7																	🟩																						2.6	1
ERBB2																								🟩															2.6	1
KIT																																			🟩				2.6	1
RAF1																																					🟩		2.6	1
SMAD4																																				🟧			2.6	1
STK11																																						⬛	2.6	1

🟧 splicing/exon skipping
🟥 copy number gain
🟩 missense substitution
⬛ indel
🟦 truncation
🟨 promoter mutation

FIGURE 3 | The spectrum of genomic alterations in NSCLC was detected by plasma NGS testing. Baseline plasma samples for 53 NSCLC cases were tested with the 49-gene panel LiquidHALLMARK® assay. Cases with ≥1 alteration are presented ($n = 38$), 15 cases with no alteration detected were excluded from the presentation. Genes with no alteration detected among all cases were also excluded from the presentation. Percentage (%) and number of cases carrying a mutation in each gene are shown in the right-most columns.

including *ALK*, *RET*, *ROS1* fusions among actionable targets, which represents a 1.9-fold increase in the number of actionable findings compared to tissue *EGFR* testing alone.

The spectrum of all the mutations (actionable and nonactionable) detected by plasma NGS in 53 NSCLC cases is shown in **Figure 3**. A total of 38 NSCLC cases (76%) had ≥ 1 alteration detectable, of which *TP53* mutations were most prevalent (60.5%), followed by mutations in clinically actionable target genes, *EGFR* (31.6%), *BRAF* (13.2%), *KRAS* (10.5%), and *MET* (7.9%).

Tissue and Plasma Concordance for EGFR Mutations and Other Variants

To assess the performance of the plasma NGS test relative to the standard tissue *EGFR* testing modality, samples with results from both plasma NGS and tissue tests were compared. Among 12 cases positive for sensitizing *EGFR* mutations by standard *EGFR* tissue testing, nine were found to have the same mutation in plasma cfDNA, for a sensitivity of 75% (9/12) (**Table 2**). Out of 26 cases negative for sensitizing *EGFR* mutations in tissue, 25 cases were tested by plasma NGS, and concordantly none were found to have any *EGFR* mutations [except for one case with an *EGFR* exon 20 insertion (*EGFR* p.A763_Y764insFQQA)] resulting in a specificity of 100% (25/25). The overall concordance of *EGFR* sensitizing mutations commonly included in the range of PCR-based *EGFR* testing and plasma NGS was 91.9% (34/37). The range of *EGFR* VAFs detected by plasma NGS was 0.057–80.3%, with a median AF of 0.98%, with 7 *EGFR* exon19 deletions and 2 L858R mutations (**Table 3**). As the detection sensitivity of NGS assays is a function of the depth of coverage achieved, which, in turn, is a function of input DNA amount, we looked at the distribution of depth of coverage across the samples for which *EGFR* mutations were expected to be found in plasma based on tissue results. For three samples in which corresponding *EGFR* mutations were not detected in plasma, the average consensus coverage (X) was 6,524X, 8,068X, and 14,565X, respectively (**Table 3**), which did not correspond to the lowest coverage among these samples. In fact, two cases with coverage of 4,538X and 4,830X, respectively, had detectable mutations at variant allele frequencies of 0.057 and 9.44% for *EGFR* p.E746_A750del (exon 19 deletion), suggesting a biological (such as low tumor shedding into circulation) rather than a technical reason for discordance. Considering all NSCLC samples tested by plasma NGS ($n = 53$), the median consensus coverage was 8183x. Among samples with coverage lower than the median coverage ($n = 26$), nine samples had no mutations detected by plasma NGS, and among samples with coverage greater than or equal to the median coverage ($n = 27$), six samples had no mutations detected by plasma NGS ($p = 0.2238$,

TABLE 2 | Concordance analysis of *EGFR* mutation detection by targeted tissue *EGFR* testing and plasma NGS for 37 NSCLC cases.

		Tissue *EGFR* testing (Sanger or targeted PCR)			
		Positive	**Negative**	**Total**	
Plasma NGS	Positive	9	0†	9	Sensitivity: 75% (95% CI: 42.8–94.5%)
	Negative	3	25	28	Specificity: 100% (95% CI: 86.3% to 100.0%) Accuracy: 91.9% (95% CI: 78.1% to 98.3%)

Sensitivity of plasma NGS for EGFR detection relative to tissue EGFR testing was 75% (9/12) and specificity was 100% (25/25), for an overall concordance of 91.9% (34/37).

†One case in plasma NGS was found to have EGFR p.A763_Y764insFQQA, an exon 20 insertion mutation, which is not part of the assay used in routine PCR-based tissue EGFR testing, and is not included in the count.

TABLE 3 | Depth of coverage by plasma NGS and detection of *EGFR* mutation and mutation allele frequency (AF %).

	Tissue *EGFR* test		Plasma NGS test		
Case	***EGFR* Mutation**	**Method**	**Average consensus coverage (X)**	***EGFR* Mutation (HGVSp)**	**AF (%)**
1	Exon19del	Sanger	9496.7	p.E746_A750del	0.33
2	Exon19del	Roche PCR	4830.58	p.E746_A750del	9.44
3	Exon19del	Roche PCR	14854.77	p.E746_A750del	7.15
4	Exon19del	Sanger	11864.58	p.E746_S752delinsV	50.7
5	Exon19del	Roche PCR	6524.41	-	ND
6	p.E746_T751delinsA	Sanger	12254.13	p.E746_T751delinsA	80.3
7	p.L858R	Roche PCR	13842.24	p.L858R	1.51
8	Exon19del	Sanger	8068.15	-	ND
9	p.L858R	Sanger	14565.16	-	ND
	p.E709K			-	ND
10	p.L747_A750delinsP	Sanger	7420.09	p.L747_A750delinsP	0.98
11	p.L858R	Roche PCR	10417.81	p.L858R	0.86
	p.S768I			p.S768I	0.25
12	Exon19del unspecified	Roche PCR	5722.85	p.E746_A750del	0.73

ND, not detected.

TABLE 4 | Panel-wide concordance of actionable mutations in 24 NSCLC cases that underwent both the tissue and plasma NGS testing.

		Tissue NGS			
		Positive	**Negative**	**Total**	
Plasma NGS	Positive	9	2	11	PPA: 75.0% (95% CI: 42.8 to 94.5%)
	Negative	3	10	13	NPA: 83.3% (95% CI: 51.6 to 97.9%) OPA: 79.2% (95% CI: 57.9 to 92.9%)

PPA, positive percent agreement; NPA, negative percent agreement; OPA, overall percent agreement.

Fisher's exact test), suggesting that coverage was not the main determining factor for detection of variants among these samples (**Supplementary Figure 3**).

Beyond *EGFR*, panel-wide concordance of mutation findings in tissue biopsy samples and plasma was studied by performing tissue NGS using the same panel (TissueHALLMARK®) on a subset of samples for which tissue samples from the original biopsy were available. A total of 24 patients with NSCLC had both the plasma NGS and tissue NGS results available, of which 14 (58.3%) cases had a therapeutically relevant target detected, either by plasma or tissue NGS or by both methods. The positive predictive agreement (PPA) between plasma and tissue NGS was 75.0% and the negative predictive agreement (NPA) was 83.3%, for an overall predictive agreement (OPA) of 79.2% (**Table 4**). There was a correlation between the plasma and tissue mutation AF among actionable mutations detected ($\rho = 0.5503$, $p = 0.0221$) (**Supplementary Figure 4**). It was observed that for cases in which tissue mutation was not detected in plasma, the AF was low in the tissue sample, below 10% AF. Conversely, two mutations identified only

TABLE 5 | Cancer stage-dependence of detection of actionable mutations in plasma.

		Stage	
		2B-3B	**4-4B**
Actionable mutation	Detected	0	9
	Not detected	6	11

Fisher's exact test, p-value = 0.0632.

TABLE 6 | Clinically actionable mutations detected in stage 4-4B cases and their concordance of detection with tissue *EGFR* tests.

Stage	Mutation (HGVSp)	AF (%)	Concordant with tissue *EGFR*
4B	*EGFR* p.E746_A750del	7.15	Yes
4	*EGFR* p.E746_A750del	0.73	Yes
4	*KRAS* p.G12D	12.36	NA
4	*EGFR* p.L747_A750delinsP	0.98	Yes
4	*BRAF* p.K601E	12.45	NA
4	*KRAS* p.G12D	27.17	NA
4	*EGFR* p.E746_A750del	0.33	Yes
4	*EGFR* p.E746_S752delinsV	50.7	Yes
4	*KRAS* p.G12D	3.32	NA

NA, not applicable as not tested by tissue EGFR.

in plasma were characterized by very low AF −0.04 and 0.3% (**Supplementary Figure 4**). To account for the discordant mutations, the extent of clinical disease was examined by comparing tumor stage information, which was available only for 49% of NSCLC cases in this study that underwent plasma NGS (26/53). Actionable mutations were detected in plasma for 0% (0/6) cases with disease stage 2B-3B, including one tissue-discordant *EGFR* sensitizing mutation (**Table 5**). In contrast, for cases with disease stage 4 or 4B ($n = 20$), an actionable mutation was detected in 45% (9/20) cases, including five tissue concordant *EGFR* sensitizing mutations (Stage 2B-3B vs. Stage 4-4B: Fisher's exact test, $p = 0.0632$) (**Tables 5**, **6**).

Plasma NGS for Non-NSCLC Cancers and Noncancer Samples

As described in **Figure 1**, plasma samples from patients initially suspected to have lung cancer, but later confirmed to have either other cancers ($n = 7$) or a noncancer diagnosis ($n = 10$), were also tested by NGS. The specificity of detection of cancer-specific mutations by plasma NGS was demonstrated by the detection of a mutation in 85% (6/7) of other cancer cases, including pathogenic *TP53* mutations in 71% (5/7) of cases (**Supplementary Table 2**). Importantly, among plasma from 10 noncancer cases, only one case harbored an *ALK* frameshift mutation of uncertain significance, which was also present in a pleural effusion sample from the same case (data not shown). This demonstrates that mutation detection by plasma NGS is reliable and specific to the presence of cancer.

Plasma NGS TAT

Plasma NGS was successfully performed in 53 patients with NSCLC and 17 patients with non-NSCLC with suspected lung cancer with an average TAT of 10 days from the time of blood draw to the time of receipt of the report. In contrast, the average TAT for tissue NGS for 38 patients with standard *EGFR* testing with tissue was 29.9 days ($p < 0.05$), with the longest duration between biopsy collection and receipt being 48 days.

DISCUSSION

In this single-center prospective study, we assessed the clinical utility of adding plasma NGS testing to the diagnostic workflow for suspected lung cancer and molecular testing workflow for diagnosed NSCLC. This approach may be labeled as "plasma-first" for cases with no tissue sample available for testing, or complementary where both tumor and plasma sample may be tested for comprehensive target coverage, or where there is uncertainty about the adequacy of a tissue sample for molecular testing (19). Plasma NGS demonstrated significantly higher sample accessibility levels, lower average reporting time, and matched specificity and accuracy when compared to standard tissue *EGFR* testing. Importantly, a range of additional actionable mutations from guideline-recommended biomarkers was found by plasma NGS, potentially enabling an appropriate targeted treatment option, even in the absence of a tissue test result.

The invasive nature of tissue biopsy makes routine diagnostic EGFR profiling unfeasible for patients with late-stage NSCLC and those of advanced age. In this study, only 70.3% (38/54) of diagnosed patients with NSCLC had informative results from tissue *EGFR* testing. On the other hand, the blood sample was collected for 99% of all the patients recruited in this prospective study (70/71), including 98.4% (53/54) of patients with NSCLC. We show the clinical value of a plasma NGS test was an average 26.8% additional diagnostic yield over tissue *EGFR* testing, from the combined contribution of (1) additional actionable mutations in six of 25 tissue *EGFR*-negative cases and (2) detection of five actionable mutations, including 2 *EGFR* sensitizing mutations, in 16 cases that had no results from tissue *EGFR* testing.

Among all the patients with NSCLC, adding plasma NGS to tissue *EGFR* testing resulted in the detection of a therapeutically actionable mutation in 43.6% (23/54) cases, whereas if only tissue *EGFR* testing had been done, only 22.2% (12/54) cases would have had a clinical actionable finding. This represents a 1.9-fold increase in the number of actionable mutations detected in this study by adding plasma NGS testing, including two *EGFR* mutations in two cases that failed standard tissue *EGFR* testing. This is consistent with past studies in larger real-world NSCLC cohorts, where the addition of comprehensive liquid biopsy to targeted tissue testing increased the number of targetable mutations up to as much as 65% (17, 26). This makes plasma NGS an especially important diagnostic tool when tissue biopsy is scant or not available.

The routine implementation of a complementary plasma or even "plasma-first" testing approach in healthcare settings significantly reduces reporting time and can enable patients to begin targeted therapy earlier. Tissue *EGFR* results took an average of 29.9 days to report, while plasma NGS took an average of 10 days to report. In this study, for 37% (20/54) of NSCLC cases, a treatment decision could have been made as soon as the plasma NGS results became available. This trend of a lower turnaround time with plasma NGS tests has been widely supported by other studies (27, 28). The length of time between the scheduling of the tissue biopsy and the procedure itself can vary widely and can add many weeks to an already long wait for a diagnosis. In contrast, in-clinic, same-day blood collection for plasma NGS can be quickly and conveniently performed.

The high specificity of diagnostics is key to ensuring that false-positive findings do not result in incorrect treatment, which can be harmful to patients and increases the financial burden of healthcare. The specificity of plasma NGS compared with PCR-based tissue *EGFR* testing in this study was 100%. This finding provides supporting evidence that positive identification of an actionable mutation by plasma NGS is sufficient evidence to initiate targeted treatments without needing additional confirmation from tissue testing (26), reducing the duration from clinical consultation to the start of the treatment program. In this study, tissue *EGFR* results would have yielded additional findings in 5.56% (3/54) of cases, for which plasma NGS did not find the *EGFR* mutation present in the tumor, supporting the complementary plasma testing would be the most informative approach for the NSCLC patient population.

Plasma NGS reported a sensitivity of 75% when compared to routine Sanger or targeted PCR, which suggests that negative results require further investigation to rule out the possibility of false negatives. Levels of circulating tumor DNA (ctDNA) are highly varied between patients, likely because ctDNA levels can vary based on the rate of turnover, perfusion, and vascularization of the tumor, and are influenced by the cancer stage (29). In this study, a disease stage-dependence was observed for both *EGFR* mutation concordance and detection rate of any actionable mutation, with 45% (9/20) of cases with stage 4 or 4B vs. 0% (0/6) of cases with stage 2B-3B having an actionable mutation detected. Further, there was a correlation between the tumor AF and plasma AF of mutations for cases where both plasma and tissue NGS were performed, suggesting ctDNA burden is a function of the actual tumor size and spread. This is in alignment with another study where patients with liver metastases had higher plasma-tissue concordance for actionable mutations compared to those with M1a disease (17), and with a study in which patients with intrathoracic metastases alone were less likely to have detectable ctDNA (30). It has been suggested that the disease stage could serve as a decision metric to decide the order in which plasma or tissue testing is requested, to maximize detection of actionable mutations detection without unnecessarily prolonging the time to result.

As an attestation of the specificity and broad applicability of plasma NGS for cancer diagnostics, we also show that among other suspected lung cancer patients eventually diagnosed to not have cancer, only one case (out of 10) had a detectable mutation (of uncertain significance), while six of seven cases diagnosed as having other non-NSCLC cancers had *TP53* mutations or other cancer-related mutations detected. Based on these results, a role for plasma NGS testing in preliminary cancer diagnosis could be envisioned.

This study has limitations in that the standard diagnostic test comparison was limited to *EGFR* mutations, and actionable fusions in *ALK*, *ROS1, RET,* and *NTRK* were not considered as they were not measured at the time of this study. Including actionable fusions in concurrent tissue and plasma, NGS tests will likely result in a similar fractional increase in actionability. Another limitation was that disease stage information was only available for a subset of patients, limiting the stage-specific analysis for plasma-tissue concordance. Furthermore, the study was conducted in a small cohort of prospectively recruited patients and no information on treatment decisions and clinical outcomes was recorded, which would have enabled the real-world clinical utility of the complementary or "plasma-first" approach to be quantified in a prospective setting. Finally, longitudinal monitoring of the efficacy of plasma NGS on this patient cohort was not captured in this study. However, the non-invasive nature and sensitive detection ability of plasma NGS make it a suitable tool for the determination of resistance mutations earlier and with greater accessibility than would be possible with an initial biopsy or rebiopsy.

This study demonstrates that integrating plasma NGS with tissue testing increases actionable yield over conventional diagnostic approaches for NSCLC by allowing more patients to achieve comprehensive biomarker profiling. Plasma NGS allows for quick and non-invasive molecular profiling that can rapidly guide treatment decisions and complement routine tissue testing or tissue NGS or could be a viable first-line alternative when tissue biopsy is not feasible.

DATA AVAILABILITY STATEMENT

The original contributions presented in the study are included in the article/**Supplementary Material**, further inquiries can be directed to the corresponding author.

ETHICS STATEMENT

The studies involving human participants were reviewed and approved by Institutional Review Board of Changi General Hospital. Study is registered under clinical trial number NCT04254497. The patients/participants provided their written informed consent to participate in this study.

AUTHOR CONTRIBUTIONS

YC, M-HT, and JM conceived and planned the experiments. JM, M-HT, and AT contributed to the samples preparation. YC, JP, and KN carried out the experiments and preliminary analysis.

YC, JP, KN, JM, and RG analyzed and interpreted the results. YC wrote the manuscript with support from RG and JM. All authors provided critical feedback and helped shape the analysis and manuscript and contributed to the article and approved the submitted version.

FUNDING

The study was funded by the Agency for Science, Technology and Research Biomedical Research Council-Economic Development Board (A*STAR BMRC-EDB) Industrial Alignment Fund (IAF) (Project No. IAF111221).

ACKNOWLEDGMENTS

We would like to sincerely acknowledge all the patients that participated in this study. We would like to thank Kim-Tien Ng and Kian-Hin Tan for their contributions to this study.

SUPPLEMENTARY MATERIAL

The Supplementary Material for this article can be found online at: https://www.frontiersin.org/articles/10.3389/fmed.2022.758464/full#supplementary-material

REFERENCES

1. Molina JR, Yang P, Cassivi SD, Schild SE, Adjei AA. Non-small cell lung cancer: epidemiology, risk factors, treatment, and survivorship. *Mayo Clin Proc.* (2008) 83:584–94. doi: 10.1016/S0025-6196(11)60735-0
2. SEER Cancer Statistics Review (CSR) 1975-2015 (2018). Available online at: https://seer.cancer.gov/archive/csr/1975_2015/
3. Lindeman NI, Cagle PT, Aisner DL, Arcila ME, Beasley MB, Bernicker EH, et al. Updated molecular testing guideline for the selection of lung cancer patients for treatment with targeted tyrosine kinase inhibitors: guideline from the college of american pathologists, the international association for the study of lung cancer, and the association for molecular pathology. *Arch Pathol Lab Med.* (2018) 142:321–46. doi: 10.5858/arpa.2017-0388-CP
4. Hanna N, Johnson D, Temin S, Baker S, Brahmer J, Ellis PM, et al. Systemic Therapy for stage IV non–small-cell lung cancer: American society of clinical oncology clinical practice guideline update. *JCO.* (2017) 35:3484–515. doi: 10.1200/JCO.2017.74.6065
5. Chen R, Manochakian R, James L, Azzouqa A-G, Shi H, Zhang Y, et al. Emerging therapeutic agents for advanced non-small cell lung cancer. *J Hematol Oncol.* (2020) 13:58. doi: 10.1186/s13045-020-00881-7
6. Alexander M, Kim SY, Cheng H. Update 2020: management of non-small cell lung cancer. *Lung*. (2020) 198:897–907. doi: 10.1007/s00408-020-00407-5
7. Skoulidis F, Li BT, Dy GK, Price TJ, Falchook GS, Wolf J. et al. Sotorasib for Lung Cancers with KRAS pG12C Mutation. *N Engl J Med.* (2021) 384:2371–81. doi: 10.1056/NEJMoa2103695
8. National Comprehensive Cancer Network (NCCN) NCCN Clinical Practice Guidelines in Oncology: Non-Small Cell Lung Cancer. Version 5.2021. Available online at: https://www.nccn.org/professionals/physician_gls/pdf/nscl.pdf
9. Gutierrez ME, Choi K, Lanman RB, Licitra EJ, Skrzypczak SM, Pe Benito R, et al. Genomic profiling of advanced non–small cell lung cancer in community settings: gaps and opportunities. *Clin Lung Cancer.* (2017) 18:651–9. doi: 10.1016/j.cllc.2017.04.004
10. Lim C, Tsao MS, Le LW, Shepherd FA, Feld R, Burkes RL, et al. Biomarker testing and time to treatment decision in patients with advanced nonsmall-cell lung cancer†. *Ann Oncol.* (2015) 26:1415–21. doi: 10.1093/annonc/mdv208
11. Makarem M, Leighl NB. Molecular testing for lung adenocarcinoma: is it time to adopt a "plasma-first" approach? *Cancer.* (2020) 126:3176–80. doi: 10.1002/cncr.32875
12. Russano M, Napolitano A, Ribelli G, Iuliani M, Simonetti S, Citarella F, et al. Liquid biopsy and tumor heterogeneity in metastatic solid tumors: the potentiality of blood samples. *J Exp Clin Cancer Res.* (2020) 39:95. doi: 10.1186/s13046-020-01601-2
13. Boskovic T, Stanic J, Pena-Karan S, Zarogoulidis P, Drevelegas K, Katsikogiannis N, et al. Pneumothorax after transthoracic needle biopsy of lung lesions under CT guidance. *J Thorac Dis.* (2014) 6 Suppl 1:S99–107. doi: 10.3978/j.issn.2072-1439.2013.12.08
14. Cescon DW, Bratman SV, Chan SM, Siu LL. Circulating tumor DNA and liquid biopsy in oncology. *Nature Cancer.* (2020) 1:276–90. doi: 10.1038/s43018-020-0043-5
15. Odegaard JI, Vincent JJ, Mortimer S, Vowles JV, Ulrich BC, Banks KC, et al. Validation of a plasma-based comprehensive cancer genotyping assay utilizing orthogonal tissue- and plasma-based methodologies. *Clin Cancer Res.* (2018) 24:3539. doi: 10.1158/1078-0432.CCR-17-3831
16. Bettegowda C, Sausen M, Leary RJ, Kinde I, Wang Y, Agrawal N, et al. Detection of circulating tumor DNA in early- and late-stage human malignancies. *Sci Transl Med*. (2014) 6:224ra24. doi: 10.1158/1538-7445.AM2014-5606
17. Aggarwal C, Thompson JC, Black TA, Katz SI, Fan R, Yee SS, et al. Clinical Implications of plasma-based genotyping with the delivery of personalized therapy in metastatic non–small cell lung cancer. *JAMA Oncology.* (2019) 5:173–80. doi: 10.1001/jamaoncol.2018.4305
18. Wang N, Zhang X, Wang F, Zhang M, Sun B, Yin W, et al. The Diagnostic accuracy of liquid biopsy in EGFR-Mutated NSCLC: a systematic review and meta-analysis of 40 studies. *SLAS Technol.* (2021) 26:42–54. doi: 10.1177/2472630320939565
19. Rolfo C, Mack P, Scagliotti GV, Aggarwal C, Arcila ME, Barlesi F, et al. Liquid biopsy for advanced non-small cell lung cancer: a consensus statement from the international association for the study of lung cancer (IASLC). *J Thorac Oncol.* (2021) 16:1647–62. doi: 10.1016/j.jtho.2021.06.017
20. Thompson JC, Yee SS, Troxel AB, Savitch SL, Fan R, Balli D, et al. Detection of Therapeutically Targetable Driver and Resistance Mutations in Lung Cancer Patients by Next-Generation Sequencing of Cell-Free Circulating Tumor DNA. *Clin Cancer Res.* (2016) 22:5772. doi: 10.1158/1078-0432.CCR-16-1231
21. Schwaederlé MC, Patel SP, Husain H, Ikeda M, Lanman RB, Banks KC, et al. Utility of genomic assessment of blood-derived circulating tumor DNA (ctDNA) in patients with advanced lung adenocarcinoma. *Clin Cancer Res.* (2017) 23:5101. doi: 10.1158/1078-0432.CCR-16-2497
22. Hsu W-H, Yang JC-H, Mok TS, Loong HH. Overview of current systemic management of EGFR-mutant NSCLC. *Ann Oncol.* (2018) 29:i3–9. doi: 10.1093/annonc/mdx702
23. Kumari N, Singh S, Haloi D, Mishra SK, Krishnani N, Nath A, et al. Epidermal growth factor receptor mutation frequency in squamous cell carcinoma and its diagnostic performance in cytological samples: a molecular and immunohistochemical study. *World J Oncol.* (2019) 10:142–50. doi: 10.14740/wjon1204
24. Liam C-K, Stone E, Andarini S, Liam Y-S, Lam DC-L, Lee P. Molecular testing of metastatic non-small cell lung cancer in the Asia-Pacific region. *Respirology.* (2020) 25:685–7. doi: 10.1111/resp.13833
25. Ettinger DS, Wood DE, Aisner DL, Akerley W, Bauman JR, Bharat A, et al. NCCN guidelines insights: non–small cell lung cancer, version 2.2021: featured updates to the NCCN guidelines. *J Natl Compr Canc Netw.* (2021) 19:254–66. doi: 10.6004/jnccn.2021.0013
26. Mack PC, Banks KC, Espenschied CR, Burich RA, Zill OA, Lee CE, et al. Spectrum of driver mutations and clinical impact of circulating tumor DNA analysis in non–small cell lung cancer: analysis of over 8000 cases. *Cancer.* (2020) 126:3219–28. doi: 10.1002/cncr.32876
27. Leighl NB, Page RD, Raymond VM, Daniel DB, Divers SG, Reckamp KL, et al. Clinical utility of comprehensive cell-free DNA analysis to identify genomic biomarkers in patients with newly diagnosed

metastatic non–small cell lung cancer. *Clin Cancer Res.* (2019) 25:4691. doi: 10.1158/1078-0432.CCR-19-0624

28. Sabari JK, Offin M, Stephens D, Ni A, Lee A, Pavlakis N, et al. A prospective study of circulating tumor DNA to guide matched targeted therapy in lung cancers. *JNCI.* (2019) 111:575–83. doi: 10.1093/jnci/djy156
29. Bronkhorst AJ, Ungerer V, Holdenrieder S. The emerging role of cell-free DNA as a molecular marker for cancer management. *Biomol Detect Quantif.* (2019) 17:100087–100087. doi: 10.1016/j.bdq.2019.100087
30. Karlovich C, Goldman JW, Sun J-M, Mann E, Sequist LV, Konopa K, et al. Assessment of EGFR mutation status in matched plasma and tumor tissue of NSCLC patients from a phase I study of rociletinib (CO-1686). *Clin Cancer Res*. (2016) 22:2386. doi: 10.1158/1078-0432.CCR-15-1260

Conflict of Interest: YC, M-HT, JP, and KN are employees of Lucence Diagnostics Pte Ltd.

The remaining authors declare that the research was conducted in the absence of any commercial or financial relationships that could be construed as a potential conflict of interest.

frontiers
in Medicine

ORIGINAL RESEARCH
published: 01 March 2022
doi: 10.3389/fmed.2022.822806

Roles of Pyroptosis-Related Gene Signature in Prediction of Endometrial Cancer Outcomes

Yili Chen[1], Yuandong Liao[1], Qiqiao Du[1], Chunliang Shang[2], Shuhang Qin[1], Kaping Lee[3], Qiaojian Zou[1], Junxiu Liu[1]* and Shuzhong Yao[1]*

[1] Department of Obstetrics and Gynecology, The First Affiliated Hospital, Sun Yat-sen University, Guangzhou, China, [2] Department of Obstetrics and Gynecology, Peking University Third Hospital, Beijing, China, [3] State Key Laboratory of Oncology in South China, Collaborative Innovation Center for Cancer Medicine, Sun Yat-sen University Cancer Center, Guangzhou, China

Edited by:
Fu Wang,
Xi'an Jiaotong University, China

Reviewed by:
Longhui Qiu,
University of California, San Francisco, United States
Jinhui Liu,
Nanjing Medical University, China
Qian Yang,
Zhejiang University, China
Chen Jierong,
Guangdong Provincial People's Hospital, China

***Correspondence:**
Shuzhong Yao
yaoshuzh@mail.sysu.edu.cn
Junxiu Liu
liujxiu@mail.sysu.edu.cn

Specialty section:
This article was submitted to Precision Medicine, a section of the journal Frontiers in Medicine

Received: *26 November 2021*
Accepted: *08 February 2022*
Published: *01 March 2022*

Citation:
Chen Y, Liao Y, Du Q, Shang C, Qin S, Lee K, Zou Q, Liu J and Yao S (2022) Roles of Pyroptosis-Related Gene Signature in Prediction of Endometrial Cancer Outcomes. Front. Med. 9:822806. doi: 10.3389/fmed.2022.822806

Endometrial cancer (EC) is one of the most common gynecological malignancies in women, accompanied by the increasing incidence and decreasing age of onset. Pyroptosis plays an important role in the occurrence and development of malignant tumors. However, the relationship between pyroptosis-related genes and tumor prognosis remains unclear. In this study, analyzing the expression levels and survival data of 33 pyroptosis-related genes in the Cancer Genome Atlas (TCGA) between normal samples and tumor samples, we obtained six pyroptosis-related prognostic differentially expressed genes (DEGs). Then, through the least absolute shrinkage and selection operator (LASSO) regression analysis, a gene signature composed of six genes (GPX4, GSDMD, GSDME, IL6, NOD2 and PYCARD) was constructed and divided patients into high- and low-risk groups. Subsequently, Kaplan-Meier (KM) plot, receiver operating characteristic (ROC) curve and principal component analysis (PCA) in two cohorts demonstrated that the gene signature was an efficient independent prognostic indicator. The enrichment analysis and immune infiltration analysis indicated that the high-risk group generally has lower immune infiltrating cells and less active immune function. In short, we constructed and validated a pyroptosis-related gene signature to predict the prognosis of EC, which is correlated to immune infiltration and proposed to help the precise diagnosis and therapy of EC.

Keywords: endometrial cancer, pyroptosis, gene signature, prognosis, immune infiltration

INTRODUCTION

Endometrial cancer (EC) is one of the most common gynecological malignancies in women. In 2020, there were 417,367 new cases and 97,370 new deaths worldwide (1). In recent years, the number of new cases is increasing while its onset age is gradually decreasing (2). The prognostic outcomes of EC patients in different stages are obviously different. Early-stage EC patients generally have a good prognosis, while advanced, metastatic or recurrent EC patients usually have a poor prognosis (3–5). Therefore, EC patients should be detected as soon as possible to improve their prognosis. The most common clinical symptom of EC is postmenopausal vaginal bleeding (PMB). However, this symptom is not specific because only 9% of women with PMB are diagnosed as EC (6). Cytology and transvaginal ultrasonography are most commonly used to screen EC, but they also lack specificity unfortunately (7). Therefore, it is particularly important to screen high-efficiency biomarkers or risk model to improve the prognosis of EC patients.

Pyroptosis is an atypical form of inflammatory programmed cell death mediated by caspase family proteins. It can be triggered by infections, malignant tumors and other pathological factors. The characteristic of pyroptosis is the rapid rupture of the cell membrane and the release of pro-inflammatory substances in the cell (8–10). The three pathways of pyroptosis are the classic pathway that depends on caspase-1 (11, 12), the non-classical pathway that depends on caspase-4/5/11 (13, 14), and the special pathway that depends on caspase-3 (15). In addition, the Gasdermin family proteins are known as the "executioners" of pyroptosis. They are the most important proteins that affect pyroptosis, especially Gasdermin D (GSDMD) and Gasdermin E (GSMDE) (9, 10, 16).

The occurrence and development of malignant tumors is an extremely complex biological process, and studies have shown pyroptosis plays a certain role in it (17–19). On one hand, promoting pyroptosis of tumor cells can effectively inhibit the occurrence and progression of tumors and enhance the effect of anti-tumor treatment (9, 20); on the other hand, pyroptosis can form a microenvironment suitable for tumor cell growth, thereby promoting tumor growth (21, 22). Recent studies demonstrated that pyroptosis is closely related to proliferation, invasion and metastasis of tumor cells, and can affect the therapeutic effect of chemotherapy (12, 15, 19, 23–25). A recent study found that hydrogen inhibits the growth of EC through the pyroptosis pathway mediated by ROS/NLRP3/caspase-1/GSDMD, revealing the close relationship between pyroptosis and EC (12). However, there is still no relevant research to clarify the prognostic value of the gene signature related to pyroptosis in EC.

Accordingly, in this study, we aim to establish a novel gene signature for predicting the prognosis of EC by mining data from the Cancer Genome Atlas (TCGA). The overall design and technical roadmap of the study are shown in **Figure 1**. To this end, we intend to analyze the mRNA expression data and clinical information of EC patients in TCGA, and identify the prognostic differentially expressed genes (DEGs) related to pyroptosis. Then, a pyroptosis-related gene signature will be established through the least absolute shrinkage and selection operator (LASSO) regression analysis from the training set, and its prediction performance will be further verified through the validation set. After that, we plan to perform enrichment analysis and immune infiltration analysis on DEGs of the high- and low-risk groups. In addition, we propose to verify mRNA and protein expression of the pyroptosis-related prognostic DEGs in the gene signature. All in all, we hope to successfully establish a gene signature related to pyroptosis, which may help the diagnosis and treatment of EC.

MATERIALS AND METHODS

Data Collection

The mRNA expression profiles and corresponding clinical information of 23 normal samples and 552 EC samples were downloaded from the TCGA database (https://portal.gdc.cancer.gov/). After deleting deletions and duplications, the "sample" function in R was used to randomly divide the remaining 539 EC patient samples into the TCGA training set ($n = 287$) and the TCGA validation set ($n = 252$) in equal proportions. In addition, 33 genes related to pyroptosis were collected from previous studies and were listed in **Supplementary Table S1** (26).

Identification of Pyroptosis-Related Prognostic DEGs

Firstly, using the false discovery rate (FDR) < 0.05 as the standard, we used the "limma" R package to perform mRNA differential expression analysis on EC samples and normal samples in the TCGA cohort to obtain pyroptosis-related DEGs. Then, taking $p < 0.05$ as the critical value standard for genes with prognostic value, we performed univariate Cox regression analysis on the overall survival (OS) of these 33 genes to obtain prognostic genes. Subsequently, the pyroptosis-related DEGs and prognostic genes were intersected to acquire the pyroptosis-related prognostic DEGs for further analysis. In order to show the differential expression level of DEGs between tumor samples and normal samples more intuitively, we adopted the "heatmap" R package to draw a heatmap. Furthermore, we utilized the STRING online tool (http://string-db.org/) to perform protein-protein interaction (PPI) analysis to further understand the relationship between pyroptosis-related prognostic DEGs.

Construction and Validation of Pyroptosis-Related Gene Signature

After obtaining the prognostic genes related to pyroptosis, we applied the "glmnet" R package to construct the prognostic model of pyroptosis-related genes through LASSO regression analysis. Then, the risk score was calculated through the following formula: risk score $= \sum_i^n Xi \times Yi$ (X: coefficient value of each gene, Y: expression level of each gene). According to the median value of the risk score, the patients were further divided into high- and low-risk groups. Kaplan-Meier (KM) curve and receiver operating characteristic (ROC) curve were drawn using the "survival" and "timeROC" R packages to evaluate the predictive efficiency of pyroptosis-associated gene signature. Further, we employed the "Rtsne" R package to perform principal component analysis (PCA) analysis on this model to visually demonstrate its predictive performance. Separately, we also carried out univariate and multivariate Cox regression analysis for further verification.

Enrichment Analysis and Immune Infiltration Analysis

We divided the EC patients into high- and low-risk groups based on the median value of the risk score. Then, with $|\log2FC| \geq 1$ and FDR < 0.05 as the specific criteria, we utilized the "limma" R package to filter out the DEGs between the high- and low-risk groups. Then, we further applied the "clusterProfiler" R package to perform Gene Ontology (GO) analysis and Kyoto Encyclopedia of Genes and Genomes (KEGG) pathway enrichment analysis on these genes. In addition, we made use of the "gsva" package to perform single sample gene set enrichment analysis (ssGSEA) to calculate the scores of immune

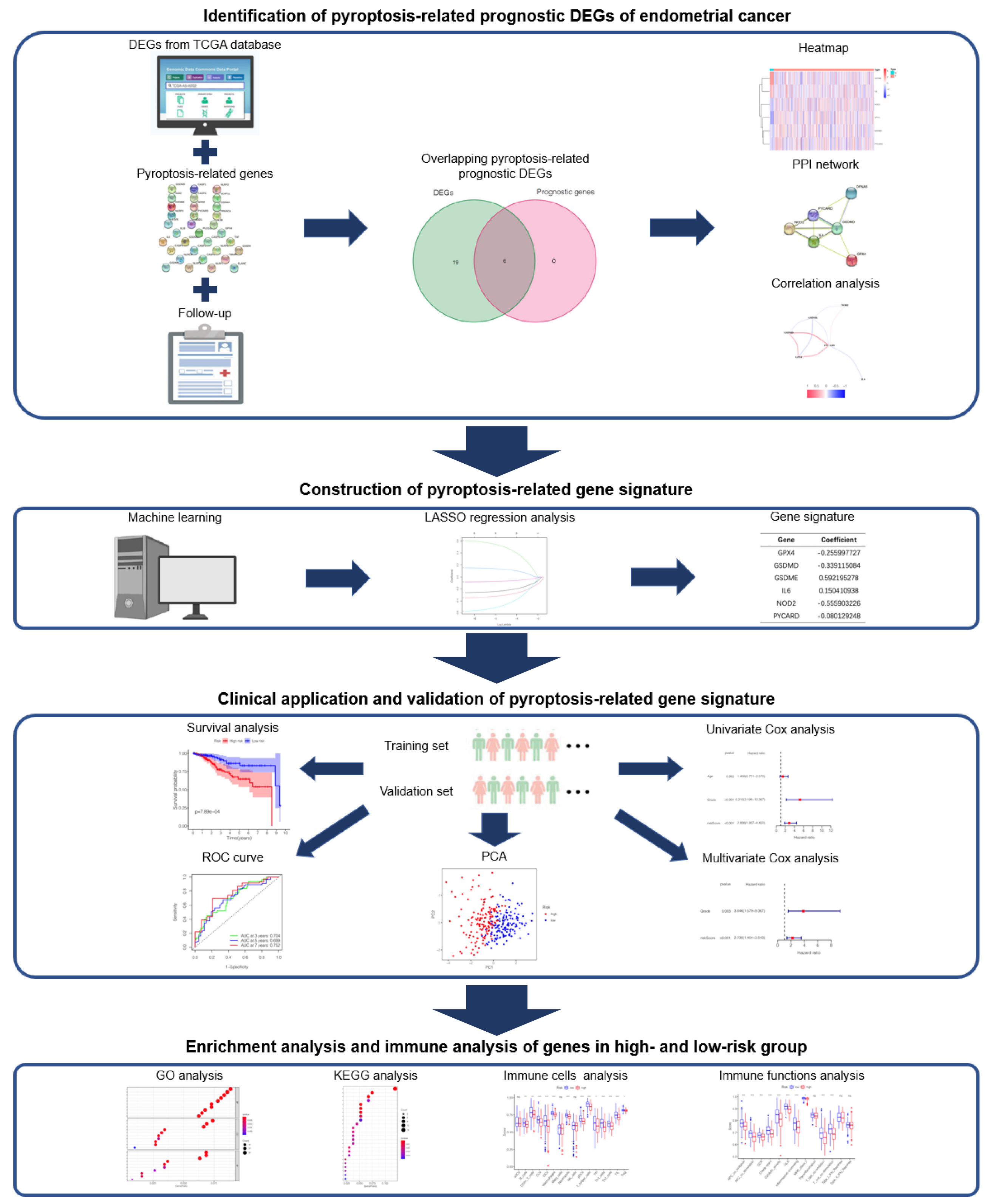

Gene	Coefficient
GPX4	-0.255997727
GSDMD	-0.339115084
GSDME	0.592195278
IL6	0.150410938
NOD2	-0.555903226
PYCARD	-0.080129248

FIGURE 1 | The overall design and technical roadmap of the study.

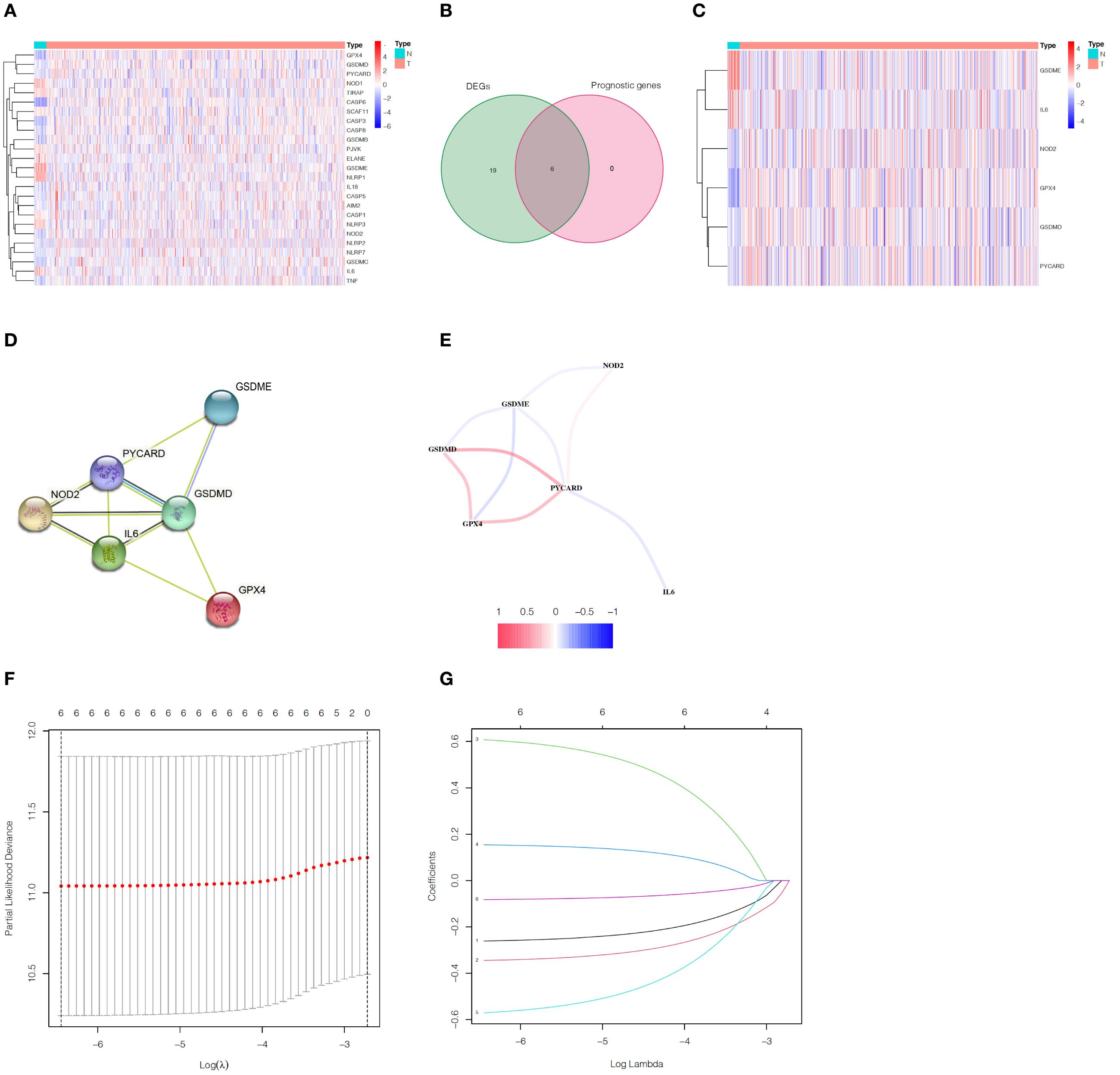

FIGURE 2 | Identification of pyroptosis-related prognostic DEGs in EC and construction of the gene signature. **(A)** The heatmap of 25 pyroptosis-related DEGs. **(B)** Venn diagram between pyroptosis-related DEGs and prognostic genes. **(C)** The heatmap of six pyroptosis-related prognostic DEGs. **(D)** The PPI network of pyroptosis-related prognostic DEGs. **(E)** The correlation network between pyroptosis-related prognostic DEGs. **(F)** The minimum criteria and **(G)** coefficients were calculated by LASSO Cox regression analysis to construct the gene signature.

infiltrating cells and immune function in the TCGA training set and validation set. Hereafter, we utilized the "limma" package to analyze the difference of the scores between the two groups.

Verification of mRNA and Protein Expression of Six Genes in the Gene Signature

The mRNA expression levels and partial representative protein expression levels of various genes in tumor samples and normal samples resourced from the UALCAN database (http://ualcan.path.uab.edu/) (27) and The Human Protein Atlas database (https:/ /www.proteinatlas.org/) (28, 29). Moreover, the genetic alteration data of the six genes in the risk model was derived from the cBioPortal database (https://www.cbioportal.org/) (30, 31).

Statistical Analysis

The Wilcoxon test was adopted to compare the mRNA expression levels between normal samples and EC samples. The KM curve of the two-sided log-rank test was used to compare the OS of patients between the high- and low-risk groups. In order to evaluate the predictive power of the risk model, we performed univariate and multivariate Cox regression analysis with hazard ratio (HR) and 95% confidence interval (95% CI). In addition, the Mann-Whitney U test was utilized to compare the scores of immune infiltrating cells and immune function in EC patients between high- and low-risk groups. All statistical analysis in this study were performed using R programming (v.1.4.1717). Unless otherwise specified, $p < 0.05$ is considered to be a statistically significant standard.

TABLE 1 | Six pyroptosis-associated genes and their coefficient value.

Pyroptosis-related gene	Coefficient
GPX4	−0.255997727
GSDMD	−0.339115084
GSDME	0.592195278
IL6	0.150410938
NOD2	−0.555903226
PYCARD	−0.080129248

RESULTS

Identification of Pyroptosis-Related Prognostic DEGs

Analyzing the expression levels of 33 genes related to pyroptosis in 23 normal samples and 552 EC samples in the TCGA database, we obtained 25 DEGs ($p < 0.05$, **Supplementary Table S2**). We can speculate that pyroptosis is related to the occurrence and development of EC, because the expression of most pyroptosis-related genes between normal samples and EC samples had statistically significant differences. The heatmap showed the expression levels of these genes (**Figure 2A**). Simultaneously, we performed univariate Cox regression analysis on 33 genes related to pyroptosis, and obtained six prognostic genes correlated to OS. By taking the intersection of DEGs and prognostic genes, we identified six pyroptosis-related prognostic DEGs, namely GPX4, GSDMD, GSDME, IL6, NOD2 and PYCARD (**Figure 2B**). Through the heatmap, we clearly found that GSDME and IL6 were downregulated in tumors while other four genes were upregulated (**Figure 2C**). In order to further explore the interaction of these prognostic DEGs related to pyroptosis, we conducted PPI analysis and correlation analysis, and the results were shown in **Figures 2D,E**, respectively.

Construction of Pyroptosis-Related Gene Signature in the TCGA Training Set

In the TCGA train set, by performing LASSO regression analysis on the above six DEGs, we constructed a pyroptosis-related gene signature according to the optimal λ value (**Figures 2F,G**). Their respective coefficient values in this model were listed in **Table 1**, and the corresponding risk score formula was as follows: Risk score = 0.592 × expression value of GSDME+0.150 × expression value of IL6-0.256 × expression value of GPX4-0.339 × expression value of GSDMD-0.556 × expression value of NOD2-0.080 × expression value of PYCARD. We could result from the KM curve that the survival probability of the high-risk group was significantly lower than that of the low-risk group ($p < 0.001$, **Figure 3A**). To assess the sensitivity and specificity of the risk model, the ROC curve was carried out and the area under the curve (AUC) for 3, 5, and 7 years was 0.704, 0.699, and 0.752, respectively (**Figure 3B**). Based on the median value of the risk score, 143 samples were assigned in the high-risk group, while 144 cases were in the low-risk group (**Figure 3C**). As the risk score increased, the survival time of patients decreased and the number of deaths increased (**Figure 3D**). Separately, PCA analysis demonstrated that the two groups of patients with high and low risk could be well distributed in the two clusters (**Figure 3E**). Univariate and multivariate Cox regression analysis were employed to determine whether the risk score in the gene signature could be adopted as an independent prognostic factor. The results instructed that whether it is univariate or multivariate Cox regression analysis, the risk score was a qualified independent prognostic indicator ($p < 0.001$). The results of univariate analysis were HR = 2.836 and 95% CI = 1.807∼4.450, while the details of multivariate analysis were HR = 2.230 and 95% CI = 1.404∼3.543 (**Figures 3F,G**). Moreover, we found that the risk score was significantly correlated with grade ($p < 0.0001$), vital status ($p = 0.0009$) and survival time ($p = 0.0151$) (**Table 2**).

Validation of the Gene Signature in the TCGA Validation Set

In the TCGA validation set, 134 patients were included in the high-risk group, while the other 118 patients were assigned to the low-risk group (**Figure 4A**). It is obviously that the higher the risk score, the higher the patient's probability of death and the lower the patient's survival time (**Figure 4B**). The KM plot revealed significant statistical differences in the survival probability of the high- and low-risk groups, and the high-risk group had a lower survival probability ($p < 0.01$, **Figure 4C**). ROC curves (AUC for 3, 5, and 7 years are 0.634, 0.648, and 0.706, respectively) further reflected the stable sensitivity and specificity of the prognostic model (**Figure 4D**). Likewise, the results of PCA analysis showed that the high- and low-risk groups of patients could still be well distributed in the two clusters in the TCGA validation set, reflecting the stability of the risk model (**Figure 4E**). In addition, using correlation analysis, we found that the risk score in the TCGA validation set was significantly correlated with grade ($p < 0.0001$) and survival time ($p = 0.0480$) (**Table 2**).

Enrichment Analysis of DEGs in Two Risk Groups

We first divided the EC patients in the TCGA training set into high- and low-risk group, and obtained 488 DEGs between the two different risk groups through differential expression analysis (**Supplementary Table S3**). Then, GO enrichment analysis was performed to explore the biological functions of DEGs in two risk groups. The results demonstrated that

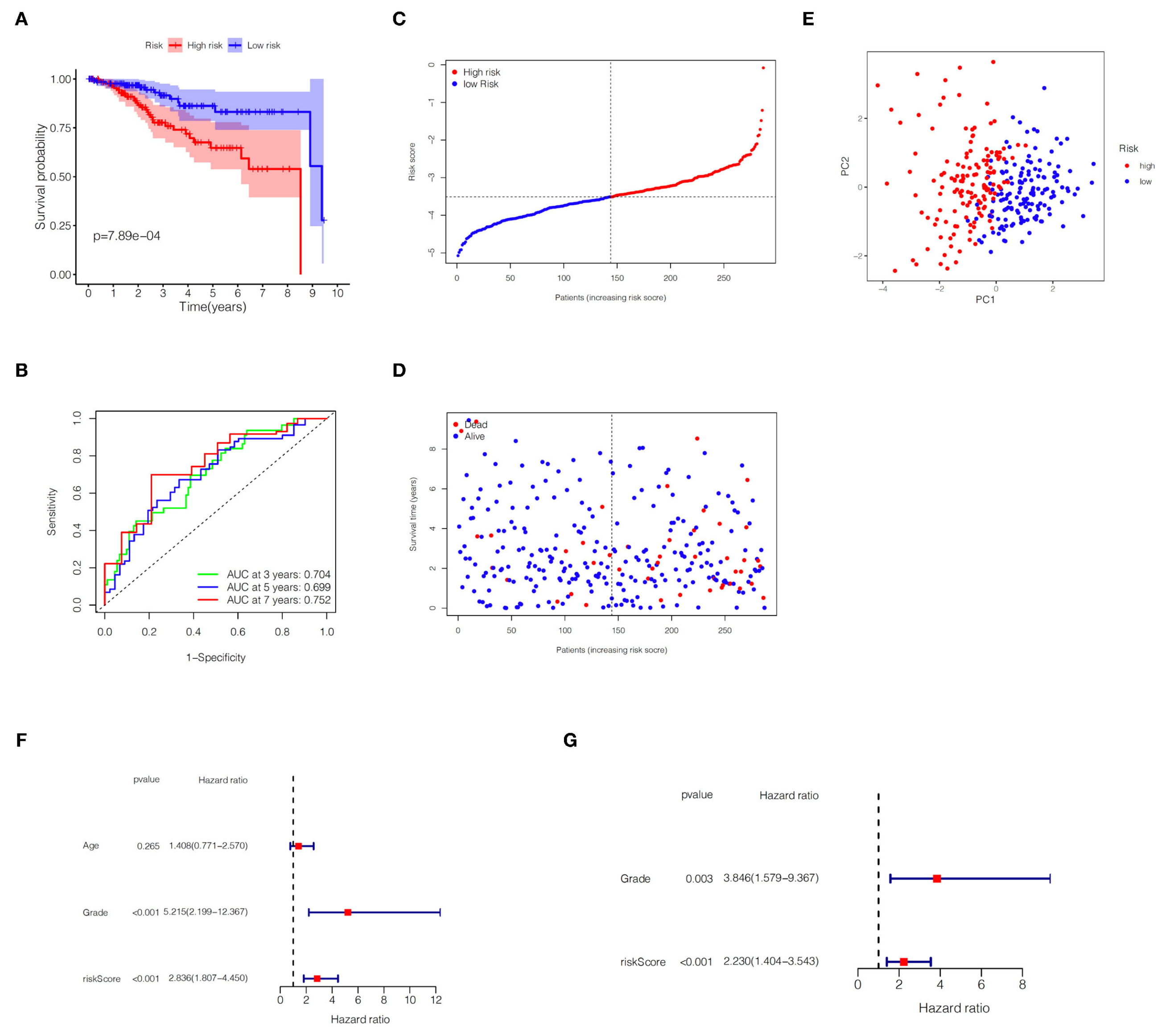

FIGURE 3 | Predictive ability of the gene signature in the TCGA training set. **(A)** KM plot for EC patients in the high- and low-risk groups. **(B)** The ROC curve of the gene signature. **(C)** Distribution of risk scores for EC patients. **(D)** Distribution of survival time with different risk scores. **(E)** PCA analysis for EC patients. **(F,G)** Univariate and multivariate Cox regression analysis of OS.

the top five significantly enriched biological progresses were immunoglobulin complex, complementary activation (classical pathway), humoral immune response mediated by circulating immunoglobulin, complement activation and immunoglobulin mediated immune response (**Figure 5A**). Besides, KEGG pathway enrichment analysis indicated DEGs-related pathways were mainly significantly enriched in cytokine-cytokine receptor interaction, hematopoietic cell lineage and cell adhesion molecules (**Figure 5C**). Hereafter, we performed the same analysis on the TCGA validation set and got 463 DEGs (**Supplementary Table S4**). The GO analysis results in the validation set were similar to the training set (**Figure 5B**), while the KEGG analysis of validation set showed that these DEGs were mainly enriched in IL-17 signaling pathway, pathogenic Escherichia coli infection, and protein digestion and absorption (**Figure 5D**).

Comparison of Immune Cells and Immune Function of EC Patients in High- and Low-Risk Groups

Using ssGSEA, we further compared the enrichment scores of immune cells and immune function of EC patients in two groups on the basis of the above enrichment analysis. Comprehensive analysis of the results in the TCGA training set and the TCGA validation set, compared with the low-risk group, the high-risk group generally has lower immune infiltrating cells, especially Dendritic cells (DCs), T helper cells and tumor-infiltrating lymphocytes (TIL) (**Figures 6A,C**). Similarly, patients in the high-risk group have less active immune function than the low-risk group, particularly in check-point, cytolytic activity, human leukocyte antigen (HLA), T cells co-inhibition and T cells co-stimulation (**Figures 6B,D**).

TABLE 2 | Correlation between risk score and clinical variables of patients with EC.

Clinical variables	TCGA training cohort			*p*-value	TCGA test cohort			*p*-value
	Total	Risk score			Total	Risk score		
	(*n*=287)	High	Low		(*n*=252)	High	Low	
Age (years)								
$\leq$ 60	104	48	56		102	51	51	
> 60	182	95	87		149	83	66	
Unknown	1	0	1	0.3246	1	0	1	0.3125
Grade								
Low (G1 & G2)	121	45	76		96	34	62	
High (G3 & G4)	166	98	68	**<0.0001******	156	100	56	**<0.0001******
Vital status								
Alive	242	112	130		210	104	106	
Dead	45	31	14	**0.0009*****	42	30	12	0.0615
Survival time (years)								
$\leq$ 3	184	97	87		146	88	58	
> 3	103	46	57	**0.0151***	106	46	60	**0.0480***

*$p < 0.05$.
***$p < 0.001$.
****$p < 0.0001$.
Bold values represent $p < 0.05$.

Verification of mRNA and Protein Expression of Six Genes in the Gene Signature

In order to further verify the expression levels of the six genes in the risk model, we utilized the UALCAN online website (http://ualcan.path.uab.edu/) to visualize their mRNA expression levels and found the expression of GPX4, GSDMD, NOD2 and PYCARD up-regulated, while GSDME and IL6 expression down-regulated (**Figure 7A**). Similarly, the representative immunohistochemical results of these genes obtained from The Human Protein Atlas illustrated that their protein expression levels have similar trends (**Figure 7B**).

Mutation Analysis of Six Genes in the Gene Signature

In order to deepen the understanding of the genetic characteristics of these pyroptosis-related genes, the cBioPortal online tool was utilized for mutation analysis. It turned out that although they had significant different expression between normal patients and EC patients in the TCGA database, their

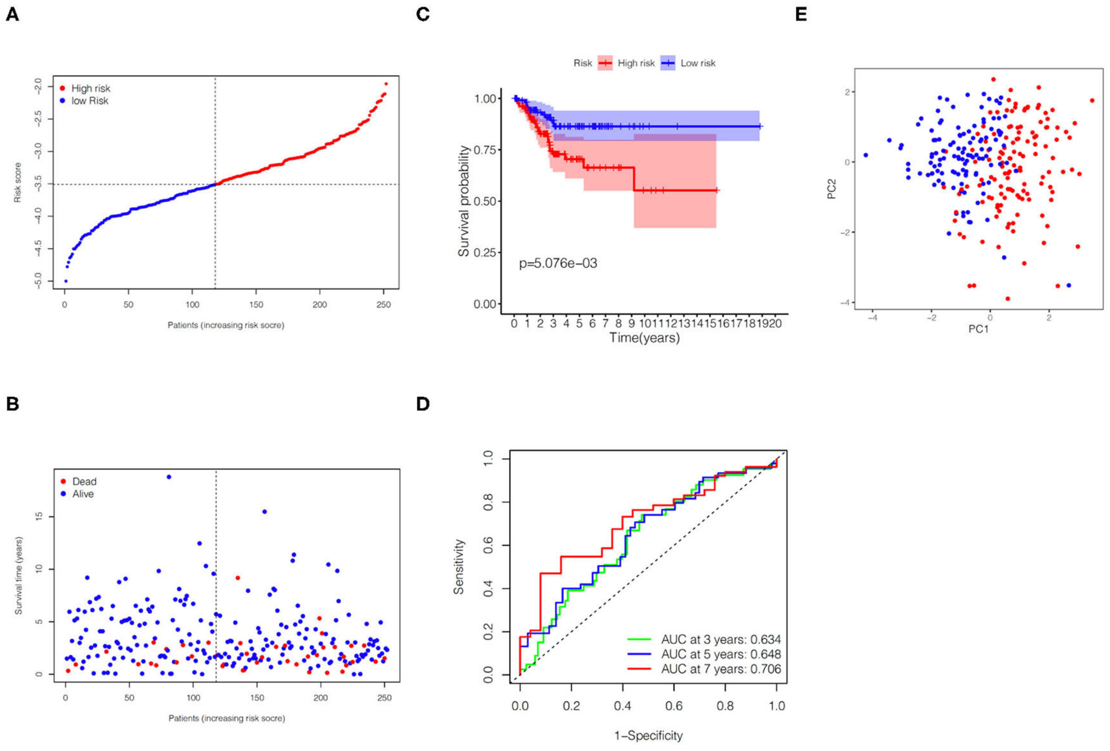

FIGURE 4 | Predictive performance of the gene signature in the TCGA validation set. **(A)** KM curve for EC patients in the high- and low-risk groups. **(B)** Verification for predictive value of the gene signature via ROC curve. **(C)** Distribution of risk scores for EC patients. **(D)** Distribution of survival time with different risk scores. **(E)** PCA analysis for EC patients.

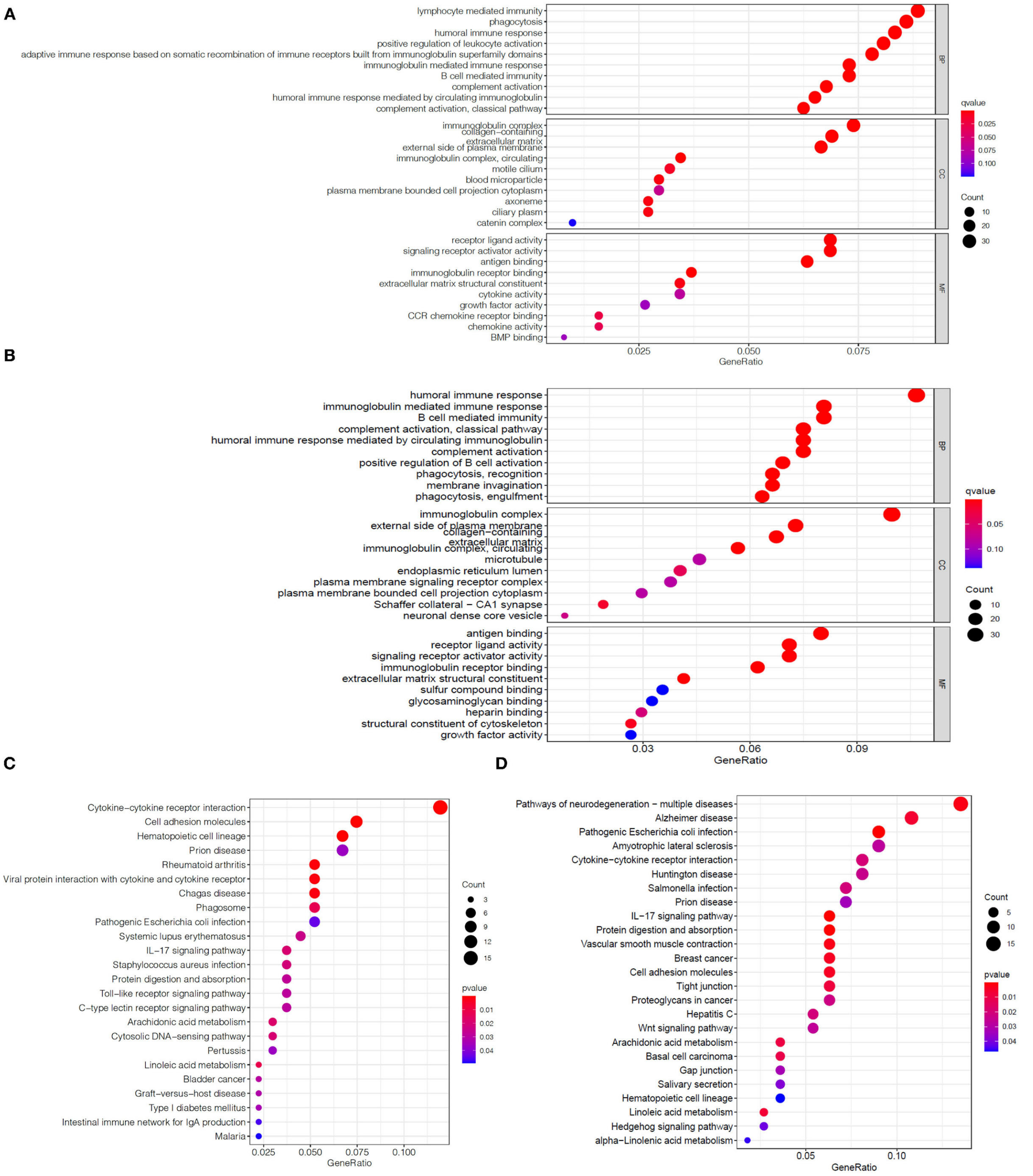

FIGURE 5 | Enrichment analysis of DEGs between two risk groups. Bubble graphs of GO enrichment analysis of DEGs in the TCGA training set **(A)** and the TCGA validation set **(B)**. Bubble graphs of KEGG pathway enrichment analysis of DEGs in the TCGA training set **(C)** and the TCGA validation set **(D)**.

mutation frequency was relatively low. Among them, the highest mutation frequency was only 7% (GSDME and NOD2), while frequency of other genes was even lower (**Figure 7C**).

DISCUSSION

EC is one of the most common gynecological malignancies in women with a relatively high number of incidences and deaths, and the age of onset has gradually become younger in recent years [(1, 2)]. Currently, it is commonly used to screen EC through clinical symptoms, cytology and transvaginal ultrasound, but the specificity of these methods is not satisfactory. With the rapid development of sequencing technology, a few single genes had been unearthed as biomarkers for predicting malignant tumors (32–34). However, since the expression of a single gene is easily regulated by different signaling pathways,

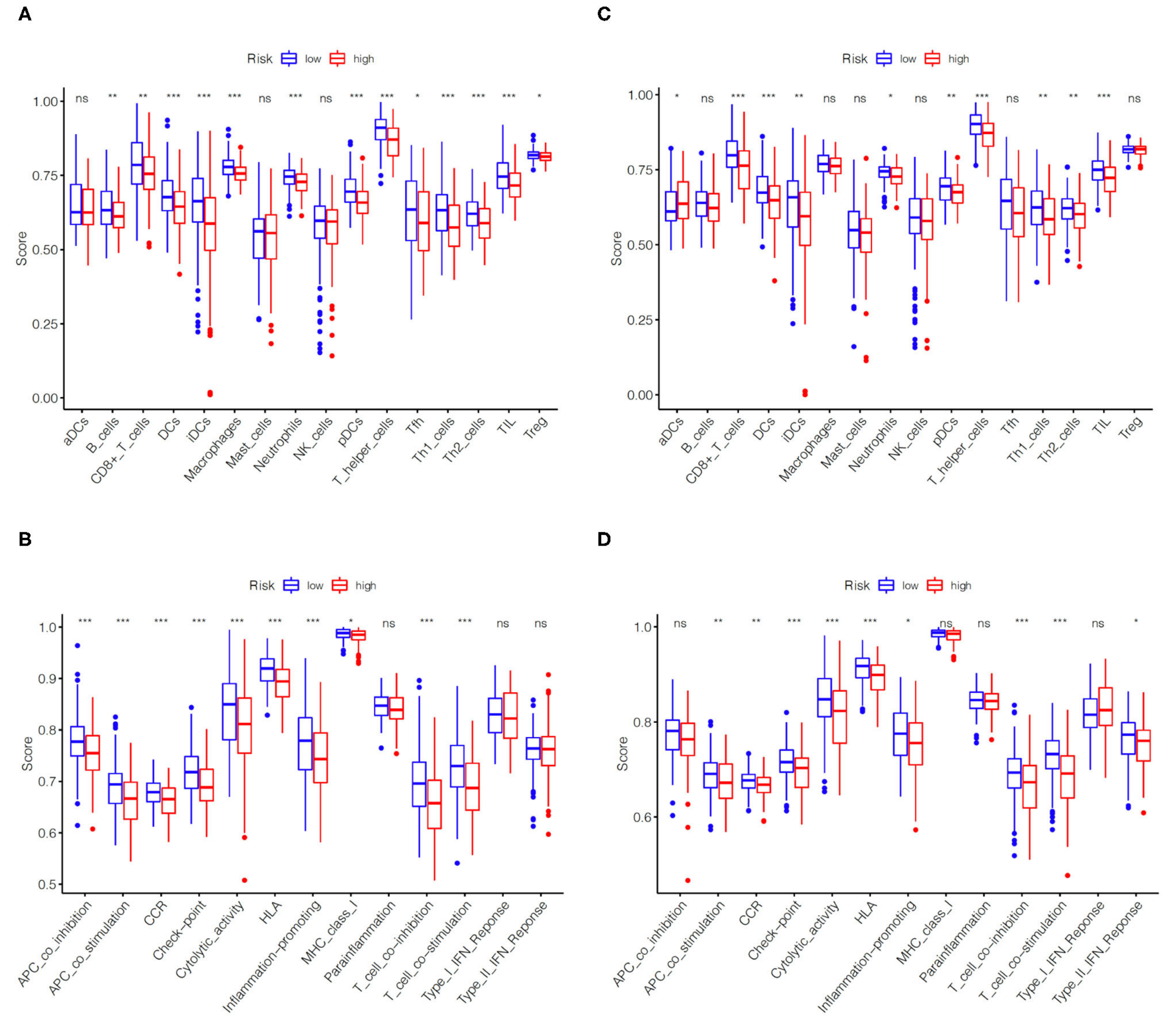

FIGURE 6 | Comparison of immune cells and immune functions of EC patients in high- and low-risk groups. Comparison of the ssGSEA scores of immune cells **(A)** and immune functions **(B)** between high- and low-risk groups in the TCGA training set. Comparison of the ssGSEA scores of immune cells **(C)** and immune functions **(D)** between high- and low-risk groups in the TCGA validation set. The statistical differences were shown as follow: ns, not significant; * $P < 0.05$; ** $P < 0.01$; *** $P < 0.001$.

its predictive effect has greater uncertainty. Thence, screening multiple key factors regulated by the same signal pathway to construct a multi-gene prediction model may be a way to improve predictive performance.

In recent years, pyroptosis had attracted the attention of researchers as a new form of programmed cell death, and many studies had confirmed that it is closely related to the proliferation, invasion, metastasis and chemotherapy effects of tumor cells (12, 15, 19, 23–25). A recent study demonstrated that hydrogen inhibited the growth of endometrial cancer through the pyroptosis pathway mediated by ROS/NLRP3/caspase-1/GSDMD, indicating there is a close relationship between pyroptosis and EC (12). However, there is no relevant reports about the connection between pyroptosis and EC prognosis.

In our study, we successfully established and verified a gene signature with six pyroptosis-related genes (GPX4, GSDMD, GSDME, IL6, NOD2, and PYCARD) that could predict the prognosis of EC.

Glutathione Peroxidase 4 (GPX4) is a member of the glutathione peroxidase (GPX) family, which converts H_2O_2 to H_2O and oxidizes glutathione to its disulfide form (GSSG). GPX4 has been proved to be a key regulator of non-apoptotic forms of programmed cell death such as ferroptosis. Inhibition of GPX4 can trigger uncontrolled oxidation of polyunsaturated fatty acids (PUFAs) and the production of

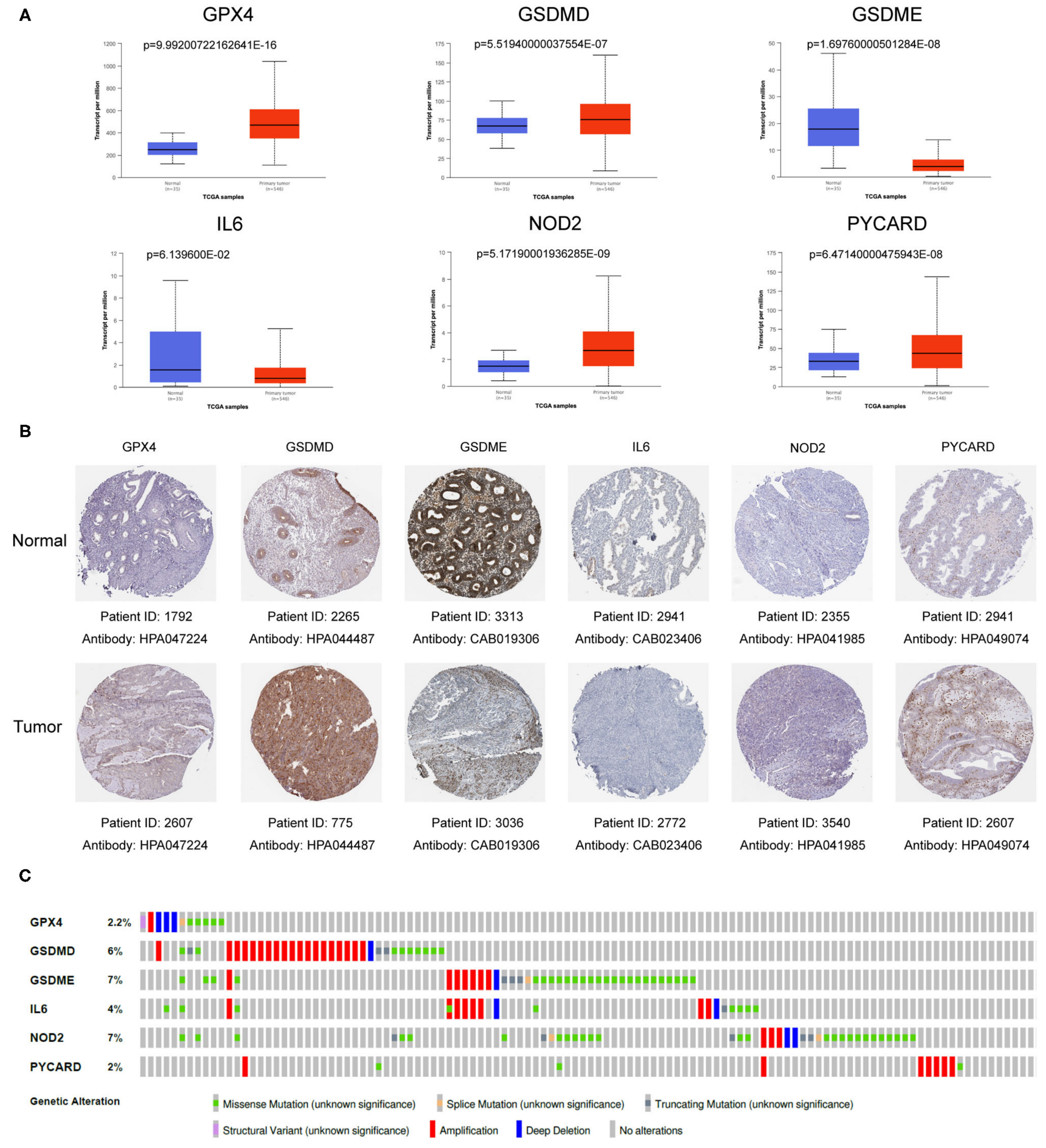

FIGURE 7 | Verification of mRNA and protein expression of six genes in the gene signature. **(A)** The mRNA expression levels of various genes in EC samples and normal samples. Data was acquired from the UALCAN (http://ualcan.path.uab.edu/). **(B)** Representative protein expression levels of each gene in tumor tissues and normal tissues. Data resourced from The Human Protein Atlas. **(C)** The genetic variation of six genes in the gene signature. The data was derived from the cBioPortal database (https://www.cbioportal.org/).

fatty acid free radicals, which can lead to ferroptosis (35, 36). Additionally, some studies had clarified that GPX4 is closely related to the occurrence and development of tumors (37–39).

Pyroptosis is also called Gasdermin (GSDM)-mediated programmed cell death. Both GSDMD and GSDME belong to the GSDM family, which are the most important proteins that affect pyroptosis. Cleaved by activated cysteine aspartate-specific protease (caspase), GSDM family releases the N-terminal domain to punch holes in cellular membranes and cause the cells to swell, burst and die (40, 41).

Interleukin 6 (IL-6) is a soluble mediator that is rapidly produced in the acute phase of infection or tissue damage, and promotes host defense by stimulating hematopoiesis, acute phase inflammation and immune response. IL-6 is a typical inflammatory cytokine that plays an important role in host defense. When infection, tissue damage or cancer occurs, IL-6 can be rapidly released from monocytes, macrophages and even fat cells. IL6 plays an important regulatory role in the occurrence and development of diseases (42, 43).

Nucleotide-binding oligomerization domain containing two (NOD2) is a member of the NOD1/Apaf-1 family involved in the regulation of apoptosis. The N-terminal encodes two Caspase Recruitment (CARD) domains, and the C-terminal consists of ten linked leucine-rich repeats (LRR). On one hand, NOD2 promotes apoptosis mainly by inducing the expression of Caspase-9. On the other hand, it can mediate the host immune response by recognizing bacterial pathogenic components such as lipopolysaccharide (LPS) in the cytoplasm, especially playing an important role in gastrointestinal immunity (44–46).

Encoding apoptosis-associated speck-like protein containing a CARD (ASC) protein, PYCARD gene acts as a key mediator of inflammation and apoptosis, and promotes caspase-mediated apoptosis (47). It mainly recruits and activates caspase-1, participates in the process of cell inflammation and pyroptosis, and plays an important role in inflammatory diseases and a variety of cancers (48, 49).

In short, these genes are closely related to inflammation and cell death. However, how they interact with each other in the process of pyroptosis remains to be studied in depth.

Through functional enrichment analysis of DEGs between high- and low-risk groups, we found that DEGs are mainly involved in immune response, especially humoral immunity. Moreover, the immune infiltration analysis of these DEGs detected that the scores of immune cell infiltration and immune function of the high-risk group were both lower than the low-risk group. It can be speculated that the poor prognosis of patients in the high-risk group may be caused by the reduced immune level. Based on the above gene composition of the risk model and results of function analysis, we can reasonably speculate that pyroptosis is involved in the regulation of tumor immune microenvironment (TIME).

Despite our research deserves a certain degree of affirmation, there are still some limitations. First, if the predictive ability of the gene signature can be verified by RNA sequencing of tissue samples from our institution, it will be better. Second, if we can explore the regulation of these genes on the TIME through *in vivo* and *in vitro* experiments, the research will be more in-depth.

In conclusion, we constructed and validated a pyroptosis-related gene signature associating with immune infiltration to predict the prognosis of EC. This gene signature provides a new choice for the prognosis prediction of EC and is proposed to help precise diagnosis and treatment of EC.

DATA AVAILABILITY STATEMENT

The datasets presented in this study can be found in online repositories. The names of the repository/repositories and accession number(s) can be found in the article/**Supplementary Material**.

AUTHOR CONTRIBUTIONS

YC designed the study and wrote the manuscript under the guidance of SY and JL. YL, QD, and CS participated in data analysis, discussion, and language editing. SQ, KL, and QZ helped statistical analysis. SY and JL contributed to the revision of the manuscript. All authors contributed to the article and approved the submitted version.

FUNDING

This work was supported by grants from the National Natural Science Foundation of China (Nos. 81672561, 81874102, and 82072874 to SY; Nos. 81502226, 81872128, and 82072884 to JL), the Science and Technology Program of Guangzhou (No. 202002020043 to SY), Sun Yat-sen University Clinical Research Foundation of 5010 Project (No. 2017006 to SY), and the Medical Scientific Research Foundation of Guangdong Province (No. A2021030 to SQ).

ACKNOWLEDGMENTS

We thank the National Natural Science Foundation of China for the grant funding. We also acknowledge the contributions from TCGA, UALCAN, cBioPortal, and the Human Protein Atlas database. In addition, we would also appreciate the developers of all the R packages mentioned in our study.

SUPPLEMENTARY MATERIAL

The Supplementary Material for this article can be found online at: https://www.frontiersin.org/articles/10.3389/fmed.2022.822806/full#supplementary-material

REFERENCES

1. Sung H, Ferlay J, Siegel RL, Laversanne M, Soerjomataram I, Jemal A, et al. Global cancer statistics 2020: GLOBOCAN estimates of incidence and mortality worldwide for 36 cancers in 185 countries. *CA Cancer J Clin.* (2021) 71:209–49. doi: 10.3322/caac.21660
2. Siegel RL, Miller KD, Jemal A. Cancer statistics, 2019. *CA Cancer J Clin.* (2019) 69:7–34. doi: 10.3322/caac.21551
3. Morice P, Leary A, Creutzberg C, Abu-Rustum N, Darai E. Endometrial cancer. *Lancet.* (2016) 387:1094–108. doi: 10.1016/S0140-6736(15)00130-0
4. McGunigal M, Liu J, Kalir T, Chadha M, Gupta V. Survival differences among uterine papillary serous, clear cell and grade 3 endometrioid adenocarcinoma

endometrial cancers: a national cancer database analysis. *Int J Gynecol Cancer.* (2017) 27:85–92. doi: 10.1097/IGC.0000000000000844

5. Urick ME, Bell DW. Clinical actionability of molecular targets in endometrial cancer. *Nat Rev Cancer.* (2019) 19:510–21. doi: 10.1038/s41568-019-0177-x
6. Clarke MA, Long BJ, Del Mar Morillo A, Arbyn M, Bakkum-Gamez JN, Wentzensen N. Association of endometrial cancer risk with postmenopausal bleeding in women: a systematic review and meta-analysis. *JAMA Intern Med.* (2018) 178:1210–22. doi: 10.1001/jamainternmed.2018.2820
7. Kinde I, Bettegowda C, Wang Y, Wu J, Agrawal N, Shih Ie M, et al. Evaluation of DNA from the Papanicolaou test to detect ovarian and endometrial cancers. *Sci Transl Med.* (2013) 5:167ra164. doi: 10.1126/scitranslmed.3004952
8. Bergsbaken T, Fink SL, Cookson BT. Pyroptosis: host cell death and inflammation. *Nat Rev Microbiol.* (2009) 7:99–109. doi: 10.1038/nrmicro2070
9. Tan Y, Chen Q, Li X, Zeng Z, Xiong W, Li G, et al. Pyroptosis: a new paradigm of cell death for fighting against cancer. *J Exp Clin Cancer Res.* (2021) 40:153. doi: 10.1186/s13046-021-02101-7
10. Wang L, Qin X, Liang J, Ge P. Induction of pyroptosis: a promising strategy for cancer treatment. *Front Oncol.* (2021) 11:635774. doi: 10.3389/fonc.2021.635774
11. Fink SL, Cookson BT. Caspase-1-dependent pore formation during pyroptosis leads to osmotic lysis of infected host macrophages. *Cell Microbiol.* (2006) 8:1812–25. doi: 10.1111/j.1462-5822.2006.00751.x
12. Yang Y, Liu PY, Bao W, Chen SJ, Wu FS, Zhu PY. Hydrogen inhibits endometrial cancer growth via a ROS/NLRP3/caspase-1/GSDMD-mediated pyroptotic pathway. *BMC Cancer.* (2020) 20:28. doi: 10.1186/s12885-019-6491-6
13. Qiao L, Wu X, Zhang J, Liu L, Sui X, Zhang R, et al. alpha-NETA induces pyroptosis of epithelial ovarian cancer cells through the GSDMD/caspase-4 pathway. *FASEB J.* (2019) 33:12760–7. doi: 10.1096/fj.201900483RR
14. Matikainen S, Nyman TA, Cypryk W. Function and regulation of noncanonical caspase-4/5/11 inflammasome. *J Immunol.* (2020) 204:3063–9. doi: 10.4049/jimmunol.2000373
15. Wang Y, Gao W, Shi X, Ding J, Liu W, He H, et al. Chemotherapy drugs induce pyroptosis through caspase-3 cleavage of a gasdermin. *Nature.* (2017) 547:99–103. doi: 10.1038/nature22393
16. Jiang M, Qi L, Li L, Li Y. The caspase-3/GSDME signal pathway as a switch between apoptosis and pyroptosis in cancer. *Cell Death Discov.* (2020) 6:112. doi: 10.1038/s41420-020-00349-0
17. Erkes DA, Cai W, Sanchez IM, Purwin TJ, Rogers C, Field CO, et al. Mutant BRAF and MEK inhibitors regulate the tumor immune microenvironment via pyroptosis. *Cancer Discov.* (2020) 10:254–69. doi: 10.1158/2159-8290.CD-19-0672
18. Hou J, Zhao R, Xia W, Chang CW, You Y, Hsu JM, et al. PD-L1-mediated gasdermin C expression switches apoptosis to pyroptosis in cancer cells and facilitates tumour necrosis. *Nat Cell Biol.* (2020) 22:1264–75. doi: 10.1038/s41556-020-0575-z
19. Zhang Z, Zhang Y, Xia S, Kong Q, Li S, Liu X, et al. Gasdermin E suppresses tumour growth by activating anti-tumour immunity. *Nature.* (2020) 579:415–20. doi: 10.1038/s41586-020-2071-9
20. Tang R, Xu J, Zhang B, Liu J, Liang C, Hua J, et al. Ferroptosis, necroptosis, and pyroptosis in anticancer immunity. *J Hematol Oncol.* (2020) 13:110. doi: 10.1186/s13045-020-00946-7
21. Wree A, McGeough MD, Inzaugarat ME, Eguchi A, Schuster S, Johnson CD, et al. NLRP3 inflammasome driven liver injury and fibrosis: Roles of IL-17 and TNF in mice. *Hepatology.* (2018) 67:736–49. doi: 10.1002/hep.29523
22. Xia X, Wang X, Cheng Z, Qin W, Lei L, Jiang J, et al. The role of pyroptosis in cancer: pro-cancer or pro-"host"? *Cell Death Dis.* (2019) 10:650. doi: 10.1038/s41419-019-1883-8
23. Tang Z, Ji L, Han M, Xie J, Zhong F, Zhang X, et al. Pyroptosis is involved in the inhibitory effect of FL118 on growth and metastasis in colorectal cancer. *Life Sci.* (2020) 257:118065. doi: 10.1016/j.lfs.2020.118065
24. An H, Heo JS, Kim P, Lian Z, Lee S, Park J, et al. Tetraarsenic hexoxide enhances generation of mitochondrial ROS to promote pyroptosis by inducing the activation of caspase-3/GSDME in triple-negative breast cancer cells. *Cell Death Dis.* (2021) 12:159. doi: 10.1038/s41419-021-03454-9
25. Wu M, Shi J, He S, Wang D, Zhang N, Wang Z, et al. cGAS promotes sepsis in radiotherapy of cancer by up-regulating caspase-11 signaling. *Biochem Biophys Res Commun.* (2021) 551:86–92. doi: 10.1016/j.bbrc.2021.03.003
26. Ye Y, Dai Q, Qi H. A novel defined pyroptosis-related gene signature for predicting the prognosis of ovarian cancer. *Cell Death Discov.* (2021) 7:71. doi: 10.1038/s41420-021-00451-x
27. Chandrashekar DS, Bashel B, Balasubramanya SAH, Creighton CJ, Ponce-Rodriguez I, Chakravarthi B, et al. UALCAN: A Portal for Facilitating Tumor Subgroup Gene Expression and survival analyses. *Neoplasia.* (2017) 19:649–58. doi: 10.1016/j.neo.2017.05.002
28. Uhlen M, Fagerberg L, Hallstrom BM, Lindskog C, Oksvold P, Mardinoglu A, et al. Proteomics. Tissue-based map of the human proteome. *Science.* (2015) 347:1260419. doi: 10.1126/science.1260419
29. Uhlen M, Zhang C, Lee S, Sjostedt E, Fagerberg L, Bidkhori G, et al. A pathology atlas of the human cancer transcriptome. *Science.* (2017) 357:6352. doi: 10.1126/science.aan2507
30. Cerami E, Gao J, Dogrusoz U, Gross BE, Sumer SO, Aksoy BA, et al. The cBio cancer genomics portal: an open platform for exploring multidimensional cancer genomics data. *Cancer Discov.* (2012) 2:401–4. doi: 10.1158/2159-8290.CD-12-0095
31. Gao J, Aksoy BA, Dogrusoz U, Dresdner G, Gross B, Sumer SO, et al. Integrative analysis of complex cancer genomics and clinical profiles using the cBioPortal. *Sci Signal.* (2013) 6:pl1. doi: 10.1126/scisignal.2004088
32. Shang C, Wang W, Liao Y, Chen Y, Liu T, Du Q, et al. LNMICC promotes nodal metastasis of cervical cancer by reprogramming fatty acid metabolism. *Cancer Res.* (2018) 78:877–90. doi: 10.1158/0008-5472.CAN-17-2356
33. Du Q, Wang W, Liu T, Shang C, Huang J, Liao Y, et al. High expression of integrin alpha3 predicts poor prognosis and promotes tumor metastasis and angiogenesis by activating the c-src/extracellular signal-regulated protein kinase/focal adhesion kinase signaling pathway in cervical cancer. *Front Oncol.* (2020) 10:36. doi: 10.3389/fonc.2020.00036
34. Li Q, Wang W, Zhang M, Sun W, Shi W, Li F. Circular RNA circ-0016068 promotes the growth, migration, and invasion of prostate cancer cells by regulating the miR-330-3p/BMI-1 axis as a competing endogenous RNA. *Front Cell Dev Biol.* (2020) 8:827. doi: 10.3389/fcell.2020.00827
35. Cardoso BR, Hare DJ, Bush AI, Roberts BR. Glutathione peroxidase 4: a new player in neurodegeneration? *Mol Psychiatry.* (2017) 22:328–35. doi: 10.1038/mp.2016.196
36. Seibt TM, Proneth B, Conrad M. Role of GPX4 in ferroptosis and its pharmacological implication. *Free Radic Biol Med.* (2019) 133:144–52. doi: 10.1016/j.freeradbiomed.2018.09.014
37. Yang WS, SriRamaratnam R, Welsch ME, Shimada K, Skouta R, Viswanathan VS, et al. Regulation of ferroptotic cancer cell death by GPX4. *Cell.* (2014) 156:317–31. doi: 10.1016/j.cell.2013.12.010
38. Hangauer MJ, Viswanathan VS, Ryan MJ, Bole D, Eaton JK, Matov A, et al. Drug-tolerant persister cancer cells are vulnerable to GPX4 inhibition. *Nature.* (2017) 551:247–50. doi: 10.1038/nature24297
39. Xu C, Sun S, Johnson T, Qi R, Zhang S, Zhang J, et al. The glutathione peroxidase Gpx4 prevents lipid peroxidation and ferroptosis to sustain Treg cell activation and suppression of antitumor immunity. *Cell Rep.* (2021) 35:109235. doi: 10.1016/j.celrep.2021.109235
40. Orning P, Lien E, Fitzgerald KA. Gasdermins and their role in immunity and inflammation. *J Exp Med.* (2019) 216:2453–65. doi: 10.1084/jem.20190545
41. De Schutter E, Roelandt R, Riquet FB, Van Camp G, Wullaert A, Vandenabeele P. Punching holes in cellular membranes: biology and evolution of gasdermins. *Trends Cell Biol.* (2021) 31:500–13. doi: 10.1016/j.tcb.2021.03.004
42. Tanaka T, Narazaki M, Kishimoto T. IL-6 in inflammation, immunity, and disease. *Cold Spring Harb Perspect Biol.* (2014) 6:a016295. doi: 10.1101/cshperspect.a016295
43. Hunter CA, Jones SA. IL-6 as a keystone cytokine in health and disease. *Nat Immunol.* (2015) 16:448–57. doi: 10.1038/ni.3153
44. Ogura Y, Inohara N, Benito A, Chen FF, Yamaoka S, Nunez G. Nod2, a Nod1/Apaf-1 family member that is restricted to monocytes and activates NF-kappaB. *J Biol Chem.* (2001) 276:4812–8. doi: 10.1074/jbc.M008072200
45. Berrebi D, Maudinas R, Hugot JP, Chamaillard M, Chareyre F, De Lagausie P, et al. Card15 gene overexpression in mononuclear and epithelial cells of the inflamed Crohn's disease colon. *Gut.* (2003) 52:840–6. doi: 10.1136/gut.52.6.840

46. Trindade BC, Chen GY. NOD1 and NOD2 in inflammatory and infectious diseases. *Immunol Rev.* (2020) 297:139–61. doi: 10.1111/imr.12902
47. Protti MP, De Monte L. Dual role of inflammasome adaptor ASC in cancer. *Front Cell Dev Biol.* (2020) 8:40. doi: 10.3389/fcell.2020.00040
48. Agrawal I, Jha S. Comprehensive review of ASC structure and function in immune homeostasis and disease. *Mol Biol Rep.* (2020) 47:3077–96. doi: 10.1007/s11033-020-05345-2
49. de Souza JG, Starobinas N, Ibanez OCM. Unknown/enigmatic functions of extracellular ASC. *Immunology.* (2021) 163:377–88. doi: 10.1111/imm.13375

Conflict of Interest: The authors declare that the research was conducted in the absence of any commercial or financial relationships that could be construed as a potential conflict of interest.

frontiers
in Oncology

ORIGINAL RESEARCH
published: 02 March 2022
doi: 10.3389/fonc.2022.841438

Factors Influencing Total Delay of Breast Cancer in Northeast of China

Sihang Ren[1], *Yuting Zhang*[2], *Pan Qin*[3*] *and Jia Wang*[1*]

[1] Department of Breast Surgery, Institute of Breast Disease, The Second Hospital of Dalian Medical University, Dalian, China, [2] Dalian No.3 People's Hospital, Dalian Medical University, Dalian, China, [3] Faculty of Electronic Information and Electrical Engineering, Dalian University of Technology, Dalian, China

Objectives: Delay in diagnosis and treatment, called total delay, could probably result in lower survival rates in breast cancer patients. This study aimed to investigate the factors associated with the comprehensive delay behaviors and to evaluate its effect on outcomes in patients with breast cancer in Dalian, a northeast city of China.

Methods: A retrospective chart review was conducted using a cancer registry dataset including 298 patients. The Kaplan–Meier survival analysis was used to identify the threshold of total delay, dividing the patients into a group with significant uncertainty and a group without substantial delay. The factors associated with the significant total delay were investigated from the potential candidates, like income level and marital status, by using the chi-squared test. The difference of the clinicopathologic characteristics between the patients grouped by the significant total delay, like tumor size and lymph node metastasis, was also investigated to find out the effect of the total delay.

Results: A total of 238 charts were used for analysis. The mean age was 57.3. The median of total delays was 3.75 months. Thirty days was identified as a threshold, more than which the total delay can lead to worse survival. Patients' marital status ($p = 0.010$), income levels ($p = 0.003$), smoking status ($p = 0.031$), initial visiting hospital level ($p = 0.005$), self-health care ($p = 0.001$), and self-concern about initial symptom ($p \approx 0.000$) were identified as the independent predictors of the total delay. Metastasis ($p \approx 0.000$) was identified as the significant result relating to the significant total delay.

Conclusions: A total delay of more than 30 days predicts worse survival in breast cancer patients in Dalian. Several factors, like patients' marital status and income levels, can be considered to be relevant to the significant total delay. We recommend that these factors be used to predict the potential patients with the significant total delay in the clinical practice.

Keywords: breast cancer, total delay, survival analysis, logistic regression, individual–environmental–social factors

Edited by:
Fu Wang,
Xi'an Jiaotong University, China

Reviewed by:
Bo Chen,
The First Affiliated Hospital of China Medical University, China
Yan Zhang,
Jilin University, China
Baoliang Guo,
Harbin Medical University, China

****Correspondence:***
Jia Wang
wang2004@dmu.edu.cn
Pan Qin
qp112cn@dlut.edu.cn

Specialty section:
This article was submitted to Breast Cancer, a section of the journal Frontiers in Oncology

Received: *24 December 2021*
Accepted: *19 January 2022*
Published: *02 March 2022*

Citation:
Ren S, Zhang Y, Qin P and Wang J (2022) Factors Influencing Total Delay of Breast Cancer in Northeast of China. Front. Oncol. 12:841438. doi: 10.3389/fonc.2022.841438

INTRODUCTION

According to the National Central Cancer Registry of China, breast cancer is the dominant cause of cancer death in women younger than 45 years (1). Longer delays of diagnosis and initial therapy have been reported to result in cancer progression and poor survival (2, 3). This research investigated the socioeconomic factors and the clinical consequences associated with the total delay of breast cancer in Chinese women. The total delay includes two parts: 1) patient delay denotes the interval between the patient's self-discovery of symptoms and the initial diagnosis; and 2) system delay denotes the interval between the initial diagnosis and the standard medical treatment. Patient delay always occurs in developing countries, and studies have reported that poor outcomes induced by patient delay are mainly due to low education and poor income status (4). Whether patient delay or system delay, some questions are pending, like the correct period of uncertainty and the possible associated factors that we could use to predict the delay cohort. Several works have investigated the associated delay factors for breast cancer patients, which show that the factors were diverse. Studies have shown that a lack of knowledge about breast cancer symptoms and screening methods is an essential factor in delaying diagnosis and seeking medical attention (5). The individual–environmental–social factors, like lower socioeconomic and recent immigration, were likely to delay medical help (6, 7). A study in South Africa found that most patients who delayed seeking help blamed poor transportation or treatment that interfered with work, dating, or even marriage (8). A cross-sectional study from China linked patient delay to perceived health competence (9). As shown by Khakbazan (10), some of the factors associated with the delay identified previously could not be generalized for different regions and races. For this reason, we collected the clinical data to infer the length of the total delay associated with the mortality, and we investigated the key factors influencing the total delay of breast cancer for women in the northeast of China.

MATERIALS AND METHODS

This cross-sectional study was conducted by data of patients diagnosed with breast cancers in the second hospital of Dalian Medical University between January 1, 2012, and December 31, 2012. Pathologists confirmed the diagnosis of breast cancer after surgery or core needle biopsy. Patients who did not complete standard adjuvant therapy were excluded. Patients with breast cancer were interviewed at the department of breast surgery after obtaining the agreement from each patient. We collected the information from the medical records of these patients. The follow-up questionnaire was conducted by phone call following the second year after patient diagnosis. All of the interviewers were previously trained residents not involved in the clinical management of the patients. We also excluded those patients who had no complete follow-up information. The record collection includes the following medical factors: initial symptom, family history of cancer, tumor molecular subtype, TNM stage, and metastasis. It also includes sociodemographic factors: age at presentation, marital status, marriage bonds, education level, residence, attitude to help-seeking, smoking habit, alcohol drinking patterns, insurance types, level of first visiting hospitals, occupation status, and self-health care. The results were analyzed using SPSS (version 25.0) and R language (version 3.5.1). We defined the significant total delay as the minimum delay leading to poor survival. The Kaplan–Meier survival analysis identifies the threshold for the significant total delay. The hypothesis test was used to distinguish the factors associated with the delay. Then, the label "1" was assigned to the patients with significant total delay and "0" to the patients without significant total delay. The multivariate logistic regression model was constructed concerning these labels to verify the factors identified using the hypothesis test.

RESULTS

Study Population

A total of 296 charts were reviewed for this study. Fifty-seven charts did not meet inclusion criteria, and 238 charts were used for analysis. The sociodemographic characteristics of patients are illustrated in **Table 1**. In all patients, the mean age of patients was 57.3 ± 12.1 years. One hundred twenty-four (52.1%) patients resided in urban areas. One hundred two (42.4%) patients were single, where single included unmarried, divorced, and windowed. One hundred four (43.5%) patients were part-time employed, and 91 patients (38.1%) were full-time employed. One hundred sixty-four (62.8%) patients' education levels were higher school or above. About the insurance status, 213 (89.1%) patients were with Medicare or Medicaid. One hundred eighteen (49.4%) patients were with no or low income. Fifty-five patients (22.2%) initially visited small local clinics. Ninety (37.7%) patients were self-concerned about the initial symptoms. Forty-six (19.2%) patients were smoking. Only 2 (0.8%) patients have an alcohol drinking habit. Forty-two (17.6%) patients conducted self-health care after discovering symptoms, like breast massage and taking traditional Chinese medicine. The medical history of patients is listed in **Table 2**. In all patients, the median of total delay was 3 months (0.1–12). Thirty-one (13.0%) died. Two hundred seven (87.0%) patients' initial symptoms were lump, six (2.5%) patients' initial symptoms were nipple changes, and fifteen (6.3%) patients' initial symptoms were breast pain. Two hundred four (85.7%) patients have no family history of cancer. Metastasis happened in 75 (31.5%) patients. About the pathological types, triple-negative, HER2-enrich, Luminal A, and HR+HER2+ were diagnosed in 41 (17.2%), 12 (5.0%), 115 (48.1%), and 58 (24.3%), respectively. In all patients, the mean tumor size is 2.7 ± 1.8 cm. The detailed population of TNM classification can also be found in **Table 2**.

Total Delay of 30 Days Affecting Survival

We conducted the Kaplan–Meier survival analysis to investigate how long the total delay can affect the survival of patients. To test the significant difference in survival, we divided the patients into two groups by a threshold value of total delay. The threshold value was initially set as 10 days and was sequentially added by 10 days. We found that the total delay of 30 days can lead to significantly different survival curves (**Figure 1**). Therefore, we divided the patients into two groups: one group included the patients with total delays less than 30 days, and one group included the patients with total delays of more than 30 days.

TABLE 1 | Sociodemographic characteristics of patients (n = 238).

		N (%)
Age at presentation (years)	Mean (± SD)	57.3 ± 12.1
Area of residence	Rural	114 (47.9)
	Urban	124 (52.1)
Marital status	Married	137 (57.6)
	Single, divorced, or widowed	101 (42.4)
Occupation	No occupation	44 (18.5)
	Part-time employed	103 (43.3)
	Full time employed	91 (38.2)
Education level	Secondary or below	88 (37.0)
	Higher or above	150 (63.0)
Insurance	Self-pay	25 (10.5)
	Rural cooperative medical care	46 (19.3)
	Social insurance	167 (69.9)
Income level	No or low income	117 (49.2)
	Middle class or upper	121 (50.8)
Initial visiting hospital level	Small local clinic	55 (22.2)
	Large pandocheum	203 (77.8)
Self-concern about initial symptom	Yes	90 (37.8)
	No	148 (62.2)
Smoking	Yes	46 (19.3)
	No	192 (80.7)
Alcohol drinking habit	Yes	2 (0.8)
	No	236 (99.2)
Self-health care	Yes	42 (17.6)
	No	196 (82.4)

TABLE 2 | Medical history of patients (n = 239).

		N (%)
Total delay (months)	Median [IQR]	3 [0.1, 12]
Vital status	Alive	207 (87.0)
	Dead	31 (13.0)
Initial symptom	Lump	208 (87.0)
	Nipple changes	7 (2.5)
	Breast pain	12 (6.3)
	Other	10 (4.2)
Family history of cancer	Yes	35 (14.6)
	No	203 (85.4)
Metastasis	Yes	75 (31.5)
	No	161 (67.6)
	Unknown	2 (0.8)
Pathological type	Triple-negative	41 (17.2)
	HER2-enrich	12 (5.0)
	Luminal A	115 (48.1)
	HR+HER2+	58 (24.3)
Tumor size	Mean (± SD)	2.7 (± 1.8)
TNM classification		
T	T0	1 (0.4)
	TI	120 (50.4)
	T2	105 (44.1)
	T3	8 (3.3)
	T4	1 (0.4)
	Unknown	3 (1.3)
N	N0	117 (49.2)
	N1	112 (47.1)
	N2	6 (2.5)
	Unknown	3 (1.3)
M	M0	235 (98.7)
	M1	3 (1.3)

IQR, interquartile range.

Significance Test for Grouped Patients

We also conducted the chi-squared test for the nominal variables to identify the significantly different factors for the grouped patients. Their marital status (p = 0.02), income levels (p = 0.003), smoking status (p = 0.03), insurance (p = 0.03), initial visiting hospital levels (p = 0.005), self-health care (p = 0.01), self-concern about initial symptom (p ≈ 0), and metastasis (p ≈ 0) were significantly different.

We consequently constructed the binomial logistic regression model by using the aforementioned significantly different variables as the covariates. The model has a percentage correction of 80.7%, which implies that significantly different factors can be used as the features for the classification of total delay.

DISCUSSION

Our study first found that the total delay of 30 days can lead to significantly different survival rates. The studies conducted in other countries and areas indicated that the diagnosis delay of cancers ranged from 2 to 15.2 weeks (11–16). Primarily, Ramirez evaluated 87 studies and suggested that the delay of 3 months could impact the long-term survival of breast cancer patients (11). Compared with this result, the delay in our investigated area was more pressing for the patients.

Various factors can prompt breast cancer patients to ignore their problems and delay medical treatment. The individual–environmental–social factors have been associated with the delay (17–19). According to the further application of the investigation results, we used the individual–environmental–social factors, including education level, occupation, income level, place of residence, particular dietary habit, smoking habit, alcohol drinking habit, insurance, marital status, insurance, first visiting the hospital, first consulted person, and self-health care.

According to our results, marital status was identified as an essential factor, not reported by other works. In our investigated area, the patients with no life partner tended to delay the medical diagnosis and treatment. Smoking was a relevant factor for 34 of 46 smoking patients who delayed seeking help. The smoking rate in our investigated cohort was 19.5%, much higher than the average level in China (the current smoking rate is 0.6%, and the ever-smoked rate is 3.4% among Chinese women) (20). Thus, the smoking status should be considered as an important factor in our investigated area.

Our results also indicated that patients with a low-income level were often associated with longer delays. This fact reflects the same panorama of other developing countries; e.g., Maghous and Fedewa confirmed that socioeconomic status appears to have a negative impact (4, 21).

We found that self-health care was a novel factor. Of 42 patients, 35 consequently conducting self-health care, like having a massage and acupuncture, have a longer delay. We suggested that self-health care could strengthen the patients' self-confidence in their health status and become mindful of their symptoms. Atypical presenting symptoms of breast cancer lead

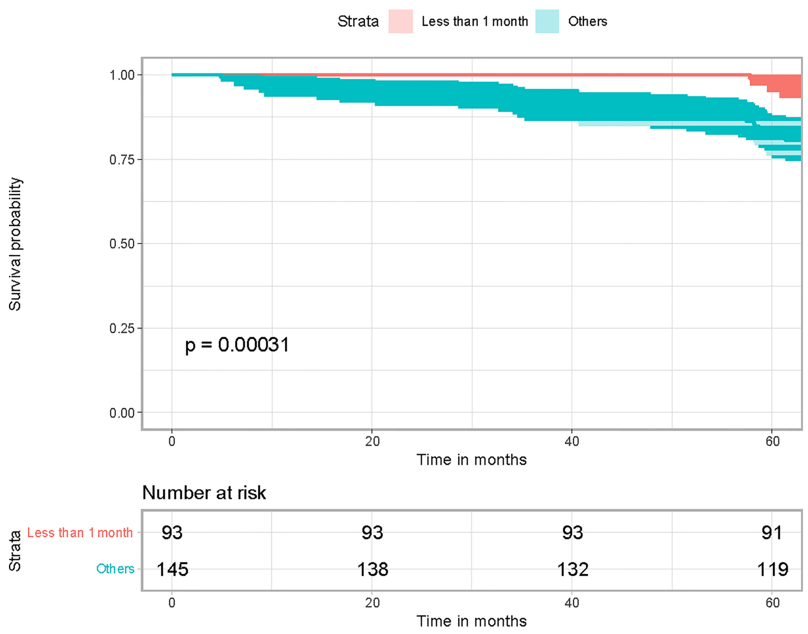

FIGURE 1 | Kaplan–Meier survival analysis results.

to diagnostic intervals. To test this theory, we included the nature of breast masses and symptoms of breast disease. Although the results were not statistically significant, we believe that the study's emphasis on a higher likelihood of delayed treatment for breast cancer patients without tumor symptoms is a reference (22).

Understanding and attention to initial symptoms and monitoring and managing symptoms have been the first and most crucial steps in the help-seeking process after symptom discovery (23, 24). In our study, the initial visiting hospital level and the patient's self-concern about initial symptom were identified to be important factors, which are considered to have effects on the initial symptom interpretation and monitoring. The initial visiting hospital level was also identified as an essential factor associated with the delays. Forty of 52 patients who initially visited the small local clinic have delays. Women's trust in the physicians' professionalism was identified to affect patients' help-seeking behavior (19, 25). This implied that the small clinics around Dalian city could not often offer proper initial symptom interpretation and monitoring. A total of 122 of 148 patients without self-concern about initial symptoms were identified to have delays. The reasons for negative attitudes toward the symptoms could be diverse. Economic status was the limiting factor for some patients. Some patients obtained the wrong symptom interpretation. The embarrassment of breast examination derived from traditional attitude could be the barriers to receiving care in Chinese middle-aged women (10).

Khokher stated that some of the factors associated with the delay identified previously could not be generalized for different races and regions (2). For example, Bleicher and Polverini have reported that the African American race was associated with delays in diagnosis and treatment (26, 27). However, the African American race often did not make up a higher percentage of Medicaid beneficiaries (28). Thus, rather than the race itself, the difference of economics between races can be considered a factor for the delay. However, such difference was not significant in Dalian, and as a result, ethics was not considered a potential factor.

To investigate what the delay will lead to, we also analyzed the difference between the delay and non-delay patients for the disease-associated factors, including the age of onset, initial symptom, family history of tumor, TNM stage, and molecular subtype. We found that 60 of 75 patients with metastasis have delays. This fact proved that the identified delay of 30 days could lead to advanced breast cancer.

As with other data analysis studies, this one has limitations. The data used in this research were collected from one large comprehensive hospital, which covered a quarter of patients in Dalian city. Our samples were not nationally representative due to its inclusion of patients seeking care at a single medical center. We did not group the negative attitudes to the symptoms, which could be directly related to other factors, like income level or self-health care. However, a similar study in Guangzhou, China, supports our research and shows that premenopausal patient status, breast disease history, and delayed physical examination affect the timing of patients' visits (29).

Some studies show that the problem of delayed treatment is not very serious and that there is an ultimate delay time within which delayed treatment seems to be tolerated. Optimal times from diagnosis are <90 days for surgery, <120 days for chemotherapy, and, where chemotherapy is administered, <365 days for radiotherapy (30). The worldwide panic caused by COVID-19, the complication of medical procedures, and the difficulty of medical treatment for middle-aged and elderly patients have also primarily affected the enthusiasm of patients seeking medical treatment. However, as the influence of this period was not included in this study, no further details can be given (31).

In the future, we will also keep collecting data to testify and justify the statistical inference. We will propose an efficient prediction method for the patients' delay status based on our identified factors. With the prediction method, we finally want to optimize the help-seeking behavior of the patients to shorten the delay.

DATA AVAILABILITY STATEMENT

The original contributions presented in the study are included in the article/supplementary material. Further inquiries can be directed to the corresponding authors.

ETHICS STATEMENT

The studies involving human participants were reviewed and approved by the Second Affiliated Hospital of Dalian Medical University. The patients/participants provided their written informed consent to participate in this study.

AUTHOR CONTRIBUTIONS

SR, JW, and PQ wrote the manuscript and collected and cleaned the dataset. PQ and JW conducted the statistical analysis. SR, YZ, PQ, and JW edited the manuscript. All authors listed have made a substantial, direct, and intellectual contribution to the work and approved it for publication.

FUNDING

This work was supported by the National Natural Science Research Foundation of China (81872247).

REFERENCES

1. Chen W, Zheng R, Baade PD, Zhang S, Zeng H, Bray F, et al. Cancer Statistics in China, 2015. *CA: Cancer J Clin* (2016) 66(2):115–32. doi: 10.3322/caac.21338
2. Khokher S, Qureshi MU, Mahmood S, Sadiq S. Determinants of Advanced Stage at Initial Diagnosis of Breast Cancer in Pakistan: Adverse Tumor Biology vs Delay in Diagnosis. *Asian Pac J Cancer Prev* (2016) 17(2):759–65. doi: 10.7314/APJCP.2016.17.2.759
3. Unger-Saldana K, Miranda A, Zarco-Espinosa G, Mainero-Ratchelous F, Bargallo-Rocha E, Miguel Lazaro-Leon J. Health System Delay and its Effect on Clinical Stage of Breast Cancer: Multicenter Study. *Cancer* (2015) 121(13):2198–206. doi: 10.1002/cncr.29331
4. Maghous A, Rais F, Ahid S, Benhmidou N, Bellahamou K, Loughlimi H, et al. Factors Influencing Diagnosis Delay of Advanced Breast Cancer in Moroccan Women. *BMC Cancer* (2016) 16:356. doi: 10.1186/s12885-016-2394-y
5. Dye TD, Bogale S, Hobden C, Tilahun Y, Deressa T, Reeler A. Experience of Initial Symptoms of Breast Cancer and Triggers for Action in Ethiopia. *Int J Breast Cancer* (2012) 2012:908547. doi: 10.1155/2012/908547
6. Lam WW, Tsuchiya M, Chan M, Chan SW, Or A, Fielding R. Help-Seeking Patterns in Chinese Women With Symptoms of Breast Disease: A Qualitative Study. *J Public Health (Oxf)* (2009) 31(1):59–68. doi: 10.1093/pubmed/fdn088
7. Unger-Saldana K, Infante-Castaneda CB. Breast Cancer Delay: A Grounded Model of Help-Seeking Behaviour. *Soc Sci Med* (2011) 72(7):1096–104. doi: 10.1016/j.socscimed.2011.01.022
8. Rayne S, Schnippel K, Kruger D, Benn CA, Firnhaber C. Delay to Diagnosis and Breast Cancer Stage in an Urban South African Breast Clinic. *South Afr Med J = Suid-Afrikaanse Tydskrif Vir Geneeskunde* (2019) 109(3):159–63. doi: 10.7196/SAMJ.2019.v109i3.13283
9. Zhang H, Wang G, Zhang J, Lu Y, Jiang X. Patient Delay and Associated Factors Among Chinese Women With Breast Cancer: A Cross-Sectional Study. *Medicine* (2019) 98(40):e17454. doi: 10.1097/MD.0000000000017454
10. Khakbazan Z, Taghipour A, Latifnejad Roudsari R, Mohammadi E. Help Seeking Behavior of Women With Self-Discovered Breast Cancer Symptoms: A Meta-Ethnographic Synthesis of Patient Delay. *PloS One* (2014) 9(12):e110262. doi: 10.1371/journal.pone.0110262
11. Ramirez AJ, Westcombe AM, Burgess CC, Sutton S, Littlejohns P, Richards MA. Factors Predicting Delayed Presentation of Symptomatic Breast Cancer: A Systematic Review. *Lancet* (1999) 353(9159):1127–31. doi: 10.1016/S0140-6736(99)02142-X
12. Mitchell E, Macdonald S, Campbell NC, Weller D, Macleod U. Influences on Pre-Hospital Delay in the Diagnosis of Colorectal Cancer: A Systematic Review. *Br J Cancer* (2008) 98(1):60–70. doi: 10.1038/sj.bjc.6604096
13. Macleod U, Mitchell ED, Burgess C, Macdonald S, Ramirez AJ. Risk Factors for Delayed Presentation and Referral of Symptomatic Cancer: Evidence for Common Cancers. *Br J Cancer* (2009) 101(Suppl 2):S92–101. doi: 10.1038/sj.bjc.6605398
14. Waller J, Robb K, Stubbings S, Ramirez A, Macleod U, Austoker J, et al. Awareness of Cancer Symptoms and Anticipated Help Seeking Among Ethnic Minority Groups in England. *Br J Cancer* (2009) 101(Suppl 2):S24–30. doi: 10.1038/sj.bjc.6605387
15. Forbes LJ, Atkins L, Thurnham A, Layburn J, Haste F, Ramirez AJ. Breast Cancer Awareness and Barriers to Symptomatic Presentation Among Women From Different Ethnic Groups in East London. *Br J Cancer* (2011) 105(10):1474–9. doi: 10.1038/bjc.2011.406
16. Smith SM, Campbell NC, MacLeod U, Lee AJ, Raja A, Wyke S, et al. Factors Contributing to the Time Taken to Consult With Symptoms of Lung Cancer: A Cross-Sectional Study. *Thorax* (2009) 64(6):523–31. doi: 10.1136/thx.2008.096560
17. de Nooijer J, Lechner L, de Vries H. A Qualitative Study on Detecting Cancer Symptoms and Seeking Medical Help; an Application of Andersen's Model of Total Patient Delay. *Patient Educ Couns* (2001) 42(2):145–57. doi: 10.1016/S0738-3991(00)00104-X
18. Harirchi I, Ghaemmaghami F, Karbakhsh M, Moghimi R, Mazaherie H. Patient Delay in Women Presenting With Advanced Breast Cancer: An Iranian Study. *Public Health* (2005) 119(10):885–91. doi: 10.1016/j.puhe.2004.11.005
19. Jones CE, Maben J, Jack RH, Davies EA, Forbes LJ, Lucas G, et al. A Systematic Review of Barriers to Early Presentation and Diagnosis With Breast Cancer Among Black Women. *BMJ Open* (2014) 4(2):e004076. doi: 10.1136/bmjopen-2013-004076
20. Liu S, Zhang M, Yang L, Li Y, Wang L, Huang Z, et al. Prevalence and Patterns of Tobacco Smoking Among Chinese Adult Men and Women: Findings of the 2010 National Smoking Survey. *J Epidemiol Community Health* (2017) 71(2):154–61. doi: 10.1136/jech-2016-207805
21. Fedewa SA, Lerro C, Chase D, Ward EM. Insurance Status and Racial Differences in Uterine Cancer Survival: A Study of Patients in the National Cancer Database. *Gynecol Oncol* (2011) 122(1):63–8. doi: 10.1016/j.ygyno.2011.03.010
22. Koo MM, von Wagner C, Abel GA, McPhail S, Rubin GP, Lyratzopoulos G. Typical and Atypical Presenting Symptoms of Breast Cancer and Their Associations With Diagnostic Intervals: Evidence From a National Audit of Cancer Diagnosis. *Cancer Epidemiol* (2017) 48:140–6. doi: 10.1016/j.canep.2017.04.010
23. Ristvedt SL, Trinkaus KM. Psychological Factors Related to Delay in Consultation for Cancer Symptoms. *Psychooncology* (2005) 14(5):339–50. doi: 10.1002/pon.850

24. Scott SE, McGurk M, Grunfeld EA. The Process of Symptom Appraisal: Cognitive and Emotional Responses to Detecting Potentially Malignant Oral Symptoms. *J Psychosom Res* (2007) 62(6):621–30. doi: 10.1016/j.jpsychores.2006.12.020
25. Drew EM, Schoenberg NE. Deconstructing Fatalism: Ethnographic Perspectives on Women's Decision Making About Cancer Prevention and Treatment. *Med Anthropol Q* (2011) 25(2):164–82. doi: 10.1111/j.1548-1387.2010.01136.x
26. Bleicher RJ, Ruth K, Sigurdson ER, Beck JR, Ross E, Wong YN, et al. Time to Surgery and Breast Cancer Survival in the United States. *JAMA Oncol* (2016) 2 (3):330–9. doi: 10.1001/jamaoncol.2015.4508
27. Polverini AC, Nelson RA, Marcinkowski E, Jones VC, Lai L, Mortimer JE, et al. Time to Treatment: Measuring Quality Breast Cancer Care. *Ann Surg Oncol* (2016) 23(10):3392–402. doi: 10.1245/s10434-016-5486-7
28. Khanna S, Raffals LE. The Microbiome in Crohn's Disease: Role in Pathogenesis and Role of Microbiome Replacement Therapies. *Gastroenterol Clinics North Am* (2017) 46(3):481–92. doi: 10.1016/j.gtc.2017.05.004
29. Li YL, Qin YC, Tang LY, Liao YH, Zhang W, Xie XM, et al. Patient and Care Delays of Breast Cancer in China. *Cancer Res Treat* (2019) 51(3):1098–106. doi: 10.4143/crt.2018.386
30. Bleicher RJ. Timing and Delays in Breast Cancer Evaluation and Treatment. *Ann Surg Oncol* (2018) 25(10):2829–38. doi: 10.1245/s10434-018-6615-2
31. Obeng-Gyasi S, Oppong B, Paskett ED, Lustberg M. Purposeful Surgical Delay and the Coronavirus Pandemic: How Will Black Breast Cancer Patients Fare? *Breast Cancer Res Treat* (2020) 182(3):527–30. doi: 10.1007/s10549-020-05740-0

Conflict of Interest: The authors declare that the research was conducted in the absence of any commercial or financial relationships that could be construed as a potential conflict of interest.

frontiers in Medicine

ORIGINAL RESEARCH
published: 17 March 2022
doi: 10.3389/fmed.2022.840378

The Efficacy and Safety of Transurethral 2 μm Laser Bladder Lesion Mucosal En Bloc Resection in the Treatment of Cystitis Glandularis

*Changyuan Zhao, Kexin Wang, Chao Men, Yue Xin and Haibo Xia**

Department of Urology, Chifeng Cancer Hospital, Chifeng, China

Objective: To study the safety and feasibility of transurethral bladder lesion mucosal en bloc resection with 2 μm laser for cystitis glandularis.

Methods: From July 2018 to July 2019, 58 patients with cystitis glandularis received surgical treatment were selected. All patients in this study were randomly divided into experimental group (transurethral 2 μm laser bladder lesion mucosal en bloc resection) and control group (traditional transurethral resection of bladder lesion mucosal). By analyzing the perioperative and follow-up clinical data of these two operation procedures, we discuss the efficacy and safety of transurethral 2 μm laser bladder lesion mucosal en bloc resection in the treatment of cystitis glandularis.

Results: Patients of two groups received operation successfully without serious complications such as bladder perforation. Compared with the experimental group, the laser treated group hadless bleeding in operation, shorter post-operative catheter indwelling time. These differences were statistically significant. No significant difference existed between two groups in terms of operative time, Bladder flushing time, irritation symptoms of bladder.

Conclusion: Transurethral 2 μm laser bladder lesion mucosal en bloc resection is safe and effective for the treatment of cystitis glandularis, and it is worthy of further clinical application.

Keywords: cystitis glandularis, 2 μm laser, en bloc resection, transurethral, bladder

Edited by:
Fu Wang,
Xi'an Jiaotong University, China

Reviewed by:
Angelo Naselli,
MultiMedica Holding SpA (IRCCS), Italy
Yi Fa-xian,
Inner Mongolia Medical University, China

****Correspondence:***
Haibo Xia
haiboxia8360101@163.com

Specialty section:
This article was submitted to Precision Medicine, a section of the journal Frontiers in Medicine

Received: *21 December 2021*
Accepted: *18 February 2022*
Published: *17 March 2022*

Citation:
Zhao C, Wang K, Men C, Xin Y and Xia H (2022) The Efficacy and Safety of Transurethral 2 μm Laser Bladder Lesion Mucosal En Bloc Resection in the Treatment of Cystitis Glandularis. Front. Med. 9:840378. doi: 10.3389/fmed.2022.840378

INTRODUCTION

Cystitis glandularis is characterized by abnormal proliferation of bladder mucosa caused by multiple factors. In recent years, the incidence of glandular cystitis is gradually increased. The etiology and pathogenesis of glandular cystitis is currently not entirely clear. And related studies have shown that there is a certain association between glandular cystitis and bladder cancer (1, 2). For the treatment of glandular cystitis, some people advocate conservative treatment such as the use of quinolone antibiotics and cyclooxygenase-2 inhibitors (3). There is a view that CG precancerous lesions should be actively treated surgically. There are open surgery methods such as resection of the bladder mucosa after incision of the bladder, partial or total bladder resection, and transurethral surgery for bladder lesions such as transurethral plasma excision or

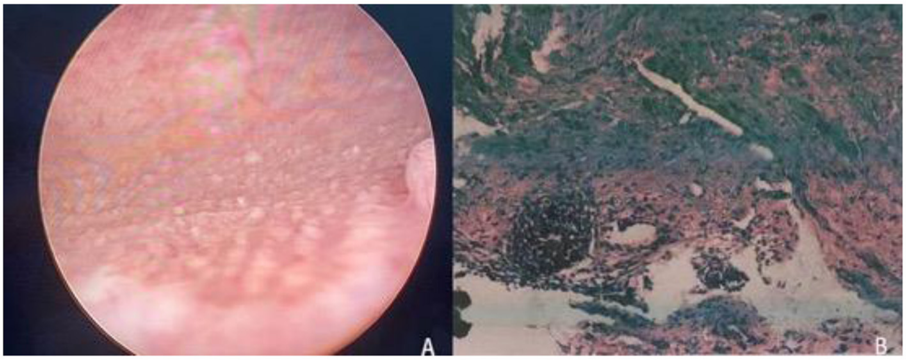

FIGURE 1 | (A) Cystoscopy revealed multiple follicular masses in the trigone of the bladder. **(B)** Pathological examination: the submucosa can be seen with adenoid-shaped cell clusters, and the surface of the glandular lumen is covered with normal urothelial cells (H.E × 40).

laser resection, etc. Due to minimally invasion of body, transurethral bladder lesion mucosal resection has become the main surgical treatment at present, but it has a high recurrence rate. With the development of scientific and technological progress and renewal of a variety of surgical devices, the clinical treatment way of glandular cystitis has varied nowadays. In this study we explored the new surgical method, transurethral 2 μm laser bladder lesion mucosal en bloc resection, and assessed its efficacy and safety for glandular cystitis treatment (4).

MATERIALS AND METHODS

Clinical Data

The patients who were diagnosed with cystitis glandularis from 2018.7 to 2019.7 and received surgical treatment were collected. Inclusion criteria: Patients diagnosed with glandular cystitis by pre-operative cystoscopy and pathological (**Figure 1**). Exclusion criteria: (1) Patients with bladder neck opening obstruction and urethral stricture. (2) Patients who do not want surgery. (3) Patients with contraindications for surgery. Display the results calculated by SPSS, a sample size of 60 patients will give us a power of 0.8 with a α of 0.05. The sample size also takes into account a pre-determined 10% drop rate. Finally, 58 patients with cystitis glandularis received surgical treatment were selected. The enrolled patients were randomly divided into two groups by statistical software: laser group (transurethral 2 μm laser bladder lesion mucosal en bloc resection, 28 cases, 8 males, 20 females,) and TUR group (traditional transurethral resection of bladder lesion mucosal, 30 cases, 6 males, 24 females) (**Figure 2**). Both groups of patients underwent intravesical instillation therapy received epirubicin once a week for 4 consecutive weeks. The average age was 55.46 ± 6.58 (range 30–67) years old in laser group and 55.67 ± 6.8 (range 28–71) years old in TUR group.

General Condition of the Patient

The incidence of glandular cystitis in male patients was lower than female patients in this study (**Table 1**).

Clinical Manifestations

Patients with glandular bladder inflammation mainly suffered bladder irritation such as dysuria, urgency, and frequency, and some patients may have hematuria.

Related Inspections

General Inspection

All patients received complete routine examinations of blood, urine, liver and kidney function, electrolytes, coagulation function, and infectious diseases. Patients need to complete the chest X-ray and ECG examination before the operation. Due to the patient's past medical history, personal medical history, age and other related factors, some patients need to complete other related examinations to exclude surgical contraindications.

Imaging Examination

Urinary System Color Doppler Ultrasound

All patients included in this experiment underwent urinary system color Doppler ultrasound examination before surgery. For male patients, the prostate should also be examined to find out whether the patient has prostate-related lesions.

Abdominal CT

CT examination should be executed to check the degree of lesions of the patient's bladder mucosa, and the relationship between diseased mucosa and different layers of tissues of the bladder, and to determine whether there is extra-bladder invasion and the condition of lymph nodes in the pelvis.

Intravenous Pyelography

For patients with clinical symptoms such as hematuria or hydronephrosis, intravenous pyelography should be executed to exclude upper urinary tract disease.

Cystoscopy Biopsy

All patients included in this experiment underwent cystoscopy before operation and biopsy was proceeded to confirm the diagnosis.

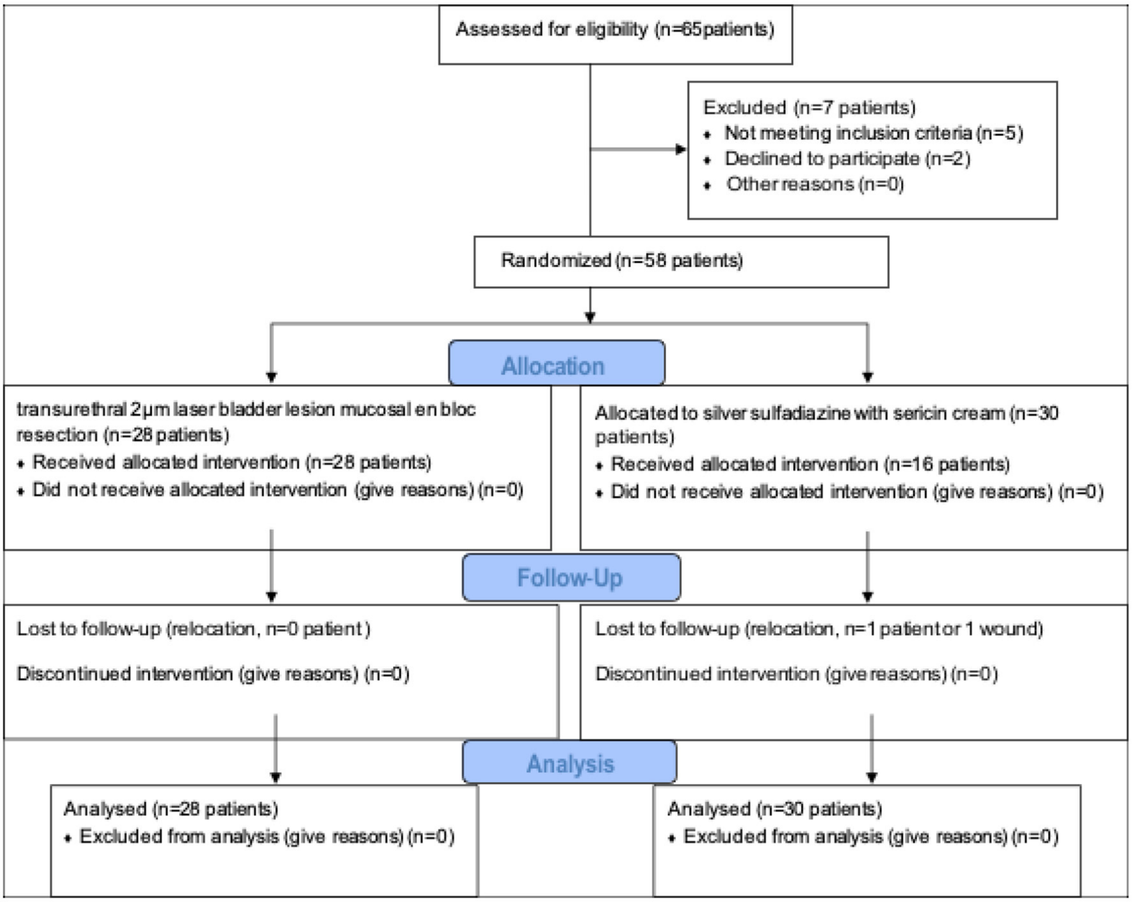

FIGURE 2 | CONSORT flow diagram.

TABLE 1 | Baseline characteristics.

Group	Sex		Age
	Male	Female	
Laser group	8 (28.57%)	20 (71.43%)	55.46 ± 6.58
TUR group	6 (25%)	24 (75%)	54.67 ± 6.8
	14 (26.92%)	44 (73.08%)	

Surgical Instruments

- Plasma cutting system (SM10).
- Medical RevoLix 2 μm continuous wave laser surgery system (LISA laser products).

Surgical Method

- Patients of two groups were performed by the same surgeon.

If there are no contraindications to anesthesia, intraspinal anesthesia was used. No obturator nerve block was performed, and normal saline was used as the rinse fluid during the operation.

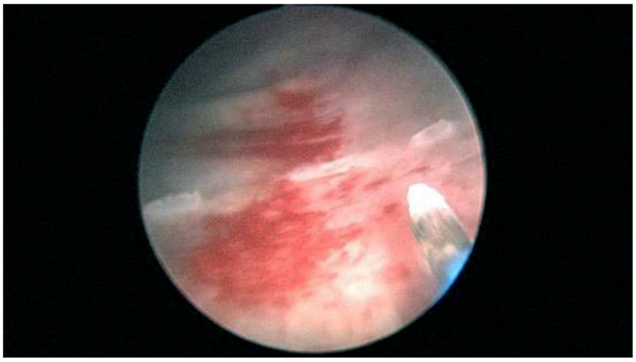

FIGURE 3 | Mark the pre-resection area.

- Laser group (transurethral 2 μm laser bladder lesion mucosal en bloc resection).

The patient adopted the lithotomy position, fully exposed the perineum, and disinfected the surgical area. To determine a general case such as the position of the lesion, the lesion number, size, range, and clarify the relationship between the diseased

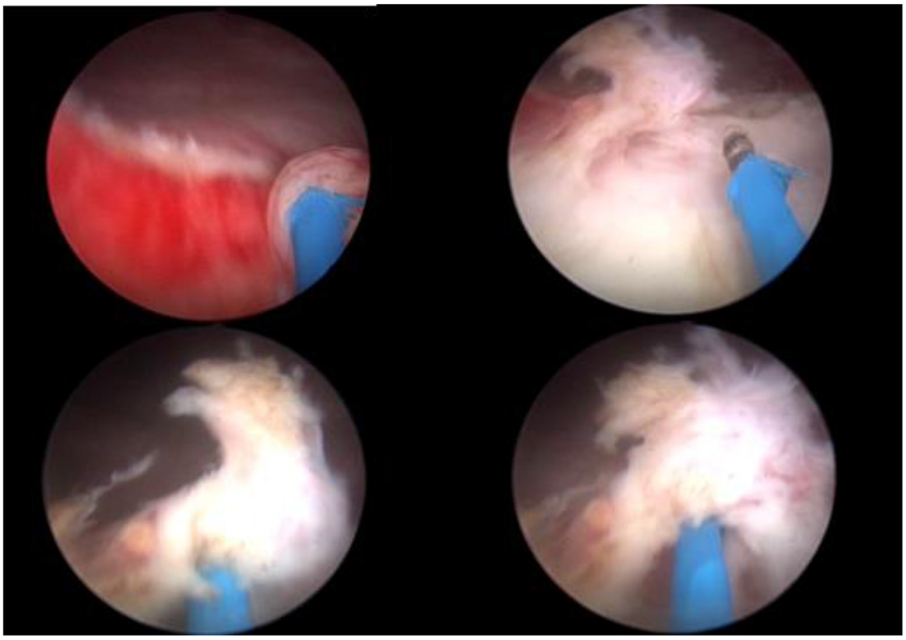

FIGURE 4 | Operation procedure.

mucosa and the ureteral orifice to avoid injury to the ureter during the operation, bladder overall situation was observed with 2 μm laser mirror into the bladder through the urethra. Then a 2 μm laser fiber was inserted and was adjust to be about 1–2 cm beyond the lens of the laser mirror. Use a 2 μm laser to mark the pre-resection area in the normal mucosa at a distance of 0.5–1.0 cm from the edge of the lesion (**Figure 3**). To reduce intraoperative bleeding, the blood vessels around the lesion could be cauterized with laser. A 2 μm laser fiber was inserted under the bladder mucosa, and bladder mucosa was lifted to maintain a certain tension with the bladder muscle layer, and then the bladder mucosa was cut and separated partly from muscle layer with a certain gap. Blunt peeling was performed along this gap with laser fiber and laser mirror. If the muscle fibers between the diseased mucosa and the bladder wall cannot be broken, using a laser to cut it (**Figure 4**). En bloc resection bladder mucosa with this method. After flushing out the diseased tissue with an irrigator, laser was used to stop bleeding on the wound (**Figure 5**). All patients underwent continuous bladder irrigation and catheterization after confirming that there was no bleeding.

- TUR group (traditional transurethral resection of bladder lesion mucosal).

The patient adopts the lithotomy position, fully exposes the perineum, and disinfects the surgical area. Use plasma electrodes to excise the diseased mucosa from front to back, with the depth of excision reaching the superficial muscle layer.

Data Collection

The perioperative and post-operative follow-up indicators of all patients were recorded. And the patient's operation time, the amount of bleeding during the operation, and the difference in hemoglobin (HGB) values before and after the operation were collected. The occurrence of bladder perforation and obturator reflex during the operation was recorded. And the duration of continuous bladder irrigation, catheter indwelling time and hospitalization days of all patients after surgery were collected and recorded in detail. Regular follow-up after operation was executed to determine whether the patient's various clinical symptoms before operation have improved.

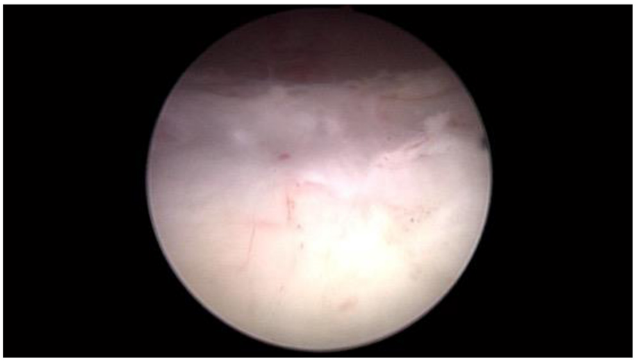

FIGURE 5 | En bloc resection bladder mucosa.

Treatment Effect Evaluation

① Cured: clinical symptoms disappear completely, no obvious abnormalities after reexamination. ② Symptom relief: the patient's symptoms are better than before, and occasionally

TABLE 2 | Perioperative indicators.

Group	Operation time (min)	Post-operative irrigation (day)	Catheter time (day)	Post-operative hospital (day)	Post-operative bleeding (ml)	HGB (ml)
Laser group	23.82 ± 5.19	1	4.07 ± 0.77	5.07 ± 0.77	11.89 ± 1.64 ml	4.61 ± 1.10 g/L
TUR group	23.77 ± 5.15	1	4.00 ± 0.64	5.00 ± 0.64	23.47 ± 1.85 ml	8.30 ± 1.26 g/L
T	0.04		0.385	0.385	−25.12	−11.83
P	0.968		0.701	0.701	<0.001	<0.001

TABLE 3 | Comparison of the effectiveness.

Group	Effective	Relapse	Sum	Effective rate (%)
Laser group	25	3	28	89.29
TUR group	27	3	30	90
Sum	52	6	58	89.66

symptoms mentioned above appear. ③ Invalid or recurrence: symptoms are not significantly improved or symptoms reappear after a period of time after improvement. Cystoscopy revealed abnormal mucosal changes at the original lesion site again, and the pathology results after biopsy showed glandular cystitis again. ④ Effective: Cured and symptom relief mentioned above.

Statistical Methods

All data were presented as mean ± SD. Student's *t*-test was used. The data were analyzed statistically using the SPSS 21.0. And *P*-value < 0.05 was considered statistically significant.

RESULTS

General Data

Laser group: 28, 8 males, 20 females, male to female ratio: 1:2.5. The average age was 55.46 ± 6.58 (range 30–67) years old. TUR group: 30, 6 males, 24 females, male to female ratio: 1:4. The average age was 55.67 ± 6.8 (range 28–71) years old. There were no significant differences between laser group and TUR group in average age and gender ($P > 0.05$; **Table 1**).

Perioperative Indicators

The average operation time of laser group was 23.82 ± 5.19 (range 15–35) min. The post-operative consecutive irrigation times was 1 day, and the mean catheter duration was 4.07 ± 0.77 days in laser group. The average of post-operative hospital stays of laser treated patients was 5.07 ± 0.77 days. As for TUR group, the average operation time was 23.77 ± 5.15 (range 15–35) min. The post-operative irrigation times was 1 day, and the mean catheter duration was 4.00 ± 0.64 days, and the mean post-operative hospital stays was 5.00 ± 0.64 days. There was no significant difference of these indicators between laser group and TUR group ($P > 0.05$).

In experimental group, intraoperative blood loss was 11.89 ± 1.64 ml, and the difference value of hemoglobin drop before and after operation was 4.61 ± 1.10 g/L. As for TUR group, intraoperative blood loss was 23.47 ± 1.85 ml, and the difference value of hemoglobin drop before and after operation was 8.30 ± 1.26 g/L. There was significant difference of these indicators between laser group and TUR group ($P < 0.05$; **Table 2**).

Post-operative Follow-Up

With 3 cases in each group having symptoms of cystitis glandularis such as irritation symptoms of bladder after the operation, there was no significant difference between the two groups ($P = 0.631$). Follow-up time ranges from 3 to 12 months. During this period, in laser group, 15 cases were cured, 10 cases improved, 3 cases relapsed, and the effective rate and recurrence rate was 89.29 and 10.71%, respectively. As for TUR group, 20 cases were cured, 7 cases improved, 3 cases relapsed, with the effective rate and recurrence rate being 90 and 10%, respectively. There was no statistically significant difference in the recurrence rate using the Fisher exact probability method of the four grid table ($p = 0.631 > 0.05$; **Table 3**).

DISCUSSION

In 1761, Morgagni et al. first proposed glandular cystitis a bladder mucosa dysplasia caused by a variety of factors (5). Glandular cystitis usually affects more women than men (6). The bladder triangle and bladder neck are regarded as the focal points of urodynamics, and their positions are relatively fixed. In addition, the bladder wall has no submucosa and lacks stretchability. Therefore, glandular cystitis is more likely to occur in the bladder triangle. Clinically, cystitis glandularis usually manifests as frequent urination, urgency, dysuria, hematuria, dysuria, pain in the suprapubic area and perineum, etc. And these symptoms are prone to recurring. In severe cases, acute urinary retention mayoccur (7). For the treatment of glandular cystitis, some people advocate conservative treatment such as the use of quinolone antibiotics and cyclooxygenase-2 inhibitors (3). Clinically, many patients with glandular cystitis have symptoms of overactive bladder. For such patients, measures can be taken to improve those symptoms. Highly selective M3 receptor blockers inhibit involuntary detrusor contractions to delayurination, having obvious effect in the treatment of symptoms of bladder over-activity (8–10).

There is a view that CG precancerous lesions, should be actively treated surgically. Currently, main treatment for glandular cystitis is transurethral resection. Among ways of it, transurethral electrocision of bladder lesion is the earliest surgical approach, and has been adopted as the most commononedue toits good results in the treatment of glandular cystitis, such as fewer traumas, shorter operation time, and faster patient recovery. However, this type of surgery has some shortcomings. During the treatment process, complications are more likely to occur, such as relatively more bleeding and post-operative bleeding, resulting in clot packing in the bladder, following too much hypertonic flushing fluid leading to dilution hyponatremia. Furthermore, it is easy to cause obturator nerve reflex during this operation process and cause bladder perforation (11, 12). The output center wavelength of the 2 μm laser ranges from 1,900 to 2,040 nm, and the maximum absorption peak of water to the laser is 1,940 nm. The process of absorption to 2 μm laser in the human tissue can produce a strong thermal effect, so as to achieve the effect of vaporization and cutting of the tissue (13, 14). Advantages of the use of 2 μm laser during operation areas follows: firstly, the combination process of 2 μm laser with water can produce efficient thermal effect for tissue cutting, vaporization and coagulation during surgery; next, the penetration depth of the 2 μm laser to tissue is only 0.2 mm, achieving precise operation during the operation and thus reduces surgical complications; finally, the use of 2 μm laser will not generate an electric field, avoiding the occurrence of obturator nerve reflex, moreover, it is also a suitable choice for high-risk patients carrying with cardiac pacemakers or cardiac stents to treat glandular cystitis surgically (13, 15).

It is these advantages mentioned above, that makes 2 μm laser in urology been widely used. We have summarized the following characteristics of clinical application of 2 μm laser to treat bladder mucosal: firstly, due to 2 μm laser performing precise cutting, the application of 2 μm laser can perform fine layered vaporization resection of the bladder mucosa and muscle layer; besides, due to its effective and rapid tissue cutting, vaporization and coagulation effects, the intraoperative operation is easy to control with clear layers of tissue and small amount of intraoperative blood loss, and the bladder blood clot packing has never occurred after the operation; next, given that the 2 μm laser penetration depth in the tissue is only 0.2 mm, bladder perforation has never occurred in the case of surgeon accurately distinguishing the bladder mucosa with muscle layer of the bladder; finally, because the 2 μm laser does not generate an electric field like an electric resection, all the transurethral 2 μm laser bladder lesion mucosal en bloc resection performed in our hospital have never caused obdurate nerve reflexes, which greatly improves the safety of the operation.

CONCLUSION

In summary, transurethral 2 μm laser bladder lesion mucosal en bloc resection in the treatment of glandular cystitis has the advantages of precise cutting, clear layers of tissue structure, less bleeding, fewer complications, shorter operation time, and faster patient recovery. Therefore, transurethral 2 μm laser bladder lesion mucosal en bloc resection for the treatment of glandular cystitis is worthy of further clinical application. It needs to be further improved and developed in the future extensive clinical practice.

DATA AVAILABILITY STATEMENT

The original contributions presented in the study are included in the article/supplementary material, further inquiries can be directed to the corresponding author.

ETHICS STATEMENT

The studies involving human participants were reviewed and approved by The Second Affiliated Hospital of Chifeng College of Science and Technology. The patients/participants provided their written informed consent to participate in this study.

AUTHOR CONTRIBUTIONS

CZ wrote this manuscript and analyzed the data. CM, YX, CZ, and KW collected the data. HX designed the study. All authors approved the submitted version.

REFERENCES

1. García Rojo D, Prera Vilaseca A, Sáez Artacho A, Abad Gairín C, Prats López J, Rosa Bella Cueto M. Transformation of glandular cystitis into bladder transitional carcinoma with adenocarcinoma areas. *Arch EspUrol.* (1997) 50:187–9.
2. Thrasher JB, Rajan RR, Perez LM, Humphrey PA, Anderson EE. Cystitis glandularis. Transition to adenocarcinoma of the urinary bladder. *NC Med J.* (1994) 55:562–4.
3. Takizawa N, Matsuzaki T, Yamamoto T, Mishima T, Miyasaka C, Tanaka S, et al. Novel strategy for cystitis glandularis: oral treatment with cyclooxygenase-2 inhibitor. *Int J Urol.* (2016) 23:706–8. doi: 10.1111/iju.13121
4. Herrmann TR, Liatsikos EN, Nagele U, Traxer O, Merseburger AS. EAU guidelines on laser technologies. *Eur Urol.* (2012) 61:783–95. doi: 10.1016/j.eururo.2012.01.010
5. Cunningham A. Pathology and the case-history in Giambattista Morgagni's "On the seats and causes of diseases investigated through anatomy (1761)". *Medizin Gesellschaft Und Geschichte Jahrbuch DesInstituts Für Geschichte Der MedizinDer Robert Bosch Stiftung.* (1996) 14:37–61.
6. Capozza N, Collura G, Nappo S, de Dominicis M, Francalanci P, Caione P. Cystitis glandularis in children. *BJU Int.* (2005) 95:411–3. doi: 10.1111/j.1464-410X.2005.05311.x
7. Zouari S, Bouassida K, Ahmed KB, Thabet AB, Krichene MA, Jebali C. Acute urinary retention due to benign prostatic

hyperplasia associated with cystitis glandularis in a 22-year-old patient. *Pan Afr Med J*. (2018) 30:30. doi: 10.11604/pamj.2018.30.30.14835

8. Pratt TS, Suskind AM. Management of overactive bladder in older women. *Curr Urol Rep*. (2018) 19:92. doi: 10.1007/s11934-018-0845-5
9. Andersson KE, Wein AJ. Pharmacology of the lower urinary tract: basis for current and future treatments of urinary incontinence. *Pharmacol Rev*. (2004) 56:581–631. doi: 10.1124/pr.56.4.4
10. Morales-Olivas FJ, Estañ L. Solifenacin pharmacology. *Arch Esp Urol*. (2010) 63:43–52. doi: 10.4321/S0004-06142010000100007
11. Hong-Yuan Y U, Xian-Kui L, Chui-Ze K. Diagnosis and treatment of cystitis glanularis (40 cases). *China J Modern Med*. (2010) 20:464–6. doi: 10.3969/j.issn.1005-8982.2010.03.040
12. Li-Gui M. Cystitis glandularis (report of 172 cases). *Chin J Urol*. (2003) 5:19–21. doi: 10.3760/j:issn:1000-6702.2003.05.006
13. Tao W, Sun C, Xue B, Yang D, Wang M, Cai C, et al. The efficacy and safety of 2-μm continuous laser in the treatment of high-risk patients with benign prostatic hyperplasia. *Lasers Med Sci*. (2017) 32:351–6. doi: 10.1007/s10103-016-2122-5
14. Wang W, Liu H, Xia S. Thulium laser treatment for bladder cancer. *Asian J Urol*. (2016) 3:130–3. doi: 10.1016/j.ajur.2016.05.002
15. Zhong C, Guo S, Tang Y, Xia S. Clinical observation on 2 micron laser for non-muscle-invasive bladder tumor treatment: single-center experience. *World J Urol*. (2010) 28:157–61. doi: 10.1007/s00345-010-0532-8

Conflict of Interest: The authors declare that the research was conducted in the absence of any commercial or financial relationships that could be construed as a potential conflict of interest.

frontiers in Medicine

ORIGINAL RESEARCH
published: 30 March 2022
doi: 10.3389/fmed.2022.855387

Identification of an Immune Classification and Prognostic Genes for Lung Adenocarcinoma Based on Immune Cell Signatures

Lili Deng[1,2], Fei Long[1], Ting Wang[1], Ling Dai[1], Huajian Chen[1,3], Yujun Yang[1] and Guoming Xie[1]**

[1] Key Laboratory of Clinical Laboratory Diagnostics (Chinese Ministry of Education), College of Laboratory Medicine, Chongqing Medical University, Chongqing, China, [2] Chongqing Health Statistics Information Center, Chongqing, China, [3] Chongqing Emergency Medical Center, Chongqing University Central Hospital, School of Medicine, Chongqing University, Chongqing, China

Edited by:
Fu Wang,
Xi'an Jiaotong University, China

Reviewed by:
Min Wei,
Shanghai Jiao Tong University, China
Zexin Zhang,
Guangzhou University of Chinese Medicine, China
Guohong Gao,
Affiliated Hospital of Weifang Medical University, China

***Correspondence:**
Guoming Xie
guomingxie@cqmu.edu.cn
Yujun Yang
yangyujun@cqmu.edu.cn

Specialty section:
This article was submitted to Precision Medicine, a section of the journal Frontiers in Medicine

Received: *15 January 2022*
Accepted: *23 February 2022*
Published: *30 March 2022*

Citation:
Deng L, Long F, Wang T, Dai L, Chen H, Yang Y and Xie G (2022) Identification of an Immune Classification and Prognostic Genes for Lung Adenocarcinoma Based on Immune Cell Signatures. Front. Med. 9:855387. doi: 10.3389/fmed.2022.855387

Objective: Current advances in immunotherapy requires accurate tumor sub-classification due to the heterogeneity of lung adenocarcinoma (LUAD). This study aimed to develop a LUAD sub-classification system based on immune cell signatures and identified prognostic gene markers.

Methods: Signatures related to the prognosis of TCGA-LUAD and 4 GSE cohorts were screened and intersected from 184 previously published immune cell signatures. The LUAD samples in the TCGA were clustered by ConsensusClusterPlus. Molecular characteristics, immune characteristics and sensitivity to immunotherapies/chemotherapies were compared. LDA score was established through Linear Discriminant Analysis (LDA). Co-expression module was constructed by Weighted Gene Co-Expression Network Analysis (WGCNA).

Results: Four LUAD subtypes with different molecular and immune characteristics were identified. Significant differences in prognosis among the four subtypes were observed. The IS1 subtype with the worst prognosis showed the highest number of TMB, mutant genes, IFN γ score, angiogenesis score and immune score. Twenty co-expression modules were generated by WGCNA. Blue module, sky blue module and light yellow module were significantly correlated with LUAD prognosis. The hub genes (CCDC90B, ARNTL2, RIPK2, SMCO2 and ADA and NBN) showing great prognostic significance were identified from the blue module. A total of 8 hub genes (NLRC3, CLEC2D, GIMAP5, CXorf65, PARP15, AKNA, ZC3H12D, and ARRDC5) were found in the light yellow module. Except for CXorf65, the expression of the other seven genes were significantly correlated with LUAD prognosis.

Conclusion: This study determined four LUAD subtypes with different molecular and immune characteristics and 13 genes closely related to the prognosis of LUAD. The current findings could help understand the heterogeneity of LUAD immune classes.

Keywords: lung adenocarcinoma, immune cell signatures, immune subtypes, molecular characteristics, weighted gene correlation network analysis (WGCNA), prognosis

INTRODUCTION

Lung cancer was estimated to account for about 1/4 of all cancer deaths in 2021 (1). As the most common type of lung histology, lung adenocarcinoma (LUAD) is characterized by a high heterogeneity at behavioral, cellular and molecular levels, with an overall survival time shorter than 5 years (2). Late diagnosis, limited treatment, recurrence and development of drug resistance are the main challenges for a successful treatment of LUAD (3). Early diagnosis, introduction of new treatments, and overcoming drug resistance are effective in reducing LUAD mortality.

Immunotherapy has greatly changed the direction of LUAD treatment (4). Immunotherapy encourages the host immune system to recognize cancer as a foreign body, stimulating immune system to inhibit cancer cell growth and spread (5). The study of LUAD immunotherapy has many advantages, such as evaluation of pathological responses and anti-tumor immune responses in combination with translational science analysis (6). Immunotherapies include immune modulators, for example, currently interleukin-2 and muramyl tripeptide, dendritic cells, immune checkpoint inhibitors, and engineered T cells have already been used in cancer treatment (7). However, immunotherapy benefits only a small number of patients. The current progress in immunotherapy requires a more accurate sub classification of tumor morphology. LUAD consists of a group of heterogeneous tumors, which can pose a diagnostic challenge, especially when using a small number of biopsy specimens. Clinically, most LUAD can be subclassified using hematoxylin & eosin (H&E) staining to assess histological characteristics. However, in some small biopsy specimens, in addition to morphological evaluation and immunohistochemical features of tumors, the subclassification of tumors is still difficult (8). Growing evidence showed that the subtype classification of LUAD based on gene expression array can provide much information for the molecular characterization and prognosis prediction of LUAD (9). Over the past 20 years, an increasing number of immune cell signatures have been identified, providing a more comprehensive knowledge for various aspects of cancer immunology (10, 11). However, so far, we still lack the study of tumor subtype classification and molecular characterization based on immune cell signatures.

At present, there are many systems biology methods to identify biomarkers related to the prognosis of LUAD and construct gene features. Zhang et al. (12) identified a 7-gene signature in the whole genome using multiomics data set. Guo et al. (13) used genomic instability to identify key lncRNAs for predicting clinical outcomes in patients with lung adenocarcinoma. Lane et al. (14) identified 28 gene markers in the hypoxia related gene expression profile to predict the clinical outcome of non-small cell lung cancer. All the three groups of authors tested their signatures in internal data sets, but they were not used clinically, which means that identifying robust molecular signatures remains a challenge.

In this study, we clustered LUAD samples based on immune cell signatures and identified four different immune subtypes (ISs). We assessed the prognostic differences, transcriptome characteristics, somatic mutation characteristics, immune characteristics, tumor microenvironment characteristics, immunotherapy and drug sensitivity of different among the four ISs, and compared them with the previously established classification. Furthermore, a scoring system was constructed based on Linear Discriminant Analysis (LDA), the modules related to LDA score were screened by WGCNA, and the modules related to the prognosis of LUAD were identified by univariate Cox analysis. Finally, LUAD prognosis-related genes were determined. The ISs we obtained contribute to better understand the heterogeneity of LUAD and the complexity of the immune microenvironment, and highlight the reference value of IS classification for clinical prognosis and treatment decision making. Also, this study identified genes associated with LUAD prognosis that may predict individualized prognosis.

MATERIALS AND METHODS

LUAD Samples Datasets

RNA-Seq data and clinicopathological characteristics of 504 samples of LUAD patients were collected from the TCGA database (https://portal.gdc.cancer.gov/). Microarray profiling dataset GSE37745 (15), GSE19188 (16), GSE50081 (17), GSE30219 (18), and GSE31210 (19) were downloaded from Gene Expression Omnibus (GEO) database (https://www.ncbi.nlm.nih.gov/gds/), and all the five GSE datasets were combined with batch effects removed using the removeBatchEffect of the Limma package (20). After the removal of batch effect, there was no difference in the samples among the GSE datasets through Principal Component Analysis (PCA) (**Supplementary Figure 1**). The clinical statistics of the samples from TCGA and GEO can be found in **Table 1**. In addition, we also obtained the exon data set of each sample from TCGA, and calculated the TMB of each patient using R software package maftools (21). **Supplementary Figure 2** shows all the workflow of this study.

Immune Cell Signatures

According to Wang et al. (10), we selected previously published 184 cancer-related immune cell signatures to calculate the enrichment scores of samples from different datasets. Survival analysis was performed to screen and intersect the immune cell signatures related to LUAD prognosis in each cohort.

Consensus Clustering of LUAD Samples

ConsensusClusterPlus (22) was used to cluster 504 LUAD samples in the TCGA cohort. According to the cumulative distribution function (CDF), the optimal number of clusters was determined. The overall survival (OS) of different subtypes was analyzed by Kaplan-Meier Plotter (KM-plotter).

Molecular Characteristics and Tumor Immune Analyses Between Subgroups

To identify the molecular characteristics of different subtypes, the mutation datasets processed by mutect2 software in TCGA were acquired to analyze the differences in tumor mutation load (TMB) and the number of mutated genes among subgroups.

TABLE 1 | Sample clinical statistics for LUAD patients from TCGA and GEO database.

Clinical Features		TCGA-LUAD	GEO
OS	0	321	352
	1	183	230
T Stage	T1	168	
	T2	269	
	T3	45	
	T4	19	
	TX	3	
N Stage	N0	325	
	N1	94	
	N2	71	
	N3	2	
	NX	12	
M Stage	M0	335	
	M1	25	
	MX	144	
Stage	I	270	
	II	119	
	III	81	
	IV	26	
	X	8	
Gender	Male	234	
	Female	270	
Age	≤65	247	
	>65	257	

Then the differences in immune checkpoint gene expression among different subgroups were compared. IFN γ scores among subgroups were recorded using Th1/IFN γ gene signatures (23). Mean expression of GZMA and PRF1 (24) were used to assess the intratumoral T cell lytic activity among subgroups. Angiogenesis-associated gene sets (25) were applied to evaluate angiogenesis scores in each subgroup. The scores and degree of immune infiltration of 22 types of immune cells in different subtypes of patients were assessed by CIBERSORT (26). TIDE (http://tide.dfci.harvard.edu/) (27) software also predicted the response of different subgroups to immunotherapy and chemotherapy.

Construction of Linear Discriminant Analysis (LDA) Model

To better understand the molecular characteristics of LUAD patients, we performed LDA using immune cell signatures with intersected genes to establish a model for evaluating the scores of different subtypes. ROC analysis was performed to determine the specificity and sensitivity of the model.

Co-expression Module Detection

Weighted Gene Co-Expression Network Analysis (WGCNA) is a biological algorithm for constructing scale-free networks based on gene expression profiles (28). Here, transcripts with discrete value of 50% expression or higher were retained. The soft threshold power was selected by the soft Connectivity function. Based on the expression matrix of LUAD, the adjacency matrix was calculated and converted to topological overlap matrix. Average-linkage hierarchical clustering method was used to cluster genes, and the modules were shown together by a tree with color assignment.

Pathway Enrichment Analysis for the Modules

Gene Ontology (GO) and Kyoto Encyclopedia of Genes and Genomes (KEGG) analyses were performed using the ClusterProfiler package (29). When there were more than 10 GO terms and pathway enrichments, only the top 10 terms with a $p < 0.05$ were shown.

RESULTS

Identification of Four Immune Subgroups Based on Immune Cell Signatures

We found that 60 out of 184 immune cell signatures were significantly correlated with the OS of LUAD by performing univariate Cox analysis. The overlaps in the Venn diagram were immune cell signatures existing in both TCGA and GEO databases and were correlated with LUAD prognosis (**Figure 1A**). The 504 LUAD samples of TCGA were clustered according to the overlapping prognostic immune cell signatures of the two databases, and the CDF delta area curve showed that CDF plot was relatively stable when the consensus index was 4 (**Figures 1B,C**). For this reason, LUAD was divided into four immune subgroups (**Figure 1D**, **Supplementary Table 1**). Significant differences in prognosis were detected among the four subgroups of ISs whether in TCGA or GEO database (**Figures 1E,F**, **Supplementary Figures 3A,B**).

Molecular Characteristics Analysis Between Four ISs

The molecular mutations among the ISs were analyzed to reveal the differences in molecular characteristics of the four ISs, which showed different TMBs and mutant gene numbers. Specifically, IS1 had the highest number of TMB and mutant genes, while IS3 patients with the best prognosis had the lowest number of TMB and mutant genes (**Figures 2A,B**). Chi-square test identified 10 genes with high frequency of mutation in all ISs, and TP53 mutations were the most common (**Figure 2C**). Furthermore, the expression of chemokines and chemokine receptors were analyzed in four ISs. More than 90% of the 41 chemokines showed differential expression in the four ISs, and the levels of most chemokines were the lowest in IS1 samples (**Figure 3A**). The same was also shown in the expression of chemokine receptors (**Figure 3B**). After examining the differences of IFN γ, CYT and angiogenesis scores in different ISs patients, we found that there were significant differences in IFN γ, CYT and angiogenesis scores in the four types of ISs patients. IS1 showed the lowest IFN γ score and angiogenesis scores, IS4 had the highest CYT score, and IS2 demonstrated the highest angiogenesis scores among the four ISs (**Figures 3C–E**).

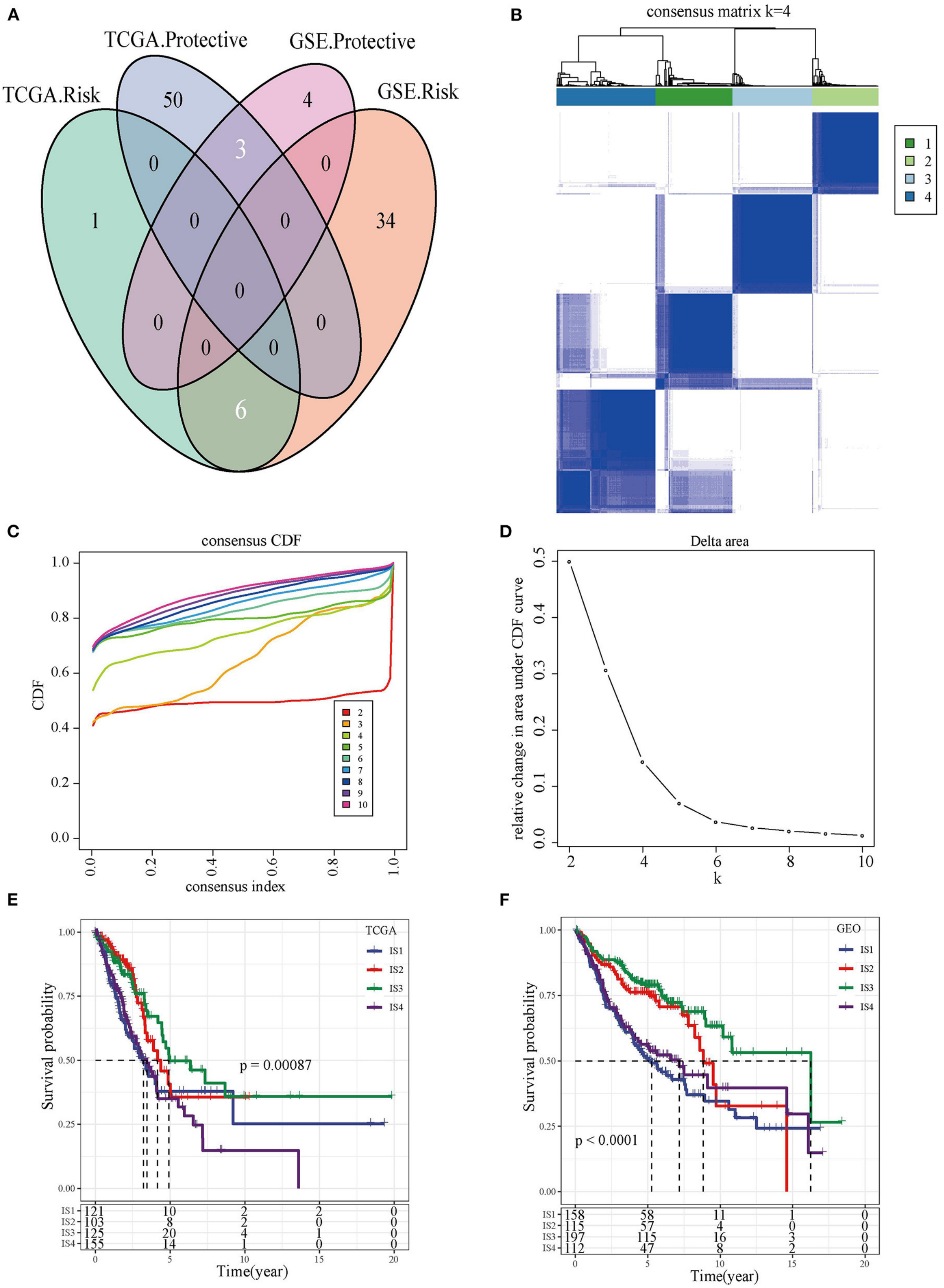

FIGURE 1 | The immune subtypes and survival analysis. **(A)** The Venn diagram showed the intersection of immune cell signatures related to LUAD prognosis in TCGA and GEO databases. **(B)** Heat map of the consensus matrix when the total samples are clustered into four ISs. **(C)** Relationship between the relative changes in the area under the CDF curve and consensus index. **(D)** Heat map of the consensus matrix when the LUAD was clustered into four immune subgroups. **(E)** Kaplan-Meier survival curve showed the OS of four types of ISs patients in TCGA. **(F)** Kaplan-Meier survival curves of four types of ISs patients in GEO.

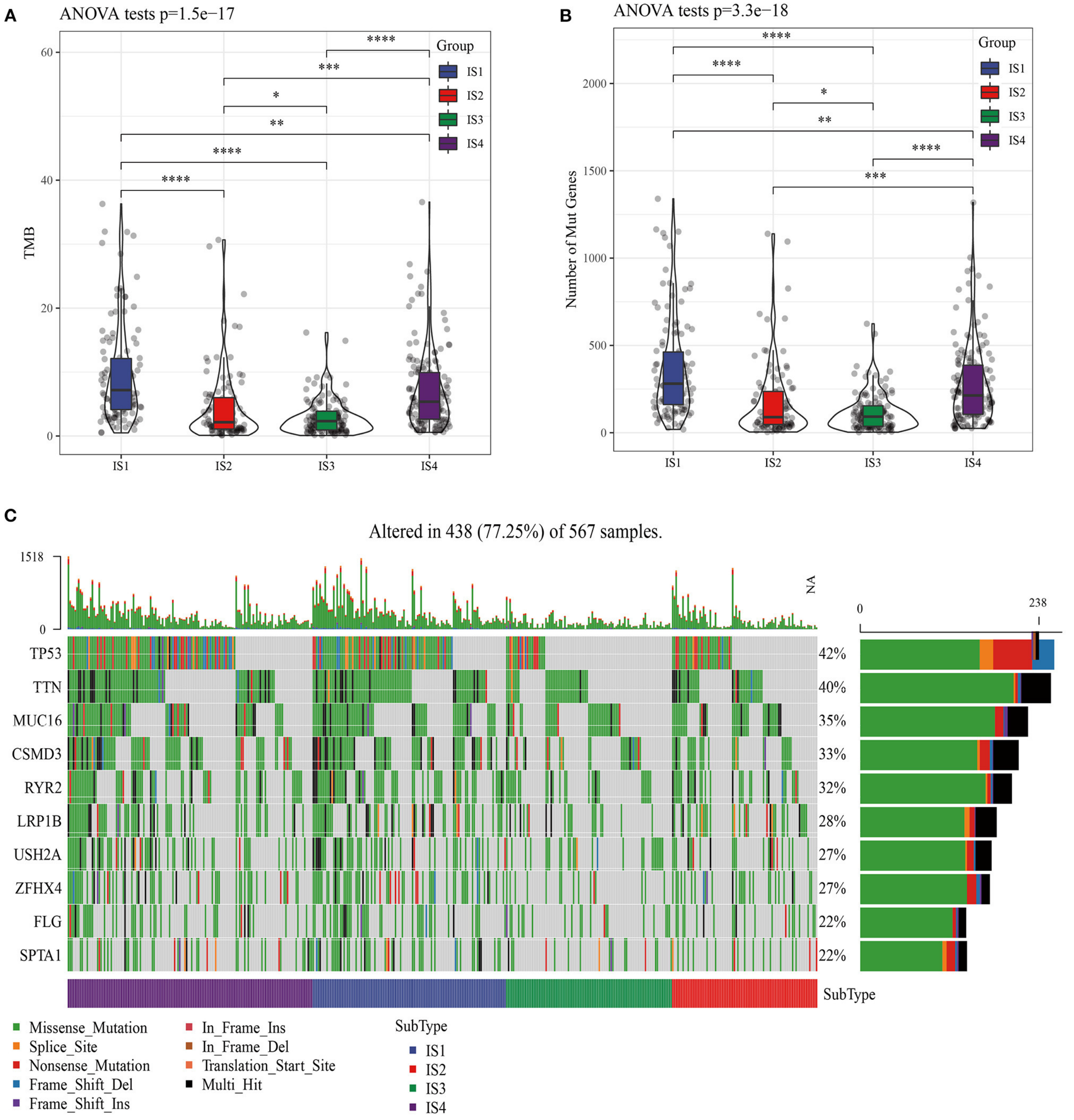

FIGURE 2 | Molecular mutation analysis of four ISs patients in LUAD. **(A)** Four kinds of ISs of LUAD have different TMB. **(B)** Comparison of the number of mutant genes in four kinds of ISs. **(C)** Significant somatic gene mutations in LUAD.

Cellular Characteristics of Four ISs

As immune system functions critically in tumors, we also explored the relationship between ISs and immune microenvironment. Among the 22 immune cell types examined by the ESTIMATE, except naive CD4 T cells, gamma delta T cells, activated dendritic cells and neutrophils, 18 immune cell displayed notably different scores in IS1-IS4 (**Figures 4A,B**). Four kinds of ISs also showed different immune scores (**Figure 4C**). It should be noted that the molecular characteristics of LUAD could be affected by the activation of specific pathways, here four types of ISs patients had significantly different enrichment scores in the 10 typical pathways (cell cycle, Hippo, Myc, Notch, Nrf2, PI3-Kinase/Akt, RTK-RAS, TGF β signaling, p53 and β-catenin/Wnt) (**Figure 4D**). Distribution of available

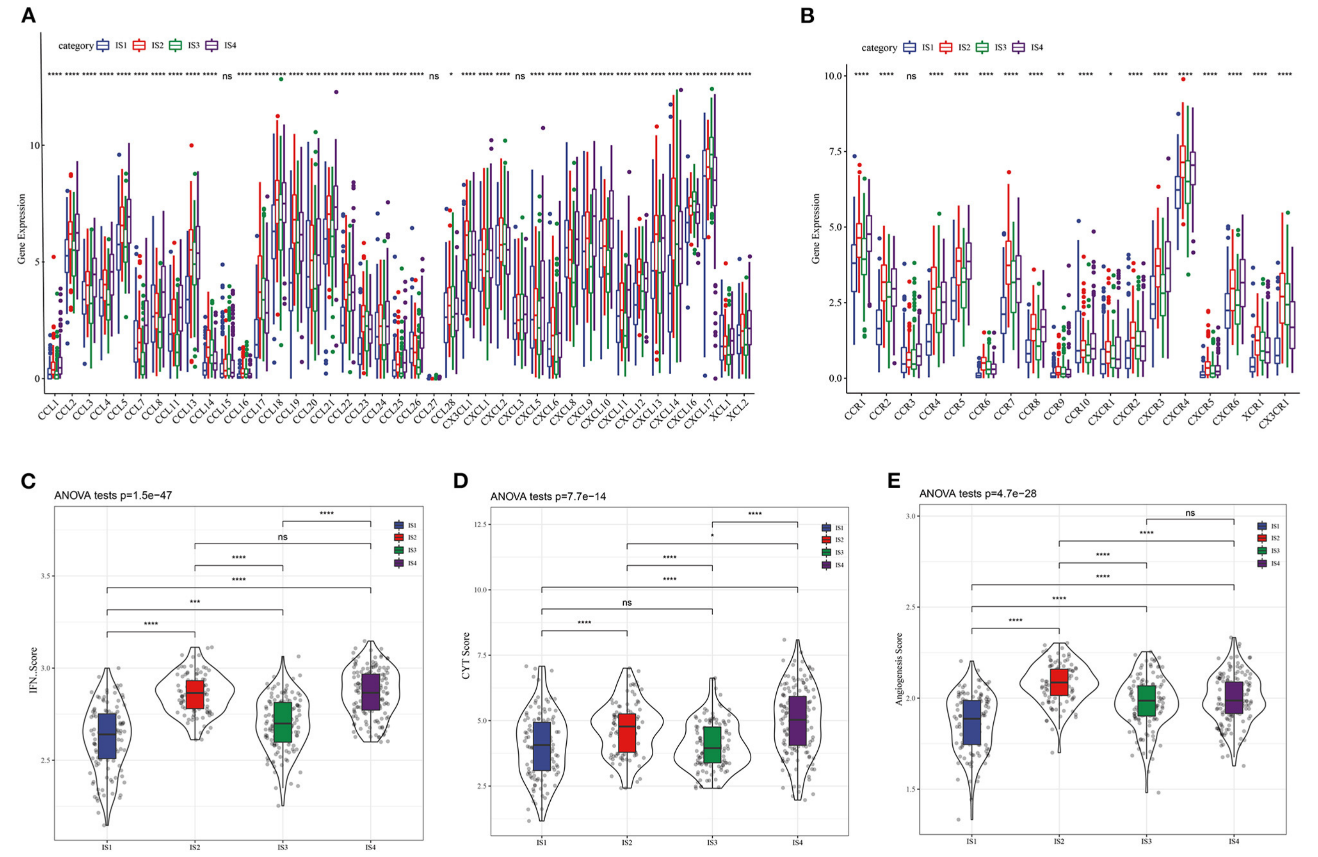

FIGURE 3 | Four LUAD subtypes showing different phenotype. **(A)** Expression of chemokine in four LUAD subtypes. **(B)** Expression of chemokine receptors in LUAD subtypes. The difference of **(C)** IFN γ score, **(D)** CYT score, and **(E)** angiogenesis scores among four ISs.

immune infiltrating subtypes molecular subtypes (30) in our molecular subtypes was analyzed, we found that C1, C2, C3, C4, and C6 subtypes all existed in TCGA data sets but were in different proportion in the four subgroups. C3 subtype has the highest proportion in IS2 and IS3, and the prognosis of these two kinds of ISs patients was better, which, to a certain extent, also confirmed the rationality of the classification of this study (**Figure 4E**).

Sensitivity of Different ISs to Immunotherapies/Chemotherapies

To explore the response of different LUAD subtypes to immunotherapy, the relationship of this immune-related classification of LUAD and immune checkpoint therapy was first analyzed, vast majority of immune checkpoint related genes showed different expression patterns in the four ISs (**Figure 5A**). As the expression of immune checkpoint is positively correlated with the effect of immunotherapy, it was speculated that the four ISs may response differently to immunotherapy. For further verification, the tumor response to immune checkpoint inhibitors (ICIs) was evaluated by the Tumor Immune Dysfunction and Exclusion (TIDE) score system (27), and the TIDE score of IS3 patients was found to be the lowest among the four ISs (**Figure 5B**), suggesting that this LUAD subtype may have a better response to ICIs and also explained the most favorable prognosis of IS3 among the four ISs. In addition, the four subtypes were also significantly correlated with T cell dysfunction score and exclusion score (**Figures 5C,D**). Considering the fact that chemotherapy is commonly used in cancer treatment, the response of four ISs to commonly used drugs were evaluated. On the basis of predictive model of the four chemo drugs (cisplatin, erlotinib, sorafenib and vinorelbine), the IC_{50} value of each subtype in the TCGA data set was analyzed. Significant differences in the IC_{50} values of all ISs were found in the four chemotherapeutic drugs, and the IS1 with the worst prognosis was more sensitive to four chemo drugs (**Figures 5E–H**).

Construction of Immune Cell Signatures-Based Scoring System Through LDA

LDA based on nine immune cell signatures could distinguish different subtypes of LUAD in TCGA (**Figure 6A**). LDA score of each subtype of LUAD patients in TCGA and GEO database was calculated and differences were analyzed. The results showed that there were significant differences in LAD score among the four

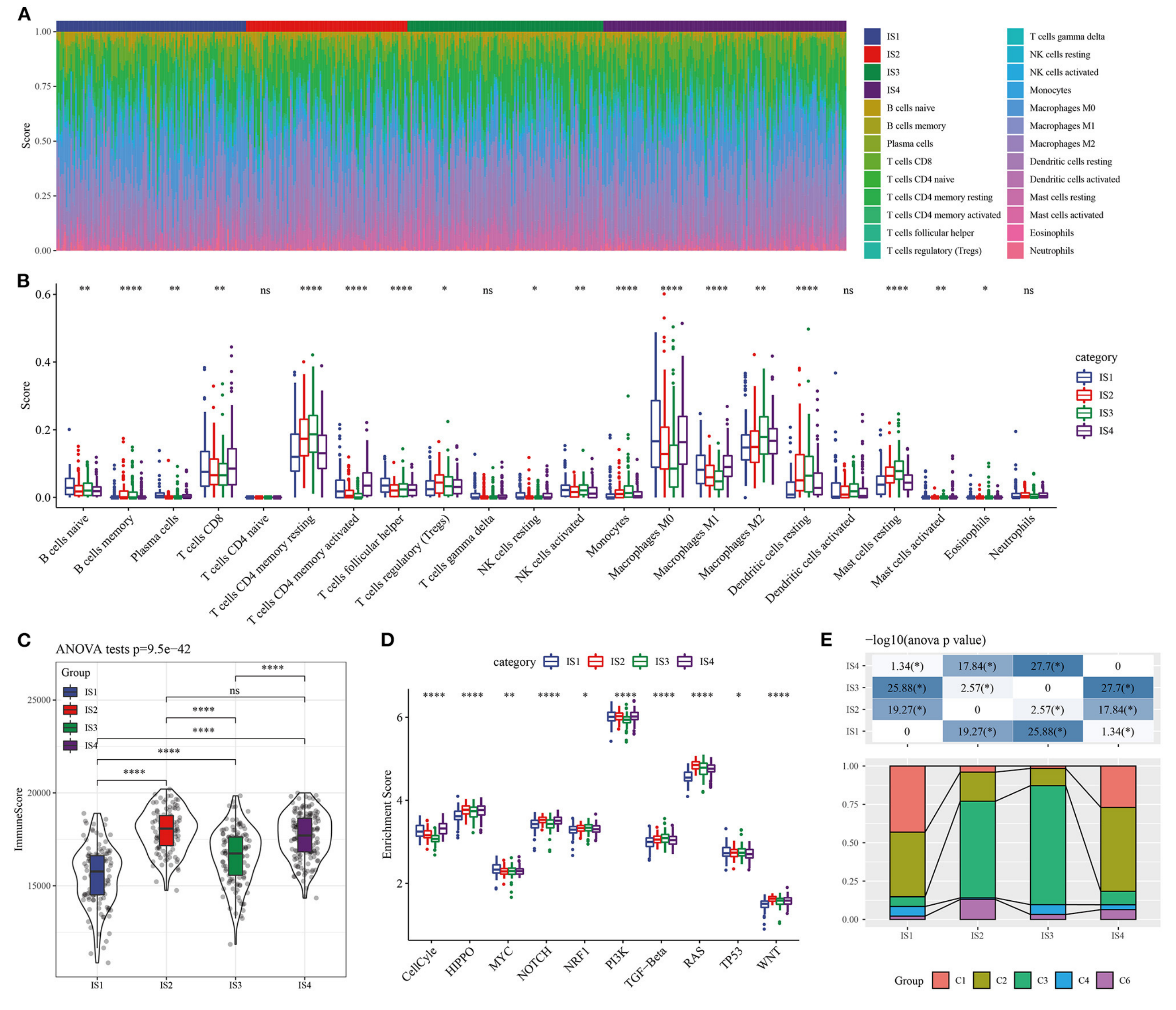

FIGURE 4 | Cellular characteristics of the ISs. **(A)** The distribution of 22 kinds of immune cells in ISs tissue. **(B)** The score of immune cell types with significant differences in two subgroups. **(C)** Distribution of immune scores in the four ISs. **(D)** Enrichment scores of four LUAD subgroups in 10 cancer signaling pathways. **(E)** Distribution of available immunoinfiltrating subtypes molecular subtypes in our subtypes.

subtypes of LUAD patients both in TCGA and GEO databases (**Figures 6B,C**). According to the results of receiver operating characteristic (ROC) curve analysis, combined area under curve (AUC) of LDA in TCGA was 0.83, similarly combined AUC of LDA in GEO was 0.83 (**Figures 6D,E**). Therefore, The LDA score model was verified to have a high accuracy in predicting immune characteristics of LUAD.

The Correlation Between LDA Score and LUAD Immunotherapy Response Was Assessed

The correlation between LDA score and immunotherapy response was examined according to the correlation between LDA score and immune checkpoints. We screened 28 immune checkpoints from 47 immune checkpoints, and their expression and LDA score was found to be significantly correlated (**Figure 7A**). Immune checkpoint blocking of PD-1, PD-L1, and CTLA-4 has emerged as a promising immunotherapy (31). Therefore, correlation analysis was conducted between LDA score and the three immune checkpoint inhibitors, and LDA score was significantly negatively correlated with the expression of PD1 (**Figure 7B**), PD-L1 (CD274) (**Figure 7C**), and CTLA-4 (**Figure 7D**), respectively. In addition, LDA scores under the states of complete response (CR), partial response (PR), stable disease (SD) and progressive disease (PD) were examined based on the expression profile data before anti-PDL1 treatment (32), and no differences were detected (**Figure 7E**). However, in another anti-PD1 pre-treatment expression profile data (33), the

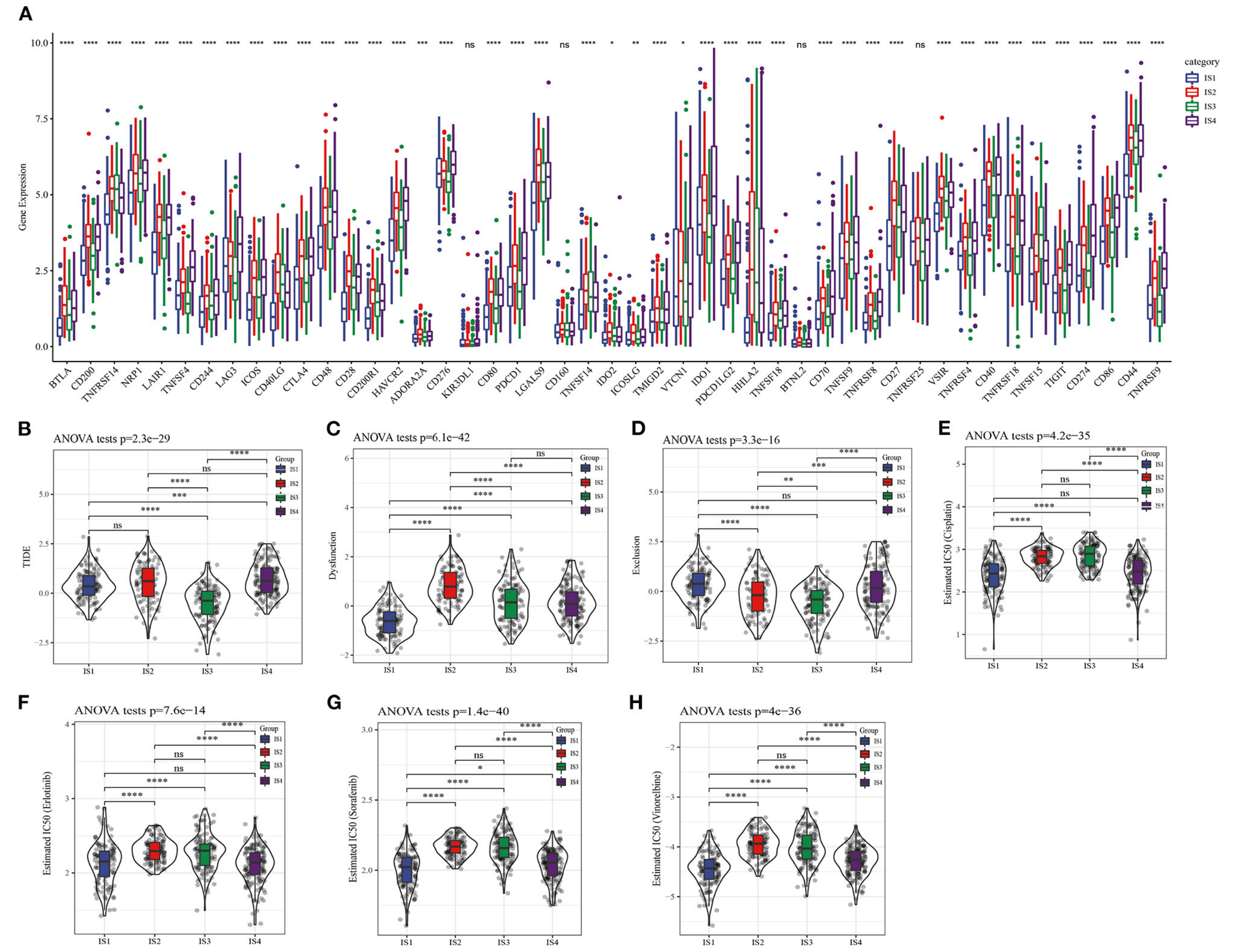

FIGURE 5 | Differential chemotherapeutic and immunotherapeutic responses of ISs. **(A)** Expression of 47 immune checkpoints in different LUAD subtypes. **(B)** The TIDE score of different subtypes. **(C)** T cell dysfunction score of four ISs. **(D)** T cell exclusion score in four subgroups. **(E–H)** All the four ISs had significant differences in the estimated cisplatin, erlotinib, sorafenib and vinorelbine IC_{50} values.

LDA score of CR/PR target lesions was significantly higher than that of PD target lesions (**Figure 7F**).

Construction of LUAD Co-expression Module and Identification of Key Modules

To identify the modules related to LDA score, firstly, the LUAD samples in TCGA were clustered. The optimal β value in the co-expression network was three, because it was the lowest power with a scale-free topology fitting index greater than 0.90 (**Figures 8A,B**). Twenty co-expression modules were generated by dynamic tree cutting method (**Figure 8C**). The transcripts for each module were counted (note that the gray module was a gene module that cannot be assigned) (**Figure 8D**). To identify ISs-related modules, correlation heatmap between a module and sample traits (age, gender, T stage, N stage, M stage, AJCC stage, IS1, IS2, IS3, IS4) was generated. From the heatmap, it could be observed that the positive correlation between IS1 and blue module was the highest ($r = 0.44$, $p < 0.05$) and the negative correlation with pink module was the strongest ($r = 0.46$, $p < 0.05$), with a significant difference. IS2 showed the highest positive correlation with gray module ($r = 0.35$, $p < 0.05$), and the most significant negative correlation with blue module ($r = 0.33$, $p < 0.05$). Among the 20 modules, IS3 was also the most significantly negatively correlated with blue ($r = 0.54$, $p < 0.05$); IS4 showed the most significant positive correlation with dark orange module ($r = 0.39$, $p < 0.05$) and blue module ($r = 0.37$, $p < 0.05$) (**Figure 8E**).

Identification of LUAD Prognostic-Related Modules and Hub Genes

Correlation analysis determined 12 modules significantly related to LDA score (**Figure 9A**). Univariate analysis showed that blue module, sky blue module and light yellow were significantly correlated with the prognosis of LUAD (**Figure 9B**). As the

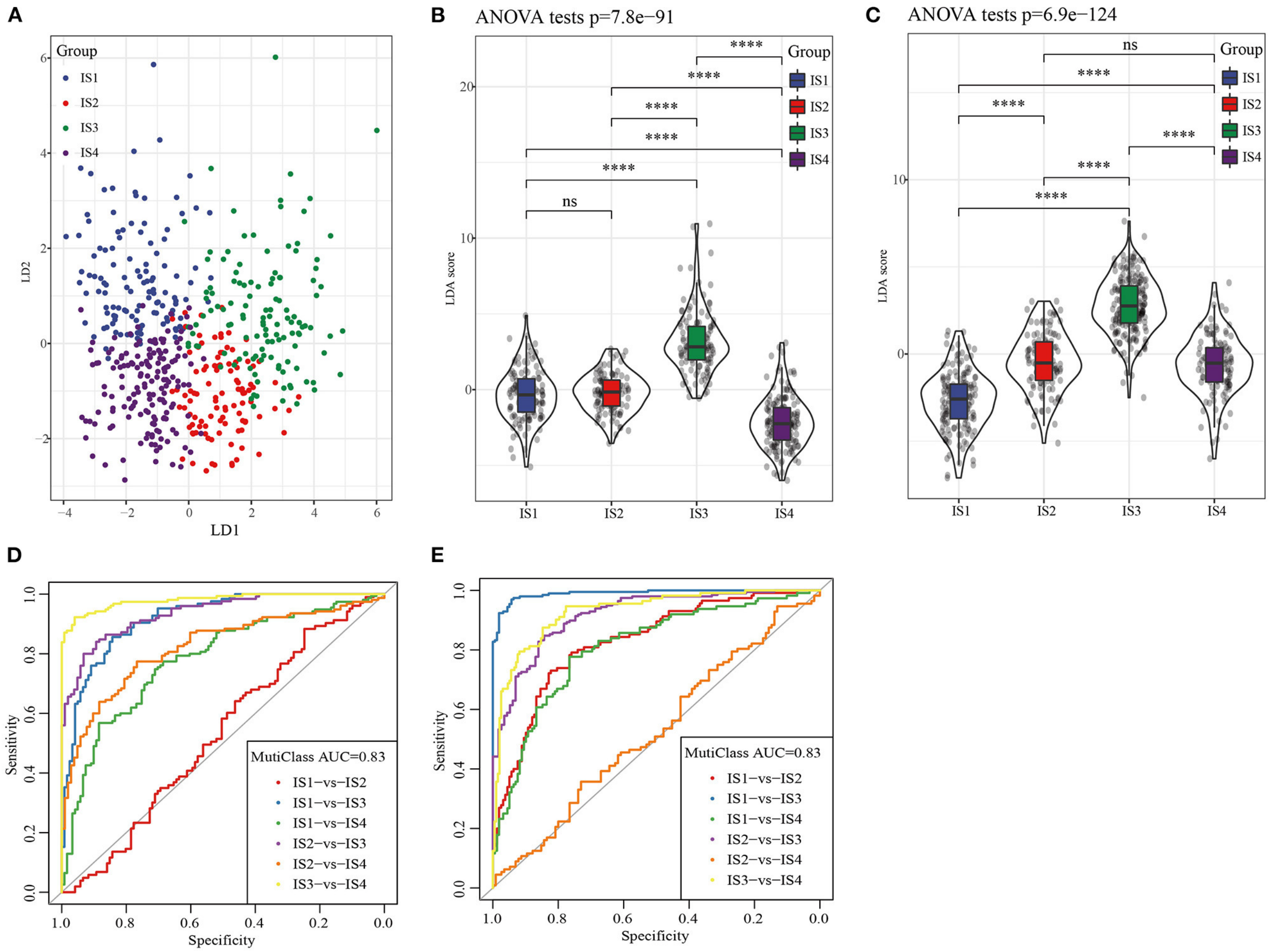

FIGURE 6 | LDA was used to construct a scoring system based on immune cell signatures. **(A)** LDA diagram of four ISs patients in TCGA cohort. **(B)** The violin diagram showed the different LDA score between IS1, IS2, IS3, and IS4 in TCGA. **(C)** Difference analysis of LDA score of four ISs patients in GEO database. **(D)** Receiver operating characteristic (ROC) curves of LDA score in the TCGA. **(E)** Receiver operating characteristic (ROC) curves of LDA score in the GEO.

number of genes in the sky blue module was too small, we then focused on the analysis of blue and light yellow modules. In the blue module, hub genes with great prognostic significance were determined to be CCDC90B, ARNTL2, RIPK2, SMCO2, and ADA and NBN (**Supplementary Figure 4**). A total of 8 hub genes, namely, NLRC3, CLEC2D, GIMAP5, CXorf65, PARP15, AKNA, ZC3H12D, and ARRDC5, were in the light yellow module. Except for CXorf65, the expression of the other seven genes were significantly associated with the prognosis of LUAD (**Supplementary Figure 5**). To further understand the biological characteristics of each module, we performed functional enrichment analysis on the genes in the blue and the light yellow modules. **Figures 9C,D** exhibited the top 10 GO terms and the top 10 KEGG pathways with blue module annotation, and genes in the light yellow module were mainly enriched in immune-related pathways (**Figures 9E,F**).

DISCUSSION

LUAD is the most common type of lung cancer, accounting for about 40% of all lung cancer cases. According to morphological characteristics, LUAD can be divided into several histological subtypes (34, 35). Among all LUAD, the most general subtype develops via tumorigenesis and progression from atypical adenomatous hyperplasia (AAH) to adenocarcinoma *in situ* (AIS), to minimally invasive adenocarcinoma (MIA), to overt invasive adenocarcinoma with a lepidic pattern (36). Amassed researchers suggested that the WHO LUAD classification should be modified for various patterns to more accurately predict LUAD prognosis (37). At present, histological features are the basis for further subdivision of LUAD into molecular subclasses, and the latest advances in sequencing technology allow LUAD to be classified according to the markers that regulate or influence certain characteristics of the cancer (34). Here, we

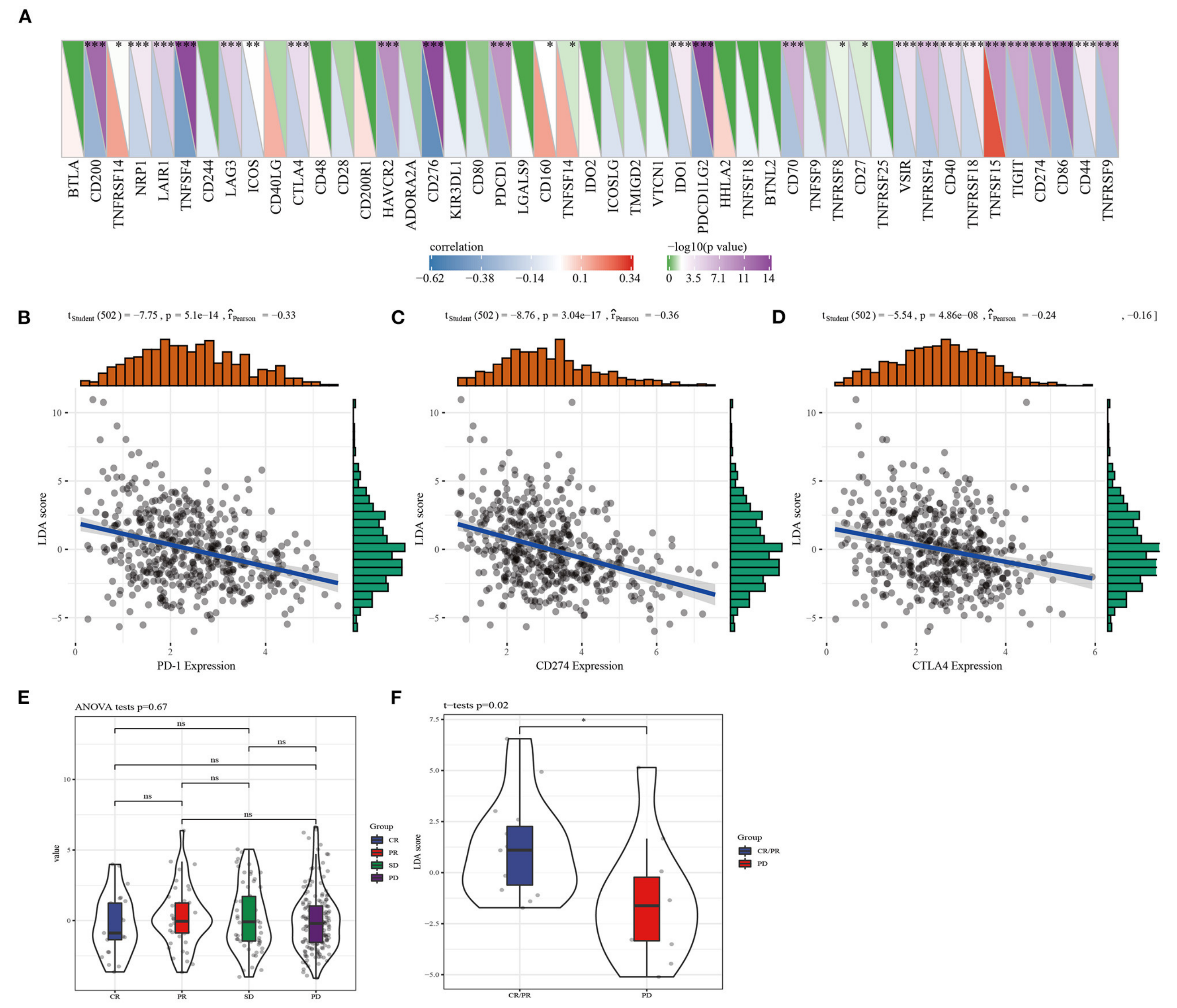

FIGURE 7 | The correlation between LDA score and LUAD immunotherapy response was assessed. **(A)** The immune checkpoints significantly related to LDA score were screened from 47 immune checkpoints. **(B)** Correlation analysis of LDA score and PD1 expression. **(C)** Analysis of correlation between LDA score and CD274 expression. **(D)** Correlation analysis of LDA score and CTLA4 expression. **(E)** LDA score evaluation between CR, PR, SD, and PD before anti-PDL1 treatment. **(F)** The difference of LDA score between CR/PR target lesions and PD target lesions was analyzed.

subdivided LUAD into four molecular subclasses based on 9 immune cell signatures of LUAD, and the results showed significant prognostic differences among the four kinds of ISs patients.

The four types of ISs presented different molecular characteristics, which were reflected in the differences in the number of TMB, mutant genes, chemokines and chemokine receptors. We observed that TP53 mutations were the most common, which was consistent with previous studies (38). A growing body of findings supported the correlation of differential existence of components of the immune system in deciding the evolution of cancer (39). We found that naive B cells, memory B cells, plasma cells, CD8 T cells, memory resting T cells CD4, activated memory T cells CD4 memory, helper follicular T cells, regulatory T cells, resting NK cells, activated NK cells, Monocytes, M0 Macrophages, M1 Macrophages, M2 Macrophages, resting dendritic cells, resting mast cells, activated mast cells and eosinophils displayed notably different scores in the four IS type. To some extent, these findings also reflected the heterogeneity of LUAD. Since the density of most T cells decreases with the progression of the tumor, B cells were related to the prolongation of survival and increase in the late stage, which had a dual effect on tumor recurrence and progression (40). Different immune cell infiltration of the four kinds of ISs may accordingly lead to variations in recurrence and survival of LUAD patients.

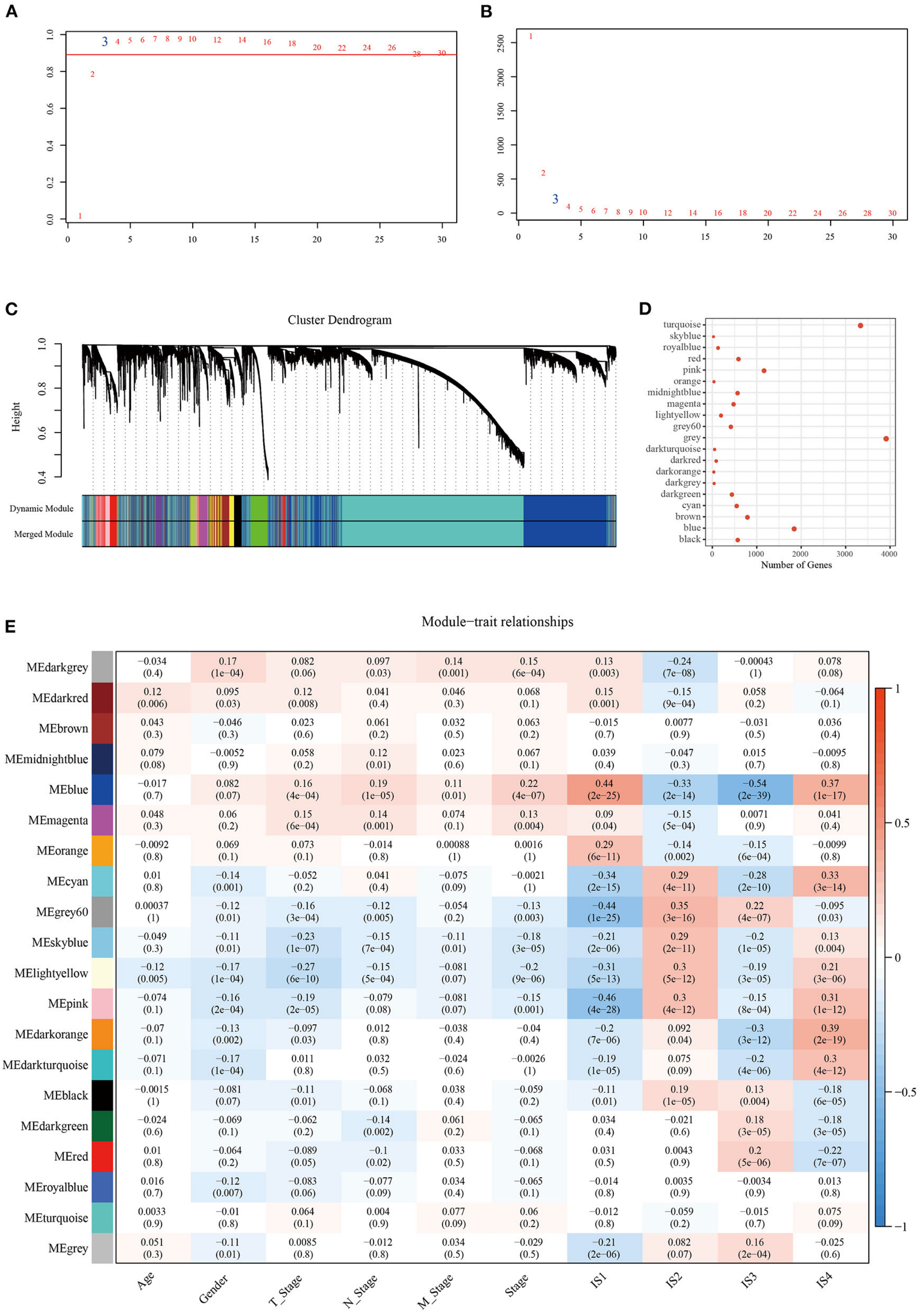

	Age	Gender	T_Stage	N_Stage	M_Stage	Stage	IS1	IS2	IS3	IS4
MEdarkgrey	−0.034 (0.4)	0.17 (1e−04)	0.082 (0.06)	0.097 (0.03)	0.14 (0.001)	0.15 (6e−04)	0.13 (0.003)	−0.24 (7e−08)	−0.00043 (1)	0.078 (0.08)
MEdarkred	0.12 (0.006)	0.095 (0.03)	0.12 (0.008)	0.041 (0.4)	0.046 (0.3)	0.068 (0.1)	0.15 (0.001)	−0.15 (9e−04)	0.058 (0.2)	−0.064 (0.1)
MEbrown	0.043 (0.3)	−0.046 (0.3)	0.023 (0.6)	0.061 (0.2)	0.032 (0.5)	0.063 (0.2)	−0.015 (0.7)	0.0077 (0.9)	−0.031 (0.5)	0.036 (0.4)
MEmidnightblue	0.079 (0.08)	−0.0052 (0.9)	0.058 (0.2)	0.12 (0.01)	0.023 (0.6)	0.067 (0.1)	0.039 (0.4)	−0.047 (0.3)	0.015 (0.7)	−0.0095 (0.8)
MEblue	−0.017 (0.7)	0.082 (0.07)	0.16 (4e−04)	0.19 (1e−05)	0.11 (0.01)	0.22 (4e−07)	0.44 (2e−25)	−0.33 (2e−14)	−0.54 (2e−39)	0.37 (1e−17)
MEmagenta	0.048 (0.3)	0.06 (0.2)	0.15 (6e−04)	0.14 (0.001)	0.074 (0.1)	0.13 (0.004)	0.09 (0.04)	−0.15 (5e−04)	0.0071 (0.9)	0.041 (0.4)
MEorange	−0.0092 (0.8)	0.069 (0.1)	0.073 (0.1)	−0.014 (0.8)	0.00088 (1)	0.0016 (1)	0.29 (6e−11)	−0.14 (0.002)	−0.15 (6e−04)	−0.0099 (0.8)
MEcyan	0.01 (0.8)	−0.14 (0.001)	−0.052 (0.2)	0.041 (0.4)	−0.075 (0.09)	−0.0021 (1)	−0.34 (2e−15)	0.29 (4e−11)	−0.28 (2e−10)	0.33 (3e−14)
MEgrey60	0.00037 (1)	−0.12 (0.01)	−0.16 (3e−04)	−0.12 (0.005)	−0.054 (0.2)	−0.13 (0.003)	−0.44 (1e−25)	0.35 (3e−16)	0.22 (4e−07)	−0.095 (0.03)
MEskyblue	−0.049 (0.3)	−0.11 (0.01)	−0.23 (1e−07)	−0.15 (7e−04)	−0.11 (0.01)	−0.18 (3e−05)	−0.21 (2e−06)	0.29 (2e−11)	−0.2 (1e−05)	0.13 (0.004)
MElightyellow	−0.12 (0.005)	−0.17 (1e−04)	−0.27 (6e−10)	−0.15 (5e−04)	−0.081 (0.07)	−0.2 (9e−06)	−0.31 (5e−13)	0.3 (5e−12)	−0.19 (3e−05)	0.21 (3e−06)
MEpink	−0.074 (0.1)	−0.16 (2e−04)	−0.19 (2e−05)	−0.079 (0.08)	−0.081 (0.07)	−0.15 (0.001)	−0.46 (4e−28)	0.3 (4e−12)	−0.15 (8e−04)	0.31 (1e−12)
MEdarkorange	−0.07 (0.1)	−0.13 (0.002)	−0.097 (0.03)	0.012 (0.8)	−0.038 (0.4)	−0.04 (0.4)	−0.2 (7e−06)	0.092 (0.04)	−0.3 (3e−12)	0.39 (2e−19)
MEdarkturquoise	−0.071 (0.1)	−0.17 (1e−04)	0.011 (0.8)	0.032 (0.5)	−0.024 (0.6)	−0.0026 (1)	−0.19 (1e−05)	0.075 (0.09)	−0.2 (4e−06)	0.3 (4e−12)
MEblack	−0.0015 (1)	−0.081 (0.07)	−0.11 (0.01)	−0.068 (0.1)	0.038 (0.4)	−0.059 (0.2)	−0.11 (0.01)	0.19 (1e−05)	0.13 (0.004)	−0.18 (6e−05)
MEdarkgreen	−0.024 (0.6)	−0.069 (0.1)	−0.062 (0.2)	−0.14 (0.002)	0.061 (0.2)	−0.065 (0.1)	0.034 (0.4)	−0.021 (0.6)	0.18 (3e−05)	−0.18 (3e−05)
MEred	0.01 (0.8)	−0.064 (0.2)	−0.089 (0.05)	−0.1 (0.02)	0.033 (0.5)	−0.068 (0.1)	0.031 (0.5)	0.0043 (0.9)	0.2 (5e−06)	−0.22 (7e−07)
MEroyalblue	0.016 (0.7)	−0.12 (0.007)	−0.083 (0.06)	−0.077 (0.09)	0.034 (0.4)	−0.065 (0.1)	−0.014 (0.8)	0.0035 (0.9)	−0.0034 (0.9)	0.013 (0.8)
MEturquoise	0.0033 (0.9)	−0.01 (0.8)	0.064 (0.1)	0.004 (0.9)	0.077 (0.09)	0.06 (0.2)	−0.012 (0.8)	−0.059 (0.2)	−0.015 (0.7)	0.075 (0.09)
MEgrey	0.051 (0.3)	−0.11 (0.01)	0.0085 (0.8)	−0.012 (0.8)	0.034 (0.5)	−0.029 (0.5)	−0.21 (2e−06)	0.082 (0.07)	0.16 (2e−04)	−0.025 (0.6)

FIGURE 8 | Construction of LUAD co-expression module and identification of key modules. Analysis of **(A)** the scale-free fit index and **(B)** the mean connectivity for various soft-thresholding powers. **(C)** Clustering dendrogram of genes based on topological overlapping. **(D)** A transcript of each module. **(E)** Analysis of module-clinical trait relationships of LUAD.

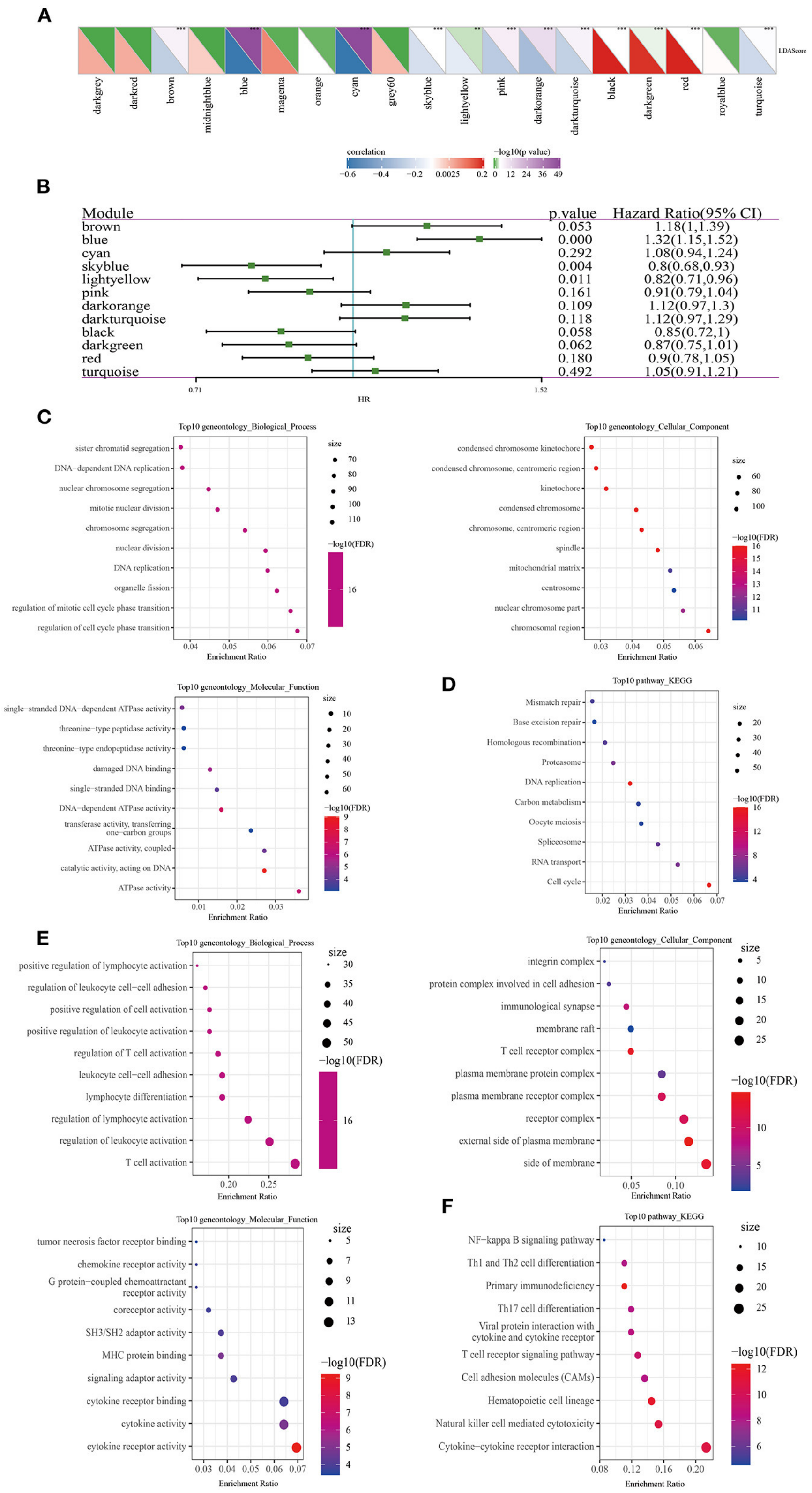

FIGURE 9 | Identification of LUAD prognostic-related modules and hub genes. **(A)** Correlation analysis between modules and LDA score. **(B)** Modules associated with LUAD prognosis were analyzed by univariate Cox screening. **(C)** The top 10 GO terms annotated by blue module annotations. **(D)** The top 10 KEGG pathways annotated by blue module annotations. **(E)** The top 10 GO terms enriched by the light yellow module. **(F)** The top 10 KEGG pathways enriched by the light yellow module.

Previous studies have found that LUAD subtypes with different molecular and immune characteristics appear different degrees of sensitivity to immunotherapies/chemotherapies (41). Consistently, the current findings showed that the four subtypes responded differently to immune/chemotherapy. It was mainly manifested in the differences in molecular expression of immune checkpoint molecules, TIDE scores, T cell dysfunction scores and exclusion scores among the four kinds of ISs, and the sensitivity to common chemotherapeutic drugs. Although the immune microenvironment of LUAD was comprehensively analyzed, these results may not correctly reflect the inherent characteristics of the tumor, which, however, is also important in regulating the function of immune cells (11). Therefore, we also characterized LUAD by the LDA score of each IS. LDA score was negatively related to the expression of immune checkpoint inhibitors, and also showed differences between CR/PR target lesions and PD target lesions.

More importantly, from 12 modules significantly associated with LDA score, we determined three modules closely associated with the prognosis of LUAD. Hub genes in blue module and light yellow module were screened. A high expression of 6 hub genes in blue module was associated with favorable LUAD prognosis, and they were mainly enriched in cell division-related pathways. In the light yellow module, seven hub genes mainly related to immunity were found to be protective of the survival of LUAD. Notably, most of these hub genes have been identified as prognostic biomarkers or regulators of cancer and were associated with pathologic progression of multiple tumor types. ARNTL2 was a prognostic biomarker of LUAD by promoting multiple organ metastasis and cell proliferation. In addition, high ARNTL2 was a poor prognostic marker for low-grade glioma, renal clear cell carcinoma and pancreatic cancer (42). RIPK2 acts as a tumor marker by regulating NF-κB signaling (43). ADA level in serum may be a biomarker for diagnosis and prognosis of oral squamous cell carcinoma (44). The variant of C. 657DEL5 in the NBN gene increases the risk of pancreatic cancer (45). NLRC3 mediates protection against colorectal cancer by inhibiting the activation of the mTOR signaling pathway (46). CLEC2D expression in lung cancer is linked to better clinical outcomes (47). AKNA is an effective target for diagnosis and treatment since it can regulate EMT-related pathways in gastric cancer (48). The expression of ZC3H12D is closely related to LUAD stage, lymph node metastasis and immune invasion (49). These findings highlight the importance of hub genes in the two modules, which are not independent but represent an important set of LUAD influencing factors for our study. In addition, we also obtained the interaction relationship of these 14 hub genes from the string database. It can be observed that there is less interaction between these genes (**Supplementary Figure 6A**), suggesting that they may play a role in their respective regulatory pathways. The R software package ClusterProfiler was used to analyze the functional enrichment of 14 hub genes. These genes were mainly enriched in biological processes such as lymphocyte activation involved in immune response, interference alpha production and so on (**Supplementary Figure 6B**). These hub genes were mainly divided into two parts, and each part of them had several high positive correlations with each other (**Supplementary Figure 6C**).

Although our study preliminarily explored the immune heterogeneity of different ISs in LUAD through bioinformatics analysis, there were still some limitations. The current sample size was small and came from public database, the population race was mainly limited to whites and blacks, therefore our results should be verified in other races. Moreover, the current research was limited to bioinformatics analysis, and further clinical studies are needed.

CONCLUSION

In this study, we identified four LUAD immune subtypes with different molecular characteristics, immune characteristics and prognostic outcomes based on immune cell signatures. In addition, ISs related modules were identified by WGCNA, and LUAD prognostic related modules and 14 hub genes was screened, of which 13 hub genes can be used as potential biomarkers to predict the prognosis of LUAD patients. Our research may provide a potential perspective for immunotherapy.

DATA AVAILABILITY STATEMENT

The datasets presented in this study can be found in online repositories. The names of the repository/repositories and accession number(s) can be found below: https://portal.gdc.cancer.gov/projects/TCGA-LUAD, https://TCGA-LUAD//www.ncbi.nlm.nih.gov/, GSE37745, GSE19188, GSE50081, GSE30219, GSE31210.

AUTHOR CONTRIBUTIONS

LD conceived and designed this study, conducted most of the experiments, data analysis, and wrote the manuscript. YY and GX provided needed funding and resources, and administrated the project. FL, TW, LD, and HC participated in collecting data and helped to draft the manuscript. All authors reviewed and approved the manuscript.

FUNDING

This work was financially supported by the National Nature Science Foundation of China (81972025, 81802115) and the Graduate Scientific Research and Innovation Project of Chongqing (CYB20162).

SUPPLEMENTARY MATERIAL

The Supplementary Material for this article can be found online at: https://www.frontiersin.org/articles/10.3389/fmed.2022.855387/full#supplementary-material

REFERENCES

1. Siegel RL, Miller KD, Fuchs HE, Jemal A. Cancer statistics, 2021. *CA Cancer J Clin*. (2021) 71:7–33. doi: 10.3322/caac.21654
2. Senosain MF, Massion PP. Intratumor heterogeneity in early lung adenocarcinoma. *Front Oncol*. (2020) 10:349. doi: 10.3389/fonc.2020.00349
3. Iqbal MA, Arora S, Prakasam G, Calin GA, Syed MA. MicroRNA in lung cancer: role, mechanisms, pathways, and therapeutic relevance. *Mol Aspects Med*. (2019) 70:3–20. doi: 10.1016/j.mam.2018.07.003
4. Duma N, Santana-Davila R, Molina JR. Non-small cell lung cancer: epidemiology, screening, diagnosis, and treatment. *Mayo Clin Proc.* (2019) 94:1623–40. doi: 10.1016/j.mayocp.2019.01.013
5. Shroff GS, de Groot PM, Papadimitrakopoulou VA, Truong MT, Carter BW. Targeted therapy and immunotherapy in the treatment of non-small cell lung cancer. *Radiol Clin North Am.* (2018) 56:485–95. doi: 10.1016/j.rcl.2018.01.012
6. Rosner S, Reuss JE, Forde PM. PD-1 blockade in early-stage lung cancer. *Annu Rev Med.* (2019) 70:425–35. doi: 10.1146/annurev-med-050217-025205
7. Miwa S, Shirai T, Yamamoto N, Hayashi K, Takeuchi A, Igarashi K, et al. Current and emerging targets in immunotherapy for osteosarcoma. *J Oncol.* (2019) 2019:7035045. doi: 10.1155/2019/7035045
8. Osmani L, Askin F, Gabrielson E, Li QK. Current WHO guidelines and the critical role of immunohistochemical markers in the sub-classification of non-small cell lung carcinoma (NSCLC): moving from targeted therapy to immunotherapy. *Semin Cancer Biol.* (2018) 52:103–9. doi: 10.1016/j.semcancer.2017.11.019
9. Tang YQ, Chen TF, Zhang Y, Zhao XC, Zhang YZ, Wang GQ, et al. The tumor immune microenvironment transcriptomic subtypes of colorectal cancer for prognosis and development of precise immunotherapy. *Gastroenterol Rep (Oxf).* (2020) 8:381–89. doi: 10.1093/gastro/goaa045
10. Wang S, Xiong Y, Zhang Q, Su D, Yu C, Cao Y, et al. Clinical significance and immunogenomic landscape analyses of the immune cell signature based prognostic model for patients with breast cancer. *Brief Bioinform*. (2021) 22:bbaa311. doi: 10.1093/bib/bbaa311
11. Amara D, Wolf DM. van 't Veer L, Esserman L, Campbell M, Yau C. Co-expression modules identified from published immune signatures reveal five distinct immune subtypes in breast cancer. *Breast Cancer Res Treat.* (2017) 161:41–50. doi: 10.1007/s10549-016-4041-3
12. Zhang S, Zeng X, Lin S, Liang M, Huang H. Identification of seven-gene marker to predict the survival of patients with lung adenocarcinoma using integrated multi-omics data analysis. *J Clin Lab Anal.* (2022) 36:e24190. doi: 10.1002/jcla.24190
13. Guo CR, Mao Y, Jiang F, Juan CX, Zhou GP Li N. Computational detection of a genome instability-derived lncRNA signature for predicting the clinical outcome of lung adenocarcinoma. *Cancer Med.* (2022) 11:864–79. doi: 10.1002/cam4.4471
14. Lane B, Khan MT, Choudhury A, Salem A, West CML. Development and validation of a hypoxia-associated signature for lung adenocarcinoma. *Sci Rep.* (2022) 12:1290. doi: 10.1038/s41598-022-05385-7
15. Goldmann T, Marwitz S, Nitschkowski D, Krupar R, Backman M, Elfving H, et al. PD-L1 amplification is associated with an immune cell rich phenotype in squamous cell cancer of the lung. *Cancer Immunol Immunother.* (2021) 70:2577–87. doi: 10.1007/s00262-020-02825-z
16. Hou J, Aerts J, den Hamer B, van Ijcken W, den Bakker M, Riegman P, et al. Gene expression-based classification of non-small cell lung carcinomas and survival prediction. *PLoS ONE.* (2010) 5:e10312. doi: 10.1371/journal.pone.0010312
17. Der SD, Sykes J, Pintilie M, Zhu CQ, Strumpf D, Liu N, et al. Validation of a histology-independent prognostic gene signature for early-stage, non-small-cell lung cancer including stage IA patients. *J Thorac Oncol.* (2014) 9:59–64. doi: 10.1097/JTO.0000000000000042
18. Rousseaux S, Debernardi A, Jacquiau B, Vitte AL, Vesin A, Nagy-Mignotte H, et al. Ectopic activation of germline and placental genes identifies aggressive metastasis-prone lung cancers. *Sci Transl Med.* (2013) 5:186ra166. doi: 10.1126/scitranslmed.3005723
19. Okayama H, Kohno T, Ishii Y, Shimada Y, Shiraishi K, Iwakawa R, et al. Identification of genes upregulated in ALK-positive and EGFR/KRAS/ALK-negative lung adenocarcinomas. *Cancer Res.* (2012) 72:100–11. doi: 10.1158/0008-5472.CAN-11-1403
20. Liu S, Wang Z, Zhu R, Wang F, Cheng Y, Liu Y. Three differential expression analysis methods for RNA sequencing: limma, EdgeR, DESeq2. *J Vis Exp*. (2021). doi: 10.3791/62528
21. Mayakonda A, Lin DC, Assenov Y, Plass C, Koeffler HP. Maftools: efficient and comprehensive analysis of somatic variants in cancer. *Genome Res.* (2018) 28:1747–56. doi: 10.1101/gr.239244.118
22. Wilkerson MD, Hayes DN. ConsensusClusterPlus: a class discovery tool with confidence assessments and item tracking. *Bioinformatics.* (2010) 26:1572–3. doi: 10.1093/bioinformatics/btq170
23. Danilova L, Ho WJ, Zhu Q, Vithayathil T, De Jesus-Acosta A, Azad NS, et al. Programmed cell death ligand-1 (PD-L1) and CD8 expression profiling identify an immunologic subtype of pancreatic ductal adenocarcinomas with favorable survival. *Cancer Immunol Res.* (2019) 7:886–95. doi: 10.1158/2326-6066.CIR-18-0822
24. Rooney MS, Shukla SA, Wu CJ, Getz G, Hacohen N. Molecular and genetic properties of tumors associated with local immune cytolytic activity. *Cell.* (2015) 160:48–61. doi: 10.1016/j.cell.2014.12.033
25. Masiero M, Simões FC, Han HD, Snell C, Peterkin T, Bridges E, et al. A core human primary tumor angiogenesis signature identifies the endothelial orphan receptor ELTD1 as a key regulator of angiogenesis. *Cancer Cell.* (2013) 24:229–41. doi: 10.1016/j.ccr.2013.06.004
26. Newman AM, Liu CL, Green MR, Gentles AJ, Feng W, Xu Y, et al. Robust enumeration of cell subsets from tissue expression profiles. *Nat Methods.* (2015) 12:453–7. doi: 10.1038/nmeth.3337
27. Jiang P, Gu S, Pan D, Fu J, Sahu A, Hu X, et al. Signatures of T cell dysfunction and exclusion predict cancer immunotherapy response. *Nat Med.* (2018) 24:1550–8. doi: 10.1038/s41591-018-0136-1
28. Zhang B, Horvath S. A general framework for weighted gene co-expression network analysis. *Stat Appl Genet Mol Biol.* (2005) 4. doi: 10.2202/1544-6115.1128
29. Yu G, Wang LG, Han Y, He QY. clusterProfiler: an R package for comparing biological themes among gene clusters. *OMICS.* (2012) 16:284–7. doi: 10.1089/omi.2011.0118
30. Thorsson V, Gibbs DL, Brown SD, Wolf D, Bortone DS, Ou Yang TH, et al. The immune landscape of cancer. *Immunity.* (2018) 48:812–30. doi: 10.1016/j.immuni.2018.03.023
31. Ramos-Casals M, Brahmer JR, Callahan MK, Flores-Chávez A, Keegan N, Khamashta MA, et al. Immune-related adverse events of checkpoint inhibitors. *Nat Rev Dis Primers.* (2020) 6:38. doi: 10.1038/s41572-020-0160-6
32. Mariathasan S, Turley SJ, Nickles D, Castiglioni A, Yuen K, Wang Y, et al. TGFβ attenuates tumour response to PD-L1 blockade by contributing to exclusion of T cells. *Nature.* (2018) 554:544–8. doi: 10.1038/nature25501
33. Hugo W, Zaretsky JM, Sun L, Song C, Moreno BH, Hu-Lieskovan S, et al. Genomic and transcriptomic features of response to anti-PD-1 therapy in metastatic melanoma. *Cell.* (2016) 165:35–44. doi: 10.1016/j.cell.2016.02.065
34. Denisenko TV, Budkevich IN, Zhivotovsky B. Cell death-based treatment of lung adenocarcinoma. *Cell Death Dis.* (2018) 9:117. doi: 10.1038/s41419-017-0063-y
35. Travis WD, Brambilla E, Noguchi M, Nicholson AG, Geisinger KR, Yatabe Y, et al. International association for the study of lung cancer/american thoracic society/european respiratory society international multidisciplinary classification of lung adenocarcinoma. *J Thorac Oncol.* (2011) 6:244–85. doi: 10.1097/JTO.0b013e318206a221
36. Inamura K. Clinicopathological characteristics and mutations driving development of early lung adenocarcinoma: tumor initiation and progression. *Int J Mol Sci.* (2018) 19:1259. doi: 10.3390/ijms19041259
37. Butnor KJ. Controversies and challenges in the histologic subtyping of lung adenocarcinoma. *Transl Lung Cancer Res.* (2020) 9:839–46. doi: 10.21037/tlcr.2019.12.30
38. Zheng Z, Deng W, Yang J. Identification of 5-gene signature improves lung adenocarcinoma prognostic stratification based on differential expression invasion genes of molecular subtypes. *Biomed Res Int.* (2020) 2020:8832739. doi: 10.1155/2020/8832739
39. Galon J, Angell HK, Bedognetti D, Marincola FM. The continuum of cancer immunosurveillance: prognostic, predictive, and mechanistic signatures. *Immunity.* (2013) 39:11–26. doi: 10.1016/j.immuni.2013.07.008

40. Bindea G, Mlecnik B, Tosolini M, Kirilovsky A, Waldner M, Obenauf AC, et al. Spatiotemporal dynamics of intratumoral immune cells reveal the immune landscape in human cancer. *Immunity*. (2013) 39:782–95. doi: 10.1016/j.immuni.2013.10.003
41. Xu F, Chen JX, Yang XB, Hong XB Li ZX, Lin L, et al. Analysis of lung adenocarcinoma subtypes based on immune signatures identifies clinical implications for cancer therapy. *Mol Ther Oncolytics*. (2020) 17:241–9. doi: 10.1016/j.omto.2020.03.021
42. Brady JJ, Chuang CH, Greenside PG, Rogers ZN, Murray CW, Caswell DR, et al. An Arntl2-driven secretome enables lung adenocarcinoma metastatic self-sufficiency. *Cancer Cell*. (2016) 29:697–710. doi: 10.1016/j.ccell.2016.03.003
43. Yang Q, Tian S, Liu Z, Dong W. Knockdown of RIPK2 inhibits proliferation and migration, and induces apoptosis via the NF-κB signaling pathway in gastric cancer. *Front Genet*. (2021) 12:627464. doi: 10.3389/fgene.2021.627464
44. Kelgandre DC, Pathak J, Patel S, Ingale P, Swain N. Adenosine deaminase - a novel diagnostic and prognostic biomarker for oral squamous cell carcinoma. *Asian Pac J Cancer Prev*. (2016) 17:1865–8. doi: 10.7314/apjcp.2016.17.4.1865
45. Borecka M, Zemankova P, Lhota F, Soukupova J, Kleiblova P, Vocka M, et al. The c657del5 variant in the NBN gene predisposes to pancreatic cancer. *Gene*. (2016) 587:169–72. doi: 10.1016/j.gene.2016.04.056
46. Karki R, Man SM, Malireddi RKS, Kesavardhana S, Zhu Q, Burton AR, et al. NLRC3 is an inhibitory sensor of PI3K-mTOR pathways in cancer. *Nature*. (2016) 540:583–7. doi: 10.1038/nature20597
47. Braud VM, Biton J, Becht E, Knockaert S, Mansuet-Lupo A, Cosson E, et al. Expression of LLT1 and its receptor CD161 in lung cancer is associated with better clinical outcome. *Oncoimmunology*. (2018) 7:e1423184. doi: 10.1080/2162402X.2017.1423184
48. Wang G, Sun D, Li W, Xin Y, AKNA. is a potential prognostic biomarker in gastric cancer and function as a tumor suppressor by modulating EMT-related pathways. *Biomed Res Int*. (2020) 2020:6726759. doi: 10.1155/2020/6726759
49. Yang B, Ji LL, Xu HL Li XP, Zhou HG, Xiao T, et al. Zc3h12d, a novel of hypomethylated and immune-related for prognostic marker of lung adenocarcinoma. *J Inflamm Res*. (2021) 14:2389–401. doi: 10.2147/JIR.S304278

Conflict of Interest: The authors declare that the research was conducted in the absence of any commercial or financial relationships that could be construed as a potential conflict of interest.

frontiers
in Medicine

ORIGINAL RESEARCH
published: 31 March 2022
doi: 10.3389/fmed.2022.828370

Effect of Hydrogen Inhalation Therapy on Hearing Loss of Patients With Nasopharyngeal Carcinoma After Radiotherapy

Xiaofeng Kong[1], *Tianyu Lu*[2], *You-Yong Lu*[3], *Zhinan Yin*[4] *and Kecheng Xu*[2]*

[1] *Hydrogen Medicine Institute, The Biomedical Translational Research Institute, Jinan University, Guangzhou, China,* [2] *Department of Oncology, Fuda Cancer Hospital, Jinan University, Guangzhou, China,* [3] *Key Laboratory of Carcinogenesis and Translational Research (Ministry of Education), Laboratory of Molecular Oncology, Peking University Cancer Hospital & Institute, Beijing, China,* [4] *Faculty of Medical Science, The Biomedical Translational Research Institute, Jinan University, Guangzhou, China*

Objective: To evaluate the clinical efficacy and safety of hydrogen inhalation in improving hearing loss in patients with long-term survival of nasopharyngeal carcinoma after radiotherapy.

Methods: The eustachian tube dysfunction score, pure tone air conduction threshold, bone conduction threshold, the score of tympanogram and otoscope were prospectively observed in patients with deafness after radiotherapy only or combined radiotherapy and chemotherapy for nasopharyngeal carcinoma. Paired t test and one-way analysis of variance were used to analyze the data before and after treatment.

Results: A total of 17 patients were observed. The median time from radiotherapy to now was 228 months, and the median time from the diagnose of deafness to now was 92 months. After 4 weeks of hydrogen inhalation, the score of eustachian tube dysfunction, air conduction and bone conduction hearing thresholds were significantly reduced, P values were 0.0293, 0.0027, 0.0404, respectively. The mean air-bone gap, the score of otoendoscopy and tympanogram were also decreased, but the differences were not significant ($P = 0.2079$, $P = 0.0536$, $P = 0.1056$). Patients with radiotherapy alone and concurrent chemo-radiotherapy had significantly lower air conduction hearing threshold after hydrogen absorption ($P = 0.0142$, $P = 0.0495$). The results of air and bone hearing thresholds before, 4 and 12 weeks after hydrogen inhalation showed a descending trend. The air and bone hearing thresholds before hydrogen inhalation were 74.69 ± 27.03 dB and 45.70 ± 21.58 dB, respectively. At the 12th week, the mean values of air and bone hearing thresholds were the lowest, which were 66.88 ± 20.88 dB and 40.94 ± 18.93 dB, respectively, but there was no significant difference in air and bone hearing thresholds among all groups ($P = 0.6755$, $P = 0.7712$). After hydrogen inhalation treatment, no adverse reactions such as nosebleed, chest pain, dyspnea, nausea, vomiting, dizziness, earache and allergic reaction were observed.

Conclusion: This is the first prospective study on the effect of hydrogen inhalation on hearing improvement in patients with deafness after radiotherapy/chemotherapy for

OPEN ACCESS

Edited by:
Fu Wang,
Xi'an Jiaotong University, China

Reviewed by:
Wei Guo,
Shanghai Jiao Tong University, China
Jun Liang,
Air Force Military Medical University, China
Chengli Li,
Shandong Provincial Hospital, China

***Correspondence:**
Kecheng Xu
xukc@vip.163.com

Specialty section:
This article was submitted to Precision Medicine, a section of the journal Frontiers in Medicine

Received: *03 December 2021*
Accepted: *28 January 2022*
Published: *31 March 2022*

Citation:
Kong X, Lu T, Lu Y-Y, Yin Z and Xu K (2022) Effect of Hydrogen Inhalation Therapy on Hearing Loss of Patients With Nasopharyngeal Carcinoma After Radiotherapy. Front. Med. 9:828370. doi: 10.3389/fmed.2022.828370

nasopharyngeal carcinoma, suggesting that continuous hydrogen inhalation may be an alternative rehabilitation therapy for these patients.

Keywords: hydrogen inhalation, hydrogen oxygen inhalation, nasopharyngeal carcinoma, radiotherapy, chemotherapy, hearing loss, hearing impairment

INTRODUCTION

As one of the most common malignant tumors in the head and neck, nasopharyngeal carcinoma (NPC) is primarily treated with radiotherapy alone or radiotherapy combined with chemotherapy. Patients' 5-year survival rate can be 77.9–87.4% (1–4). Due to the fact that the entire auditory system including the middle ear, cochlea, auditory nerves, brainstem and auditory cortex are all located at or close to the irradiation area for nasopharyngeal cancer treatment, the radiation from radiotherapy inevitably implicates the aforementioned anatomical structure of the nasopharynx. Radiotherapy is usually followed by such complications as secretory otitis media, ossicular chain necrosis, and cochlea & auditory nerve damage. Hearing impairment is the most common late-stage adverse reaction after nasopharyngeal carcinoma radiotherapy (5, 6). As patients survive longer, this complication becomes progressively worse and seriously compromises the quality of life. So far, there has been no special treatment, making tumor rehabilitation a major challenge (7, 8).

Hydrogen (H_2) is the lightest and smallest gas in nature. Dole et al. (9) first reported the therapeutic effect of high-pressure and high-concentration hydrogen on mouse models with squamous cell carcinoma in 1975. In 2001, Gharib et al. (10) proved that inhalation of high-pressure hydrogen alleviates the inflammatory response caused by liver parasite infection. In 2007, Ohsawa et al. (11) found that low-concentration hydrogen selectively neutralizes hydroxyl radicals (OH) and peroxynitrite (ONOO-); and possesses antioxidant properties. In recent years, a large number of preclinical studies and a few clinical studies have observed the preventive and therapeutic effects of this gas on different system diseases (12), including the effects on inhibiting cancer cell growth, invasion and metastasis; and in reducing adverse reactions of radiotherapy/chemotherapy (12–15). In respect of the hearing system, some studies have revealed that molecular hydrogen protects hair cells of the hearing system through antioxidant effects, and ameliorates hearing (16–19).

This study observes the changes of hearing-related indexes before and after hydrogen inhalation by 17 patients with 5-year-long or longer hearing impairment after nasopharyngeal carcinoma treatment, with a focus on assessing the effectiveness and safety of hydrogen in improving hearing. As far as we know, this is the first report of research findings in this domain. With the hope to reduce hearing loss after radiotherapy or chemotherapy, we wish to provide a new, safe and effective treatment and rehabilitation option for patients with nasopharyngeal carcinoma.

SUBJECTS AND METHODS

Subjects

From May 2019 to October 2020, a total of 34 nasopharyngeal carcinoma patients with post-radiotherapy hearing loss from the Nasopharyngeal Carcinoma Group of the Light of Life Cancer Rehabilitation Association of Guangdong Province were enrolled in this study after signing informed consent. According to the registered clinical trial (ClinicalTrials.gov, ID: NCT03818347; Registration Date: January 24, 2019), all the enrolled patients met the following conditions: (1) Diagnosed with Stage I to IVb nasopharyngeal carcinoma after pathological examinations; (2) Received conventional radiotherapy (radiotherapy) or radiotherapy combined with chemotherapy (chemoradiotherapy) 5 years ago; (3) Hearing and hearing test results before anti-tumor treatment were normal; (4) Experienced hearing loss at the age of 60 or lower, which excluded the probability of presbycusis; (5) Having inhaled hydrogen for at least 4 weeks. Patients with the following conditions were excluded from this study: (1) Severe hypertension, diabetic autoimmune disease, history of head trauma, and experience of long-time working in noisy environment; (2) Recurrence or metastasis of existing tumor(s); (3) Middle ear disease or hearing impairment developed before anti-tumor treatment; (4) Head and neck radiotherapy due to other reasons; (5) Middle ear effusion as evidenced by otoscopy.

The three patients who did not keep inhaling hydrogen daily and 14 patients who failed to complete regular relevant examinations were excluded from analysis. A total of 17 patients (34 ears) completed the study eventually.

The 17 patients, including seven males and 10 females, aged from 47 to 67 years old, with a median of 58 years old. According to AJCC (American Joint Committee on Cancer) tumor staging (7th edition), 10 cases were in Stage I, 4 cases in Stage II, 1 case in Stage III, and 2 cases in Stage IV. Eleven of the cases had received radical radiotherapy alone; and 6 cases radiotherapy combined with chemotherapy. During radiotherapy, the radiation dose of 68–72 Gy was applied to nasopharyngeal carcinoma and draining lymph node areas; 70.0 Gy to positive cervical lymph nodes; and 50.0–60.0 Gy to negative cervical lymph nodes. The patients were exposed to radiation 34 to 38 times in total once a day for five times a week, with dose fractionation set at 1.8–2.0 Gy each time. Concurrent chemotherapy was performed with the regimen 40 mg/m2 cisplatin (DDP) given through intravenous drips once a week. It has been 100 to 355 months (a median of 259 months) since the aforementioned treatment was completed. Hearing loss occurred 24 to 289 months after the completion of radiotherapy or chemoradiotherapy, with a median of 117 months. It persisted for 30–186 months, with a median of 90 months (**Table 1**). The patients received hearing loss treatments including: glucocorticoid treatment in 12 cases, acupuncture in seven cases, Chinese medicine treatment in 16 cases, and hyperbaric oxygen treatment in one case. None of the patients showed improvement from the treatments.

Hydrogen Inhalation Method

The subjects inhaled hydrogen-oxygen mixture, which contained 2.0 L/min hydrogen and 1.0 L/min oxygen (produced by hydrogen-oxygen nebulizer AMS-H-03, Shanghai Asclepius Meditec Co., Ltd.), through nasal tubes in quite conditions. Daily inhalation lasted 3–6 h for 4–12 weeks, with eight cases for 12 weeks, six cases for 8 weeks and three cases for 4 weeks. The test period was divided into three periods for assessment: before hydrogen treatment, after 4 weeks of hydrogen treatment, and after 12 weeks of hydrogen treatment.

Eustachian Tube Dysfunction Questionnaire-7 (ETDQ-7) Survey

Eustachian tube dysfunction questionnaire-7 (ETDQ-7) survey (20, 21) was adopted. The scale included seven items, representing seven levels (from 1 to 7 scores) according to the severity of symptoms. The higher the score, the more severe the symptoms. Patients were given face-to-face questionnaire surveys 1–3 days before hydrogen inhalation and 1–3 days after 4 weeks of hydrogen inhalation.

Tympanic Membrane Detection

Scoring was performed according to otoscope-based examination: 1 score: tympanic membrane turbidity and thickening; 2 scores: tympanic membrane congestion and indentation as well as disappearance of light cone; 3 scores: tympanic membrane effusion; and 4 scores: tympanic membrane perforation.

Tympanogram Changes

Acoustic impedance tester was used to assess the changes in calm breathing tympanogram (17, 18). Tympanogram scoring rules were: 3 scores for type Ad; 2 scores for type A or As; 1 score for type C; and 0 score for type B.

Pure-Tone Hearing Threshold Testing

Pure-tone hearing threshold testing (with AT235 from a Danish international hearing health care company) was carried out in a standard sound-proof chamber. With acoustic standard set at GB/T16296 and reverberation time at 0.3 ± 0.15 s, pure-tone hearing thresholds in conditions of 0.5, 1, 2, 4, and 8 kHz were tested in sequence. The average air-conduction threshold, bone-conduction threshold, and air-bone gap under 0.5–4 kHz were calculated. The average pure tone hearing threshold (PTA) of four frequencies divides hearing loss into the following levels: normal hearing is defined as the mean of pure tone hearing threshold $\leq$ 25 dB; 26–40 dB HL was mild hearing loss, 41–55 dB HL was moderate hearing loss, 56–70 dB HL was moderately severe hearing loss, 71–90 dB HL was severe hearing loss, and $\geq$91 dB HL was very severe hearing loss. Pure tone hearing threshold test by hearing detection professional testing.

Safety Assessment

According to Common Terminology Criteria for Adverse Events (CTCAE-4.0 version) defined by the National Cancer Institute of U.S. Department of Health and Human Services (22), symptoms or side effects are graded from Grade 1–5. Safety evaluation was conducted once every 4 weeks after hydrogen inhalation, covering symptoms of nose bleeding, cough, chest pain, dyspnea, nausea, vomiting, dizziness, earache and allergic reaction.

Statistical Analysis

Measurement data were expressed as x ± s. The data before and after hydrogen inhalation were compared by paired *t* test. Different hydrogen uptake durations were compared using one-way analysis of variance. $P \leq 0.05$ indicated that the difference is statistically significant. All analyses and figures were produced using GraphPad Prism 5.0 (GraphPad software, San Diego, CA, USA).

RESULTS

Eustachian Tube Function

A total of 17 cases received the survey using 7-item questionnaires about eustachian tube dysfunction. 34 questionnaires were returned back, with 100% effective response rate. The score before hydrogen inhalation was 3.25 ± 2.00, and that after 4 weeks of hydrogen inhalation was 2.59 ± 1.65. The difference between the two groups was statistically significant ($P < 0.05$) (**Table 2**).

Scoring of Tympanic Membrane Under Otoscope and Tympanogram

Tympanic membrane perforation occurred in five ears before hydrogen inhalation and persisted after treatment. After 4 weeks of hydrogen inhalation, the tympanic membrane score based on otoscopy stabilized in 10 cases, improved in 6 cases, and worsened in one case. However, the difference compared to before hydrogen inhalation was not statistically significant ($P > 0.05$). Tympanogram scores before and after hydrogen inhalation showed no statistically significant difference ($P > 0.05$) (**Table 2**).

Hearing Changes

Hearing Changes After 4 Weeks of Hydrogen Inhalation

The average air conduction, bone conduction and air-bone gap before hydrogen inhalation in 17 patients (34 ears) were 77.46 ± 28.12, 46.76 ± 20.73, and 30.70 ± 11.12 dB, respectively. After 4 weeks of hydrogen inhalation treatment, both air conduction threshold and bone conduction threshold were significantly lower than those before hydrogen inhalation, being 73.35 ± 28.20 dB ($P = 0.0027$) and 44.56 ± 19.50dB ($P = 0.0404$), respectively (**Figures 1A,B**). Among them, the threshold of air conductivity was significantly improved, with a decrease in 64.71% of the patients (**Table 3**). The mean air bone gap(ABG) decreased from that before treatment (28.78 ± 13.44 dB), but the difference was not statistically significant ($P = 0.2079$) (**Figure 1C**).

TABLE 1 | Basic information of the 17 patients with hearing loss after nasopharyngeal carcinoma radiotherapy/chemoradiotherapy.

Case no.	Age (Y)	Gender	Staging at time of treatment	Tumor treatment	End of treatment till now (month)	End of treatment to discovery of hearing loss (month)	End of treatment to receiving hydrogen treatment (month)	Hydrogen inhalation duration (week)
1	66	Female	I	Radiotherapy	300	246	54	12
2	47	Male	III	Chemoradiotherapy	173	83	90	12
3	63	Female	I	Chemoradiotherapy	220	114	106	12
4	62	Male	II	Radiotherapy	271	115	156	8
5	47	Female	I	Radiotherapy	120	54	66	12
6	67	Female	I	Radiotherapy	147	117	30	8
7	64	Female	IV	Chemoradiotherapy	259	114	145	12
8	63	Female	II	Chemoradiotherapy	113	54	59	12
9	60	Male	II	Radiotherapy	275	149	126	4
10	53	Male	I	Radiotherapy	354	168	186	8
11	53	Female	I	Radiotherapy	355	289	66	4
12	60	Female	II	Chemoradiotherapy	183	117	66	8
13	56	Male	I	Radiotherapy	268	130	138	4
14	67	Female	I	Radiotherapy	310	196	114	8
15	48	Female	IV	Chemoradiotherapy	100	56	44	12
16	54	Male	I	Radiotherapy	114	24	90	12
17	60	Male	I	Radiotherapy	228	144	84	8

TABLE 2 | Eustachian tube dysfunction 7-item score, otoscopy score and tympanogram score.

	Number of ears	Before hydrogen-oxygen inhalation x ± s	4 weeks after hydrogen- oxygen inhalation x ± s	*P* value
Eustachian tube disfunction 7-item score		3.25 ± 2.00	2.59 ± 1.65	0.0293*
Otoscopy score	34	1.76 ± 1.26	1.44 ± 1.24	0.0536
Tympanogrom score	34	0.68 ± 0.98	0.97 ± 1.06	0.1056

*$P < 0.05$.

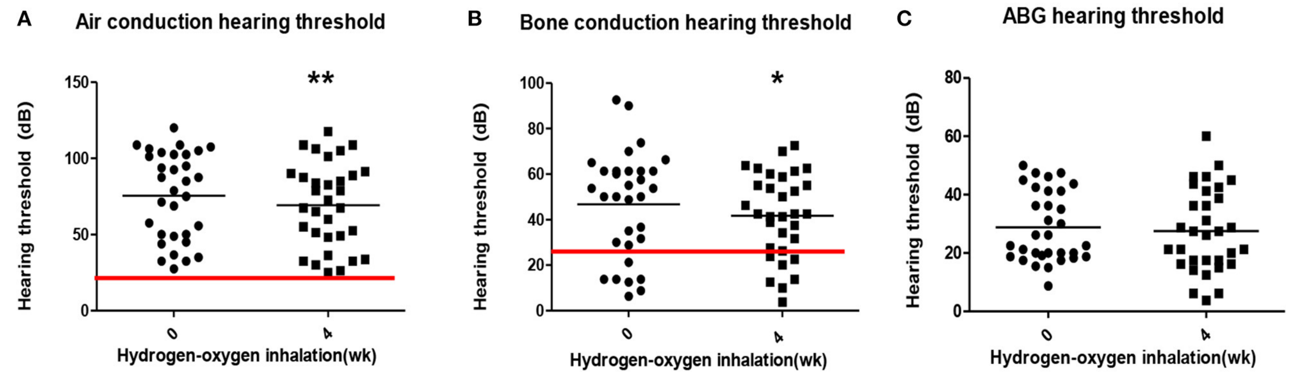

FIGURE 1 | Pure tone hearing threshold tests result before and after hydrogen-oxygen mixed gas inhalation on hearing loss patients with long-term survival after combined modality treatment of nasopharyngeal carcinoma. **(A)** Test results of the air conduction hearing threshold. **(B)** Test results of the bone conduction hearing threshold. **(C)** Test results of the air bone gap (ABG) hearing threshold. The parallel red long lines in the figure represent the normal range,the black short lines represent the average value at each time point. Data are analyzed by paired *t* test. $^{*}P < 0.05$, $^{**}P < 0.01$.

TABLE 3 | Air conductance threshold improvement before and 4 weeks after hydrogen and oxygen inhalation therapy.

Air-conduction hearing threshold improvement decibel (dB)	Number of ears	Percentage (%)
≤0	12	35.29%
0–10	18	52.94%
11–20	3	8.82%
21–30	1	2.94%

Hearing Improvement in Patients With Different Initial Treatment Regimens for Tumors

According to the initial methods of tumor treatment, 17 patients (34 ears) were separated to radiotherapy group (22 ears) and concurrent chemoradiotherapy group (12 ears). The average air-conduction threshold, bone-conduction threshold and air-bone gap of the radiotherapy group before hydrogen inhalation were 76.70 ± 28.25, 47.05 ± 22.30, and 29.66 ± 9.86 dB, respectively. After 4 weeks of hydrogen inhalation, the air-conduction threshold showed decline with significant difference (73.98 ± 30.29 dB, $P = 0.0142$, **Figure 2A**); and bone-conduction and air-bone gap hearing thresholds showed decrease without significant difference ($P = 0.6137$ and $P = 0.1699$, respectively. **Figures 2C,E**). Before hydrogen inhalation, the average air-conduction threshold, bone-conduction threshold and air-bone gap of patients with concurrent chemoradiotherapy were 78.85 ± 28.55, 47.05 ± 17.72, and 31.81 ± 14.63 dB, respectively. After hydrogen inhalation, the thresholds of air conduction and bone conduction were significantly reduced, being 72.19 ± 25.13 dB and 39.04 ± 12.61 dB, respectively. P values were 0.0495 and 0.0134, respectively (**Figures 2B,D**). The average air-bone gap between the two groups was increased (33.15 ± 18.48 dB) compared to before treatment, but the difference was not statistically significant ($P = 0.7283$, **Figure 2F**).

Hearing Threshold Changes in Patients With Different Hydrogen Inhalation Durations

Eight of the deaf patients (16 ears) were treated with hydrogen inhalation for 12 weeks. The results of air conduction threshold and bone conduction threshold were compared before, 4 weeks and 12 weeks after hydrogen inhalation treatment, showing a downward trend. Before hydrogen inhalation, air and bone hearing thresholds were 74.69 ± 27.03 dB and 45.70 ± 21.58 dB, respectively. At 12 weeks of treatment, the mean values of air conduction threshold and bone conduction threshold were the lowest, which were 66.88 ± 20.88 dB and 40.94 ± 18.93 dB, respectively. However, there was no significant difference in air and bone hearing threshold among all groups ($P = 0.6755$,$P = 0.7712$, **Figures 3A,B**).

Patients' Hearing Changes After Suspension of Hydrogen-Oxygen Inhalation

Five patients (10 ears) were given hearing checkups 6–9 months after they stopped hydrogen-oxygen gas inhalation. According to the checkup results, the bone- and air-conduction hearing thresholds of three ears were stable or showed continuous improvement; and the hearing thresholds of seven ears increased in decibels. Average decibels of both air- and bone-conduction hearing thresholds for the affected ears were higher than before, but no significant difference was observed with P value of 0.0596 and 0.3473 respectively (see **Figures 4A,B**).

Adverse Reactions Related to Hydrogen-Oxygen Inhalation

No such common adverse reaction as nose bleeding, chest pain, dyspnea, nausea, vomiting, dizziness, earache or skin allergy was observed after hydrogen-oxygen inhalation. Ten patients (58.8%) complained of mild cough before hydrogen inhalation, and 11 patients (64.7%) complained of cough 4 weeks after hydrogen inhalation. Earache occurred before hydrogen inhalation in one of the cases and no change of earache after the treatment. As time passed, the aforementioned symptoms did not worsen (**Table 4**).

DISCUSSION

Hearing Impairment After Radiotherapy

Nasopharyngeal carcinoma (NPC) is the most common malignant tumor of the head and neck, with more than half of the world's cases found in China. And such cases are mostly seen in southern and southeastern coastal areas of China. Currently, radiotherapy is the most effective treatment for NPC. As radiotherapy technology advances, the efficacy has improved gradually. Early-stage NPC patients'5-year survival rate may reach as high as 95% (23). As the most common adverse reaction after radiotherapy, hearing impairment takes place in the following three circumstances: (1) Hearing impairment occurs directly after radiotherapy and is usually temporary. Patients recover from it after several weeks or months (24). (2) Sudden deafness or sudden hearing loss occurs without any apparent cause at a certain time point after the end of radiotherapy (25). (3) Hearing loss occurs gradually after radiotherapy or chemoradiotherapy after a "latency period" of varying lengths (26). This is the case with the group of patients included in this study. The median interval (shortest at 100 months) from the completion of radiotherapy or chemoradiotherapy till now is 259 months. Hearing loss occurred at the median time of 117 months (ranging from 24 months to 285 month) after the completion of radiotherapy or chemoradiotherapy. It persisted for a median time of 90 months (shortest at 30 months). In these cases, there is neither evidence of the existence or recurrence of any primary tumor, nor other factor that could have caused hearing impairment.

Hearing loss is a major late complication for long-term surviving patients after radiotherapy or radiotherapy combined with chemotherapy. As a patient survives longer, the incidence of hearing loss increases, and hearing loss becomes more serious (27). The hearing loss rate of patients who survive more than 5 years can reach 60.5–94% (6, 28–30). Due to the lack of

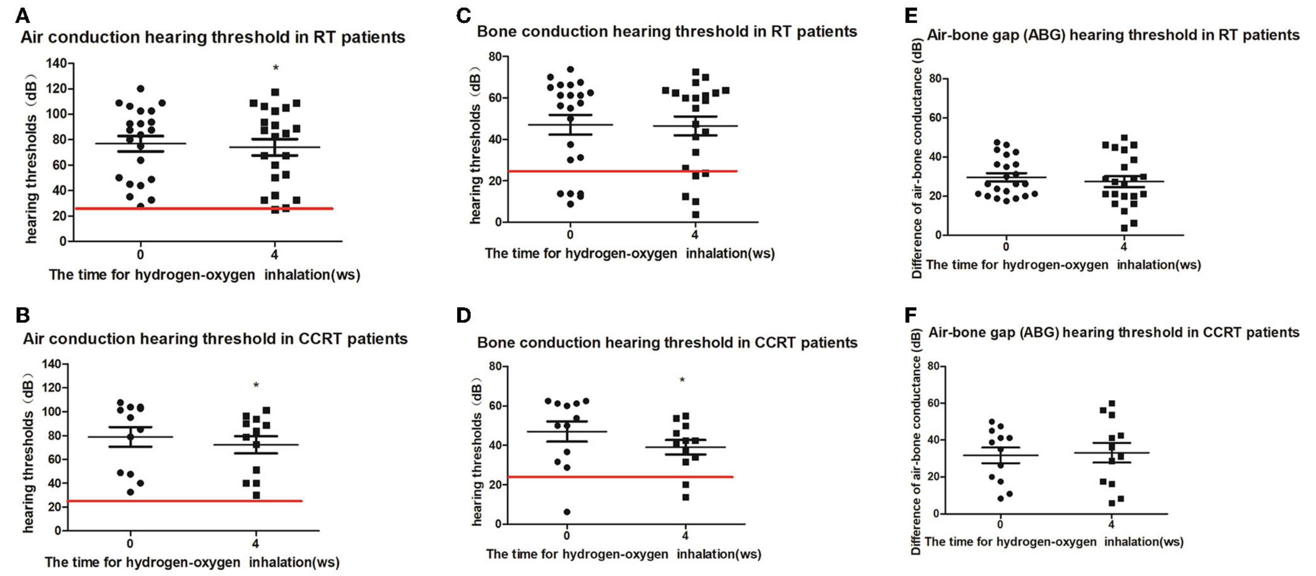

FIGURE 2 | Pure tone hearing threshold tests result before and after hydrogen-oxygen mixed gas inhalation on hearing loss patients with long-term survival after radiotherapy only and concurrent chemoradiotherapy of nasopharyngeal carcinoma. **(A)** Test results of the air conduction hearing threshold in RT patients. **(B)** Test results of the air conduction hearing threshold in CCRT patients. **(C)** Test results of the bone conduction hearing threshold in RT patients. **(D)** Test results of the bone conduction hearing threshold in CCRT patients. **(E)** Test results of the air bone gap (ABG) hearing threshold in RT patients. **(F)** Test results of the air bone gap(ABG) hearing threshold in CCRT patients. The parallel red long lines rep in the figure represent the normal range. Data are analyzed by paired t test. $^{*}P < 0.05$.

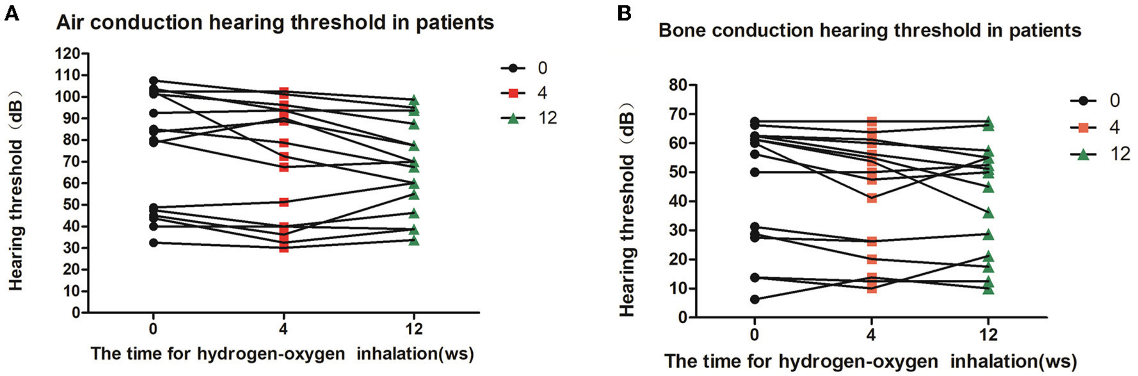

FIGURE 3 | Patients' hearing changes at different time points of hydrogen-oxygen inhalation. **(A)** Diagram of changes of air conduction hearing threshold at different time point after hydrogen-oxygen gas inhalation; **(B)** Diagram of changes of bone conduction hearing threshold at different time point after hydrogen-oxygen gas inhalation. One-way analysis of variance was used for data analysis.

targeted treatments, existing treatments are usually based on symptomatic treatments, with limited effects (31). It has been reported that hearing improved after sudden deafness was treated with Intratympanic steroids (32). All the patients in this study group received a variety of treatments, including oral steroids or ear drops, acupuncture and hyperbaric oxygen. But the treatments failed to relieve hearing damage or prevent the aggravation.

Observation on Hydrogen-Based Treatment of Hearing Loss

In 2020, we (33) reported about three cases of NPC patients with hearing loss after radiotherapy. The patients had significant improvement in hearing after hydrogen inhalation. In a real-world evidence survey of cancer patients who took hydrogen inhalation voluntarily as a means of rehabilitation, a 63-year-old male patient with nasopharyngeal carcinoma

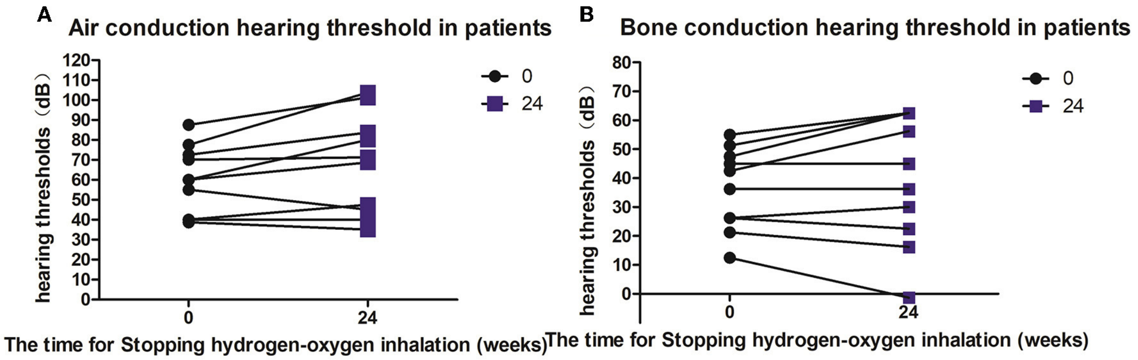

FIGURE 4 | Hearing changes in patients after hydrogen and oxygen inhalation therapy was discontinued. **(A)** Diagram of changes in air conduction hearing threshold after stopping hydrogen-oxygen inhalation therapy for 24 weeks; **(B)** Figure of changes in bone conduction hearing threshold after stopping hydrogen-oxygen inhalation therapy for 24 weeks. Paired *t* test was used for data analysis.

radiotherapy 19 years ago was observed. After radiotherapy, the patient experienced hearing loss, which showed no substantial improvement in spite of symptomatic treatments, and had to use hearing aid for smooth communication. On January 17, 2019, he started to inhale hydrogen on a daily basis. After March 2019, his hearing improved tremendously, ridding him of the hearing aid. The patient's experience led us to the unexpected discovery that hydrogen might be effective in treating hearing loss. Therefore, with a request and support from the Nasopharyngeal Cancer Group of Light of Life Cancer Rehabilitation Association in the patient's place of living, we conducted this prospective study. The 17 patients in the study had clear history of nasopharyngeal carcinoma and radiotherapy or chemoradiotherapy. In quiet environment, the patients inhaled hydrogen (mixture of hydrogen and oxygen) through nasal tubes at least 3 h a day for more than 4 weeks. Results indicated that hearing was improved in most cases. After 4 weeks of hydrogen inhalation, the patients' eustachian tube function scale scores were significantly lower than before treatment; and both their air- and bone-conduction hearing thresholds of the affected ears declined notably. As the treatment continued, the patients' hearing decibels of the affected ears decreased more than before. After hydrogen inhalation was stopped, hearing in some of the cases continued to improve. For subgroups with different initial treatments, the air-conduction hearing thresholds of ears affected by radiotherapy alone and air- and bone-conduction hearing thresholds of ears affected by concurrent radiotherapy and chemotherapy were significantly improved.

It is worth noting that the hydrogen inhalation is very safe. Few patients in the study experienced hydrogen-specific adverse reactions.

Hydrogen inhalation by the 17 patients in this study group was carried out under strict medical supervision and was not given any other medical intervention during the entire period. Therefore, it can be concluded that the hearing improvement found in these patients is undoubtedly attributable to hydrogen inhalation.

Mechanism of Hydrogen in Improving Hearing Loss

The mechanism by which hydrogen improves hearing loss in patients with nasopharyngeal carcinoma after radiotherapy or chemoradiotherapy remains unclear. However, if we connect the biological effect of radiation (or chemotherapy drugs) with the mechanism of action of hydrogen, it is not difficult to note that hydrogen represents a "tit-to-tat" "pathogenesis treatment" for post-radiation hearing loss.

First of all, hydrogen has anti-oxidant and anti-inflammatory effects that resist oxidative stress and inflammation caused by radiotherapy. In the process of radiotherapy, reactive oxygen species (ROS), especially hydroxyl radicals (OH-) and peroxy-nitrosamine, are generated in large volume. Excessive levels of ROS destroy the composition of mitochondrial electron transport chains; trigger imbalance of intracellular redox systems (34); and cause lipid peroxidation, protein misfolding and DNA strand breakage. In the meantime, they activate the JNK signaling system; up-regulate pro-oxidant genes; and inhibit antioxidants related to nuclear factor-e2 related factor (Nrf2) (35), thereby causing oxidative stress and meanwhile inducing matrix metalloproteinases (MMP); triggering secretion of inflammatory chemokines including tumor necrosis factors (TNFs), interleukin (IL)—1, IL-6 and IL-8; and precipitating inflammation. Peroxidation and inflammation promote cell apoptosis. Subsequently, pro-fibrotic cytokines such as platelet-derived growth factors (PDGFs), insulin-like growth factors (IGFs) and basic fibroblast growth factors (FGFs) are released, promoting differentiation of monocytes into M2 macrophages; strengthening fibroblasts to proliferate and differentiate into myofibroblasts; and then amplifying inflammation and fibrosis formation. Radiation can also induce the expression of several miRNAs including miRNA-1 and miRNA-21. And the up-regulation of miRNA-21 expression is related to fibrosis.

The dose of radical radiotherapy for nasopharyngeal carcinoma is far higher than the normal tissue tolerance

TABLE 4 | Adverse reactions at different time points after hydrogen inhalation.

	Before hydrogen inhalation (17 patients)					4 weeks after hydrogen inhalation(17 patients)					8 weeks after hydrogen inhalation (8 patients)					12 weeks after hydrogen inhalation (8 patients)				
Adverse reaction	1	2	3	4	5	1	2	3	4	5	1	2	3	4	5	1	2	3	4	5
Nose bleeding	0	0	0	0	0	0	0	0	0	0	0	0	0	0	0	0	0	0	0	0
Cough	10 (58.82%)	0	0	-	-	11 (64.70%)	0	0	-	-	7(87.5%)	0	0	-	-	6(75%)	0	0	-	-
Chest pain	0	0	0	-	-	0	0	0	-	-	0	0	0	-	-	0	0	0	-	-
Dyspnea	0	0	0	0	0	0	0	0	0	0	0	0	0	0	0	0	0	0	0	0
Nausea	0	0	0	-	-	0	0	0	-	-	0	0	0	-	-	0	0	0	-	-
Vomiting	0	0	0	0	0	0	0	0	0	0	0	0	0	0	0	0	0	0	0	0
Dizziness	0	0	0	-	-	0	0	0	-	-	0	0	0	-	-	0	0	0	-	-
Earache	1(5.88%)	0	0	-	-	1(5.88%)	0	0	-	-	1(12.5%)	0	0	-	-	1(12.5%)	0	0	-	-
Allergic reaction	-	-	0	0	0	-	-	0	0	0	-	-	0	0	0	-	-	0	0	0

dose. Therefore, oxidative stress, inflammation and fibrosis that accompany radiotherapy inevitably damage the auditory system in the radiation field (36–39), leading to middle ear, inner ear and auditory nerve cell damages. Eventually, conductive, sensorineural or mixed hearing loss occurs. Although intensity-modulated radiotherapy helps reduce the dose to surrounding normal tissues (6, 40, 41), ear symptoms are still unavoidable for nasopharyngeal cancer survivors (42–44). The hearing loss of patients receiving radiotherapy combined with chemotherapy is usually more severe than that of patients with radiotherapy alone (39). This might be attributed to the fact that cisplatin, which is commonly used in chemotherapy, has a strong effect on inducing ROS generation.

Hydrogen molecule is a weak reducing agent with very low molecular weight. It can quickly diffuse and pass through cell membranes and lipid bilayers; reach cell nuclei and mitochondria where abundant invasive ROS gather; and selectively neutralize highly reactive toxic ROS (such as •OH) directly (11). Further studies have revealed that hydrogen regulates the Nrf2 pathway (45). Nrf2 is considered to be an important regulator of electrophilic/antioxidant homeostasis, and is especially capable of maintaining the functional integrity of cells under oxidative stress conditions. Hydrogen helps activate the Nrf2-Keap1 system; induce activation of antioxidant response elements (AREs); and promote expression of multiple cytoprotective proteins such as glutathione, catalase (CAT), superoxide dismutase (SOD), glutathione peroxidase and heme-1 oxygenase; activate transcription factor FoxO1; reduce damage of OH to mitochondria; and inhibit overproduction of ROS. Moreover, hydrogen inhibits infiltration of phagocytes to sites of inflammation and subsequent release of reactive substances; and down-regulates various pro-inflammatory and inflammatory cytokines including interleukin (IL)-1β, IL-6, TNF-α and intracellular adhesion molecules (ICAM)-1, thereby achieving anti-inflammatory effect (46, 47). Hydrogen also weakens abnormal expression of miRNA induced by radiation and reduces fibrotic damage (45).

According to the findings of existing studies, hydrogen treatment helps significantly mitigate hearing loss caused by cisplatin; reduce Organ of Corti hair cell damage from cisplatin; improve levels of malondialdehyde (MDA) and isoprostanes F2α (8-iso-PGF2α) in serum and cochlea tissues (48); significantly increase the number of residual acoustic hair cells in the cochlea; and reduce formation of hydroxyl radicals in the cochlea (49). These facts support the aforementioned mechanism.

Second, hydrogen has cytoprotective activity that improves cell apoptosis induced by radiotherapy. Apoptosis plays an important role in progression of radiation injury. Hydrogen significantly inhibits ectopic expression of death promoter Bcl-2 related X protein (bax) and expression of caspase-3, and meanwhile, promotes expression of the anti-apoptotic protein Bcl-2, thereby achieving cytoprotective activity (50, 51).

Third, hydrogen improves blood perfusion and alleviates vascular damage as a result of radiotherapy. Vascular injury and endothelial dysfunction play key roles in development of radiation injury (52). Within a few minutes of exposure to ionization radiation (IR) and as ROS is generated in excessive amount, vascular protectant nitric oxide (NO) is eliminated, triggering nitrosylation of protein tyrosine residues and lipid peroxidation. Ultimately, vasomotor response is weakened, and vascular stenosis appears (53, 54). After radiation, NADPH oxidases (NOXs), especially NOX2 and NOX4 that are abundantly expressed in vascular endothelial cells, are up-regulated. This promotes excessive production of ROS; changes calcium homeostasis and calcium metabolism disorders; and triggers antifibrinolysis-coagulation cascade action, leading to blood clotting and vascular occlusion (55–57). Radiation facilitates migration of monocytes to inner membranes, induces expression of inflammatory adhesion molecules, enhances adhesive capacity of monocytes, recruits monocyte chemotactic protein-1 into inner membranes, absorbs low-density lipoproteins, and promotes arteriosclerosis (58), which eventually leads to arterial stenosis and lower blood perfusion. Since the neck is usually included in the irradiation scope of radiotherapy for patients with nasopharyngeal cancer, carotid artery damage (59) and cochlear vascular damage are inevitable, causing blood supply disorders. This may also directly incur damage to outer hair cells and spiral ganglion cells of the cochlea (60).

Evidence suggests that hydrogen protects damaged blood vessels and improves blood perfusion, including inhibiting degradation of cyclic guanosine monophosphate (cGMP) through phosphodiesterase, increasing cGMP levels and promoting protein kinase activation. It can also increase intracellular calcium levels and stimulate vascular endothelial growth factors, thereby increasing production of nitric oxide. Moreover, hydrogen functions to open the potassium channel sensitive to adenosine triphosphate and activate downstream mitogen-activated protein kinase pathways, thus promoting angiogenesis (61). Further experimental studies indicate that hydrogen prevents arterial intimal hyperplasia and atherosclerosis by inhibiting ROS and TNF-α/NF-κB pathways (62, 63); inhibits macrophage-derived foam cell apoptosis; stabilizes atherosclerotic plaques (64); reduces vascular stenosis; and promotes formation of vascular collaterals using the FIk1-Notch signal stimulated by paracrine VEGFs, thereby improving local microcirculation (61).

Discussion on Hydrogen Therapy

There are multiple ways to introduce hydrogen into the body, including oral and intravenous injection of hydrogen water. However, since hydrogen has short half-life in the body and cannot be retained in the body's tissues for a long time, non-inhalation methods may not deliver satisfactory results. The therapeutic effects of this study group appeared at least 2 weeks after hydrogen inhalation in all the cases. From patients with long-term hydrogen inhalation, it has been observed that as hydrogen inhalation was continued for longer time, the patients' air- and bone-conduction hearing thresholds decreased more significantly. Fransson AE and his team also found repeated administration of H_2 inhalation may further improve the therapeutic effect (65). After hydrogen inhalation was stopped, the patients' bone- and air-conduction hearing thresholds rose. Given that hearing loss in this study group lasted for months or even years, it is speculated that the disease had "aged". The effect of hydrogen depends on sufficient dose and time. It seems that only inhalation of hydrogen can meet these requirements.

The concentration level and flow rate of inhaled hydrogen are also important. The hydrogen inhaled by this study group has a flow rate of 3L/min and concentration level at 67%. These are the maximum levels that can be provided by the only hydrogen inhalation equipment approved by the Chinese authority.

So far, there has been no evidence as to whether inhalation of pure hydrogen is better or inhalation of hydrogen-oxygen mixture is. If high-concentration pure hydrogen is to be inhaled, oxygen intake is inevitably affected. Inhaling a mixture of hydrogen and oxygen helps at least prevent hypoxia. Studies have revealed that during inhalation of hydrogen-oxygen mixture, hydrogen molecules, which are extremely small and permeable, can "carry" larger molecules of oxygen to the deep areas of tissues and improve oxygen supply (66). The mixture inhaled by this study group contains 33% oxygen, which exceeds the oxygen level in normal air.

CONCLUSION

Hearing loss is a common and persisting adverse reaction for nasopharyngeal carcinoma patients with radiotherapy. The hearing loss of such patients is usually long-lasting, chronical and gradual, thus affecting the quality of life in a serious manner. Unfortunately, there has been no special treatment available so far. Hydrogen inhalation can improve the hearing of long-term surviving patients with nasopharyngeal carcinoma after radiotherapy, and achieves more significant efficacy as the duration of treatment is extended. Its mechanism of action might be associated with hydrogen's functions in controlling oxidative stress and inflammation; protecting cells; and improving blood perfusion. This study represents the first effort to adopt hydrogen inhalation as an independent measure for improving hearing loss in the patients with long-term survival of nasopharyngeal cancer. If this study would be supported by more experiments and verification in the future, hydrogen inhalation would be proven a safe and effective means of rehabilitation for the challenge in the medical world.

DATA AVAILABILITY STATEMENT

The raw data supporting the conclusions of this article will be made available by the authors, without undue reservation.

ETHICS STATEMENT

The studies involving human participants were reviewed and approved by the Ethics Committee of Fuda Cancer Hospital, Jinan University, China. The patients/participants provided their written informed consent to participate in this study.

AUTHOR CONTRIBUTIONS

KX developed the idea for and was involved in the design of this study. XK and TL reviewed available data sources and drafted the manuscript. Y-YL, ZY, and KX critically revised the manuscript. All authors read and approved the final manuscript.

ACKNOWLEDGMENTS

To Prof. Zongyuan Zeng who participated in technical editing of the manuscript.

REFERENCES

1. Lin C, Lin SW, Weng SF, Lin YS. Risk of developing sudden sensorineural hearing loss in patients with nasopharyngeal carcinoma: a population-based cohort study. *Head Neck.* (2014) 36:203–8. doi: 10.1002/hed.23278
2. Lee AW, Sze WM, Au JS, Leung SF, Leung TW, Chua DT, et al. Treatment results for nasopharyngeal carcinoma in the modern era:the Hong Kong experience. *Int J Radiat Oncol Biol Phys.* (2005) 61:1107–16. doi: 10.1016/j.ijrobp.2004.07.702
3. Langendijk JA, Leemans CR, Buter J, Berkhof J, Slotman BJ. The additional value of chemotherapy to radiotherapy in locally advanced nasopharyngeal carcinoma: a meta-analysis of the published literature. *J Clin Oncol.* (2004) 22:4604–12. doi: 10.1200/JCO.2004.10.074
4. Zhang MX Li J, Shen GP, Zou X, Xu JJ, Jiang R, et al. Intensity-modulated radiotherapy prolongs the survival of patients with nasopharyngeal carcinoma compared with conventional two-dimensional radiotherapy: a 10-year experience with a large cohort and long follow-up. *Eur J Cancer.* (2015) 51:2587–95. doi: 10.1016/j.ejca.2015.08.006
5. Wang J, Chen YY, Tai A, Chen XL, Huang SM, Yang C, et al. Sensorineural hearing loss after combined intensity modulated radiation therapy and cisplatin-based chemotherapy for nasopharyngeai carcinoma. *TransIational oncology.* (2015) 8:456–62. doi: 10.1016/j.tranon.2015.10.003
6. Wei Y, Zhou T, Zhu J, Zhang Y, Sun M, Ding X, et al. Long-term outcome of sensorineural hearing loss in nasopharyngeal carcinoma patients: comparison between treatment with radiotherapy alone and chemoradiotherapy. *Cell Biochem Biophys.* (2014) 69:433–7. doi: 10.1007/s12013-014-9814-x
7. Zhu W, Chen F, Li J, Wang W, Zhang H, Yang G, et al. Dosimetric parameters associated with conductive or sensorineural hearing loss 5 years after intensity-modulated radiation therapy in nasopharyngeal carcinoma. *Acta Otolaryngol.* (2019) 139:263–8. doi: 10.1080/00016489.2019.1566778
8. Lee A W, Lin J C, Ng W T. Current management of nasopharyngeal cancer. *Semin Radiat Oncol*. (2012) 22:233–44. doi: 10.1016/j.semradonc.2012.03.008
9. Dole M, Wilson FR, Fife WP. Hyperbaric hydrogen therapy: a possible treatment for cancer. *Science.* (1975) 190:152–4. doi: 10.1126/science.1166304
10. Gharib B, Hanna S, Abdallahi OM, Lepidi H, Gardette B, De Reggi M. Anti-inflammatory properties of molecular hydrogen: investigation on parasite-induced liver inflammation. *C R Acad Sci III.* (2001) 324:719–24. doi: 10.1016/S0764-4469(01)01350-6
11. Ohsawa I, Ishikawa M, Takahashi K, Watanabe M, Nishimaki K, Yamagata K, et al. Hydrogen acts as a therapeutic antioxidant by selectively reducing cytotoxic oxygen radicals. *Nat Med*. (2007). 13(6):688-694. doi: 10.1038/nm1577
12. Ge L, Yang M, Yang NN, Yin XX, Song WG. Molecular hydrogen: a preventive and therapeutic medical gas for various diseases. *Oncotarget.* (2017) 8:102653–73. doi: 10.18632/oncotarget.21130
13. Wang D, Wang L, Zhang Y, Zhao Y, Chen G. Hydrogen gas inhibits lung cancer progression through targeting SMC3. *Biomed Pharmacother.* (2018) 104:788–97. doi: 10.1016/j.biopha.2018.05.055
14. Yang Y, Liu PY, Bao W, Chen SJ, Wu FS, Zhu PY. Hydrogen inhibits endometrial cancer growth via a ROS/NLRP3/caspase-1/GSDMD-mediated pyroptotic pathway. *BMC Cancer.* (2020) 20:28. doi: 10.1186/s12885-019-6491-6
15. Li S, Liao R, Sheng X, Luo X, Zhang X, Wen X, et al. Hydrogen gas in cancer treatment. *Front Oncol.* (2019) 9:696. doi: 10.3389/fonc.2019.00696
16. Kikkawa YS, Nakagawa T, Horie RT, Ito J. Hydrogen protects auditory hair cells from free radicals. *Neuroreport.* (2009) 20:689–94. doi: 10.1097/WNR.0b013e32832a5c68
17. Lin Y, Kashio A, Sakamoto T, Suzukawa K, Kakigi A, Yamasoba T. Hydrogen in drinking water attenuates noise-induced hearing loss in guinea pigs. *Neurosci Lett.* (2011) 487:12–6. doi: 10.1016/j.neulet.2010.09.064
18. Zhou Y, Zheng H, Ruan F, Chen X, Zheng G, Kang M, et al. Hydrogen-rich saline alleviates experimental noise-induced hearing loss in guinea pigs. *Neuroscience.* (2012) 209:47–53. doi: 10.1016/j.neuroscience.2012.02.028
19. Chen L, Yu N, Lu Y, Wu L, Chen D, Guo W, et al. Hydrogen-saturated saline protects intensive narrow band noise-induced hearing loss in guinea pigs through an antioxidant effect. *PLoS ONE.* (2014) 9:e100774. doi: 10.1371/journal.pone.0100774
20. McCoul ED, Anand VK. Christos PJ. Validating the clinical assessment of eustachian tube dysfunction: the Eustachian tube dysfunction questionnaire (ETDQ-7). *Laryngoscope.* (2012) 122:1137–41. doi: 10.1002/lary.23223
21. Tarabichi M, Poe DS, Nogueira JF, Alicandri-Ciufelli M, Badr-El-Dine M, Cohen MS, et al. The eustachian tube redefined. *Otolaryngol Clin North Am.* (2016) 49:XVII–XX. doi: 10.1016/j.otc.2016.07.013
22. US Department of Health and Human Services, National Institutes of Health(NIH) and National Cancer Institute (NCI). *Common terminology criteria for adverse events (CTCAE) version 4.0 [EB/OL].* Bethesda, NIH Publication.
23. Au KH, Ngan RKC, Ng AWY, Poon DMC, Ng WT, Yuen KT, et al. Treatment outcomes of nasopharyngeal carcinoma in modern era after intensity modulated radiotherapy (IMRT) in Hong Kong: a report of 3328 patients (HKNPCSG 1301 study). *Oral Oncol.* (2018) 77:16–21. doi: 10.1016/j.oraloncology.2017.12.004
24. Low WK, Toh ST, Wee J, Fook-Chong SM, Wang DY. Sensorineural hearing loss after radiotherapy and chemoradiotherapy: a single, blinded, randomized study. *J Clin Oncol.* (2006) 24:1904–9. doi: 10.1200/JCO.2005.05.0096
25. Young YH, Lou PJ. Post-irradiation sudden deafness. *J Laryngol Otol.* (1999) 113:815–7. doi: 10.1017/S0022215100145281
26. Yilmaz YF, Aytas FI, Akdogan O, Sari K, Savas ZG, Titiz A, et al. Sensorineural hearing loss after radiotherapy for head and neck tumors: a prospective study of the effect of radiation. *Otol Neurotol.* (2008) 29:461–3. doi: 10.1097/MAO.0b013e31816c7c9e
27. Zheng Y, Han F, Xiao W, Xiang Y, Lu L, Deng X, et al. Analysis of late toxicity in nasopharyngeal carcinoma patients treated with intensity modulated radiation therapy. *Radiat Oncol.* (2015) 10:17. doi: 10.1186/s13014-014-0326-z
28. McDowell LJ, Rock K, Xu W, Chan B, Waldron J, Lu L, et al. Long-term late toxicity, quality of life, and emotional distress in patients with nasopharyngeal carcinoma treated with intensity modulated radiation therapy. *Int J Radiat Oncol Biol Phys.* (2018) 102:340–52. doi: 10.1016/j.ijrobp.2018.05.060
29. Huang TL, Chien CY, Tsai WL, Liao KC, Chou SY, Lin HC, et al. Long-term late toxicities and quality of life for survivors of nasopharyngeal carcinoma treated with intensity-modulated radiotherapy versus non-intensity-modulated radiotherapy. *Head Neck.* (2016) 38:E1026–32. doi: 10.1002/hed.24150
30. Lan XH,Tang AZ, Zhou Y. The audiologic study of the long-term survivors with Nasopharyngeal carcinoma after radiotherapy. *Can J Speech-Lang Pathol Audiol*. (2012) 20:336–8. doi: 10.3969/j.issn.1006-7299.2012.4.009
31. Michels TC, Duffy MT, Rogers DJ. Hearing Loss in Adults: Differential Diagnosis and Treatment. *Am Fam Physician.* (2019) 100:98–108.
32. Peng Y, Xiong S, Cheng Y, Qi YF, Yang Y. Clinical investigation of different routes of administration of dexamethasone on sudden deafness.

Lin Chung Er Bi Yan Hou Tou Jing Wai Ke Za Zhi. (2008) 22:442–5. doi: 10.3969/j.issn.1001-1781.2008.10.004

33. Chen J, Kong X, Mu F, Lu T, Du D, Xu K. Hydrogen-oxygen therapy can alleviate radiotherapy-induced hearing loss in patients with nasopharyngeal cancer. *Ann Palliat Med.* (2019) 8:746–51. doi: 10.21037/apm.2019.11.18
34. Kam WW, Banati RB. Effects of ionizing radiation on mitochondria. *Free Radic Biol Med.* (2013) 65:607–19. doi: 10.1016/j.freeradbiomed.2013.07.024
35. Faraonio R, Vergara P, Di Marzo D, Pierantoni MG, Napolitano M, Russo T, et al. p53 suppresses the Nrf2-dependent transcription of antioxidant response genes. *J Biol Chem.* (2006) 281:39776–84. doi: 10.1074/jbc.M605707200
36. Hus MM, Young YH. Lin KL. Eustachian tube function of patients with nasopharyngeal carcinoma. *Ann Oto Rhinol Laryngol.* (1995) 104:453–5. doi: 10.1177/000348949510400607
37. Low WK, Burgess R, Fong KW. Wang DY. Effect of Radiotherapy on Retro-Cochlear Auditory Pathways. *The Laryngoscope.* (2005) 115:1823–6. doi: 10.1097/01.mlg.0000175061.59315.58
38. Wang SZ, Chen ZC, McNamar JP, Wang SY. Cheng QF. The relationship between the protective effect of amifostine and decreased intercellular adhesion molecule expression. *Am J Otolaryngol Head Neck Med Surg.* (2005) 26:118–22. doi: 10.1016/j.amjoto.2004.11.002
39. Xiao J, Luo ZQ, Shi DZ, Huang YJ, Tan YF. Short-term results of audiological change of nasopharyngeal carcinoma patient after radiotherapy and chemotherapy. *Zhonghua Er Bi Yan Hou Tou Jing Wai Ke Za Zhi.* (2008) 43:906–9.
40. Lee N, Xia P, Quivey JM, Sultanem K, Poon I, Akazawa C, et al. Intensity-modulated radiotherapy in the treatment of nasopharyngeal carcinoma: an update of the UCSF experience. *Int J Radiat Oncol Biol Phys.* (2002) 53:12–22. doi: 10.1016/S0360-3016(02)02724-4
41. Hsin CH, Chen TH, Young YH, Liu WS. Comparison of otologic complications between intensity-modulated and two-dimensional radiotherapies in nasopharyngeal carcinoma patients. *Otolaryngol Head Neck Surg.* (2010) 143:662–8. doi: 10.1016/j.otohns.2010.07.012
42. Young YH, Ko JY, Sheen TS. Post-irradiation dizziness in nasopharyngeal carcinoma survivors. *Otol Neurotol.* (2004). 25:366–70. doi: 10.1097/00129492-200405000-00027
43. Chi FH. Young YH Inner ear deficits in irradiated nasopharyngeal carcinoma survivors. *Laryngoscope.* (2015) 125:2565–71. doi: 10.1002/lary.25329
44. Hsin CH, Chen TH, Liang KL, Tseng HC, Liu WS. Postirradiation otitis media with effusion in nasopharyngeal carcinoma patients treated by intensity-modulated radiotherapy. *Laryngoscope.* (2013) 123:2148–53. doi: 10.1002/lary.23215
45. LeBaron TW, Kura B, Kalocayova B, Tribulova N, Slezak J. A new approach for the prevention and treatment of cardiovascular disorders: molecular hydrogen significantly reduces the effects of oxidative stress. *Molecules.* (2019) 24:2076. doi: 10.3390/molecules24112076
46. Nogueira JE, de Deus JL, Amorim MR, Batalhão ME, Leão RM, Carnio EC, et al. Inhaled molecular hydrogen attenuates intense acute exercise-induced hippocampal inflammation in sedentary rats. *Neurosci Lett.* (2020) 715:134577. doi: 10.1016/j.neulet.2019.134577
47. Nogueira JE, Passaglia P, Mota CMD, Santos BM, Batalhão ME, Carnio EC, et al. Molecular hydrogen reduces acute exercise-induced inflammatory and oxidative stress status. *Free Radic Biol Med.* (2018) 129:186–93. doi: 10.1016/j.freeradbiomed.2018.09.028
48. Qu J, Li X, Wang J, Mi W, Xie K, Qiu J. Inhalation of hydrogen gas attenuates cisplatin-induced ototoxicity via reducing oxidative stress. *Int J Pediatr Otorhinolaryngol.* (2012) 76:111–5. doi: 10.1016/j.ijporl.2011.10.014
49. Kikkawa YS, Nakagawa T, Taniguchi M, Ito J. Hydrogen protects auditory hair cells from cisplatin-induced free radicals. *Neurosci Lett.* (2014) 579:125–9. doi: 10.1016/j.neulet.2014.07.025
50. Zhao YS, An JR, Yang S, Guan P, Yu FY Li W, et al. Hydrogen and oxygen mixture to improve cardiac dysfunction and myocardial pathological changes induced by intermittent hypoxia in rats. *Oxid Med Cell Longev.* (2019) 2019:7415212. doi: 10.1155/2019/7415212
51. Mo XY Li XM, She CS, Lu XQ, Xiao CG, Wang SH, et al. Hydrogen-rich saline protects rat from oxygen glucose deprivation and reperusion-induced apoptosis through VDAC1 via Bcl-2. *Brain Res.* (2019) 1706:110–5. doi: 10.1016/j.brainres.2018.09.037
52. Wang B, Wang H, Zhang M, Ji R, Wei J, Xin Y, et al. Radiation-induced myocardial fibrosis: mechanisms underlying its pathogenesis and therapeutic strategies. *J Cell Mol Med.* (2020) 24:7717–29. doi: 10.1111/jcmm.15479
53. Venkatesulu BP, Mahadevan LS, Aliru ML, Yang X, Bodd MH, Singh PK, et al. Radiation-induced endothelial vascular injury: a review of possible mechanisms. *JACC Basic Transl Sci.* (2018) 3:563–72. doi: 10.1016/j.jacbts.2018.01.014
54. Wang Z, Yang B, Chen X, Zhou Q, Li H, Chen S, et al. Nobiletin regulates ROS/ADMA/DDAHII/ eNOS/NO pathway and alleviates vascular endothelium injury by iron overload. *Biol Trace Elem Res.* (2020) 198:87–97. doi: 10.1007/s12011-020-02038-6
55. Zhang Y, Murugesan P, Huang K, Cai H, NADPH. oxidases and oxidase crosstalk in cardiovascular diseases: novel therapeutic targets. *Nat Rev Cardiol.* (2020) 17:170–94. doi: 10.1038/s41569-019-0260-8
56. Ping Z, Peng Y, Lang H, Xinyong C, Zhiyi Z, Xiaocheng W, et al. Oxidative stress in radiation-induced cardiotoxicity. *Oxid Med Cell Longev.* (2020) 2020:1–15. doi: 10.1155/2020/3579143
57. Farhood B, Goradel NH, Mortezaee K, Khanlarkhani N, Salehi E, Nashtaei MS, et al. Intercellular communications-redox interactions in radiation toxicity; potential targets for radiation mitigation. *J Cell Commun Signal.* (2019) 13:3–16. doi: 10.1007/s12079-018-0473-3
58. Stewart FA, Hoving S, Russell NS. Vascular damage as an underlying mechanism of cardiac and cerebral toxicity in irradiated cancer patients. *Radiat Res.* (2010) 174:865–9. doi: 10.1667/RR1862.1
59. Li CS, Schminke U, Tan TY. Extracranial carotid artery disease in nasopharyngeal carcinoma patients with post-irradiation ischemic stroke.*Clin Neurol Neurosurg.* (2010) 112:682–6. doi: 10.1016/j.clineuro.2010.05.007
60. Young YH, Sheen TS. Preservation of tubal function in patients with nasopharyngeal carcinoma, post-irradiation. *Acta Otolaryngol.* (1998) 118:280–3. doi: 10.1080/00016489850155026
61. KC Xu. *Hydrogen-Oxygen Inhalation for Treatment of COVID-19.* Singapore: World Sci. (2020) p. 23–25
62. Qin ZX Yu P, Qian DH, Song MB, Tan H, Yu Y, et al. Hydrogen-rich saline prevents neointima formation after carotid balloon injury by suppressing ROS and the TNF-alpha/NF-kappaB pathway. *Atherosclerosis.* (2012) 220:343–50. doi: 10.1016/j.atherosclerosis.2011.11.002
63. Ohsawa I, Nishimaki K, Yamagata K, Ishikawa M, Ohta S. Consumption of hydrogen water prevents atherosclerosis in apolipoprotein E knockout mice. *Biochem Biophys Res Commun.* (2008) 377:1195–8. doi: 10.1016/j.bbrc.2008.10.156
64. Song G, Zong C, Zhang Z, Yu Y, Yao S, Jiao P, et al. Molecular hydrogen stabilizes atherosclerotic plaque in low-density lipoprotein receptor-knockout mice. *Free Radic Biol Med.* (2015) 87:58–68. doi: 10.1016/j.freeradbiomed.2015.06.018
65. Fransson AE, Videhult Pierre P, Risling M, Laurell GFE. Inhalation of molecular hydrogen, a rescue treatment for noise-induced hearing loss. *Front Cell Neurosci.* (2021) 15:658662. doi: 10.3389/fncel.2021.658662
66. Zhou ZQ, Zhong CH, Su ZQ Li XY, Chen Y, Chen XB, et al. Breathing hydrogen-oxygen mixture decreases inspiratory effort in patients with tracheal stenosis. *Respiration.* (2019) 97:42–51. doi: 10.1159/000492031

Conflict of Interest: The authors declare that the research was conducted in the absence of any commercial or financial relationships that could be construed as a potential conflict of interest.

frontiers | Frontiers in Medicine

ORIGINAL RESEARCH
published: 11 April 2022
doi: 10.3389/fmed.2022.827585

Nonoxid-HMGB1 Attenuates Cognitive Impairment After Traumatic Brain Injury in Rats

Jun-Quan Chen†, Shuang-Qi Gao†, Lun Luo, Zong-Yuan Jiang, Chao-Feng Liang, Hai-Yong He and Ying Guo**

Department of Neurosurgery, The Third Affiliated Hospital, Sun Yat-sen University, Guangzhou, China

Traumatic brain injury (TBI) is a major global burden of health. As an accepted inflammatory mediator, high mobility group box 1 (HMGB1) is found to be effective in facilitating neurogenesis and axonal regeneration. SH3RF2 (also known as POSHER), an E3 ligase SH3 domain-containing ring finger 2, belongs to the SH3RF family of proteins. Here, we aimed to investigate the role of redox states of HMGB1 on neurite outgrowth and regeneration both *in vitro and in vivo*. In this study, distinct recombinant HMGB1 redox isoforms were used. Sequencing for RNA-seq and data analysis were performed to find the potential downstream target of nonoxid-HMGB1 (3S-HMGB1). Protein changes and distribution of SH3RF2 were evaluated by western blot assays and immunofluorescence. Lentivirus and adeno-associated virus were used to regulate the expression of genes. Nonoxid-HMGB1-enriched exosomes were constructed and used to treat TBI rats. Neurological function was evaluated by OF test and NOR test. Results demonstrated that nonoxid-HMGB1 and fr-HMGB1, but not ds-HMGB1, promoted neurite outgrowth and axon elongation. RNA-seq and western blot assay indicated a significant increase of SH3RF2 in neurons after treated with nonoxid-HMGB1 or fr-HMGB1. Notably, the beneficial effects of nonoxid-HMGB1 were attenuated by downregulation of SH3RF2. Furthermore, nonoxid-HMGB1 ameliorated cognitive impairment in rats post-TBI *via* SH3RF2. Altogether, our experimental results suggest that one of the promoting neurite outgrowth and regeneration mechanisms of nonoxid-HMGB1 is mediated through the upregulated expression of SH3RF2. Nonoxid-HMGB1 is an attractive therapeutic candidate for the treatment of TBI.

Keywords: cognitive impairment, redox state, HMGB1, traumatic brain injury, SH3RF2

Edited by:
Fu Wang,
Xi'an Jiaotong University, China

Reviewed by:
Yuqin Ye,
Airforce Military Medical University,
China

***Correspondence:**
Hai-Yong He
jlhhy007@126.com
Ying Guo
guoy@mail.sysu.edu.cn

†These authors have contributed equally to this work

Specialty section:
This article was submitted to
Precision Medicine,
a section of the journal
Frontiers in Medicine

Received: *02 December 2021*
Accepted: *11 March 2022*
Published: *11 April 2022*

Citation:
Chen J-Q, Gao S-Q, Luo L, Jiang Z-Y,
Liang C-F, He H-Y and Guo Y (2022)
Nonoxid-HMGB1 Attenuates
Cognitive Impairment After Traumatic
Brain Injury in Rats.
Front. Med. 9:827585.
doi: 10.3389/fmed.2022.827585

INTRODUCTION

Traumatic brain injury (TBI) is a major cause of death and disability around the world (1, 2). Survivors often suffer from a variety of neurological symptoms, such as cognitive dysfunction, disorders of balance, paresthesia, memory problems, etc. (3, 4). The mechanism of brain damage after TBI has been proved to involve both direct mechanical damage and indirect damage (5, 6). Direct mechanical damage results from initial impact and is considered irreversible. Secondary damage is mainly caused by the delayed neurochemical process such as excitotoxicity, mitochondrial dysfunction, oxidative stress, and inflammation, which is reversible (7). However, despite extensive research into the process of TBI disease, there is, still, a lack of effective treatments to promote neurological recovery, and the prognosis remains unfavorable.

HMGB1 (high mobility group box 1) is a nuclear protein, but extracellular HMGB1 works as a damage-associated molecular pattern (DAMP) to stimulate the innate immune system (8, 9). HMGB1 exerts varying biological activities according to the redox states of cysteines, which are at positions C23, C45, and C106 within a protein (10–12). Three isoforms of HMGB1 have been identified, namely, fully reduced HMGB1 (fr-HMGB1), disulfide HMGB1 (ds-HMGB1), and fully oxidized HMGB1 (ox-HMGB1) (13). They interact with different pathogen recognition receptors to participate in different pathophysiological processes. Fr-HMGB1 exhibits that the three cysteines are in the thiol state (reducing status). It elicits intracellular actions *via* binding to RAGE and/or CXCR4 (14). In contrast, in ds-HMGB1, a disulfide bond is formed between C23 and C45 residues due to the oxidation, while C106 remains unchanged. It induces cytokine production *via* binding to TLR4 (15). The final variant, namely, ox-HMGB1, is reportedly non-active, with all three cysteines terminally oxidized (16).

In TBI, HMGB1 has been shown to enhance neuroinflammation and subsequently exacerbate neurocognitive impairment (17, 18). Extracellular HMGB1 is released by necrotic neurons and other immune cells recruited to the injury site (19). It can act both as a chemoattractant for leukocytes and as a proinflammatory mediator to induce the release of proinflammatory cytokines (12). However, the critical role of HMGB1 in facilitating neurogenesis and neural regeneration is neglected. It has been reported that HMGB1 stimulates hippocampal and cortical neurogenesis post-TBI (20). HMGB1 is upregulated in axons of injury-conditioned neurons and enhances axon outgrowth (21). Furthermore, a previous study shows that the overexpression of HMGB1 in motoneurons promotes neuroregeneration in SCI (spinal cord injury) (22). Together, these observations suggest that HMGB1 plays dual and antagonistic roles during neurogenesis and neuroregeneration after CNS (central nervous system) injury.

In this study, to investigate the effects of HMGB1 redox isoforms on neurite outgrowth and regeneration *in vitro*, fr-HMGB1, ds-HMGB1, and nonoxid-HMGB1 (3S-HMGB1) were selected. Nonoxid-HMGB1 is a mutant to mimic fr-HMGB1 functions in which all cysteines are replaced with serines and maintains structural stability in oxidizing milieu (23). In addition, we assessed the effects of nonoxid-HMGB1 in TBI rats and tried to explore the potential molecular mechanism.

MATERIALS AND METHODS

Animals

The post-natal day 1–3 Sprague-Dawley (SD) rats were provided by Southern Medical University SPF Animal Experimental Center (Guangzhou, China). Male adult SD rats were purchased from the Vital River Laboratory Animal Technology Co., Ltd. (Beijing, China), weighing 190–210 g (8–10 weeks old). The animals were fed in a standard environment with a light-dark cycle (12/12-h day/night, 25°C) and had 1 week to adapt to the new environment before surgery. All the animal studies were approved by the Review Committee for the Use of Human or Animal Subjects of Sun Yat-Sen University.

Primary Culture of Cortical Neurons

Cortical neurons were isolated from the neonatal rats under a microscope. In brief, cerebral cortices were isolated carefully. The separated cortical tissue was shredded and dissociated with a papaya enzyme (Sigma-Aldrich, USA). In the first 2 h, cells were cultured in a high-glucose DMEM-F12 (Gibco, USA) medium. After that, the medium was changed into a neurobasal medium (Gibco, USA). The neurons were cultured in a 5% CO2 incubator for 7 days, and then treated with three different forms of recombinant HMGB1 (ds-HMGB1, fr-HMGB1, and nonoxid-HMGB1; 100 ng/ml, respectively; HMGBiotech, Italy). The dosage of HMGB1 referred to a previous research (24).

Immunofluorescence

Cortical neurons were fixed with paraformaldehyde for 15 min, and then permeabilized with 0.3% Triton X-100 for 30 min. After washing with PBS, the cells were blocked with 5% BSA for 1 h at room temperature, followed by incubation with a MAP2 antibody (1:100; Abcam, UK), a NeuN antibody (1:100; Millipore, USA), and an SH3RF2 antibody (1:100; Novus, USA) overnight at 4°C. The day after, neurons were incubated with Alexa Fluor 488-conjugated (1:500; Abcam, UK) and Alexa Fluor 555-conjugated (1:500; Abcam, UK) for 1 h at room temperature. Finally, nuclei were visualized with DAPI (1:1,000; Abcam, UK). Images were acquired with a confocal laser scanning microscope (LSM 780; Zeiss, Germany) and analyzed by Image J software.

Bioinformatics Analyses

Total RNA was isolated from cultured cortical neurons. Sequencing for RNA-seq and data analysis were performed at JinWeiZhi (Suzhou) BIOTECHNOLOGY LLC (https://www.genewiz.com.cn/). In the present analysis, an FDR below 0.05 was identified as the criterion for differentially expressed genes (DEGs). Differences in the mRNA expressions were displayed on heatmaps. GO pathway enrichment analyses were performed to find possible biological processes and signaling pathways associated with the correlated target genes of neurite outgrowth and regeneration.

Western Blotting Analysis

As previously described (25), 30 μg protein samples were separated by 10% SDS-PAGE gel, and then transferred to polyvinylidene fluoride (PVDF, pore size, 0.45 um) membranes (Millipore Billerica, USA). The membranes were blocked with 5% non-fat dry milk for 1 h, followed by incubation overnight at 4°C with the following primary antibodies: rabbit anti-SH3RF2 (1:1,000), rabbit anti-HMGB1 (1:1,000), mice anti-EGFP (1:1,000, mice anti-GAPDH (1:1,000), and mice anti-β-actin (1:1,000). The day after, the membranes were incubated with secondary antibody HRP-conjugated goat anti-rabbit (1:3,000) or an HRP-conjugated goat anti-mouse (1:3,000) at room temperature for 1 h. The secondary antibody was diluted with 1% non-fat dry milk. Specific bands were detected with a GE AI600 system. ImageJ software was used to quantify the expression of protein.

Lentiviral Transfection

The lentivirus targeting SH3RF2, pLKD-CMV-mcherry-2A-puro-U6-shSH3RF2, was purchased from Obio Technology Corp., Ltd (Shanghai, China). pLKD-CMV-mcherry-2A-puro-U6 served as negative control. Multiplicity of infection (MOI) was 20. Neurons were transfected at day in Culture 7, and the effect of gene interference was verified after 72 h using western blot assays.

Stereotaxic Injection

Gene overexpression *in vivo* was achieved by ScAAV vectors. ScAAV vectors carrying Nonoxid-HMGB1 (3S-HMGB1), ScAAV-hSyn-HMGB1 (C23S C45S C106S)-EGFP-WPREs, were purchased from BrainVTA Co., Ltd (Wuhan, China). ScAAV-hSyn-EGFP-WPREs served as negative control. After being anesthetized, rats were placed in a stereotaxic apparatus (RWD, CN). The hole was drilled above the right hippocampus, and viruses were microinfused *via* a 10-μl Hamilton microsyringe. The stereotactic coordinates were as follows: bregma −3. mm, midline 3. mm, 2.5 mm below dura.

Establishment of the TBI Rat Model

The controlled cortex injury (CCI) device (RWD68099II, China) was used to establish the TBI model. A diameter craniotomy of 5. mm on the right parietal (centered 3. mm posterior and 3. mm lateral from the Bregma) was performed to expose the dura. The CCI was delivered to a depth of 1. mm at a velocity of 5 m/s with a duration of 500 ms. Sham rats received the same craniotomy but not brain injury.

Isolation, Culture, and Transfection of BMSCs

As previously described, BMSCs were harvested from the femurs and tibias of neonatal rat femurs (26). The adherent cells were passaged when they reached 80∼90% confluency, and P3 BMSCs were used for subsequent experiments. The nonoxid-HMGB overexpression plasmids carrying EGFP were purchased from BrainVTA Co., Ltd (Wuhan, China). All plasmids were transfected into BMSCs using Lipofectamine 2000 (Invitrogen, USA).

Isolation and Identification of BMSC-Derived Exosomes

When BMSCs reached 70∼80% confluence, a medium was replaced. After 48 h, the medium was collected. The exosomes were extracted through traditional ultracentrifugation and preserved in a freezer at −80°C. The morphology of exosomes was observed under a transmission electron microscope (FEI, CZ). A BCA protein quantification kit (Beyotime, China) was used to detect protein content. Western blot was used to identify the expression of Exo-specific markers TSG101 (Abcam, USA) and Flotillin-1 (Abcam, USA). Exosomes (5 ug) were injected into the caudal vein after TBI (27).

Behavioral Procedures

Before testing, rats were transferred to the testing room and adapted to the surroundings for at least 1 h.

Open Field Test (OF)

OF test was used to measure locomotor activity of rats post-TBI. The rats were individually placed in an open-field chamber (120 cm × 120 cm × 40 cm) and allowed to explore for 5 min freely. The total distance traveled was used to evaluate motor function, which was recorded by SMART 3.0 software.

Novel Object Recognition Test (NOR)

NOR test is widely used to evaluate object recognition memory (28). The discrimination of recognition novelty was assessed by preference index (PI) (time exploring the new object)/(total time spent exploring both objects) (29).

Statistical Analysis

In this study, data were expressed as mean ± SEM and analyzed by employing the GraphPad 8.0 software (San Diego, USA). The differences between any given two groups throughout this study were analyzed by unpaired Student's *T*-tests, unless otherwise specified. In different treatment groups, one-way ANOVA followed by Fisher's LSD test was employed. Multiple comparisons involving more than one variable were analyzed by two-way ANOVA followed by Tukey's *post-hoc* test. Two-tailed $p < 0.05$ was considered as statistically significant.

RESULTS

Nonoxid-HMGB1 and fr-HMGB1 Promote Growth of Primary Cortical Neurons

Extracellular HMGB1 has been evaluated to be a DAMP. Interestingly, HMGB1 has also been found to promote neurite outgrowth and regeneration. Different redox isoforms of HMGB1 may play different roles. We first characterized the cultured cortical neurons with two specific markers (MAP2 and NeuN), and the cells were confirmed as neurons (**Supplementary Figure 1**).

The biological activity of extracellular HMGB1 is determined by the redox state (30). We tested the role of the nonoxid-HMGB1 and fr-HMGB1 as well as ds-HMGB1 in neuron growth. Compare with the control group, a significantly increased number of neurites were detected in the nonoxid-HMGB1 group and the fr-HMGB1 group (**Figures 1A,B**). Furthermore, average axon length was measured in the nonoxid-HMGB1 group and the fr-HMGB1 group, and both were significantly increased than the control group (**Figure 1C**). The average number of neurites was not affected by ds-HMGB1 (**Figure 1B**). However, the axon length was decreased after ds-HMGB1 treatment (**Figure 1C**). Thus, these results confirmed that HMGB1-mediated neurite outgrowth and axon elongation of neurons require the reduced state of the protein.

Differential Gene Expression and Functional Enrichment Analysis

To identify genes and pathways involved in the promotion of neurite outgrowth and regeneration, we performed RNA-seq analysis. Heatmap showed clear clusters of up- and downregulated genes (**Supplementary Figure 2A**).

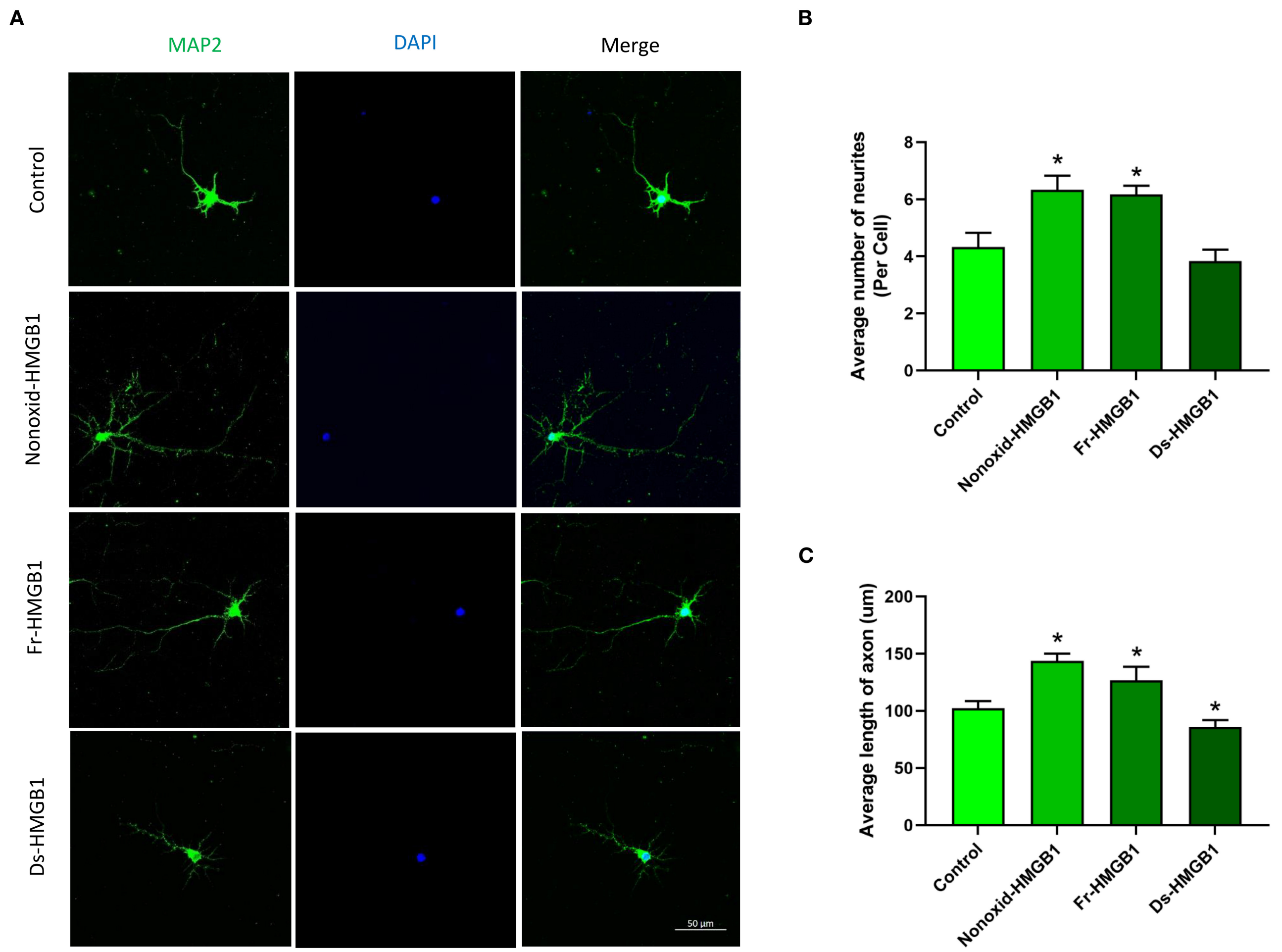

FIGURE 1 | Effects of HMGB1 in different redox forms on neurite outgrowth and axon elongation of cortical neurons. **(A)** Immunocytochemistry was used to label neurites and axons after 24 h of treatment with HMGB1. **(B)** Nonoxid-HMGB1 and fr-HMGB1 significantly increased the average number of neurites compared to the control group. Ds-HMGB1 failed to significantly affect neurite outgrowth. **(C)** Nonoxid-HMGB1 and fr-HMGB1 significantly increased the average axon length compared to control; however, the average axon length was decreased after ds-HMGB1 treatment. Mean + SEM. $^*p < 0.05$.

Through differential expression analysis of RNA-Seq data, we identified top 50 DEGs (differential expressed genes) (**Figures 2A,B**). Gene ontology (GO) analysis revealed that the majority of biological processes had correlations with neurodevelopment and nerve regeneration, such as nervous system development, axon extension, neuroblast proliferation, neurotransmitter secretion, myelination, cortical cytoskeleton organization, and so on (**Figures 2C,D**). In addition, we also found that four accepted pathways for nerve regeneration were activated to varying degrees by nonoxid-HMGB1 (**Supplementary Figures 2B–E**). As nonoxid-HMGB1 and fr-HMGB1 have the similar activity, they may regulate neurite outgrowth and regeneration by the same mechanism. To identify the potential downstream target of nonoxid-HMGB1 and fr-HMGB1, we compared two sets of DEGs data, and a co-upregulated gene SH3RF2 was detected (**Figures 2A,B**).

Expression and Distribution of SH3RF2 in Cortical Neurons

To validate the expression of SH3RF2 in neurons, we performed immunostaining of SH3RF2. The results showed that green fluorescence intensity of SH3RF2 was significantly increased in the nonoxid-HMGB1 group and the fr-HMGB1 group as compared with the control (**Figures 3A,B**). Interestingly, we found that SH3RF2 was widely distributed in the cell bodies and neurites (**Figure 3A**). To further evaluate the effect of extracellular HMGB1 on the expression of SH3RF2 and HMGB1 in neurons, western blot analysis was performed. As expected, we detected the relative protein level of SH3RF2 was significantly increased in the nonoxid-HMGB1 group and the fr-HMGB1 group. In addition, we found that extracellular nonoxid-HMGB1 and fr-HMGB1 did not influence the expression of HMGB1 in neurons (**Figures 3C–F**). These results confirmed the expression change of SH3RF2, which were consistent with the bioinformatic

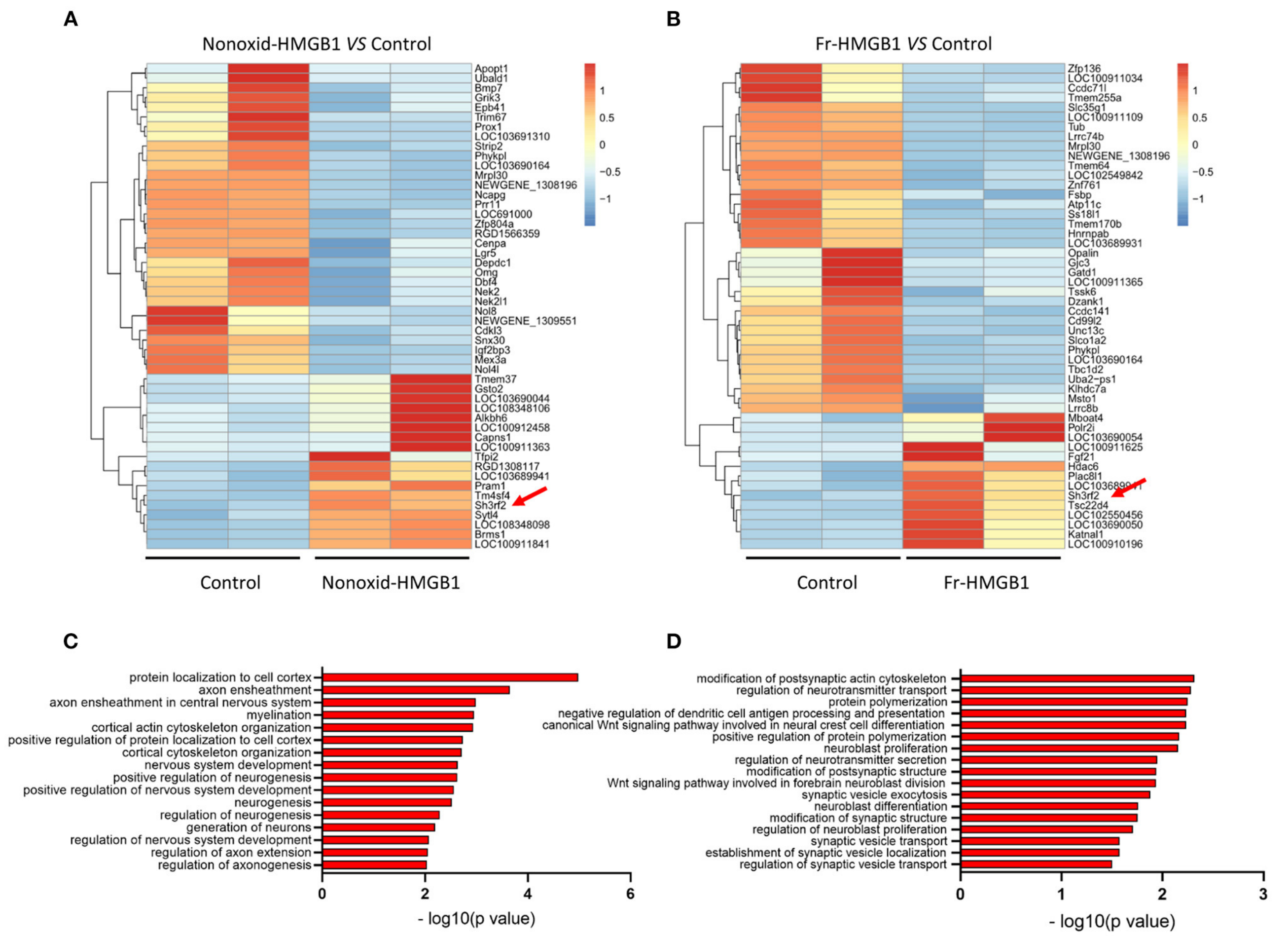

FIGURE 2 | The transcriptome sequence and bioinformatics analysis. **(A)** The heat map of top 50 DEGs in the nonoxid-HMGB1 group vs. the control group. **(B)** The heat map of top 50 DEGs in the fr-HMGB1 group vs. the control group. **(C)** GO analysis for DEGs in the nonoxid-HMGB1 group compared with the control group. **(D)** GO analysis for DEGs in the fr-HMGB1 group compared with the control group.

analysis result. SH3RF2 could be the potential downstream target of nonoxid-HMGB1 and fr-HMGB1 to participate in neurite outgrowth and axon elongation.

Nonoxid-HMGB1 Enhances Axon Growth by SH3RF2

To validate the potential downstream target gene SH3RF2, we designed this experiment. Because of the instability of fr-HMGB1 in the oxidizing environment, a mutant of fr-HMGB1, nonoxid-HMGB1 (3S-HMGB1), was adopted in this experiment. LV-shSH3RF2 was designed to silence SH3RF2, and empty vectors (LV-vector) were used as control lentivirus. Neurons were transfected with lentivirus at day in Culture 7. After transfection for 72 h, a great number of neurons with strong red fluorescence were observed (**Figure 4A**), and the SH3RF2 level decreased significantly in the LV-shSH3RF2 group (**Figures 4B,C**). After infection, nonoxid-HMGB1 was added to the cultured neurons and remained present until fixation after 24 h. Compared with the LV-vector group, the average length of axons was increased in LV-vector + 3S-HMGB1 group. Moreover, no differences were observed between the LV-vector controls and the LV-shSH3RF2 group in axon length. As expected, there was also no diversity between the LV-vector group and the LV-shSH3RF2 + 3S-HMGB1 group (**Figures 4D,E**). The number of neurites per neuron was no change in different groups (**Figure 4F**). Taken together, these results demonstrate that silence SH3RF2 antagonizes nonoxid-HMGB1-induced axon growth.

Nonoxid-HMGB1 Attenuates Object Recognition Memory Deficits in CCI Rats

To further investigate *in vivo* effects of nonoxid-HMGB1, the CCI model was employed; we injected an ScAAV-3S-HMGB1 expressing vector to increase levels of nonoxid-HMGB1 after TBI, using injections of an empty vehicle as the matched group (ScAAV-Vehicle). The experimental CCI was established at 10 days after ScAAV injection. OF test and novel NOR test were conducted at 3 weeks after CCI (**Figure 5A**). After virus injection for 10 days, strong green fluorescence was observed in the cortex and hippocampus, and nonoxid-HMGB1 was strongly expressed (**Figure 5B**, **Supplementary Figure 3**). We examined

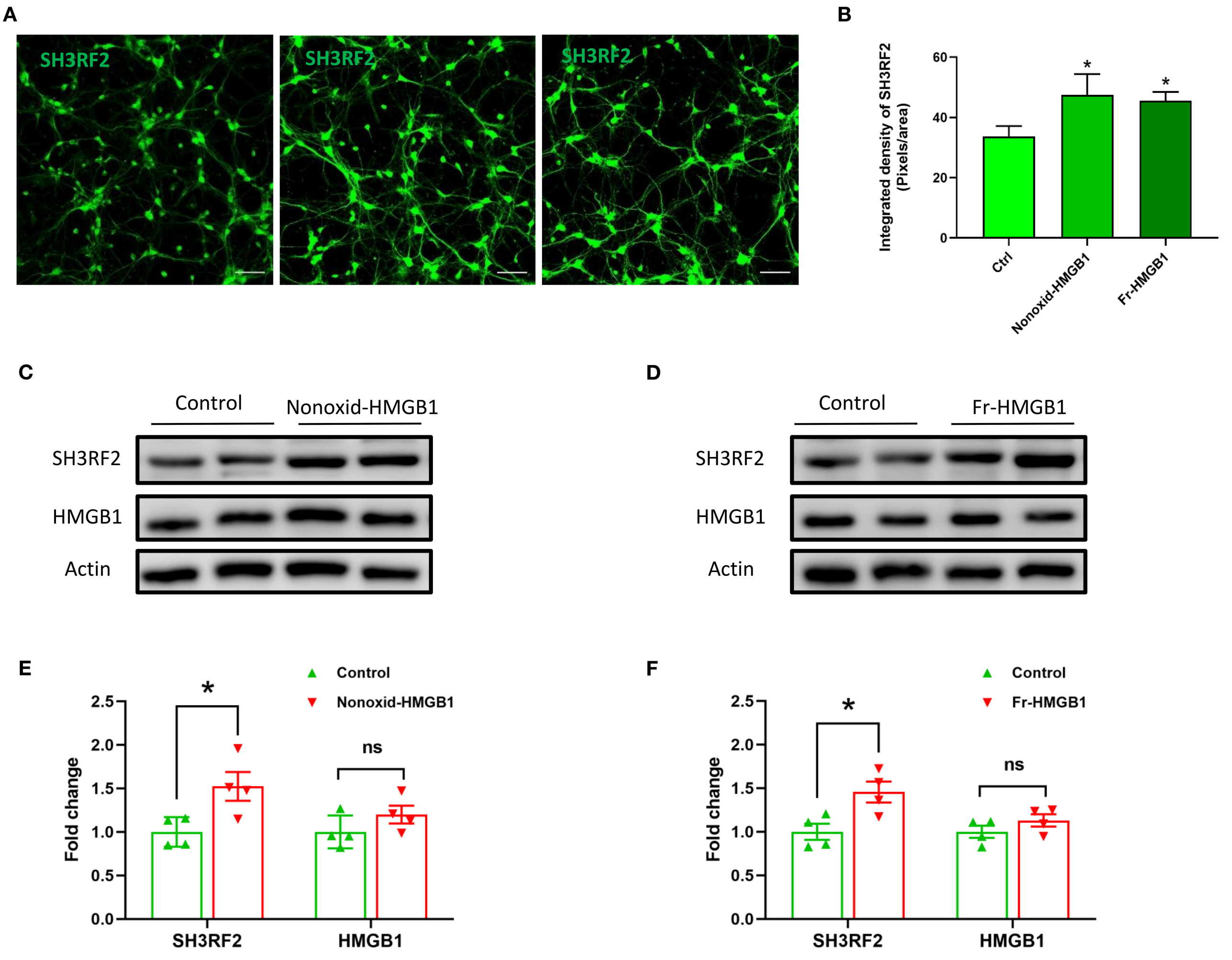

FIGURE 3 | Validation and expression analysis of SH3RF2 in neurons after being treated with nonoxid-HMGB1 or fr-HMGB1. **(A)** Representative fluorescence images of neurons. Scale bars, 50 um. **(B)** Relative quantification of the fluorescence signal. **(C–F)** Western blot for SH3RF2 and HMGB1. Mean ± SEM, $^*p < 0.05$.

the locomotor activity of rats with the OF test, and all three experimental groups displayed similar locomotor activity post-TBI (**Figure 5C**). For the NOR test, as presented in **Figure 5D**, the new object reference index in the CCI + ScAAV-Vehicle group was lower than Sham + ScAAV-Vehicle group, indicating that CCI results in an impairment in memory behavior. In the ScAAV-3S-HMGB1 group, the new object preference index was higher than CCI + ScAAV-Vehicle group, but lower than Sham + ScAAV-Vehicle group (**Figure 5D**). Taken together, these results indicate that nonoxid-HMGB1 improved rats' learning and memory function to a certain extent.

SH3RF2 Is Required for Nonoxid-HMGB1 Improving CCI-Induced Learning and Memory Damage

To further disclose whether SH3RF2 is required for nonoxid-HMGB1 improving CCI-induced learning and memory impairments, we knocked down the expression of SH3RF2 in hippocampus by lentivirus (LV-shSH3RF2). Nonoxid-HMGB1-enriched exosomes (Exo-3S-HMGB1) were employed to increase levels of nonoxid-HMGB1 in brain after CCI. The schematic timeline of experiments was presented in **Figure 6A**.

Exo-3S-HMGB1 was first constructed, and then was administrated into rats after the establishment of CCI. To construct Exo-3S-HMGB1, the BMSCs with high expression of nonoxid-HMGB1 were generated by plasmid transfection, and the green fluorescence was obviously observed in BMSCs after transfection (**Supplementary Figures 4A,B**). Then, exosomes were identified by analyzing their shape and size (**Supplementary Figure 4C**) and detecting the specific protein TSG101 and Flotillin-1 (**Supplementary Figure 4D**). In addition, nonoxid-HMGB1 was detected in exosomes of the transfected BMSCs (**Supplementary Figure 4E**). All of these results suggest that the Exo-3S-HMGB1 was successfully constructed.

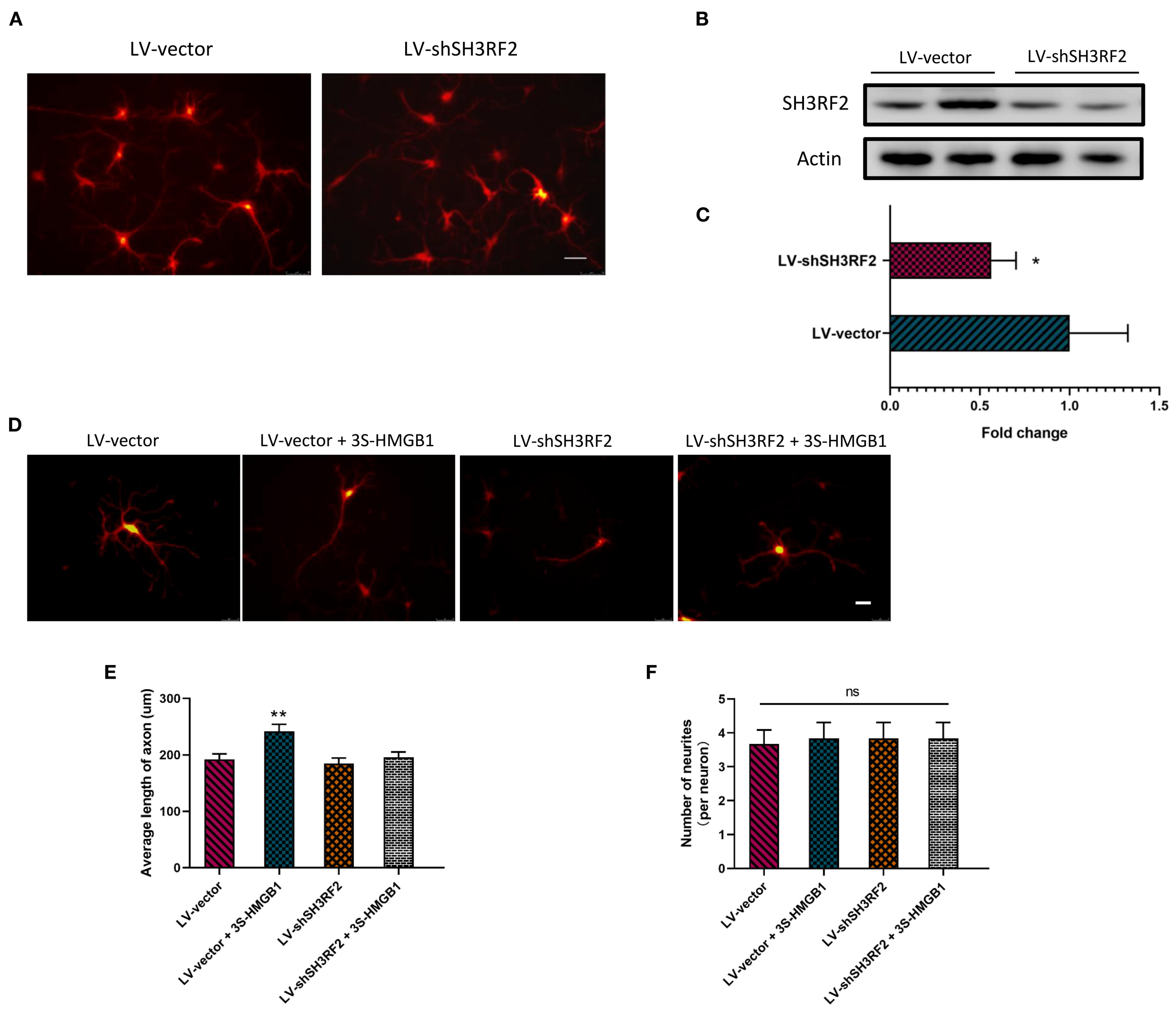

FIGURE 4 | Nonoxid-HMGB1 promotes axon growth by SH3RF2. **(A)** Representative images of neurons after transfection for 72 h. Scale bars, 50 um. **(B,C)** Assessment of silencing efficiency by relative quantification of SH3RF2. **(D,E)** Representative electron microscopy images show that nonoxid-HMGB1 promotes axon growth in control (LV-vector) primary neurons, and it does not cause marked changes of axon growth in shSH3RF2 primary neurons. Scale bars, 50 um. **(F)** Treatment with nonoxid-HMGB1 did not alter the neurites number in control (LV-vector) primary neurons and in shSH3RF2 primary neurons. Mean ± SEM, $^{*}p < 0.05$, $^{**}p < 0.01$, ns: no significance.

The subsequent study was aimed to explore whether knockdown of SH3RF2 could eliminate the recovery of memory function induced by nonoxid-HMGB1 in CCI. We injected LV-shSH3RF2 to knocked-down SH3RF2 in hippocampus, and decreased SH3RF2 expression was observed after 2 weeks (**Figure 6B**). Next, we constructed the TBI model of rats and injected exosomes into rats. The OF test results showed that there were no significant differences in total distance traveled among all five groups, suggesting that motor abilities did not interfere with NOR training and test (**Figure 6C**). For the NOR test, the preference index of a new object in the CCI-PBS group and the CCI-Exo-control group was both significantly lower than a familiar object, indicating that Exo-control could not improve the memory impairment caused by CCI. Rats injected with Exo-3S-HMGB1 showed an improvement in memory function. However, SH3RF2 silencing attenuated the improvement of memory defect induced by Exo-3S-HMGB1 (**Figure 6D**). All of these data indicated that SH3RF2 silencing could partly eliminate the recovery of memory function induced by nonoxid-HMGB1.

DISCUSSION

As mentioned before, extracellular HMGB1 exists in three different redox states, and different forms of HMGB1 interact

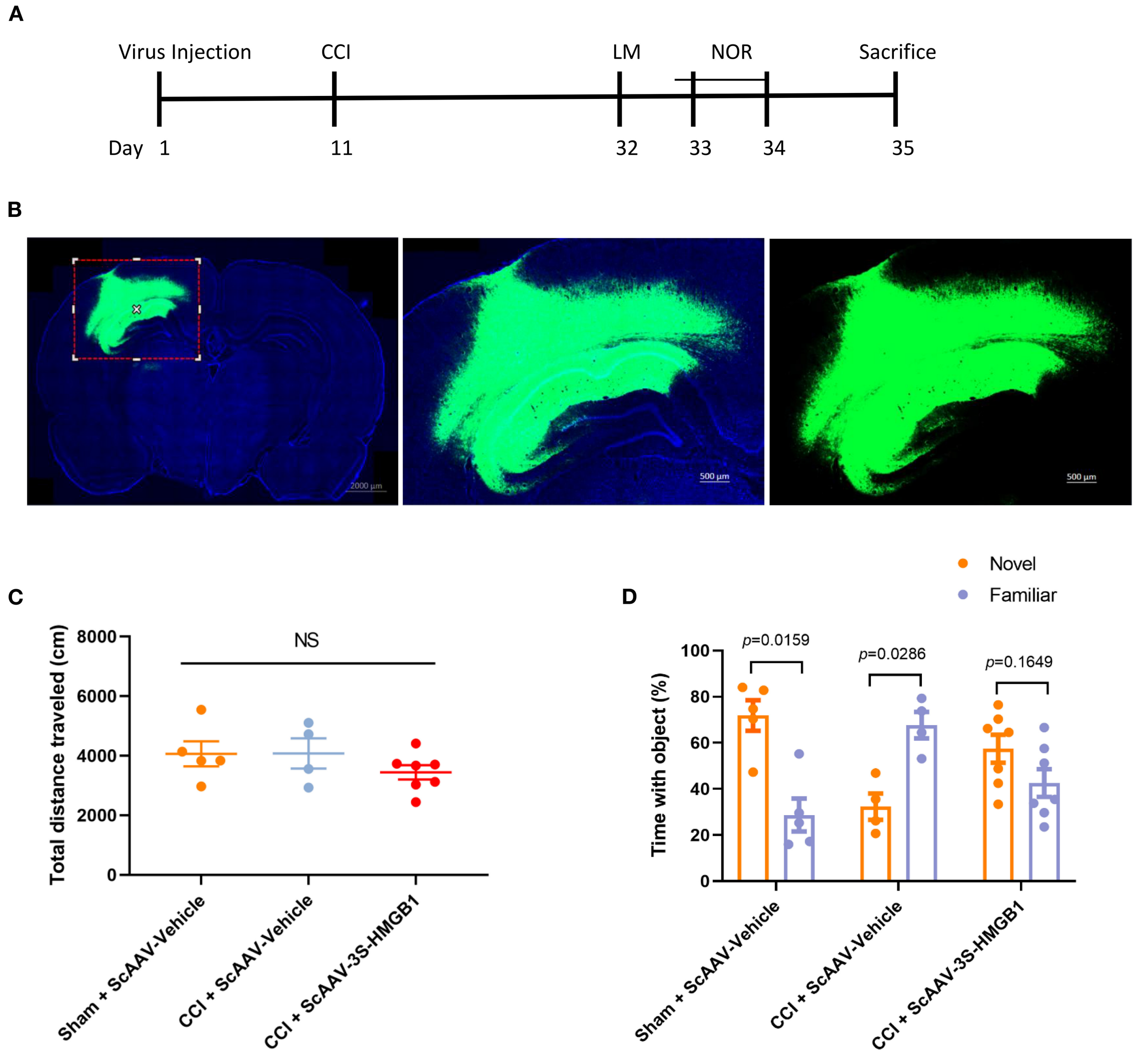

FIGURE 5 | Nonoxid-HMGB1 attenuates learning and memory impairments in CCI rats. **(A)** The experimental timeline for the neurobehavioral testing. **(B)** Representative electron microscopy images of brain sections from rats intervened with ScAAV-3S-HMGB1 or ScAAV-Vehicle for 10 days. **(C)** In the open field test, no differences were observed among three experimental groups. **(D)** Exploration times and discrimination indices were calculated in NOR test. Mean ± SEM; NS: no significance.

with different receptors (13). Several lines of evidence support that ds-HMGB1 serves as a proinflammatory cytokine *via* interactions with TLR4 (14, 15), whereas fr-HMGB1 mediates tissue regeneration by binding to RAGE (12). Interestingly enough, RAGE signaling has been demonstrated to promote neurite outgrowth and nerve regeneration (31–36). In addition, HMGB1-RAGE axis has been turned out to mediate cell migration and tissue regeneration (37, 38). However, few studies have investigated the potential relationship between different redox states of HMGB1 and nerve growth or regeneration. Against this background, we sought to further confirm if HMGB1 would enhance neurite outgrowth of neurons and, if so, by which kind of redox state. We found that nonoxid-HMGB1 (3S-HMGB1) and fr-HMGB1 promote neurite outgrowth and axon elongation, which is consistent with prior reports that HMGB1 contributes to facilitate neurogenesis and neural regeneration (20–22). However, the neurite outgrowth and axon elongation of neuron were inhibited by ds-HMGB1. Frank et al. reported that ds-HMGB1, but not fr-HMGB1, contributes to inflammatory responses (39). This phenomenon might be caused by activating TLR4 and evoking the production of proinflammatory cytokines subsequently (14, 15).

In order to understand the molecular mechanism through which nonoxid-HMGB1 and/or fr-HMGB1 acts in neurons, we have performed RNA-seq analysis. We noted that nonoxid-HMGB1 shows stronger effects than fr-HMGB1 in genes related to neurogenesis, axon extension, and myelination, but weaker influences on neuroblast proliferation, neuroblast differentiation, and neurotransmitter transport. The divergent results may be due to the inability of nonoxid-HMGB1 to be oxidized to

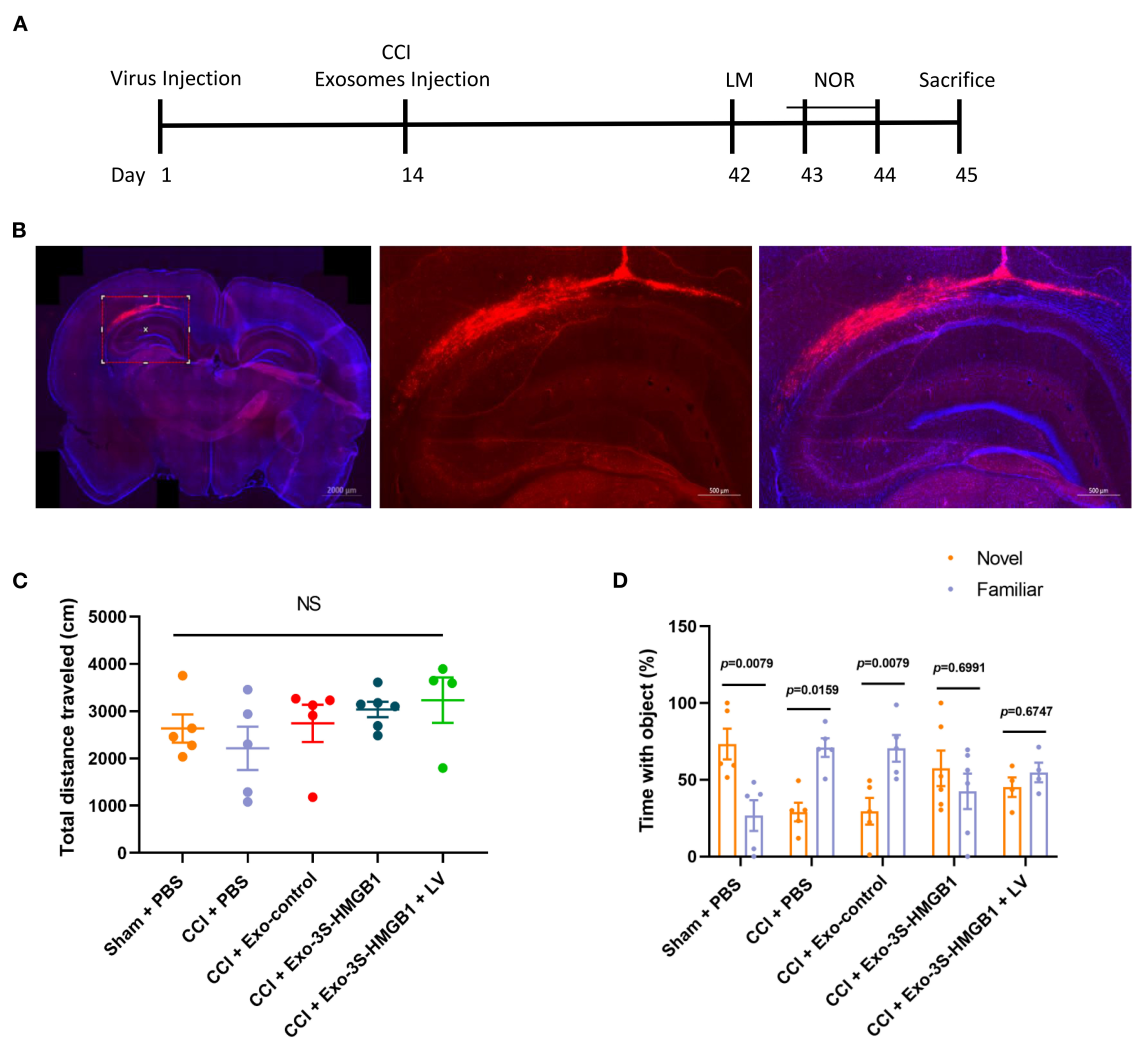

FIGURE 6 | LV-shSH3RF2 attenuated the effect of Exo-3S-HMGB1 to improve the recovery of memory function in CCI. **(A)** The experimental timeline for the neurobehavioral testing. **(B)** Representative electron microscopy images of brain sections from rats intervened with LV-shSH3RF2. **(C)** No differences were observed in the open field test. **(D)** Exploration times and discrimination indices were calculated in NOR test. Mean ± SEM, NS: no significance.

other forms of HMGB1. Notably, we found that SH3RF2 is a co-upregulated DEG in the nonoxid-HMGB1 group and the fr-HMGB1 group. SH3RF2 is a multidomain scaffold protein participated in promoting cell survival, and the knockdown of SH3RF2 promoted apoptosis of cultured cortical neurons (40, 41). Besides, mice with SH3RF2 haploinsufficiency exhibit synaptic plasticity deficits and synaptic dysfunction (42). In this study, we revealed that nonoxid-HMGB1 promotes neurite outgrowth and axon elongation in neurons by increasing SH3RF2 expression. Combined with previous pieces of research, we speculated that SH3RF2 might be a target gene in HMGB1-RAGE axis.

Prior pieces of evidence have indicated that HMGB1 is implicated in neuroinflammation in TBI and exacerbates neurocognitive impairments (17, 18). The release of HMGB1 from damaged tissues has been reported to enhance cerebral edema and neurological deficits (43, 44). In addition, some studies declared that the use of HMGB1 antagonists could reduce cerebral edema, suppress pro-inflammatory cytokine release and microglial activation, and improve neurological outcomes (45–47). As the cysteines of HMGB1 are easily oxidized in oxidizing milieu (13), few studies have further investigated the role of different redox states of HMGB1 in TBI. Interestingly, we found that nonoxid-HMGB1 effectively ameliorates cognitive function, and the inhibition of SH3RF2 attenuated the beneficial effects of nonoxid-HMGB1 on cognitive function. The behavioral improvement induced by nonoxid-HMGB1 post-TBI might result from the neurite outgrowth and axon regeneration of neurons.

Notably, this study has certain limitations. HMGB1 is released from injured cells or death cells (13). Extracellular

HMGB1 mainly exists in the form of Disulfide HMGB1 (ds-HMGB1). To avoid these destabilizing factors, we choose a normal cell model in an *in vitro* experiment, but not the neuronal injury model. Further studies are needed to explore the effects of nonoxid-HMGB1 on injured neurons. In addition, the *in vivo* findings indicated that nonoxid-HMGB1 ameliorated cognitive function in rats post-TBI *via* SH3RF2. Further studies will be required to clarify the detailed molecular biological mechanisms in the recovery of cognitive function post-TBI.

Taken together, our findings indicate that nonoxid-HMGB1 reduces TBI-mediated cognitive impairment. This beneficial effect might be through two mechanisms: (i) SH3RF2-induced modulation of neurite outgrowth and regeneration and (ii) SH3RF2-induced modulation of neuronal survival and apoptosis (40, 41). Our experimental results suggest that nonoxid-HMGB1 is an attractive therapeutic candidate for the treatment of TBI, and regulating the redox state of extracellular HMGB1 may be a novel therapeutic approach to treat TBI.

DATA AVAILABILITY STATEMENT

The raw data supporting the conclusions of this article will be made available by the authors, without undue reservation.

ETHICS STATEMENT

The animal study was reviewed and approved by the Review Committee for the Use of Human or Animal Subjects of Sun Yat-sen University.

AUTHOR CONTRIBUTIONS

J-QC performed the experiments and wrote the manuscript. S-QG performed all behavior tests. LL, Z-YJ, and C-FL worked with cell culture and exosome extraction. H-YH and YG designed the project and revised the manuscript. All authors contributed to the article and approved the submitted version.

FUNDING

This work was supported by the Science and Technology Program of Guangzhou, China under (Grant No. 201604020080 to YG) and the Guangdong Basic and Applied Basic Research Foundation under (Grant Nos. 2018B0303110014 and 2020B090924004 to YG).

ACKNOWLEDGMENTS

We acknowledge and appreciate our colleagues for their valuable efforts and comments on this paper.

SUPPLEMENTARY MATERIAL

The Supplementary Material for this article can be found online at: https://www.frontiersin.org/articles/10.3389/fmed.2022.827585/full#supplementary-material

Supplementary Figure 1 | Identification of cultured cortical neurons. After 7 days in culture, two specific markers for neurons were used to identify the cultured cells. The expression of NeuN and MAP2 was detected in the cells.

Supplementary Figure 2 | Bioinformatics analysis. **(A)** The heat map illustrates the intensity of signals about transcription for each sample. **(B–E)** Four classical pathways for nerve regeneration were activated to varying degrees by non-oxidized HMGB1.

Supplementary Figure 3 | The expression of nonoxid-HMGB1 in neurons. **(A)** Representative images of neurons after ScAAV transfection. **(B)** Western blot for nonoxid-HMGB1.

Supplementary Figure 4 | The construction and identification of Exo-3S-HMGB1. **(A)** Representative electron microscopy image of ordinary BMSCs. **(B)** BMSCs transfected with plasmid. Scale bars, 100 um. **(C)** Representative electron microscope image of exosomes. Scale bars, 200 nm. **(D)** Western blot for the markers of exosome TSG101 and Flotin. **(E)** Nonoxid-HMGB1 was detected in the modified exosomes derived from BMSCs.

REFERENCES

1. Capizzi A, Woo J, Verduzco-Gutierrez M. Traumatic brain injury: an overview of epidemiology, pathophysiology, and medical management. *Med Clin North Am.* (2020) 104:213–38. doi: 10.1016/j.mcna.2019.11.001
2. Maas AIR, Menon DK, Adelson PD, Andelic N, Bell MJ, Belli A, et al. Traumatic brain injury: integrated approaches to improve prevention, clinical care, and research. *Lancet Neurol.* (2017) 16:987–1048. doi: 10.1016/S1474-4422(17)30371-X
3. Marshall S, Bayley M, McCullagh S, Velikonja D, Berrigan L. Clinical practice guidelines for mild traumatic brain injury and persistent symptoms. *Can Fam Physician.* (2012) 58:257–67, e128–40.
4. Stern RA, Riley DO, Daneshvar DH, Nowinski CJ, Cantu RC, McKee AC. Long-term consequences of repetitive brain trauma: chronic traumatic encephalopathy. *Pm r.* (2011) 3:S460–7. doi: 10.1016/j.pmrj.2011.08.008
5. Kochanek PM, Clark RSB, Ruppel RA, Adelson PD, Bell MJ, Whalen MJ, et al. Biochemical, cellular, and molecular mechanisms in the evolution of secondary damage after severe traumatic brain injury in infants and children: lessons learned from the bedside. *Pediatr Crit Care Med.* (2000) 1:4–19. doi: 10.1097/00130478-200007000-00003
6. Marjani S, Zirh S, Sever-Bahcekapili M, Cakir-Aktas C, Muftuoglu SF, Mut M. Doxycycline alleviates acute traumatic brain injury by suppressing neuroinflammation and apoptosis in a mouse model. *J Neuroimmunol.* (2021) 359:577672. doi: 10.1016/j.jneuroim.2021.577672
7. Pearn ML, Niesman IR, Egawa J, Sawada A, Almenar-Queralt A, Shah SB, et al. Pathophysiology associated with traumatic brain injury: current treatments and potential novel therapeutics. *Cell Mol Neurobiol.* (2017) 37:571–85. doi: 10.1007/s10571-016-0400-1
8. Andersson U, Tracey KJ. HMGB1 is a therapeutic target for sterile inflammation and infection. *Annu Rev Immunol.* (2011) 29:139–62. doi: 10.1146/annurev-immunol-030409-101323
9. Harris HE, Andersson U, Pisetsky DS. HMGB1: a multifunctional alarmin driving autoimmune and inflammatory disease. *Nat Rev Rheumatol.* (2012) 8:195–202. doi: 10.1038/nrrheum.2011.222
10. Bianchi M E, Manfredi A A. High-mobility group box 1 (HMGB1) protein at the crossroads between innate and adaptive immunity. *Immunol Rev.* (2007) 220:35–46. doi: 10.1111/j.1600-065X.2007.00574.x

11. Yang H, Lundbäck P, Ottosson L, Erlandsson-Harris H, Venereau E, Bianchi ME, et al. Redox modification of cysteine residues regulates the cytokine activity of high mobility group box-1 (HMGB1). *Mol Med.* (2012) 18:250–9. doi: 10.2119/molmed.2011.00389
12. Venereau E, Casalgrandi M, Schiraldi M, Antoine DJ, Cattaneo A, De Marchis F, et al. Mutually exclusive redox forms of HMGB1 promote cell recruitment or proinflammatory cytokine release. *J Exp Med.* (2012) 209:1519–28. doi: 10.1084/jem.20120189
13. Kang R, Chen R, Zhang Q, Hou W, Wu S, Cao L, et al. HMGB1 in health and disease. *Mol Aspects Med.* (2014) 40:1–116. doi: 10.1016/j.mam.2014.05.001
14. Lian YJ, Gong H, Wu TY, Su WJ, Zhang Y, Yang YY, et al. Ds-HMGB1 and fr-HMGB induce depressive behavior through neuroinflammation in contrast to nonoxid-HMGB1. *Brain Behav Immun.* (2017) 59:322–32. doi: 10.1016/j.bbi.2016.09.017
15. Frank MG, Weber MD, Watkins LR, Maier SF. Stress sounds the alarmin: the role of the danger-associated molecular pattern HMGB1 in stress-induced neuroinflammatory priming. *Brain Behav Immun.* (2015) 48:1–7. doi: 10.1016/j.bbi.2015.03.010
16. Tang Y, Zhao X, Antoine D, Xiao X, Wang H, Andersson U, et al. Regulation of posttranslational modifications of HMGB1 during immune responses. *Antioxid Redox Signal.* (2016) 24:620–34. doi: 10.1089/ars.2015.6409
17. Gadani SP, Walsh JT, Lukens JR, Kipnis J. Dealing with danger in the CNS: the response of the immune system to injury. *Neuron.* (2015) 87:47–62. doi: 10.1016/j.neuron.2015.05.019
18. Paudel YN, Angelopoulou E, Piperi C, Othman I, Shaikh MF. HMGB1-mediated neuroinflammatory responses in brain injuries: potential mechanisms and therapeutic opportunities. *Int J Mol Sci.* (2020) 21:4609. doi: 10.3390/ijms21134609
19. Bianchi ME. DAMPs, PAMPs and alarmins: all we need to know about danger. *J Leukoc Biol.* (2007) 81:1–5. doi: 10.1189/jlb.0306164
20. Manivannan S, Marei O, Elalfy O, Zaben M. Neurogenesis after traumatic brain injury - the complex role of HMGB1 and neuroinflammation. *Neuropharmacology.* (2021) 183:108400. doi: 10.1016/j.neuropharm.2020.108400
21. Merianda TT, Coleman J, Kim HH, Kumar Sahoo P, Gomes C, Brito-Vargas P, et al. Axonal amphoterin mRNA is regulated by translational control and enhances axon outgrowth. *J Neurosci.* (2015) 35:5693–706. doi: 10.1523/JNEUROSCI.3397-14.2015
22. Fang P, Pan HC, Lin SL, Zhang WQ, Rauvala H, Schachner M, et al. HMGB1 contributes to regeneration after spinal cord injury in adult zebrafish. *Mol Neurobiol.* (2014) 49:472–83. doi: 10.1007/s12035-013-8533-4
23. Careccia G, Saclier M, Tirone M, Ruggieri E, Principi E, Raffaghello L, et al. Rebalancing expression of HMGB1 redox isoforms to counteract muscular dystrophy. *Sci Transl Med.* (2021) 13:eaay8416. doi: 10.1126/scitranslmed.aay8416
24. Zhu L, Ren L, Chen Y, Fang J, Ge Z, Li X. Redox status of high-mobility group box 1 performs a dual role in angiogenesis of colorectal carcinoma. *J Cell Mol Med.* (2015) 19:2128–35. doi: 10.1111/jcmm.12577
25. Chen C, Ling C, Gong J, Li C, Zhang L, Gao S, et al. Increasing the expression of microRNA-126–5p in the temporal muscle can promote angiogenesis in the chronically ischemic brains of rats subjected to two-vessel occlusion plus encephalo-myo-synangiosis. *Aging.* (2020) 12:13234–54. doi: 10.18632/aging.103431
26. Hou B, Ye Z, Ji W, Cai M, Ling C, Chen C, et al. Comparison of the effects of BMSC-derived Schwann cells and autologous schwann cells on remyelination using a rat sciatic nerve defect model. *Int J Biol Sci.* (2018) 14:1910–22. doi: 10.7150/ijbs.26765
27. Kim DK, Nishida H, An SY, Shetty AK, Bartosh TJ, Prockop DJ. Chromatographically isolated CD63+CD81+ extracellular vesicles from mesenchymal stromal cells rescue cognitive impairments after TBI. *Proc Natl Acad Sci USA.* (2016) 113:170–5. doi: 10.1073/pnas.1522297113
28. Antunes M, Biala G. The novel object recognition memory: neurobiology, test procedure, and its modifications. *Cogn Process.* (2012) 13:93–110. doi: 10.1007/s10339-011-0430-z
29. Mumby DG, Glenn MJ, Nesbitt C, Kyriazis DA. Dissociation in retrograde memory for object discriminations and object recognition in rats with perirhinal cortex damage. *Behav Brain Res.* (2002) 132:215–26. doi: 10.1016/S0166-4328(01)00444-2
30. Di Maggio S, Milano G, De Marchis F, D'Ambrosio A, Bertolotti M, Palacios BS, et al. Non-oxidizable HMGB1 induces cardiac fibroblasts migration via CXCR4 in a CXCL12-independent manner and worsens tissue remodeling after myocardial infarction. *Biochim Biophys Acta.* (2017) 1863:2693–704. doi: 10.1016/j.bbadis.2017.07.012
31. Saleh A, Smith DR, Tessler L, Mateo AR, Martens C, Schartner E, et al. Receptor for advanced glycation end-products (RAGE) activates divergent signaling pathways to augment neurite outgrowth of adult sensory neurons. *Exp Neurol.* (2013) 249:149–59. doi: 10.1016/j.expneurol.2013.08.018
32. Kim J, Wan CK, O'Carroll JS, Shaikh SB, Nicholson LF. The role of receptor for advanced glycation end products (RAGE) in neuronal differentiation. *J Neurosci Res.* (2012) 90:1136–47. doi: 10.1002/jnr.23014
33. Rong LL, Trojaborg W, Qu W, Kostov K, Yan SD, Gooch C, et al. Antagonism of RAGE suppresses peripheral nerve regeneration. *FASEB J.* (2004) 18:1812–7. doi: 10.1096/fj.04-1899com
34. Xue X, Chen X, Fan W, Wang G, Zhang L, Chen Z, et al. High-mobility group box 1 facilitates migration of neural stem cells via receptor for advanced glycation end products signaling pathway. *Sci Rep.* (2018) 8:4513. doi: 10.1038/s41598-018-22672-4
35. Huttunen HJ, Kuja-Panula J, Sorci G, Agneletti AL, Donato R, Rauvala H. Coregulation of neurite outgrowth and cell survival by amphoterin and S100 proteins through receptor for advanced glycation end products (RAGE) activation. *J Biol Chem.* (2000) 275:40096–105. doi: 10.1074/jbc.M006993200
36. Huttunen HJ, Fages C, Rauvala H. Receptor for advanced glycation end products (RAGE)-mediated neurite outgrowth and activation of NF-kappaB require the cytoplasmic domain of the receptor but different downstream signaling pathways. *J Biol Chem.* (1999) 274:19919–24. doi: 10.1074/jbc.274.28.19919
37. Meng X, Chen M, Su W, Tao X, Sun M, Zou X, et al. The differentiation of mesenchymal stem cells to vascular cells regulated by the HMGB1/RAGE axis: its application in cell therapy for transplant arteriosclerosis. *Stem Cell Res Ther.* (2018) 9:85. doi: 10.1186/s13287-018-0827-z
38. Tancharoen S, Gando S, Binita S, Nagasato T, Kikuchi K, Nawa Y, et al. HMGB1 promotes intraoral palatal wound healing through RAGE-dependent mechanisms. *Int J Mol Sci.* (2016) 17:1961. doi: 10.3390/ijms17111961
39. Frank MG, Weber MD, Fonken LK, Hershman SA, Watkins LR, Maier SF. The redox state of the alarmin HMGB1 is a pivotal factor in neuroinflammatory and microglial priming: a role for the NLRP3 inflammasome. *Brain Behav Immun.* (2016) 55:215–24. doi: 10.1016/j.bbi.2015.10.009
40. Wilhelm M, Kukekov NV, Schmit TL, Biagas KV, Sproul AA, Gire S, et al. Sh3rf2/POSHER protein promotes cell survival by ring-mediated proteasomal degradation of the c-Jun N-terminal kinase scaffold POSH (Plenty of SH3s) protein. *J Biol Chem.* (2012) 287:2247–56. doi: 10.1074/jbc.M111.269431
41. Kim TW, Kang YK, Park ZY, Kim YH, Hong SW, Oh SJ, et al. SH3RF2 functions as an oncogene by mediating PAK4 protein stability. *Carcinogenesis.* (2014) 35:624–34. doi: 10.1093/carcin/bgt338
42. Wang S, Tan N, Zhu X, Yao M, Wang Y, Zhang X, et al. Sh3rf2 haploinsufficiency leads to unilateral neuronal development deficits and autistic-like behaviors in mice. *Cell Rep.* (2018) 25:2963–71.e6. doi: 10.1016/j.celrep.2018.11.044
43. Chen X, Chen C, Fan S, Wu S, Yang F, Fang Z, et al. Omega-3 polyunsaturated fatty acid attenuates the inflammatory response by modulating microglia polarization through SIRT1-mediated deacetylation of the HMGB1/NF-κB pathway following experimental traumatic brain injury. *J Neuroinflamm.* (2018) 15:116. doi: 10.1186/s12974-018-1151-3
44. Laird MD, Shields JS, Sukumari-Ramesh S, Kimbler DE, Fessler RD, Shakir B, et al. High mobility group box protein-1 promotes cerebral edema after traumatic brain injury via activation of toll-like receptor 4. *Glia.* (2014) 62:26–38. doi: 10.1002/glia.22581
45. Evran S, Calis F, Akkaya E, Baran O, Cevik S, Katar S, et al. The effect of high mobility group box-1 protein on cerebral edema, blood-brain barrier, oxidative stress and apoptosis in an

experimental traumatic brain injury model. *Brain Res Bull.* (2020) 154:68–80. doi: 10.1016/j.brainresbull.2019.10.013

46. Pang H, Huang T, Song J, Li D, Zhao Y, Ma X. Inhibiting HMGB1 with glycyrrhizic acid protects brain injury after DAI via its anti-inflammatory effect. *Mediators Inflamm.* (2016) 2016:4569521. doi: 10.1155/2016/4569521
47. Chen X, Wu S, Chen C, Xie B, Fang Z, Hu W, et al. Omega-3 polyunsaturated fatty acid supplementation attenuates microglial-induced inflammation by inhibiting the HMGB1/TLR4/NF-κB pathway following experimental traumatic brain injury. *J Neuroinflamm.* (2017) 14:143. doi: 10.1186/s12974-017-0917-3

Conflict of Interest: The authors declare that the research was conducted in the absence of any commercial or financial relationships that could be construed as a potential conflict of interest.

frontiers | Frontiers in Medicine

ORIGINAL RESEARCH
published: 13 May 2022
doi: 10.3389/fmed.2022.897392

A Network Pharmacology Study: Reveal the Mechanisms of Palovarotene Against Heterotopic Ossification

*Junchao Huang[1]†, Dachuan Liu[2]†, Jingwei Zhang[1] and Haijun Xiao[1]**

[1] Department of Orthopedics, Shanghai Fenxian District Central Hospital/Anhui University of Science and Technology Affiliated Fengxian Hospital, Shanghai, China, [2] Department of Orthopaedic Surgery, Orthopaedic Institute, The First Affiliated Hospital of Soochow University, Suzhou, China

Edited by:
Fu Wang,
Xi'an Jiaotong University, China

Reviewed by:
Xiaogang Zhong,
People's Hospital of Guangxi Zhuang Autonomous Region, China
Dandan Yuan,
The Second Affiliated Hospital of Harbin Medical University, China
Shuxia Ma,
Jiamusi University, China

***Correspondence:**
Haijun Xiao
xiaohaijun89@163.com

† These authors have contributed equally to this work

Specialty section:
This article was submitted to Precision Medicine, a section of the journal Frontiers in Medicine

Received: *16 March 2022*
Accepted: *14 April 2022*
Published: *13 May 2022*

Citation:
Huang J, Liu D, Zhang J and Xiao H (2022) A Network Pharmacology Study: Reveal the Mechanisms of Palovarotene Against Heterotopic Ossification. Front. Med. 9:897392. doi: 10.3389/fmed.2022.897392

Heterotopic ossification (HO) occurs when bone forms within non-ossifying tissues, such as in muscle. Palovarotene, an activator of retinoic acid receptor γ (RAR-γ), has been shown to inhibit the formation of ectopic bone in HO model mice, but its specific mechanism of action remains unclear. This study will explore the target and molecular mechanism of Palovarotene's action on HO by network pharmacology study. We collected the relevant targets of Palovarotene and HO from the database, obtained the potential targets of Palovarotene acting on HO through Venn analysis, and constructed the protein-protein interaction (PPI) network. Then, Gene Ontology (GO) and KEGG (Kyoto Encyclopedia of Genes and Genomes) enrichment Analysis and Module-based Network Analysis were performed for potential targets, and in addition, PPI Network Topology Analysis and Gene-Phenotype Correlation Analysis were performed. The results suggested that MAPK1, MDM2, and other targets as well as P53 signaling pathway and PI3K–Akt signaling pathway may be closely related to Palovarotene treatment of HO. We carried out verification experiments to confirm our finding, alkaline phosphatase and alizarin red staining *in vitro* and Micro-CT as well as hematoxylin-eosin staining *in vivo* were performed to verify treatment for HO of Palovarotene, reverse transcription polymerase chain reaction was also used to explore the transcription changes of MAPK1, MDM2, and osteogenic genes. This study systematically elucidated the possible mechanism of Palovarotene in the treatment of HO through network pharmacology study, revealing a new direction for the further application of Palovarotene in the treatment of HO.

Keywords: Palovarotene, heterotopic ossification, network pharmacology, module-based network analysis, topological analysis, Gene-Phenotype Correlation Analysis

INTRODUCTION

Heterotopic ossification (HO) refers to bone formation in tissues that do not have ossification properties under normal conditions (1). Heterotopic ossification can be either congenital or acquired. The latter is usually related to trauma (2). Patients with early heterotopic ossification have obvious local swelling and pain, the range of motion of the joints gradually narrows, and movement is restricted; in the late stage, due to the loss of more soft tissue and the formation of bone tissue, the joints may even lose the ability to move (3). Because heterotopic ossification brings serious consequences to patients. Therefore, the search for drugs to prevent and treat heterotopic ossification has become a contemporary research hotspot.

Palovarotene is a retinoic acid receptor-gamma (RAR-γ) agonist that inactivates activin receptor-like kinase 2 (Alk2) receptors. This receptor usually interacts with bone morphogenetic protein (BMP), which can inhibit the formation of new bone tissue outside the bone (4). According to research, the combined use of corticosteroids and retinoic acid receptor gamma agonist Palovarotene can significantly inhibit heterotopic ossification (5). It has broad prospects in the treatment of heterotopic ossification.

As the requirements for drug research and development continue to increase, innovative drug research and development are facing huge difficulties. The development of highly selective single-target drugs has shown obvious limitations. In order to change this deep-rooted concept of "one gene, one drug, one disease," network pharmacology was proposed by Hopkins (6, 7). Since the human body is a dynamic and interactive complex environment, if any organ's homeostasis is disrupted, it will cause the change in the body environment, and this dynamic network will be destroyed (8). Network pharmacology emphasizes the analysis of the molecular association rules between drugs and treatment targets from the perspective of biological networks, providing new scientific and technological support for clinical rational drug use and new drug research and development.

Currently, various studies have been conducted on the mechanism of Palovarotene in treating HO, but these views are one-sided and static. The mechanism of Palovarotene's action on HO should be multi-signal pathway and multi-target. Therefore, in order to explore as much and comprehensive mechanisms by which Palovarotene acts on HO as possible, we used the method of network pharmacology. In addition, we also carry out conceptual verification by a series of experiments (**Figure 1**).

TABLE 1 | The database and related analysis platform used in this study.

Names	URL	Purpose
PubChem	https://pubchem.ncbi.nlm.nih.gov	Get the Palovarotene structure
ChEMBL	http://www.ebi.ac.uk/chembl/	Obtain the Palovarotene target
SwissTarget Prediction	http://www.swisstargetprediction.ch	Obtain the Palovarotene target
UniProt	http://www.uniprot.org/	Target name standardization
DisGeNET	http://www.disgenet.org/	Obtain related genes of HO
Comparative Toxicogenomics Database	http://ctdbase.org/	Obtain related genes of HO
STRING	https://www.string-db.org/	Construction of PPI network
Metascape	www.metascape.org/	Perform module-based network analysis
VarElect	http://ve.genecards.org	Analyze the relationship between hub genes and disease

METHODS

Software and Database

The database and related analysis platform used in this study are shown in **Table 1**.

Target Gene Screening of Palovarotene

PubChem can provide structural information and bioactivity information about chemical substances. We collected potential protein targets of Palovarotene through PubChem. Using Palovarotene as the search term, the 3D molecular structure of Palovarotene can be obtained through the PubChem database. The obtained information was input into ChEMBL and SWisStar prediction database to predict palovarotene-related targets. Finally, the English names of the screened target proteins were input into Uniprot database for standardization (**Supplementary Table 1**).

Acquisition of Palovarotene and HO Intersection Targets

Search DisGeNET Database and Comparative Genomics Database by search terms for heterotopic ossification (9). The disease target of HO was obtained by integration after elimination of repetitions, detailed information of genes was shown in **Supplementary Table 2**. Then we performed Venny analysis on HO disease targets and Palovarotene-related targets. Intersection targets of Palovarotene and HO in Venn diagram were regarded as potential targets.

PPI Network Construction

In order to clarify the interaction between intersection targets, drug-disease intersection target data was imported into STRING database (10). Homo sapiens was set as species, a PPI (protein-protein interaction) network of intersection targets was obtained. The network analysis function of Cytoscape 3.7.2 was utilized to analyze the obtained protein interaction information. It uses a confidence range to define PPI (Low confidence: Score < 0.4; Moderate: 0.4–0.7; Height: > 0.7). Take into account these scores, this study retained a PPI with a comprehensive score > 0.4. Visualize the PPI network by using Cytoscape 3.7.2.

GO and KEGG Enrichment Analysis

R software package WebGestaltR (V0.4.4) was used for KEGG pathway analysis and GO functional enrichment analysis of differential genes (11), $P < 0.05$. The biological process (BP), cell component (MF), molecular function (MF), and pathways were screened in descending order according to the enrichment degree of the target. Finally, the data was visualized.

Module-Based Network Analysis

Metascape was used for modular network analysis (12). Mature MCODE algorithm was used to find a few closely connected protein groups in a large and complex target network, and the biological functions of each protein group were also labeled.

Topological Analysis of PPI Network

We used the Network Analyzer function in CytoScape3.7.2 to conduct topological analysis on PPI Network (13), its

Node degree distribution, Betweenness centrality and Closeness centrality were calculated, the node with the highest ranking among the three parameters can be identified as the core target.

Gene–Phenotype Correlation Analysis

To further defined the relationship between genes and phenotypes, we used the VarElec tool (10). VarElect's algorithm can verify the direct or indirect relationship between genes and phenotypes, and it can select the genes with the highest correlation with phenotypes from a group of genes. We were input genes screened from Palovarotene's potential therapeutic targets against HO and phenotype of HO into VarElect to obtain the results.

Preparation of Bone Mesenchymal Stem Cells

Bone marrow mesenchymal stromal cells (BMSCs) were selected as our validation cells in subsequent experiments. BMSCs have been found to have osteogenic potential, which is one of HO progenitor cells (14), BMSCs (Procell, #CP-M131) were purchased from Wuhan Procell. The cells were cultured in an incubator at 37°C and 5% CO_2. BMSCs were cultured in osteogenic induction medium for 14 to 21 days to induce osteogenic differentiation. The osteogenic induction medium used in this study consisted of 10 nM Dexamethasone, 50 μg/mL ascorbic acid, 10 mM B-GP disodium, 10% fetal bovine serum, and high-glucose Dulbecco's Modified Eagle Medium DMEM (Gibco, MA, USA). We used IL-1β to mimic inflammatory stimuli. The dosage of IL-1 β is 10 ng/mL *in vitro*. And the dosage of Palovarotene is 0.25 μM *in vitro*. These above concentrations were supported by our preliminary experimental verification. In *in vitro* experiments, we are grouped into: Control group (Control), IL-1β group (IL-1β), IL-1β group plus Palovarotene group (Palo).

Alizarin Red and Alkaline Phosphatase Staining

After 14 days of osteogenesis, alkaline phosphatase (ALP) staining was performed; 40 uL of reagent A was added to 1 mL of reaction buffer, and 40 uL of reagent B was added to the mix, that is, the reaction working solution (ready for use) was prepared (the reagents were purchased from Beyotime, #C3206). Subsequently, 1 mL of PBS was added to each well and was removed after 1 min, and the cells were washed twice. Subsequently, 500 μL of fixing solution was added to each well, and the cells were fixed at 37°C (or room temperature) for 30 min. Add the prepared reaction solution into each well, and the cells were dyed at 37°C (or room temperature) for 30 min. Lastly, 1 mL of washing solution was added to each well; the cells were washed twice, The cells were washed twice and examined under a microscope.

Then, after 21 days of osteogenesis, alizarin red staining (ARS) was performed as follows: 1 mL of PBS was added to each well and was removed after 1 min. Furthermore, 1 mL of 70% ethanol or 10% neutral formaldehyde was added to each well, and the cells were fixed at 37°C (or room temperature) for 30 min. After discarding the fixed solution in the well, 1 mL washing solution was added to each well. The cells were washed thrice, and 3 mL of alizarin red S staining solution (purchased from Sigma, #A5533) was added to each well; the stained cells were incubated for 15–20 min at 37°C. The cells were washed twice with the washing solution and were observed under a microscope.

TABLE 2 | Primer sequences.

Gene	Primers
OCN-mouse-F	CTGACCTCACAGATCCCAAGC
OCN-mouse-R	TGGTCTGATAGCTCGTCACAAG
Runx2-mouse-F	CCAACTTCCTGTGCTCCGTG
Runx2-mouse-R	TCTTGCCTCGTCCGCTCC
MAPK1-mouse-F	ATGGTTTGCTCTGCTTAT
MAPK1-mouse-R	TGATGCCAATGATGTTCT
MDM2-mouse-F	GGTCTATCGGGTCACAGT
MDM2-mouse-R	TTATCTTTCCCCTTATCGT
ACE-mouse-F	CGTTACCCGACAACTATC
ACE-mouse-R	CGTTACCCGACAACTATC
Actin-mouse-F	GTCCCTCACCCTCCCAAAAG
Actin-mouse-R	GCTGCCTCAACACCTCAACCC

TABLE 3 | Topological parameters of hub genes in the PPI network.

Number	Genes	Degree	Betweenness centrality	Closeness centrality
1	PPARG	26	0.25539816	0.60784314
2	CASP3	23	0.15038421	0.58490566
3	PPARA	20	0.15050133	0.56363636
4	HSP90AA1	18	0.08021818	0.52542373
5	MAPK1	17	0.10085056	0.52542373
6	STAT3	16	0.06892525	0.51666667
7	GSK3B	13	0.02914279	0.496
8	CNR1	12	0.13782789	0.48062016
9	CASP8	12	0.00986503	0.484375
10	REN	11	0.06854053	0.48062016
11	RXRA	11	0.04907326	0.45588235
12	MDM2	11	0.02154882	0.47328244
13	PBRM1	3	0.06345849	0.41610738

RT-PCR

After 14 days of osteogenesis, the transcription level of osteogenic genes was detected by reverse transcription PCR (RT-PCR). We added an additional group of BMSCs that were cultured without osteogenic induction medium but with normal medium. The reaction system used was SYBR Green Mix (Takara, RR420A), and the fluorescence signal was obtained by a detecting instrument (Roche, Light Cycler 480). The primer sequences used in this study shown in **Table 2**.

Construction of HO Animal Model

The experimental rats were 24 males SD rats (4 weeks, weight 200 ± 5 grams), eight in each group and three groups in total according to our experimental requirements. Rats are purchased from Shanghai Jiesjie Experimental Animal Co., LTD. In our animal experiments, we are grouped into: sham-operated group (Sham), HO model group (Vehicle), HO model and administered Palovarotene group (Palo). Anesthesia was performed by intraperitoneal injection of 10% chloral hydration, control drug flow per minute. After fixation, hair removal and disinfection, a 0.5–1 cm longitudinal incision was made along the lateral superficial skin groove between tibiofibular bone and the Achilles tendon according to the marking point of the Achilles tendon. Cut the skin and subcutaneous tissue, step by step after exposure of the Achilles tendon tissue fully, to identify the middle point of the Achilles tendon, The Achilles tendon was clamped repeatedly with vascular forceps five times, once at the midpoint of the Achilles tendon, and then twice above and below the midpoint caused considerable trauma, in Model group and Palov group, we pricked the outer sheath membrane, to the middle point of tendon and surrounding tissues thoroughly after separation, use eye or knife cut transverse form completely cut off the Achilles tendon, then on both sides of the Achilles tendon end in normal tissue, in the sham operation group, only the Achilles tendon was exposed and then sutured. Penicillin was injected intramuscularly for 3 consecutive days after surgery at a dose of 800,000 IU/ days to prevent infection in the surgical field. Palovarotene was dissolved in DMSO solvent, and 100 ul oral solution was obtained by mixing 30 ul drug solution and 70 ul corn oil during administration. The Sham group and HO Model group were given DMSO+ corn oil solution in the same proportion, Palovarotene concentration was 1 mg/kg/ day, and Palovarotene was orally administered by no. 20 gavage needle. Throughout the 21-day period, the Palovarotene was administered continuously.

Micro-CT

Micro-CT analysis was performed after 12 weeks of feeding. Achilles tendons with lower tibia and calcaneus from mice were fixed in 10 % formalin overnight. The X-ray tube settings were 50 kV and 60 uA and images were acquired at 50-um resolution. A 0.5 rotation step through a 360 angular range with a 50 ms exposure per step was used. The images were reconstructed and analyzed with Skysan 1275 software.

Hematoxylin-Eosin Staining

The rats were sacrificed by excessive intraperitoneal injection of 10% chloral hydrate, and then the tissues below the bilateral knee joints of rats were immediately severed with a scalpel. Residual blood stains were washed with physiological saline for several time, then fixed in a 50 mL centrifuge tube

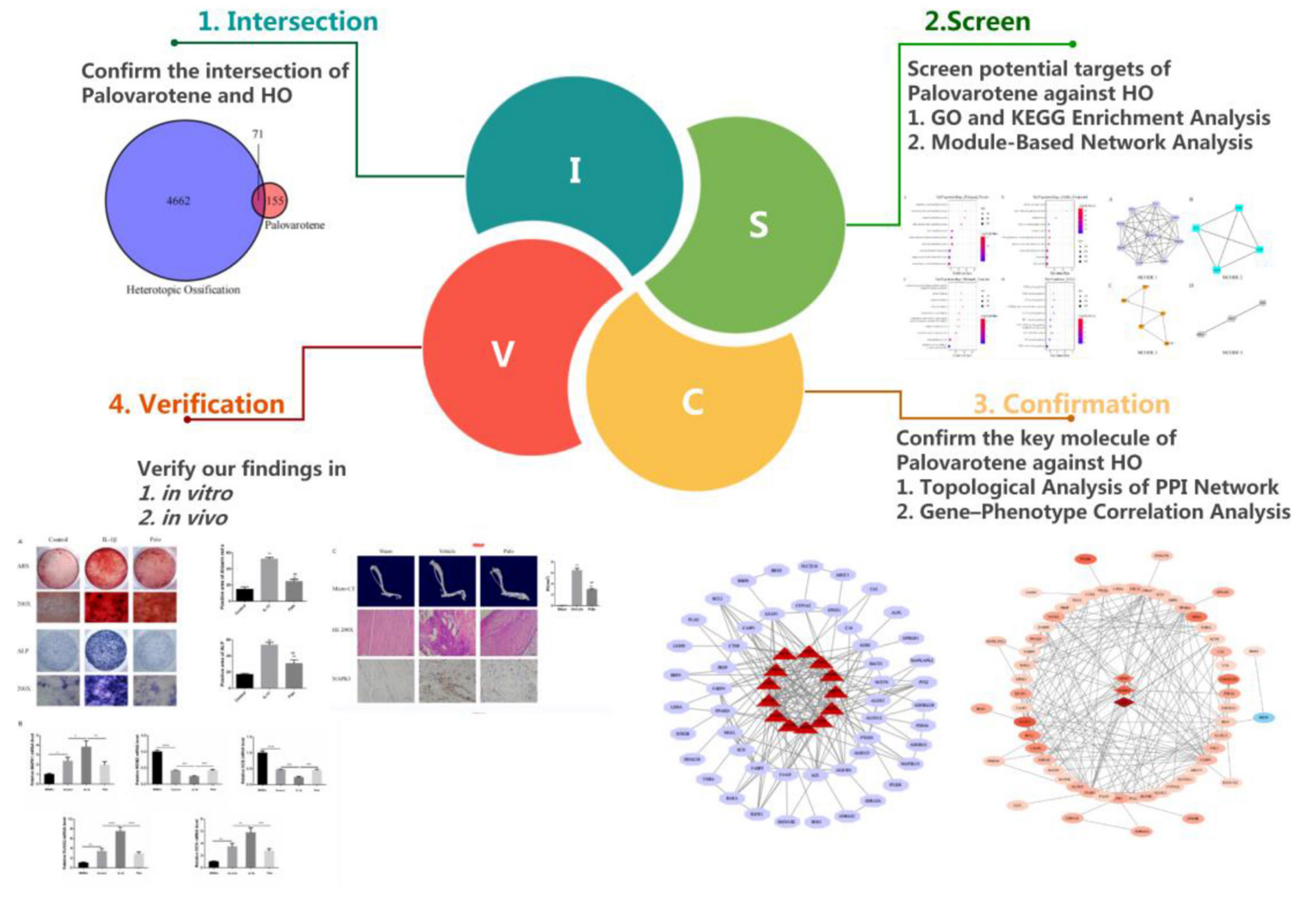

FIGURE 1 | Workflow diagram of method.

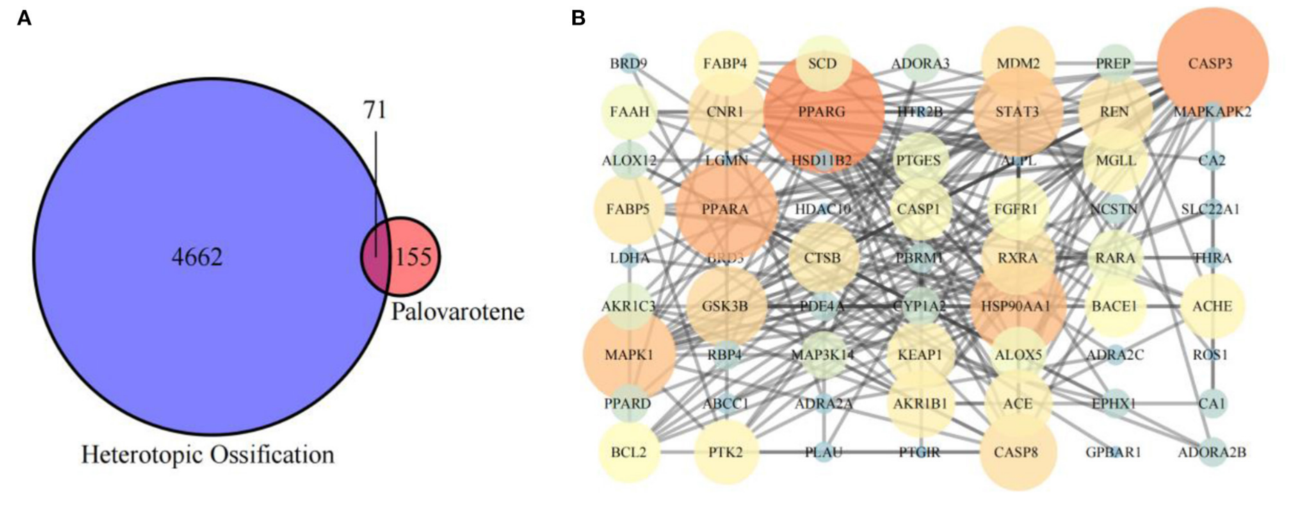

FIGURE 2 | (A) Intersection of Palovarotene-related genes and heterotopic ossification related genes; **(B)** PPI network of potential targets of Palovarotene to treat heterotopic ossification.

containing 4% paraformaldehyde solution. After being fixed in 4% paraformaldehyde for 24–48 h, the Achilles tendon tissue were decalcified, dehydrated and embedded. The tissue sections required by the experiment were dewaxed and hydrated. The original hematoxylin solution and alcohol-soluble eosin solution were successively covered on the tissue surface for staining. After staining, the slices were sealed. Observed them under a microscope 24 h later.

Statistical Analysis

Statistical analysis was performed using SPSS 25.0 software. Results are presented as mean ± standard deviation (x ± s). The comparison of multiple groups of independent data was performed by one-way analysis of variance. Pairwise comparisons between multiple groups were performed using the LSD-*t* test. $P < 0.05$ indicated that the difference was statistically significant.

RESULTS

Intersection Target of Palovarotene and HO

We obtained 226 Palovarotene-related genes from ChEMBL and SwissTargetPrediction databases. 4733 HO related genes were obtained from DisGeNET and Comparative Toxicogenomics Database. Then, their intersection was taken to obtain 71 common targets of Palovarotene and HO, and this set is the possible target of Palovarotene for HO (**Figure 2A**).

Construction of Palovarotene and HO Intersection Target Network and Target Protein-Protein Interaction Analysis

Intersection targets of Palovarotene-HO were imported into Cytoscape software to construct the compound-target interaction network diagram of Palovarotene's direct or indirect action against HO, and then the intersection targets were imported into String database (15). Seventy-one targets were reserved with a confidence score > 0.4 out of all the intersection targets. Acquire protein-protein interaction (PPI) relationships. Then Cytoscap was utilized to draw the network diagram of the relationship between targets. After deleting the nodes with fewer edges in PPI network, 63 targets were finally reserved for follow-up studies (**Figure 2B** and **Supplementary Table 3**).

GO and KEGG Enrichment Analysis of Potential Targets

Analysis of GO and KEGG enrichment analysis on 63 targets was performed using WebGestaltR After systematic analysis, it was found that in the biological process of Palovarotene treatment of HO, the top 10 correlation of biological process GO entries ($p < 0.05$), including arachidonic acid metabolic process, unsaturated fatty acid metabolic process, icosanoid metabolic process, monocarboxylic acid metabolic process. Molecular function GO entries ($p < 0.05$), concluding cysteine-type endopeptidase activity involved in apoptotic signaling pathway, retinoid binding, fatty acid binding, peptidase activity, acting on L-amino acid peptides and cellular components GO entries ($p < 0.05$), including nuclear envelope lumen, death–inducing signaling complex, endolysosome, lytic vacuole. KEGG pathway enrichment found that P53 signaling pathway, PI3K-Akt signaling pathway, PPAR signaling pathway, VEGF signaling pathway, and AGE-RAGE and other signaling pathways were significantly enriched (**Figure 3**, original data can be found in **Supplementary Material 1**).

Module-Based Network Analysis

In order to screen out the 63 intersection targets highly associated targets of Palovarotene against HO, we performed a module-based network analysis using Metascape, and used the MCODE

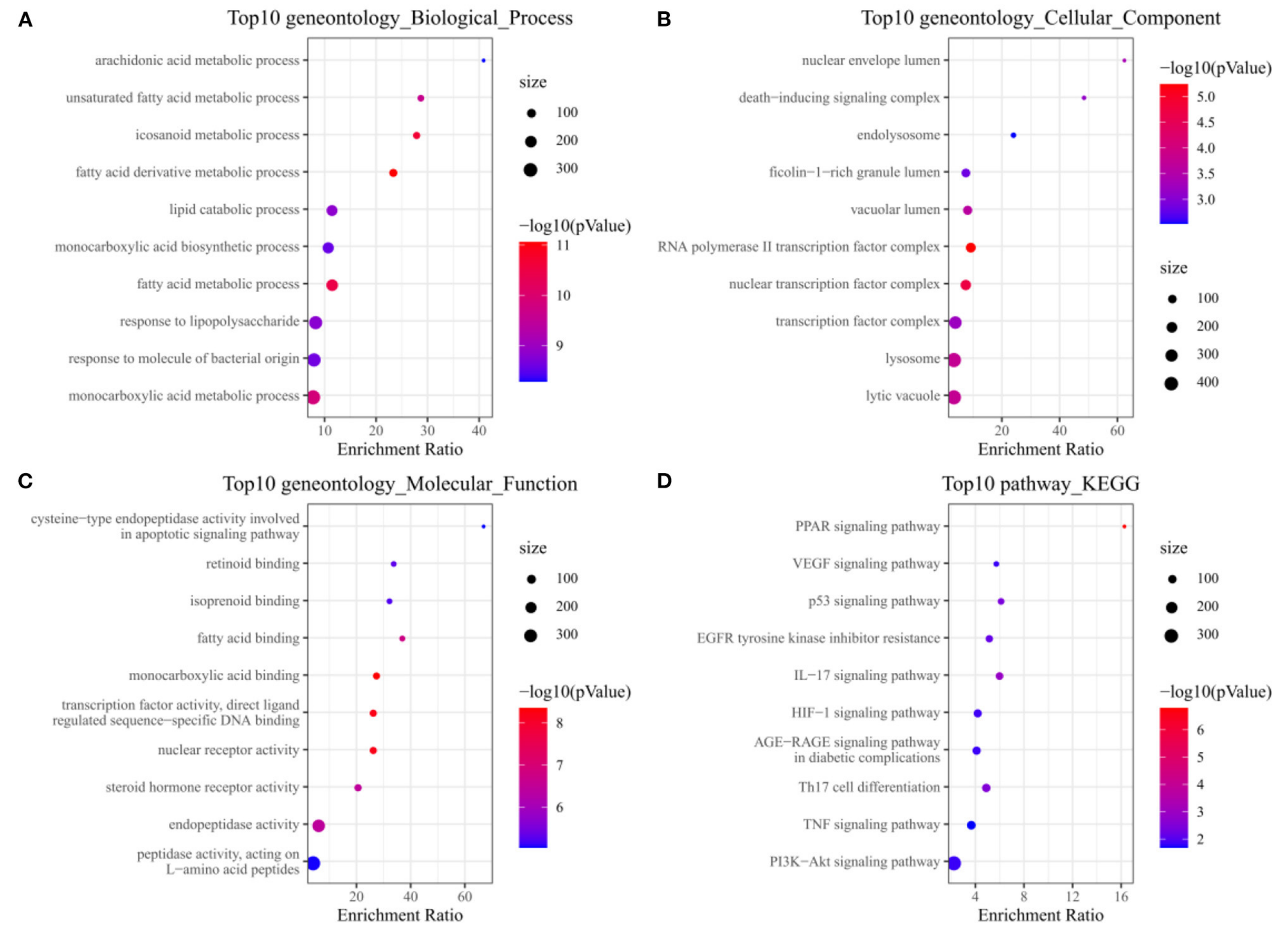

FIGURE 3 | (A) Annotation diagram of biological process; **(B)** Annotation diagram of cellular component; **(C)** Annotation diagram of molecular function; **(D)** Annotation diagram of KEGG.

algorithm to screen these 63 intersecting targets with their respective mutual. The linked targets are called protein groups (**Supplementary Material 2**). These screened protein groups often have their own biological functions. GO and KEGG analysis of these protein groups found that these protein groups are related to p53 signaling pathway, PI3K-Akt signaling pathway, PPAR signaling pathway, cGMP-PKG signaling pathway, FoxO signaling pathway, etc. are significantly related (**Figure 4**, original data can be found in **Supplementary Material 3**).

Topological Analysis of PPI Network

We have constructed a PPI network, and 63 targets were initially screened, and the 63 key targets were used to communicate with Cytoscape and visualized. Sort by topological parameters of degree, betweenness central, and closeness central, the highest number of nodes as Hub Genes (**Figure 5**). The more important of the rank is more important in the PPI network. In this network, PPARG, CASP3, PPARA, HSP90AA1, MAPK1, STAT3, GSK3B, CNR1, CASP8, REN, RXRA, MDM2, and PBRM and other genes were HUB Gene (**Table 3**).

Gene-Phenotype Correlation Analysis of Anti-heterotopic Ossification Targets of Palovarotene

After performing Topological Analysis on the PPI network, we screened out the most relevant hub genes. For identifying the most core genes, we employed VarElect to perform Gene-Phenotype Correlation Analysis. The VarElect algorithm can verify the relationship between genes and phenotypes. The direct or indirect relationship can be used to screen out the genes with the highest phenotype correlation in a group of genes. The results showed that, of the 63 potential targets, three were directly related to the HO phenotype and 60 were indirectly related (**Table 4**). Directly related targets are Angiotensin I Converting Enzyme (ACE), Mitogen-Activated Protein Kinase 1 (MAPK1), and MDM2 Proto-Oncogene (MDM2) (**Figure 6**).

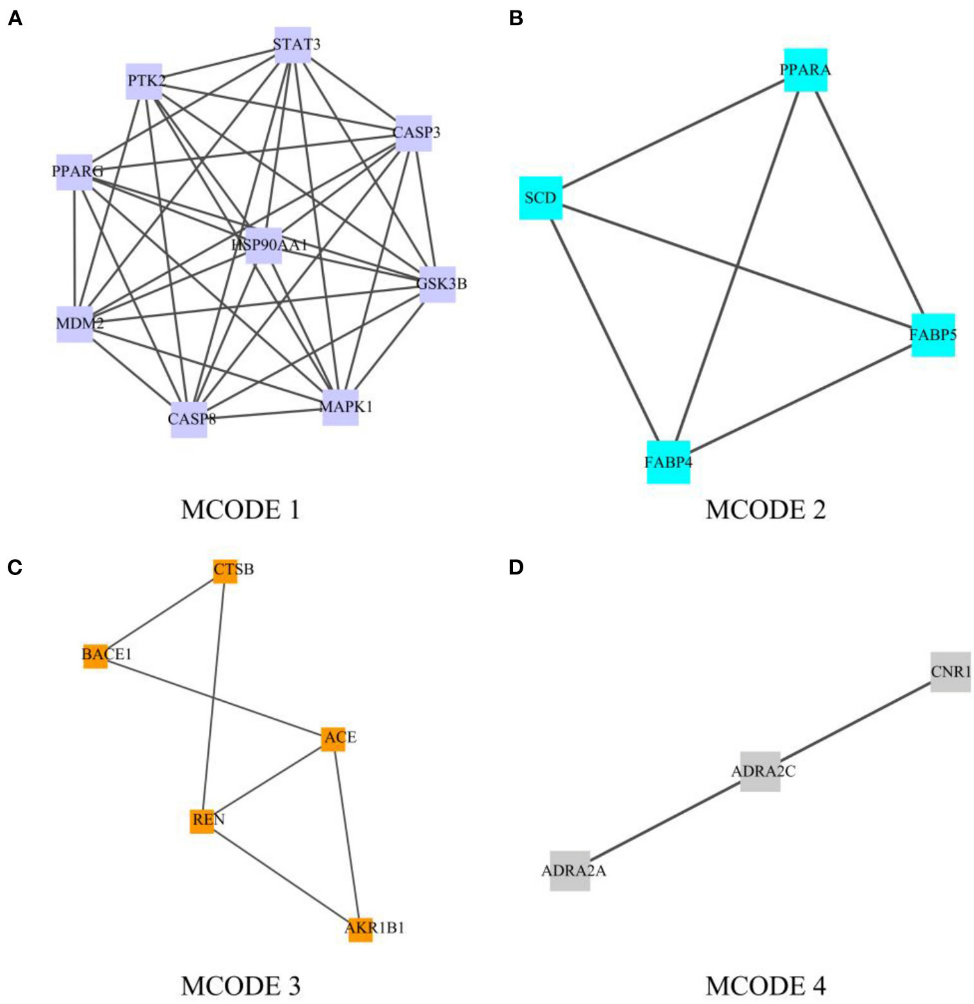

FIGURE 4 | Module-based network analysis of potential targets of Palovarotene against heterotopic ossification. **(A–D)** Different functional modules in targets of Palovarotene against heterotopic ossification.

After Administration of Palovarotene, the Osteogenic Differentiation of BMSCs Was Inhibited and the Volume of Heterotopic Bone Was Significantly Reduced in Animal Models

In *in vitro* experiments, we are grouped into: Control group (Control), IL-1β group (IL-1β), IL-1β group plus Palovarotene group (Palo), in the PCR experiments performed *in vitro*, we added an additional group of BMSCs that were cultured without osteogenic induction medium but with normal medium. In animal experiments, we are grouped into: sham-operated group (Sham), HO model group (Vehicle), HO model, and administered Palovarotene group (Palo). *In vitro*, after culturing BMSCs for 14–21 days after osteogenic induction, we performed ARS, ALP staining, and RT-PCR experiments *in vitro*. The results showed that under the osteogenic induction and the stimulation of IL-1β, the calcium deposition and alkaline phosphatase content of BMSCs were significantly increased, and the calcium deposition and alkaline phosphatase are classic markers of osteogenic differentiation, and the expression and transcription levels of osteogenic-related molecules OCN and RUNX2 were significantly up-regulated. This indicated that BMSCs differentiated into osteoblasts in the context of osteogenic induction. The PCR results also showed that the transcription levels of the key molecules MAPK1 and MDM2 we screened were significantly regulated, MAPK1 is a positive regulator of PI3K–Akt signaling pathway, while MDM2 is a key negative regulator of p53 signaling pathway. The results showed that MAPK1 was significantly up-regulated, while MDM2 was significantly down-regulated. After administration of Palovarotene, the above trend was reversed, the calcium deposition and alkaline phosphatase contents were significantly reduced, and the osteogenesis-related molecules and the screened key molecules transcriptions were down-regulated. In our animal model, Micro-CT showed that the model group produced obvious ectopic bone, while the

TABLE 4 | Top 20 targets directly or indirectly associated with the HO phenotype.

Number	Symbol	Description	Direct/indirect	Score	Average disease causing likelihood
1	ACE	Angiotensin I Converting Enzyme	Direct	2.38	15.8
2	STAT3	Signal Transducer And Activator Of Transcription 3	Indirect	1.97	78.9
3	PTGIR	Prostaglandin I2 Receptor	Indirect	1.36	43.3
4	MAPK1	Mitogen-Activated Protein Kinase 1	Direct	1.31	73.8
5	THRA	Thyroid Hormone Receptor Alpha	Indirect	1.17	89.8
6	ADORA2B	Adenosine A2b Receptor	Indirect	1.16	58.2
7	CASP8	Caspase 8	Indirect	1.13	68.6
8	BCL2	BCL2 Apoptosis Regulator	Indirect	1.1	48.6
9	MDM2	MDM2 Proto-Oncogene	Direct	1.03	86.2
10	FGFR1	Fibroblast Growth Factor Receptor 1	Indirect	1.01	76.3
11	ROS1	ROS Proto-Oncogene 1, Receptor Tyrosine Kinase	Indirect	0.89	22.3
12	PDE4A	Phosphodiesterase 4A	Indirect	0.82	57.4
13	CA2	Carbonic Anhydrase 2	Indirect	0.8	60.1
14	KEAP1	Kelch Like ECH Associated Protein 1	Indirect	0.8	86.2
15	PPARG	Peroxisome Proliferator Activated Receptor Gamma	Indirect	0.73	58.4
16	CNR1	Cannabinoid Receptor 1	Indirect	0.7	87.5
17	HTR2B	5-Hydroxytryptamine Receptor 2B	Indirect	0.7	20.5
18	PTK2	Protein Tyrosine Kinase 2	Indirect	0.68	83
19	ADRA2A	Adrenoceptor Alpha 2A	Indirect	0.65	43.2
20	CASP3	Caspase 3	Indirect	0.63	64.2

ectopic bone formation in the sham-operated group and the Palovarotene-administered group was significantly inhibited. A large number of disorganized ectopic bones were generated between tissues, while in the sham-operated group and the Palovarotene-administered group, the trend of the model group was suppressed, and there was no obvious abnormality except for the partial tissue destruction caused by modeling. Immunohistochemical results showed that the positive rate of MAPK1, a positive regulator of PI3K-Akt signaling pathway, was higher in Vehicle group, but lower in Sham group and Palo Group. The above results suggest that the PI3K-Akt signaling pathway is activated when HO occurs, and the administration of Palovarotene can effectively inhibit the activation of PI3K-Akt signaling pathway, which is consistent with our cell validation experiment (**Figure 7**).

DISCUSSION

Clinically, heterotopic ossification is currently mainly divided into two types: one is hereditary heterotopic ossification, with low incidence but severe symptoms and high mortality; the other is acquired heterotopic ossification, with mild symptoms and death. The incidence is low, but the morbidity is high. The severity of symptoms in patients is often proportional to the severity of the trauma, and is closely related to the site of the trauma and the source of the trauma (3). Because the pathogenesis of heterotopic ossification is complex, it involves heredity and gene mutation, the participation of osteogenic precursor cells, the up-regulation of BMP signal transduction pathway, and the overexpression of BMP (16). At present, the treatment methods of heterotopic ossification include drug therapy, radiotherapy, surgery, rehabilitation therapy, etc. (17). Since the exact mechanism of the formation of heterotopic ossification is still unclear, there is no clear drug for the treatment of heterotopic ossification (18). The reason is that the targets of the currently isolated and purified drugs are various, and it is impossible to truly screen a drug against heterotopic ossification through clinical practice. Palovarotene is a retinoic acid receptor agonist. Studies have shown that this receptor interacts with bone morphogenetic protein (BMP), which is shown to prevent ectopic bone and blood vessel formation, and inhibit osteogenic gene expression (19), it can also be used in combination with corticosteroids to treat heterotopic ossification (20). Through the above studies, it can be found that Palovarotene can improve disease progression through multiple pathways and targets, which is a feature of drugs for complex diseases.

Network pharmacology explains the occurrence and development of diseases from the perspective of systems biology and biological network balance, understands the interaction between drugs and the body from the overall perspective of improving or restoring biological network balance, and guides the discovery of new drugs (21). It emphasizes the analysis of molecular associations between drugs and treatment of diseases from the perspective of the system level and the overall biological network (22). Considering that Palovarotene has the characteristics of being multi-target, and multi-pathways for treating diseases, it shows great promise for treating HO. Compared with traditional pharmacology, network pharmacology can comprehensively explain the potential mechanism of drug action by scientific analysis methods. The

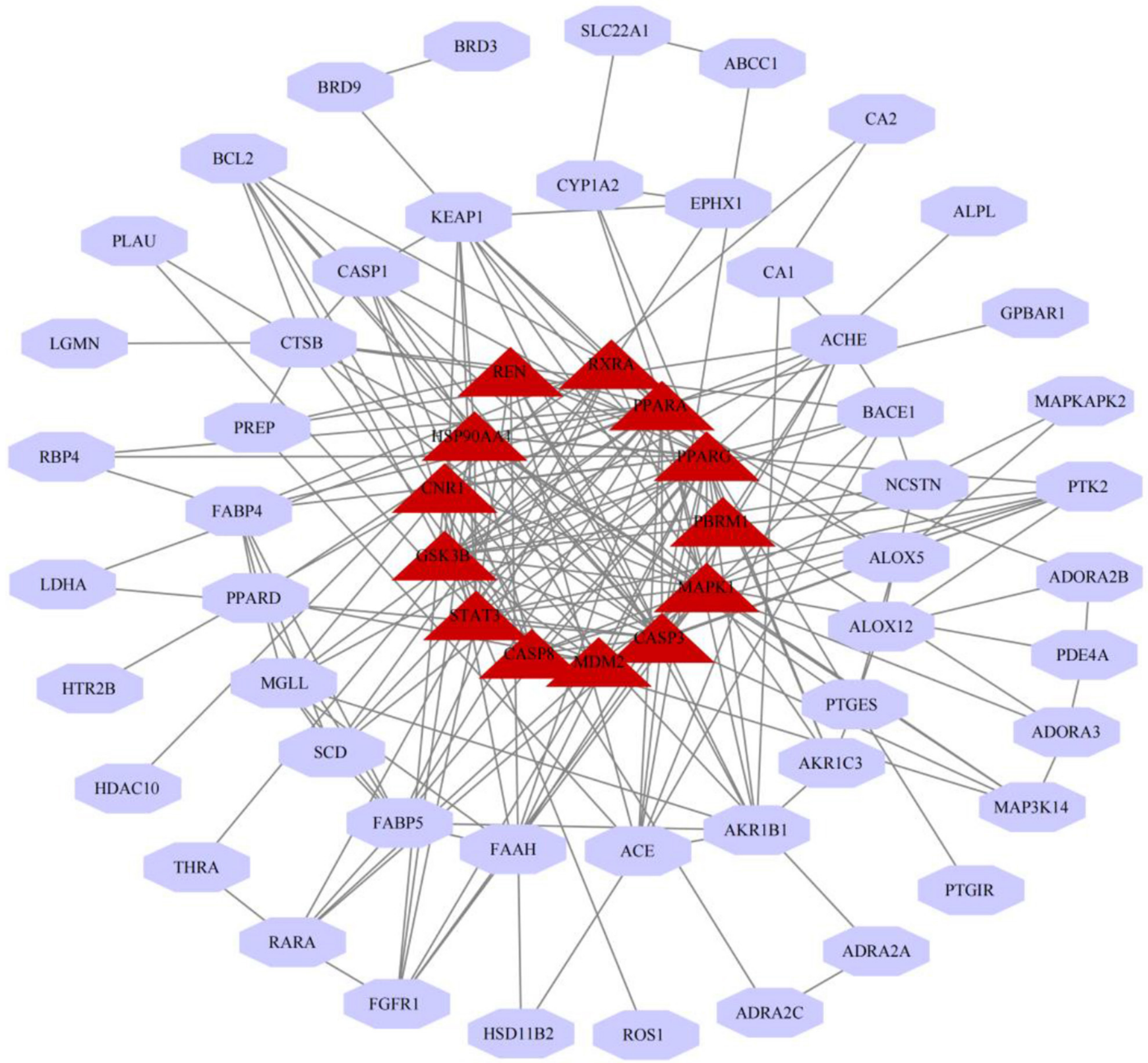

FIGURE 5 | Topological analysis of PPI network. Red nodes on the inner circle indicate hub genes.

potential mechanism of action in the treatment of heterotopic ossification provides new scientific and technological support for clinical rational drug use, interpretation of the overall mechanism of action, and analysis of the law of drug combination (23).

To evaluate the efficacy of Palovarotene in the treatment of heterotopic ossification, a network pharmacology analysis was performed. First, 71 potential targets of Palovarotene for the treatment of heterotopic ossification were obtained through Venn analysis by searching different databases. After constructing PPI, edge nodes were removed, and 63 targets were obtained for follow-up research. Afterwards, to elucidate the multiple mechanisms by which Palovarotene treats HO, we performed GO and KEGG enrichment analysis on these targets. The GO results indicated that the potential targets of Palovarotene in the treatment of heterotopic ossification are closely related to the following molecular functions: cysteine-type endopeptidase activity involved in apoptotic signaling pathway, retinoid binding, fatty acid binding, peptidase activity, acting on L-amino acid peptides; closely related to the following biological processes: arachidonic acid metabolic process, unsaturated fatty acid metabolic process, icosanoid metabolic process, monocarboxylic acid metabolic process. It is closely related to the following cellular components: nuclear envelope lumen, death-inducing signaling complex, endolysosome, and lytic vacuole. The results suggest that many molecules, cellular components, and biological processes may play a role in the

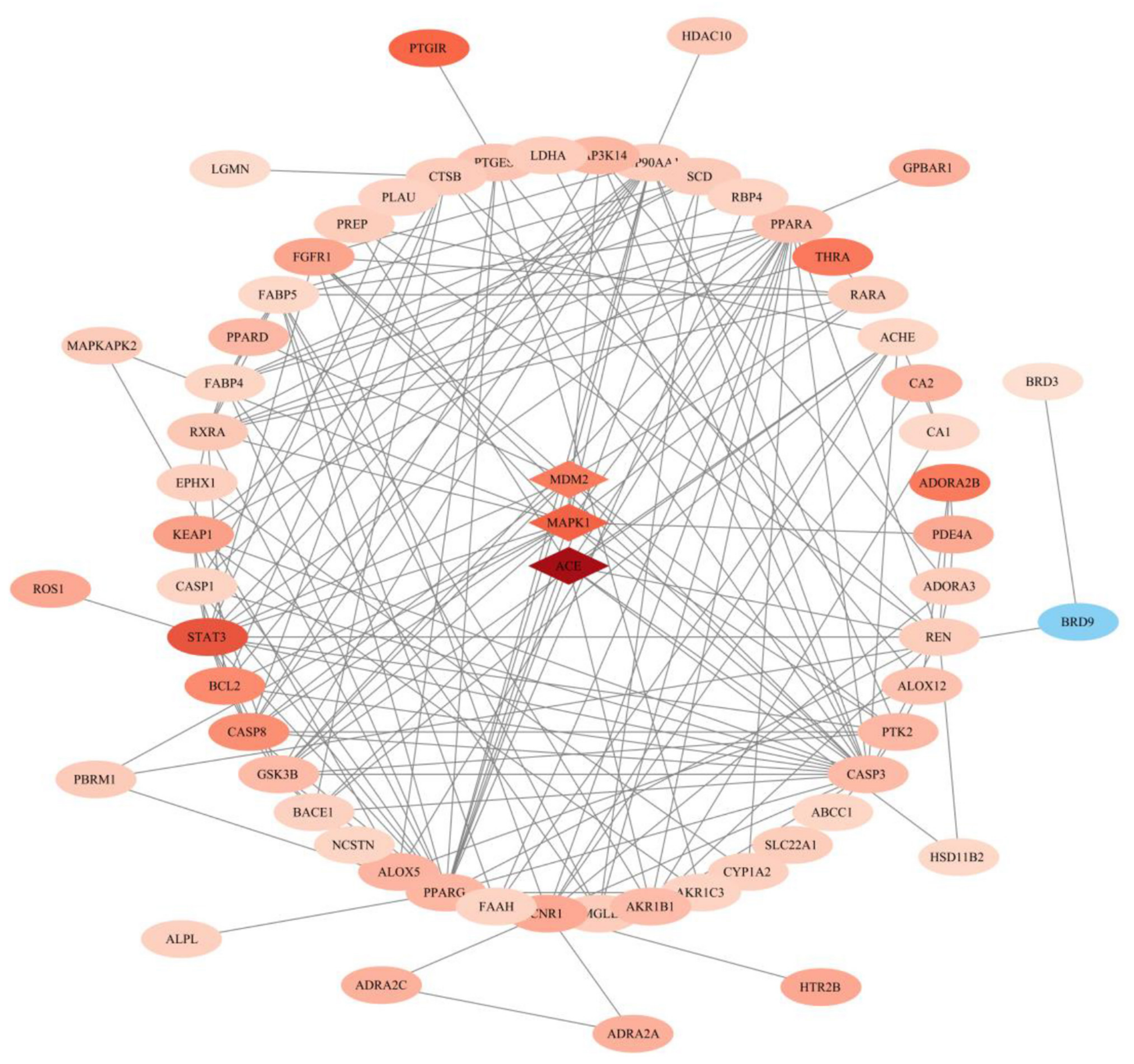

FIGURE 6 | Gene–phenotype correlation analysis of anti- heterotopic ossification targets of Palovarotene. Intersection genes were categorized as directly (the diamond in the middle) or indirectly (outer ellipse) associated with the HO phenotype. The darker the color, the larger the score value, the lighter the color, the smaller the score value.

signal transduction and metabolism of Palovarotene-treated HO, and these molecules, cellular components, and biological processes are highly correlated with the results of our screening of core targets. In addition, the results of KEGG enrichment analysis showed that the signaling pathways involving these targets in heterotopic ossification diseases mainly include PI3K-Akt signaling pathway, PPAR signaling pathway, P53 signaling pathway, and VEGF signaling pathway. Dong et al. demonstrated that the PTEN/PI3K/AKT signaling pathway plays a key role in the development of ectopic bone formation (24). Targeting the PI3K/AKT pathway with inhibitors may be a potential molecular therapy for HO (25). Chen et al. confirmed that the activation of PI3K-Akt signaling pathway by leptin combined with mechanical stress stimulation plays an important role in the ossification of the posterior longitudinal ligament (26). Hwang et al. found that mesenchymal-derived VEGFA is an important expression signal in the occurrence of heterotopic ossification, and the treatment of VEGF pathway may reduce the occurrence of heterotopic ossification (27). AGE/RAGE signaling heavily influences both cellular and systemic responses to increase bone matrix proteins

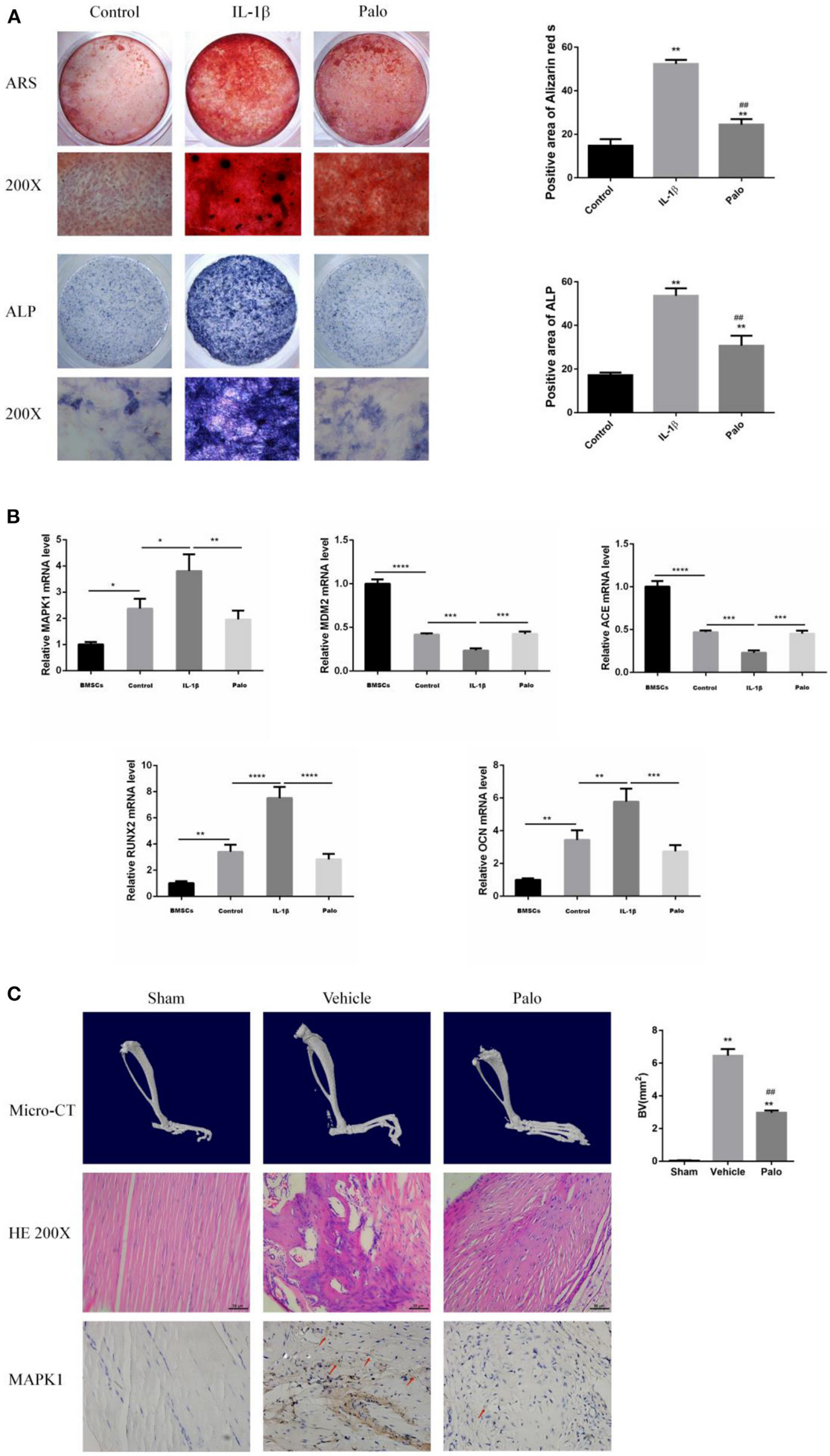

FIGURE 7 | Screening target validation and Palovarotene against HO validation experiments. **(A)** ALP and ARS staining in BMSCs after culture with osteogenesis induction. Data are means ± SD ($n = 3$) $^{*}P < 0.05$, $^{**}P < 0.01$, * compared with the Control group. $^{\#}P < 0.05$, $^{\#\#}P < 0.01$, and # compared with the IL-1β group. Scale bar: 100 μm; **(B)** The mRNA expression and relevant quantitative analysis of MAPK1, MDM2, ACE, Runx2, and OCN. Data are means ± SD ($n = 3$) $^{*}P < 0.05$, $^{**}p < 0.01$, $^{***}P < 0.001$, and $^{****}P < 0.0001$; **(C)** images of Micro-CT, HE staining and IHC. Data are means ± SD ($n = 8$) $^{*}P < 0.05$, $^{**}p < 0.01$, and * compared with the Sham group. $^{\#}P < 0.05$, $^{\#\#}P < 0.01$, and # compared with the Vehicle group. Scale bar =50 μm.

through PKC, p38 MAPK, fetuin-A, TGF-β, NFκB, and ERK1/2 signaling pathways in both hyperglycemic and calcification conditions (28) and researcher found that the Advanced Glycation End-Products (AGE)/Receptor for AGEs (RAGE) signaling pathway exacerbates diabetes-mediated vascular calcification (VC) in vascular smooth muscle cells (VSMCs), so the relationship between age-rage signaling pathway and osteogenesis was confirmed (29). In recent years, more and more experimental studies have shown that retinoic acid receptors play a negative regulatory role in the process of osteogenesis and chondrogenesis, and chondrogenic differentiation under physiological conditions requires a low concentration of endogenous retinoic acid (30). The researchers used a retinoic acid receptor agonist to effectively prevent heterotopic ossification in mice and found that the effect continued even after the mice were no longer taking the agonist (31). In additions, the nuclear transcription factor peroxisome-proliferator-activated receptor-gamma (PPAR-γ) has been found expressed in both osteoblasts and adipocytes, as well as in mesenchymal stem cells, suggesting its crucial role in regulating adipocyte formation and osteoblast development. In addition, Ju et al. found that in models of heterotopic ossification such as traumatic brain injury/burn/tenotomy, the NF-kB/p53 signaling pathway plays an important role in the occurrence and development of heterotopic ossification, and ammonium pyrrolidine dithiocarbamate Pharmacological inhibition of NF-kB signaling pathway (PDTC) can significantly reduce the expression level of p53 and the size of heterotopic ossification (32).

Further targeting of Palovarotene in the treatment of heterotopic ossification, we performed a modular network analysis of parovatine's anti-heterotopic ossification targets. The result of the modular network analysis is likely to be a protein group that plays a role in the treatment of HO with Palovarotene, so we propose a modular network analysis method to highlight the protein group of parovarotene in the treatment of heterotopic ossification. The results show that these protein groups are closely related to p53 signaling pathway, PI3K-Akt signaling pathway, PPAR signaling pathway, cGMP-PKG signaling pathway, FoxO signaling pathway, etc., which are very similar to our KEGG results. Next, we further conducted topological analysis of the PPI network, and we screened out PPARG, PPARA, MDM2, MAPK1, and other genes as hub genes that are highly related to the HO process of Palovarotene treatment, which is consistent with the above GO and KEGG enrichment analysis results and Module-Based. The results of Network Analysis are consistent, both PPARG and PPARA are related to PPAR signaling pathway; MDM2 is a key negative regulator of p53 signaling pathway; MAPK1 is an important component of PI3K-Akt signaling pathway. Finally, in order to confirm the relationship between the screened key genes and the HO phenotype, we carried out Gene–Phenotype Correlation Analysis, the results showed that PPARG, MAPK1, MDM2, and other targets are directly related to the HO phenotype, among which the role of MAPK1 and MDM2 most closely, our research has gradually confirmed that MAPK1 and MDM2 may be the core targets of Palovarotene in the treatment of heterotopic ossification, and the corresponding PI3K-Akt signaling pathway and p53 signaling pathway are likely to be involved in the treatment process play an important role in. To verify our point, we conduct a series of verification experiments.

The verification experiment found that in the osteogenic induction environment, the calcium deposition and alkaline phosphatase content of BMSCs were significantly increased, and the expression levels of osteogenesis-related molecules OCN and RUNX2 were significantly up-regulated. The results indicated that BMSCs differentiated into osteoblasts, which confirmed the validity of our *in vitro* model. The PCR results showed that the transcription levels of the key molecules MAPK1 and MDM2 we screened were significantly up-regulated. After administration of Palovarotene, the above trend was reversed, the calcium deposition and alkaline phosphatase contents were significantly reduced, and the osteogenesis-related molecules and the screened key molecules were transcribed level down. In our animal model, Micro-CT showed that the model group produced obvious ectopic bone, while the ectopic bone formation in the sham-operated group and the Palovarotene-administered group was significantly inhibited, and the volume of the ectopic bone was significantly reduced. Consistent with Mircro-CT, in the model group, the muscle tissue was disordered, angiogenesis was formed, and a large number of disorganized ectopic bones were generated between tissues, while in the sham-operated group and the administered Palovarotene group, the trend of the model group was suppressed, except for some tissues caused by modeling. No obvious abnormality was found outside the damage. Our results show that when BMSCs differentiate into osteoblasts, MAPK1 and MDM2 play a role and their transcription levels are up-regulated. After administration of Palovarotene, the transcription levels are decreased, indicating that Palovarotene is likely to act on MAPK1, MDM2 targets and their corresponding PI3K- Akt signaling pathway and p53 signaling pathway play a role.

This study attempted to clarify a key target and mechanism of Palovarotene in the treatment of heterotopic ossification, screened out the possible core targets and related signaling pathways by means of network pharmacology, and carried out verification experiments. Our study confirmed the role of the screened core targets in the treatment of HO with Palovarotene, and confirmed the effectiveness of Palovarotene in the treatment of HO. Nevertheless, there are some limitations to our study. Although we have collected a large database for parovatine-related targets and heterotopic ossification-related targets, the data are certainly incomplete and some of the latest studies have not been uncovered. Secondly, our study found that the mechanism of Palovarotene in the treatment of HO is complex and multi-factorial. It's not sufficiently investigated for the details of its relevant molecular mechanism, and there is a lack of further experimental verification. More experiments are needed to verify these goals and key points path.

DATA AVAILABILITY STATEMENT

The datasets presented in this study can be found in online repositories. The names of the repository/repositories and accession number(s) can be found in the article/**Supplementary Material**.

ETHICS STATEMENT

The animal study was reviewed and approved by the Bioethics Committee of the Shanghai Sixth People's Hospital.

AUTHOR CONTRIBUTIONS

JH and HX: conceptualization. JH: methodology, formal analysis, resources, data curation, writing—original draft preparation, and visualization. JH and DL: software and writing—review and editing. JZ: validation. DL and JZ: investigation. HX: supervision, project administration, and funding acquisition. All authors have read and agreed to the published version of the manuscript.

FUNDING

This research was funded by Shanghai Fengxian District Health Committee, grant number fxlczlzx-a-202103.

SUPPLEMENTARY MATERIAL

The Supplementary Material for this article can be found online at: https://www.frontiersin.org/articles/10.3389/fmed.2022.897392/full#supplementary-material

REFERENCES

1. Eisenstein N, Stapley S, Grover L. Post-traumatic heterotopic ossification: an old problem in need of new solutions. *J Orthop Res.* (2018) 36:1061–68. doi: 10.1002/jor.23808
2. Xu Y, Huang M, He W, He C, Chen K, Hou J, et al. Heterotopic ossification: clinical features, basic researches, and mechanical stimulations. *Front Cell Dev Biol.* (2022) 10:770931. doi: 10.3389/fcell.2022.770931
3. Ranganathan K, Loder S, Agarwal S, Wong VW, Forsberg J, Davis TA, et al. Heterotopic ossification: basic-science principles and clinical correlates. *J Bone Joint Surg.* (2015) 97:1101–11. doi: 10.2106/JBJS.N.01056
4. Semler O, Rehberg M, Mehdiani N, Jackels M, Hoyer-Kuhn H. Current and emerging therapeutic options for the management of rare skeletal diseases. *Paediatr Drugs.* (2019) 21:95–106. doi: 10.1007/s40272-019-00330-0
5. Sinha S, Uchibe K, Usami Y, Pacifici M, Iwamoto M. Effectiveness and mode of action of a combination therapy for heterotopic ossification with a retinoid agonist and an anti-inflammatory agent. *Bone.* (2016) 90:59–68. doi: 10.1016/j.bone.2016.02.008
6. Hopkins AL. Network pharmacology: the next paradigm in drug discovery. *Nat Chem Biol.* (2008) 4:682–90. doi: 10.1038/nchembio.118
7. Li W, Yuan G, Pan Y, Wang C, Chen H. Network pharmacology studies on the bioactive compounds and action mechanisms of natural products for the treatment of diabetes mellitus: a review. *Front Pharmacol.* (2017) 8:74. doi: 10.3389/fphar.2017.00074
8. Cheng X, Song Z, Wang X, Xu S, Dong L, Bai J, et al. Network pharmacology study on the molecular mechanism of protocatechualdehyde in the treatment of diabetic cataract. *Drug Des Devel Ther.* (2021) 15:4011–23. doi: 10.2147/DDDT.S334693
9. Zhang L, Han L, Wang X, Wei Y, Zheng J, Zhao L, et al. Exploring the mechanisms underlying the therapeutic effect of *Salvia miltiorrhiza* in diabetic nephropathy using network pharmacology and molecular docking. *Biosci Rep.* (2021) 41:BSR20203520. doi: 10.1042/BSR20203520
10. Barshir R, Fishilevich S, Iny-Stein T, Zelig O, Mazor Y, Guan-Golan Y, et al. GeneCaRNA: a comprehensive gene-centric database of human non-coding RNAs in the genecards suite. *J Mol Biol.* (2021) 433:166913. doi: 10.1016/j.jmb.2021.166913
11. Nam S, Lee S, Park S, Lee J, Park A, Kim YH, et al. PATHOME-Drug: a subpathway-based poly-pharmacology drug-repositioning method. *Bioinformatics.* (2021) 38:444–52. doi: 10.1093/bioinformatics/btab566
12. Ye M, Luo G, Ye D, She M, Sun N, Lu YJ, et al. Network pharmacology, molecular docking integrated surface plasmon resonance technology reveals the mechanism of Toujie Quwen Granules against coronavirus disease 2019 pneumonia. *Phytomedicine.* (2021) 85:153401. doi: 10.1016/j.phymed.2020.153401
13. Piñero J, Saüch J, Sanz F, Furlong LI. The DisGeNET cytoscape app: exploring and visualizing disease genomics data. *Comput Struct Biotechnol J.* (2021) 19:2960–7. doi: 10.1016/j.csbj.2021.05.015
14. Kan C, Chen L, Hu Y, Lu H, Li Y, Kessler JA, et al. Microenvironmental factors that regulate mesenchymal stem cells: lessons learned from the study of heterotopic ossification. *Histol Histopathol.* (2017) 32:977–85. doi: 10.14670/HH-11-890
15. Qin X, Huang C, Wu K, Li Y, Liang X, Su M, et al. Anti-coronavirus disease 2019 (COVID-19) targets and mechanisms of puerarin. *J Cell Mol Med.* (2021) 25:677–85. doi: 10.1111/jcmm.16117
16. Wu J, Ren B, Shi F, Hua P, Lin H. BMP and mTOR signaling in heterotopic ossification: does their crosstalk provide therapeutic opportunities? *J Cell Biochem.* (2019) 120:12108–22. doi: 10.1002/jcb.28710
17. Ampadiotaki MM, Evangelopoulos DS, Pallis D, Vlachos C, Vlamis J, Evangelopoulos ME, et al. New strategies in neurogenic heterotopic ossification. *Cureus.* (2021) 13:e14709. doi: 10.7759/cureus.14709
18. Hu X, Sun Z, Li F, Jiang C, Yan W, Sun Y, et al. Burn-induced heterotopic ossification from incidence to therapy: key signaling pathways underlying ectopic bone formation. *Cell Mol Biol Lett.* (2021) 26:34. doi: 10.1186/s11658-021-00277-6
19. Pavey GJ, Qureshi AT, Tomasino AM, Honnold CL, Bishop DK, Agarwal S, et al. Targeted stimulation of retinoic acid receptor-γ mitigates the formation of heterotopic ossification in an established blast-related traumatic injury model. *Bone.* (2016) 90:159–67. doi: 10.1016/j.bone.2016.06.014
20. Łegosz P, Drela K, Pulik Ł, Sarzyńska S, Małdyk M. Challenges of heterotopic ossification-Molecular background and current treatment strategies. *Clin Exp Pharmacol Physiol.* (2018) 45:1229–35. doi: 10.1111/1440-1681.13025
21. Zhou Z, Chen B, Chen S, Lin M, Chen Y, Jin S, et al. Applications of network pharmacology in traditional Chinese medicine research. *Evid Based Complement Alternat Med.* (2020) 2020:1646905. doi: 10.1155/2020/1646905
22. Kibble M, Saarinen N, Tang J, Wennerberg K, Mäkelä S, Aittokallio T, et al. Network pharmacology applications to map the unexplored target space and therapeutic potential of natural products. *Nat Product Rep.* (2015) 32:1249–66. doi: 10.1039/C5NP00005J
23. Boezio B, Audouze K, Ducrot P, Taboureau O. Network-based approaches in pharmacology. *Mol Informat*. (2017) 36:48. doi: 10.1002/minf.201700048
24. Dong J, Xu X, Zhang Q, Yuan Z, Tan B. Critical implication of the PTEN/PI3K/AKT pathway during BMP2-induced heterotopic ossification. *Mol Med Rep*. (2021) 23:11893. doi: 10.3892/mmr.2021.11893
25. Valer JA, Sánchez-de-Diego C, Gámez B, Mishina Y, Rosa JL, Ventura F, et al. Inhibition of phosphatidylinositol 3-kinase α (PI3Kα) prevents heterotopic ossification. *EMBO Mol Med.* (2019) 11:e10567. doi: 10.15252/emmm.201910567
26. Chen S, Zhu H, Wang G, Xie Z, Wang J, Chen J, et al. Combined use of leptin and mechanical stress has osteogenic effects on ossification of the posterior longitudinal ligament. *Eur Spine J.* (2018) 27:1757–66. doi: 10.1007/s00586-018-5663-4
27. Hwang C, Marini S, Huber AK, Stepien DM, Sorkin M, Loder S, et al. Mesenchymal VEGFA induces aberrant differentiation in heterotopic ossification. *Bone Res.* (2019) 7:36. doi: 10.1038/s41413-019-0075-6

28. Kay AM, Simpson CL, Stewart JA. The role of AGE/RAGE signaling in diabetes-mediated vascular calcification. *J Diabetes Res.* (2016) 2016:6809703. doi: 10.1155/2016/6809703
29. Kennon AM, Stewart JA. RAGE differentially altered in vitro responses in vascular smooth muscle cells and adventitial fibroblasts in diabetes-induced vascular calcification. *Front Physiol.* (2021) 12:676727. doi: 10.3389/fphys.2021.676727
30. Hoffman LM, Garcha K, Karamboulas K, Cowan MF, Drysdale LM, Horton WA, et al. BMP action in skeletogenesis involves attenuation of retinoid signaling. *J Cell Biol.* (2006) 174:101–13. doi: 10.1083/jcb.200604150
31. Pignolo RJ, Pacifici M. Retinoid agonists in the targeting of heterotopic ossification. *Cells.* (2021) 10:113245. doi: 10.3390/cells10113245
32. Ju J, Yu D, Xue F, Zhao Y, Shi W, Pan M, et al. Inhibition of Nf-κb prevents trauma-induced heterotopic ossification in rat model. *Connect Tissue Res.* (2019) 60:304–10. doi: 10.1080/03008207.2018.1530771

Conflict of Interest: The authors declare that the research was conducted in the absence of any commercial or financial relationships that could be construed as a potential conflict of interest.

frontiers | Frontiers in Medicine

ORIGINAL RESEARCH
published: 19 May 2022
doi: 10.3389/fmed.2022.895564

Deep Sequencing of Serum Exosomal microRNA Level in Psoriasis Vulgaris Patients

Xiu-Min Chen[1,2,3,4]†, Dan-Ni Yao[2]†, Mao-Jie Wang[1,2,4], Xiao-Dong Wu[2], Jing-Wen Deng[2], Hao Deng[2], Run-Yue Huang[1,2,4] and Chuan-Jian Lu[1,2,4]**

[1] State Key Laboratory of Dampness Syndrome of Chinese Medicine, The Second Affiliated Hospital of Guangzhou University of Chinese Medicine (Guangdong Provincial Hospital of Chinese Medicine), Guangzhou, China, [2] The Second Affiliated Hospital, Guangzhou University of Chinese Medicine (Guangdong Provincial Hospital of Chinese Medicine), Guangzhou, China, [3] Guangdong Provincial Key Laboratory of Chinese Medicine for Prevention and Treatment of Refractory Chronic Diseases, Guangzhou, China, [4] Guangdong-Hong Kong-Macau Joint Lab on Chinese Medicine and Immune Disease Research, Guangzhou University of Chinese Medicine, Guangzhou, China

Psoriasis is a chronic skin disease affecting 1% to 3% of the world population. Psoriasis vulgaris (PV) is the most common form of psoriasis. PV patients suffer from inflamed, pruritic and painful lesions for years (even a lifetime). However, conventional drugs for PV are costly. Considering the need for long-term treatment of PV, it is urgent to discover novel biomarkers and therapeutic targets. Serum exosomal miRNAs have been identified as the reliable biomarkers and therapy targets of human diseases. Here, we described the levels of serum exosomal miRNAs in PV patients and analyzed the functional features of differently expressed miRNAs and their potential target genes for the first time. We identified 1182 miRNAs including 336 novel miRNAs and 246 differently expressed miRNAs in serum exosomes of healthy people and PV patients. Furthermore, the functional analysis found differently expressed miRNA-regulated target genes enriched for specific GO terms including primary metabolic process, cellular metabolic process, metabolic process, organic substance metabolic process, and Kyoto Encyclopedia of Genes and Genomes (KEGG) pathway containing cellular processes, human diseases, metabolic pathways, metabolism and organismal systems. In addition, we found that some predicted target genes of differentially expressed miRNAs, such as CREB1, RUNX2, EGFR, are both involved in inflammatory response and metabolism. In summary, our study identifies many candidate miRNAs involved in PV, which could provide potential biomarkers for diagnosis of PV and targets for clinical therapies against PV.

Keywords: psoriasis vulgaris, serum, exosome, miRNA, inflammatory response, metabolism

OPEN ACCESS

Edited by:
Fu Wang,
Xi'an Jiaotong University, China

Reviewed by:
Zhang Wang,
South China Normal University, China
Jin-Jian Lu,
University of Macau, China

****Correspondence:***
Run-Yue Huang
ryhuang@gzucm.edu.cn
Chuan-Jian Lu
luchuanjian888@vip.sina.com

†These authors have contributed equally to this work

Specialty section:
This article was submitted to Precision Medicine, a section of the journal Frontiers in Medicine

Received: *14 March 2022*
Accepted: *27 April 2022*
Published: *19 May 2022*

Citation:
Chen X-M, Yao D-N, Wang M-J, Wu X-D, Deng J-W, Deng H, Huang R-Y and Lu C-J (2022) Deep Sequencing of Serum Exosomal microRNA Level in Psoriasis Vulgaris Patients. Front. Med. 9:895564. doi: 10.3389/fmed.2022.895564

INTRODUCTION

Psoriasis is a chronic, inflammatory,systemic skin disease (1, 2). 1% to 3% of the world population suffers from psoriasis (3). PV is the most common form of psoriasis occurred in 80%–90% psoriasis patients who manifest erythematous papules covered with pearly scales on extensor surface of extremities, scalp and sacral region (1, 4). Due to its prevalence, diversity and duration, scientists and medical workers pay more and more attention to discovering novel biomarkers and therapeutic targets for psoriasis vulgaris.

As membrane-bound nanovesicles of 30–100 nm in diameter, exosomes are secreted by most cell types and exit in almost all bodily fluids (5–7). Various components including lipid, protein, mRNAs, microRNAs (miRNAs), long non-coding RNA (lncRNA) have been identified in exosomes (5, 6, 8). Numerous studies have indicated that recipient cells can be regulated by the above exosomal RNAs through the uptake of circulating exosomes (9, 10). Of these, serum exosomal miRNAs have been identified as the reliable biomarkers and therapy targets of human diseases, such as cancers, respiratory illness, diabetic nephropathy and autoimmune diseases (11–14). For example, the serum exosomal miR-24-3p level in nasopharyngeal carcinoma has been revealed to correlate with worse disease-free survival of patients (15). Furthermore, serum exosomal miRNA miR-126 have potential to predict acute respiratory distress syndrome (16). A subset of serum exosomal miRNAs (miR-4449, miR-642a-3p, miR-1255b-5p, let-7c-5p, miR-1246, let-7i-3p, miR-5010-5p, miR-150-3p) associate with diabetic nephropathy (17). More importantly, a recent study has demonstrated that extrinsic microRNA *let-7i* transferred by serum exosomes might have an active role in triggering autoimmune diseases (18).

Considering that plasma exosomal microRNAs modulate immune response (11), serum exosomal microRNAs might have the potential to predict immune disorders including psoriasis vulgaris. In this study, the high-throughput RNA sequencing was employed to identify differentially expressed serum exosomal miRNAs in patients with psoriasis vulgaris, and results were validated by quantitative real-time polymerase chain reaction (qRT-PCR). Subsequently, the enrichment analysis of the GO term and Kyoto Encyclopedia of Genes and Genomes (KEGG) for target genes of differently expressed miRNA were conducted to provide insights exploring reliable candidates for the diagnosis and treatment of psoriasis vulgaris.

MATERIALS AND METHODS

Ethics Statement

All experimental procedures of the present study were approved by the Institutional Review Board of Guangdong Provincial

TABLE 1 | Demographic characteristics of psoriasis vulgaris (PV) patients and healthy control.

Variable	Healthy control (*n* = 15)	PV (*n* = 15)
Age, years#	49.33 (8.15)	53.73 (14.88)
Age, group, n		
≤ 25	0	1 (6.67%)
26–40	2 (13.33%)	2 (13.33%)
41–55	10 (66.67%)	4 (26.67%)
≥ 56	3 (20.00%)	8 (53.33%)
Sex, n		
Male	9 (60.00%)	11 (73.33%)
Female	6 (40.00%)	4 (26.67%)
PASI		
0	15 (100.00%)	0 (100.00%)
1	0	0
2	0	5 (33.30%)
3	0	3 (20.00%)
4	0	4 (26.67%)
5	0	2 (13.33%)
6	0	1 (6.67%)

#Age data are presented as the mean (SD). PV: psoriasis vulgaris; HC: healthy controls.

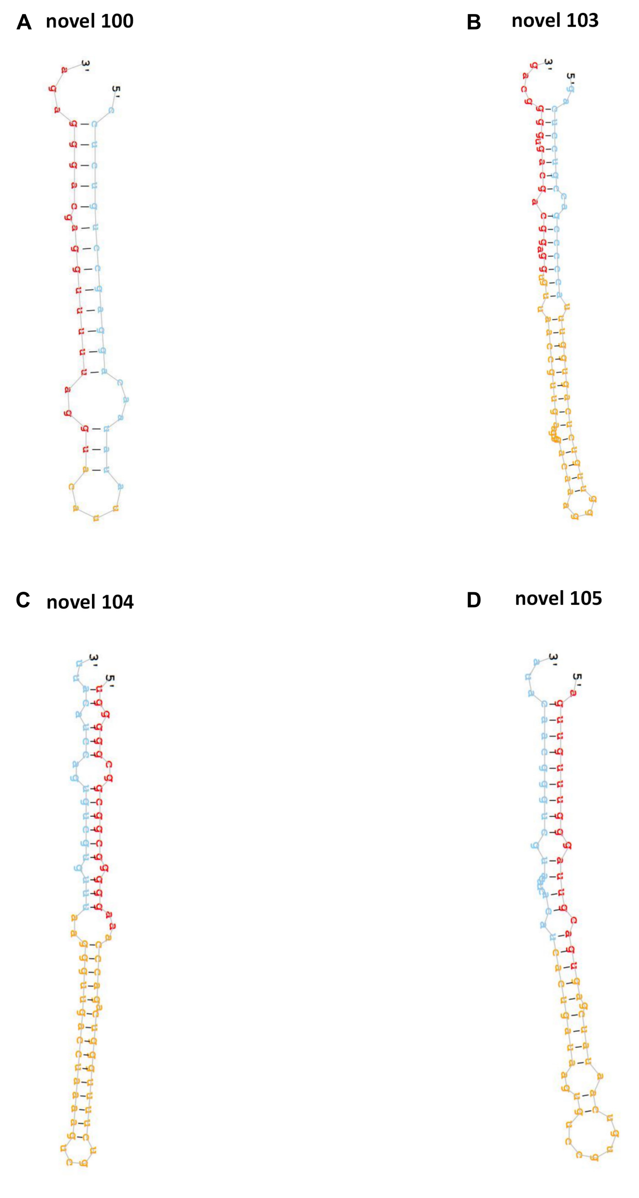

FIGURE 1 | The hairpin structures of four novel precursor miRNAs. The secondary structures of four novel precursor miRNA identified in this study, including novel-100 **(A)**, novel-103 **(B)**, novel-104 **(C)** and novel-105 **(D)**.

Hospital of Chinese Medicine and conducted in accordance with the Declaration of Helsinki (#B2014-029-01). Written informed consent was obtained from all recruited participants.

Patients

The clinical characteristics of 15 healthy people and 15 PV patients recruited for this study were shown in **Table 1**. All selected PV patients fulfilled the Clinical Guidelines of Psoriasis 2008 formulated by the Chinese Medical Association (19). The inclusion criteria were: (1) patients meeting diagnosis standards of PV; (2) patients corresponding the progressive stage of PV; (3) patients diagnosed by two clinicians regarding relevance to PV. Besides, patients combined with tumor, serious cardiovascular, liver and kidney comorbidities, hematopoietic system disease, high fever, tuberculosis, acute suppurative and other infectious diseases were excluded. In addition, women in pregnancy and lactation were also excluded. Fasting venous blood was drawn and centrifuged, then the separated plasma was stored at −80° until detection.

Exosome Isolation

Exosomes were isolated from 500µl serum samples according to the manufacturer's protocols using Exo Quick Exosome Precipitation Solution Kit (20), and identified by scanning electron microscopy (SEM) (FEI XL30, The Netherlands) with low-voltage (1 KeV) and magnification of 20,000, NanoSight and Western blot analysis in our previous study (20), which shared exosomes used in the present study.

Small RNA Library Construction, Sequencing, and miRNA Identification

After the extraction of total RNA from serum exosome by TRIzol (Thermo Fisher Scientific, Waltham, MA, United States), the RNAs ranged from 18 to 30bp were enriched. Then adapters were ligated to RNAs followed by the reverse transcription of adapter-ligated RNAs, and the 140–160bp size products were collected for the construction of cDNA library and sequencing by Illumina HiSeq^{TM} 4000.

Subsequently, raw reads were analyzed by in-house Perl scripts to collect clean tags. After discarding dirty reads with over 10% poly-N sequences or whose Phred scores were $< 5\%$, all clean tags were aligned with miRNAs using GeneBank database and Rfam database (v11.0). Besides, all clean tags were also aligned with human reference genome (Grch37) utilizing TopHat v2.0.9 (21). Next, clean tags were blasted in miRBase database (v21) to screen known miRNAs. Moreover, all unannotated tags were predicted using Mireap_v0.2 software based on their genome positions and hairpin structures to identify novel miRNA candidates.

miRNA Levels

The levels of total miRNAs were calculated and normalized to transcripts per million (TPM) using the following formula: TPM = Actual miRNA counts/Total counts of

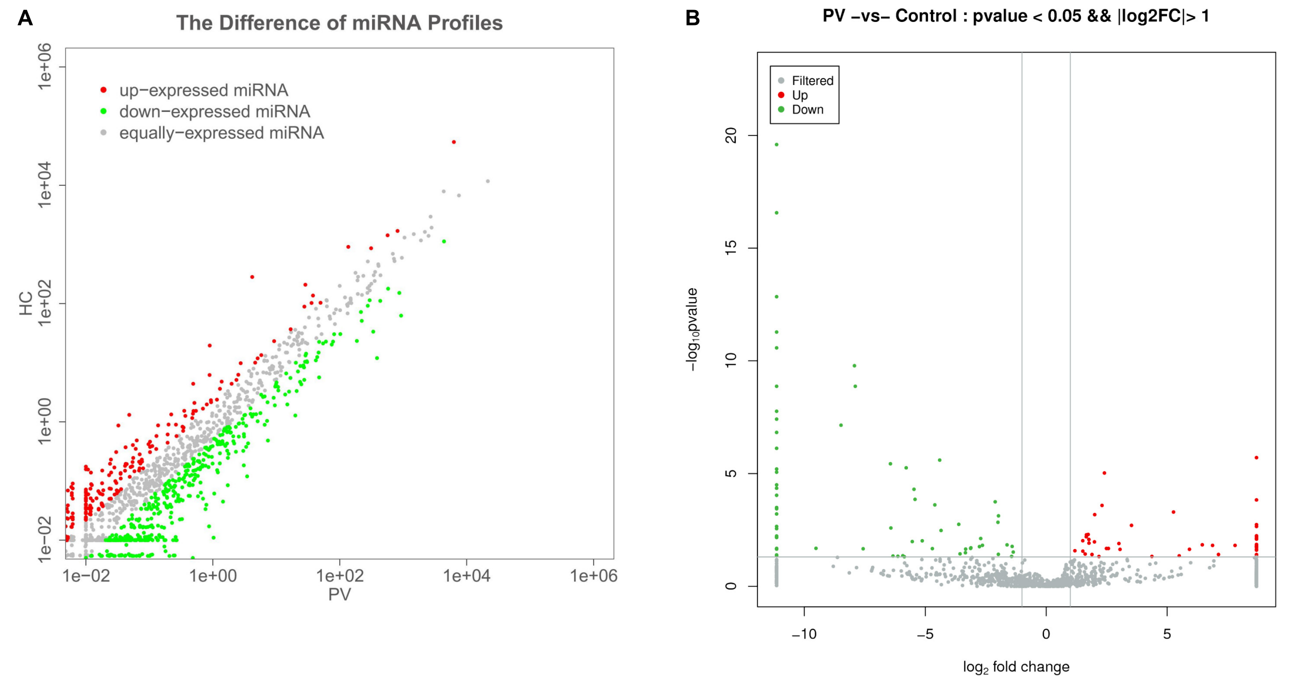

FIGURE 2 | Characteristics of miRNA levels between control group and PV group. **(A,B)** All miRNA levels are shown, and miRNAs with differentially levels are shown in red (up-regulated) or green (down-regulated).

clean tags × 10^6. Besides, levels of miRNAs in different groups were displayed by the heatmaps to cluster miRNAs with similar level patterns.

Analysis of miRNA Differential Levels

The formula used to determine miRNA differential levels across groups was shown as follows:

$$p(x|y) = (\frac{N_2}{N_1})^y \frac{(x+y)!}{x!y!(1+\frac{N_2}{N_1})^{(x+y+1)}} \quad \begin{matrix} C(y \leq y_{\min}|x) = \sum_{y=0}^{y \leq y_{\min}} p(y|x) \\ D(y \geq y_{\max}|x) = \sum_{y \geq y_{\max}}^{\infty} p(y|x) \end{matrix}$$

Besides, miRNAs with a fold change (FC) ≥ 2 and P value < 0.05 in a comparison were considered as significant differently expressed miRNAs.

Prediction of Target Genes of Differently Expressed miRNAs

The candidate target genes of differently expressed miRNAs of miRNAs were predicted by RNAhybrid (v2.1.2), Miranda (v3.3a) and TargetScan (v7.0) software based on sequences. Besides, the miRNA-target gene network was established using Cytoscape software (v3.6.0).

Gene Ontology and Kyoto Encyclopedia of Genes and Genomes Pathway Enrichment Analysis for Target Genes

All target genes of different expressed miRNAs were mapped to GO terms based on Gene Ontology database. Besides, significantly enriched GO terms were identified by hypergeometric test. KEGG is an important public pathway-related database. Therefore, KEGG was used for analyzing pathway enrichment to determine significantly enriched pathways for target genes of different expressed miRNAs.

Validation of Small RNA Sequencing Data by Quantitative Real-Time Polymerase Chain Reaction

Quantitative real-time polymerase chain reaction (qRT-PCR) assays were performed to confirm the reliability of the small RNA-seq data according to previous studies (22, 23). Small RNA was reversed transcripted by the miRcute miRNA First-Strand cDNA Synthesis Kit (Tiangen, Beijing, China). Besides, miRNA levels were normalized to the level of U6 according to the $\Delta\Delta$ CT method.

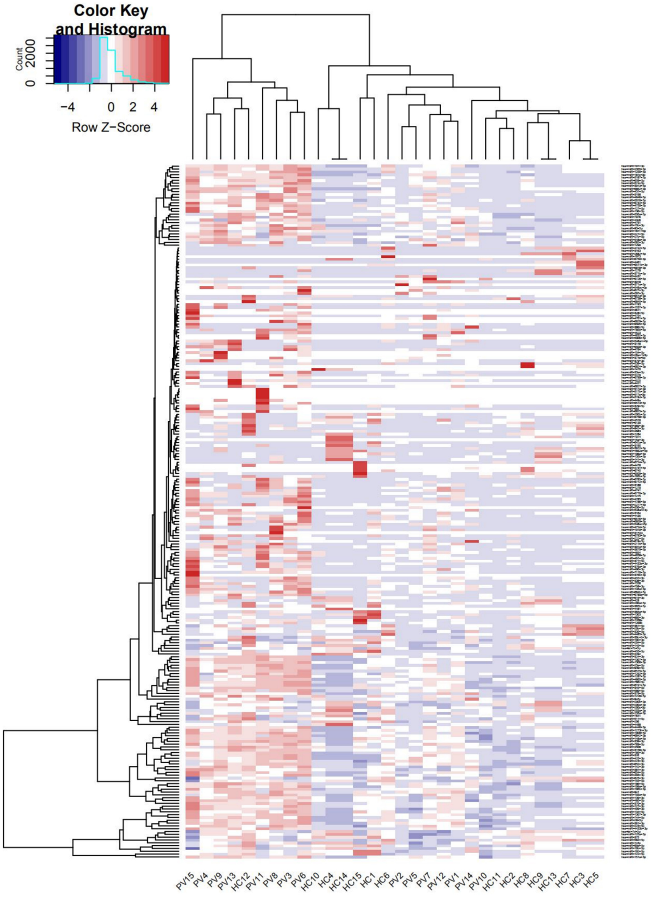

FIGURE 3 | Characteristics of miRNA levels between different groups. Heat map showing the levels of miRNAs ($P < 0.05$) in different groups. Colors from blue to red stand for z-score got through the dimensionality reduction of FPKM value and reveal decreasing miRNA levels in each group.

Statistical Analysis

Statistical differences of data in this study were analyzing by the unpaired Student's *t*-test between two groups using SPSS software (v20.0, SPSS Inc., Chicago, United States). Besides, $P < 0.05$ indicated statistically significant.

RESULTS

Analysis of Small RNA Sequencing

Thirty small RNA libraries, including 15 PV samples (PV1-15) and 15 samples (HC1-15), were constructed and sequenced to reveal miRNA profiles. After the filter of low-quality reads, approximately 13 million clean tags were obtained from PV groups while the number of clean tags obtained from control groups was about 11 million. The percentage of clean reads in each group was approximately 88%. Then, clean reads were mapped to the human reference genome (Grch37) by TopHat. Results showed that more than 90% of clean reads were mapped.

Identification of miRNA

After the alignment with GenBank and Rfam (11.0), rRNA, scRNA, snoRNA, snRNA, tRNA were removed from clean tags. Results of the mapping to human reference genome revealed that 751 and 846 known miRNAs were found in clean tags of control and PV groups, respectively (**Supplementary Table 1**). Moreover, 257 and 336 novel miRNAs were uncovered from clean tags of in clean tags of control and PV groups, respectively (**Supplementary Table 2**). The hairpin structures of four novel precursor miRNAs (novel 100, novel 103, novel 104, novel 105) were displayed in **Figures 1A–D**.

miRNA Differential Levels

Levels of total miRNAs were quantified the read count and TPM analyses. Compared with the control group, 246 differently expressed miRNAs (166 up-regulated and 80 down-regulated) were found in PV group (**Figures 2A,B** and **Supplementary Table 3**), including hsa-let-7d-3p, hsa-miR-125a-5p, hsa-miR-134-5p, hsa-miR-142-3p, hsa-miR-155-5p, hsa-miR-375-3p, hsa-miR-485-5p, hsa-miR-941, and hsa-miR-1228-5p. In addition, the heat map (**Figure 3**) revealed the differentially expressed miRNAs ($P < 0.05$) between the control group and the PV group. Besides, top differential miRNAs between PV patients and healthy control were stated in **Table 2**. Subsequently, qRT-PCR was performed to validate data of small RNA sequencing in 20 healthy control samples (control group) and 20 PV samples (case group). Except hsa-miR-125a-5p, hsa-miR-142-3p and hsa-miR-375-3p, qRT-PCR results of other miRNAs were consistent with those in small RNA sequencing (**Figures 4A–I**).

Target Prediction of Differently Expressed miRNAs

Usually, miRNAs play roles in biology progresses through regulating target gene expression. To understand the roles of differently expressed miRNAs responded to PV, target prediction was assessed. Target genes of differently expressed miRNAs were identified including DEAD-box helicase 5 (DDX5), SEC11 homolog A, signal peptidase complex subunit (SEC11A), TSR1 ribosome maturation factor (TSR1), ribosomal protein L13a (RPL13A), epidermal growth factor receptor (EGFR) and UTP6 small subunit processome component (UTP6) (**Figure 5** and **Supplementary Tables 4**, **5**). Moreover, miRNA-mRNA network indicated that a target gene could be modified both by up-regulated and down-regulated miRNAs (**Figure 5**).

Functional Analysis of Differently Expressed miRNAs

To further identify cellular processes and pathways related to differently expressed miRNAs, GO and KEGG pathway enrichment were further utilized to analyze their targets. GO enrichment analysis revealed that significantly enriched biological process for target genes of differently expressed miRNAs included primary metabolic process, cellular metabolic process, organic substance metabolic process, metabolic process, regulation of cellular process, signal-organism cellular process, regulation of biological process, biological regulation, cellular process (**Figures 6A,B** and **Supplementary Table 6**). In addition, the KEGG pathway enrichment analysis indicated that targets of up-regulated miRNAs were associated with metabolic pathways, endocytosis, apoptosis, alcoholism, spliceosome (**Figure 7A** and **Supplementary Table 7**), while targets of down-regulated miRNAs were involved in metabolic pathways, alcoholism, measies, spliceosome, toxoplasmosis (**Figure 7B** and **Supplementary Table 7**).

DISCUSSION

Here, we identified the levels of serum exosomal miRNAs in PV patients. 1182 miRNAs including 336 novel miRNAs were investigated. In addition, 246 differently expressed miRNAs were identified including hsa-let-7d-3p, hsa-miR-125a-5p, hsa-miR-134-5p, hsa-miR-142-3p, hsa-miR-155-5p, hsa-miR-375-3p, hsa-miR-485-5p, hsa-miR-941and hsa-miR-1228-5p.

TABLE 2 | Top differential miRNAs between psoriasis vulgaris (PV) patients and healthy control.

miRNA	TPM		Up/Down	Log2 (Fold change)
	HC	PV		
hsa-miR-222-5p	0.005	0.4845	Up	6.5984
hsa-miR-376b-3p	0.011	1.028	Up	6.5462
hsa-miR-449a	0.0028	0.174	Up	5.9575
hsa-miR-2115-5p	0.0171	0.8727	Up	5.6734
hsa-miR-4785	0.0055	0.2507	Up	5.5104
hsa-miR-4488	281.3985	4.1762	Down	−6.0743
hsa-miR-6513-3p	0.1356	0.004	Down	−5.0832
hsa-miR-4485-3p	1.3131	0.0482	Down	−4.7678
hsa-miR-4481	0.8671	0.0325	Down	−4.7377
hsa-miR-203a-3p	19.5013	0.8938	Down	−4.4475

PV: psoriasis vulgaris; HC: healthy controls; TPM: transcripts per million.

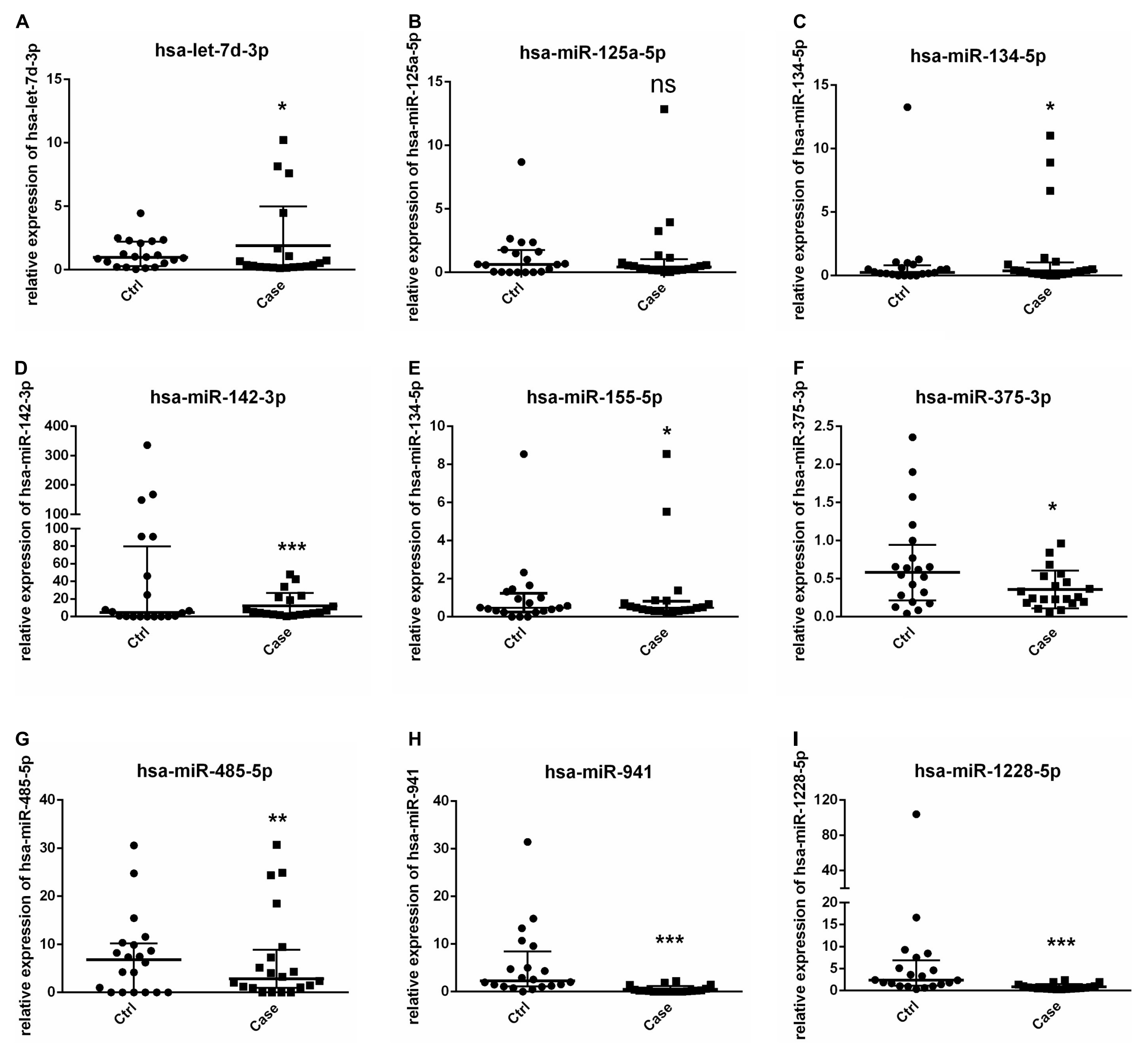

FIGURE 4 | Validation of miRNAs by RT-PCR. **(A–I)** Levels of 9 selected miRNAs are determined by RT-PCR. * $P < 0.05$, ** $P < 0.01$, *** $P < 0.001$. Ctrl: healthy control samples; Case: PV samples.

Previous studies have indicated that some of these differently expressed miRNAs associate with psoriasis. For example, serum hsa-miR-142-3p is significantly downregulated in patients with psoriasis after anti-tumor necrosis factor-α (TNF–α) therapy (24). In addition, hsa-miR-142-3p is highly upregulated in psoriatic skin (25). Moreover, miR-155 promotes proliferation and suppresses apoptosis of psoriasis cells (26), while treatment of methotrexate (MTX) and narrow-band ultraviolet B phototherapy (NB-UVB) decrease hsa-miR-155-5p expression in psoriatic skin lesions (27). Therefore, these miRNAs may exert influence on PV through exosome.

PV is an inflammatory skin disease (2, 28). Consistently, numerous of target genes of differently expressed miRNAs are involved in immunity. cAMP-response element binding protein 1 (CREB1), RUNX family transcription factor 2 (RUNX2) and epidermal growth factor receptor (EGFR) are targets of up-regulated miRNAs. CREB1 can activate the transcription of cytokine interleukin (IL) 33 as a transcription factor (29). CREB1 also enhances the production of IL-1 and TNF-α (30). Moreover, RUNX2 suppresses antitumor immunity in multiple myeloma cells (31). In contrast, RUNX2 contributes to clear viral infections through promoting IL-1 production in plasmacytoid dendritic cells (32). Recent studies have indicated that EGFR is a target of immunotherapy for tumors including lung cancer and glioblastoma multiforme (33–35).

Prediction of target genes revealed that insulin like growth factor binding protein 5 (IGFBP5), interleukin 13 receptor subunit alpha 1 (IL13RA1), cyclin D1 (CCND1) were modified by

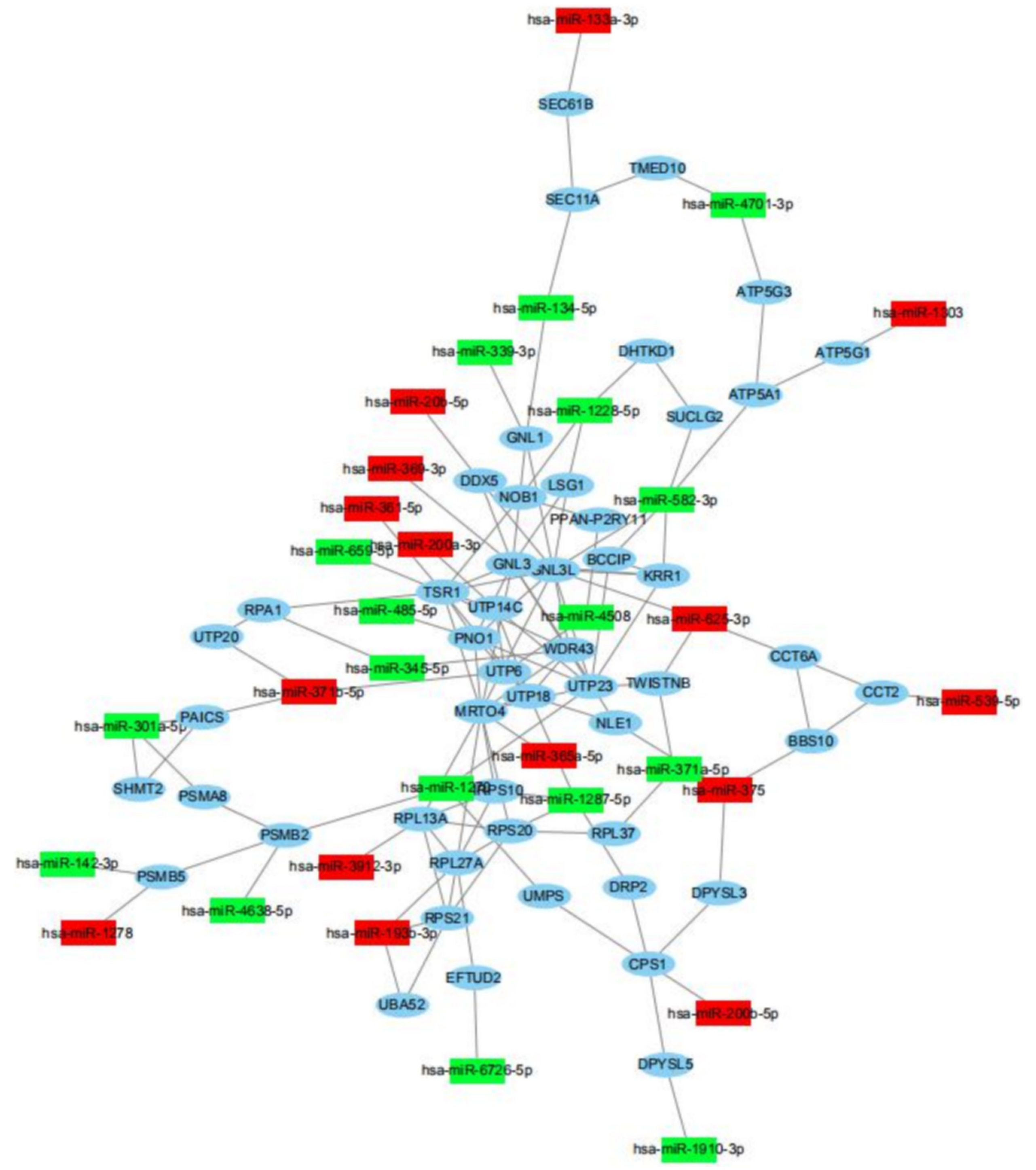

FIGURE 5 | miRNA-mRNA regulatory network between differently expressed miRNAs and target genes. View of miRNA-mRNA regulatory network according to miRNAs with differently levels and their regulated target genes.

down-regulated miRNAs. IGFBP5 is essential for IL-6 production in human fibroblasts (36). IL-13Ralpha1 plays a critical role in immune responses for T helper type 2 -mediated disease (37). Furthermore, CCND1 is a target of immunotherapy for numerous cancers (38–40). Thus, serum exosomal miRNAs may contribute to the inflammatory response in PV patients.

However, analysis of GO and KEGG pathway for target genes of differently expressed miRNAs demonstrated that these target

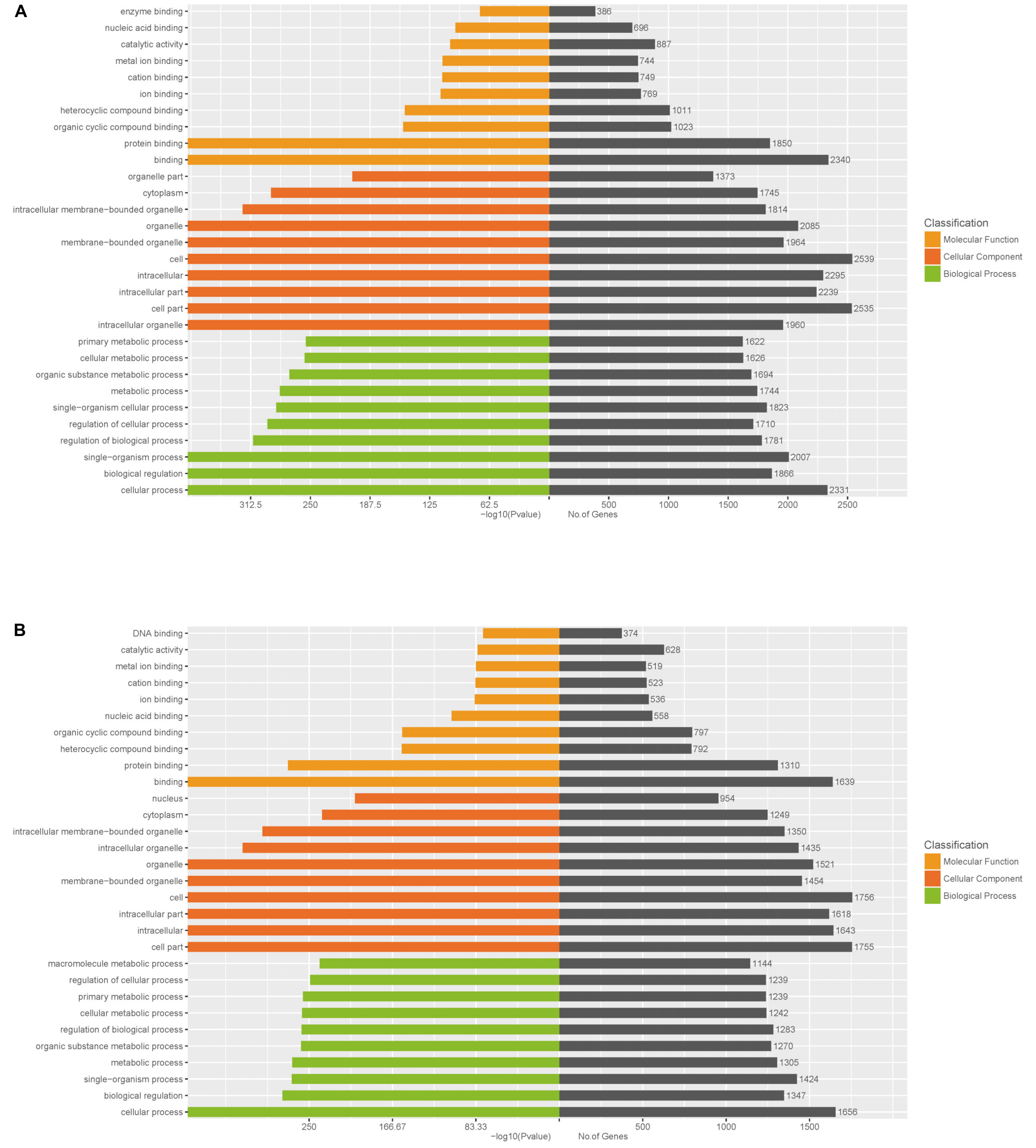

FIGURE 6 | GO enrichment analysis for target genes of miRNAs with differently levels. The GO enrichment histograms and GO terms for target genes of up-regulated miRNAs **(A)** and down-regulated miRNAs **(B)** are shown.

genes were not enriched in inflammatory response or immunity but metabolic processes and metabolism pathways, indicating that most of target genes associated with metabolism. Metabolism fundamentally influences inflammatory response and ultimately affect progression of numerous diseases (41). T lymphocytes (T cells) are sentinels of immune system, and cellular metabolism activates T cell upon immune challenge through regulating blast, proliferation and differentiation (41). T cell metabolism is dynamically regulated with activation state (42). Upon antigen encounter, T cells are activated in a high rate of glycolysis for

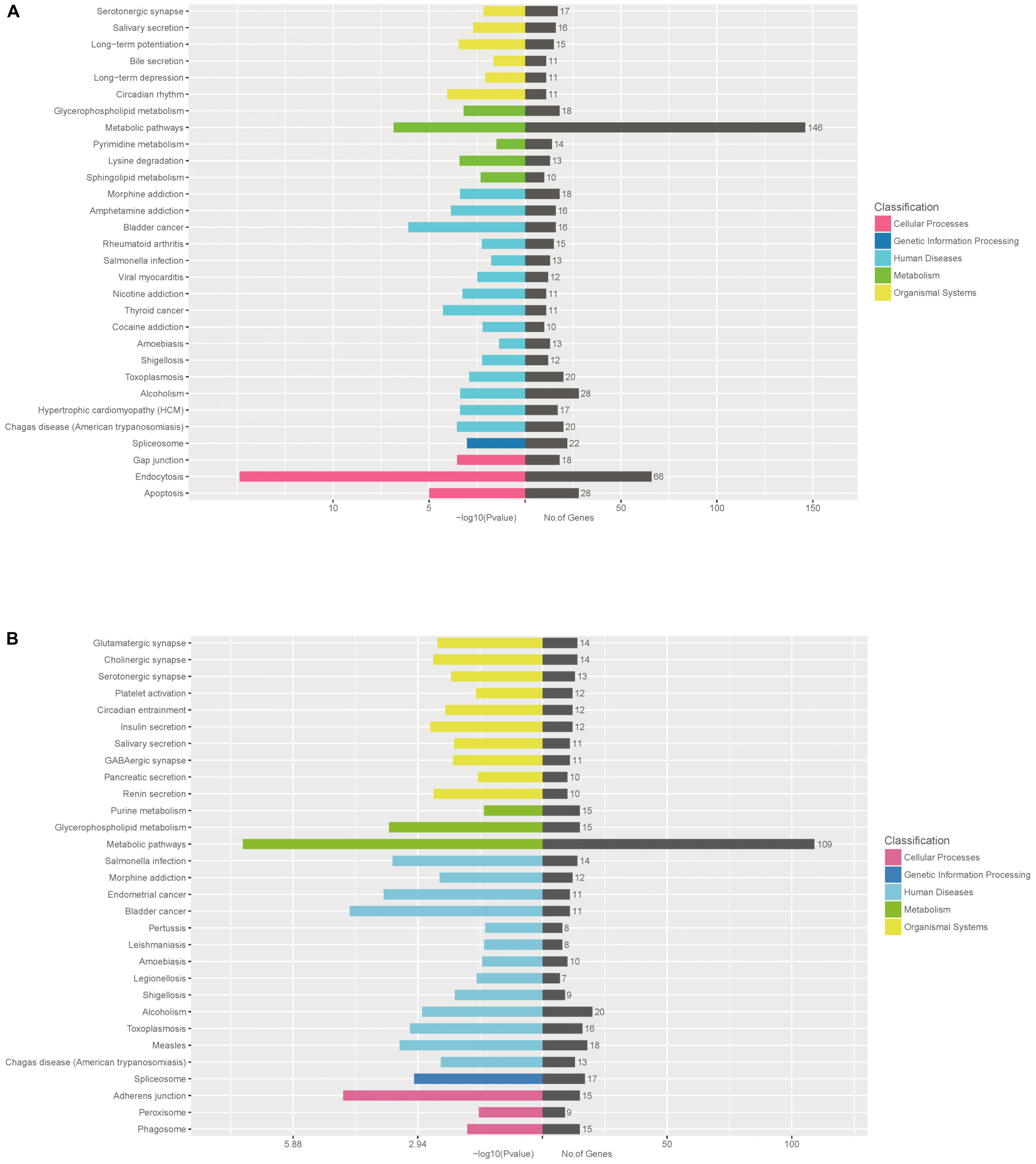

FIGURE 7 | KEGG pathway enrichment analysis for target genes of miRNAs with differently levels. The KEGG pathway enrichment scatter plots for target genes of up-regulated miRNAs **(A)** and down-regulated miRNAs **(B)** are shown.

extensive proliferation and differentiation into effector. After pathogen clearance, most of effector T cells die while a few antigen-specific memory T cells were maintained (41–45). In addition, metabolism may contribute to the transition of effector T cells to memory T cells (46–48).

In detail, iron metabolism contributes to the proliferation of immune cells and cytokine action (49), consistent with the enriched GO terms "iron binding " and "metal iron binding." Moreover, cholinergic metabolism is essential for vagus nerve-mediated immune function and proinflammatory responses (50).

Furthermore, arginine metabolism, Vitamin D metabolism, Zinc metabolism, Myo-Inositol metabolism are crucial for immune cell growth and immunity (51–54). More importantly, some of immunity-related target genes in this study also contribute to metabolism. For example, CREB1 suppresses hepatic glucose metabolism (55). RUNX2 alters nutrient metabolism including glucose metabolism in cancers (56, 57). EGFR also regulates glucose metabolism in chondrosarcomas (58). Thus, serum exosomal miRNAs may regulate immunity through modifying metabolism in PV patients.

However, the small size of the patient group was the limitation of this study. More PV patients would be recruited in the future study.

CONCLUSION

In summary, the present study revealed candidate serum exosomal miRNAs associated with PV and the signaling pathways modulated by miRNAs. These findings could provide potential biomarkers for diagnosis of PV and targets for clinical therapies against PV. However, the small size of the patient group was the limitation of this study. More PV patients would be recruited in the future study.

DATA AVAILABILITY STATEMENT

The original contributions presented in the study are included in the article/**Supplementary Material**, further inquiries can be directed to the corresponding authors.

ETHICS STATEMENT

The studies involving human participants were reviewed and approved by Institutional Review Board of Guangdong Provincial Hospital of Chinese Medicine. The patients/participants provided their written informed consent to participate in this study.

AUTHOR CONTRIBUTIONS

X-MC, D-NY, R-YH, and C-JL: study conception and design and draft manuscript preparation. X-MC, D-NY, X-DW, and M-JW: data collection. X-MC, D-NY, X-DW, M-JW, J-WD, and HD: analysis and interpretation of results. All authors reviewed the results and approved the final version of the manuscript.

FUNDING

This work was supported by the following funds: National Natural Science Foundation of China (81873302 and 81473681); The China-Dutch special projects of Guangdong Provincial Hospital of Chinese Medicine (YN2019HL01, YN2019HL02, and YN2019HL03); Natural Science Foundation of Guangdong Province (2021A1515011477); grant from Guangzhou Basic Research Program (202102010256); Guangdong Provincial Key laboratory of Chinese Medicine for Prevention and Treatment of Refractory Chronic Diseases (2018) (2018B030322012); The 2020 Guangdong Provincial Science and Technology Innovation Strategy Special Fund (Guangdong-Hong Kong-Macau Joint Lab) (2020B1212030006); and grant from Guangdong Provincial Hospital of Chinese Medicine (YN2018ZD01).

SUPPLEMENTARY MATERIAL

The Supplementary Material for this article can be found online at: https://www.frontiersin.org/articles/10.3389/fmed.2022.895564/full#supplementary-material

REFERENCES

1. Menter A, Gottlieb A, Feldman SR, Van Voorhees AS, Leonardi CL, Gordon KB, et al. Guidelines of care for the management of psoriasis and psoriatic arthritis: section 1. Overview of psoriasis and guidelines of care for the treatment of psoriasis with biologics. *J Am Acad Dermatol.* (2008) 58:826–50. doi: 10.1016/j.jaad.2008.02.039
2. Lowes MA, Suarez-Farinas M, Krueger JG. Immunology of psoriasis. *Annu Rev Immunol.* (2014) 32:227–55.
3. Ljubenovic M, Lazarevic V, Golubovic M, Binic I. Integrative approach to psoriasis vulgaris. *Holist Nurs Pract.* (2018) 32:133–9. doi: 10.1097/HNP.0000000000000180
4. Nast A, Boehncke WH, Mrowietz U, Ockenfels HM, Philipp S, Reich K, et al. S3 – Guidelines on the treatment of psoriasis vulgaris (English version). Update. *J Dtsch Dermatol Ges.* (2012) 10:S1–95. doi: 10.1111/j.1610-0387.2012.07919.x
5. Simons M, Raposo G. Exosomes–vesicular carriers for intercellular communication. *Curr Opin Cell Biol.* (2009) 21:575–81. doi: 10.1016/j.ceb.2009.03.007
6. Mathivanan S, Ji H, Simpson RJ. Exosomes: extracellular organelles important in intercellular communication. *J Proteomics.* (2010) 73:1907–20. doi: 10.1016/j.jprot.2010.06.006
7. Gupta A, Kashte S, Gupta M, Rodriguez HC, Gautam SS, Kadam S. Mesenchymal stem cells and exosome therapy for COVID-19: current status and future perspective. *Hum Cell.* (2020) 33:907–18. doi: 10.1007/s13577-020-00407-w
8. Simpson RJ, Lim JW, Moritz RL, Mathivanan S. Exosomes: proteomic insights and diagnostic potential. *Expert Rev Proteomics.* (2009) 6:267–83. doi: 10.1586/epr.09.17
9. Sato-Kuwabara Y, Melo SA, Soares FA, Calin GA. The fusion of two worlds: non-coding RNAs and extracellular vesicles–diagnostic and therapeutic implications (Review). *Int J Oncol.* (2015) 46:17–27. doi: 10.3892/ijo.2014.2712
10. Zhang J, Li S, Li L, Li M, Guo C, Yao J, et al. Exosome and exosomal microRNA: trafficking, sorting, and function. *Genomics Proteomics Bioinformatics.* (2015) 13:17–24. doi: 10.1016/j.gpb.2015.02.001
11. Giudice V, Banaszak LG, Gutierrez-Rodrigues F, Kajigaya S, Panjwani R, Fernandez Ibanez MDP, et al. Diagnostic and prognostic roles of circulating exosomal microRNAs in acquired aplastic anemia and myelodysplastic syndromes. *Haematologica.* (2018) 103:1150–9. doi: 10.3324/haematol.2017.182824
12. Mori MA, Ludwig RG, Garcia-Martin R, Brandao BB, Kahn CR. Extracellular miRNAs: from biomarkers to mediators of physiology and disease. *Cell Metab.* (2019) 30:656–73. doi: 10.1016/j.cmet.2019.07.011

13. Avgeris M, Panoutsopoulou K, Papadimitriou MA, Scorilas A. Circulating exosomal miRNAs: clinical significance in human cancers. *Expert Rev Mol Diagn.* (2019) 19:979–95. doi: 10.1080/14737159.2019.1673732
14. Hernandez-Walias FJ, Vazquez E, Pacheco Y, Rodriguez-Fernandez JM, Perez-Elias MJ, Dronda F, et al. Risk, diagnostic and predictor factors for classical Hodgkin lymphoma in HIV-1-infected individuals: role of plasma exosome-derived miR-20a and miR-21. *J Clin Med.* (2020) 9:760. doi: 10.3390/jcm9030760
15. Kapetanakis NI, Baloche V, Busson P. Tumor exosomal microRNAs thwarting anti-tumor immune responses in nasopharyngeal carcinomas. *Ann Transl Med.* (2017) 5:164. doi: 10.21037/atm.2017.03.57
16. Wu X, Wu C, Gu W, Ji H, Zhu L. Serum exosomal microRNAs predict acute respiratory distress syndrome events in patients with severe community-acquired pneumonia. *Biomed Res Int.* (2019) 2019:3612020. doi: 10.1155/2019/3612020
17. Kim H, Bae YU, Jeon JS, Noh H, Park HK, Byun DW, et al. The circulating exosomal microRNAs related to albuminuria in patients with diabetic nephropathy. *J Transl Med.* (2019) 17:236. doi: 10.1186/s12967-019-1983-3
18. Kimura K, Hohjoh H, Yamamura T. The role for exosomal microRNAs in disruption of regulatory T cell homeostasis in multiple sclerosis. *J Exp Neurosci.* (2018) 12:1179069518764892. doi: 10.1177/1179069518764892
19. PGoDaVCM Association. Clinical guidelines of psoriasis 2008. *Chin J Dermatol.* (2009) 42:2.
20. Chen XM, Zhao Y, Wu XD, Wang MJ, Yu H, Lu JJ, et al. Novel findings from determination of common expressed plasma exosomal microRNAs in patients with psoriatic arthritis, psoriasis vulgaris, rheumatoid arthritis, and gouty arthritis. *Discov Med.* (2019) 28:47–68.
21. Trapnell C, Roberts A, Goff L, Pertea G, Kim D, Kelley DR, et al. Differential gene and transcript expression analysis of RNA-seq experiments with TopHat and cufflinks. *Nat Protoc.* (2012) 7:562–78. doi: 10.1038/nprot.2012.016
22. Xu Y, Niu J, Xi G, Niu X, Wang Y, Guo M, et al. TGF-beta1 resulting in differential microRNA expression in bovine granulosa cells. *Gene.* (2018) 663:88–100. doi: 10.1016/j.gene.2018.04.036
23. Zhong JX, Zhou L, Li Z, Wang Y, Gui JF. Zebrafish Noxa promotes mitosis in early embryonic development and regulates apoptosis in subsequent embryogenesis. *Cell Death Differ.* (2014) 21:1013–24. doi: 10.1038/cdd.2014.22
24. Pivarcsi A, Meisgen F, Xu N, Stahle M, Sonkoly E. Changes in the level of serum microRNAs in patients with psoriasis after antitumour necrosis factor-alpha therapy. *Br J Dermatol.* (2013) 169:563–70. doi: 10.1111/bjd.12381
25. Joyce CE, Zhou X, Xia J, Ryan C, Thrash B, Menter A, et al. Deep sequencing of small RNAs from human skin reveals major alterations in the psoriasis miRNAome. *Hum Mol Genet.* (2011) 20:4025–40. doi: 10.1093/hmg/ddr331
26. Xu L, Len H, Shi X, Ji J, Fu J, Len H. MiR-155 promotes cell proliferation and inhibits apoptosis by PTEN signaling pathway in the psoriasis. *Biomed Pharmacother.* (2017) 90:524–30. doi: 10.1016/j.biopha.2017.03.105
27. Soonthornchai W, Tangtanatakul P, Meephansan J, Ruchusatsawat K, Reantragoon R, Hirankarn N, et al. Down-regulation of miR-155 after treatment with narrow-band UVB and methotrexate associates with apoptosis of keratinocytes in psoriasis. *Asian Pac J Allergy Immunol.* (2019) 39:206–13. doi: 10.12932/AP-031218-0451
28. Boehncke WH, Schon MP. Psoriasis. *Lancet.* (2015) 386:983–94.
29. Gorbacheva AM, Korneev KV, Kuprash DV, Mitkin NA. The risk G allele of the single-nucleotide polymorphism rs928413 creates a CREB1-binding site that activates IL33 promoter in lung epithelial cells. *Int J Mol Sci.* (2018) 19:2911. doi: 10.3390/ijms19102911
30. Yang S, Li L, Zhu L, Zhang C, Li Z, Guo Y, et al. Aucubin inhibits IL-1beta-or TNF-alpha-induced extracellular matrix degradation in nucleus pulposus cell through blocking the miR-140-5p/CREB1 axis. *J Cell Physiol.* (2019) 234:13639–48. doi: 10.1002/jcp.28044
31. Gowda PS, Wildman BJ, Trotter TN, Xu X, Hao X, Hassan MQ, et al. Runx2 suppression by miR-342 and miR-363 inhibits multiple myeloma progression. *Mol Cancer Res.* (2018) 16:1138–48. doi: 10.1158/1541-7786.MCR-17-0606
32. Chopin M, Preston SP, Lun ATL, Tellier J, Smyth GK, Pellegrini M, et al. RUNX2 mediates plasmacytoid dendritic cell egress from the bone marrow and controls viral immunity. *Cell Rep.* (2016) 15:866–78. doi: 10.1016/j.celrep.2016.03.066
33. Akbay EA, Koyama S, Carretero J, Altabef A, Tchaicha JH, Christensen CL, et al. Activation of the PD-1 pathway contributes to immune escape in EGFR-driven lung tumors. *Cancer Discov.* (2013) 3:1355–63. doi: 10.1158/2159-8290.CD-13-0310
34. Biton J, Mansuet-Lupo A, Pecuchet N, Alifano M, Ouakrim H, Arrondeau J, et al. TP53, STK11, and EGFR mutations predict tumor immune profile and the response to anti-PD-1 in lung adenocarcinoma. *Clin Cancer Res.* (2018) 24:5710–23. doi: 10.1158/1078-0432.CCR-18-0163
35. Chistiakov DA, Chekhonin IV, Chekhonin VP. The EGFR variant III mutant as a target for immunotherapy of glioblastoma multiforme. *Eur J Pharmacol.* (2017) 810:70–82. doi: 10.1016/j.ejphar.2017.05.064
36. Kojima H, Kunimoto H, Inoue T, Nakajima K. The STAT3-IGFBP5 axis is critical for IL-6/gp130-induced premature senescence in human fibroblasts. *Cell Cycle.* (2012) 11:730–9. doi: 10.4161/cc.11.4.19172
37. Ramalingam TR, Pesce JT, Sheikh F, Cheever AW, Mentink-Kane MM, Wilson MS, et al. Unique functions of the type II interleukin 4 receptor identified in mice lacking the interleukin 13 receptor alpha1 chain. *Nat Immunol.* (2008) 9:25–33. doi: 10.1038/ni1544
38. Sobti RC, Kaur P, Kaur S, Singh J, Janmeja AK, Jindal SK, et al. Effects of cyclin D1 (CCND1) polymorphism on susceptibility to lung cancer in a North Indian population. *Cancer Genet Cytogenet.* (2006) 170:108–14. doi: 10.1016/j.cancergencyto.2006.05.017
39. Khemlina G, Ikeda S, Kurzrock R. The biology of Hepatocellular carcinoma: implications for genomic and immune therapies. *Mol Cancer.* (2017) 16:149. doi: 10.1186/s12943-017-0712-x
40. Han Y, Wu Y, Yang C, Huang J, Guo Y, Liu L, et al. Dynamic and specific immune responses against multiple tumor antigens were elicited in patients with hepatocellular carcinoma after cell-based immunotherapy. *J Transl Med.* (2017) 15:64. doi: 10.1186/s12967-017-1165-0
41. Pearce EL, Poffenberger MC, Chang CH, Jones RG. Fueling immunity: insights into metabolism and lymphocyte function. *Science.* (2013) 342:1242454. doi: 10.1126/science.1242454
42. Sinclair LV, Rolf J, Emslie E, Shi YB, Taylor PM, Cantrell DA. Control of amino-acid transport by antigen receptors coordinates the metabolic reprogramming essential for T cell differentiation. *Nat Immunol.* (2013) 14:500–8. doi: 10.1038/ni.2556
43. Frauwirth KA, Riley JL, Harris MH, Parry RV, Rathmell JC, Plas DR, et al. The CD28 signaling pathway regulates glucose metabolism. *Immunity.* (2002) 16:769–77. doi: 10.1016/s1074-7613(02)00323-0
44. Pearce EL, Pearce EJ. Metabolic pathways in immune cell activation and quiescence. *Immunity.* (2013) 38:633–43. doi: 10.1016/j.immuni.2013.04.005
45. O'Neill LA, Hardie DG. Metabolism of inflammation limited by AMPK and pseudo-starvation. *Nature.* (2013) 493:346–55. doi: 10.1038/nature11862
46. Pearce EL, Walsh MC, Cejas PJ, Harms GM, Shen H, Wang LS, et al. Enhancing CD8 T-cell memory by modulating fatty acid metabolism. *Nature.* (2009) 460:103–7. doi: 10.1038/nature08097
47. Shackelford DB, Shaw RJ. The LKB1-AMPK pathway: metabolism and growth control in tumour suppression. *Nat Rev Cancer.* (2009) 9:563–75. doi: 10.1038/nrc2676
48. Rao RR, Li Q, Odunsi K, Shrikant PA. The mTOR kinase determines effector versus memory CD8+ T cell fate by regulating the expression of transcription factors T-bet and eomesodermin. *Immunity.* (2010) 32:67–78. doi: 10.1016/j.immuni.2009.10.010
49. Weiss G, Wachter H, Fuchs D. Linkage of cell-mediated immunity to iron metabolism. *Immunol Today.* (1995) 16:495–500. doi: 10.1016/0167-5699(95)80034-4
50. Pavlov VA, Tracey KJ. The vagus nerve and the inflammatory reflex–linking immunity and metabolism. *Nat Rev Endocrinol.* (2012) 8:743–54. doi: 10.1038/nrendo.2012.189

51. Peranzoni E, Marigo I, Dolcetti L, Ugel S, Sonda N, Taschin E, et al. Role of arginine metabolism in immunity and immunopathology. *Immunobiology.* (2007) 212:795–812. doi: 10.1016/j.imbio.2007.09.008
52. Lagishetty V, Liu NQ, Hewison M. Vitamin D metabolism and innate immunity. *Mol Cell Endocrinol.* (2011) 347:97–105. doi: 10.1016/j.mce.2011.04.015
53. Kidd MT, Ferket PR, Qureshi MA. Zinc metabolism with special reference to its role in immunity. *Worlds Poult Sci J.* (1996) 52:309–24. doi: 10.1079/wps19960022
54. Meng PH, Raynaud C, Tcherkez G, Blanchet S, Massoud K, Domenichini S, et al. Crosstalks between myo-inositol metabolism, programmed cell death and basal immunity in Arabidopsis. *PLoS One.* (2009) 4:e7364. doi: 10.1371/journal.pone.0007364
55. Potthoff MJ, Boney-Montoya J, Choi M, He T, Sunny NE, Satapati S, et al. FGF15/19 regulates hepatic glucose metabolism by inhibiting the CREB-PGC-1alpha pathway. *Cell Metab.* (2011) 13:729–38. doi: 10.1016/j.cmet.2011.03.019
56. Choe M, Brusgard JL, Chumsri S, Bhandary L, Zhao XF, Lu S, et al. The RUNX2 transcription factor negatively regulates SIRT6 expression to alter glucose metabolism in breast cancer cells. *J Cell Biochem.* (2015) 116:2210–26. doi: 10.1002/jcb.25171
57. Nagel AK, Ball LE. O-GlcNAc modification of the runt-related transcription factor 2 (Runx2) links osteogenesis and nutrient metabolism in bone marrow mesenchymal stem cells. *Mol Cell Proteomics.* (2014) 13:3381–95. doi: 10.1074/mcp.M114.040691
58. Song Y, Zhang K, Dong L, Guo Y, Wang D, Cui M, et al. Inhibition of EGFR-induced glucose metabolism sensitizes chondrosarcoma cells to cisplatin. *Tumor Biol.* (2014) 35:7017–24. doi: 10.1007/s13277-014-1902-4

Conflict of Interest: The authors declare that the research was conducted in the absence of any commercial or financial relationships that could be construed as a potential conflict of interest.

frontiers | Frontiers in Medicine

ORIGINAL RESEARCH
published: 23 May 2022
doi: 10.3389/fmed.2022.906001

Construction and Analysis of a Joint Diagnosis Model of Random Forest and Artificial Neural Network for Obesity

Jian Yu[1], Xiaoyan Xie[1], Yun Zhang[1], Feng Jiang[2] and Chuyan Wu[1]**

[1] Department of Rehabilitation Medicine, The First Affiliated Hospital of Nanjing Medical University, Nanjing, China,
[2] Department of Neonatology, Obstetrics and Gynecology Hospital of Fudan University, Shanghai, China

Obesity is a significant global health concern since it is connected to a higher risk of several chronic diseases. As a consequence, obesity may be described as a condition that reduces human life expectancy and significantly impacts life quality. Because traditional obesity diagnosis procedures have several flaws, it is vital to design new diagnostic models to enhance current methods. More obesity-related markers have been discovered in recent years as a result of improvements and enhancements in gene sequencing technology. Using current gene expression profiles from the Gene Expression Omnibus (GEO) collection, we identified differentially expressed genes (DEGs) associated with obesity and found 12 important genes (CRLS1, ANG, ALPK3, ADSSL1, ABCC1, HLF, AZGP1, TSC22D3, F2R, FXN, PEMT, and SPTAN1) using a random forest classifier. ALPK3, HLF, FXN, and SPTAN1 are the only genes that have never been linked to obesity. We also used an artificial neural network to build a novel obesity diagnosis model and tested its diagnostic effectiveness using public datasets.

Keywords: obesity, gene sequencing technology, random forest classifier, artificial neural network, diagnosis model

Edited by:
Fu Wang,
Xi'an Jiaotong University, China

Reviewed by:
Zhouxiao Li,
Ludwig Maximilian University of Munich, Germany
XIN LIAO,
Affiliated Hospital of Zunyi Medical College, China

****Correspondence:***
Feng Jiang
dxyjiang@163.com
Chuyan Wu
chuyan_w@hotmail.com

Specialty section:
This article was submitted to Precision Medicine, a section of the journal Frontiers in Medicine

Received: *28 March 2022*
Accepted: *19 April 2022*
Published: *23 May 2022*

Citation:
Yu J, Xie X, Zhang Y, Jiang F and Wu C (2022) Construction and Analysis of a Joint Diagnosis Model of Random Forest and Artificial Neural Network for Obesity. Front. Med. 9:906001. doi: 10.3389/fmed.2022.906001

INTRODUCTION

Obesity, defined by the European Association for the Study of Obesity (EASO) (1), as an adiposity-related chronic illness, is a continuing global health concern because it is frequently linked to increased risks for a variety of chronic illnesses, including hypertension, type 2 diabetes (T2D), and cardiovascular disease (CVD). As a consequence, obesity may be described as a condition that reduces human life expectancy and significantly impacts life quality. Obesity has a complicated etiology, with environmental, social, physiological, medicinal, behavioral, genetic, epigenetic, and other variables all contributing to cause and development (2). Obesity has surged globally in the previous two decades, according to a study, and is spreading like an epidemic illness.

Obesity is categorized into two types: physical obesity and feeding obesity. Simple obesity seems to be the most prevalent kind. Secondary obesity is defined by excessive fat stores in the body, but it also has the clinical signs of primary illness. It is induced by hormonal or metabolic abnormalities. Drugs that cause gaining weight as a side effect are becoming more widely used, which contributes to drug-induced obesity. As a result, the therapies for these three forms of obesity are distinct. Obesity is traditionally treated with behavioral modification, medication therapy, and weight reduction surgery. Weight reduction surgery, which would be a risky invasive operation, is the only long-term therapy. Obesity and diabetes are now being treated using neuromodulation techniques which include vagal nerve stimulation as well as intestinal electrical stimulation.

Obesity diagnostic procedures that are routinely utilized have certain drawbacks. Currently, BMI (body mass index) is by far the most widely used metric for determining obesity. However, a BMI diagnosis alone will not be able to determine the site of fat distribution (3). The WHO included waist circumference as just a criterion of abdominal adiposity in its obesity categorization paradigm because it offered extra information about the risk of CVD as a consequence of the BMI category (4). It's worth noting that BMI, as well as waist circumference cut-offs, change by ethnicity since these measurements are associated with a higher risk of heart illness and diabetes in distinct ways (5–9). As a result, new diagnostic models must be developed to enhance current procedures.

The fast advancement of 2nd sequencing technology has aided in the discovery of marker genes linked to a wide range of disorders in recent years, laying a strong basis for the creation of a novel gene-related diagnostic approach for obesity. In this work, we searched the gene expression comprehensive database (GEO) for differentially expressed genes (DEGs) between obese patients' fat samples and normal fat samples. We apply the random forest approach to determine the important genes activated in obesity based on this DEGs data. Then, using an artificial neural network, we built a genetic diagnostic model of obesity based on these critical genes (see the analysis process in **Figure 1**).

MATERIALS AND METHODS

Downloading and Analyzing Data

Gene Expression Omnibus (GEO, http://www.ncbi.nlm.nih.gov/geo) was used to find DEGs. The following were the selection criteria: **Table 1** shows the expression pattern and clinical phenotypic data from chip datasets GSE24883, GSE25401, as well as RNA-seq datasets GSE156909 and GSE159924, that were downloaded using the query tool. The GEO database was used to collect the annotation data for the chip probes of the appropriate platforms. Multiple probes were identified to match one gene symbol during the translation of chip probe ID as well as the gene symbol. The median probe expression was taken as the level of gene expression in this situation.

Differentially Expressed Genes and Enrichment Investigation

A differential study was made on 34 lean and 38 obese GSE24883 and GSE25401 samples using the R software package limma. To filter DEGs, the limma software tool employs traditional Bayesian data analysis. For DEGs, the significant thresholds were established at an adjusted *P*-value of <0.05 and a log Fold Chang (logFC) larger than 1. The heatmap of DEGs was created using the heatmap software program. We used the R package cluster profile to undertake GO function enrichment analysis as well as KEGG enrichment analysis on associated genes, and we found three kinds of significantly enriched GO terms ($P < 0.05$) and considerably enriched pathways ($P < 0.05$) using metascope cluster analysis (http://metascape.org/gp/index,html).

Construction of Protein-Protein Interaction (PPI)-Network

In the sting database (https://www.string-db.org/), we utilized the screened differential genes to create a PPI network. The interaction score for the PPI network's minimum requirement is set at 0.4. Simultaneously, while constructing a PPI network, we conceal solitary points that are not connected.

Random Forest Screening for DEGs

For the DEGs, the Random Forest software tool was utilized to create a random forest model. Firstly, the average model inaccuracy rate for all genes was estimated using out-of-band data. The optimal variable value for the binary tree in the node has been set to 6, and the best number of trees in the random forest was decided to be 500. The dimensional effect size from the random forest model then was determined using the diminishing accuracy approach (Gini coefficient method). For the ensuing model development, illness genetic factors with an essential point larger than 1.2 were picked. The unstructured hierarchical groups of the 12 significant genes in the merging dataset were reclassified and a heatmap was produced using the freeware tool pheatmap.

Modeling of an Artificial Neural Network

For neural network-based training, the GSE24883 and GSE25401 merging datasets were used. The R software package neural net has been used to develop a deep learning model of the main variables after the data was standardized to the maximum and lowest values. The model parameters for constructing an obese classification model using the collected gene weight information were set at four hidden layers. The illness classification score was calculated using the sum of the weight scores scaled by the differential expression of the key genes in this model. The validation outcomes of AUC classification results were then calculated using the pROC software tool.

Evaluation of AUC

The validity of the categorization score model of slim and obese samples is evaluated using the following data sets (the merging dataset of GSE156906 and GSE159924). To check the classification efficiency, use the proc software tool to build the ROC curve for each and compute the area under the Curve. Simultaneously, the appropriate ROC curve threshold was determined, as well as the specificity and sensitivity of categorizing obese and healthy samples under this threshold.

Estimation of the Immune Landscape and Correlation Test

Using the R package "complot" with 1000 permutations, CIBERSORT (https://cibersortx.stanford.edu/) has been used to infer the 22 immune-cell values in the obese cohort by analyzing the proportion of patients with the transcription of Leukocyte signature matrix (LM22) core genes. Cases with a

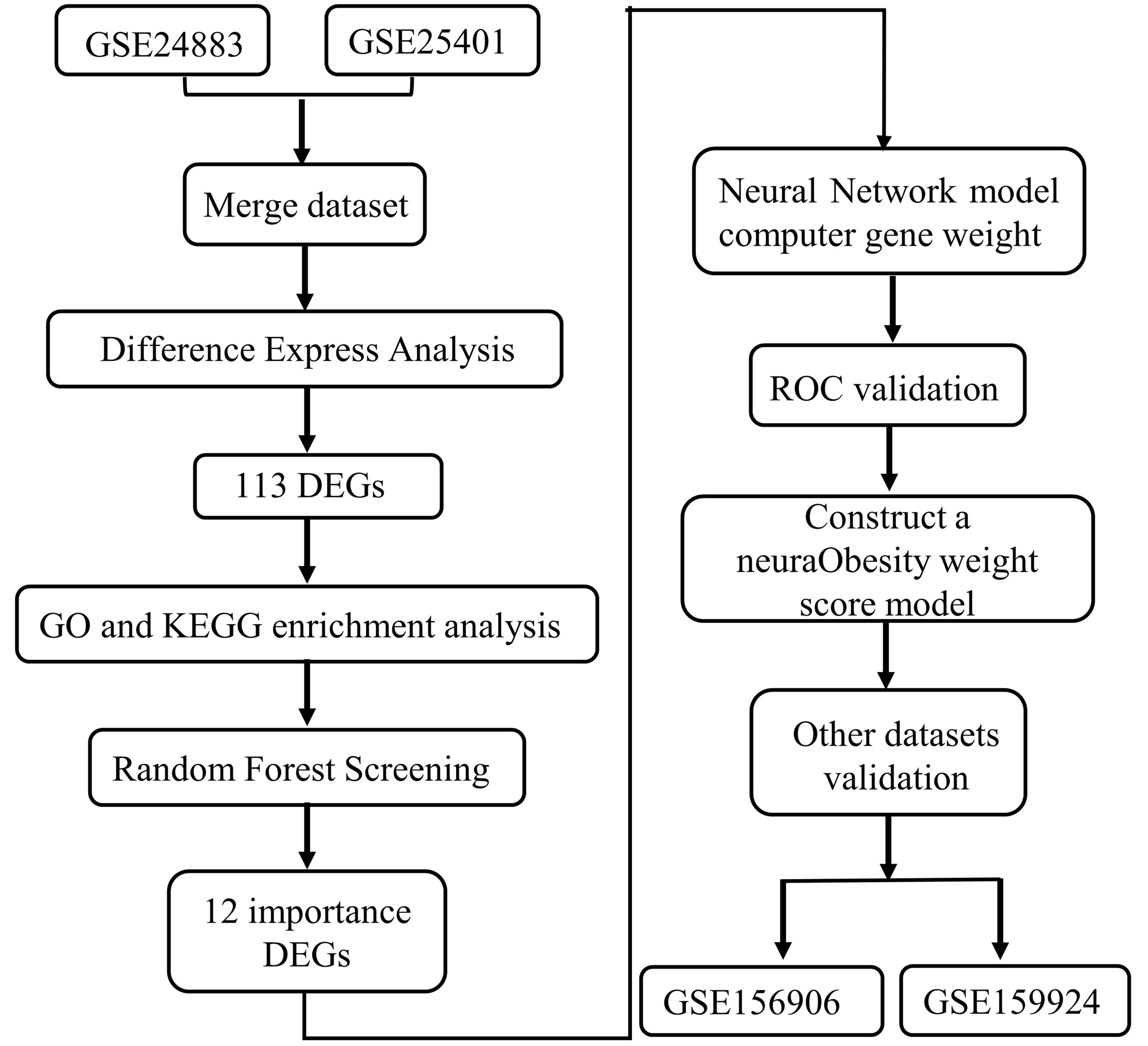

FIGURE 1 | Flowchart.

TABLE 1 | Data download.

ID	GSE number	Data type	Samples	Source type	Group
1	GSE24883	Microarray	8Lean8Obesity	subcutaneous adipose tissue	Discovery cohort
2	GSE25401	Microarray	26Lean30Obesity	subcutaneous adipose tissue	Discovery cohort
3	GSE156906	RNA-Seq	14Lean28Obesity	subcutaneous adipose tissue	Validation cohort
4	GSE159924	RNA-Seq	12Lean21Obesity	subcutaneous adipose tissue	Validation cohort

CIBERSORT result of $P < 0.05$ were selected for the following analysis. Violin plots were constructed in R using the "vioplot" package to show the differences in immune-cell infiltration between the two groups. The association between the found gene indication and the quantity of invading immune cells was investigated using Spearman's correlation research in R. The charm method of the "ggplot2" package was used to depict the resulting correlations.

RESULT

Identification of DEGs

The Bayesian test was utilized to discover DEGs between obese chip dataset samples and lean control samples using the limma program. The DEGs' findings are depicted in the volcano diagram (**Figure 2A**) as well as the heatmap (**Figure 2B**). The search found 113 significant DEGs associated with obesity depending on fold change values of >1 as well as a significance threshold of $P < 0.05$ (**Supplementary File 1**).

Metascape Analysis of DEGs

The matescape database was used to enrich and evaluate differential genes. GO Biological Processes, KEGG Pathway, Canonical Pathways, Cell Type Signatures, Reactome Gene Sets, CORUM, TRUST, DisGeNET, PaGenBase, Transcription Factor Targets, WikiPathways, PANTHER Pathway, and COVID were used to enrich the DEGs list using pathway and process enrichment investigation. The enrichment background was made up of every gene in the genome. Terms having a p-value < 0.01, a baseline count of 3, and contributing factors more than 1.5 (the maximum enhancement is the proportion between the known numbers and the counts anticipated by chance) are gathered and classified depending on membership commonalities. The top 20 words from the matescape enrichment analysis are shown in **Figures 3A,B**. **Supplement File 2** contains the findings of the route and process enrichment study.

Enrichment Analysis in Samples From Obese Patients and Lean People

The cluster profile software was used to conduct GO enrichment analysis on the 113 noteworthy DEGs. The Benjamini–Hochberg correction technique was applied, with the P and Q levels set at 0.05 and 0.05, respectively. We conducted compression on the GO enrichment words and excluded phrases with a gene overlap of >0.75 to prevent repetition in the GO enrichment findings. The findings of 3 areas of GO enrichment are shown in **Figure 4**. **Figure 4A** displays the GO enrichment findings for all three categories (only the –log10 (adj P) >5 GO terms are presented). Protein kinase B signaling, leukocyte chemotaxis, cell chemotaxis, modulation of protein kinase B signaling, and myeloid leukocyte migration are among the associated biological processes implicated in obesity, according to the findings. Cell leading edge and collagen-containing cellular components are involved. Integral interaction and other critical activities were among the molecular functionalities. Parts of the GO enriched words and the key DEGs implicated are shown in **Figures 4B,C**. On the DEGs, we also ran a KEGG pathway enrichment analysis. **Figures 4D–F** demonstrate the findings of substantially enriched biological KEGG pathways implicated, as well as the accompanying DEGs.

Random Forest Tree Screening

The random forest algorithm received the 113 DEGs. We did a recurrent random forest categorization for all possible values among the 1–113 factors and estimated the mean error rate of the model to determine the ideal parameter mtry (that is, to describe the best number of factors for the binary trees inside the nodes). As the variable number's argument, we picked 12. The set of variables was kept to a minimum, and out-of-band error was kept to an absolute minimum. We chose 500 trees as the variable of the final model based on the association plot between both the model uncertainties and the number of selection trees (**Figure 5A**), which demonstrated a steady error. The variable relevance of the output findings (Gini coefficient method) was assessed in the context of decreasing accuracy and decreasing mean square error throughout the construction of the random forest model (see **Supplementary File 3** for the important output results). The potential genes for further investigation were then identified as twelve DEGs with a significance larger than 1.2. **Figure 5B** demonstrates that ALPK3, ADSSL1, ABCC1, ANG, CRLS1, HLF, AZGP1, TSC22D3, F2R, FXN, PEMT, and SPTAN1 were the most significant of the twelve variables. We used k-means unsupervised clustering to cluster the merging dataset using these twelve critical factors. The twelve genes might be utilized to differentiate between illness and normal samples, as shown in **Figure 5C**. FXN, SPTAN1, ABCC1, F2R, and PEMT are a group of genes with low or undetectable positive control and reach this point in treated samples. CRLS1, ANG, ALPK3, ADSSL1, HLF, AZGP1, and TSC22D3, on the other hand, belong to a different cluster, having a high level of expression in healthy samples but a low level of expression in ill samples.

Constructing an Artificial Neural Network Model

We utilized the GSE24881 and GSE25403 merging datasets to build an artificial neural network model using the neural net package. Data preparation was the initial phase, which was used to standardize the data. To segregate the magnification information before training the network, the min-max technique [0,1] was chosen and pushed. The maximum and lowest data values were normalized before the computation began, and the number of hidden layers was set to 5. There was no set guideline for how many layers and neurons to employ when choosing parameters. The number of neurons should be around two-thirds of the input layer size and one-third of the output layer size. As a result, the number of neurons parameter was adjusted to 12. A training data set and a validation set was created at random from the dataset. The objective of the training group was to figure out how much each candidate's DEG was worth. The validation set was utilized to test the model score's classification performance using the expression of genes and gene weight. The following is the formula for calculating the categorization score of the produced illness neural network model: $\text{neuraObesity} = \sum(\text{Gene Expression} \times \text{Neural Network Weight})$ (**Figure 6A**). To create the neural network model, we utilize all of the data. The experimental group demonstrated that the model's area under the ROC curve (AUC) was near 1 (average AUC > 0.99), indicating that it was robust. To check that the area under the ROC curve (AUC) remains near 0.9, we examined the merged data sets of two more data sets, GSE156906 and GSE159924 (**Figures 6B,C**).

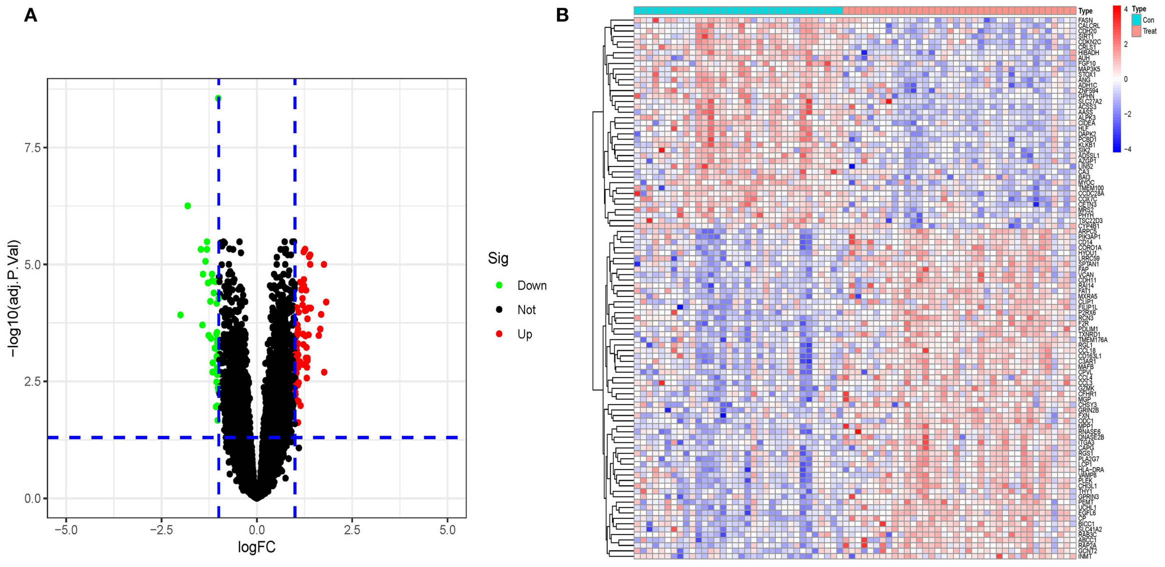

FIGURE 2 | (A) A volcano plot representing the findings of differential expression investigation. The remaining functional genes are shown by the black dots. **(B)** A DEG heatmap. The graph's hues, which range from red to green, represent high to low expressiveness. The red band in the top half of the heatmap represents illness samples, whereas the blue band represents normal samples.

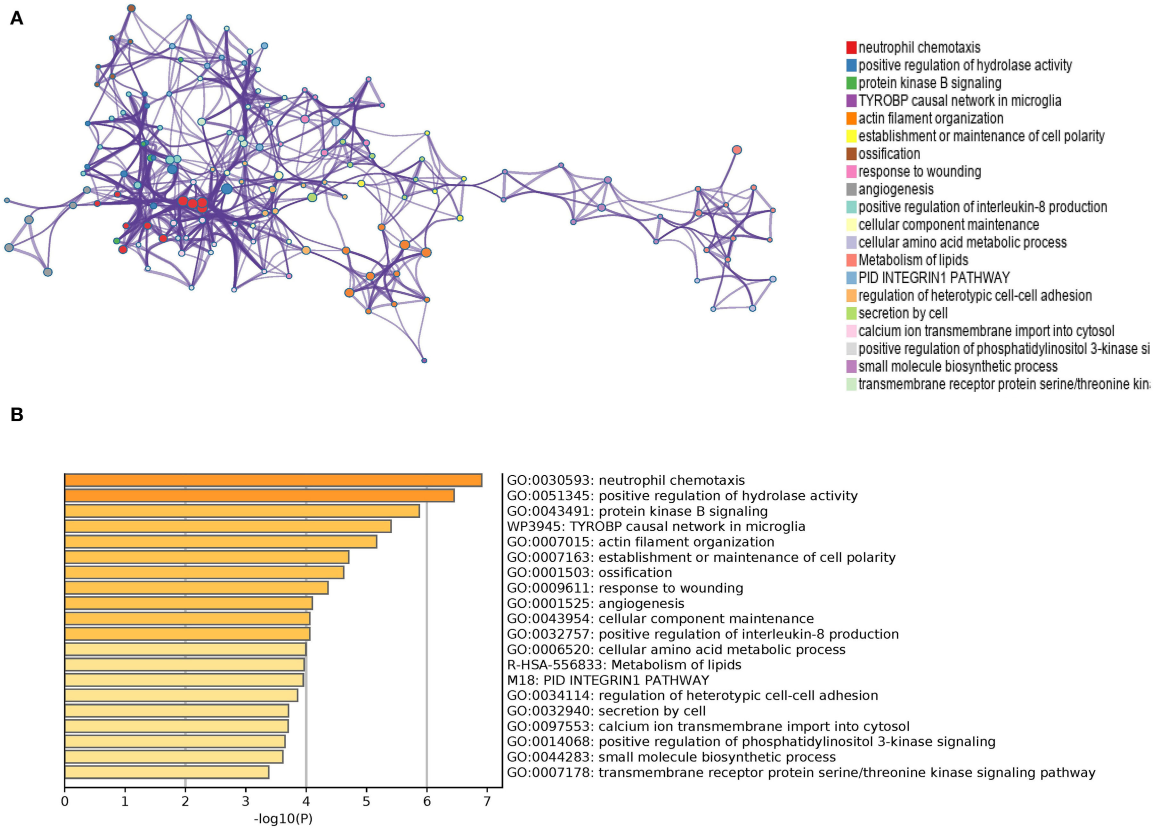

FIGURE 3 | (A) An enhanced terms network. Cluster-ID is used to color the notes, and notes with the same cluster-ID are often closer to one other. **(B)** *P*-Value-colored bar graph of enhanced phrases across DEGs lists.

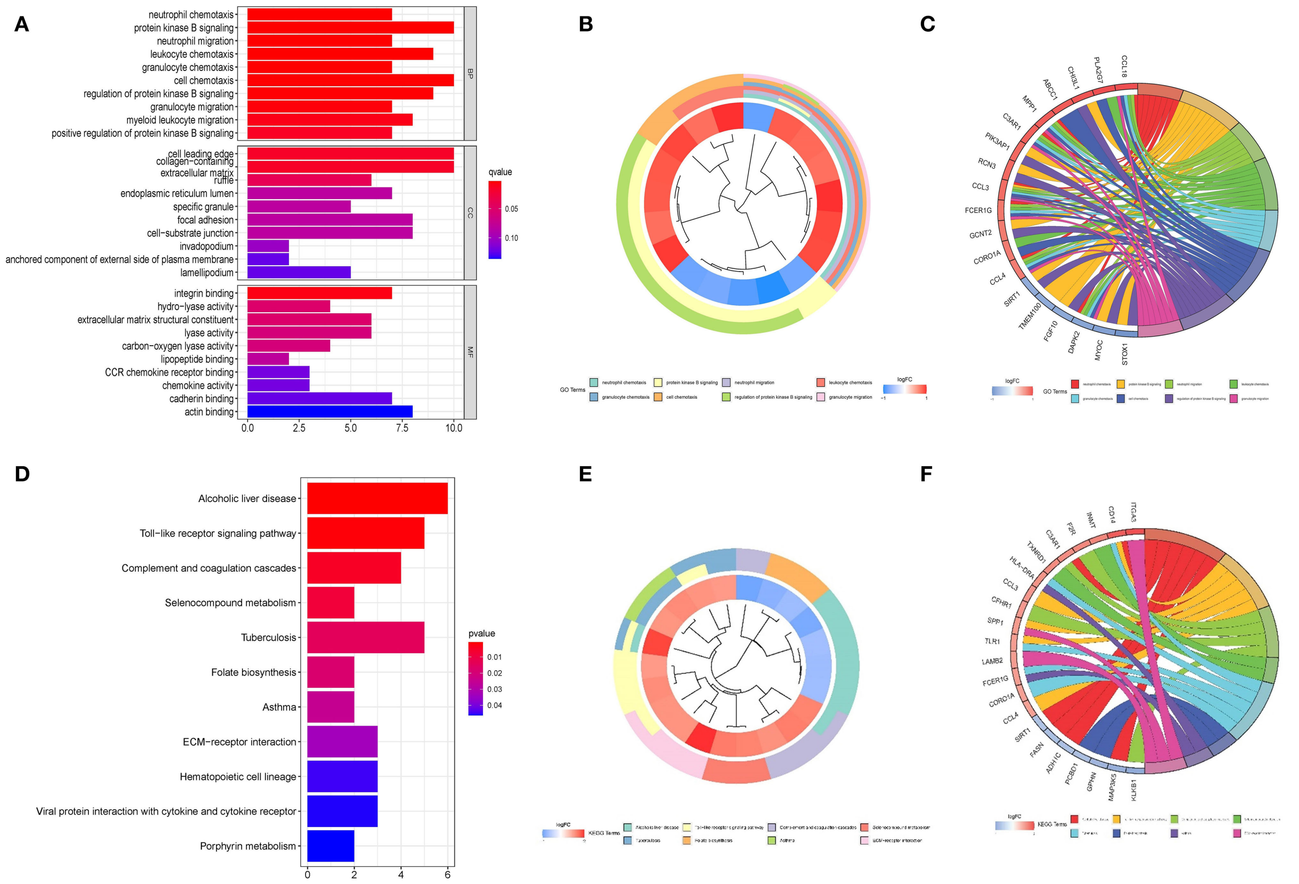

FIGURE 4 | Graph depicting the findings of the enrichment analysis. **(A)** GO enrichment findings in a bar graph. The *z*-score is shown on the *x*-axis, while the log 10 (adj *P*) values are represented on the *y*-axis. **(B)** Gene clustering circle: the inner circle indicates DEGs, the red circle represents up-regulated genes, the blue circle indicates down-regulated genes, and the outside circle represents GO keywords. **(C)** GO enrichment ring plot. The DEGs are shown on the left, with the red gene band indicating upregulation and the blue gene band indicating downregulation. The right-hand band, which is colored differently, indicates several GO concepts. The gene's inclusion in the GO word is shown by the connecting line. **(D)** KEGG pathway enrichment findings in a bubble chart. The z-score is shown on the x-axis, while the log 10 (adj *P*) value is represented on the y-axis. A KEGG pathway is represented by a bubble, the size of which indicates the number of genes in the route. The route enrichment findings in the figure with a log 10 (adj *P*) > 1.3 ($P < 0.05$) are highlighted and listed in the table. **(E)** Gene clustering circle: the inner circle indicates DEGs, the red circle represents up-regulated genes, the blue circle indicates down-regulated genes, and the outside circle represents KEGG terms. **(F)** KEGG pathway enrichment ring plot. The DEGs are shown on the left side, with red gene bands indicating upregulation and blue gene bands indicating downregulation. Distinct colored bands on the right-hand side symbolize different paths. The gene's involvement in the route is shown by the connecting line.

Immune Landscape Associated With the Characteristics of Obesity Patients

Immune-related networks were enhanced in the obese sample vs. in the lean category, according to functional enrichment analysis. Adipose tissue genomic information from the fusion dataset of GSE24881 and GSE25403 has been processed to investigate the immune landscape differences between obese patients and lean persons. The proportion of 22 distinct types of immune cells in the data was also calculated using the program CIBERSORTx. CIBERSORTx is an online tool that determines the relative quantity of immune adult tissues using a background subtraction algorithm. The location of 22 distinct immune cell types in obese and thin subjects is shown in **Figure 7A**. We compared the relationship between immune cells with Spearman's correlation analysis. The largest positive connection, $R = 0.84$, was found between T cells CD4 naïve and T cells gamma delta, whereas the strongest negative correlation, $R = -0.64$, was found between T cells CD4 memory resting and T cells CD8 (**Figure 7B**). In addition, the proportion of B cells with memory was significantly lower ($P = 0.012$) in the obese group than in the no-obese group (**Figure 7C**).

DISCUSSION

For the first time, we computed DEGs associated with obesity and discovered twelve key candidate DEGs using the classifier model in this work. We employed a neural network model to compute the anticipated weights of linked genes, create the neuraObesity classification model score, and test the model score's classification performance in 2 autonomous sample

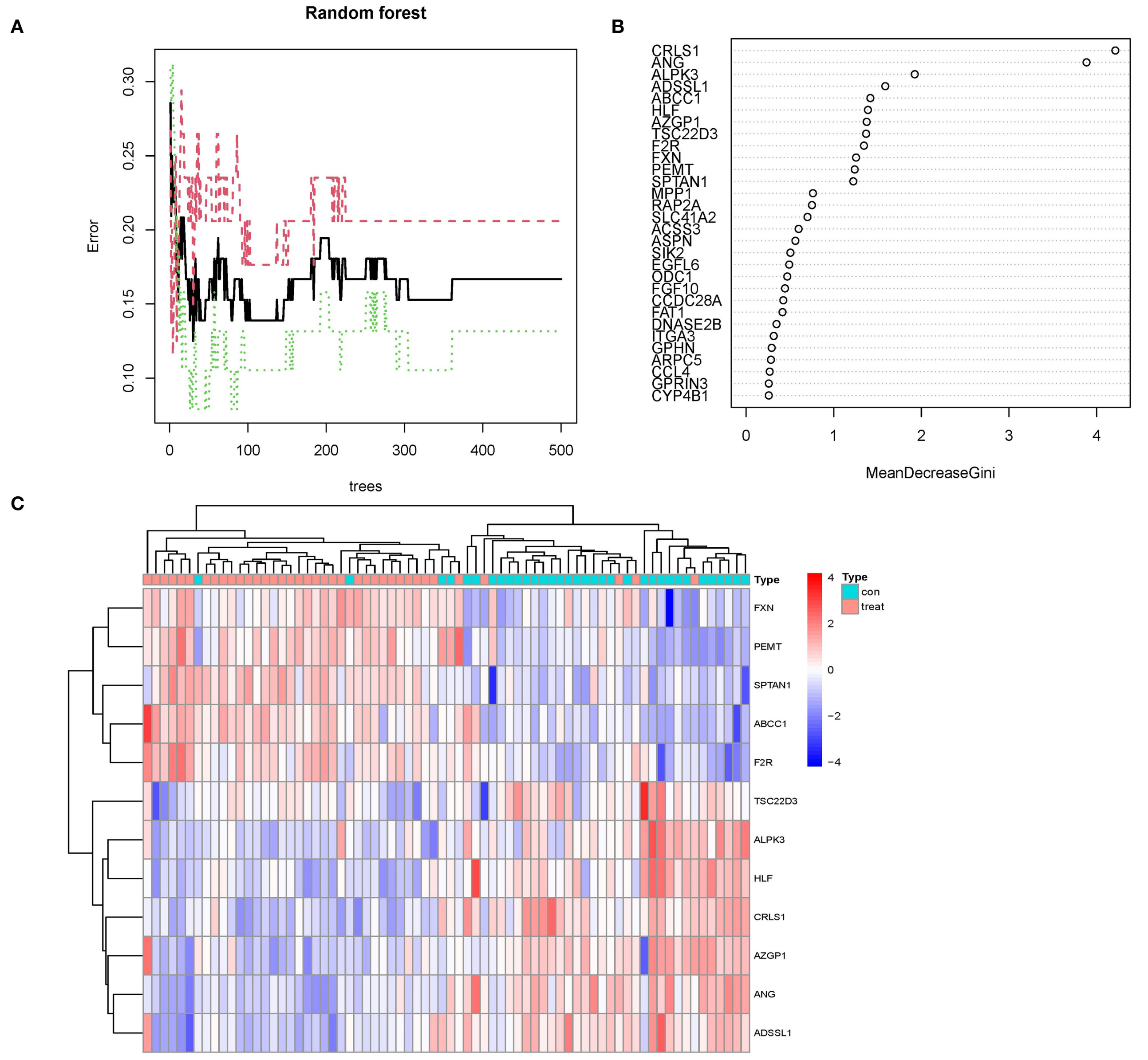

FIGURE 5 | (A) The mistake rate is influenced by the number of selection trees. The amount of decision trees is shown on the *x*-axis, while the mistake rate is represented on the *y*-axis. **(B)** Random forest classifier results using the Gini coefficient approach. **(C)** Unsupervised clustering heatmap demonstrating the hierarchical clustering formed by the twelve significant genes created by the random forest in the GSE24881 and GSE25403 merging dataset. The red band on the upper portion of the heatmap suggests normal samples, while the blue band indicates obesity disorder samples. Red color demonstrates genes with elevated expression in the samples, the blue color implies genes with low or undetectable in the samples.

datasets. The AUC efficiency was outstanding, and it was discovered that neuraObesity had a high classification efficiency.

CRLS1 is a variation linked with insulin resistance, and adipose CRLS1 expression positively connects with insulin sensitivity among these twelve genes. By reducing the expression and activity of ATF3, CRLS1 reduces insulin resistance, hepatic steatosis, inflammation, and fibrosis during the pathological phase of non-alcoholic steatohepatitis (NASH) (10, 11). The angiotensin-angiotensin system is a critical regulator of metabolism, with the angiotensin 1-7 (ANG 1-7) peptide having positive effects. Treatment with ANG 1-7 lowered body weight, increased thermogenesis, and improved glucose homeostasis without changing food intake. Paternal inflammation-induced metabolic abnormalities in children are linked to ANG-mediated synthesis of 5'-tsRNAs in sperm, and offspring of inflamed fathers have metabolic diseases such as glucose intolerance and obesity (12, 13).

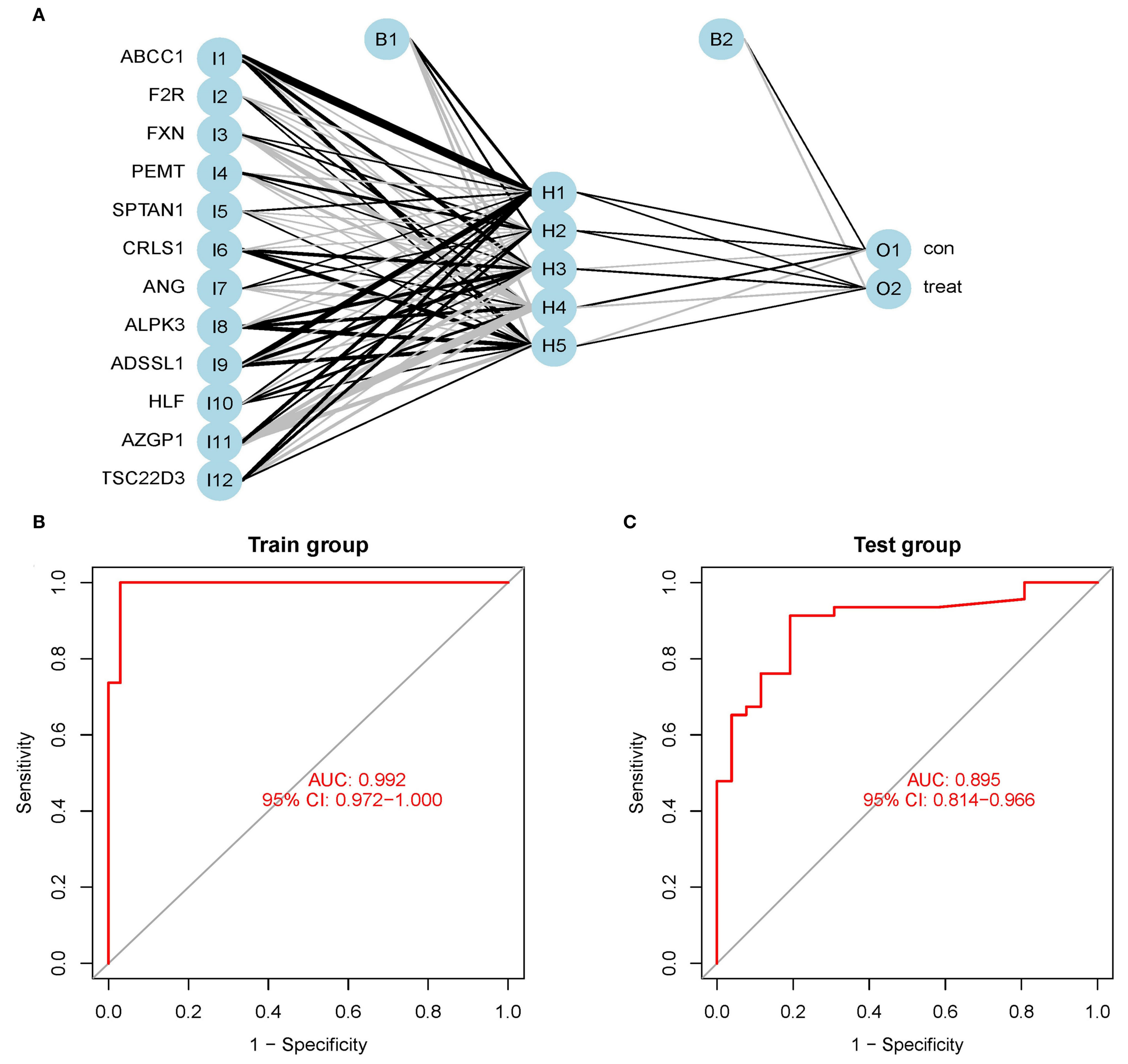

FIGURE 6 | (A) Neural network visualization results. **(B)** The training group verifies the ROC curve findings (merge dataset of GSE24881 and GSE25403). **(C)** The testing group verifies the ROC curve findings (merge dataset of GSE156906 and GSE159924).

ABCC1 is a protein found in human adipocytes. ABCC1 mRNA is increased in adult adipose tissue, while tissue plasma cortisol concentrations are continuously low (14, 15). In the epidemic of obesity, AZGP1 is implicated in polygenic traits and age-dependent alterations in the genetic regulation of obesity. Reduced AZGP1 expression resulted in a considerable increase in lipogenic gene expression, resulting in increased serum lipid in KD cells. By negatively regulating TNF-α, AZGP1 reduces the severity of Nonalcoholic fatty liver disease (NAFLD) by lowering inflammation, speeding lipolysis, boosting proliferation, and minimizing apoptosis. AZGP1 has been proposed as a potential new treatment target for NAFLD. Circulating AZGP1 has been linked to polycystic ovary syndrome (PCOS) and might be a significant adipokine in the onset and progression of PCOS. A large number of literatures have confirmed that PCOS is closely related to obesity and insulin resistance (16). AZGP1 might be used as a novel observational biomarker in the management of PCOS patients. AZGP1 levels in the blood are lower in women with PCOS, and AZGP1 could be a cytokine linked to insulin resistance in PCOS patients (17–21). Adipogenesis was aided by the coagulation factor II thrombin receptor (F2R), which encodes coagulation factor II. Obesity, T2D, steatosis, atherosclerosis,

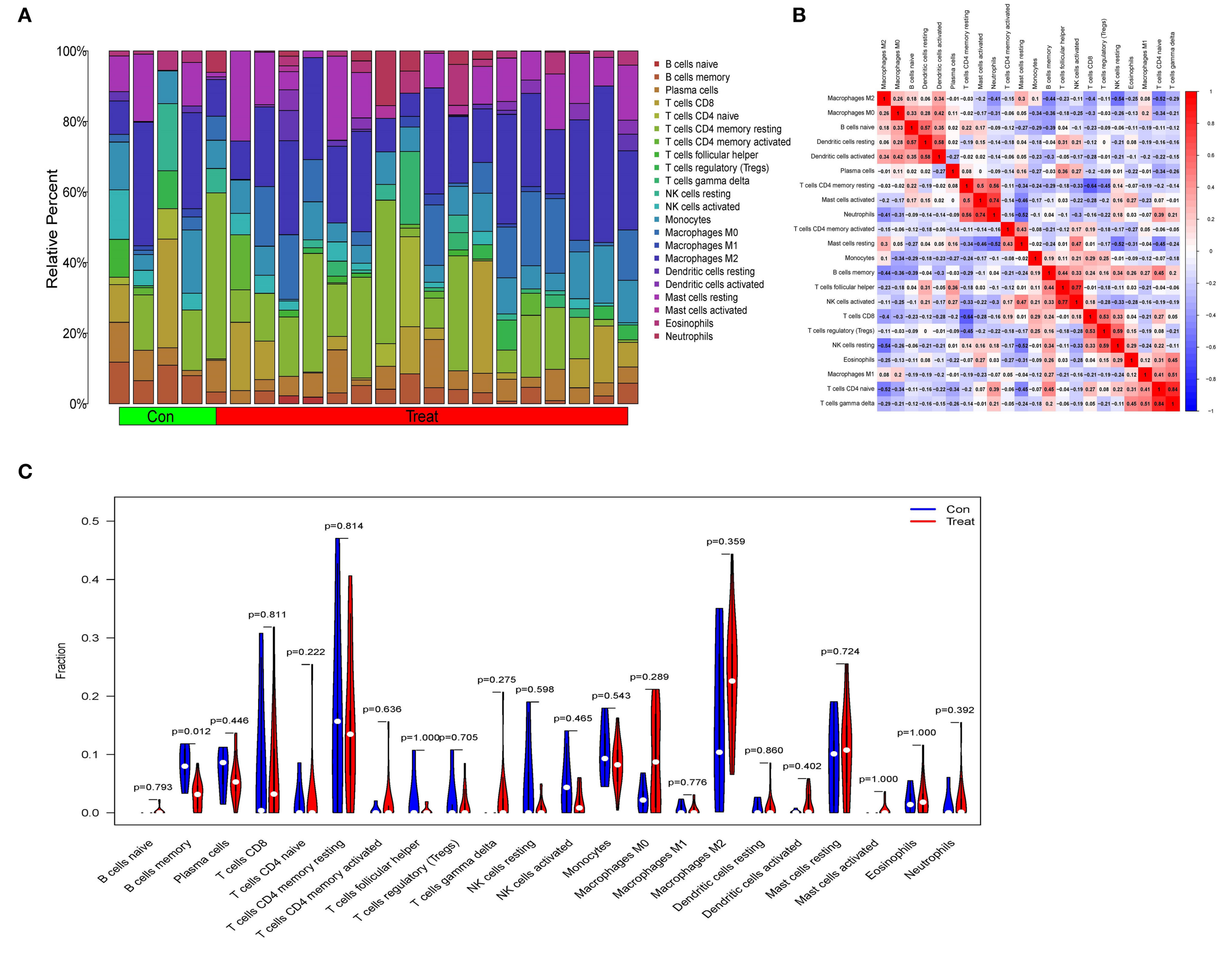

FIGURE 7 | An examination of the immunological landscape of obesity. **(A)** Overview of predicted proportions of 22 immune-cell categories in con and treat groups using the CIBERSORT algorithm. **(B)** Correlation analysis of infiltrating immune cells. **(C)** Con and treat groups were compared on 22 immune-cell subtypes.

as well as osteoporosis are all metabolic disorders, and the gene F2R might be exploited as an adipogenic marker to give a possible target for understanding them. F2R was identified as a potentially relevant biomarker related to the polycystic ovarian syndrome as a result of the PCOS pathway network that was created (PCOS) (22, 23). PEMT is a tiny integral membrane protein that transforms phosphatidylethanolamine (PE) to phosphatidylcholine (PC). PEMT knockdown prevented lipid droplet formation, lowered triacylglycerol concentration, and decreased leptin release from adipocytes (24–26). Fat migration into the periphery of the vast lateral, gastrocnemius, as well as soleus muscles, was seen in all ADSSL1 myopathy patients, as were increased lipid droplets (27).

Interestingly, none of the following four genes (ALPK3, HLF, FXN, and SPTAN1) have been shown to be involved in obesity-related disorders. Familial cardiomyopathy may be caused by ALPK3 mutations. Cardiomyocytes missing ALPK3 may have abnormal calcium handling, offering useful insights into the molecular processes driving ALPK3-mediated cardiomyopathy (28). HIF-2 activates the production of hypoxia-inducible, lipid droplet-associated protein in renal CCCs, which preferentially enriches polyunsaturated lipids, the rate-limiting precursors for lipid peroxidation (HILPDA) (29). Friedreich's ataxia (FRDA) is a neurological illness with T2D as severe comorbidity caused by reduced expression of mitochondrial frataxin (FXN). Hyperlipidemia, impaired energy expenditure, insulin sensitivity, as well as higher plasma leptin are all shown in the FXN knock-in/knock-out (KIKO) mouse, which mimics T2D-like symptoms. In BAT, FXN deficiency causes mitochondrial ultrastructure disruption, oxygen consumption, and lipid buildup (30). SPTAN1 is a potential gene for ataxia and spastic paraplegia, and also the disruption of spectrin helices' interlinking might be a crucial aspect of the pathomechanism for the mutations (31).

The majority of research have shown that proinflammatory T lymphocytes and macrophages play a key role in insulin resistance (IR) induced by visceral adipose tissue inflammation (VAT) (32). The invasion and activation of immune cells define adipose tissue inflammation. Immune cells release cytokines and chemokines, which lead to chronic inflammation and exacerbate the metabolic pathway deterioration associated with obesity.

In obese individuals, CD8 + and Th1 CD4 + T cells enter VAT and stimulate the release of proinflammatory cytokines by M1 macrophages, according to studies (33). B cells are capable of presenting antigens to T cells, secreting proinflammatory cytokines and pathogenic antibodies. Lipolysis products in VAT may activate B cells, causing them to produce proinflammatory mediators and causing systemic and local inflammation. Our findings also indicated that obese persons had more T cells and macrophages, although there was no substantial difference when compared to healthy people. This might be due to the research sample size being too small (34, 35).

The current research contained several flaws. First, we searched DEGs in the GEO database comparing fat tissues from obese patients and normal fat samples without subtyping obese individuals. Second, the clinical applicability of the random forest, as well as the artificial neural network joint diagnostic model for obesity, has to be further evaluated and externally verified. This information will be made available in future research.

Finally, our findings clearly showed that a combined random forest and artificial neural network obesity diagnostic model is acceptable for forecasting obesity occurrence in clinical practice.

DATA AVAILABILITY STATEMENT

The datasets used during the present study are available from GEO (https://www.ncbi.nlm.nih.gov/geo/) database.

AUTHOR CONTRIBUTIONS

CW is the corresponding author of the article who contributes the most. She designed the whole study. YZ and XX collaborated on data curation. Statistical analysis was carried out by FJ and CW. The original draft of the manuscript was completed by JY. CW revised the manuscript. All of the authors approved the final manuscript.

FUNDING

This work was supported by the National Natural Science Foundation of China (Grant No. 82172539) and funded by the Nanjing Municipal Science and Technology Bureau (Grant number of 2019060002). The funding bodies had no role in the study design, data collection, analysis, and interpretation of data.

SUPPLEMENTARY MATERIAL

The Supplementary Material for this article can be found online at: https://www.frontiersin.org/articles/10.3389/fmed.2022.906001/full#supplementary-material

Supplement File 1 | 113 significant DEGs related to obesity.

Supplement File 2 | Results of path and process enrichment analysis.

Supplement File 3 | Results of random forest classifier.

REFERENCES

1. Frühbeck G, Busetto L, Dicker D, Yumuk V, Goossens GH, Hebebrand J, et al. The ABCD of obesity: An EASO position statement on a diagnostic term with clinical and scientific implications. *Obes Facts.* (2019) 12:131–6. doi: 10.1159/000497124
2. Heymsfield SB, Wadden TA. Mechanisms, pathophysiology, and management of obesity. *N Engl J Med.* (2017) 376:254–66. doi: 10.1056/NEJMra1514009
3. Weir CB, Jan A. BMI classification percentile and cut off points. In: *StatPearls [Internet]*. Treasure Island, FL: StatPearls Publishing (2022).
4. Obesity: Preventing and managing the global epidemic. Report of a WHO consultation. *World Health Organ Tech Rep Ser*. (2000) 894:1–253.
5. Hsu WC, Araneta MR, Kanaya AM, Chiang JL, Fujimoto W, BMI. cut points to identify at-risk Asian Americans for type 2 diabetes screening. *Diabetes Care.* (2015) 38:150–8. doi: 10.2337/dc14-2391
6. Katzmarzyk PT, Bray GA, Greenway FL, Johnson WD, Newton RJ, Ravussin E, et al. Ethnic-specific BMI and waist circumference thresholds. *Obesity (Silver Spring).* (2011) 19:1272–8. doi: 10.1038/oby.2010.319
7. He W, Li Q, Yang M, Jiao J, Ma X, Zhou Y, et al. Lower BMI cutoffs to define overweight and obesity in China. *Obesity (Silver Spring).* (2015) 23:684–91. doi: 10.1002/oby.20995
8. Caleyachetty R, Barber TM, Mohammed NI, Cappuccio FP, Hardy R, Mathur R, et al. Ethnicity-specific BMI cutoffs for obesity based on type 2 diabetes risk in England: A population-based cohort study. *Lancet Diabetes Endocrinol.* (2021) 9:419–26. doi: 10.1016/S2213-8587(21)00088-7
9. Hu Y, Zeng N, Ge Y, Wang D, Qin X, Zhang W, et al. Identification of the shared gene signatures and biological mechanism in type 2 diabetes and pancreatic cancer. *Front Endocrinol.* (2022) 13:847760. doi: 10.3389/fendo.2022.847760
10. Elahu GS, Tao M, Matthew DL, Michael L, Iuliia K, Jesper FH, et al. Cardiolipin synthesis in brown and beige fat mitochondria is essential for systemic energy homeostasis. *Cell Metab.* (2018) 28. 159–74.e11. doi: 10.1016/j.cmet.2018.05.003
11. Tu C, Xiong H, Hu Y, Wang W, Mei G, Wang H, et al. Cardiolipin synthase 1 ameliorates NASH through activating transcription factor 3 transcriptional inactivation. *Hepatology.* (2020) 72:1949–67. doi: 10.1002/hep.31202
12. Morimoto H, Mori J, Nakajima H, Kawabe Y, Tsuma Y, Fukuhara S, et al. Angiotensin 1-7 stimulates brown adipose tissue and reduces diet-induced obesity. *Am J Physiol Endocrinol Metab.* (2018) 314:E131–8. doi: 10.1152/ajpendo.00192.2017
13. Zhang Y, Ren L, Sun X, Zhang Z, Liu J, Xin Y, et al. Angiogenin mediates paternal inflammation-induced metabolic disorders in offspring through sperm tsRNAs. *Nat Commun.* (2021) 12:6673. doi: 10.1038/s41467-021-26909-1
14. Zhou S, Wang R, Xiao H. Adipocytes induce the resistance of ovarian cancer to carboplatin through ANGPTL4. *Oncol Rep.* (2020) 44:927–38. doi: 10.3892/or.2020.7647
15. Nixon M, Mackenzie SD, Taylor AI, Homer NZ, Livingstone DE, Mouras R, et al. ABCC1 confers tissue-specific sensitivity to cortisol versus corticosterone: a rationale for safer glucocorticoid replacement therapy. *Sci Transl Med.* (2016) 8:109r—352r. doi: 10.1126/scitranslmed.aaf9074
16. Jiang F, Wei K, Lyu W, Wu C. Predicting risk of insulin resistance in a chinese population with polycystic ovary syndrome: Designing and testing a new predictive nomogram. *Biomed Res Int.* (2020) 2020:8031497. doi: 10.1155/2020/8031497
17. Choi JW, Liu H, Mukherjee R, Yun JW. Downregulation of fetuin-B and zinc-alpha2-glycoprotein is linked to impaired fatty acid metabolism in liver cells. *Cell Physiol Biochem.* (2012) 30:295–306. doi: 10.1159/000339065
18. Gohda T, Makita Y, Shike T, Tanimoto M, Funabiki K, Horikoshi S, et al. Identification of epistatic interaction involved in obesity using the KK/Ta

mouse as a Type 2 diabetes model: Is Zn-alpha2 glycoprotein-1 a candidate gene for obesity? *Diabetes*. (2003) 52:2175–81. doi: 10.2337/diabetes.52.8.2175

19. Zheng S, Liu E, Zhang Y, Long T, Liu X, Gong Y, et al. Circulating zinc-alpha2-glycoprotein is reduced in women with polycystic ovary syndrome, but can be increased by exenatide or metformin treatment. *Endocr J.* (2019) 66:555–62. doi: 10.1507/endocrj.EJ18-0153
20. Lai Y, Chen J, Li L, Yin J, He J, Yang M, et al. Circulating Zinc-alpha2-glycoprotein levels and insulin resistance in polycystic ovary syndrome. *Sci Rep.* (2016) 6:25934. doi: 10.1038/srep25934
21. Liu T, Luo X, Li ZH, Wu JC, Luo SZ, Xu MY. Zinc-alpha2-glycoprotein 1 attenuates non-alcoholic fatty liver disease by negatively regulating tumour necrosis factor-alpha. *World J Gastroenterol.* (2019) 25:5451–68. doi: 10.3748/wjg.v25.i36.5451
22. Yi X, Wu P, Liu J, Gong Y, Xu X, Li W. Identification of the potential key genes for adipogenesis from human mesenchymal stem cells by RNA-Seq. *J Cell Physiol.* (2019) 234:20217–27. doi: 10.1002/jcp.28621
23. Liu L, He D, Wang Y, Sheng M. Integrated analysis of DNA methylation and transcriptome profiling of polycystic ovary syndrome. *Mol Med Rep.* (2020) 21:2138–50. doi: 10.3892/mmr.2020.11005
24. Presa N, Dominguez-Herrera A, van der Veen JN, Vance DE, Gomez-Munoz A. Implication of phosphatidylethanolamine N-methyltransferase in adipocyte differentiation. *Biochim Biophys Acta Mol Basis Dis.* (2020) 1866:165853. doi: 10.1016/j.bbadis.2020.165853
25. Dong H, Wang J, Li C, Hirose A, Nozaki Y, Takahashi M, et al. The phosphatidylethanolamine N-methyltransferase gene V175M single nucleotide polymorphism confers the susceptibility to NASH in Japanese population. *J Hepatol.* (2007) 46:915–20. doi: 10.1016/j.jhep.2006.12.012
26. Watanabe M, Nakatsuka A, Murakami K, Inoue K, Terami T, Higuchi C, et al. Pemt deficiency ameliorates endoplasmic reticulum stress in diabetic nephropathy. *PLoS ONE.* (2014) 9:e92647. doi: 10.1371/journal.pone.0092647
27. Saito Y, Nishikawa A, Iida A, Mori-Yoshimura M, Oya Y, Ishiyama A, et al. ADSSL1 myopathy is the most common nemaline myopathy in Japan with variable clinical features. *Neurology.* (2020) 95:e1500–11. doi: 10.1212/WNL.0000000000010237
28. Phelan DG, Anderson DJ, Howden SE, Wong RC, Hickey PF, Pope K, et al. ALPK3-deficient cardiomyocytes generated from patient-derived induced pluripotent stem cells and mutant human embryonic stem cells display abnormal calcium handling and establish that ALPK3 deficiency underlies familial cardiomyopathy. *Eur Heart J.* (2016) 37:2586–90. doi: 10.1093/eurheartj/ehw160
29. Zou Y, Palte MJ, Deik AA Li H, Eaton JK, Wang W, et al. A GPX4-dependent cancer cell state underlies the clear-cell morphology and confers sensitivity to ferroptosis. *Nat Commun.* (2019) 10:1617. doi: 10.1038/s41467-019-09277-9
30. Turchi R, Tortolici F, Guidobaldi G, Iacovelli F, Falconi M, Rufini S, et al. Frataxin deficiency induces lipid accumulation and affects thermogenesis in brown adipose tissue. *Cell Death Dis.* (2020) 11:51. doi: 10.1038/s41419-020-2253-2
31. Van de Vondel L, De Winter J, Beijer D, Coarelli G, Wayand M, Palvadeau R, et al. *De novo* and dominantly inherited SPTAN1 mutations cause spastic paraplegia and cerebellar ataxia. *Mov Disord.* (2022).
32. Nishimura S, Manabe I, Nagasaki M, Eto K, Yamashita H, Ohsugi M, et al. CD8+ effector T cells contribute to macrophage recruitment and adipose tissue inflammation in obesity. *Nat Med.* (2009) 15:914–20. doi: 10.1038/nm.1964
33. Lumeng CN, Bodzin JL, Saltiel AR. Obesity induces a phenotypic switch in adipose tissue macrophage polarization. *J Clin Invest.* (2007) 117:175–84. doi: 10.1172/JCI29881
34. Winer DA, Winer S, Shen L, Wadia PP, Yantha J, Paltser G, et al. B cells promote insulin resistance through modulation of T cells and production of pathogenic IgG antibodies. *Nat Med.* (2011) 17:610–7. doi: 10.1038/nm.2353
35. Frasca D, Ferracci F, Diaz A, Romero M, Lechner S, Blomberg BB. Obesity decreases B cell responses in young and elderly individuals. *Obesity (Silver Spring).* (2016) 24:615–25. doi: 10.1002/oby.21383

Conflict of Interest: The authors declare that the research was conducted in the absence of any commercial or financial relationships that could be construed as a potential conflict of interest.

frontiers | Frontiers in Medicine

ORIGINAL RESEARCH
published: 16 June 2022
doi: 10.3389/fmed.2022.892593

Identification of Epigenetic-Dysregulated lncRNAs Signature in Osteosarcoma by Multi-Omics Data Analysis

Junchao Huang[†], *Jingwei Zhang*[†] *and Haijun Xiao*[*]

Department of Orthopedics, Anhui University of Science and Technology Affiliated Fengxian Hospital, Shanghai, China

Edited by:
Fu Wang,
Xi'an Jiaotong University, China

Reviewed by:
Xin Chen,
Second Hospital of Hebei Medical University, China
Dandan Yuan,
The Second Affiliated Hospital of Harbin Medical University, China
Ruixiang Tang,
The First Affiliated Hospital of Xi'an Jiaotong University, China

***Correspondence:**
Haijun Xiao
xiaohaijun89@163.com

[†] *These authors have contributed equally to this work*

Specialty section:
This article was submitted to Precision Medicine, a section of the journal Frontiers in Medicine

Received: *09 March 2022*
Accepted: *16 May 2022*
Published: *16 June 2022*

Citation:
Huang J, Zhang J and Xiao H (2022) Identification of Epigenetic-Dysregulated lncRNAs Signature in Osteosarcoma by Multi-Omics Data Analysis. Front. Med. 9:892593. doi: 10.3389/fmed.2022.892593

Background: Alterations of epigenetic modification patterns are potential markers of cancer. The current study characterized six histone modifications in osteosarcoma and identified epigenetically dysregulated long non-coding RNAs (epi-lncRNAs).

Methods: Multi-omics data were obtained from osteosarcoma cell line SJSA1 and a normal cell line. Differentially expressed lncRNAs (DElncRNAs) between osteosarcoma and normal skeletal muscle were analyzed using Limma. MACS2 was applied to identify the "peaks" modified by each histone in the cell. Promoters or enhancers of DElncRNA were overlapped with differential histone-modified regions (DHMR) to screen epi-lncRNAs. Univariate and multivariate Cox regression analysis were performed to detect the genes closely related to the prognosis of osteosarcoma and to construct risk models.

Results: A total of 17 symbolic epi-lncRNA in osteosarcoma were screened, and 13 of them were differentially expressed between osteosarcoma and normal samples. Eight epi-lncRNAs were retained by Univariate Cox regression analysis. Four of these epi-lncRNAs were used to construct an epi-lncRNA signature. The risk score of each osteosarcoma sample in the high- or low-risk group was estimated according to the epi-lncRNA signature. The overall survival (OS) of the low-risk group was significantly better than that of the high-risk group. The area under the receiver operating characteristic (ROC) curve of the model was 0.79 and 0.82 for 1-, 3-, and 5-year OS, respectively.

Conclusion: Our results revealed the histone modification pattern in osteosarcoma and developed 4-epi-lncRNA signature to predict the prognosis of osteosarcoma, laying a foundation for the identification of highly specific epigenetic biomarkers for osteosarcoma.

Keywords: osteosarcoma, histone modification, long non-coding RNAs, multiomics, prognosis

INTRODUCTION

Osteosarcoma is the most common primary malignant tumor in children and adolescents (1). This tumor mainly occurs in the long bones (femur, tibia, humerus), the growth plates near the diaphysis, as well as all areas characterized by extensive bone rearrangement, and occurs less frequently in flat bones and the spine (2). Osteosarcoma is characterized by the presence of transformed osteoblastic cells producing osteoid matrix. Currently identified subtypes of osteosarcoma include typical intramedullary or central (osteoblastic, chondroblastic and fibroblastic); telangiectasic; small cell; high-grade surface; secondary osteosarcoma; parosteal; periostal; and central with a low degree of malignancy (3). Osteosarcoma exhibits a high tendency for local invasion and metastasis, and although many factors that predict metastasis have been identified, there is no effective therapeutic strategy other than surgery to reduce the number of patients with metastatic disease or to cure these patients with metastatic disease (4). At advanced stages, the survival rate of these metastatic patients is still only 20% (5). Therefore, improving the therapeutic unit of osteosarcoma there remains a constant and primary goal for many global research and clinical communities.

Epigenetics is the study of alterations caused by modifications in gene expression patterns that occurred during organismal development or cell proliferation without any change in DNA sequences (6). Histone modification could be resulted from the regulation of chromatin condensation level, and is therefore important in regulating gene expression and other nuclear events. Histone modification together with DNA methylation constitute are the foundation of epigenetic regulation of cell functions (7). Epigenetic modifications that work in conjunction with genetic mechanisms, which regulate transcriptional activity, are maladjusted in many diseases, including in cancers (8). Several epigenetic drugs, including inhibitors of EZH2, IDH, histone deacetylases (HDACis), and DNA methyltransferases (DNMTs) with many others undergoing clinical trials for treating solid have been designed to reverse cancer-specific epigenetic modification to normal epigenetic state, and have been approved by Food and Drug Administration (FDA) (9). To date, the efficacy and use of epigenetic therapy have been demonstrated mainly in the treatment of hematological malignancies, with limited supporting data for solid malignancies (10). Epigenetic therapies also face problems with their lack of specificity for cancer cells. Targeting a combination of epigenetic modifications specific to or preferentially present in cancer cells is a feasible strategy (11).

Several previous studies have shown that lncRNA transcription is affected by epigenetic mechanisms, including DNA methylation and histone modification. Abnormally low level of DNA methylation mediates the activation of lncRNA SNHG12, enabling it to play a role in glioblastoma resistance (12). Analysis on the relationship between lncRNA expression and histone modification of its promoter showed that trimethylation of histone H3 at lysine 4 (H3K4me3) and histone H3 trimethylated at lysine 27(H3K27me3) are generally correlated to lncRNA activation and repression, respectively (13). A study integrating bioinformatics with *in vitro* and *in vivo* biological experiments demonstrated that HOXC-AS3 is obviously activated by gain of H3K4me3, and that H3K27ac is involved in the regulation of gastric cancer (14). In basal-like breast cancer, the expression of BLAT1 is regulated at epigenetic level by DNA methylation of the CpG island in the promoter. On the contrary, lncRNAs also mediate epigenetic modification. Mohammad reported a lncRNA that can induce DNA methylation in specific regions of the Kcnq1 locus (15). Endogenous unspliced lncRNA ANRASSF1 binds to its transcriptional site to form an RNA/DNA hybrid, which then binds to polycomb repressive complex 2. This complex is only recruited to the RASSF1A promoter and could increase H3K27me3 repressive histone mark (16). The relationship between lncRNAs and epigenetic modifications may be exploited as an effective regulator of epigenetic mechanism (17). However, the data collected so far on the involvement of lncRNA in epigenetic regulation is still the tip of the iceberg in this emerging field, and the further expansion of these data may simultaneously reveal a large number of undeveloped targets and pathways suitable for epigenetic therapy (18).

In this study, we explored the relationship between histone modification and abnormal lncRNA expression through integrating six histone modified CHIP-seq data and RNA-seq data of osteosarcoma. We analyzed epigenetic-dysregulated lncRNAs (epi-lncRNAs) and its genome landscape, and identified osteosarcoma-specific epi-lncRNAs to develop a prognostic signature, which may be of great significance to improve the understanding of the tandem of lncRNAs and histone modification. **Figure 1A** shows the overall design process of this study.

MATERIALS AND METHODS

Six groups of histone modified replicated narrowPeak data were acquired from osteosarcoma cell line SJSA1 in Encyclopedia of DNA Elements (ENCODE) (19), including histone H3 monomethylated at lysine 4 (H3K4me1), H3K4me3, histone H3 trimethylated at lysine 9 (H3K9me3), histone H3 acetylated at lysine 27(H3K27ac), H3K27me3, histone H3 trimethylated at lysine 36 (H3K36me3). Normal human osteoblast was used as a control. Transcriptome data of osteosarcoma came from TRAGET database (https://ocg.cancer.gov/programs/target). The transcriptome data of normal skeletal muscle were obtained from GTEx database (https://www.genome.gov/Funded-Programs-Projects/Genotype-Tissue-Expression-Project). The batch effect of the two datasets was eliminated by removeBatchEffect in LIMMA R package. The GTF file (version 40, https://ftp.ebi.ac.uk/pub/databases/gencode/Gencode_human/release_40/gencode.v40.annotation.gff3.gz) of the transcript was obtained from GENCODE database (https://www.gencodegenes.org/human/), and the lncRNA and protein coding genes were determined according to the geneType attribute.

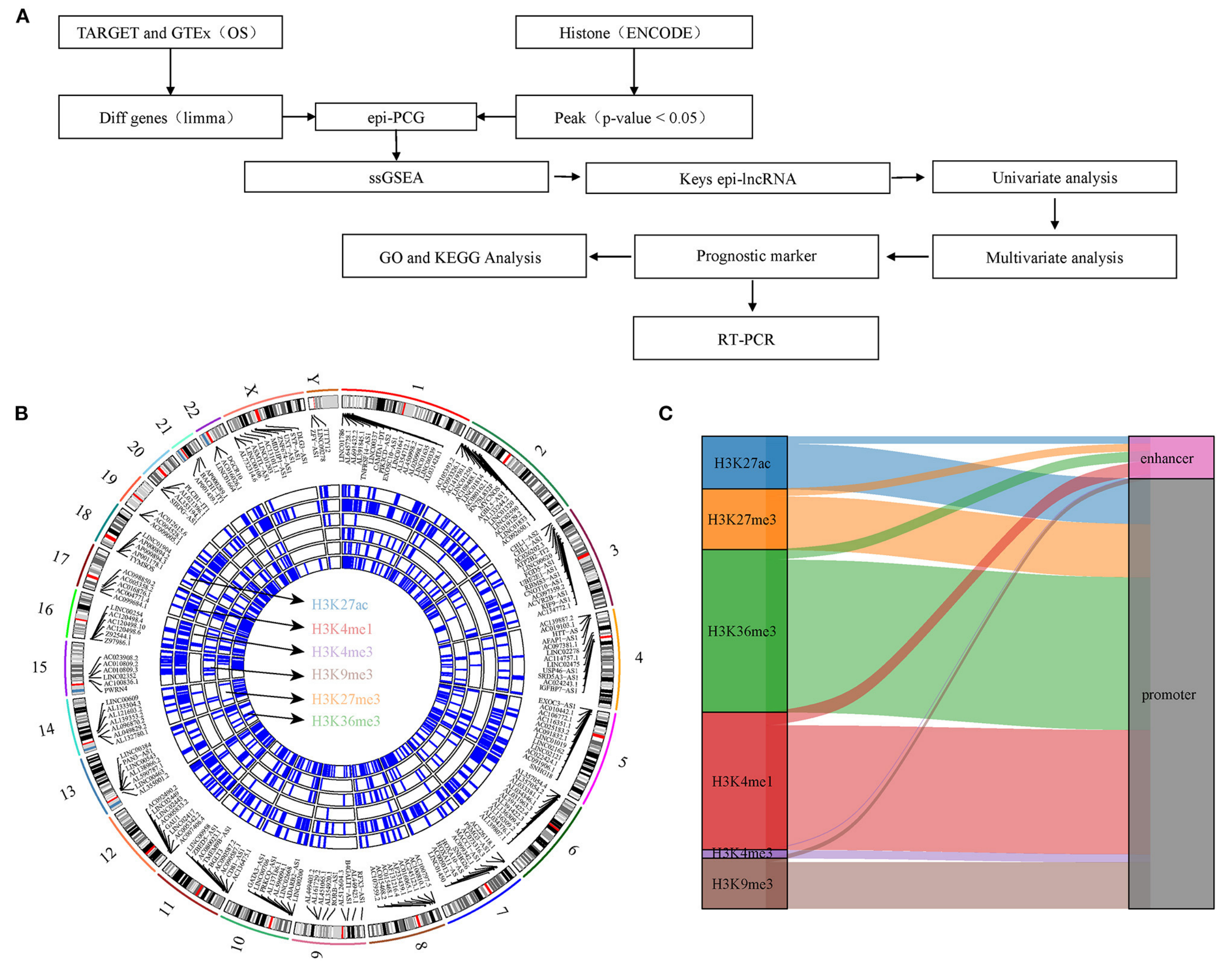

FIGURE 1 | Work flow chart and genomic landscape of epi-lncRNAs. **(A)** Workflow diagram of the study. **(B)** The locations on the chromosome of epi-lncRNAs shows the global apparent modification distribution. Epi-lncRNAs is marked in the appropriate location. **(C)** Alluvial diagram of six histone modification distributions of promoter and enhancer.

Identification of Epigenetic-Dysregulated lncRNAs and Protein-Coding Genes

The difference between osteosarcoma and normal skeletal muscle was analyzed by Limma (20) to obtain differentially expressed lncRNA (DElncRNAs) and PCGs (DEPCGs). The threshold was adjusted by benjamini-Hochberg method ($P < 0.05$). Histone-modified "peaks" with a region of $q < 0.05$ in each cell line of the six groups was detected by MACS2 (https://github.com/taoliu/MACS/) (21). The upstream 2 kb and downstream 0.5 kb of the transcriptional initiation site (TSS) were defined as promoters, which were identified by CHIPseeker (22). The chromatin immunoprecipitation sequencing (ChIP-seq) data of H3K27ac in FANTOM5 were integrated into our study, and high H3K27ac signal was defined as an active enhancer. Differential histone modified regions (DHMR) were screened by MACS2 bdgdiff. DElncRNAs/DEPCGs with at least one promoter or enhancer overlapping with DHMR were identified as epigenetic-dysregulated lncRNAs/PCGs (epi-lncRNAs/epi-PCGs).

Identification of Genomic Characteristic for Epigenetic Modifications

To examine the genomic characteristics of epigenetic disorders of lncRNA/PCGs, genes were divided into four different groups, namely, epi-lncRNAs, non-epi-lncRNAs, epi-PCGs, non-epi-PCGs, according to the characteristics and gene types of modification. The number and length of exons and transcripts in each group were summarized, and differences between epi-lncRNAs/epi-PCGs and non-epi-lncRNAs/non-epi-PCGs were compared. In addition, different genomic distributions of abnormally epigenetically modified lncRNA were analyzed.

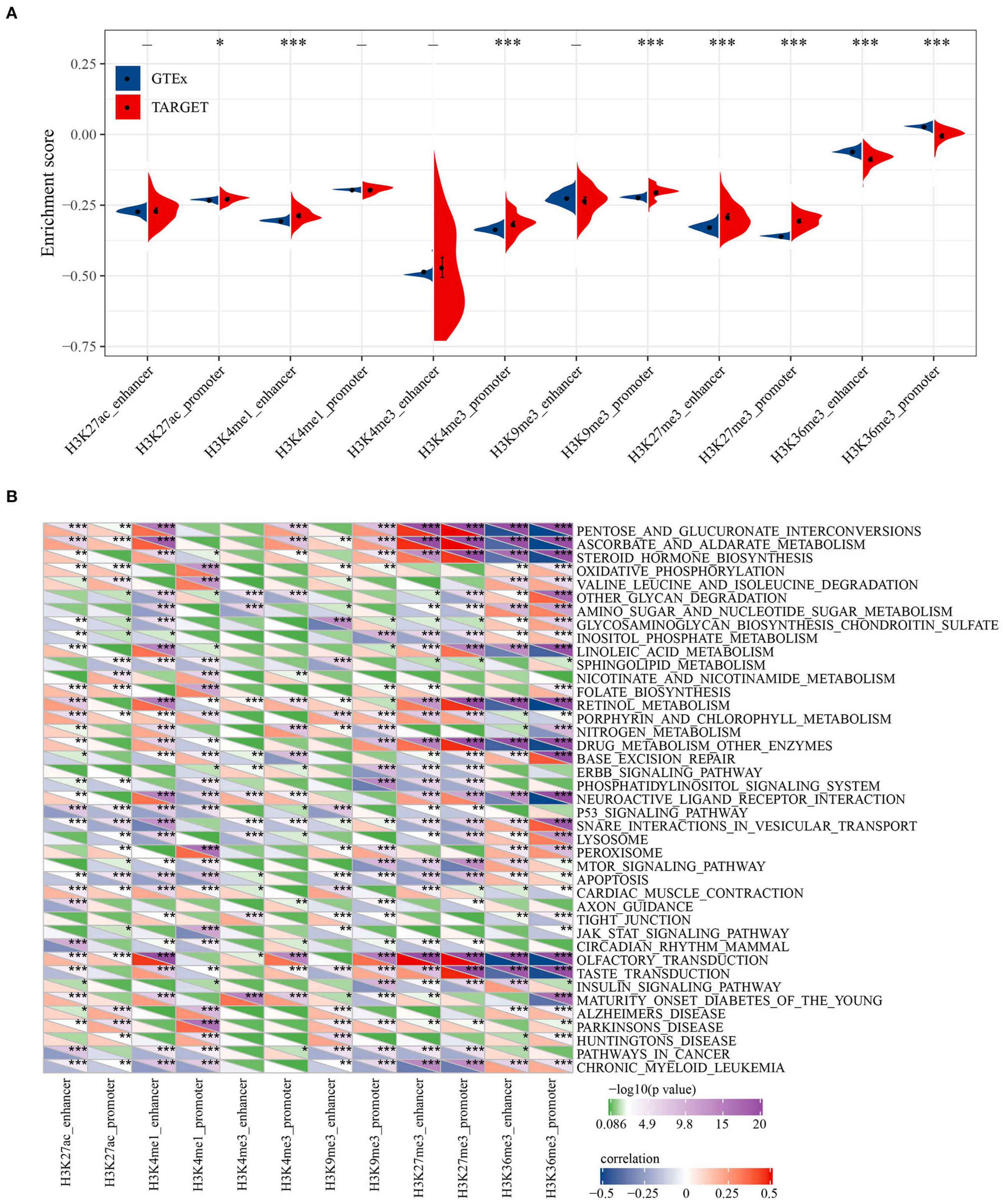

FIGURE 2 | Biological characteristics of histone modification regulation. **(A)** The difference for enrichment scores of six histone modified promoters and enhancers between normal samples and osteosarcoma samples. **(B)** Correlation between KEGG pathway and six histone-modified promoters and enhancers. *$P < 0.05$, **$P < 0.01$, ***$P < 0.001$.

FIGURE 3 | Identification of epi-lncRNAs specifically expressed in osteosarcoma. **(A)** The venn diagram of the intersection of cancer-related lncRNAs and osteosarcoma epi-lncRNAs in Lnc2Cancer. **(B)** Analysis of the expression of 17 osteosarcoma emblematical epi-lncRNAs in normal samples and osteosarcoma samples. **(C)** Histone modification profiles of MALAT and SNHG20. *$P < 0.05$, **$P < 0.01$, ***$P < 0.001$.

Single Sample Gene Set Enrichment Analysis

Lnc2Cancer is a database providing lncRNA-cancer correlations between 216 human cancers subtypes and 2,659 lncRNAs (23). The relationship between epi-lncRNAs and different types of cancer was analyzed using Lnc2Cancer database, and epi-lncRNAs related to osteosarcoma were screened. The ssGSEA scores of osteosarcoma samples were evaluated by R packet "GSVA" (24). At the same time, the Kyoto Encyclopedia of Genes and Genomes (KEGG) pathway score of each sample was calculated to investigate the relationship between osteosarcoma-related epilncRNAs and different biological pathways.

Construction of Osteosarcoma Prognosis-Related Signature Based on epi-lncRNAs

Univariate Cox regression analysis on osteosarcoma-related epi-lncRNAs and overall survival (OS) was performed to screen OS-related epi-lncRNAs in osteosarcoma. Furthermore, based on its expression, max_stat R package was used to evaluate the risk of osteosarcoma samples. Then stapAIC with step-by-step regression was used to eliminate unnecessary epi-lncRNAs, and then multivariate Cox regression analysis was conducted to identify closely related genes and build an epi-lncRNAs risk model with the strongest prognostic significance.

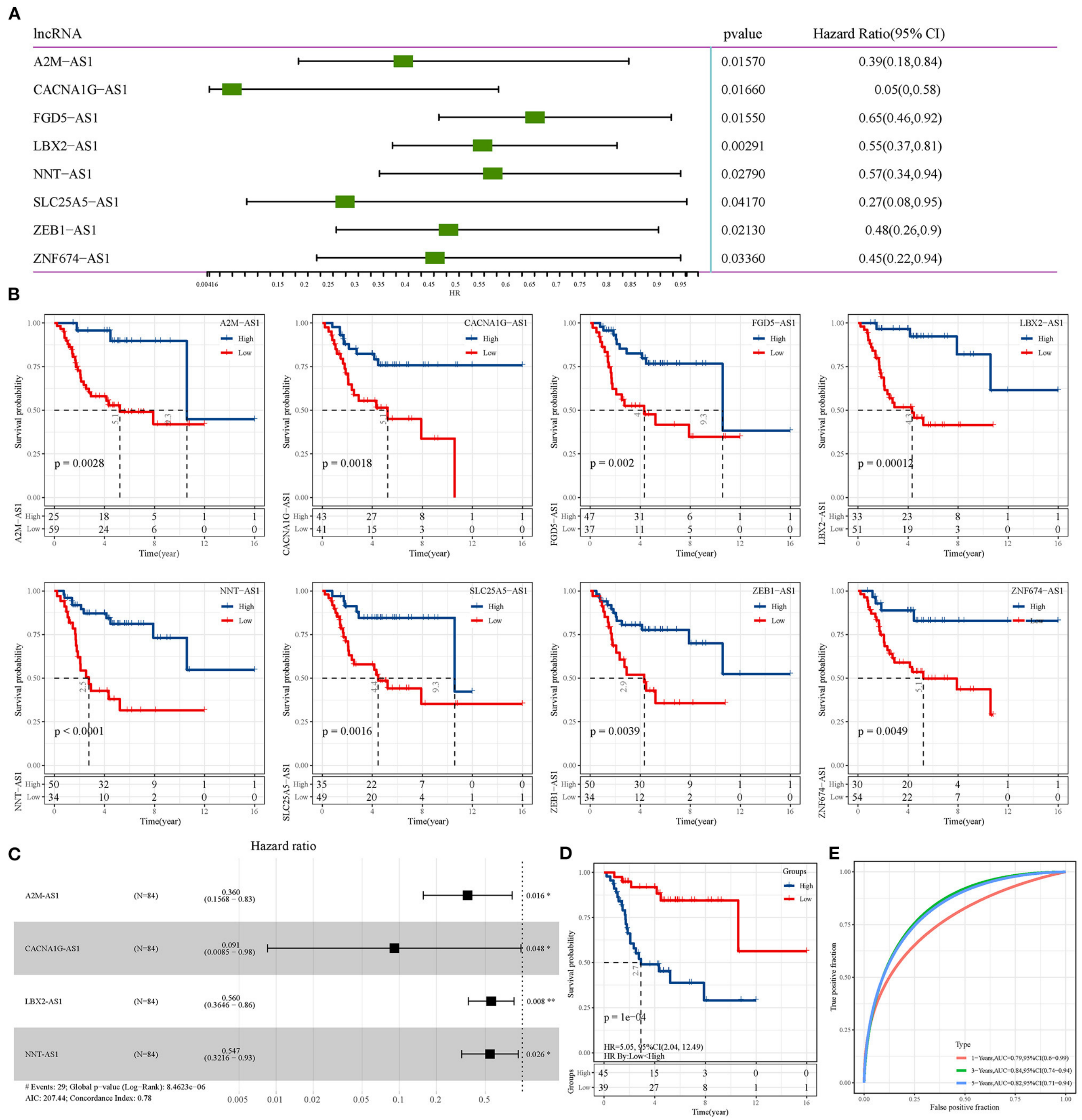

FIGURE 4 | Construction of osteosarcoma prognostic signature based on epi-lncRNAs. **(A)** Univariate Cox regression analysis of 8 epi-lncRNAs significantly correlated with OS of osteosarcoma. **(B)** The OS of osteosarcoma patients was evaluated according to the expression of each of the 8 epi-lncRNAs. **(C)** Forest map of 4 epi-lncRNAs by multivariate Cox regression analysis. **(D)** The survival curve of patients with different risks assessed by the 4-epi-lncRNA signature. **(E)** The ROC curve shows the area under curve (AUC) of the 1-, 3-, and 5-year OS calculated by the 4-epi-lncRNA signature.

Functional Enrichment Analysis on the epi-lncRNAs Risk Model

The Pearson correlation analysis was performed to analyze the correlation between epi-PCGs and epi-lncRNA in TARGET (threshold: $|\text{Corr}| > 0.4$ epi-PCGs $P < 0.05$). The epi-PCGs identified were integrated into the "WebGestaltR" R package (25) for KEGG and Gene Ontology (GO) analysis to further evaluate its functional characteristics. FDR < 0.05 was considered as the pathway of significant enrichment.

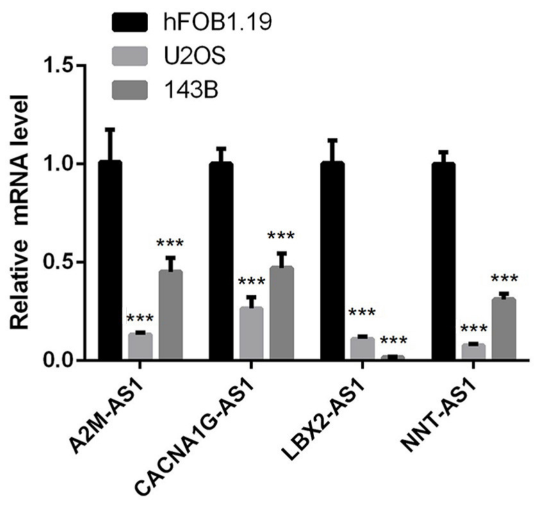

FIGURE 5 | qRT-PCR was used to detect the expression of lncRNA in human osteoblast and osteosarcoma cells in 4-epi-lncRNA signature. (*P < 0.05, ** P < 0.01, *** P < 0.001, **** P < 0.0001).

Cell Culture

Human SV40-transfected osteoblasts hFOB1.19 (BNCC255176), human osteosarcoma cell line U2OS (item number) and 143B (BNCC337683) were obtained from BeNa Culture Collection (Beijing, China). All of them were subcultured in dulbecco's modified eagle medium (DMEM) containing 10% fetal bovine serum and 1% penicillin-streptomycin at 37°C and 5% CO_2 concentration.

Quantitative Real-Time PCR

The cells in logarithmic growth phase were taken and their density was adjusted to 1×10^5 cells/mL and then inoculated into 6-well cell culture plates with 2 mL per well and 3 multiple holes in each group. TRIzol reagents (Invitrogen, Carlsbad, California, USA) were used to extract total RNA. We followed the instructions provided by the manufacturer. Then, RevertAid First Strand cDNA Synthesis kit (Thermo Fisher Scientific, United States) was used for reverse transcription of RNA to synthesize cDNA. qRT-PCR was performed on the ABI StepOnePlus Real-Time PCR System (Applied Biosystems, Foster City, CA, USA) by utilizing SYBR Green qPCR Master Mix (2x) (Bimake, United States) and 40 cycles were amplified. All expression data was normalized to β-actin as an internal control utilizing the 2−ΔΔCt method. The primer sequences involved are as follows:

A2M-AS1 – forward: AGCCTACTCAGACCGACA
A2M-AS1- reverse: GAAATGCTTGAAGACCAC
CACNA1G-AS1-forward: GGACAGAAGACACCAAGGG
CACNA1G-AS1-reverse: GAGTTGCGAAGGCAGTTA
LBX2-AS1-forward: TAGAAGCCGTGGAGTCAG
LBX2-AS1-reverse: TTCAAGGAACAAAAGGGA
NNT-AS1-forward: GACTGCTTTGAGGATTTG
NNT-AS1-reverse: GAGTGACATTCTTTACTACCG
β-actin-froward: AGCGAGCATCCCCCAAAGTT
β-actin -reverse: GGGCACGAAGGCTCATCATT.

Statistical Analysis

All statistical data were analyzed and the results were presented by R language v4.0.2 (https://www.r-project.org/). The Kaplan-Meier method and log-rank Tests were used to compare the sample OS. The accuracy of the epi-lncRNAs risk model was evaluated by drawing the Receiver Operating Characteristic (ROC) curve. $P < 0.05$ was defined as having a statistical significance standard.

RESULTS

Identification of epi-lncRNAs and epi-PCGs

In this study, DHMR was identified by CHIP-seq analysis on six histone-modified markers. A total of 9,995 lncRNAs and 5,141 PCGs were screened from osteosarcoma by difference analysis. 1,148 epi-lncRNAs, 12,902 non-epi-lncRNAs, 1,729 epi-PCGs and 17,805 non-epiPCGs were identified by overlapping analysis on DElncRNA/DEPCG promoter or enhancers with DHMR. The number of transcripts and exons in epi-lncRNAs was significantly higher than that in non-epi-lncRNAs. The exon of epi-lncRNAs was also significantly longer than that of non-epi-lncRNAs. The number of transcripts and exons of Epi-PCG was significantly fewer than that of non-epi-PCGs (**Supplementary Figure S1**). The locations of abnormal histone-modified epi-lncRNAs on the chromosome showed a wide distribution of apparent modification, noticeably, H3K4me1, H3K9me3, H3K27ac, H3K27me3, and H3K36me3 were the main histone-modified epi-lncRNAs (**Figure 1B**). These histone modifications are mainly covered in the promoter region (**Figure 1C**).

Biological Characteristics of Histone Modification Regulation

To reveal the biological significance of lncRNA regulated by epigenetic dysregulation, ssGSEA was performed to calculate the score of each osteosarcoma sample. The enrichment scores of six histone-modified promoters and enhancers in normal samples and osteosarcoma samples were determined. Significant differences were found in H3K27ac promoter, H3K4me1 enhancer, H3K4me3 promoter, H3K9me3 promoter, H3K27me3 enhancer, H3K27me3 promoter, H3K36me3 enhancer, and H3K36me3 promoter between normal samples and osteosarcoma samples. Osteosarcoma samples showed high enrichment scores of H3K27ac promoter, H3K4me1 enhancer, H3K4me3 promoter, H3K9me3 promoter, H3K27me3 enhancer and H3K27me3 promoter, but low enrichment scores of H3K36me3 enhancer and H3K36me3 promoter (**Figure 2A**). Pearson correlation analysis showed that 41 KEGG pathways were related to most of the six histone-modified promoters and enhancers. The KEGG pathways involved in malignant tumors included metabolism, cancer cell proliferation, apoptosis, autophagy, etc. (**Figure 2B**).

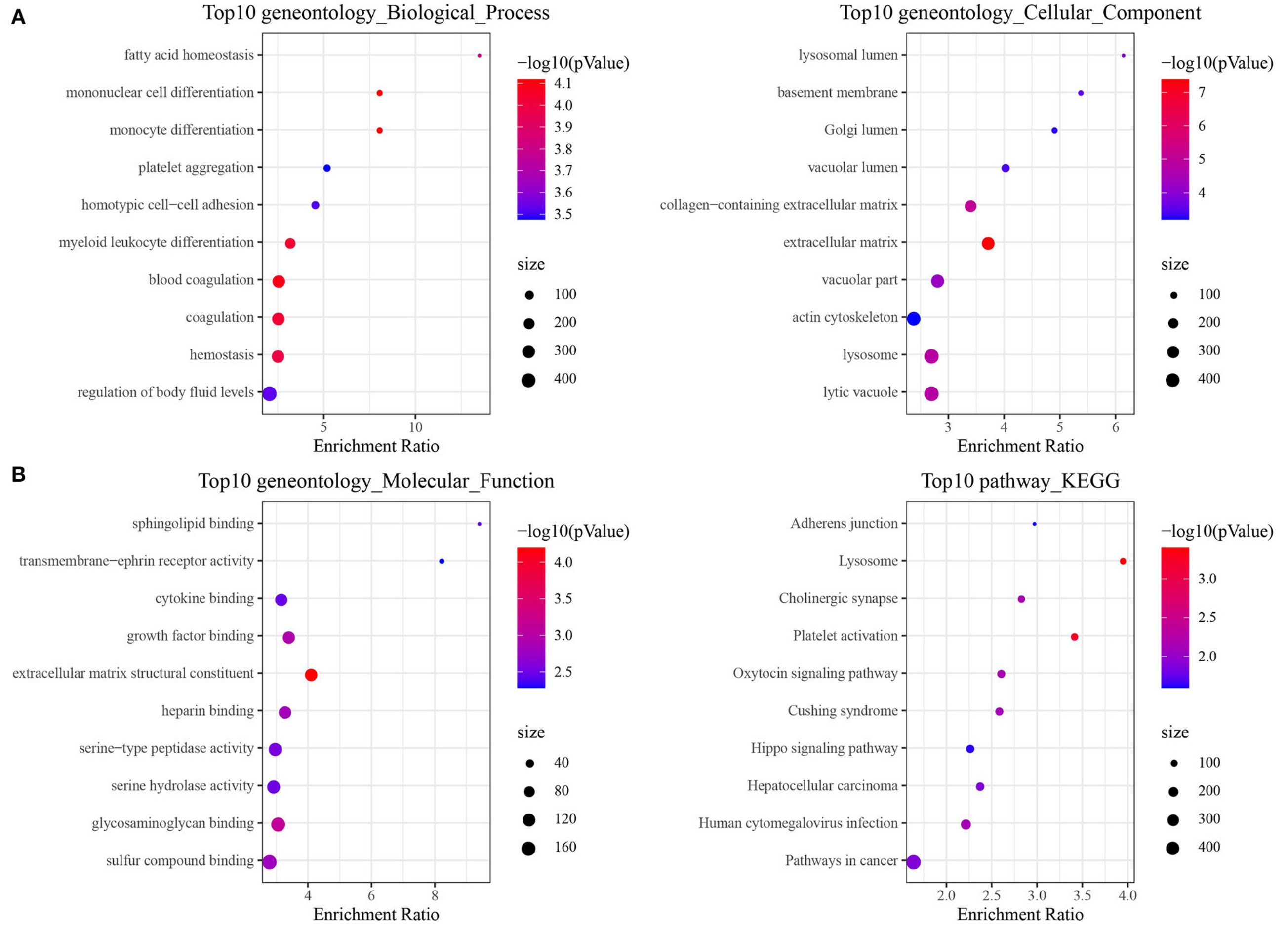

FIGURE 6 | Enrichment pathway analysis of epi-lncRNAs in osteosarcoma prognostic signature. **(A)** GO analysis of 486 epi-lncRNAs-related PCGs, including biological process (BP), cellular component (CC) and molecular function (MF). **(B)** KEGG analysis of 486 epi-lncRNAs-related PCGs showed the highest 10 pathways of enrichment ratio.

Identification of epi-lncRNAs Specifically Expressed in Osteosarcoma

A total of 101 osteosarcoma-related epi-lncRNAs were found in epi-lncRNAs through Lnc2Cancer database (**Figure 3A**), and 17 epi-lncRNAs were selected as the markers for osteosarcoma. Through the difference analysis on 17 epi-lncRNAs between normal samples and osteosarcoma samples, 13 DEepi-lncRNAs, including 10 abnormally down-regulated epi-lncRNAs and 3 abnormally down-regulated epi-lncRNAs, were obtained (**Figure 3B**). MALAT showed increased H3K27me3 enrichment in promoter and distal enhancer in SJSA1, while the downstream region of MALAT was significantly enriched by H3K4me1 and H3K9me3. On the other hand, the H3K36me3 enrichment of SNHG20 promoter in SJSA1 increases, and the downstream region was covered by H3K4me1. It should be noted that H3K4me1 and H3K36me3 were enhancer markers, while H3K27me3 and H3K9me3 were inhibitory markers, indicating that a variety of histone modifications reshaped the acquisition/loss of active promoters and/or enhancers through enrichment at different sites of genes, which could synergistically affect gene expression (**Figure 3C**).

Construction of an Osteosarcoma Prognostic Signature Based on epi-lncRNAs

Univariate Cox regression analysis of epi-lncRNAs related to osteosarcoma identified 8 epi-lncRNAs significantly correlated with OS of osteosarcoma (**Figure 4A**). Each OS-related epi-lncRNA can group osteosarcoma samples according to its expression, and the survival of different risk groups can be clearly distinguished (**Figure 4B**). To integrate establish an overall effective osteosarcoma scoring model, 4 epi-lncRNAs were removed according to stepAIC, and the remaining four epi-lncRNAs (A2M-AS1, CACNA1G-AS1, LBA2-AS1, and NNT-AS1) were recruited to build a risk model (**Figure 4C**). According to the 4-epi-lncRNA signature, the samples were divided into two risk groups with significant OS differences. Specifically, the OS of the low-risk group was much better than that of the high-risk group (**Figure 4D**). The area under ROC curve of 4- epi-lncRNA signature reached 0.79, 0.84, and 0.82 in 1-, 3-, and 5-year OS, respectively (**Figure 4E**), indicating a high prediction accuracy. In addition, we also evaluated the relationship between these lncRNAs and immunity. It can be observed that LBX2-AS1 has a significant positive correlation with a variety of immune infiltrating cells, such as Activated dendritic cell, Macrophage and Central memory CD8 T cell, and CACNA1G-AS1 has a significant negative correlation with a variety of immune infiltrating cells, such as Type 17 T helper cell, Immature dendritic cell and Activated dendritic cell (**Supplementary Figure 2A**). Further, we also observed that patients in the high-risk group have significantly higher Activated CD8 T cell infiltration (**Supplementary Figure 2B**) and lower fibroblasts and CD8 T cells infiltration (**Supplementary Figure 2C**), Similarly, the matrix score in high-risk patients was significantly lower than that in low-risk patients (**Supplementary Figure 2D**).

Expression of lncRNA in 4-epi-lncRNA Signature

To verify whether lncRNAs in the 4-epi-lncRNA signature are abnormally expressed in osteosarcoma as predicted, we detected their expression levels in human osteoblasts and osteosarcoma cells by qRT-PCR. The results showed that the expression of A2M-AS1, CACNA1G-AS1, LBA2-AS1, and NNT-AS1 was significantly lower in osteosarcoma cells U2OS and 143B compared with hFOB1.19 cells (**Figure 5**). According to the results of survival analysis obtained by **Figure 4B**, the low expression of these four lncRNA was associated with poor prognosis. This also implies to some extent that our predicted trend is of practical significance.

Regulatory Role of epi-lncRNAs in Prognosis of Osteosarcoma

LncRNAs play a critical role in cancer through directly or indirectly regulating the coding genes. Therefore, the function of epi-lncRNAs-related PCGs in prognostic signature was studied. Firstly, 486 PCGs related to epi-lncRNAs in TARGET were filtered by Pearson correlation analysis (306 PCGs with positive correlation, 180 PCGs with negative correlation). GO analysis based on these PCGs demonstrated that the most relevant GO biological process (BP) included fatty acid homeostasis, mononuclear cell differentiation, homotypic cell–cell adhesion and myeloid leukocyte differentiation; the most related cellular component (CC) were lysosomal lumen, basement membrane and Golgi lumen and vacuolar lumen. Most of the PCGs were enriched in the signal molecules binding (cytokine binding, growth factor binding) and cellular activity-related molecules in TME (**Figure 6A**). KEGG analysis based on 486 PCGs showed that the PCGs were enriched in a variety of pathways, which regulate cancer, such as adherens junction, Hippo signaling pathway, hepatocellular carcinoma, and pathways in cancer (**Figure 6B**). In addition, we also analyzed the expression of genes downstream of the four key lncRNAs. It can be observed that TLX2 and PAIP1 in the latest four genes downstream of the four lncRNAs are significantly related to poor prognosis, suggesting that these genes may affect the expression of downstream genes through cis-regulation (**Supplementary Figure 3A**). Further, the targeted miRNAs of the four lncrnas are predicted from the microT, miRanda, mircode, miRDB, miRmap, miRtarbase, PicTar, PITA, RNA22, starbase, TargetMiner and TargetScan database according to the Cerna hypothesis. Then, we use 12 databases to predict the target encoding gene (mRNA) of miRNA and retain the target mRNA that appears in at least 6 databases. The ceRNA network is constructed. The network contains 4 lncRNA, 14 miRNA and 325 mRNA (**Supplementary Figure 3B**). Using the gene analysis of the regulatory network of the ceRNA, we can observe that these genes are enriched into many tumor pathways, such as liver cancer, breast cancer, Glioma and non-small cell lung cancer etc. (**Supplementary Figure 3C**). These results show that the potential ceRNA networks of these four lncRNAs are closely related to the occurrence and development of tumors.

DISCUSSION

Histone modification, a common epigenetic mechanism, is the process of histone modification by enzymes, including post-translational modifications such as methylation, acetylation, phosphorylation and ubiquitin (26). Recent evidence suggests that post-translational modification of histones accompanied by lncRNAs profiles is involved in several clinical cancer parameters, including histopathology progression, prognosis, and/or responsiveness to unique or combined oncological therapies (27). In this work, we explored the relationship between histone modification and abnormal lncRNAs in osteosarcoma according to 6 emerging classes of histone modifications subjected for epigenome profiling by International Human Epigenome Consortium (http://www.ihec-epigenomes.org/), and screened epi-lncRNAs in osteosarcoma.

The difference of RNA modification pattern between normal tissue and osteosarcoma tissue was explored, and we found that osteosarcoma samples showed high levels of H3K27ac promoter, H3K4me1 enhancer, H3K4me3 promoter, H3K9me3 promoter, H3K27me3 promoter and enhancer enrichment scores, but low levels of H3K36me3 promoter and enhancer enrichment scores, indicating the diversity of histone modification in osteosarcoma. These combinations of epigenetic modifications that stimulate cancer cell development are considered to be candidate targets for cancer therapy (28). In osteosarcoma, we found 13 specific lncRNAs related to these histone modifications, and analyzed histone modification spectra of two of them. The results demonstrated that MALAT showed increased H3K27me3 enrichment in promoter and distal enhancer in osteosarcoma cell lines, while the downstream region was significantly enriched by H3K4me1 and H3K9me3. On the other hand, the H3K36me3 enrichment of SNHG20 promoter in SJSA1 increased, and the downstream region was covered by H3K4me1. These two kinds of lncRNAs were found to be greatly overexpressed in osteosarcoma cells (29, 30). The modification activity of these active histones may be an important factor in regulating their expression.

Finally, 4 epi-lncRNAs were identified from 13 epi-lncRNAs specifically expressed in osteosarcoma to develop a prognostic signature for survival prediction of osteosarcoma. The function of A2M-AS1 as a positive regulatory factor to promote the metastasis of breast cancer has been characterized, and is related to a poor prognosis (31). CACNA1G-AS1 is highly expressed in colorectal cancer (32) and hepatocellular carcinoma tissues (33), which accelerates the malignant biological process of both cancers. The up-regulated expression of LBX2-AS1 in gastric cancer cells and tissues contributes to the malignant transformation of this cancer (34). In ovarian cancer, LBX2-AS1 is also an oncogenic factor, enhancing the proliferation and migration of cancer cells and promoting the formation of solid tumors (35). NNT-AS1 induces cell proliferation and invasion in prostate cancer (36) and lung cancer (37). Notably, herein, qRT-PCR was utilized to detect the expression of these four lncRNAs in human osteoblasts and osteosarcoma cells, and we found that compared with human osteoblasts, the expression of all of this lncRNA in osteosarcoma cells was significantly down-regulated. Survival analysis showed that low expression of each of the four lncRNAs was significantly associated with a good prognosis in patients with osteosarcoma. Therefore, our results suggested that all 4 lncRNAs are protective factors in osteosarcoma. We speculated that the reason for this result might be the heterogeneity of lncRNA between tumors. At present, the relationship between them and histone modification is still unclear. LncRNAs located in the nucleus are involved in chromatin interactions, transcriptional regulation and RNA processing, while cytoplasmic lncRNAs can modulate mRNA stability or translation and influence cellular signaling cascades (38). It can be seen that lncRNA regulates cell behavior by affecting PCG. Therefore, we finally analyzed four epi-lncRNA-related PCGs and analyzed the functions of these PCGs. There are various pathways enriched by PCGs, and the most notable ones were adherens junction, Hippo signaling pathway, hepatocellular carcinoma and pathways in cancer. Adherens junction is the initiator and maintenance of adhesion between cancer cells and regulation of tumor cell proliferation and migration (39). Hippo signaling pathway was identified by Atlas as one of the eight major signaling pathways in human cancers (40). Therefore, we speculated that the 4 epi-lncRNAs we identified may interact with the screened PCGs through specific mechanisms and ultimately regulate the pathological progression of osteosarcoma.

Our research has certain potential limitations. Firstly, DNA methylation is the most important modification in epigenetics, we did not analyze the effects of DNA methylation. Secondly, Innovations in bioinformatics analysis are not abundant, and the limited sample size prevented us from addressing specific epigenetic or transcriptome differences between potentially important epigenetic modification factors such as age. Finally, Our data are all from public data sets, and the functional and molecular mechanism of 4 epi-lncRNAs in the malignant progression of osteosarcoma is still unknown, and whether they are cross-talk remains unclear, which needs to be further explored in future experimental studies.

In summary, our study revealed different patterns of epigenetic modification in osteosarcoma and identified epigenetically dysregulated epi-lncRNAs based on epigenetic and transcriptional analyses, which provided new insights into epigenetic regulation and identification of prognostic biomarkers in osteosarcoma.

DATA AVAILABILITY STATEMENT

Publicly available datasets were analyzed in this study. This data can be found here: transcriptome data of osteosarcoma came from TRAGET database (https://ocg.cancer.gov/programs/target). The transcriptome data of normal skeletal muscle were obtained from GTEx database (https://www.genome.gov/Funded-Programs-Projects/Genotype-Tissue-Expression-Project). The batch effect of the two datasets was eliminated by removeBatchEffect in LIMMA R package.

AUTHOR CONTRIBUTIONS

Conceptualization: JH and HX. Methodology, software, formal analysis, resources, data curation, writing—original draft preparation, and visualization: JH. Validation, investigation, and writing—review and editing: JZ. Supervision, project administration, and funding acquisition: HX. All authors have read and agreed to the published version of the manuscript.

FUNDING

This research was funded by Shanghai Fengxian District Health Committee, Grant Number fxlczlzx-a-202103.

SUPPLEMENTARY MATERIAL

The Supplementary Material for this article can be found online at: https://www.frontiersin.org/articles/10.3389/fmed.2022.892593/full#supplementary-material

Supplementary Figure S1 | Genomic characteristics of epi-lncRNA vs. non-epi-lncRNA and epi-PCG vs. non-epi- PCG.

Supplementary Figure S2 | Relationship between key lncRNA and immunity. **(A)** Correlation Heatmap between immune infiltration score calculated by three immune infiltration methods and four key lncRNAs. **(B)** Distribution differences of 28 kinds of immune infiltrating cells in patients with high and low risk groups. **(C)** Distribution differences of 10 kinds of immune infiltrating cells in patients with high and low risk groups. **(D)** Distribution difference of immune infiltration in patients with high and low risk groups. $^{*}P < 0.05$, $^{**}P < 0.01$, $^{***}P < 0.001$.

Supplementary Figure S3 | Potential regulatory role of lncRNA. **(A)** Prognostic K-M curve of adjacent genes downstream of four lncRNAs. **(B)** Four lncRNAs potential Cerna networks. **(C)** Four lncRNAs potential Cerna networks were enriched into the KEGG pathway.

REFERENCES

1. Mailankody S, Kumar VS, Khan SA, Banavali SD, Bajpai J. Resource-appropriate selection of osteosarcoma treatment protocols in low- and middle-income countries. *Pediatr Blood Cancer*. (2022) 69:29540. doi: 10.1002/pbc.29540
2. Kansara M, Teng MW, Smyth MJ, Thomas DM. Translational biology of osteosarcoma. *Nat Rev Cancer*. (2014) 14:722–35. doi: 10.1038/nrc3838
3. De Martino V, Rossi M, Battafarano G, Pepe J, Minisola S, Del Fattore A, et al. Extracellular vesicles in osteosarcoma: antagonists or therapeutic agents? *Int J Mol Sci*. (2021) 22:86. doi: 10.3390/ijms222212586
4. Odri GA, TchicayaBouanga J, Yoon DJY, Modrowski D. Metastatic progression of osteosarcomas: a review of current knowledge of environmental versus oncogenic drivers. *Cancers*. (2022) 14:360. doi: 10.3390/cancers14020360
5. Sadoughi F, Dana PM, Asemi Z, Yousefi B. DNA damage response and repair in osteosarcoma: defects, regulation and therapeutic implication. *DNA Repair*. (2021) 102:103105. doi: 10.1016/j.dnarep.2021.103105
6. Ning B, Li WY, Zhao W, Wang RF. Targeting epigenetic regulations in cancer. *Acta Biochimica Et Biophysica Sinica*. (2016) 48:97–109. doi: 10.1093/abbs/gmv116
7. Biancotto C, Frigè G, Minucci S. Histone modification therapy of cancer. *Adv Genet*. (2010) 70:341–86. doi: 10.1016/B978-0-12-380866-0.60013-7
8. Park JW, Han JW. Targeting epigenetics for cancer therapy. *Arch Pharm Res*. (2019) 42:159–70. doi: 10.1007/s12272-019-01126-z
9. Garcia-Martinez L, Zhang Y, Nakata Y, Chan HL, Morey L. Epigenetic mechanisms in breast cancer therapy and resistance. *Nat Commun*. (2021) 12:1786. doi: 10.1038/s41467-021-22024-3
10. Wu Y, Sarkissyan M, Vadgama JV. Epigenetics in breast and prostate cancer. *Methods Mol Biol*. (2015) 1238:425–66. doi: 10.1007/978-1-4939-1804-1_23
11. Takeshima H, Wakabayashi M, Hattori N, Yamashita S, Ushijima T. Identification of coexistence of DNA methylation and H3K27me3 specifically in cancer cells as a promising target for epigenetic therapy. *Carcinogenesis*. (2015) 36:192–201. doi: 10.1093/carcin/bgu238
12. Lu C, Wei Y, Wang X, Zhang Z, Yin J, Li W. DNA-methylation-mediated activating of lncRNA SNHG12 promotes temozolomide resistance in glioblastoma. *Mol Cancer*. (2020) 19:28. doi: 10.1186/s12943-020-1137-5
13. Wu SC, Kallin EM, Zhang Y. Role of H3K27 methylation in the regulation of lncRNA expression. *Cell Res*. (2010) 20:1109–16. doi: 10.1038/cr.2010.114
14. Zhang E, He X, Zhang C, Su J, Lu X, Si X. A novel long noncoding RNA HOXC-AS3 mediates tumorigenesis of gastric cancer by binding to YBX1. *Genome Biol*. (2018) 19:154. doi: 10.1186/s13059-018-1523-0
15. Mohammad F, Pandey GK, Mondal T, Enroth S, Redrup L, Gyllensten U. Long noncoding RNA-mediated maintenance of DNA methylation and transcriptional gene silencing. *Development*. (2012) 139:2792–803. doi: 10.1242/dev.079566
16. Beckedorff FC, Ayupe AC, Crocci-Souza R, Amaral MS, Nakaya HI, Soltys DT, et al. The intronic long noncoding RNA ANRASSF1 recruits PRC2 to the RASSF1A promoter, reducing the expression of RASSF1A and increasing cell proliferation. *PLoS Genetics*. (2013) 9:e1003705. doi: 10.1371/journal.pgen.1003705
17. Aguilo F, Zhou MM, Walsh MJ. Long noncoding RNA, polycomb, and the ghosts haunting INK4b-ARF-INK4a expression. *Cancer Res*. (2011) 71:5365–9. doi: 10.1158/0008-5472.CAN-10-4379
18. Hanly DJ, Esteller M, Berdasco M. Interplay between long non-coding RNAs and epigenetic machinery: emerging targets in cancer? Philosophical transactions of the Royal Society of London. *Series B Biol Sci*. (2018) 373:74. doi: 10.1098/rstb.2017.0074
19. Qu H, Fang X. A brief review on the Human Encyclopedia of DNA Elements (ENCODE) project. *Genom Proteom Bioinform*. (2013) 11:135–41. doi: 10.1016/j.gpb.2013.05.001
20. Ritchie ME, Phipson B, Wu D, Hu Y, Law CW, Shi W, et al. Limma powers differential expression analyses for RNA-sequencing and microarray studies. *Nucleic Acids Res*. (2015) 43:e47. doi: 10.1093/nar/gkv007
21. Zhang Y, Liu T, Meyer CA, Eeckhoute J, Johnson DS, Bernstein BE, et al. Model-based analysis of ChIP-Seq (MACS). *Genome Biol*. (2008) 9:R137. doi: 10.1186/gb-2008-9-9-r137
22. Yu G, Wang LG, He QY. ChIPseeker: an R/Bioconductor package for ChIP peak annotation, comparison and visualization. *Bioinformatics*. (2015) 31:2382–3. doi: 10.1093/bioinformatics/btv145
23. Gao Y, Shang S, Guo S, Li X, Zhou H, Liu H, et al. Lnc2Cancer 3.0: an updated resource for experimentally supported lncRNA/circRNA cancer associations and web tools based on RNA-seq and scRNA-seq data. *Nucleic Acids Res*. (2021) 49:D1251–8. doi: 10.1093/nar/gkaa1006
24. Hänzelmann S, Castelo R, Guinney J. GSVA: gene set variation analysis for microarray and RNA-seq data. *BMC Bioinform*. (2013) 14:7. doi: 10.1186/1471-2105-14-7
25. Liao Y, Wang J, Jaehnig EJ, Shi Z, Zhang B. WebGestalt 2019: gene set analysis toolkit with revamped UIs and APIs. *Nucleic Acids Res*. (2019) 47:W199–205. doi: 10.1093/nar/gkz401
26. Harr JC, Gonzalez-Sandoval A, Gasser SM. Histones and histone modifications in perinuclear chromatin anchoring: from yeast to man. *EMBO Reports*. (2016) 17:139–55. doi: 10.15252/embr.201541809
27. Herrera-Solorio AM, Armas-López L, Arrieta O, Zúñiga J, Piña-Sánchez P, Áhezta-Solo F., et al. Histone code and long non-coding RNAs (lncRNAs) aberrations in lung cancer: implications in the therapy response. *Clin. Epigen*. (2017) 9:98. doi: 10.1186/s13148-017-0398-3
28. Kikutake C, Yahara K. Identification of epigenetic biomarkers of lung adenocarcinoma through multi-omics data analysis. *PLoS ONE*. (2016) 11:e0152918. doi: 10.1371/journal.pone.0152918
29. Liu C, Han X, Li B, Huang S, Zhou Z, Wang Z, et al. MALAT-1 is associated with the doxorubicin resistance in U-2OS osteosarcoma cells. *Cancer Manag Res*. (2021) 13:6879–89. doi: 10.2147/CMAR.S304922
30. Zhang J, Ju C, Zhang W, Xie L. LncRNA SNHG20 is associated with clinical progression and enhances cell migration and invasion in osteosarcoma. *IUBMB Life*. (2018) 70:1115–21. doi: 10.1002/iub.1922
31. Fang K, Caixia H, Xiufen Z, Zijian G, Li L. Screening of a novel upregulated lncRNA, A2M-AS1, that promotes invasion and migration and signifies poor prognosis in breast cancer. *BioMed Res Int*. (2020) 2020:9747826. doi: 10.1155/2020/9747826
32. Wei LJ, Bai DM, Wang ZY, Liu BC. Upregulated lncRNA CACNA1G-AS1 aggravates the progression of colorectal cancer by downregulating p53. *Eur Rev Med Pharmacol Sci*. (2020) 24:130–6. doi: 10.26355/eurrev_202001_19902
33. Yang J, Li C, Li H, Changyong E. LncRNA CACNA1G-AS1 facilitates hepatocellular carcinoma progression through the miR-2392/C1orf61 pathway. *J Cell Physiol*. (2019) 234:18415–22. doi: 10.1002/jcp.28477
34. Yang Z, Dong X, Pu M, Yang H, Chang W, Ji F, et al. LBX2-AS1/miR-219a-2-3p/FUS/LBX2 positive feedback loop contributes to the proliferation of gastric cancer. *Gastric Cancer*. (2020) 23:449–63. doi: 10.1007/s10120-019-01019-6
35. Cao J, Wang H, Liu G, Tang R, Ding Y, Xu P, et al. LBX2-AS1 promotes ovarian cancer progression by facilitating E2F2 gene expression *via* miR-455-5p and miR-491-5p sponging. *J Cell Mol Med*. (2021) 25:1178–89. doi: 10.1111/jcmm.16185
36. Yao C, Cheng X, Guo X, Lu X, Bu F, Xu Y, et al. NNT-AS1 modulates prostate cancer cell proliferation, apoptosis and migration through miR-496/DDIT4 axis. *Cancer Cell Int*. (2020) 20:463. doi: 10.1186/s12935-020-01505-3
37. He W, Zhang Y, Xia S. LncRNA NNT-AS1 promotes non-small cell lung cancer progression through regulating miR-22-3p/YAP1 axis. *Thoracic Cancer*. (2020) 11:549–60. doi: 10.1111/1759-7714.13280
38. Batista PJ, Chang HY. Long noncoding RNAs: cellular address codes in development and disease. *Cell*. (2013) 152:1298–307. doi: 10.1016/j.cell.2013.02.012
39. Garcia MA, Nelson WJ, Chavez N. Cell-cell junctions organize structural and signaling networks. *Cold Spring Harbor Perspect Biol*. (2018) 10:9181. doi: 10.1101/cshperspect.a029181

40. Sanchez-Vega F, Mina M, Armenia J, Chatila WK, Luna A, La KC, et al. Oncogenic signaling pathways in the cancer genome atlas. *Cell.* (2018) 173:321–37.e10. doi: 10.1016/j.cell.2018.03.035

Conflict of Interest: The authors declare that the research was conducted in the absence of any commercial or financial relationships that could be construed as a potential conflict of interest.

Frontiers in Medicine

Translating medical research and innovation into improved patient care

A multidisciplinary journal which advances our medical knowledge. It supports the translation of scientific advances into new therapies and diagnostic tools that will improve patient care.

Discover the latest Research Topics

See more →

frontiers

Frontiers in
Medicine

Frontiers

Avenue du Tribunal-Fédéral 34
1005 Lausanne, Switzerland
frontiersin.org

Contact us

+41 (0)21 510 17 00
frontiersin.org/about/contact

frontiers | Research Topics